



2016 AAAS ANNUAL MEETING

Global Science Engagement | Washington, DC

Science

\$10
23 OCTOBER 2015
sciencemag.org

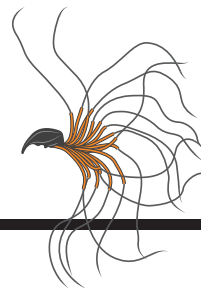
AAAS

Seeing the light

Restoring sight
in Indian children
illuminates the
brain p. 372

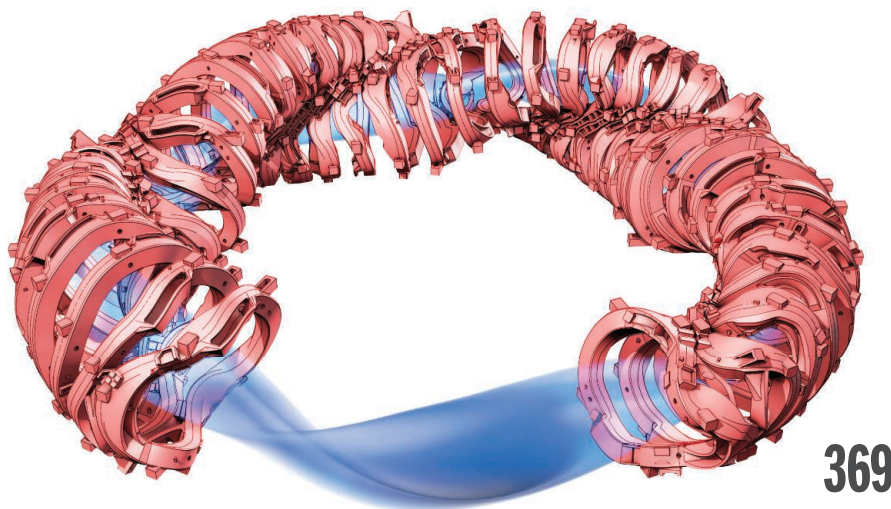
CONTENTS

23 OCTOBER 2015 • VOLUME 350 • ISSUE 6259



385 & 442

Inhibiting sperm maturation



369

NEWS

IN BRIEF

360 Roundup of the week's news

IN DEPTH

363 U.S. TARGETS MATTER-ANTIMATTER FRONTIER

Search for rare nuclear decay would test whether the neutrino is its own antiparticle *By A. Cho*

364 SHINING A LIGHT ON SEXUAL HARASSMENT IN ASTRONOMY

Astronomer Joan Schmelz talks about what needs to change in the wake of the Marcy case *By D. Clery*

365 SECOND BID FOR BRAIN OBSERVATORY

Workshop explores facilities to give neuroscience access to high-tech tools *By E. Underwood*

366 PROTEIN 'DROPS' MAY SEED DISEASE

Cellular droplets promote vital biochemistry—but may dangerously solidify *By K. Garber*

368 EUROPE'S FOOD WATCHDOG EMBRACES TRANSPARENCY

Industry uneasy at European Food Safety Authority pledge to make data underlying its decisions public *By T. Rabesandratana*

FEATURES

369 TWISTED LOGIC

Germany completes the epic construction of the reactor designed in hell. Its tortuous shape may point the way forward for fusion *By D. Clery*

372 OUT OF THE DARKNESS

Defying expectations, cataract surgery in Indian children is endowing them with vision—and shedding light on how the brain learns to see *By R. Chatterjee*

► PODCAST; SLIDESHOW

INSIGHTS

PERSPECTIVES

376 ASSEMBLING THE WHEEL OF DEATH

A single ligand-activated protein triggers the assembly of an entire inflammasome *By Z. Liu and T. S. Xiao*

► RESEARCH ARTICLE P. 399; REPORT P. 404

378 CHIRAL ANOMALY WITHOUT RELATIVITY

A condensed matter system exhibits an effect usually associated with particle physics *By A. Burkov*

► REPORT P. 413

379 THE UNKNOWN OF COGNITIVE ENHANCEMENT

Can science and policy catch up with practice? *By M. J. Farah*

381 SNAPSHOTS OF A PROTEIN QUAKE

Release of CO induces ultrafast collective motions in myoglobin *By R. Neutze*

► REPORT P. 445

382 MAKING WAVES: THE SCIENCE AND POLITICS OF OCEAN PROTECTION

Mature science reveals opportunities for policy progress *By J. Lubchenco and K. Grorud-Colvert*

384 BEYOND KNOWN METHANOGENS

DNA sequences from a coal-bed reservoir show that methane can be generated by unexpected microbes *By K. Lloyd*

► REPORT P. 434

385 TOWARD A RAPID AND REVERSIBLE MALE PILL

Sperm-specific calcineurin is a novel fertility and contraceptive target *By J. Castaneda and M. M. Matzuk*

► REPORT P. 442

386 SYSTEMS BIOLOGY (UN)CERTAINTIES

How can modelers restore confidence in systems and computational biology? *By P. D. W. Kirk et al.*

388 HOW SAFE ARE NANOMATERIALS?

There is still no consensus on the toxicity of nanomaterials *By E. Valsami-Jones and I. Lynch*

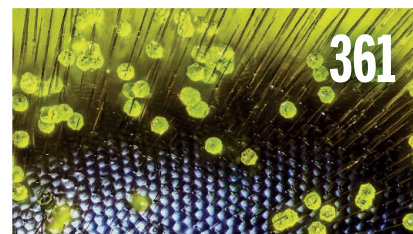
BOOKS ET AL.

390 DARK MATTER AND THE DINOSAURS

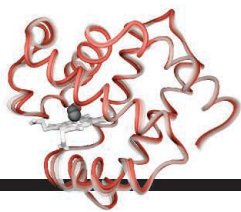
By L. Randall,
reviewed by J. Smit and R. Smit

391 HOUSTON, WE HAVE A NARRATIVE

By R. Olson, reviewed by R. E. Luna

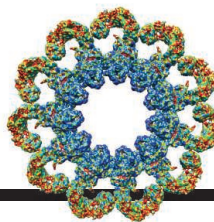


Science Staff	358
New Products	460
AAAS Meeting Program	461
Science Careers	471



381 & 445

Visualizing ultrafast
protein motion



376, 399, & 404

A complex that signals cell death

LETTERS

392 IRAN'S ENVIRONMENT UNDER SIEGE

By H. Akhiani

392 IRAN'S EDUCATION AND RESEARCH POTENTIAL

By D. N. Rahni

393 WITH MORALIZING GODS, EXCLUSION REIGNS

By R. Blanton and L. Fargher

RESEARCH

IN BRIEF

394 From *Science* and other journals

RESEARCH ARTICLES

398 CLATHRIN ADAPTORS

HIV-1 Nef hijacks clathrin coats by stabilizing AP-1:Arf1 polygons
Q.-T. Shen et al.

RESEARCH ARTICLE SUMMARY; FOR FULL TEXT:
dx.doi.org/10.1126/science.aac5137

399 INNATE IMMUNITY

Structural and biochemical basis for induced self-propagation of NLRC4
Z. Hu et al.

► PERSPECTIVE P. 376; REPORT P. 404

REPORTS

404 INNATE IMMUNITY

Cryo-EM structure of the activated NAIP2-NLRC4 inflammasome reveals nucleated polymerization
L. Zhang et al.

► PERSPECTIVE P. 376;

RESEARCH ARTICLE P. 399

409 SUPERCONDUCTIVITY

Metallic ground state in an ion-gated two-dimensional superconductor
Y. Saito et al.

413 TOPOLOGICAL MATTER

Evidence for the chiral anomaly in the Dirac semimetal Na₃Bi
J. Xiong et al.

► PERSPECTIVE P. 378

417 MAGNETIC RESONANCE

Electron paramagnetic resonance of individual atoms on a surface
S. Baumann et al.

420 QUANTUM OPTICS

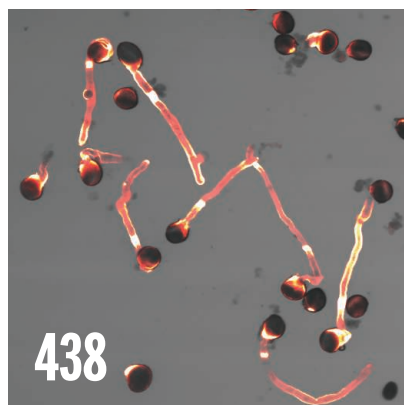
Direct sampling of electric-field vacuum fluctuations
C. Riek et al.

423 ASTEROSEISMOLOGY

Asteroseismology can reveal strong internal magnetic fields in red giant stars
J. Fuller et al.

426 PLANT DEVELOPMENT

Transcriptional control of tissue formation throughout root development
M. A. Moreno-Risueno et al.



430 ALZHEIMER'S DISEASE

Reduced grid-cell-like representations in adults at genetic risk for Alzheimer's disease
L. Kunz et al.

434 MICROBIAL METABOLISM

Methane metabolism in the archaeal phylum Bathyarchaeota revealed by genome-centric metagenomics
P. N. Evans et al.

► PERSPECTIVE P. 384

438 PLANT SCIENCE

Mechanosensitive channel MSL8 regulates osmotic forces during pollen hydration and germination
E. S. Hamilton et al.

442 REPRODUCTIVE BIOLOGY

Sperm calcineurin inhibition prevents mouse fertility with implications for male contraceptive
H. Miyata et al.

► PERSPECTIVE P. 385

445 PROTEIN DYNAMICS

Direct observation of ultrafast collective motions in CO myoglobin upon ligand dissociation
T. R. M. Barends et al.

► PERSPECTIVE P. 381

450 CHLOROPLASTS

Ubiquitin facilitates a quality-control pathway that removes damaged chloroplasts
J. D. Woodson et al.

455 AUTOIMMUNITY

The Ro60 autoantigen binds endogenous retroelements and regulates inflammatory gene expression
T. Hung et al.

DEPARTMENTS

359 EDITORIAL

Smart villages

By John Holmes et al.

478 WORKING LIFE

The power of mentoring

By Carol Lynn Curchoe

ON THE COVER



Since 2003, Project Prakash has restored vision in hundreds of Indian children who were blind from birth and thought to be beyond medical help, including 14-year-old Dilip Kumar Yadav

(pictured) and his brother, Manoj. The project is revealing new insights into how the brain interprets the visual world. See page 372. Photo: Graham Crouch/AP

SCIENCE (ISSN 0036-8075) is published weekly on Friday, except the last week in December, by the American Association for the Advancement of Science, 1200 New York Avenue, NW, Washington, DC 20005. Periodicals mail postage (publication No. 484460) paid at Washington, DC, and additional mailing offices. Copyright © 2015 by the American Association for the Advancement of Science. The title SCIENCE is a registered trademark of the AAAS. Domestic individual membership and subscription (51 issues): \$153 (\$74 allocated to subscription). Foreign postage extra: Mexico, Caribbean (surface mail) \$55; other countries (air assist delivery) \$85. First class, airmail, student, and emeritus rates on request. Canadian rates with GST available upon request. GST #R1254 88122. Publications Mail Agreement Number 1069624. Printed in the U.S.A. Change of address: Allow 4 weeks, giving old and new addresses and 8-digit account number. Postmaster: Send change of address to AAAS, P.O. Box 96178, Washington, DC 20090-6178. Single-copy sales: \$10.00 current issue, \$15.00 back issue prepaid includes surface postage; bulk rates on request. Authorization to photocopy material for internal or personal use under circumstances not falling within the fair use provisions of the Copyright Act is granted by AAAS to libraries and other users registered with the Copyright Clearance Center (CCC) Transactional Reporting Service, provided that \$30.00 per article is paid directly to CCC, 222 Rosewood Drive, Danvers, MA 01923. The identification code for Science is 0036-8075. Science is indexed in the Reader's Guide to Periodical Literature and in several specialized indexes.

Editor-in-Chief Marcia McNutt

Executive Editor Monica M. Bradford **News Editor** Tim Appenzeller

Managing Editor, Research Journals Katrina L. Kelner

Deputy Editors Barbara R. Jasny, Andrew M. Sugden(UK), Valda J. Vinson, Jake S. Yeston

Research and Insights

SR. EDITORS Caroline Ash(UK), Gilbert J. Chin, Lisa D. Chong, Julia Fahrenkamp-Uppenbrink(UK), Pamela J. Hines, Stella M. Hurlty(UK), Paula A. Kiberstis, Marc S. Lavine(Canada), Kristen L. Mueller, Ian S. Osborne(UK), Beverly A. Purnell, L. Bryan Ray, Guy Riddihough, H. Jesse Smith, Jelena Stajic, Peter Stern(UK), Phillip D. Szurmi, Brad Wible, Nicholas S. Wigginton, Laura M. Zahn **ASSOCIATE EDITORS** Brent Grocholski, Keith T. Smith, Sacha Vignieri **ASSOCIATE BOOK REVIEW EDITOR** Valerie B. Thompson **ASSOCIATE LETTERS EDITOR** Jennifer Sills **CHIEF CONTENT PRODUCTION EDITOR** Cara Tate **SR. CONTENT PRODUCTION EDITOR** Harry Jack **CONTENT PRODUCTION EDITORS** Jeffrey E. Cook, Chris Filiatreau, Cynthia Howe, Lauren Kmec, Barbara P. Ordway, Catherine Wolner **SR. EDITORIAL COORDINATORS** Carolyn Kyle, Beverly Shields **EDITORIAL COORDINATORS** Ramatoulaye Diop, Joi S. Granger, Lisa Johnson, Anita Wynn **PUBLICATIONS ASSISTANTS** Aneera Dobbins, Jeffrey Hearn, Dona Mathieu, Le-Toya Mayne Flood, Shannon McMahon, Scott Miller, Jerry Richardson, Rachel Roberts(UK), Alice Whaley(UK), Brian White **EXECUTIVE ASSISTANT** Anna Bashkirova **ADMINISTRATIVE SUPPORT** Janet Clements(UK), Lizanne Newton(UK), Maryrose Madrid, Laura-Nadine Schuhmacher (UK, Intern), Alix Welch (Intern), John Wood(UK)

News

NEWS MANAGING EDITOR John Travis **INTERNATIONAL EDITOR** Richard Stone **DEPUTY NEWS EDITORS** Daniel Clery(UK), Robert Coontz, Elizabeth Culotta, David Grimm, David Malakoff, Leslie Roberts **CONTRIBUTING EDITOR** Martin Enserink(Europe) **SR. CORRESPONDENTS** Jeffrey Mervis, Elizabeth Pennisi **NEWS WRITERS** Adrian Cho, Jon Cohen, Jennifer Couzin-Frankel, Carolyn Gramling, Eric Hand, Jocelyn Kaiser, Catherine Maticic, Kelly Servick, Robert F. Service, Erik Stokstad(Cambridge, UK), Emily Underwood **INTERNS** Hanae Armitage, Emily DeMarco, Annick Laurent, Laura Olivieri, Juan David Romero **CONTRIBUTING CORRESPONDENTS** Michael Balter(Paris), John Bohannon, Ann Gibbons, Mara Hvistendahl, Sam Kean, Eli Kirsch, Kai Kupferschmidt(Berlin), Andrew Lawler, Christina Larson(Beijing), Mitch Leslie, Charles C. Mann, Eliot Marshall, Virginia Morell, Dennis Normile(Tokyo), Heather Pringle, Tania Rabesandratana(London), Gretchen Vogel(Berlin), Lizzie Wade(Mexico City) **CAREERS** Donisha Adams, Rachel Bernstein **COPY EDITORS** Julia Cole, Jennifer Levin (Chief) **ADMINISTRATIVE SUPPORT** Jessica Williams

Executive Publisher Rush D. Holt

Publisher Kent R. Anderson **Chief Digital Media Officer** Rob Covey

BUSINESS OPERATIONS AND PORTFOLIO MANAGEMENT DIRECTOR Sarah Whalen **BUSINESS SYSTEMS AND FINANCIAL ANALYSIS DIRECTOR** Randy Yi **MANAGER OF FULFILLMENT SYSTEMS** Neal Hawkins **SYSTEMS ANALYST** Nicole Mehmedovic **ASSISTANT DIRECTOR, BUSINESS OPERATIONS** Eric Knott **MANAGER, BUSINESS OPERATIONS** Jessica Tierney **BUSINESS ANALYSTS** Cory Lipman, Cooper Tilton, Celeste Troxler **FINANCIAL ANALYST** Robert Clark **RIGHTS AND PERMISSIONS ASSISTANT DIRECTOR** Emilie David **PERMISSIONS ASSOCIATE** Elizabeth Sandler **RIGHTS, CONTRACTS, AND LICENSING ASSOCIATE** Lili Kiser

MARKETING DIRECTOR Elise Swinehart **ASSOCIATE DIRECTOR OF ACQUISITION AND RETENTION** Julianne Wielga **MARKETING ASSOCIATE** Elizabeth Sattler **SR. MARKETING EXECUTIVE** Jennifer Reeves **ASSOCIATE DIRECTOR, CREATIVE SERVICES** Tzeitel Sorrosa **ART ASSOCIATE** Seil Lee **JR. ART ASSOCIATE** Kim Huynh **ASSISTANT COMMERCIAL EDITOR** Selby Frame **MARKETING PROJECT MANAGER** Angelissa McArthur **PROGRAM DIRECTOR, AAAS MEMBER CENTRAL** Peggy Mihelich **FULFILLMENT SYSTEMS AND OPERATIONS** membership@aaas.org **MANAGER, MEMBER SERVICES** Pat Butler **SPECIALISTS** LaToya Casteel, Terrance Morrison, Latasha Russell **MANAGER, DATA ENTRY** Mickie Napoleoni **DATA ENTRY SPECIALISTS** JJ Regan, Brenden Aquilino, Fiona Giblin

DIRECTOR, SITE LICENSING Tom Ryan **DIRECTOR, CORPORATE RELATIONS** Eileen Bernadette Moran **SR. PUBLISHER RELATIONS SPECIALIST** Kiki Forsythe **PUBLISHER RELATIONS MANAGER** Catherine Holland **PUBLISHER RELATIONS, EASTERN REGION** Keith Layson **PUBLISHER RELATIONS, WESTERN REGION** Ryan Rexroth **SALES RESEARCH COORDINATOR** Aiesha Marshall **MANAGER, SITE LICENSE OPERATIONS** Iqo Edim **SENIOR PRODUCTION SPECIALIST** Robert Koepke **SENIOR OPERATIONS ANALYST** Lana Guz **FULFILLMENT SPECIALIST** Judy Lillibridge **ASSOCIATE DIRECTOR, MARKETING** Christina Schlecht **MARKETING ASSOCIATES** Thomas Landreth, Isa Sesay-Bah

WEB TECHNOLOGIES SR. DEVELOPER Chris Coleman **DEVELOPERS** Dan Berger, Jimmy Marks, Ryan Jensen **SR. PROJECT MANAGER** Trista Smith

CREATIVE DIRECTOR, MULTIMEDIA Martyn Green **DIRECTOR OF ANALYTICS** Enrique Gonzales **SR. WEB PRODUCER** Sarah Crespi **WEB PRODUCER** Alison Crawford **VIDEO PRODUCER** Nguyen Nguyen **SOCIAL MEDIA PRODUCER** Meghna Sachdev

DIRECTOR OF OPERATIONS PRINT AND ONLINE Lizabeth Harman **DESIGN/PRINT STRATEGY MANAGER** Jason Hillman **QUALITY TECHNICAL MANAGER** Marcus Spiegel **PROJECT ACCOUNT MANAGER** Tara Kelly **DIGITAL PRODUCTION MANAGER** Lisa Stanford **ASSISTANT MANAGER DIGITAL/PRINT** Rebecca Doshi **SENIOR CONTENT SPECIALISTS** Steve Forrester, Antoinette Hodal, Lori Murphy, Anthony Rosen **CONTENT SPECIALISTS** Jacob Hedrick, Kimberley Oster

DESIGN DIRECTOR Beth Rakouskas **DESIGN EDITOR** Marcy Atarod **SENIOR DESIGNER** Garvin Grullón **DESIGNER** Chrystal Smith **GRAPHICS MANAGING EDITOR** Alberto Cuadra **SENIOR SCIENTIFIC ILLUSTRATORS** Chris Bickel, Katharine Sutliff **SCIENTIFIC ILLUSTRATOR** Valerie Altounian **SENIOR ART ASSOCIATES** Holly Bishop, Nathalie Cary, Preston Huey **SENIOR PHOTO EDITOR** William Douthitt **PHOTO EDITORS** Leslie Blizard, Christy Steele

DIRECTOR, GLOBAL COLLABORATION, CUSTOM PUBLICATIONS, ADVERTISING Bill Moran **EDITOR, CUSTOM PUBLISHING** Sean Sanders: 202-326-6430 **ASSISTANT EDITOR, CUSTOM PUBLISHING** Tianna Hicklin: 202-326-6463 **ADVERTISING MARKETING MANAGER** Justin Sawyers: 202-326-7061 **science_advertising@aaas.org** **ADVERTISING MARKETING ASSOCIATE** Javia Flemmings **ADVERTISING SUPPORT MANAGER** Karen Foote: 202-326-6740 **ADVERTISING PRODUCTION OPERATIONS MANAGER** Deborah Tompkins **SR. PRODUCTION SPECIALIST/GRAPHIC DESIGNER** Amy Hardcastle **PRODUCTION SPECIALIST** Yuse Lajimimuhup **SR. TRAFFIC ASSOCIATE** Christine Hall **SALES COORDINATOR** Shirley Young **ASSOCIATE DIRECTOR, COLLABORATION, CUSTOM PUBLICATIONS/CHINA/TAIWAN/KOREA/SINGAPORE** Ruolei Wu: +86-186 0082 9345, rwu@aaas.org **COLLABORATION/ CUSTOM PUBLICATIONS/JAPAN** Adarsh Sandhu + 81532-81-5142 asandhu@aaas.org **EAST COAST/E. CANADA** Laurie Faraday: 508-747-9395, FAX 617-507-8189 **WEST COAST/W. CANADA** Lynne Stickrod: 415-931-9782, FAX 415-520-6940 **MIDWEST** Jeffrey Dembski: 847-498-4520 x3005, Steven Loerch: 847-498-4520 x3006 **UK EUROPE/ASIA** Roger Gonçalves: TEL/FAX +41 43 243 1358 **JAPAN** Katsuyoshi Fukamizu(Tokyo): +81-3-3219-5777 kfukamizu@aaas.org **CHINA/TAIWAN** Ruolei Wu: +86-186 0082 9345, rwu@aaas.org

WORLDWIDE ASSOCIATE DIRECTOR OF SCIENCE CAREERS Tracy Holmes: +44 (0) 1223 326525, FAX +44 (0) 1223 326532 tholmes@science-int.co.uk **CLASSIFIED advertise@sciencemag.org** **U.S. SALES** Tina Burks: 202-326-6577 **Nancy Toema:** 202-326-6578 **SALES ADMINISTRATOR** Marci Gallun **EUROPE/ROW SALES** Axel Gesatzki, Sarah Lelange **ASSISTANT Kelly Grace** **JAPAN** Hiroyuki Mashiki(Kyoto): +81-75-823-1109 hmashiki@aaas.org **CHINA/TAIWAN** Ruolei Wu: +86-186 0082 9345 rwu@aaas.org **MARKETING MANAGER** Allison Pritchard **MARKETING ASSOCIATE** Aimee Aponte

AAAS BOARD OF DIRECTORS **RETIRING PRESIDENT, CHAIR** Gerald R. Fink **PRESIDENT** Geraldine (Geri) Richmond **PRESIDENT-ELECT** Barbara A. Schaaf **TREASURER** David Evans **SHAW CHIEF EXECUTIVE OFFICER** Rush D. Holt **BOARD** Bonnie L. Bassler, May R. Berenbaum, Carlos J. Bustamante, Stephen P. A. Fodor, Claire M. Fraser, Michael S. Gazzaniga, Laura H. Greene, Elizabeth Loftus, Mercedes Pascual

SUBSCRIPTION SERVICES For change of address, missing issues, new orders and renewals, and payment questions: 866-434-AAAS (2227) or 202-326-6417, FAX 202-842-1065. Mailing addresses: AAAS, P.O. Box 96178, Washington, DC 20090-6178 or AAAS Member Services, 1200 New York Avenue, NW, Washington, DC 20005

INSTITUTIONAL SITE LICENSES 202-326-6730 **REPRINTS:** Author Inquiries 800-635-7181 **COMMERCIAL INQUIRIES** 803-359-4578 **PERMISSIONS** 202-326-6765, permissions@aaas.org **AAAS Member Services** 202-326-6417 or http://membercentral.aaas.org/discouints

Science serves as a forum for discussion of important issues related to the advancement of science by publishing material on which a consensus has been reached as well as including the presentation of minority of conflicting points of view. Accordingly, all articles published in Science—including editorials, news and comment, and books reviews—are signed and reflect the individual views of the authors and not official points of view adopted by AAAS or the institutions with which the authors are affiliated.

INFORMATION FOR AUTHORS See pages 678 and 679 of the 6 February 2015 issue or access www.sciencemag.org/about/authors

SENIOR EDITORIAL BOARD

Robert H. Grubbs, *California Institute of Technology*, Gary King, *Harvard University*
Susan M. Rosenberg, *Baylor College of Medicine*, Ali Shalithard, *Northwestern University*
Feinberg School of Medicine, Michael S. Turner, *U. of Chicago*

BOARD OF REVIEWING EDITORS (Statistics board members indicated with \$)

Adriano Aguzzi, *U. Hospital Zurich*
Takuzo Aida, *U. of Tokyo*
Leslie Aiello, *Wenner-Gren Foundation*
Judith Allen, *U. of Edinburgh*
Sonia Altizer, *U. of Georgia*
Sebastian Amigorena, *Institut Curie*
Kathryn Anderson, *Memorial Sloan-Kettering Cancer Center*
Meinrat O. Andreae, *Max-Planck Inst. Mainz*
Paola Arlotta, *Harvard U.*
Johan Auwerx, *EPFL*
David Awechselom, *U. of Chicago*
Clare Baker, *University of Cambridge*
Jordi Bascompte, *ETH Zurich*
Jacundo Batista, *London Research Inst.*
Ray H. Baughman, *U. of Texas, Dallas*
David Baum, *U. of Wisconsin*
Carlo Beenakker, *Leiden U.*
Kamran Behnia, *ESPCI-ParisTech*
Yasmine Belkaid, *NIH, NIH*
Philip Benfey, *Duke U.*
Stephen J. Benkovic, *Penn State U.*
May Berenbaum, *U. of Illinois*
Gabriele Bergers, *U. of California, San Francisco*
Bradley Bernstein, *Massachusetts General Hospital*
Peer Bork, *EMBL*
Bernard Bourdon, *Ecole Normale Supérieure de Lyon*
Chris Bowler, *Ecole Normale Supérieure*
Ian Boyd, *U. of St. Andrews*
Emily Brodsky, *U. of California, Santa Cruz*
Ron Brookmeyer, *U. of California Los Angeles (\$)*
Christian Büchel, *U. Hamburg-Eppendorf*
Joseph A. Burns, *Cornell U.*
Carter Tribble Butts, *U. of California, Irvine*
Gyorgy Buzsaki, *New York U. School of Medicine*
Blanche Capel, *Duke U.*
Mats Carlsson, *U. of Oslo*
Ib Chorkendorff, *U. of Denmark*
David Clapham, *Children's Hospital Boston*
David Clary, *U. of Oxford*
Joel Cohen, *Rockefeller U., Columbia U.*
James J. Collins, *MIT*
Robert Cook-Deegan, *Duke U.*
Alan Cowman, *Walter & Eliza Hall Inst.*
Robert H. Crabtree, *Yale U.*
Roberta Croce, *Vrije Universiteit*
Janet Currie, *Princeton U.*
Jeff L. Dangi, *U. of North Carolina*
Tom Daniel, *U. of Washington*
Frans de Waal, *Emory U.*
Stanislas Dehaene, *Collège de France*
Robert Desimone, *MIT*
Claude Desplan, *New York U.*
Ap Dijksterhuis, *Radboud U. of Nijmegen*
Dennis Discher, *U. of Pennsylvania*
Gerald W. Dorn II, *Washington U. School of Medicine*
Jennifer A. Doudna, *U. of California, Berkeley*
Bruce Dunn, *U. of California, Los Angeles*
William Dunphy, *Caltch*
Christopher Dye, *WHO*
Todd Ehlers, *U. of Tübingen*
David Ehrhardt, *Carnegie Inst. of Washington*
Tim Elston, *U. of North Carolina at Chapel Hill*
Gerhard Ertl, *Fritz-Haber-Institut, Berlin*
Barry Everitt, *U. of Cambridge*
Ernst Fehr, *U. of Zurich*
Anne C. Ferguson-Smith, *U. of Cambridge*
Michael Feuer, *The George Washington U.*
Toren Finkel, *NHLBI, NIH*
Kate Fitzgerald, *U. of Massachusetts*
Peter Fratzl, *Max-Planck Inst.*
Elaine Fuchs, *Rockefeller U.*
Daniel Geschwind, *UCLA*
Karl-Heinz Glassmeier, *TU Braunschweig*
Ramon Gonzalez, *Rice U.*
Julia R. Greer, *Caltch*
Elizabeth Grove, *U. of Chicago*
Nicolas Gruber, *ETH Zurich*
Kip Guy, *St. Jude's Children's Research Hospital*
Taekjip Ha, *U. of Illinois at Urbana-Champaign*
Christian Hassel, *Ludwig Maximilians U.*
Michael Hasselmo, *Boston U.*
Martin Heimann, *Max-Planck Inst. Jena*
Yka Helariutta, *U. of Cambridge*
James A. Hendler, *Rensselaer Polytechnic Inst.*
Janet G. Hering, *Swiss Fed. Inst. of Aquatic Science & Technology*
Kai-Uwe Hinrichs, *U. of Bremen*
Kei Hirose, *Tokyo Inst. of Technology*
David Hodell, *U. of Cambridge*
David Holden, *Imperial College*
Lora Hooper, *UT Southwestern Medical Ctr. at Dallas*
Raymond Huey, *U. of Washington*
Auke Ijspeert, *EPFL Lausanne*
Steven Jacobsen, *U. of California, Los Angeles*
Kai Jonsson, *EPFL Lausanne*
Peter Jonas, *Inst. of Science & Technology (IST) Austria*
Matt Kaebberlein, *U. of Washington*
William Kaelin Jr., *Dana-Farber Cancer Inst.*
Daniel Kahne, *Harvard U.*
Daniel Kammen, *U. of California, Berkeley*
Masashi Kawasaki, *U. of Tokyo*
Y. Narry Kim, *Seoul National U.*
Joel Kingsolver, *U. of North Carolina at Chapel Hill*
Robert Kingston, *Harvard Medical School*
Etienne Kochlin, *Ecole Normale Supérieure*
Alexander Koldkin, *Johns Hopkins U.*
Leonid Kruglyak, *UCLA*
Thomas Langer, *U. of Cologne*
Mitchell A. Lazar, *U. of Pennsylvania*
David Lazer, *Harvard U.*
Thomas Lecuit, *IBDM*
Virginia Lee, *U. of Pennsylvania*
Stanley Lemon, *U. of North Carolina at Chapel Hill*
Ottoline Leyser, *Cambridge U.*
Wendell Lim, *U.C. San Francisco*
Marcia C. Linn, *U. of California, Berkeley*
Jianguo Liu, *Michigan State U.*
Luis Liz-Marzan, *CIC biomaGUNE*
Jonathan Losos, *Harvard U.*
Kai. Chinese Acad. of Sciences
Christian Lüscher, *U. of Geneva*
Laura Machesky, *CRUK Beatson Inst. for Cancer Research*
Anne Magurran, *U. of St. Andrews*
Oscar Marin, *CSIC & U. Miguel Hernández*
Charles Marshall, *U. of California, Berkeley*
C. Robertson McClung, *Dartmouth College*
Graham Medley, *U. of Warwick*
Tom Misteli, *NCI*
Yasushi Miyashita, *U. of Tokyo*
Mary Ann Moran, *U. of Georgia*
Richard Morris, *U. of Edinburgh*
Alison Mutsaers-Reif, *NC State U. (\$)*
Thomas Murray, *The Hastings Center*
James Neuman, *Stanford U. School of Med.*
Daniel Neukarth, *U. of California, Berkeley*
Kitty Niemeijer, *U. of Twente*
Pär Nordlund, *Karolinska Inst.*
Helga Nowotny, *European Research Advisory Board*
Ben Olken, *MIT*
Joe Orenstein, *U. of California Berkeley & Lawrence Berkeley National Lab*
Harry Orr, *U. of Minnesota*
Andrew Oswald, *U. of Warwick*
Steve Palumbi, *Stanford U.*
Jane Parker, *Max-Planck Inst. of Plant Breeding Research*
Giovanni Parmigiani, *Dana-Farber Cancer Inst. (\$)*
Donald R. Paul, *U. of Texas, Austin*
John H. J. Petrini, *Memorial Sloan-Kettering Cancer Center*
Samuel Pfaff, *Salk Institute for Biological Studies*
Joshua Plotkin, *U. of Pennsylvania*
Albert Polman, *FOM Institute AMOLF*
Philippe Pouchin, *CNRS*
Jonathan Pritchard, *Stanford U.*
David Randall, *Colorado State U.*
Colin Renfrew, *U. of Cambridge*
Felix Rey, *Institut Pasteur*
Trevor Robbins, *U. of Cambridge*
Jim Roberts, *Fred Hutchinson Cancer Research Ctr.*
Barbara A. Romanowicz, *U. of California, Berkeley*
Amy Rosenzweig, *Northwestern University*
Jens Rostrup-Nielsen, *Haldor Topsøe*
Mike Ryan, *U. of Texas, Austin*
Mitsunori Saitou, *Kyoto U.*
Shimon Sakaguchi, *Kyoto U.*
Miguel Salmeron, *Lawrence Berkeley National Lab*
Jürgen Sandkühler, *University of Vienna*
Alexander Schier, *Harvard U.*
Randy Seeley, *U. of Cincinnati*
Vladimir Shalaev, *Purdue U.*
Robert Siliciano, *Johns Hopkins School of Medicine*
Deni Simon, *Arizona State U.*
Uri Simonsohn, *U. of Pennsylvania*
Alison Smith, *John Innes Centre*
Richard Smith, *U. of North Carolina (\$)*
John Speakman, *U. of Aberdeen*
Allan C. Spradling, *Carnegie Institution of Washington*
Jonathan Sprent, *Garvan Inst. of Medical Research*
Eric Steig, *U. of Washington*
Paula Stephan, *George State U. and National Bureau of Economic Research*
Molly Stevens, *Imperial College London*
V. S. Subrahmanian, *U. of Maryland*
Ira Tabas, *Columbia U.*
Sarah Teichmann, *Cambridge U.*
John Thomas, *North Carolina State U.*
Shubha Tole, *Tata Institute of Fundamental Research*
Christopher Tyler-Smith, *The Wellcome Trust Sanger Inst.*
Herbert Virgin, *Washington U.*
Bern Vogelstein, *Johns Hopkins U.*
Cynthia Volkert, *U. of Göttingen*
Douglas Wallace, *Dalhousie U.*
David Wallace, *Weizmann Inst. of Science*
Ian Walmsey, *U. of Oxford*
Jane-Ling Wang, *U. of California, Davis*
David A. Wardle, *Swedish U. of Agric. Sciences*
David Waxman, *Fudan U.*
Jonathan Weissman, *U. of California, San Francisco*
Chris Wikle, *U. of Missouri (\$)*
Ian A. Wilson, *The Scripps Res. Inst. (\$)*
Timothy D. Wilson, *U. of Virginia*
Rosemary Wyse, *Johns Hopkins U.*
Jan Zaenen, *Leiden U.*
Kenneth Zaret, *U. of Pennsylvania School of Medicine*
Jonathan Zehr, *U. of California, Santa Cruz*
Len Zon, *Children's Hospital Boston*
Maria Zuber, *MIT*

BOOK REVIEW BOARD

David Bloom, *Harvard U.*, Samuel Bowring, *MIT*, Angela Creager, *Princeton U.*, Richard Sweder, *U. of Chicago*, Ed Wasserman, *DuPont*

Smart villages

Last month in New York, the world adopted the Sustainable Development Goals (SDGs), defining the global development agenda for the next 15 years. Among the 17 goals is Goal 7's aim to ensure "access to affordable, reliable, sustainable and modern energy for all." Given that an estimated 1.3 billion people have no access to electricity and that 70% of the world's poor live off-grid in the countryside, this is indeed ambitious. How do we ensure that these remote communities have access to energy?

Energy is a catalyst for improving the quality of life. The value of a \$5 solar lantern stretches well beyond simply providing light at night. It allows children to study after sunset, for instance, and therefore compete with peers who live in towns. Larger power systems provide commensurately greater benefits, such as lighting for security, refrigeration for food and medicines, and the ability to set up enterprises that support the community. Furthermore, the availability of electricity opens up space for technological innovations, such as remote education or handheld medical devices that can transmit information hundreds of miles away.

Access to sustainable energy is a necessary precursor to all the other SDGs and offers opportunities for synergy that integrated strategies might bring. One such strategy is the "smart village," a rural analog of the "smart city" concept, in which access to sustainable energy, together with modern information and communication technologies, enables holistic development, including cultural changes in the provision of good education and health care; access to clean water, sanitation, and nutrition; and the growth of social and industrial enterprises to boost incomes. This approach in Terrat, in the Maasai region of northern Tanzania, underlies a biodiesel-fueled generating plant that now supports schools, health centers, a radio station, and the sprouting of local enterprises. Indeed, access to

electricity helped a local dairy, whose prize-winning cheese has doubled the incomes of the Maasai women.

The reality is that extending existing grids to remote areas is often prohibitively expensive. What are needed instead are local solutions, and governments must adopt policy and regulatory frameworks for these local answers. This has been the case for establishing solar home systems in Bangladesh and mini-grids in Rwanda. New frameworks must address several key issues with clarity: appropriately targeted subsidies, tariffs that are commercially viable, and capital for entrepreneurs at affordable rates. A true game-changer would be enabling small- and medium-scale village-level energy projects to access large-scale international climate change funds.

Important areas for future research and development include improved control systems that can balance the supply and demand of electricity throughout the day, and "plug-and-play" technologies for installing and maintaining home-based power systems, which would minimize the need for scarce

local skills. Energy storage also needs a dedicated international research program to develop affordable and efficient batteries. More sharing of information and experiences between countries could drive systematic analyses of the knowledge and local skills required to implement and maintain energy services.

In the 15-year SDG marathon that lies ahead, something more than the warm words and sentiments of Goal 7 must be done to cover the "last mile": the millions of people living in remote communities with no realistic chance of being connected to a grid. Smart villages are not the only approach for the sustainable development of rural populations, but they are certainly a strategy that can improve the quality of life and give younger generations positive reasons to stay rather than migrate.

– John Holmes, Bernie Jones, Brian Heap

John Holmes, Bernie Jones, and Brian Heap are research associates at the Smart Villages Initiative supported by the Cambridge Malaysian Education and Development Trust and the Templeton World Charity Foundation, c/o Trinity College, Cambridge CB2 1TQ, UK. E-mail: john.holmes@earth.ox.ac.uk; bernie@e4sv.org; rbh22@cam.ac.uk



"...access to sustainable energy... enables holistic development..."

“Please give Maddie one more day to complete her homework. We had some big family news and did not get to this. Her grandpa won the Nobel Prize in chemistry!”

Note sent to Maddie's teacher this month; her grandfather is Swedish chemist Tomas Lindahl.

IN BRIEF

Predator wannabe just another *T. rex*



A 3D reconstruction of this skull suggests it is a *Tyrannosaurus rex*, not a *Nanotyrannus*.

Some scientists think that *Tyrannosaurus rex*, which roamed the western United States between 68 million and 66 million years ago, had a smaller cousin named *Nanotyrannus*. But a new study, presented this week at the Society of Vertebrate Paleontology meeting in Dallas, Texas, supports the argument that *Nanotyrannus* is simply a juvenile version of *T. rex*. Scientists have wrangled over *Nanotyrannus* for decades: A skull found in Montana was first described in 1946 as a member of the tyrannosaur family, but other researchers later concluded that it was a separate, smaller taxon based on the fusing of the bones in its skull. Years later, another paleontologist concluded that the skull bones weren't fused and that it was a juvenile *T. rex* after all. A second skull and partial skeleton, found in 2002 in Montana, seemed to bolster this case. Now, the new study, based on a 3D computer reconstruction of the second skull and skeleton, counted microscopic “growth rings” in its calf bone and concluded that it was indeed a juvenile. Yet the debate isn't quite over: Scientists in the *Nanotyrannus* camp argue that a third skeleton—found in 2006 but mired in controversy after its owners tried to auction it—would provide the best evidence for their case. <http://scim.ag/nanotyranno>

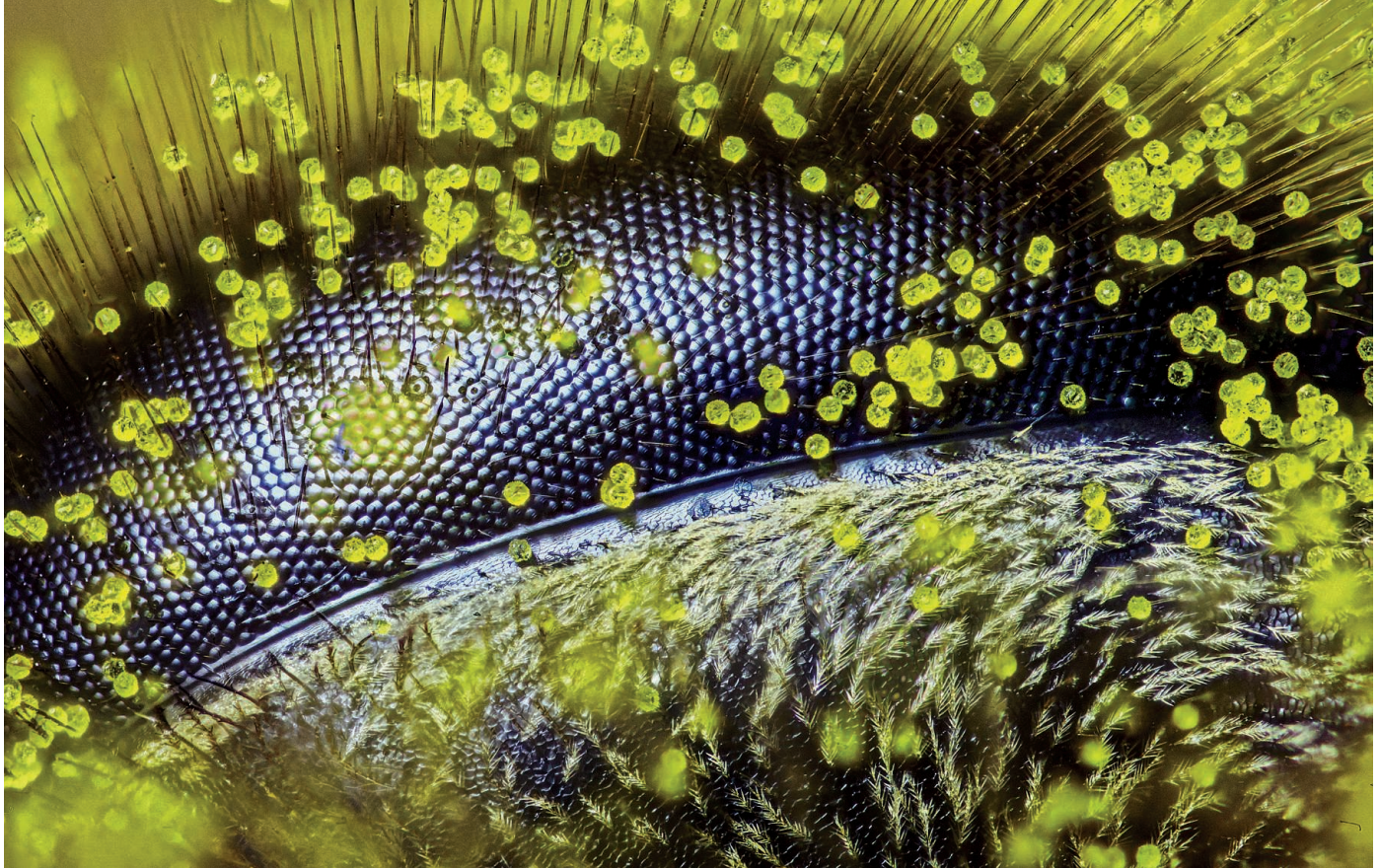
AROUND THE WORLD

Health research via iPhone

CUPERTINO, CALIFORNIA | Apple's open-source health research platform ResearchKit, launched in April, is expanding as it continues to garner interest from researchers; the platform added three new apps designed and managed by academic investigators, the company announced last week. ResearchKit is a software framework that lets researchers run large studies with data collected from participants' iPhones. An initial five apps released in March focus on tracking conditions including asthma, Parkinson's disease, and diabetes. Last week, three new studies came online: the EpiWatch app, developed by Johns Hopkins University, aims to track seizures using the accelerometer and heart rate sensor in the Apple Watch; Duke University's Autism & Beyond app explores ways to detect developmental disorders with the iPhone's front-facing camera; and a melanoma app from Oregon Health & Science University has users photograph their moles to enable new cancer detection algorithms.

EPA targets refrigerants

WASHINGTON, D.C. | The U.S. Environmental Protection Agency (EPA) proposed rules last week that will tighten restrictions on hydrofluorocarbons (HFCs), a class of refrigerants that pack up to 10,000 times the greenhouse warming power of CO₂. The new rules for HFCs in air conditioners and refrigerators would cover the sales, handling, and recovery of the chemicals; if adopted, EPA estimates that the greenhouse gas reduction would be equivalent to the removal of 7 million tons of CO₂ emissions in 2025. These new steps should propel international talks next month in the United Arab Emirates that are aimed at limiting emissions of HFCs, says David Doniger of the Natural Resources Defense Council. Furthermore, he says, a “crucial contribution” to the global effort has been new data from the U.S. Department of Energy showing that replacement chemicals for HFCs can perform well in warm climates, which will



Pollen-covered honey bee eye wins Nikon photography prize

If honey bees were publicity hounds, this one might have stars in its eyes. But the winning entry in this year's Nikon Small World photography competition has an eye full of pollen instead. Photographer and former beekeeper Ralph Grimm captured this extreme close-up after 4 hours of a painstakingly careful setup. Grimm, a high school fine arts teacher, says he hopes to call attention to the honey bees' continued struggle to regain a stable population. Honey bees are a crucial

facilitator in food diversity and stability—contributing more than \$15 billion to crop value annually in the United States. But over the last decade or so, the bees have fallen victim to a number of problems like parasites, pesticides, and disease, causing their numbers to dwindle 30% each year since 2006. Grimm tells Nikon that his image, though beautiful, comes with a word of caution—we need to stay connected to our planet by listening to little creatures, like bees.

help countries with hot climates upgrade their cooling systems.

Elections cheer scientists

OTTAWA | Many Canadian scientists are celebrating the result of this week's federal election, which saw Stephen Harper's Conservative government defeated after nearly 10 years in power by the center-left Liberal Party under Justin Trudeau. Harper's government was extremely unpopular with scientists, who accused it of ignoring evidence in policymaking, "muzzling" government scientists, and focusing too much funding on commercially driven applied research. The Liberals have promised to reinstate a chief science officer, embrace "evidence based policy," do more to address climate change, protect endangered species, and review the environmental impact of major projects. Jim Woodgett, director of research at the Lunenfeld-Tanenbaum

Research Institute at Mount Sinai Hospital in Toronto, says the government must also address a neglect of basic research funding. "We are at serious risk of a lost generation of scientists," he says. "It's critical that younger researchers are given a clear indication that Canada is open to their ideas and needs." http://scim.ag/_2015Canada

NIH funds chimp brain resource

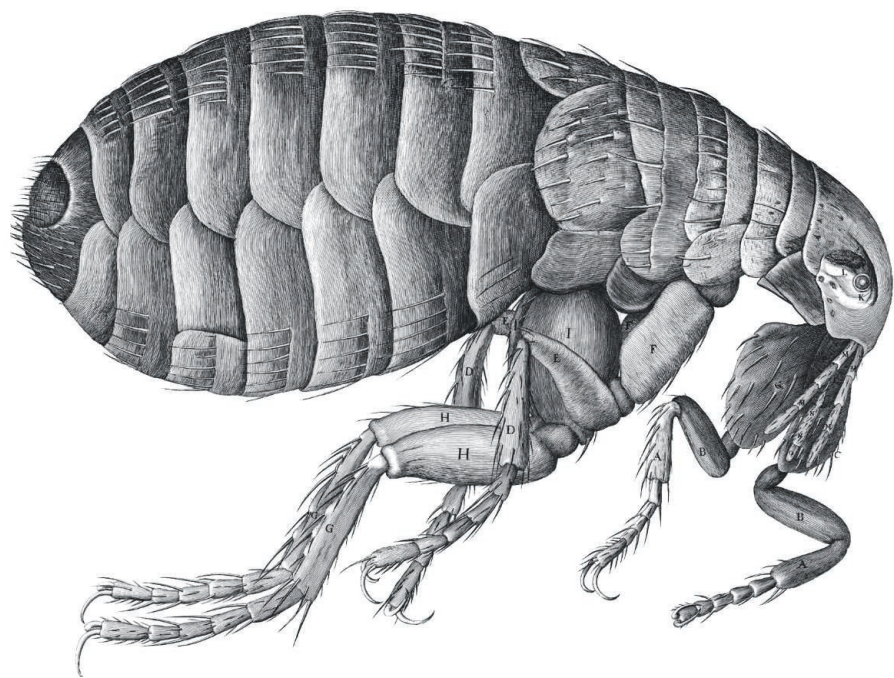
WASHINGTON, D.C. | Researchers at the George Washington University are developing the first national chimpanzee brain repository with the aid of a \$1 million National Institutes of Health (NIH) grant awarded last month. The university has a collection of more than 650 mammalian brains, including 60 species of primates. The grant, to be spread across 4 years, would provide funding to make the brains more accessible to other researchers, through open data

sharing and coordinated projects with other primate centers. The team, led by anthropologist Chester Sherwood, is planning to first launch an online portal this year that would offer data on MRI scans and tissue samples and allow other scientists to request samples and data. Plans for the site also include a chimp brain atlas and gene expression map. NIH began retiring many of its chimpanzees used in research in 2013.

FINDINGS

Parts of Ebola virus hide in semen

Researchers have known since 1999 that traces of the Ebola virus could remain in semen for months; but two papers published in *The New England Journal of Medicine* last week offer details about the frightening possibility that survivors of an Ebola infection could rekindle outbreaks. In one study of 93 survivors in Sierra



An early glimpse into a tiny world

Some things can never be unseen: the microscopic mandibles of a fruit fly; the leggy limbs of a hairy flea (shown). Three hundred and fifty years ago, scientist and amateur artist Robert Hooke's exquisite illustrations of tiny things showed people for the first time what the parasites that plagued them looked like. In his 1665 book *Micrographia*—the first major work of illustrated observations made through a microscope—Hooke chronicled dozens of parasites, plants, and other microscopic wonders. The Royal Society celebrated the book's anniversary this week with a microscopy drawing event and an exhibition in London. Robert Hooke made profound contributions to timekeeping, astronomy, physics, and microscopy—and coined the word “cell.” In *Micrographia*, he also argued, controversially, that fossils were the mineralized remains of ancient living organisms.

Leone, researchers found Ebola viral RNA in semen samples from 46 men; the likelihood of finding viral RNA declined over time. But there isn't enough information yet to assess how that translates to risk of transmission, the authors noted. However, the second paper documents a clear case of sexual transmission of Ebola virus: A

44-year-old Liberian woman was diagnosed with Ebola on 20 March, although there had been no cases of Ebola in the country in the previous 30 days. However, she reported having unprotected vaginal intercourse with an Ebola survivor on 7 March. The man had contracted Ebola in September 2014 and tested negative in



In some Ebola survivors, the virus (shown) is detectable in semen up to 9 months after infection.

BY THE NUMBERS

6.9–8.5

Average number of hours of sleep per day among hunter-gatherers in three preindustrial societies (*Current Biology*).

70%

Fraction of U.S. citizens who believe in climate science—an increase of 7% in the last 6 months (Poll by University of Michigan and Muhlenberg College).

76%

Fraction of U.S. respondents with no formal religious affiliation who think science and religion are often in conflict; only 16% of respondents with no formal religious affiliation think their own beliefs conflict with science (Pew Research Center survey).

early October; but a semen sample taken in March 2015 tested positive for Ebola. <http://scim.ag/Ebolasemen>

Specks of oldest life?

Scientists have found potential evidence that life on Earth existed 300 million years earlier than previously thought. Researchers examined microscopic flecks of graphite in a 4.1-billion-year-old zircon crystal from the Jack Hills in Western Australia. Based on the ratio of light and heavy isotopes of carbon, the authors suggest the material is consistent with a biological origin, they report this week in the *Proceedings of the National Academy of Sciences*. If confirmed, the results would demonstrate that life evolved shortly after the formation of the planet 4.5 billion years ago. The authors acknowledge that nonbiological processes could also explain their results, but hope to find more graphite inclusions in other ancient zircons to help confirm their hypothesis. <http://scim.ag/Zirconlife>



Researchers assemble the Majorana Demonstrator, which they hope will be a precursor to a larger experiment to search for a new type of nuclear decay.

NUCLEAR PHYSICS

U.S. targets matter-antimatter frontier

Search for rare nuclear decay would test whether the neutrino is its own antiparticle

By Adrian Cho

The neutrino is the hottest particle in physics. Two weeks ago, two physicists won the Nobel Prize for showing that the ghostly particle is not, as once thought, massless (*Science*, 9 October, p. 145). And last week nuclear physicists in the United States urged government funders to swiftly launch a new experiment to test whether the neutrino is— weirdly—its own antiparticle. If it is, the discovery would rewrite textbooks in both nuclear and particle physics.

First, though, the U.S. Department of Energy (DOE) must come up with roughly \$250 million to build a massive detector deep underground. It would search for a new type of nuclear decay, called neutrinoless double β decay, which can occur only if the neutrino and antineutrino are one. The United States will have to hustle to beat other nations to the potential prize, say physicists, who hope to start building the experiment in 2018. “The neutrinoless double β decay arena is very competitive,” says Robert McKeown, a physicist at Thomas Jefferson National Accelerator Facility (Jefferson Lab) in Newport News, Virginia. “If

the U.S. wants to lead, we can’t wait.”

The call for the decay experiment is just one part of a new long-range plan that physicists presented to DOE’s Nuclear Science Advisory Committee (NSAC) on 15 October in Washington, D.C. The road map is meant to help set priorities for DOE’s nuclear physics program, which has a 2015 budget of \$596 million, and for a smaller program at the National Science Foundation. The plan

“The ... arena is very competitive. If the U.S. wants to lead, we can’t wait.”

Robert McKeown, Thomas Jefferson National Accelerator Facility

mainly calls for continuing current projects; the exotic decay experiment would be the one large near-term initiative.

Neutrinoless double β decay would be a strange cousin of common β decay, in which a neutron in a radioactive nucleus changes into a proton by ejecting an electron and an antineutrino. Some nuclei, such as selenium-82, can exhibit double β decay, si-

multaneously spitting out two electrons and two antineutrinos. But in neutrinoless double β decay, only the electrons would emerge. For that to happen, the neutrino would have to be its own antiparticle, as the antineutrino emitted with one electron would instantly be reabsorbed as a neutrino to trigger emission of the second electron.

Being its own antiparticle would make the neutrino unique among the building blocks of matter (although force-carrying particles like the photon and gluon are their own antiparticles). It would also mean that the neutrino acquires its mass differently from other particles, which gain weight by the so-called Higgs mechanism (*Science*, 14 September 2012, p. 1286).

Spotting the rare decay won’t be easy. It can occur only in certain nuclei—such as germanium-76, tellurium-130, and xenon-136—so physicists must watch highly enriched samples of such isotopes for long periods, waiting to see the decay. They also must work far underground, where background radiation is low and won’t interfere with observations.

Smaller experiments are already underway around the world. Scientists at the 1480-meter-deep Sanford Underground Research

Facility in Lead, South Dakota, are working on a prototype detector known as the Majorana Demonstrator; their counterparts at Italy's 1400-meter-deep Gran Sasso National Laboratory are developing one called CUORE. But these prototypes use relatively small amounts of the key nuclei; physicists think they will need a detector containing a tonne to have a good chance of spotting the decay.

Last week's recommendation could accelerate development of a bigger experiment. "It's certainly putting it in a different category of probability than it has been in," says Timothy Hallman, DOE's associate director for nuclear physics.

In the meantime, the new plan's top recommendation is for U.S. nuclear physicists to fully exploit the three major facilities they already have. Jefferson Lab is completing a \$338 million upgrade to its Continuous Electron Beam Accelerator Facility, which scientists use to probe the innards of protons and neutrons. Physicists at Michigan State University in East Lansing are building the \$730 million Facility for Rare Isotope Beams, which starting in 2022 will generate and study exotic nuclei. And since 2000, researchers at Brookhaven National Laboratory in Upton, New York, have used their Relativistic Heavy Ion Collider (RHIC) to smash heavy nuclei and create a plasma of the quarks and gluons that make up their protons and neutrons—like the one that filled the infant universe.

Just 2 years ago, it seemed unlikely that DOE could afford to run all three facilities, and researchers decided to sacrifice RHIC if they had to (*Science*, 1 February 2013, p. 498). But DOE's nuclear physics budget rebounded, and the report says it now should be possible to run all of them. "We want to run RHIC for another 5 to 7 years," says NSAC chair Donald Geesaman of Argonne National Laboratory in Lemont, Illinois.

The report also recommends the United States build a new collider to probe the proton and neutron far more deeply by smashing electrons into protons or heavier nuclei. But that billion-dollar electron-ion collider could not be completed until the late 2020s, the report says. "I think it's defining the goal," says Patricia Dehmer, acting director of DOE's \$5.1 billion Office of Science.

To afford the whole plan, the report estimates that DOE's nuclear physics budget must increase annually by 1.6% above inflation over the next 10 years, or between 3.5% and 4% in absolute terms. That may be a tall order, Dehmer cautioned—although she noted that the budget has grown at that pace in recent years. If the budget just inches up with inflation, the report notes, the new collider will have to wait even longer. ■

Q&A

Shining a light on sexual harassment in astronomy

Astronomer Joan Schmelz talks about what needs to change in the wake of the Marcy case

By Daniel Clery

The field of astronomy has been reeling since one of its most prominent members, exoplanet pioneer Geoff Marcy, was found guilty of sexually harassing female students at the University of California, Berkeley, over a decade. The university did not publish the results of its 6-month investigation, triggered by complaints from four former students, and it simply admonished Marcy to change his behavior. But a 9 October article in the online publication BuzzFeed and pressure from Berkeley students and faculty as well as the wider astronomy community persuaded Marcy to resign from his Berkeley professorship and other positions.

Astronomer Joan Schmelz, chair of the American Astronomical Society's (AAS's) Committee on the Status of Women in Astronomy for 6 years until she finished her second term in August, played a key role in identifying victims of Marcy's activities and letting them know they were not alone. *Science* spoke with her this week. Her comments have been edited for clarity and brevity.

Q: You and others started looking into Marcy after complaints about his behavior at the 2010 AAS meeting. What did you find out?

A: We found out that there were many other targets of Marcy. That he used similar techniques to approach them, to befriend them, to get close to them, all with the idea that he was mentoring them, that women in astronomy was an important topic for him. [Marcy has not responded to *Science's* request for comment.]

I started hearing from women who couldn't figure out what to do at their own universities and more than one of these women were contacting me about Marcy. My goal was always to help them

to do what was right for them. And in many cases that was not filing a Title IX complaint. [Title IX is the federal law covering sexual discrimination in publicly funded organizations.]

I reached out to some friends and colleagues of mine who were or had been at Berkeley, and we started to identify some women who were targeted by Marcy. In almost every case, they thought their interaction with Marcy was the only one; they did not know about the other women involved. So I think it was, at least for these four complainants, really the fact that there were other women and there was this long pattern of behavior going back many years that convinced them they should file with the Title IX office.



Joan Schmelz says too much burden is put on the shoulders of women.

Q: Marcy's behavior has been called an "open secret" in the community. Why has it taken so long to come to light?

A: Part of the problem is the way we handle all of this in terms of Title IX: All of the burden is put on the shoulders of the young women who were targeted. There is not a real avenue for, say, senior men who knew the secret or who knew about the behavior to intervene in any sort of sanctioned way. That is one of the things we should see if we can change.

It is not very common in academia that young women will come forward [with Title IX complaints] because they correctly fear retribution. They are in the most vulnerable phases of their career. They are relying on their advisers for letters of recommendation to get into graduate school, to get their first job. It is very much like the old medieval master-apprentice system, where you are completely reliant on these letters. That's a system that's worked in academia for hundreds of years, and I don't know how we're going to change that. But it is a system that can breed this sort of unprofessional behavior.

PHOTO: COURTESY OF JOAN SCHMELZ

Q: Will this case encourage other victims to come forward?

A: I'm not aware of anyone filing a Title IX complaint. I know I've received emails from people wanting advice, and those are all ongoing.

Marcy is not the only sexual harasser in astronomy. In this particular case, there were a number of victims who could be identified and therefore they could talk to each other and get support from each other. That's not necessarily as easy to do in some of the other cases. Even in the Marcy case it was incredibly difficult. It took many years to get to this point.

Q: Institutions have a conflict of interest in disciplining their own faculty. Is there another way complaints can be handled?

A: One of the problems with the current system is that one individual complaint feels very much like a he-said/she-said. The he in this situation is almost always a professor, and the she is always a student or postdoc. As he has a lot more power than she, that means that she doesn't come forward. But there's no way to account for many shes. There's no office that will keep a confidential complaint on file until, for example, they get a second confidential complaint from another person.

That's one of the things I'd like to see going forward. The Committee on the Status of Women in Astronomy had been acting like that, and I had been acting like that in a very informal way. That's not the best way to do it or the right way to do it, but right now it's the only way to do it.

Some campuses are much better than others at having offices where women can go and speak confidentially about this, before they would ever go to the Title IX office and file an official complaint. Some campuses are also better at making students aware of their options and resources. It seems that the Berkeley campus was not very good at that.

Q: Is there anything about astronomy that makes harassment a particular problem?

A: I don't think astronomy is any better or any worse than any other academic field that is male-dominated. I think that for a number of years we have been shining a light on this problem, and it's harder for the problem to hide in the shadows if you're shining a light on it.

Q: Will the field's collective action over this case have a galvanizing effect to tackle the issue of harassment?

A: I hope we all find a way to use this incident to build momentum toward changing the situation. We just have to move away from the status quo. Almost every sexual harassment survivor that I have talked to has always said to me, "I want the problem to stop." It's not that they're looking for revenge or punishment; they just want the problem to stop. They want to be treated like everybody else and do their science. If anything positive can come out of this, I hope it is awareness that we can all work together to make our community a safer place for everyone. ■

NEUROSCIENCE

Second bid for brain observatory

Workshop explores facilities to give neuroscience access to high-tech tools

By Emily Underwood

Bobby Kasthuri appreciates the value of high-tech tools for studying the brain. While working on a master's degree at Harvard University, he had access to one of the country's most powerful electron microscopes, able to image individual synapses in slices of mouse brain. Now, he is at Argonne National Laboratory (ANL) in Lemont, Illinois, which has its own cutting-edge electron microscope, plus an accelerator 1.6 kilometers around that can perform x-ray microscopy on brain tissue.

Kasthuri, who is continuing to image nanoscale connections in mouse and human brains, wants others to share his good fortune. Last Friday at ANL, prior to the Society for Neuroscience meeting in nearby Chicago, he and colleagues hosted nearly 100 researchers and government officials to discuss a bold proposal: the creation of a National Brain Observatory, a network of neurotechnology centers tied to the Department of Energy's (DOE's) National Laboratories.

The call to equip neuroscientists with the type of big, expensive facilities historically built for physicists and astronomers dates from 3 years ago, when Rafael Yuste of Columbia University and five other neuroscientists drafted the proposal for what would ultimately become President Obama's Brain Research through Advancing Innovative Neurotechnologies (BRAIN) Initiative. They argued that mapping the intricacies of the brain and managing the resulting data requires "big science" investments similar to national telescopes and particle accelerators. But the first round of federal BRAIN funding—roughly \$100 million—went almost exclusively for technology development by individual labs, a "tepid" response, Yuste says. Last week, he and the same five colleagues made their case again in the journal *Neuron* and at the ANL workshop. "Something has been left out from the orig-

Astronomer Geoff Marcy has been a leader in the hunt for exoplanets.



PHOTO: NIKLAS HALLEN/GETTY IMAGES

inal vision, and that is why we are making all this noise,” Yuste says.

At the meeting, attendees discussed four broad goals: expanding access to large-scale electron microscopes; providing fabrication facilities for new, nanosized electrode systems that can monitor thousands of neurons at once; developing new optical and magnetic resonance technologies for mapping brain activity; and finding new ways to analyze and store the staggering amount of data that detailed brain studies can produce. Participants differed, however, about just how much federal support they will need. Fabricating nanoelectrodes, for example, will require the same types of costly foundries that build semiconductor chips, says Michael Roukes, a physicist at the California Institute of Technology in Pasadena. But for data storage and analysis, distributed networks of programmers who create and share code might ultimately be more effective than government-run facilities, says neuroscientist Jeremy Freeman of Janelia Research Campus in Ashburn, Virginia.

Either way, building support for the initiative among neuroscientists and at funding agencies will require “an extraordinary scientific mission, something where you sit up and say we have to do this,” says Clay Reid, a neuroscientist at the Allen Institute for Brain Science in Seattle, Washington. One such mission—creating a map of roughly half of the human brain’s 100,000 km of axons, the threadlike extensions that project from neurons—generated widespread enthusiasm at the meeting. Created by imaging micron-thick slices of a postmortem human brain, the map would not show synapses for the entire brain, but would reveal every neuron, axon, and potentially hard-to-distinguish glial cell, Kasthuri says.

It would “push the envelope” of current optical imaging and data analysis, and create a core of trained staff that could support later projects, said David Kleinfeld, a neuroscientist and physicist at the University of California, San Diego. It would also be the first complete map of the human brain’s neural pathways, which would be useful for physicians and surgeons and help “ground truth” techniques such as functional magnetic resonance imaging, which lack anatomical detail, says Jeffrey Lichtman, a neuroscientist at Harvard University.

Still murky is how a National Brain Observatory would be organized and how much it would cost. It could harness existing electron microscopes and x-ray sources at DOE and university facilities, but Yuste says that even so, the initiative would require at least \$50 million per year, on top of existing BRAIN funding. And any effort will have to serve DOE’s mission of advancing basic physical and computational science, notes Brad Aimone, a computational neuroscientist at Sandia National Laboratories in Albuquerque, New Mexico.

Long-time neuroscience supporter Representative Chaka Fattah (D-PA), who helped secure \$3 million in National Science Foundation (NSF) funding for developing the National Brain Observatory project this year, attended the workshop and told attendees that the idea has bipartisan support. And DOE seems on board. ANL Director Peter Littlewood has asked NSF for roughly \$1 million annually for 5 years to develop the concept through collaborations between the lab and the University of Chicago in Illinois. Now, it’s up to the neuroscience community, Congress, and the White House to determine whether the National Brain Observatory becomes more than a lofty vision. ■

CELL BIOLOGY

Protein ‘drops’ may seed brain disease

Cellular droplets promote vital biochemistry—but may dangerously solidify

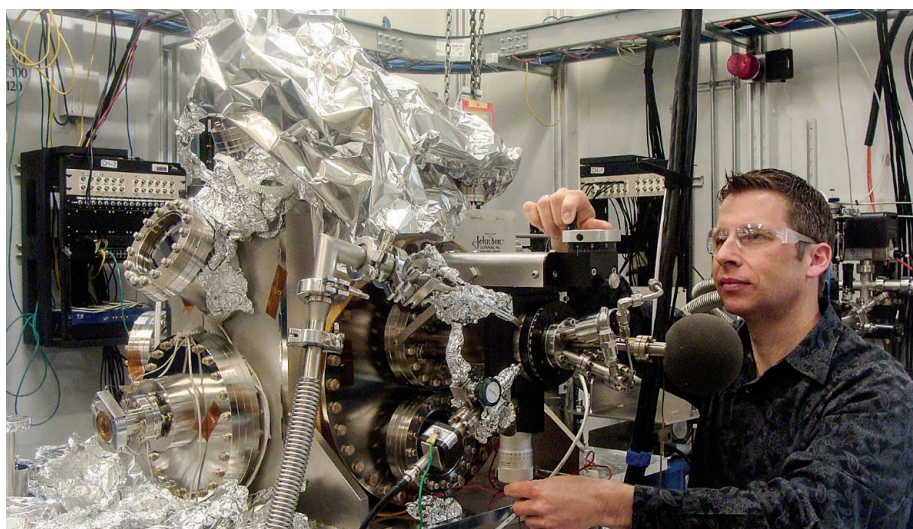
By Ken Garber

One day last year, a graduate student brought molecular geneticist Paul Taylor an ice bucket holding a test tube that contained a white solution. When she lifted the tube from the bucket, the solution became clear—and it went white again when she put it back in. Taylor was baffled at first, because the tube held a dissolved protein, and proteins are normally clear in solution. So he examined the white version under a microscope. The protein had apparently “demixed” out of water, forming tiny droplets in a process analogous to the separation of vinaigrette into oil and vinegar. What made the observation especially interesting was the identity of the protein: It was the normal product of a gene that, when mutated, Taylor’s team had found to cause amyotrophic lateral sclerosis (ALS), or Lou Gehrig’s disease.

Taylor is not the only biologist captivated by these liquid transformations. Over the past year, several other groups have independently seen protein droplets form in test tubes and in cells, and four papers on the unusual phenomenon have just been published in *Cell* and *Molecular Cell*. Already, investigators are proposing that droplet formation is a key part of the machinery regulating gene expression in cells. When the process goes awry, they suggest, it can lead to the solid protein aggregates that are a hallmark of ALS and other neurodegenerative diseases.

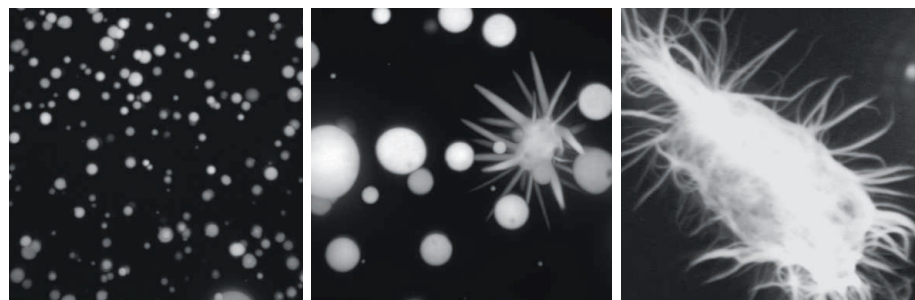
“Together the papers are a tour de force and really a very large advance,” says James Shorter, a cell biologist at the University of Pennsylvania.

Steve McKnight, a biochemist at the University of Texas Southwestern Medical Center (UTSW) in Dallas, agrees that the field is on the cusp of something profound. “We are seeing the first glimpses of ... a whole new understanding of how cells are organized.”



An Argonne National Laboratory physicist works on a prototype high-resolution microscope, the type of tool neuroscientists would have access to at a National Brain Observatory.

PHOTO: ARGONNE NATIONAL LABORATORY/FLICKR



Mutant proteins linked to some cases of amyotrophic lateral sclerosis transition from normal liquid droplets to various structures (bottom, left to right, and top), which may lead to aggregates that cause disease.

The new work addresses a biological puzzle. Gene expression, and thus most of biology, depends on two large families of proteins: transcription factors, which turn on genes, and RNA-binding proteins (RBPs), which transport RNA to the correct parts of the cell so that they're in the right place at the right time to be translated into proteins. "The crown jewels of biology," McKnight calls these families. Oddly, many of these proteins have tails that resemble the self-propagating infectious particles called prions, which cause mad cow disease and, in humans, Creutzfeldt-Jakob disease. But why? "It's been an enigma," McKnight says.

The new papers provide an answer, at least for RBPs: The prionlike domains

drive the assembly of RBPs into the droplets that fascinated Taylor. These droplets, he and others hypothesize, serve to protect and concentrate the proteins and their attached RNAs, keeping them from dispersing into the cell fluid and ferrying them intact to their proper cellular destinations.

Such structures, speculates Tony Hyman, a cell biologist at the Max Planck Institute of Molecular Cell Biology and Genetics in Dresden, Germany, and co-author of one of the new papers, may have played a key role in the emergence of life more than 3 billion years ago by protecting its chemical reactions from a hostile environment, before cell membranes came about. "As soon as organized molecules would have formed in a primitive soup they

would have started to phase separate to form reaction centers," he says.

But the proteins' ability to assemble into droplets has a potentially dangerous flip side—they can then solidify in a manner that causes disease. In the 27 August and 24 September issues of *Cell*, Hyman's and Taylor's groups reported that given enough time and under the right conditions, RBP droplets can become fibrous structures resembling those that aggregate in the brain cells of people with ALS and Alzheimer's disease. The teams also found that abnormal RBPs, encoded by mutant genes known to cause ALS, are quicker to aggregate. "This work is important because it provides a novel mechanism for formation of pathological aggregates," says Ben Wolozin, an Alzheimer's disease researcher at Boston University.

However, the aggregation has been seen only in purified RBPs in solution, not in living cells. "We've tried very hard," Hyman says. "In vivo they don't convert from liquid to solid." He suspects that the molecular machinery that eliminates aberrant proteins normally prevents aggregation, and that dangerous aggregates appear when quality control mechanisms are weakened by aging or disease.

The study of protein droplets has become a lively subfield. In the 15 October issue of *Molecular Cell*, a UTSW–University of Colorado, Boulder, collaboration provides independent confirmation that the droplets assemble from prionlike protein tails. And in the same issue, a Brown University team used nuclear magnetic resonance to show that RBPs and RNAs are not so much enclosed by the droplet, but rather the RBPs interact with each other's prionlike tails to assemble it.

Just how the prionlike domains initially drive droplet formation remains a mystery. Taylor thinks that weak bonding between the domains is enough to make it happen. McKnight's lab 3 years ago was the first to suggest a role for these prionlike domains. In his hands, instead of droplets, they formed protein fibers, with similarities to disease aggregates but looser. He doesn't dispute the droplet work: "They're finding neat things, cool things, and if there's a controversy it'll be sorted out in short order."

Drug companies are already paying close attention, because understanding how the droplets solidify in disease could lead to new ways to treat neurodegeneration. "I have been swamped with requests to teach pharmaceutical companies how to target this process," Taylor says. "This is the biggest thing to happen in cell biology in my career." ■

REGULATORY SCIENCE

Europe's food watchdog embraces transparency

Industry uneasy at European Food Safety Authority pledge to make data underlying its decisions public

By Tania Rabesandratana, in Milan, Italy

Europe's transparency advocates are hoping for a new victory in the battle for the public's right to scrutinize the data behind regulatory decisions. Last year, the European Medicines Agency (EMA) in London changed its rules to make public the massive amounts of clinical trial data that it receives as part of marketing applications. The move will allow anyone to see the evidence underpinning EMA's decisions to allow (or reject) medicinal products on the European market.

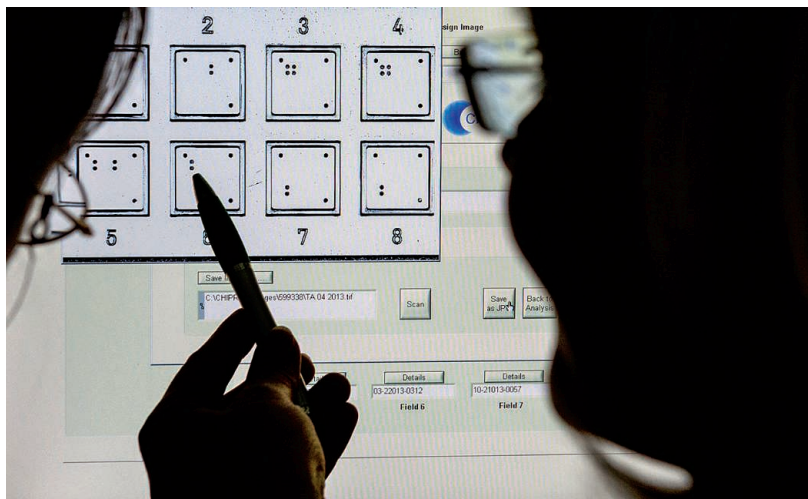
Now, a sister agency in Parma, Italy, says it will follow EMA's example. The European Food Safety Authority (EFSA) plans to make public the data it uses to assess whether products such as pesticides, food additives, and genetically modified (GM) crops are safe to use, eat, or grow. "We want to make our data as open as possible and make it reusable," EFSA Executive Director Bernhard Url pledged on 14 October at the opening session of EFSA's second scientific conference here. Industry, however, worries that the openness—which will extend to detailed industry reports—could threaten trade secrets, and some say it could stir unwarranted concerns.

EFSA itself cannot decide whether a product should be sold in the European Union, but it produces "opinions," written by panels of scientists, that form the basis of such decisions by the European Commission. EFSA opinions rely partly on company-sponsored studies that sometimes aren't published; even when they are, the raw data usually are not, making it harder for watchdogs to examine and critique a study.

Groups like the Corporate Europe Observatory, which seeks to expose undue industry lobbying, and the Pesticide Action

Network Europe (PAN Europe) have pressured EFSA to publish the content of all applications submitted by manufacturers, in a usable format, just as EMA is preparing to do. (Pesticides and GM foods are among their targets.) "There is no reason for EFSA not to follow EMA's footsteps," says Martin Dermine, honey bee project coordinator at PAN Europe.

EFSA will begin doing so next year, sharing data submitted by E.U. member states—a "treasure trove" that includes information on antimicrobial resistance, food consump-



Food samples are tested for horse meat at a lab in Germany. The European Food Safety Authority plans to begin sharing data submitted by E.U. countries next year.

tion, and pesticide residues, Url tells *Science*. But it will take several years before EFSA starts sharing company data filed as part of the product risk assessments.

Dermine is unhappy about the slow pace. The data and studies that EFSA deals with are easier to share than clinical trials, he says, because they usually don't include sensitive patient information. Dermine is concerned that EFSA's pledges to make openness "intelligent" or "useful" may mean that there will be limits to what will be released.

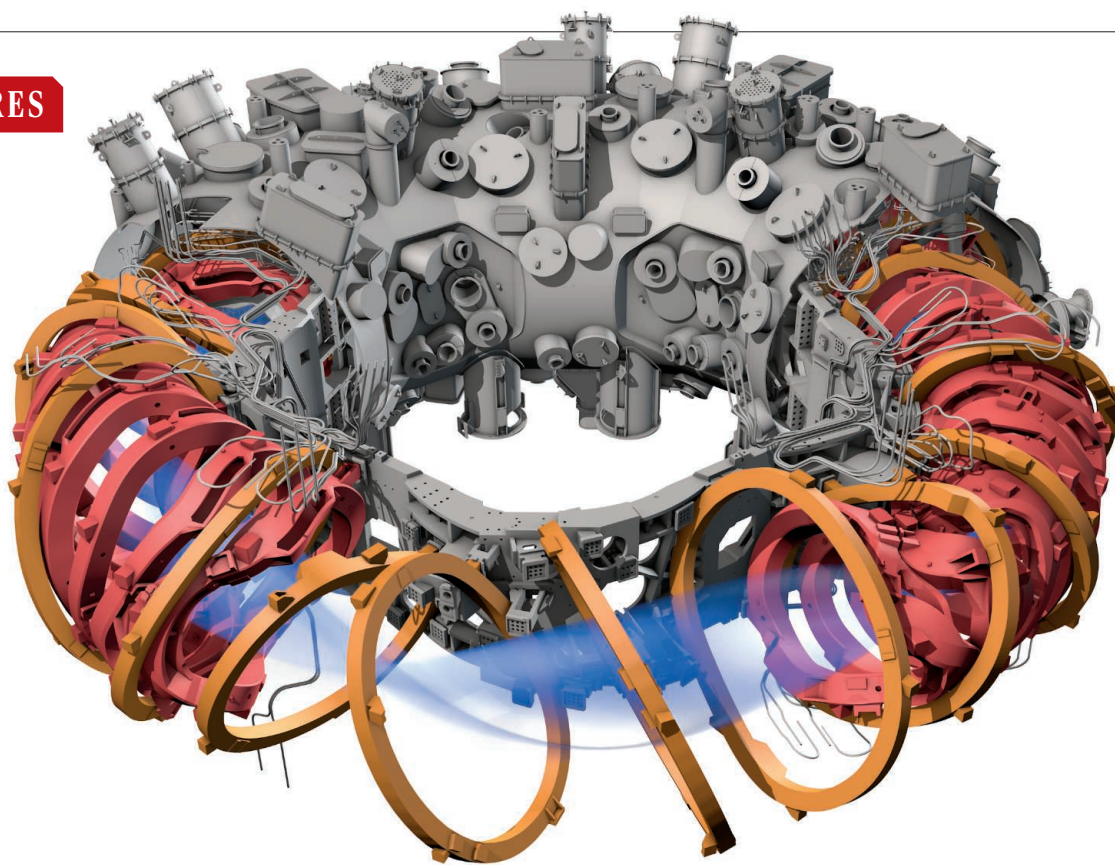
EFSA's scientific adviser Hubert Deluyker acknowledges that his agency is facing resistance from industry. Companies say competitors might run with their trade secrets. Another worry is that consumers or activists

could zoom in on scientific details that may seem scary but are of little importance. "Industry needs to know in advance whether, how, and when data submitted to public authorities will be disclosed to third parties," says a spokesperson for EuropaBio, a lobby group for the biotech industry. Although EuropaBio supports the drive toward openness, the spokesperson says, EFSA should first focus on better explaining its work to the public, and "on better protecting information provided by applicants from misuse."

EMA's experiences so far suggest that industry will adapt. Some drug companies are still dragging their feet, EMA's Senior Medical Officer Hans-Georg Eichler told last week's meeting, but most executives have now "understood that the train has left the station." EMA moved from "acrimonious" discussions with companies that refused to share clinical trial reports in the name of commercial confidentiality to discussing which elements in these reports can be confidential. "It started as a nasty story but may have a very happy end," Eichler says. "All the research enterprise will become more efficient if [researchers] can learn from the mistakes their predecessors have made."

Jean-Louis Bresson, a nutrition researcher at Paris Descartes University, says there is a risk that releasing raw data will cause misunderstandings, health scares, and rumors—but EFSA "cannot not do it." Bresson, who sits on EFSA's Dietetic Products, Nutrition and Allergies panel, says patients and consumers have "the right to know."

But transparency alone is not enough to improve regulation, says Axel Decourtye, an ecotoxicologist at France's National Institute for Agricultural Research whose studies on the effects of neonicotinoid pesticides on honey bees contributed to a partial ban on three such compounds in the European Union (*Science*, 20 April 2012, p. 348). EFSA also needs to collect the right data, he says. Neonicotinoids were approved based partly on studies that looked at the effect of a single pesticide dose on adult bees, Decourtye says; the studies should also have included information about chronic effects at low doses and effects on larvae. "Transparency is all very well," Decourtye says, "but we need to make sure that the data is relevant in the first place." ■



TWISTED LOGIC

Germany completes the epic construction of the reactor designed in hell. Its tortuous shape may point the way forward for fusion

By Daniel Clery in Greifswald, Germany

If you've heard of fusion energy, you've probably heard of tokamaks. These doughnut-shaped devices are meant to cage ionized gases called plasmas in magnetic fields while heating them to the outlandish temperatures needed for hydrogen nuclei to fuse. Tokamaks are the workhorses of fusion—solid, symmetrical, and relatively straightforward to engineer—but progress with them has been plodding.

Now, tokamaks' rebellious cousin is stepping out of the shadows. In a gleaming research lab in Germany's northeastern corner, researchers are preparing to switch on a fusion device called a stellarator, the largest ever built. The €1 billion machine, known as Wendelstein 7-X (W7-X), appears now as a 16-meter-wide ring of gleaming metal bristling with devices of all shapes

and sizes, innumerable cables trailing off to unknown destinations, and technicians tinkering with it here and there. It looks a bit like Han Solo's Millennium Falcon, towed in for repairs after a run-in with the Imperial fleet. Inside are 50 6-tonne magnet coils, strangely twisted as if trampled by an angry giant.

Although stellarators are similar in principle to tokamaks, they have long been dark horses in fusion energy research because tokamaks are better at keeping gas trapped and holding on to the heat needed to keep reactions ticking along. But the Dali-esque devices have many attributes that could make them much better prospects for a commercial fusion power plant: Once started, stellarators naturally purr along in a steady state, and they don't spawn the poten-

tially metal-bending magnetic disruptions that plague tokamaks. Unfortunately, they are devilishly hard to build, making them perhaps even more prone to cost overruns and delays than other fusion projects. "No one imagined what it means" to build one, says Thomas Klinger, leader of the German effort.

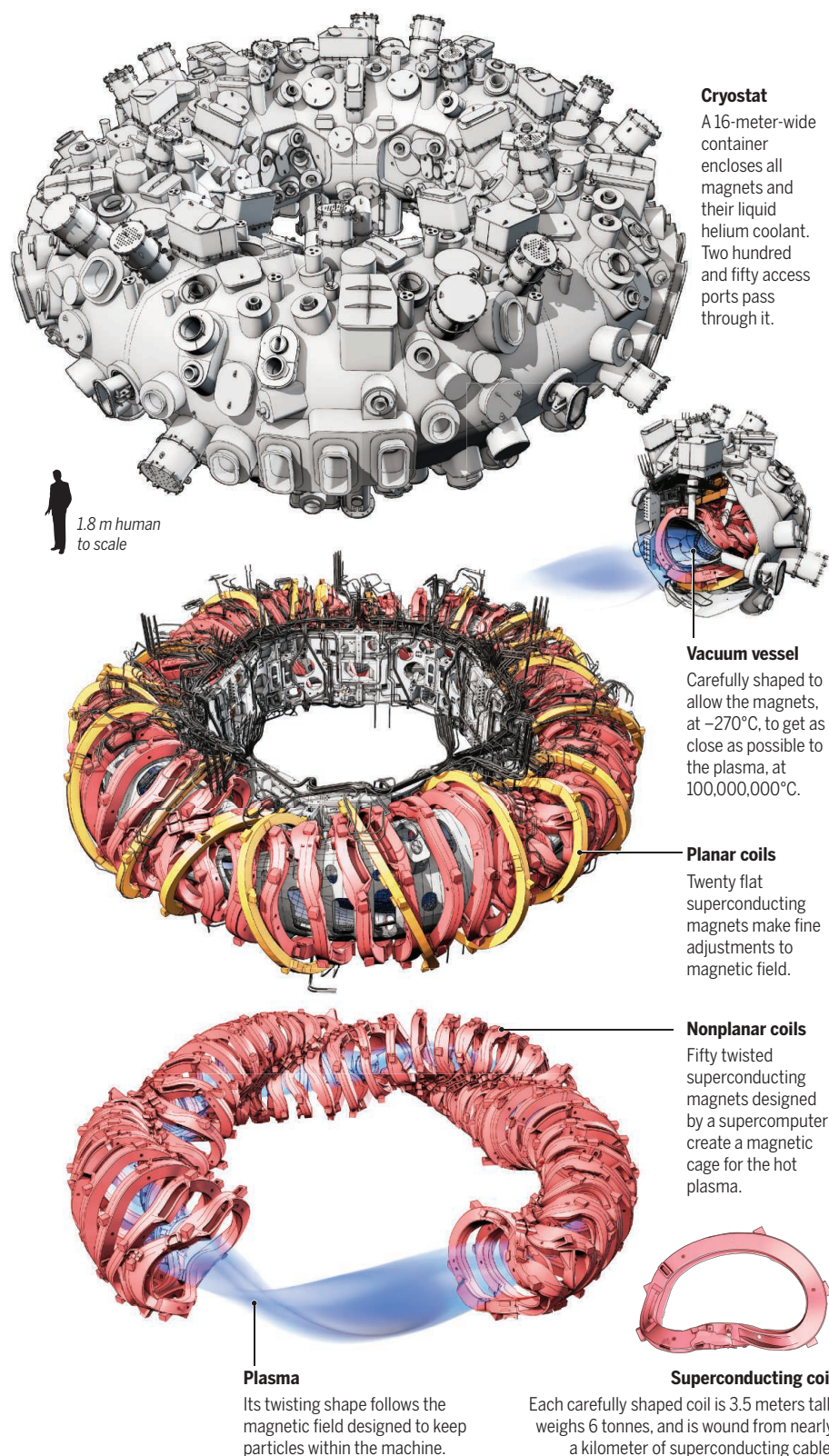
W7-X could mark a turning point. The machine, housed at a branch of the Max Planck Institute for Plasma Physics (IPP) that Klinger directs, is awaiting regulatory approval for a startup in November. It is the first large-scale example of a new breed of supercomputer-designed stellarators that have had most of their containment problems computed out. If W7-X matches or beats the performance of a similarly sized tokamak, fusion researchers may have to reassess the future course of

VIDEO

To watch a video about stellarators, go to http://scim.ag/vid_6259.

A fusion reactor with a twist

Wendelstein 7-X, the first large-scale optimized stellarator, took 1.1 million working hours to assemble, using one of the most complex engineering models ever devised, and must withstand huge temperature ranges and enormous forces.



their field. “Tokamak people are waiting to see what happens. There’s an excitement around the world about W7-X,” says engineer David Anderson of the University of Wisconsin (UW), Madison.

STELLARATORS FACE THE SAME challenge as all fusion devices: They must heat and hold on to a gas at more than 100 million degrees Celsius—seven times the temperature of the sun’s core. Such heat strips electrons from atoms, leaving a plasma of electrons and ions, and it makes the ions travel fast enough to overcome their mutual repulsion and fuse. But it also makes the gas impossible to contain in a normal vessel.

Instead, it is held in a magnetic cage. A current-carrying wire wound around a tube creates a straight magnetic field down the center of the tube that draws the plasma away from the walls. To keep particles from escaping at the ends, many early fusion researchers bent the tube into a doughnut-shaped ring, or torus, creating an endless track.

But the torus shape creates another problem: Because the windings of the wire are closer together inside the hole of the doughnut, the magnetic field is stronger there and weaker toward the doughnut’s outer rim. The imbalance causes particles to drift off course and hit the wall. The solution is to add a twist that forces particles through regions of high and low magnetic fields, so the effects of the two cancel each other out.

Stellarators impose the twist from outside. The first stellarator, invented by astrophysicist Lyman Spitzer at Princeton University in 1951, did it by bending the tube into a figure-eight shape. But the lab he set up—the Princeton Plasma Physics Laboratory (PPPL) in New Jersey—switched to a simpler method for later stellarators: winding more coils of wire around a conventional torus tube like stripes on a candy cane to create a twisting magnetic field inside.

In a tokamak, a design invented in the Soviet Union in the 1950s, the twist comes from within. Tokamaks use a setup like an electrical transformer to induce the electrons and ions to flow around the tube as an electric current. This current produces a vertical looping magnetic field that, when added to the field already running the length of the tube, creates the required spiraling field lines.

Both methods work, but the tokamak is better at holding on to a plasma. In part that’s because a tokamak’s symmetry gives particles smoother paths to follow. In stellarators, Anderson says, “particles see lots of ripples and wiggles” that cause many of them to be lost. As a result, most

fusion research since the 1970s has focused on tokamaks—culminating in the huge ITER reactor project in France, a €16 billion international effort to build a tokamak that produces more energy than it consumes, paving the way for commercial power reactors.

But tokamaks have serious drawbacks. A transformer can drive a current in the plasma only in short pulses that would not suit a commercial fusion reactor. Current in the plasma can also falter unexpectedly, resulting in “disruptions”: sudden losses of plasma confinement that can unleash magnetic forces powerful enough to damage the reactor. Such problems plague even up-and-coming designs such as the spherical tokamak (*Science*, 22 May, p. 854).

Stellarators, however, are immune. Their fields come entirely from external coils, which don’t need to be pulsed, and there is no plasma current to suffer disruptions. Those two factors have kept some teams pursuing the concept.

The largest working stellarator is the Large Helical Device (LHD) in Toki, Japan, which began operating in 1998. Lyman Spitzer would recognize the design, a variation on the classic stellarator with two helical coils to twist the plasma and other coils to add further control. The LHD holds all major records for stellarator performance, shows good steady-state operation, and is approaching the performance of a similarly sized tokamak.

Two researchers—IPP’s Jürgen Nührenberg and Allen Boozer of PPPL (now at Columbia University)—calculated that they could do better with a different design that would confine plasma with a magnetic field of constant strength but changing direction. Such a “quasi-symmetric” field wouldn’t be a perfect particle trap, says IPP theorist Per Helander, “but you can get arbitrarily close and get losses to a satisfactory level.” In principle, it could make a stellarator perform as well as a tokamak.

The design strategy, known as optimization, involves defining the shape of magnetic field that best confines the plasma, then designing a set of magnets to produce the field. That takes considerable computing power, and supercomputers weren’t up to the job until the 1980s.

The first attempt at a partially optimized stellarator, dubbed Wendelstein 7-AS, was built at the IPP branch in Garching near Munich and operated between 1988 and 2002. It broke all stellarator records for machines of its size. Researchers at UW Madison set

out to build the first fully optimized device in 1993. The result, a small machine called the Helically Symmetric Experiment (HSX), began operating in 1999. “W7-AS and HSX showed the idea works,” says David Gates, head of stellarator physics at PPPL.

That success gave U.S. researchers confidence to try something bigger. PPPL began building the National Compact Stellarator Experiment (NCSX) in 2004 using an optimization strategy different from IPP’s. But the difficulty of assembling the intricately shaped parts with millimeter accuracy led to cost hikes and schedule slips. In 2008, with 80% of the major components either built or purchased, the Department of Energy pulled the plug on the project



Wendelstein 7-X’s bizarrely shaped components must be put together with millimeter precision. All welding was computer controlled and monitored with laser scanners.

(*Science*, 30 May 2008, p. 1142). “We flat out underestimated the cost and the schedule,” says PPPL’s George “Hutch” Neilson, manager of NCSX.

BACK IN GERMANY, the project to build W7-X was well underway. The government of the recently reunified country had given the green light in 1993 and 1994 and decided to establish a new branch institute at Greifswald, in former East Germany, to build the machine. Fifty staff members from IPP moved from Garching to Greifswald, 800 kilometers away, and others made frequent trips between the sites, says Klinger, director of the Greifswald branch. New hires brought staff numbers up to today’s 400. W7-X was scheduled to start up in 2006 at a cost of €550 million.

But just like the ill-fated American NCSX, W7-X soon ran into problems. The machine

has 425 tonnes of superconducting magnets and support structure that must be chilled close to absolute zero. Cooling the magnets with liquid helium is “hell on Earth,” Klinger says. “All cold components *must* work, leaks are not possible, and access is poor” because of the twisted magnets. Among the weirdly shaped magnets, engineers must squeeze more than 250 ports to supply and remove fuel, heat the plasma, and give access for diagnostic instruments. Everything needs extremely complex 3D modeling. “It can only be done on computer,” Klinger says. “You can’t adapt anything on site.”

By 2003, W7-X was in trouble. About a third of the magnets produced by industry failed in tests and had to be sent back. The forces acting on the reactor structure turned out to be greater than the team had calculated. “It would have broken apart,” Klinger says. So construction of some major components had to be halted for redesigning. One magnet supplier went bankrupt. The years 2003 to 2007 were a “crisis time,” Klinger says, and the project was “close to cancellation.” But civil servants in the research ministry fought hard for the project; finally, the minister allowed it to go ahead with a cost ceiling of €1.06 billion and first plasma scheduled for 2015.

After 1.1 million construction hours, the Greifswald institute finished the machine in May 2014 and spent the past year carrying out commissioning checks, which W7-X passed without a hitch. Tests with electron beams show that the magnetic field in the still-empty reactor is the right shape. “Everything looks, to an extremely high accuracy, exactly as it should,” IPP’s Thomas

Sunn Pedersen says.

Approval to go ahead is expected from Germany’s nuclear regulators by the end of this month. The real test will come once W7-X is full of plasma and researchers finally see how it holds on to heat. The key measure is energy confinement time, the rate at which the plasma loses energy to the environment. “The world’s waiting to see if we get the confinement time and then hold it for a long pulse,” PPPL’s Gates says.

Success could mean a course change for fusion. The next step after ITER is a yet-to-be-designed prototype power plant called DEMO. Most experts have assumed it would be some sort of tokamak, but now some are starting to speculate about a stellarator. “People are already talking about it,” Gates says. “It depends how good the results are. If the results are positive, there’ll be a lot of excitement.” ■



OUT OF THE DARKNESS

Defying expectations, cataract surgery in Indian children is endowing them with vision—and shedding light on how the brain learns to see

By **Rhithu Chatterjee**, in New Delhi; photography by **Graham Crouch**

Manoj Kumar Yadav came into this world with cataracts. In developed countries, a simple surgery cures this disabling eye affliction within the first few months of life. But like the vast majority of people in India, Yadav was born in a village, with limited access to health care. His parents are poor and uneducated. They didn't even realize their infant son was blind until he began to bump into things while crawling. Years later, when regional doctors examined Yadav, they told him he

would never see. "So we gave up," recalls Yadav, now 22. "We thought there was no point in running around anymore trying to find treatment."

Then in 2011, a team of eye specialists from New Delhi visited Yadav's village in Uttar Pradesh state. They screened him and other blind children and kindled hope that Yadav might someday be able to see after all. That August, he and his father took a 13-hour train journey to India's capital. Here at the Dr. Shroff Charity Eye Hospital, a surgeon excised his cataract-ridden lenses and slipped in synthetic ones in their place.

When the doctors removed the bandages a day later, Yadav's world was filled with light, and shapes that to him were inscrutable. He couldn't tell people from objects, or where one thing ended and another began. His brain, deprived of information from his eyes for 18 years, didn't know what to make of the flood of visual stimuli. But over the coming months, his brain gradually learned to interpret the signals it was receiving from his eyes, and the blurry and confusing world began to come into focus.

Yadav is among hundreds of blind children, teenagers, and young adults who are



Manoj Yadav, 22, reads while visiting a hostel in Gorakhpur, a small city in northern India. Born blind in both eyes, Yadav began training his brain to see in 2011 after cataract surgery.

now able to see thanks to a project called Prakash, which means “light” in Sanskrit. India may have the largest number of blind children in the world. Estimates range from 360,000 to nearly 1.2 million. The vast majority live in rural areas, their quality of life worsened by poverty, lack of access to health care, and a dearth of facilities for the disabled. Nearly 40% of these children are thought to have preventable or treatable blindness, caused by congenital cataracts, damaged corneas, and eye infections.

Led by neuroscientist Pawan Sinha, Project Prakash began in 2004 as a humanitarian effort to address this problem. But it also had a scientific goal. Sinha, based at the Massachusetts Institute of Technology in Cambridge, hypothesized that the newly sighted children could help answer a question that had long intrigued him: How does the brain learn to see? Initially

funded by the U.S. National Institutes of Health as an exploratory grant, Prakash has since grown into a groundbreaking effort in neuroscience. For years, physicians assumed that once a blind person passed a critical age in early childhood without vision, their brain would never be able to make sense of the visual world. Through patients like Yadav, Prakash has demolished that assumption.

“It took me about one-and-a-half years before I could see everything clearly,” Yadav says. Short and slight, Yadav is polite and soft-spoken, and his eyes restlessly dart back and forth. The condition, nystagmus, is a relic of his congenital blindness. But with the cataracts gone, it doesn’t keep him from seeing. “Now, I can even ride a bicycle through a crowded market,” he says.

Prakash “beautifully demonstrates that there is still room for plasticity and recovery” in patients who have grown up blind, says Olivier Collignon, a neuroscientist at the University of Trento in Italy. That doesn’t mean the newly sighted will be able to see as well as those born sighted, he cautions. “That is not supported by data.”

Still, the surprising capacity of Prakash patients to gain substantial vision is rewriting visual neuroscience. As the medical payoff of their efforts became clear, project leaders have launched a series of studies, from low-tech tests of patients’ responses to visual illusions to functional MRI (fMRI) imaging of their brains reorganizing in response to visual input. While probing how the newly sighted process visual cues, project scientists are peeling away layers of mystery about which aspects of sight come preprogrammed and which are shaped by experience.

OPHTHALMOLOGY TEXTBOOKS have long suggested that trying to give sight to teenagers who have been blind since birth is unlikely to succeed. In a series of groundbreaking studies in cats and monkeys that won them the Nobel Prize in Physiology or Medicine in 1981, Torsten Wiesel and David Hubel showed that if the brain is deprived

of visual signals during a critical period soon after birth, vision is impaired for life. There have been no similar experiments in humans for ethical reasons, but scientists assumed our critical window slams shut

between ages 6 and 8. That belief guided surgeons at Shroff, who turned away congenitally blind children older than 8 years.

However, Sinha unearthed a couple of studies from several decades ago that suggested congenitally blind adults could gain at least some vision after cataract surgery. Then in 2002 and 2003, while traveling across India to understand the extent and causes of blindness, Sinha met four individuals, all of whom had had cataracts removed as adolescents and had acquired some vision. The anecdotal evidence was enough to persuade Sinha that, given recent advances in medicine, Project Prakash was worth pursuing, and he convinced the Shroff surgeons to give it a try.

The team’s eye specialists and health workers set up screening camps in rural areas to identify children who could benefit from surgery and nonsurgical interventions like eyeglasses, eye drops, and medication. So

far, more than 1400 children have received nonsurgical care and nearly 500 children and young adults have undergone cataract operations. About half of those patients—the ones that the scientists are convinced were blind from birth—become research subjects.

Their recent studies show that experience isn’t critical for certain visual functions. Instead, the brain appears to be prewired to interpret at least some simple aspects of the visual world. The evidence comes from tests of visual illusions that are also helping settle a longstanding debate about why the brain misinterprets particular kinds of images.

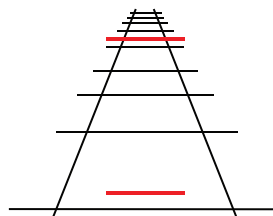
When our perception of an image differs from reality, we experience a visual illusion. Some neuroscientists think the innate wiring of our brains is responsible for illusions; others think they are a product of learning. Resolving this debate has proved difficult, says Susana Martinez-Conde, a neuroscientist at the State University of New York Downstate Medical Center who

Truth from deception

Project Prakash patients are susceptible to these two visual illusions immediately after surgery, suggesting our brains are preprogrammed to misread certain images.

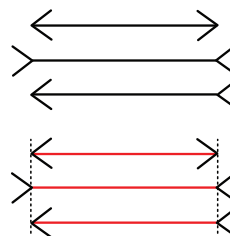
Ponzo illusion

The red lines are equal length, but the “farther” line appears longer.



Müller-Lyer illusion

The horizontal lines are equal length, but the ones capped with inward arrows appear longer.



PODCAST

To hear a podcast with author Rihitu Chatterjee, go to http://scim.ag/pod_6259.

studies illusions. “Babies can’t report on visual experience,” she says. “And it wouldn’t be ethical to deprive a baby of visual experience to test this.” The answer was “anybody’s guess,” she says—until Project Prakash started studying the newly sighted children, whose vision, when first acquired, is close to a newborn’s.

In 2010 and 2011, Sinha’s team picked nine children from those about to undergo cataract surgery. The subjects had been blind since birth, according to the parents and surgeons at Shroff Charity Eye Hospital. Soon after their bandages were removed, the scientists showed them the Ponzo illusion. First demonstrated more than a century ago, this illusion typically involves lines converging on the horizon (like train tracks) and two short parallel lines cutting across them. Although the horizontal lines are identical, the one nearer the horizon looks longer.

The dominant explanation for the Ponzo illusion is that it is a result of the brain’s experience interpreting 2D images as 3D scenes, with the individual elements of images perceived to be at various depths and distances. “That learning leads us to associate these two identical lines in this illusion as being at two different distances from us,” Sinha explains. The brain interprets the line nearer the apparent horizon as farther away and therefore longer than the other identical line.

If the Ponzo illusion were the result of visual learning, the Prakash kids wouldn’t fall for it. But to the team’s surprise, the children were just as susceptible to the Ponzo illusion as were control subjects with normal vision: They consistently found the line closer to the horizon longer, the team reported in *Current Biology* in May.

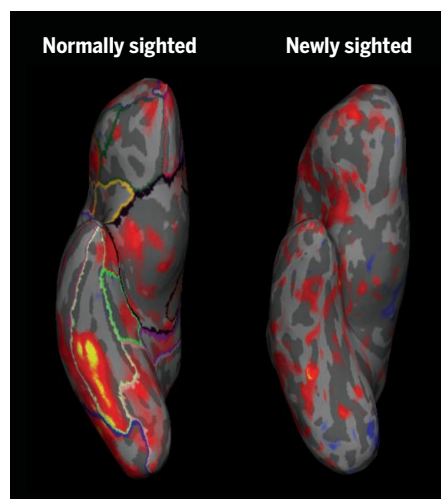
The kids also fell for the Müller-Lyer illusion, a pair of lines with arrowheads on both ends; one set of arrowheads points outward, the other inward toward the line. The line with the inward arrowheads seems longer. “All we can say based on these results is that it’s not experience,” Sinha says. “It’s something else. It’s probably being driven by very simple factors in the image that the brain is probably innately programmed to respond to.”

Martinez-Conde is willing to hazard a guess at how the Müller-Lyer illusion works. Her past research has shown that our eyes tend to notice corners more than straight lines. Perhaps, she says, our brain focuses on the corners of the outward arrowheads, making the line between them look shorter than the line with inward arrowheads. “But this should be taken with a big grain of salt because I don’t have any data to prove it.”

Whatever the mechanism, the new study adds to growing evidence “that we are not

blank slates when we’re born,” Martinez-Conde says. Other evidence comes from a recent study by Amir Amedi, a neuroscientist at the Hebrew University of Jerusalem, and colleagues in which they used fMRI to compare the visual cortex of congenitally blind individuals with that of normally sighted ones. They found that the basic organization of the visual cortex of congenitally blind people is similar to that of the normally sighted, and both have similar connections between different parts of the cortex. That means “we’re born with this machinery for seeing that in a way doesn’t require visual experience to emerge,” Amedi says. “The visual system comes with certain connections and computational biases.”

SUCH PREWIRING MAY HELP the Prakash children gain functional vision in the months following surgery, Amedi specu-



Functional MRI shows activity in the visual cortex of a newly sighted Prakash patient who is starting to perceive human faces. Prakash kids gradually learn to use the same region of the cortex that supports face perception in normally sighted people.

lates. But experience and learning seem to play a bigger role in visual acquisition. “There is growing evidence that [even] adult brains can change in structure and function,” says Brigitte Roeder, a neuropsychologist at the University of Hamburg in Germany. For example, studies have shown that adults who regularly play action video games become better at certain visual tasks, like reading the fine print on a prescription bottle or tracking several friends moving through a crowd.

More relevant to the Prakash children is the ability to create a mental image of a 3D space. “Spatial imagery is very important in our lives,” says Prakash team member Tapan Gandhi, a neuroscientist at the Indian Institute of Technology, Delhi, in New Delhi. “If

I ask you, think about your kitchen, where you’ve kept what, you can visualize it. This is very important for our daily lives.” But blind people aren’t adept at imagining spaces. When tested for this ability using a matrix and movable pegs, Prakash children before surgery perform poorly compared with normally sighted people, Gandhi says. Soon after surgery, however, they start to improve at spatial imagery tasks. Vision must be crucial to helping the brain create mental maps of spaces, he says. And the brain either does not have a critical window for this ability, or the window remains open until much later in life, Gandhi and colleagues reported in the 12 March 2014 issue of *Psychological Science*.

The team found similar adaptability in the ability to distinguish a human face from facelike images. Soon after surgery, Prakash patients cannot tell the difference. That too contradicts dogma: Homing in on faces is one visual capability that scientists think is innate. But after a few weeks, the newly sighted can identify a human face and start to recognize different faces. The team has also found that their patients quickly learn to connect touch with sight. In other words, they are soon able to recognize objects they touched while blindfolded when they see those objects from a distance.

But plasticity has its limits. Collignon and his colleagues studied a group of adults in Canada who were born with cataracts but had corrective surgery before they turned 1. Despite at least 2 decades of restored sight, every individual had slightly impaired vision. Their 3D perception and their ability to detect movement were also compromised, according to unpublished results. The researchers found that the brains of these individuals appear to be wired differently: Unlike normally sighted people, their visual cortexes also process sound, they reported in August in *Current Biology*.

“What is really striking here is that we are speaking of people who are deprived [of sight] for a few weeks to a few months, but it leads to longstanding reorganization of the brain to respond more to sound,” Collignon says. Prakash patients, who are blind for years, are also likely to have their visual cortex reorganized, he says, which could hinder recovery. “They have a trace of their past [in their brains], and their past is blindness,” he says. “These people will never be able to recover vision like someone who’s seen before.”

Sinha’s findings confirm this. The Prakash patients do not develop vision as sharp as normally sighted people’s. “Despite following these kids for several years, we do not find a progression of acuity to normalcy,” Sinha says. That suggests a critical



Manoj Yadav bicycles to work in Gorakhpur, India. "I can ride a bicycle even in a crowded market," he says.

window for acuity that closes sometime before they turn 8—the youngest age Prakash has so far treated.

Yadav's experiences are typical. "I can read newspaper headlines with my glasses," he says. But 4 years since his surgery, he still has trouble reading the finer print in newspapers and books.

The window also seems to close early for contrast sensitivity: the ability to discern contrasts, shades, and patterns, one of the most basic functions of vision. In one test, Sinha's team shows Prakash kids four patterns—a house, a square, an apple, and a circle—and asks them to identify the patterns as they change in size and contrast. Normally sighted people can detect these patterns for a range of sizes, if the contrast is above a certain threshold. For Prakash kids, their contrast sensitivity improves significantly up to several months after surgery, but never reaches normal levels. They remain stuck at detecting a limited range of sizes, and only when the contrast is fairly high.

Taken together, the findings demonstrate that there is no single critical period governing vision, says Amy Kalia, a postdoctoral fellow with Sinha. "Is vision recoverable or not," she says, "is a more complex story."

Training could help the Prakash children recover more visual function, says Uri Polat, a neuroscientist at Tel Aviv University in Israel. "The window doesn't shut," he says. "It becomes less sensitive."

In 2004, Polat was the first to show that training can restore eyesight in adults with amblyopia, or lazy eye. A lazy eye prevents normal development of the visual cortex during early childhood. Patients have impaired binocular vision, as well as poor acuity and contrast sensitivity; the diminished sight was considered irreversible after age 10. Polat had patients look at a computer screen with variations of a Gabor Patch image, which has blurry black-and-white patterns that change in size and contrast. After just a month of training, his patients had better acuity and contrast sensitivity.

Amedi agrees that training is key, but thinks that it should involve touch and sound, too—senses that blind people rely on to navigate the world. His research has shown that to interpret sound or touch, they rely on parts of their visual cortex normally dedicated to vision. For example, they use the same part of the brain for braille that the sighted use for reading. Project Prakash plans to open a residential school next year to rehabilitate and educate children after cataract surgery using physical exercises and multisensory experiences.

ULTIMATELY, the Prakash team wants to reveal how restoring vision alters the visual cortex. They are beginning to probe changes in the brain with fMRI.

When they image the visual cortex of a patient before and 2 days after surgery, dif-

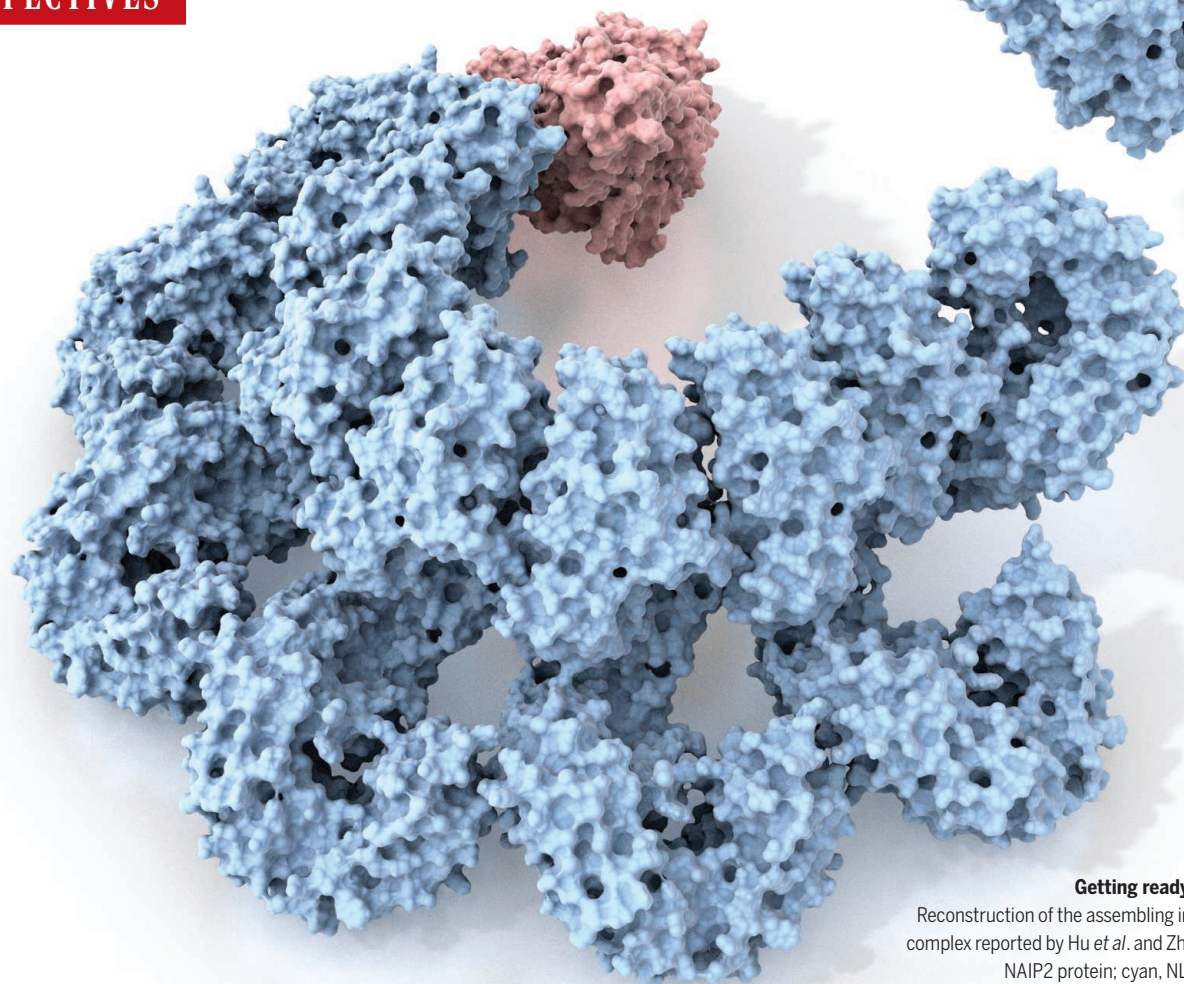
ferent areas of the cortex appear to be working in synchrony. "So if you have high activity in one part of the cortex, you'll have similar activity in another part of the cortex," Sinha says. "It's as if much of the visual cortex is pulsating together."

However, just a couple of months after surgery, the fMRI picture starts to change. Different regions of the visual cortex light up differentially, suggesting a division of labor. Pictures of human faces shown to patients, for example, activate an area of the cortex known to respond to faces in normally sighted people.

"It makes a lot of sense," Amedi says. "When they start processing visual information, they cannot perform tasks. They cannot identify an object, a person. It is all the same nonsense to them." But as time goes by, and the brain learns to distinguish objects, shapes, and faces, different areas of the visual cortex start to specialize.

Sinha, for one, did not expect these changes in the brain. "I was amazed by just how much, how massive the changes are and how quickly it happens, and how late in life it can happen," he says. He also didn't expect the gusher of results the project has generated. "I was worried that having to work with fairly old children, we were setting ourselves up for failure." Instead, the project has brought hundreds of young people like Yadav into the light—while putting the field of visual neuroscience in a new light as well. ■

PERSPECTIVES



Getting ready for defense.

Reconstruction of the assembling inflammasome complex reported by Hu *et al.* and Zhang *et al.* Red, NAIP2 protein; cyan, NLRC4 proteins.

STRUCTURAL BIOLOGY

Assembling the wheel of death

A single ligand-activated protein triggers the assembly of an entire inflammasome

By **Zhonghua Liu** and **Tsan Sam Xiao**

Inflammation is an essential defense strategy mounted by the innate immune system to eradicate infections and repair tissue damage. The inflammasome is an intracellular signaling complex involved in inflammation initiation and perpetuation. These multimeric

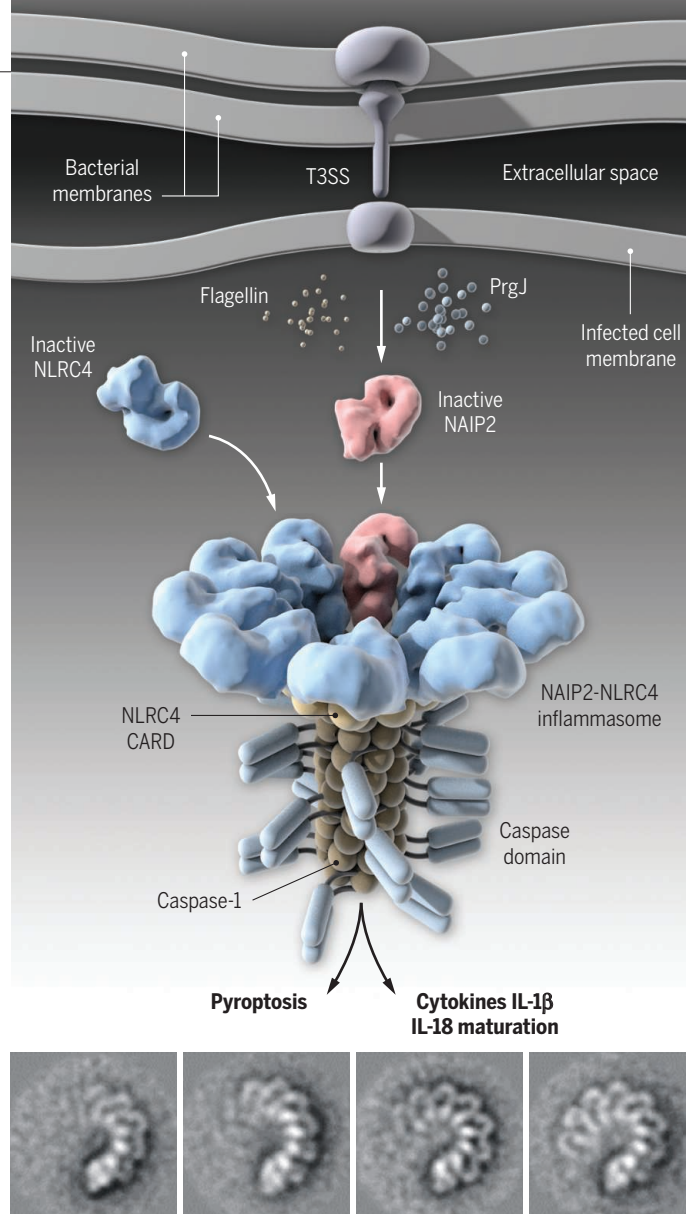
protein assemblies promote the activation of proteases and the maturation of proinflammatory cytokines, as well as a form of cell death (pyroptosis) that incites further inflammation (1). Excessive inflammasome activation has been implicated in chronic inflammatory disorders such as diabetes, atherosclerosis, multiple sclerosis, and Alzheimer's disease (2). However, inflamma-

some also play protective roles in response to microbial pathogens. On pages 404 and 399 of this issue, Zhang *et al.* (3) and Hu *et al.* (4) report the structural basis for activation of an inflammasome implicated in both infectious disease response and autoinflammatory disorders (see the first figure).

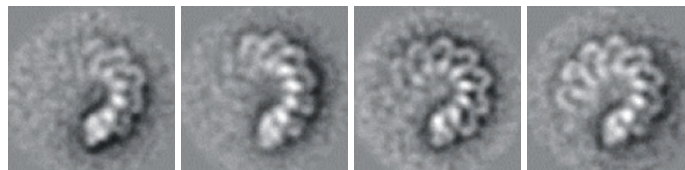
Several inflammasomes have been shown to be activated by both microbial and host

stimuli. Among these inflammasomes, NLRC4 [where NLR denotes NOD-like receptor and C denotes caspase activation and recruitment domain (CARD)] is a unique inflammasome that uses host NAIP proteins (NLR family apoptosis inhibitory proteins) to recognize two bacterial proteins, flagellin and PrgJ, which are essential for bacterial movement and pathogenesis (see the second figure) (5, 6). Previous work suggested that the flagellin-activated NLRC4 inflammasome adopts disk-like structures containing 11 or 12 protomers (7), but the details of the inflammasome assembly are lacking.

Using cryo-electron microscopy (cryo-EM) methods, Hu *et al.* and Zhang *et al.* now show that just one PrgJ-bound NAIP2 molecule is sufficient to trigger a dramatic conformational change in NLRC4; 9 to 11 activated NLRC4 molecules then oligomerize around one NAIP2 molecule to form a 10- to 12-spoke wheel-like structure (see the second figure). Nanogold labeling demonstrated that there was only one NAIP2 and one PrgJ molecule in the inflammasome wheel (see the second figure). Unlike the assembly of the Apaf-1 (apoptotic protease activating factor-1) apoptosome, which requires ligand binding by each of its seven protomers (8), a single ligand-bound NAIP2 molecule triggers the assembly of an entire NAIP2-NLRC4 inflammasome complex. This complex then oligomerizes the caspase-1 protein and promotes its activation (see the second figure). Comparison of the cryo-EM structures and a previous crystal structure of NLRC4 in an autoinhibited state reveals striking conformational changes in NLRC4. In particular, NLRC4's C-terminal half pivots on a helix within the NOD (nucleotide-binding oligomerization) domain, leading to a ~90° rotation. This large structural reorganization is necessary to expose two oligomerization surfaces that facilitate the protein's progressive oligomerization. Mutations near the NLRC4 hinge region cause severe autoinflammatory



Add just one NAIP. Bacterial infections activate the NAIP2-NLRC4 inflammasomes, which promote the activation of caspase-1 and maturation of proinflammatory cytokines interleukin-1 β (IL-1 β) and IL-18, as well as pyroptotic cell death. Hu *et al.* and Zhang *et al.* show that a single ligand-bound NAIP2 protein triggers the progressive assembly of the NAIP2-NLRC4 inflammasomes through large conformational changes in NLRC4 and perhaps NAIP2. Similar mechanisms could govern the assembly of the NLRP3 inflammasome. **(Bottom)** Cryo-EM images of the assembling inflammasome.



diseases typified by recurrent fever and pyroptotic cell death (9–11). The two new structural studies (3, 4) reveal the molecular mechanisms for this autoinflammatory pathology involving NLRC4.

Notwithstanding the remarkable new findings, many mysteries remain regarding inflammasome activation. A key question is the mode of ligand binding. Tenthorey *et al.* have shown that the NAIP NOD domains confer the capacity to recognize flagellin or T3SS proteins (12). The resolution of the current cryo-EM structures was too low to identify the ligand-bound NAIP2 molecule within the wheel-like structures. Therefore, the structural basis for ligand recognition by the NOD

modules remains to be deciphered. Because the NAIP2 NOD module also recruits NLRC4, it is possible that the ligand may engage both NAIPs and NLRC4 in the fully assembled inflammasomes. Therefore, NLRC4 may function as a co-receptor instead of an adapter.

Another unsolved mystery is the role of adenosine diphosphate (ADP) or adenosine triphosphate (ATP). The assembly of the apoptosome requires the exchange of ADP for ATP (8). Halff *et al.* have shown that ATP binding by NAIP5 was not essential for inflammasome assembly, but the role of ATP for NLRC4 function was not clear (7). It remains to be shown whether exchange of ADP for ATP is necessary for inflammasome assembly or disassembly or whether, as suggested by Zhang *et al.*, release of ADP suffices.

The results presented by Hu *et al.* and Zhang *et al.* may also help in understanding the NLRP3 inflammasome, which is perhaps the most intensively studied because it is activated by various microbial and environmental stimuli. Because of their similar domain architecture, the NLRP3 inflammasome may adopt quaternary structures resembling the NAIP2-NLRC4 inflammasome. Many chemically distinct stimuli for the NLRP3 inflammasome may converge on as yet unidentified host protein(s), which then trigger the assembly of the NLRP3 inflammasome in a fashion similar to how NAIP2 accomplishes the NLRC4 oligomerization. ■

REFERENCES AND NOTES

1. K. Schroder, J. Tschoop, *Cell* **140**, 821 (2010).
2. H. Guo, J. B. Callaway, J. P. Y. Ting, *Nat. Med.* **21**, 677 (2015).
3. L. Zhang *et al.*, *Science* **350**, 404 (2015).
4. Z. Hu *et al.*, *Science* **350**, 399 (2015).
5. E. M. Kofoed, R. E. Vance, *Nature* **477**, 592 (2011).
6. Y. Zhao *et al.*, *Nature* **477**, 596 (2011).
7. E. F. Halff *et al.*, *J. Biol. Chem.* **287**, 38460 (2012).
8. J. Chai, Y. Shi, *Natl. Sci. Rev.* **1**, 101 (2014).
9. S. W. Canna *et al.*, *Nat. Genet.* **46**, 1140 (2014).
10. N. Romberg *et al.*, *Nat. Genet.* **46**, 1135 (2014).
11. A. Kitamura, Y. Sasaki, T. Abe, H. Kano, K. Yasutomo, *J. Exp. Med.* **211**, 2385 (2014).
12. J. L. Tenthorey, E. M. Kofoed, M. D. Daugherty, H. S. Malik, R. E. Vance, *Mol. Cell* **54**, 17 (2014).

ACKNOWLEDGMENTS

In memory of William E. Paul, a mentor, colleague and friend to T.S.X.

10.1126/science.aad3981

Department of Pathology, Case Western Reserve University, Cleveland, OH 44106, USA. E-mail: tsx@case.edu

PHYSICS

Chiral anomaly without relativity

A condensed matter system exhibits an effect usually associated with particle physics

By Anton Burkov

The Dirac equation, which describes relativistic fermions (like electrons moving at nearly the speed of light), has a mathematically inevitable but puzzling feature: negative-energy solutions. The physical reality of these solutions is unquestionable, as one of their direct consequences—the existence of antimatter—is confirmed by experiment. However, the interpretation of the solutions has always been somewhat controversial. Dirac's own idea was to view the vacuum as a state in which all the negative energy levels are physically filled. This “Dirac sea” idea seems to contradict a common-sense view of the vacuum as a state in which matter is absent. On the other hand, the Dirac sea is a very natural concept from the point of view of condensed

ing seems to be hard to achieve without assigning physical reality to the Dirac sea. This phenomenon, the chiral anomaly, presents a quantum mechanical violation of chiral symmetry; it was first observed experimentally in particle physics as a decay of a neutral pion into two photons. On page 413 of this issue, Xiong *et al.* (1) report the observation of this phenomenon in a condensed matter system—a crystal of Na_3Bi —manifesting as an unusual negative longitudinal magnetoresistance; the vacuum/insulating crystal analogy is now all the more tangible.

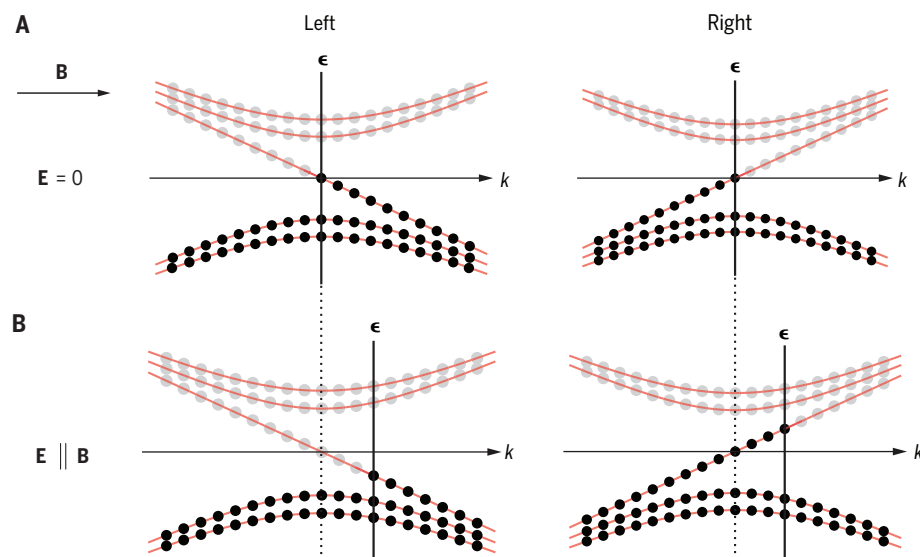
The chiral anomaly is an unexpected feature of relativistic quantum field theory. If the Dirac equation is applied to a hypothetical massless fermion, then the particle is expected to possess a strictly conserved physical quantity called chirality, which refers to the handedness (left or right) of its internal

the negative-energy solutions of the Dirac equation), the chiral symmetry disappears once another fundamental physical principle, that of gauge invariance, is taken into account. Chirality is no longer conserved when the fermions are placed in an electromagnetic field with collinear electric and magnetic components. This property was discovered by Adler and by Bell and Jackiw (2, 3), who were trying to explain the observed decay of a neutral pion into two photons, which seemed to be prohibited by the chiral symmetry.

The chiral anomaly is readily understood when the Dirac sea is considered real (4). In this case, the chiral anomaly follows from the form of the energy eigenvalues of the Dirac equation for a massless left- or right-handed charged fermion in the presence of a constant magnetic field (see the figure). These solutions have the form of Landau levels, discrete energy levels that disperse continuously as a function of the component of the linear momentum along the direction of the field. The handedness of the particles is reflected in the existence in each case of a special Landau level whose dispersion is chiral; that is, it has a slope of a specific sign, positive or negative. Whereas all other Landau levels have either strictly positive or strictly negative energy, the chiral Landau levels necessarily contain both negative and positive energy states. The chiral anomaly arises as a direct consequence of the existence of these chiral Landau levels.

Invoking the Dirac sea picture, all the negative energy states are filled by fermions while all the positive energy states are empty. Now suppose that in addition to the magnetic field, an electric field is applied in the same direction. The electric field will accelerate the particles, which means their momentum will change with time. This implies (see the figure) the simultaneous production of particles of one chirality and antiparticles of the opposite one. The total charge is conserved but the chirality is not.

The observation of the phenomenon reported by Xiong *et al.* was made possible by the recent discovery of Weyl and Dirac semimetals, which are crystalline materials whose electronic structure mimics the energy-momentum relation of relativistic fermions (5–9). The specific material studied by Xiong *et al.*, Na_3Bi , is a Dirac semimetal, which means that the left- and right-chirality electrons coexist at the same point in the



Illustrating the chiral anomaly. (A) Energy spectrum of the left- and right-handed fermions in the presence of a magnetic field B . Filled states with negative energy are shown as black dots, empty states with positive energy as gray dots. (B) Same spectrum, but in the additional presence of an electric field E parallel to the magnetic field B . Right-handed particles and left-handed antiparticles have been produced. ϵ , energy; k , wavevector.

matter physics, as there is a direct and simple analogy: filled valence bands of an insulating crystal. There exists, however, a phenomenon within the context of relativistic quantum field theory, whose satisfactory understand-

angular momentum (i.e., spin) relative to the direction of its linear momentum. This conservation of chirality may be viewed as a consequence of chiral symmetry of the Dirac equation for massless particles: It has no preference for either chirality and does not mix the two chiralities.

However, when one passes from the Dirac equation to the corresponding relativistic field theory (which is made unavoidable by

Department of Physics and Astronomy, University of Waterloo, Waterloo, Ontario N2L 3G1, Canada, and National Research University ITMO, St. Petersburg 197101, Russia. E-mail: aburkov@waterloo.edu

crystal momentum space. This, however, is not important, as a similar effect should be observed in Weyl semimetals, where opposite-chirality fermions exist at distinct points in momentum space. The way that the chiral anomaly manifests in Na_3Bi is through magnetoresistance (a dependence of the electrical resistance of the material on an applied magnetic field). The physical picture of the chiral anomaly, when applied to a Dirac or Weyl semimetal, implies a magnetic field-dependent contribution to the resistance, which is negative (the resistance is reduced and the material becomes a better conductor when the magnetic field is applied) and quadratic in the field (10, 11). The effect also exists only when the current is aligned with the direction of the field (the magnetoresistance is longitudinal), survives up to a temperature of about 90 K, and is large (quickly rising to more than 100% as the temperature decreases below 90 K). These features are unusual and cannot be explained by any other known mechanism but the chiral anomaly.

What makes the observed effect important, apart from the analogy to particle physics, is that the chiral anomaly is a purely quantum mechanical phenomenon without any clas-

“...the chiral anomaly is a purely quantum mechanical phenomenon without any classical analogs. Yet the observed longitudinal magnetoresistance is a macroscopic effect...”

sical analogs. Yet the observed longitudinal magnetoresistance is a macroscopic effect, seen in a large sample. Such macroscopic quantum phenomena are typically observed only at very low temperatures. The fact that the chiral anomaly manifestation in Na_3Bi is observed at temperatures as high as 90 K makes it especially interesting and potentially useful technologically. ■

REFERENCES

1. J. Xiong *et al.*, *Science* **350**, 413 (2015).
2. S. L. Adler, *Phys. Rev.* **177**, 2426 (1969).
3. J. S. Bell, R. Jackiw, *Nuov. Cim.* **A 60**, 4 (1969).
4. H. Nielsen, M. Ninomiya, *Phys. Lett. B* **130**, 389 (1983).
5. X. Wan, A. M. Turner, A. Vishwanath, S. Y. Savrasov, *Phys. Rev. B* **83**, 205101 (2011).
6. A. A. Burkov, L. Balents, *Phys. Rev. Lett.* **107**, 127205 (2011).
7. Z. K. Liu *et al.*, *Science* **343**, 864 (2014).
8. S.-Y. Xu *et al.*, *Science* **349**, 613 (2015).
9. L. Lu *et al.*, *Science* **349**, 622 (2015).
10. D. T. Son, B. Z. Spivak, *Phys. Rev. B* **88**, 104412 (2013).
11. A. A. Burkov, *Phys. Rev. B* **91**, 245157 (2015).

10.1126/science.aad2713

NEUROSCIENCE

The unknowns of cognitive enhancement

Can science and policy catch up with practice?

By Martha J. Farah

“Man is not going to wait passively for millions of years before evolution offers him a better brain.” These words are attributed to the 20th century Romanian psychopharmacologist Corneliu Giurgea, an early advocate of cognitive enhancement—that is, the use of medications or other brain treatments for improving normal healthy cognition. Contemporary attempts at cognitive enhancement involve an array of drugs and devices for modifying brain function, such as pills taken by students to help them study, or electrical stimulators focused on prefrontal cortex by electronic game players (“e-gamers”) to sharpen their skills. What is known about current methods of cognitive enhancement? What specifically do they enhance, for whom, and with what risks? We know surprisingly little.

In the United States, stimulants such as amphetamine and methylphenidate (sold under trade names such as Adderall and Ritalin, respectively) are widely used for nonmedical reasons (1). However, it is not known how many of these users are seeking cognitive enhancement, as opposed to getting “high,” losing weight, or some other effect—there is simply a lack of epidemiological data. Student surveys suggest that cognitive enhancement with stimulants is commonplace on college campuses, where students with prescriptions sell pills to other students, who use them to help study and finish papers and projects (2). Similar use by college faculty and other professionals to enhance workplace productivity has been documented, but prevalence is unknown (3, 4).

These practices have been interpreted as paradigm cases of cognitive enhancement (which is distinct from treatment for a cognitive disorder) generally aimed at improving executive function—the ability to marshal cognitive resources for flexible multitasking or focusing, as needed. Because these drugs are widely used to treat attention deficit hyperactivity disorder

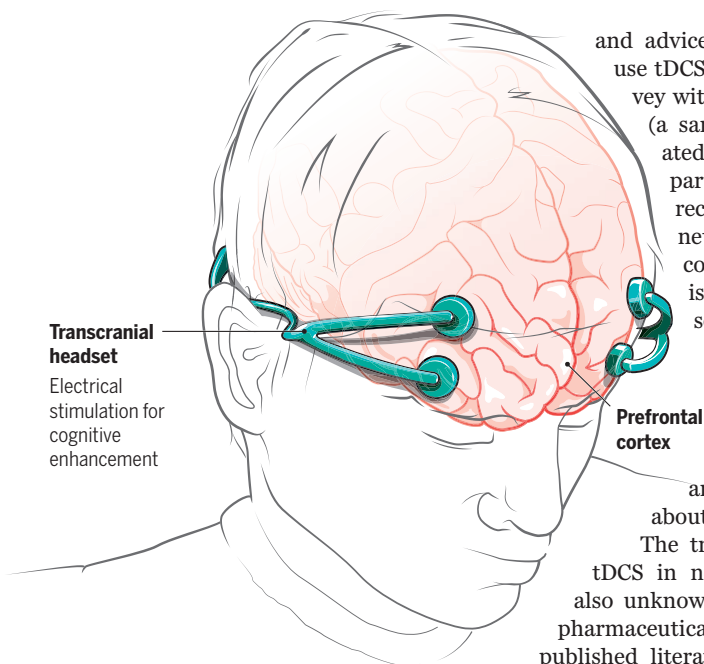
(ADHD), in which executive function is impaired, they are assumed to enhance executive function in healthy individuals as well. However, the current evidence suggests a more complex state of affairs. The published literature includes substantially different estimates of the effectiveness of prescription stimulants as cognitive enhancers. A recent meta-analysis suggests that the effect is most likely real but small for executive function tests stressing inhibitory control, and probably nonexistent for executive function tests stressing working memory (5).

Why, then, do these drugs continue to be used for enhancement? One possibility is that there are important individual differences in people’s response to them, with some people benefiting (2). In addition, stimulants have other effects for which they may be used. In a report entitled “Just How Cognitive Is ‘Cognitive Enhancement’?”, sociologist Scott Vrecko interviewed students who used Adderall and found that they emphasized motivational and mood effects as reasons for using the drugs for schoolwork (6). Subsequent research confirmed the role of these noncognitive factors for students enhancing with Adderall; although they differed minimally from nonusers on attention task performance, they exhibited substantially greater differences in motivation and worse study habits, along with more depressed mood (7).

There is, of course, a close relation between cognitive performance, on the one hand, and motivation, on the other. Even if one’s laboratory-measured executive function is not appreciably increased, one is likely to get more done, and of better quality, if one is feeling cheerful and “into” the tasks at hand. Unfortunately, the mood- and motivation-boosting abilities of stimulants are related to their well-known dependence potential, and that potential is a major concern. How likely is it that cognitive enhancement use of stimulants will lead to dependence? The prevalence of drug dependence among enhancement users is not currently known.

Another drug used for cognitive enhancement is modafinil (trade name Provigil). Best known for its ability to preserve alertness and cognitive function under

Department of Psychology, University of Pennsylvania, Philadelphia, PA 19104, USA. E-mail: mfarah@psych.upenn.edu



New trends. Transcranial electric stimulation for cognitive enhancement in healthy individuals is becoming more popular, yet little is known about the effectiveness or long-term safety of these devices.

conditions of sleep deprivation, it may also enhance aspects of cognition in rested individuals. As with amphetamine, studies have produced conflicting results. A recent literature review of the cognitive effects of modafinil found a range of outcomes: enhancement, null effects, and occasionally impairment. Enhancement was the most common finding, especially in complex cognitive tasks requiring multiple components of executive function to be used together, although effect sizes were not synthesized through meta-analysis to yield a quantitative summary measure of effectiveness (8). A recent study reported a “striking increase in task motivation,” suggesting that this may contribute to modafinil’s value as a cognitive enhancer in the workplace (9), but motivational effects are inconsistent across studies (8). Modafinil’s dependence potential is believed to be low, although some would not discount the risk (10).

The newest trend in cognitive enhancement is the use of transcranial electric stimulation (11). In the most widely used form, called transcranial direct current stimulation (tDCS), a weak current flows between an anode and a cathode placed on the head, altering the resting potential of neurons in the current’s path. The simplicity and low cost of tDCS devices have enabled broad use of the technology for research and, increasingly, for home use. No epidemiological data exist on the use of these devices, but the Internet abounds with discussion

and advice on how to build and use tDCS systems. An initial survey with a convenience sample (a sample not expressly created to be representative of particular types of people) recruited from the Internet sites indicates that cognitive enhancement is the most common reason for personal use of tDCS (12). Subscribers to the main tDCS interest website number in the thousands, but actual prevalence and related information about tDCS use is unknown.

The true cognitive benefit of tDCS in normal healthy users is also unknown. As with research on pharmaceutical enhancement, the published literature includes a mix of findings. One recent attempt to synthesize the literature with meta-analysis concluded that tDCS has no effect whatsoever on a wide range of cognitive abilities (13). However, the methods of this analysis have been criticized as unnecessarily conservative and even biased (14). Newer transcranial electric stimulation protocols involving alternating current stimulation (tACS), random noise stimulation (tRNS), and pulsed stimulation (tPCS) have different physiological effects and hence potentially different psychological effects, although the empirical literature is still developing.

Transcranial electric stimulation is expanding beyond home users, with new companies selling compact, visually appealing, user-friendly devices. These have been exempted from regulation as medical devices by the U.S. Food and Drug Administration. One company, Foc.us, markets its systems to e-gamers to improve attention and performance. Thync, which began selling its system in June of this year, targets a broader set of lifestyle uses, comparable to coffee for work and meditation for relaxation. At present, there is little to no scientific evidence for or against the effectiveness of these specific systems, nor is there evidence concerning the physiological and psychological effects of regular use over months or years in humans or in animals.

It remains difficult to say what cognitive benefits these various practices offer in the laboratory, let alone in the classroom or workplace, and their attendant risks are even harder to gauge. Although surveys have estimated the number of college students using stimulants for enhancement, little is known about other people and

other practices. Without knowing more about the prevalence, risks, and benefits of these brain interventions, it is difficult to formulate useful policy.

Why are we so ignorant about cognitive enhancement? Several factors seem to be at play. The majority of studies on enhancement effectiveness have been carried out on small samples, rarely more than 50 subjects, which limits their power. Furthermore, cognitive tasks typically lend themselves to a variety of different but reasonable outcome measures, such as overall errors, specific types of errors (for example, false alarms), and response times. In addition, there is usually more than one possible statistical approach to analyze the enhancement effect. Small samples and flexibility in design and analysis raise the likelihood of published false positives (15). In addition, pharmacologic and electric enhancements may differ in effectiveness depending on the biological and psychological traits of the user, which complicates the effort to understand the true enhancement potential of these technologies. Industry is understandably unmotivated to take on the expense of appropriate large-scale trials of enhancement, given that the stimulants used are illegally diverted and transcranial electric stimulation devices can be sold without such evidence. The inferential step from laboratory effect to real-world benefit adds another layer of challenge. Given that enhancements would likely be used for years, long-term effectiveness and safety are essential concerns but are particularly difficult and costly to determine. As a result, the only large-scale trial we may see is the enormous but uncontrolled and poorly monitored trial of people using these drugs and devices on their own. ■

REFERENCES

1. *Results from the 2013 National Survey on Drug Use and Health: Summary of National Findings* (Substance Abuse and Mental Health Services Administration, Rockville, MD, 2013).
2. M. E. Smith, M. J. Farah, *Psychol. Bull.* **137**, 717 (2011).
3. B. Maher, *Nature* **452**, 674 (2008).
4. A. Schwarz, “Workers Seeking Productivity in a Pill Are Abusing A.D.H.D. Drugs,” *New York Times*, 18 April 2015.
5. I. P. Ilieva, C. J. Hook, M. J. Farah, *J. Cognit. Neurosci.* **27**, 1069 (2015).
6. S. Vrecko, *AJOB Neurosci.* **4**, 4 (2013).
7. I. P. Ilieva, M. J. Farah, *J. Atten. Disord.* **1087054715591849** (2015).
8. R. M. Battleday, A. K. Brem, *Eur. Neuropsychopharmacol.* **10.1016/j.euroneuro.2015.07.028** (2015).
9. U. Müller et al., *Neuropharmacology* **64**, 490 (2013).
10. N. D. Volkow et al., *JAMA* **301**, 1148 (2009).
11. V. Dubljević, V. Saigle, E. Racine, *Neuron* **82**, 731 (2014).
12. A. Jwa, *J. Law Biosci. lsv017* (2015).
13. J. C. Horvath, J. D. Forte, O. Carter, *Brain Stim.* **8**, 318 (2015).
14. A. R. Price, R. H. Hamilton, *Brain Stim.* **8**, 663 (2015).
15. J. P. A. Ioannidis, *PLOS Med.* **2**, e124 (2005).

10.1126/science.5893

Snapshots of a protein quake

Release of CO induces ultrafast collective motions in myoglobin

By Richard Neutze

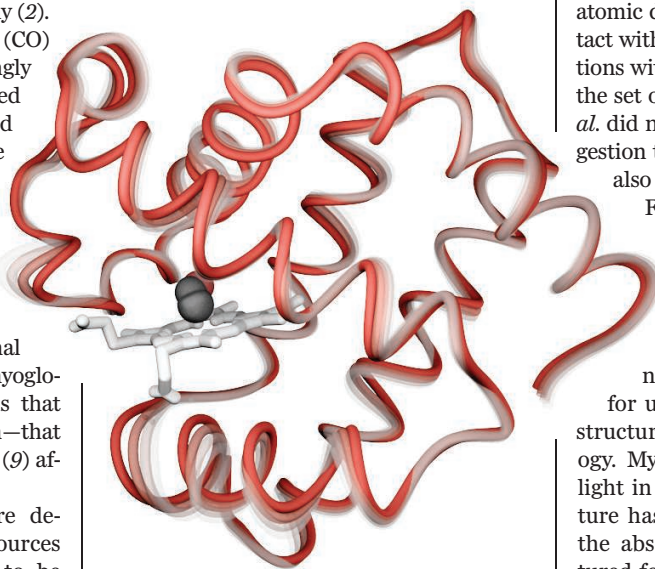
“Everything that living things do can be understood in terms of the jiggings and wiggings of atoms,” Richard Feynman famously surmised (1). This question has captured the imagination of biologists since the first protein structure, that of myoglobin, an oxygen (O_2) carrier in muscles, was solved by x-ray crystallography (2). Myoglobin binds carbon monoxide (CO) two orders of magnitude more strongly than O_2 . Bound CO can be dislodged from the active-site heme by light, and the subsequent structural response of the protein has been the focus of intense study by spectroscopic (3), x-ray scattering (4), and x-ray diffraction (XRD) (5, 6) methods, yet complex structural questions remain (7). On page 445 of this issue, Barends *et al.* (8) provide three-dimensional snapshots of structural changes in myoglobin—low-amplitude collective motions that rapidly spread throughout the protein—that occur during the first few picoseconds (9) after the CO photodissociation.

Time-resolved XRD methods were developed at synchrotron radiation sources to enable the movement of atoms to be observed in real time during a biological reaction. Synchrotron-based time-resolved XRD studies of the photo-dissociation of CO from the active site of myoglobin first achieved a time resolution of a 4000 ps (5), and technical developments later facilitated a 30-fold improvement (6). These studies beautifully illustrated how dislodging a bound ligand may induce a coordinated sequence of structural changes throughout a protein, and suggested that collective motions may be coupled to opening and closing a gateway for CO (or O_2) to enter or exit the active site of the protein (7).

Because of technical limitations associated with circulating electron bunches around a ring, it is not possible to isolate x-ray pulses shorter than 100 ps in duration with synchrotron radiation sources. This fundamental limitation hampers time-resolved studies of the most rapid structural changes in biology, because spectroscopic evidence suggests that

collective motions in proteins may occur two orders of magnitude faster (3).

Barends *et al.* overcame this restriction by performing time-resolved diffraction studies at an x-ray free-electron laser (XFEL). Rather than circulating electrons around a ring, XFELs utilize a linear accelerator to inject a very short (hundredths of a millimeter) electron bunch through a very long (~100 m) array of oppositely aligned magnetic fields. A



Ultrafast collective motions in myoglobin. Myoglobin consists of six α helices, which enclose a heme containing an iron atom (Fe^{2+}) bound within a porphyrin ring (light gray). CO (gray spheres) is bound to Fe^{2+} in the resting state, and the Fe-CO bond is broken by a rapid laser flash, whereupon CO moves to its primary docking position (red) within 0.1 ps. Strain is released as functionally important motions that evolve collectively throughout the protein. The resting myoglobin conformation is shown as light gray, whereas protein motions are implied by a sequence of increasingly opaque excited conformations (red). Movements of the backbone carbon atoms are exaggerated up to ninefold to better illustrate these small-amplitude motions.

feedback mechanism termed “lasing” creates a revolutionary x-ray source that delivers extremely intense x-ray pulses 0.1 ps in duration (10). XFEL radiation has enabled high-resolution protein structures to be determined from a continuous stream of tiny crystals approximately a thousandth of a millimeter across (microcrystals), which mitigates the effects of damage from these very intense pulses (11). When used in combination with

a suitably short laser pulse to initiate a light-driven reaction within microcrystals (12), an XFEL can be used to visualize the most rapid structural changes in biology.

A tenth of a picosecond after photo-activation by a short laser flash, Barends *et al.* observed a 1.6 Å displacement of a CO molecule away from the iron atom of the heme and into a transient docking site atop the heme’s porphyrin ring. This movement of the ligand releases strain energy, which is transported away from the active site as collective motions of the protein’s backbone atoms (see the figure). The amplitude of these motions is small (~0.2 Å), yet the power of averaging diffraction data from thousands of microcrystals allows the accurate recording of a high-resolution movie. Most strikingly, the atomic displacements of the residues in contact with the heme undergo coherent oscillations with a period of ~0.5 ps. Unfortunately, the set of time delays sampled by Barends *et al.* did not allow verification of a recent suggestion that longer-period global oscillations also arise in myoglobin (4).

Functionally important motions that arise on this time scale have been coined a “protein-quake” (3). Barends *et al.* provide a direct observation of such motions at high resolution and provide new insight of generic importance for understanding the relation between structure and dynamics throughout biology. Myoglobin, however, does not utilize light in its natural function. Whenever nature has evolved proteins to harvest light, the absorbed photons are invariably captured for their energy or their information content. Future XFEL-based time-resolved XRD studies are likely to facilitate unprecedented structural insights into the most rapid structural changes in photo-biology, revealing how the proteins that partake in photosynthesis and vision have been optimized for function throughout evolution. It will be fascinating to see how the collective movement of the atoms of light receptors initiate vision. ■

REFERENCES AND NOTES

1. R. P. Feynman, R. B. Leighton, M. L. Sands, *The Feynman Lectures on Physics* (Addison-Wesley, Reading, MA, 1963).
2. J. C. Kendrew *et al.*, *Nature* **181**, 662 (1958).
3. A. Ansari *et al.*, *Proc. Natl. Acad. Sci. U.S.A.* **82**, 5000 (1985).
4. M. Levantino *et al.*, *Nat. Commun.* **6**, 6772 (2015).
5. V. Srajer *et al.*, *Science* **274**, 1726 (1996).
6. F. Schotte *et al.*, *Science* **300**, 1944 (2003).
7. H. Frauenfelder, B. H. McMahon, P. W. Fenimore, *Proc. Natl. Acad. Sci. U.S.A.* **100**, 8615 (2003).
8. T. R. M. Barends *et al.*, *Science* **350**, 445 (2015).
9. Light travels 0.3 mm in 1 ps, which is 10^{-12} s.
10. P. Emma *et al.*, *Nat. Photon.* **4**, 641 (2010).
11. S. Boutet *et al.*, *Science* **337**, 362 (2012).
12. J. Tenboer *et al.*, *Science* **346**, 1242 (2014).

Department of Chemistry and Molecular Biology, University of Gothenburg, Sweden. E-mail: richard.neutze@chem.gu.se

OCEAN

Making waves: The science and politics of ocean protection

Mature science reveals opportunities for policy progress

By Jane Lubchenco and Kirsten Grorud-Colvert*

The ocean has recently taken a more prominent role on the international policy stage. In June, the United Nations (UN) initiated development of a treaty for conservation of biodiversity on the High Seas. One of the Sustainable Development Goals (SDGs) adopted by the UN in September focuses on the ocean. In early October, the second Our Ocean Conference (OO-2015) provided a high-profile platform for nations to tout progress or make promises to protect and restore the ocean. We discuss recent progress in creating and enforcing strongly protected areas, and we emphasize the need to accelerate the pace and draw on scientific knowledge.

POLICY

to protect and restore the ocean. We discuss recent progress in creating and enforcing strongly protected areas, and we emphasize the need to accelerate the pace and draw on scientific knowledge.

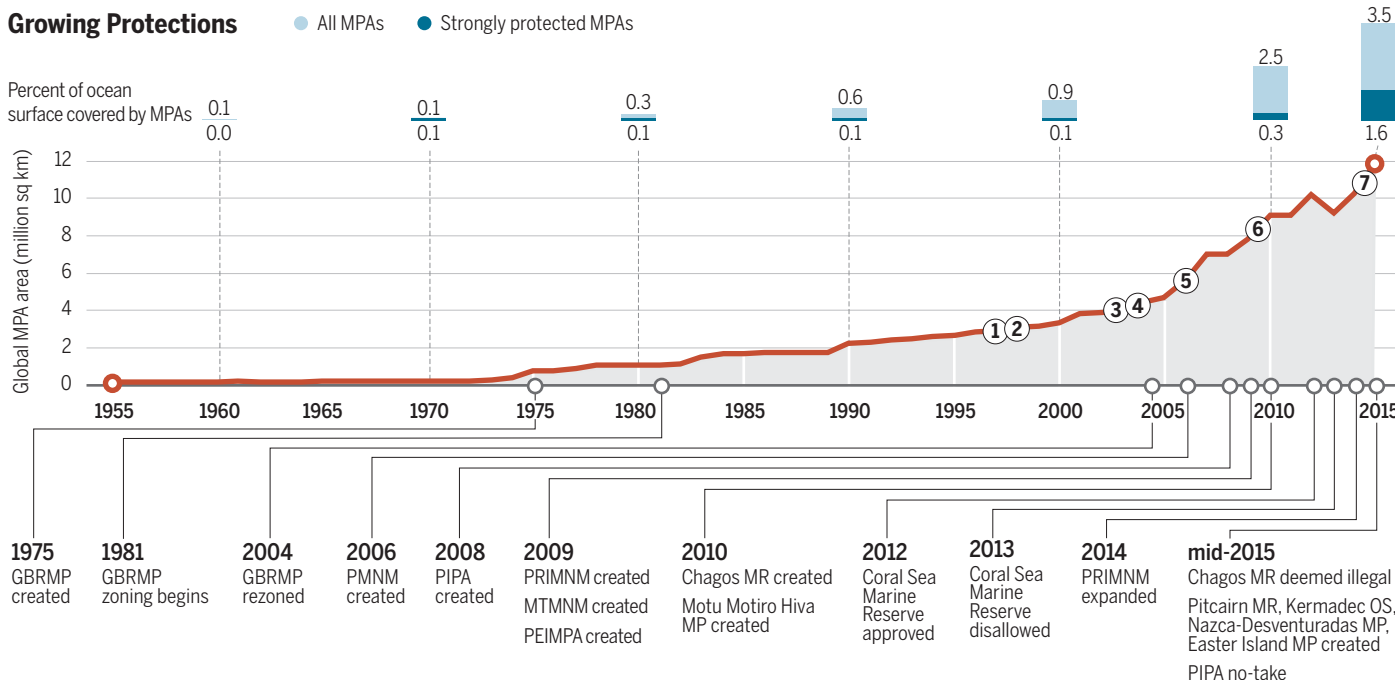
Two new large marine reserves were announced by Chile at OO-2015: Easter Island Marine Park and Nazca-Desventuradas Marine Park. These join other recent reserves, including a sixfold expansion of the U.S. Pacific Remote Islands Marine National Monument (2014); Kiribati's ban on commercial fishing in its Phoenix Island Protected Area (2015); the United Kingdom's Pitcairn Islands Marine Reserve (2015), which will be the world's largest fully protected marine area; and New Zealand's Kermadec Ocean Sanctuary (2015). Each of these new protected areas, if fully implemented and enforced, should bring significant ecological benefit.

These areas contribute to global targets set in SDG Goal 14 and the Convention on Biological Diversity's (CBD) Aichi Target 11 to protect at least 10% of coastal and marine areas by 2020. These targets employ a

loose definition of "protection." We find it more useful to distinguish among "lightly protected" (some protection exists but significant extractive activity is allowed), "strongly protected" (all commercial activity prohibited, only light recreational and subsistence fishing allowed), and "fully protected" (no extractive activities allowed; also called "marine reserves"). The term "Marine Protected Area" (MPA) encompasses all three categories, among which ecological benefits vary greatly (1).

Even lumping all categories together, only 3.5% of the ocean is protected (see the figure). Only 1.6% is "strongly" or "fully" protected. In contrast, the CBD 17% target for terrestrial protection is likely to be met by 2020—it currently stands at ~15% (2). Conservation organizations and scientific analyses support ocean protection ranging from 20 to 50% (3). Existing MPAs are solely within countries' jurisdictions, leaving the High Seas (~58% of the ocean) without any permanent protection (hence the new UN High Seas process). Protecting the High Seas could bring significant fishery enhancement in addition to the primary goal of biodiversity benefit (4). Representativeness of protection across diverse habitats may be more important than total area (5), but no adequate measure exists to

Growing Protections



Increases in global MPA coverage over time. The line graph shows increasing MPA area. MPAs and year established are shown below the x axis. Data include formal commitments for large MPAs made in mid-2015. Bar graphs (decadal from 1960 to 2010, plus 2015) show percent ocean surface area that is strongly or fully protected (dark blue) out of the total percent MPA coverage (light blue). Circled numbers highlight key international events or agreements: 1) First AAAS Marine Reserves Symposium; 2) First NCEAS Marine Reserves Working Group; 3) UN World Summit on Sustainable Development; 4) Vth IUCN World Parks Congress; 5) UN Convention on Biological Diversity (CBD); 6) CBD, Aichi Targets; 7) UN SDG 14. Chagos MR currently in negotiation (see SM). GBRMP, Great Barrier Reef Marine Park; PRIMNM, Pacific Remote Islands Marine National Monument; MP, Marine Park; MR, Marine Reserve; MTMNM, Marianas Trench Marine National Monument; OS, Ocean Sanctuary; PEI MPA, Prince Edward Islands Marine Protected Area; PIPA, Phoenix Islands Protected Area; PMNM, Papahānaumokuākea Marine National Monument. Pre-2015 data from World Database on Protected Areas and MPAtlas, collated by R. Moffitt, and from (6). Mid-2015 large MPA data compiled by authors from data made public as formal MPA commitments are announced. See SM for MPA sizes.

assess how protection is distributed globally or within nations' exclusive economic zones [see the supplementary materials (SM)].

Despite the low fraction of the ocean protected, significant progress has been made in the last decade (6) (see the figure and the SM)—from less than 0.1% to 1.6% strongly protected. This reflects increasingly strong scientific evidence about the social, economic, and environmental benefits of full protection; greater attention to community, stakeholder, and governance dynamics; increasing recognition of the need for more protection due to threats to biodiversity, overfishing, and the lack of assessment for many marine stocks; dedicated campaigns by nongovernmental organizations (NGOs); funding by philanthropies; and new technologies that enable more effective enforcement. Complementary changes are under way in some fishery management to achieve more sustainable fisheries outside marine reserves [e.g., (7)].

MATURE SCIENCE. Although the science of MPAs is mature and extensive, political discussions are frequently disconnected from that knowledge, and resistance from resource extractors is often intense. We highlight seven important, relevant findings.

Full protection works. Fully protected, effectively enforced reserves almost always achieve their primary goal of significant ecological gains, including more species in greater numbers and larger sizes [e.g., (8, 9)]. Fully protected areas have ecological benefits up to an order of magnitude greater than partially protected areas (1). Strong potential also exists to help recover some depleted fisheries outside a reserve [e.g., (4)]. They also provide a control to evaluate the impact of fishing and thus improve fishery management.

Habitats are connected. Networks of reserves that extend beyond coastal waters into deeper waters can protect more biodiversity; many species move among habitats during their life cycles. If seamounts are fully protected within a strategically placed reserve, they can also benefit migratory animals such as tuna and marine mammals.

Networks allow fishing. Connected networks of reserves can protect species while allowing extractive use between reserves. Connectivity occurs through movement of larvae, juveniles, or adults, sometimes across political jurisdictions, leading to greater benefits than from a set of unconnected reserves (10). Simply having multiple relatively small reserves within a region, without thoughtful design, does not guarantee connectivity.

Engaging users usually improves outcomes. Reserves or networks planned with fishers and managers can address both conservation and fishery goals. For example, Territorial User Rights Fisheries (TURFs) can be combined with reserves, as fishing cooperatives with secure access recognize the benefits of creating neighboring “fish banks” to provide spillover into their fishing areas (7).

“An accelerated pace of protection will be needed...”

Reserves can enhance resilience. Large and strategically placed reserves with their full component of trophic levels and greater genetic and species diversity are likely to be more resilient to some environmental changes and could be important tools in climate adaptation [e.g., (11, 12)].

Planning saves money. Thoughtful planning can minimize the costs of reserves, including foregone revenue [e.g., (13)]. Reserves can increase economic benefits, such as through spillover of adults to fished areas or enhanced tourism revenues; in some cases, the value of the reserve can exceed the pre-reserve value (14).

Ecosystems matter. Complementary efforts beyond reserves and MPAs are needed to fully protect and restore ecosystem functioning. Smart planning using science- and ecosystem-based approaches can enable a combination of sustainable uses (fishing, aquaculture, energy generation, recreation, and the like) and protected places (15).

POLICY CONNECTIONS. Cognizant of the disparity between existing protection and policy—or scientific—targets, we offer six recommendations.

Embrace options. MPAs have been implemented using myriad top-down (politically mandated) and bottom-up (citizen-driven) approaches (see SM). Both are needed to achieve adequate protection.

Bring users to the table. Involving stakeholders during all stages can assist successful MPA planning, improving outcomes of resource protection while minimizing the effects on resource users (see SM).

Change users' incentives. Push-back is understandable from those who bear the immediate costs, especially if there is no guarantee of direct benefit. This has been the single biggest impediment to the creation of reserves. Good reserve design and explicit transition strategies can help minimize economic and social effects (e.g., fisheries buyouts, phasing out fishing over time, or training for alternative livelihoods).

Even more powerful approaches turn losers into winners—for example through TURF-reserves or other rights-based fishery management (7) or by treating reserves as a new business, with users as investors and shareholders, and a return on investment expected in future years (14).

Use new technologies for enforcement. Partnerships between NGOs, the technology industry, and agencies use satellite tracking to visualize boat traffic, identify potential illegal fishing, and direct law enforcement to offenders. These complement international initiatives to reduce what has been a major threat to fishery management and biodiversity protection: Illegal, Unregulated, and Unreported (IUU) Fishing.

Integrate reserves with other management measures. Reserves cannot address all stressors affecting the ocean. Complementary management, ideally integrated with reserves, is necessary to address issues such as bycatch, unsustainable and IUU fishing, climate change, and ocean acidification.

Expect surprises and use adaptive management. When reserve goals are identified, so, too, should plans be laid for accommodating unexpected changes. Monitoring is key to track progress and signal when management plans should be reviewed. Management agencies need the capacity to effectively evaluate reserve outcomes and use sound data for adapting appropriately.

An accelerated pace of protection will be needed for the ocean to provide the full range of benefits people want and need. ■

REFERENCES AND NOTES

1. S. E. Lester, B. S. Halpern, *Mar. Ecol. Prog. Ser.* **367**, 49 (2008).
2. Secretariat of the Convention on Biological Diversity, “Global Biodiversity Outlook 4” (Montréal, Canada, 2014).
3. K. Grorud-Colvert, J. Lubchenco, A. Barner, in *Science for Parks, Parks for Science: The Next Century*, S. R. Beissinger, D. Ackerly, H. Doremus, G. Machlis, Eds. (University of Chicago Press, Chicago, in press).
4. C. White, C. Costello, *PLoS Biol.* **12**, e1001826 (2014).
5. B. Pressey et al., *Nature* **515**, 28 (2014).
6. R. J. Toonen et al., Big Ocean Think Tank, *Mar. Pollut. Bull.* **77**, 7 (2013).
7. A. K. Barner et al., *Oceanography* **28**, 252 (2015).
8. S. E. Lester et al., *Mar. Ecol. Prog. Ser.* **384**, 33 (2009).
9. J. E. Caselle, A. Rassweiler, S. L. Hamilton, R. R. Warner, *Scientific Reports* **5**, 14102 (2015).
10. K. Grorud-Colvert et al., *PLoS ONE* **9**, e102298 (2014).
11. A. D. Olds et al., *Glob. Change Biol.* **20**, 3050 (2014).
12. F. Micheli et al., *PLoS ONE* **7**, e40832 (2012).
13. C. J. Klein et al., *Conserv. Biol.* **22**, 691 (2008).
14. E. Sala et al., *PLoS ONE* **8**, e58799 (2013).
15. K. L. McLeod, H. Leslie, *Ecosystem-Based Management for the Oceans* (Island Press, Washington, DC, 2009).

ACKNOWLEDGMENTS

We thank R. Moffitt, B. Pike, and the MPAtlas team, along with M. Rand and the Global Ocean Legacy team at the Pew Charitable Trusts for assistance with MPA data; and M. Pessino for graphic design.

SUPPLEMENTARY MATERIALS

www.sciencemag.org/content/350/6259/382/suppl/DC1

Published online 15 October 2015

10.1126/science.aad5443

Oregon State University, Corvallis, OR 97331, USA. The authors contributed equally to this work.

*E-mail: grorudck@science.oregonstate.edu

MICROBIOLOGY

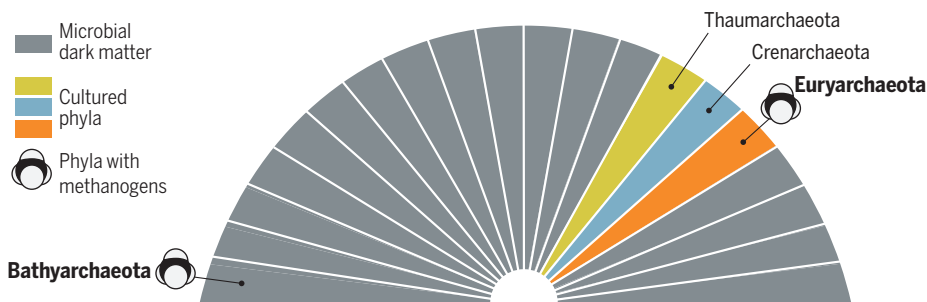
Beyond known methanogens

DNA sequences from a coal-bed reservoir show that methane can be generated by unexpected microbes

By Karen Lloyd

Recent advances in DNA sequencing and analysis have shown that much of the microbial life on Earth differs from previously described organisms. The organisms in this “microbial dark matter” are globally ubiquitous and numerous but have largely unknown physiologies (1–4). Given their great evolutionary distance from all laboratory cultures, these mysterious organisms may harbor unique functions with potentially useful biotechnological applications. Like most environments on Earth, coal-bed reservoirs contain microbial dark matter. On page 434 of this issue, Evans *et al.* (5) show that members of the microbial dark matter phylum Bathyarchaeota

reservoirs. This approach differs from past ones in that nearly all the DNA in the environment is sequenced, so that genomes can be reconstructed without preselection bias. The *mcrA* genes that the authors ascribe to the Bathyarchaeota match the four-letter frequencies of the rest of the Bathyarchaeota genes in their study and thus do not belong to other microbes in the community. Additionally, the Bathyarchaeota *mcrA* genes differ significantly from all previously discovered *mcrA* genes. It is therefore likely that these genes, along with other genetic components of the methanogenic pathway, were transferred vertically (rather than being brought in recently by a virus or a transposon). These genes thus likely originated before this ancient lineage diverged.



Early divergence. The Bathyarchaeota diverged early from other archaea, including the methane-generating Euryarchaeota. Evans *et al.* now show that Bathyarchaeota likely generate methane with the help of genes that differ fundamentally from those found in Euryarchaeota.

(6) from coal beds have the genetic potential to generate methane.

Coal-bed methanogens, if properly nurtured, could increase natural gas production from existing wells (7). Past studies of methane-generating microbes (methanogens) in any environment, including coal-bed reservoirs, have searched for either taxonomic marker genes or methyl coenzyme M reductase (*mcrA*) genes found in cultivated methanogens (8). Any methanogen from a new taxonomic group, or one that performs methanogenesis by an as-yet-undiscovered pathway, will have been missed by these studies.

Evans *et al.* now report the reconstruction of two bathyarchaeotal genomes from DNA sequences derived from coal-bed reser-

All cultivated methanogens are members of a single phylum, the Euryarchaeota, in the domain Archaea (see the figure). Because methanogenesis only requires substrates that were abundant on early Earth, it is thought to be one of life's earliest metabolisms (9, 10). Expanding methanogenesis to the Bathyarchaeota provides support for this theory because it places the evolution of genes for methanogenesis before the divergence of the Euryarchaeota and Bathyarchaeota.

Support for the placement of Bathyarchaeota as a phylum-level group comes from their deeply branching evolutionary history (4, 6) and their broad environmental distribution, ranging from the deep-sea subsurface to anoxic land environments (11). Another characteristic of phyla is that they contain species with diverse physiologies and ecological functions. Bathyarchaeota have been associated with degradation of

protein-derived matter (4) and aromatics (6). By adding a third type of metabolism to the Bathyarchaeota, Evans *et al.* make it clear that it is a phylum-level group with a wide range of physiological capabilities.

It is impossible to draw definitive proof that an organism performs a particular metabolism based on its genes alone. However, the Mcr protein inferred from the Bathyarchaeota genome has many key features of the active site known to be essential for its function in cultured methanogens. Furthermore, the presence of these organisms in a deep coal bed, where methanogenesis is known to occur, supports the possibility that this is a previously unknown type of methanogen.

Evans *et al.* show that common microbial processes in the environment can occur through genes that have been completely missed in previous DNA-sequencing efforts. Most understanding of the roles of specific types of genes in the environment requires amplification. To be amplified, the target DNA sequence of the environmental DNA must match small strands of synthesized DNA (primers) that are designed to match all known target sequences. Because only the environmental DNA matching the sequence of those primers is amplified, this method will miss the target gene if it diverges strongly from the primers.

Genomic sequencing of uncultivated microorganisms has always held the promise of removing this preselection for known genotypes. The work by Evans *et al.* fulfills that promise. The *mcrA* gene they found in the Bathyarchaeota has 10 to 18 mismatched DNA bases with commonly used primers. Two or three mismatches are usually sufficient to prevent primer binding. Clearly, all known primers would have missed this particular *mcrA* gene. After the genomic bin showed them what to look for, Evans *et al.* found homologs of the novel methanogenesis genes in other coal-bed reservoirs, demonstrating the presence of previously uninvestigated forms of *mcrA* in those environments. Future investigations of this kind are likely to reveal further genetic adaptations to known metabolic processes, in addition to discovering new processes or combinations of processes not seen in pure cultures. ■

REFERENCES

1. C. Rinke *et al.*, *Nature* **499**, 431 (2013).
2. C. T. Brown *et al.*, *Nature* **523**, 208 (2015).
3. K. C. Wrighton *et al.*, *Science* **337**, 1661 (2012).
4. K. G. Lloyd *et al.*, *Nature* **496**, 215 (2013).
5. P. N. Evans *et al.*, *Science* **350**, 434 (2015).
6. J. Meng *et al.*, *ISME J.* **8**, 650 (2014).
7. D. Ritter *et al.*, *Int. J. Coal Geol.* **146**, 28 (2015).
8. B. A. Hales *et al.*, *Appl. Environ. Microbiol.* **62**, 668 (1996).
9. F. U. Battistuzzi, A. Feijao, S. B. Hedges, *BMC Evol. Biol.* **14**, 1 (2004).
10. J. G. Ferry, C. H. House, *Mol. Biol. Evol.* **23**, 1286 (2006).
11. K. Kubo *et al.*, *ISME J.* **6**, 1949 (2012).

Department of Microbiology, University of Tennessee, Knoxville, TN 37996, USA. E-mail: klloyd@utk.edu

Toward a rapid and reversible male pill

Sperm-specific calcineurin is a novel fertility and contraceptive target

By **Julio Castaneda**^{1,2,3} and
Martin M. Matzuk^{1,2,3,4,5,6}

The population of our planet continues to rise at a rapid rate and is reaching unsustainable numbers. The Strategic Plan 2000 of the National Institute of Child Health and Human Development (NICHD) states that uncontrolled fertility “is one of the most pressing public health challenges facing the world today” (1). However, while women have had the freedom to control their own reproductive destiny with the “pill” for more than 50 years, there remains no oral contraceptive for men. On page 442 of this issue, Miyata *et al.* (2) demonstrate that genetic disruption of either the catalytic subunit (PPP3CC) or the regulatory subunit (PPP3R2) of sperm-specific calcineurin or short-term in vivo pharmacological inhibition with cyclosporine A or FK506 yields dysfunctional mouse sperm incapable of proper motility toward the egg.

An exciting feature of this new study is that both the genetic knockout and the small-molecule inhibitor leave the testes functionally intact and only influence sperm maturation in the epididymis (see the first figure), which is a reservoir for maturation and transit of the sperm once they exit the testis. This feature of the work therefore has the added benefit that small-molecule inhibitors of sperm-specific calcineurin could act both quickly and reversibly.

Why is the work of Miyata *et al.* so globally important? During the time that the contraceptive pill has been available to women, the world's population has increased more than 2.4-fold, growing from 3 billion people in 1960 to over 7.2 billion today (see the second figure). This continued high rate of population growth (where the birth

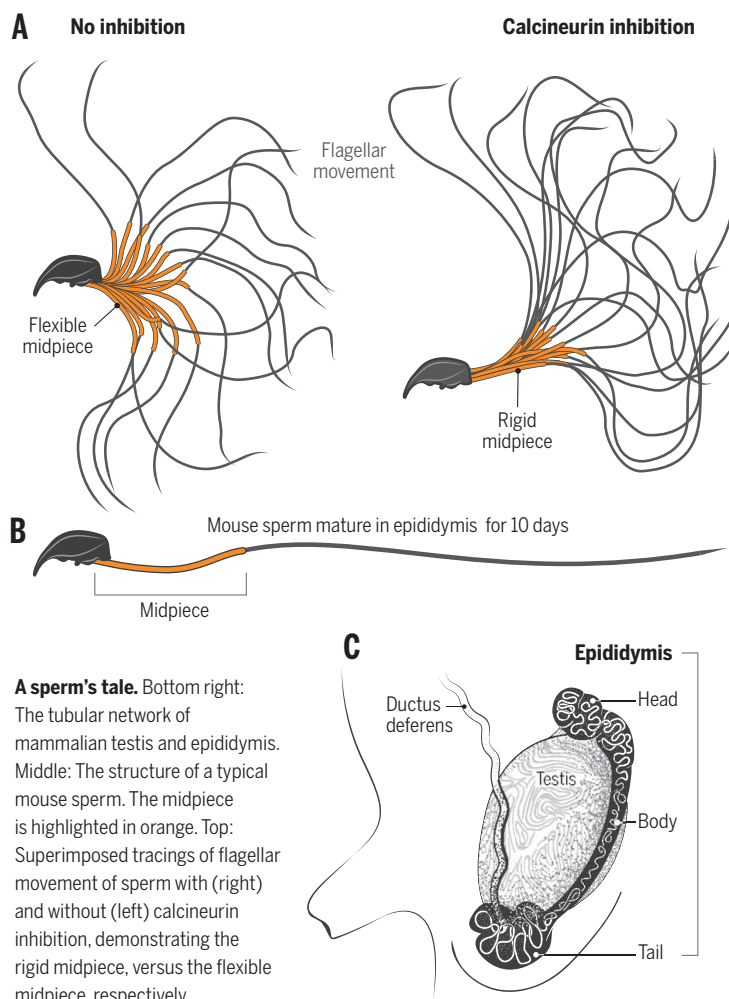
rate exceeds the death rate) calls into question whether every child born will have sufficient food, water, and education (3). In the United States, more than 50% of all women have experienced an unplanned pregnancy, and unlike other areas of the world, unintended pregnancy rates have not fallen (4). Contraception should be advocated globally to curb this population explosion, and we must come up with new approaches to contraception. One such prospect is a male pill that targets the male reproductive tract in a reversible manner while both sparing the other cells in the body of a reproductively healthy man and leaving the concentrations of male reproductive hormones (e.g., testosterone) unaltered.

Miyata *et al.* identified a potential avenue for the development of a male contracep-

tive pill by targeting calcium signaling. Calcium signaling is important for many cell types, especially in the immune system. It is mediated by the calcineurin protein complex (5). Small-molecule inhibitors of calcineurin, FK506 and cyclosporine A, have long been used to suppress the immune response following organ transplantation (6). In addition, both FK506 and cyclosporine A have adverse effects on sperm function in animals (7). Using mouse genetics, Miyata *et al.* were able to pinpoint the mechanism of decreased sperm function upon exposure to FK506 and cyclosporine A and the role of calcineurin in sperm production.

Calcineurin is composed of a regulatory subunit and a catalytic subunit (8). Mammals contain three versions of the catalytic subunit (PPP3CA, PPP3CB, and PPP3CC) and only two versions of the regulatory subunit (PPP3R1 and PPP3R2). Whereas most of these subunits are present in all cell types of the body, PPP3CC and PPP3R2 are relatively more abundant in the testis. Using different experimental approaches, Miyata *et al.* demonstrated that PPP3CC and PPP3R2 form a testis-specific calcineurin complex that localizes to the sperm tail.

When Miyata *et al.* depleted PPP3CC from mice using genetic tools, males became infertile, whereas females were unaffected. Testis morphology, spermatogenesis, sperm counts, and sperm motility were not affected in mice lacking PPP3CC. In addition, sperm from these males could reach the site of fertilization in the female reproductive tract, which seems at odds with the observation that males are sterile. Using video recordings and computer analysis, the authors found that sperm lacking PPP3CC have a subtle yet noticeable rigidity in the sperm tail (see the first figure, top right). Through careful anal-



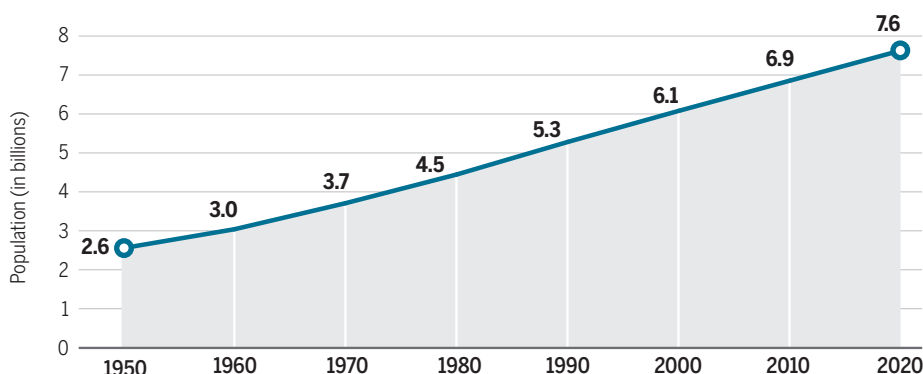
ysis using in vitro fertilization, Miyata *et al.* discovered that these rigid sperm were unable to penetrate the zona pellucida (a glycoprotein layer surrounding oocytes). The infertility defect could be suppressed if the zona pellucida was removed. The offspring generated from this in vitro fertilization procedure had no abnormalities, which suggests that the sperm-specific calcineurin is not needed for normal development.

In the next set of experiments, Miyata *et al.* used FK506 and cyclosporine A to pinpoint when functional calcineurin was needed in sperm development. When isolated sperm were exposed to these inhibitors in vitro, sperm flexibility and fertilization rates were unaffected. However, when male mice were subcutaneously in-

sibility of generating a male contraceptive pill by targeting sperm-specific calcineurin, several important considerations remain. One major issue is the similarities between the testis-specific calcineurin and the calcineurins present in other cell types. An effective and safe male contraceptive pill will need to target only testis-specific calcineurin, as global inhibitors of this complex have (undesirable) effects elsewhere in the body. Another consideration is public attitudes regarding gender-specific stereotypes toward a “male pill.” Men worldwide, especially those in long-term relationships, may be more accepting of taking a pill that renders them only temporarily “infertile” (i.e., if the potential of rapid reversibility can be demonstrated, as in Miyata *et al.*),

Billions and billions

The global population growth by decade since 1950



jected with these inhibitors, rigid sperm appeared as early as 4 days after administration. In normal sperm production, the final maturation steps (which span 10 days in the mouse) occur in the epididymis of the male reproductive tract. The appearance of rigid sperm after 4 days suggests that calcineurin function is needed during these final maturation steps. The most exciting finding from a human health perspective is that sperm flexibility and fertilization rates recovered completely within 7 days of cessation of administration of these drugs. The rapid inhibition of male fertility and its reversibility identify the sperm-specific calcineurin complex as a tantalizing male contraceptive target.

Although the study of Miyata *et al.* has global implications in identifying the pos-

and there are also economic benefits of family planning that does not rely only on the woman to be solely responsible for contraception.

Uncontrolled fertility has been identified as a pressing public health issue facing this and future generations worldwide (9). For the previous 50 years, contraceptive pills have only been available to half the population (women). While a male “pill” is many years away, the study of Miyata *et al.* lays the groundwork for research into the production of new small-molecule contraceptives. ■

REFERENCES

1. NICHD. Strategic Plan 2000 From Cells to Selves. (National Institute of Child Health and Human Development, 2000).
2. H. Miyata *et al.*, *Science* **350**, 442 (2015).
3. http://consensusforaction.stanford.edu/see-scientific-consensus/consensus_english.pdf
4. S. Singh, G. Sedgh, R. Hussain, *Stud. Fam. Plann.* **41**, 241 (2010).
5. N. A. Clipstone, G. R. Crabtree, *Nature* **357**, 695 (1992).
6. T. E. Starzl *et al.*, *Lancet* **334**, 1000 (1989).
7. L. Seethalakshmi, M. Menon, R. K. Malhotra, D. A. Diamond, *J. Urol.* **138**, 991 (1987).
8. F. Rusnak, P. Mertz, *Physiol. Rev.* **80**, 1483 (2000).
9. R. J. Aitken *et al.*, *J. Clin. Invest.* **118**, 1330 (2008).

¹Department of Pathology and Immunology, Baylor College of Medicine, Houston, TX 77030, USA. ²Department of Molecular and Cellular Biology, Baylor College of Medicine, Houston, TX 77030, USA. ³Center for Reproductive Medicine, Baylor College of Medicine, Houston, TX 77030, USA. ⁴Department of Molecular and Human Genetics, Baylor College of Medicine, Houston, TX 77030, USA. ⁵Department of Pharmacology, Baylor College of Medicine, Houston, TX 77030, USA. ⁶Center for Drug Discovery, Baylor College of Medicine, Houston, TX 77030, USA. E-mail: mmatzuk@bcm.tmc.edu

SYSTEMS BIOLOGY

Systems biology (un)certainities

How can modelers restore confidence in systems and computational biology?

By P. D. W. Kirk,¹ A. C. Babbie,² M. P. H. Stumpf^{2*}

Systems biology, some have claimed (1), attempts the impossible and is doomed to fail. Possible definitions abound, but systems biology is widely understood to be an approach for studying the behavior of systems of interacting biological components that combines experiments with computational and mathematical reasoning. Modeling complex systems occurs throughout the sciences, so it may not be immediately clear why it should attract greater skepticism in molecular and cell biology than in other scientific disciplines. The way in which biological models are often presented and interpreted (and overinterpreted) may be partly to blame. As with experimental results, the key to successfully reporting a mathematical model is to provide an honest appraisal and representation of uncertainty in the model's predictions, parameters, and (where appropriate) in the structure of the model itself.

Deriving mathematical models in biology is rarely straightforward. Although biology is, of course, subject to the same fundamental physical laws—for example, conservation of mass, energy, and momentum—as the other sciences, these laws often do not provide a good starting point for understanding how biological organisms and systems work. Biological modeling is an example of the so-called inverse problem (1), and instead emphasizes context-specific levels of abstraction and relies upon experimental observations to decide if a particular model is useful.

Typically, not all terms or parameters in a biological model are known or observable directly, and—except for some highly specific systems—the abundances of all the key players (molecules, cells, or individuals) cannot be measured simultaneously and continuously. Thus, despite being often overlooked, the challenge is not only

to identify suitable mathematical descriptions of biological systems (such as gene regulatory networks) and mathematical representations of such systems that provide mechanistic insight, but also to communicate the inevitable uncertainty in the model's (possibly many) unknowns. Although substituting these unknowns for estimates obtained from exogenous experimental assays that are related to the biological system in question has been advocated (2), this is usually fraught with problems: It is often impossible to perform all of the necessary experiments to measure missing parameters directly; frequently these measurements are themselves subject to considerable uncertainty, or are only possible to make under very different conditions; and the approach misses an opportunity to extract this information from the original, and potentially most relevant, experimental data. In this context, Bayesian inference procedures (3), which naturally permit the integration of external prior knowledge or beliefs with newly observed data, may provide the most natural framework for expressing and reporting uncertainty, and for this reason have become increasingly popular in systems biology. For example, a recent application provides insight into a debated mechanism for the way in which organisms may ameliorate dangerous damage to mitochondrial DNA (3).

The number of unknowns in a model is partly determined by the scale of the system being studied. A biological system may range in scale from a few interacting molecules to whole populations of organisms, and this can have a huge impact on both the modeling approach and the associated assessment of uncertainty (see the figure). For small systems, it might be possible to rely solely on strong prior knowledge and specify a model structure that reflects known interactions. For larger systems, automated "network inference" algorithms have been employed (4, 5). These aim to identify statistical dependencies, such as those between messenger RNA expression measurements, to highlight potential (co)regulatory interactions. But here, too, information about known transcription factor targets can be used as prior information to guide network inference. These data-driven, hypothesis-generating approaches for creating a biological model from data alone are often opposed, because as the biological systems in ques-

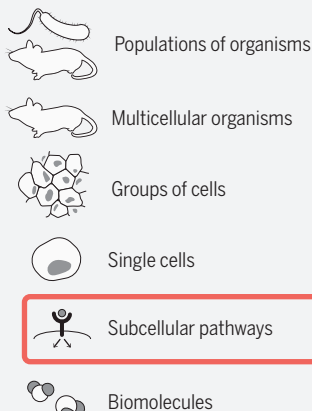
tion become larger and more complex, it becomes increasingly impossible to learn the "true" and complete underlying network (1). However, this opposition seems to be predicated upon misconceptions of the aims of large-scale network inference, which are typically to highlight and explore dependencies in data sets—and thereby help to generate new hypotheses worthy of further investigation—rather than to uncover a single grand unifying model of the system. Unfortunately, not all network inference algorithms are equally effective,

Question

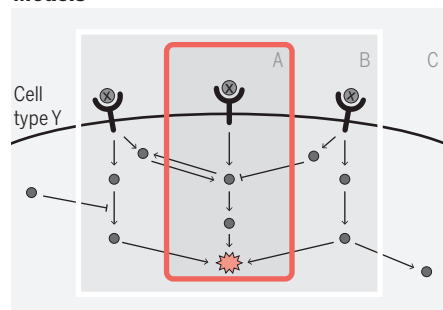
How does factor X affect proliferation of cell type Y?



Scales of biological systems



Models



Abstraction and simplification. Mathematical models usually represent elements of a biological system at one scale. Choosing the appropriate degree of abstraction and simplification can be influenced by current knowledge about the system, the quality and quantity of experimental data, the computational demands of a particular modeling approach, and the modeling aims. For example, when studying a signaling pathway, the scope of the model may be restricted to a single pathway or it might include the influence of parts of a wider interconnected network of signaling pathways.

and the most popular approach—using the correlation among expression levels of genes (6)—results in a particularly poor basis on which to conduct further studies, let alone mechanistic models. Several alternative network inference approaches exist (4, 5) that provide better, more robust candidate networks, and can incorporate expert or domain knowledge. These methods may be used to investigate gene-regulatory relationships, and how interactions between genes change over time or differ between disease cases and healthy controls.

Although large-scale grand unifying biological models have occasionally been sought (for example, whole-cell models, which are designed to be comprehensive models of cells that are expressed in terms of each cell's molecular components) (7), these efforts remain the exception and only exist in early draft forms. Many challenges remain for models of such scope, including how to validate their quality and adequately report the uncertainty in both their overall global structure and their implied submodels. Whatever the scale of the system and data set, many different models are likely to provide plausible fits, while still remaining consistent with current knowledge. Even for a small-scale (five-gene) regulatory network, it can be possible to find tens of thousands of models that provide qualitatively perfect fits even to dense, low-noise data sets, but that yield a variety of (often contradictory) insights into the regulatory relationships between genes (8). Assessing robustness of predictions and inferences across multiple alternative models can therefore be illuminating (8–10), provided the conclusions are still understood to be dependent on the particular set of models that are specified, and influenced by the experiments that are chosen (11, 12).

Models should not be expected to work in every conceivable context, and the most exciting results are frequently those that break existing models. Model uncertainty, as characterized by the ability to identify multiple models that explain current observations, therefore calls for the design of maximally discriminative experiments that will break as many models as possible (12, 13). For example, dose-response curves typically provide too little discriminatory power, whereas carefully designed time-resolved analyses allow the study of even complicated models, such as proteasomal dynamics (14).

Many of the criticisms of model development in systems biology stem from a lack of appreciation of the variety of roles that can be played by mathematical modeling (1). This is partly driven by overstating implications and consequences of models, perhaps due to poor understanding of the power of

¹MRC Biostatistics Unit, Cambridge Institute of Public Health, Cambridge CB2 0SR, UK. ²Centre for Integrative Systems Biology and Bioinformatics, Department of Life Sciences, Imperial College London, London SW7 2AZ, UK. E-mail: a.babbie@imperial.ac.uk; paul.kirk@mrc-bsu.cam.ac.uk; m.stumpf@imperial.ac.uk *All authors contributed equally to this work.

modern statistical approaches and machine learning. Overstating can also be attributed to a lack of understanding the value of reporting uncertainties. Frequent fallacies and bad practices continue to thrive, including the use of correlation to capture causal relationships, failure to address the multiple comparison problem (for example, when testing for the presence of potential regulatory interaction among all pairs of genes, one cannot apply standard hypothesis testing, which would result in excessive numbers of false-positives; to prevent this, the threshold for significance must be adjusted to account for the large number of tests carried out), and a lack of error bars or more general confidence sets/intervals (8) for parameters and models.

Models are simplified (but not simplistic) representations of real systems, and this is

“Deriving mathematical models in biology is rarely straightforward.”

precisely the property that makes them attractive to explore the consequences of our assumptions, and to identify where we lack understanding of the principles governing a biological system. Models are tools to uncover mechanisms that cannot be directly observed, akin to microscopes or nuclear magnetic resonance machines (15). Used and interpreted appropriately, with due attention paid to inherent uncertainties, the mathematical and computational modeling of biological systems allows the exploration of hypotheses. But the relevance of these models depends on the ability to assess, communicate, and, ultimately, understand their uncertainties. ■

REFERENCES

1. S. Brenner, *Philos. Trans. R. Soc. Lond. B Biol. Sci.* **365**, 207 (2010).
2. E. U. Azeloglu, R. Iyengar, *Sci. Signal.* **8**, fs8 (2015).
3. I. G. Johnston *et al.*, *eLife*, **4**, e07464 (2015).
4. C. A. Penfold, D. L. Wild, *Interface Focus* **1**, 857 (2011).
5. C. J. Oates, R. Amos, S. E. F. Spencer, *Stat. Appl. Genet. Mol. Biol.* **13**, 611 (2014).
6. S.-J. Dunn, G. Martello, B. Yordanov, S. Emmott, A. G. Smith, *Science* **344**, 1156 (2014).
7. J. R. Karr *et al.*, *Cell*, **150**, 389 (2012).
8. A. C. Babbie, P. Kirk, M. P. H. Stumpf, *Proc. Natl. Acad. Sci. U.S.A.* **111**, 18507 (2014).
9. P. Meyer *et al.*, *BMC Syst. Biol.* **8**, 13 (2014).
10. A. F. Villaverde *et al.*, *Comput. Methods Programs Biomed.* **119**, 17 (2015).
11. J. Ruess, A. Milias-Argetis, J. Lygeros, *J. R. Soc. Interface* **10**, 20130588 (2013).
12. M. Sunnåker *et al.*, *Sci. Signal.* **6**, ra41 (2013).
13. D. Silk *et al.*, *PLOS Comput. Biol.* **10**, e1003650 (2014).
14. J. Liepe *et al.*, *eLife*, **4**, e07545 (2015).
15. J. E. Cohen, *PLOS Biol.* **2**, e439 (2004).

10.1126/science.aac9505

NANOSAFETY

How safe are nanomaterials?

There is still no consensus on the toxicity of nanomaterials

By Eugenia Valsami-Jones and Iseult Lynch

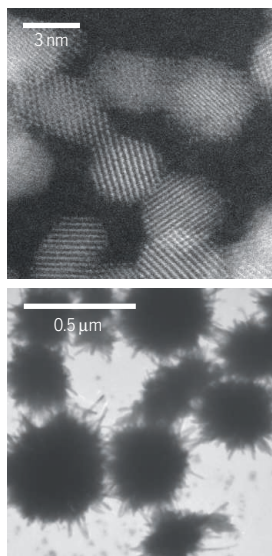
Engineered nanomaterials are widely used in consumer products such as cosmetics, paints, fabrics, and electronics. Because of their small size (diameter <100 nm), they often have unusual properties. Once released into the human body or the environment, they are also fiendishly difficult to find again. In 2006, Nel *et al.* described possible mechanisms by which engineered nanomaterials interact with biological entities and the toxicological responses that may be triggered (1). Despite much research since then, mechanistic understanding remains limited. Evidence for acute toxicity from nanomaterials at realistic doses is limited; there also is no simple correlation between toxic responses and nanoparticle size or other predictable pattern of toxicity. For answers to emerge, the nanosafety community must embrace recent technical advances and build consensus on testing methodologies.

Upon entering the environment, some engineered nanomaterials, such as metals (silver, copper) and metal oxides (zinc oxide, iron oxide), may dissolve quickly, whereas others are more persistent (for example, titanium dioxide, silicon dioxide, carbon nanotubes, and graphene). From a safety point of view, soluble nanomaterials represent a best-case scenario, because any hazard from exposure is likely to be no different from that of their constituent ions. Given their small size and the limited quantities used in applications, such release is unlikely to amount to a major environmental threat. Direct exposure of humans or organisms would, however, still be a concern, particularly if the nanomaterials were internalized by cells as particles, only to dissolve and deliver toxic metals inside the cell after entry—a mechanism known as “Trojan horse” (2) (see the second figure) in analogy with Greek mythology.

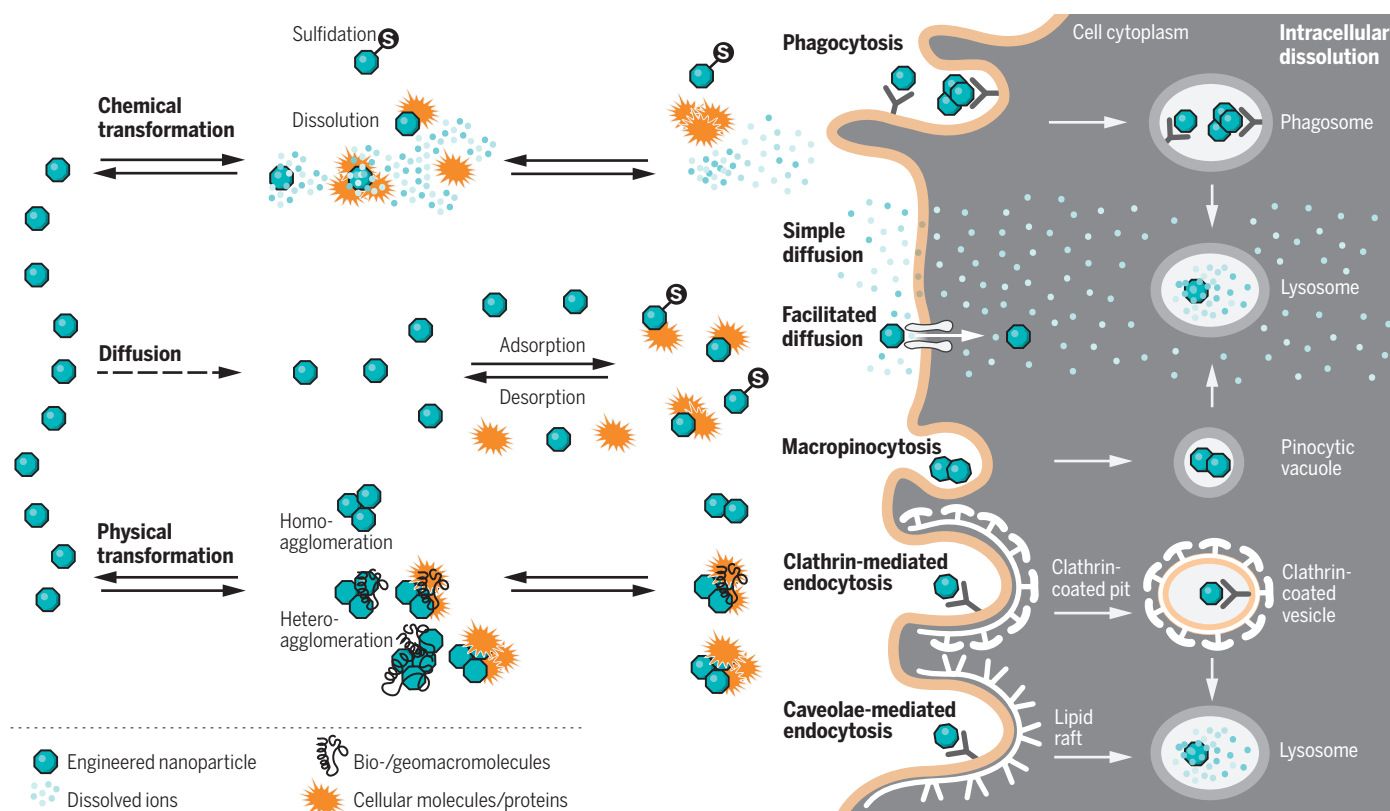
The Trojan horse effect is specific to the nanometer scale and results from the potential of small particles to be actively internalized by cells via inadvertent recognition by cellular receptors. It remains unclear how prevalent such nanospecific effects are. In a recent review, Notter *et al.* found that most published ecotoxicity studies report no more harm from engineered nanomaterials than from their dissolved metal counterparts (3). However, some of these studies may have missed subtle effects or failed to monitor the fate of nanomaterials and ensure exposure throughout the experiment. The review also considered only three types of nanomaterials (Ag, CuO, and ZnO).

Even a casual survey of the literature would find many studies reporting a nanospecific effect. For example, uptake of silver nanoparticles by snails differs from that of dissolved ions and depends on whether the snails are exposed to them through their diet or via water that they consume (4). Also, some engineered nanomaterials may cause damage to the digestive or pulmonary system of different organisms and humans (4, 5) and even to secondary organs, such as the liver, after translocation (5). At the bottom of the food chain, algae take up metal nanoparticles in fundamentally different ways from dissolved metals (Zn, Cu, Ag) (6). In the case of nanoparticles, metal concentrations were highest in the cell walls, whereas for dissolved metals, concentrations were highest in the cell. However, for all metals, toxicity was the same for both types of exposure.

Aging of nanoparticles is another recently discovered issue. For example, Stegemeier *et al.* have reported very different uptakes of pristine and aged particles by plants (7). Most published work to date has focused on pristine nanomaterials, which can be structurally and chemically distinct from their aged counterparts (see the first figure) and may thus have



Young and old. Nanomaterials change or “age” upon release into the environment, as shown here for ceria nanoparticles. Data for the pristine nanomaterial are therefore meaningless for interpreting the environmental and toxicological impacts of the aged form.



Nanoparticle complexity. Schematic illustration of the competing environmental transformation and organismal uptake processes that occur for a nanomaterial in aquatic environments, illustrated using a silver nanoparticle.

different toxicity. The nanosafety community must demonstrate biological and environmental relevance of the studied nanomaterials, especially if aging is insufficiently accounted for. This will not be easy, because consensus in the literature is often lacking even for pristine nanomaterials (8).

Nanosafety is of course no different from many other areas of science where issues with reproducibility occur. Openness and data sharing can go a long way toward resolving the issues (9). The nanosafety community could benefit from harmonization of methodologies and approaches, given that in this young field, there is no consensus even on basic laboratory protocols. Characterization must also be sufficiently detailed, particularly given that recent studies linking nanomaterial structure with toxicity point to subtle physicochemical characteristics (such as redox activity, band gap energy, and surface properties) not included in routine characterization (10). A recent review by the Organisation for Economic Cooperation and Development (OECD) also concluded that standardized hazard testing methods must be critically revised to correctly address hazards from engineered nanomaterials (11).


Recent advances may point the way toward resolution and consensus. In particular, genomic approaches enable hypothesis-independent discovery of potential toxicity pathways. Ivask *et al.* recently used such an approach to demonstrate not only differences between ionic and nanoparticle toxicity, but also different mechanisms of toxicity triggered by different forms of nanomaterial surface modification (12). These methods allow subtle effects to be picked up and attributed correctly.

High-throughput screening techniques also hold great potential, enabling faster and more reproducible toxicity testing of engineered nanomaterials (13). Further progress is likely from novel approaches to quantitative structure-activity relationships (QSARs), computational models that link specific structures or properties to the responses that they elicit. The models can, for example, use the specific combination of proteins and their relative concentrations on a nanomaterial's surface (the "corona") to predict its potential for cell association and internalization (14). Mechanistic models of toxicity could be the ultimate weapon against uncertainty, if they provide a reproducible link between specific nanomaterial features and a particular biological response; a less toxic material might then result from "designing-out" features identified as causing toxicity (15).

Nanosafety research has reached a crossroads, with opportunities still compromised by uncertainties, but with great potential for answers to emerge from application of state-of-the-art approaches. Future success will depend on converting laboratory and field discoveries into computational models and on ensuring that consistent language is used to describe these findings. This will ensure reliable answers to the question of nanomaterials toxicity and allow prediction of toxicity from structure and/or properties. ■

REFERENCES

1. A. Nel, T. Xia, L. Madler, N. Li, *Science* **311**, 622 (2006).
2. Z. Wang *et al.*, *ACS Nano* **7**, 4171 (2013).
3. D. A. Nottter, D. M. Mitrano, B. Nowack, *Environ. Toxicol. Chem.* **33**, 2733 (2014).
4. M. N. Croteau, S. K. Misra, S. N. Luoma, E. Valsami-Jones, *Environ. Sci. Technol.* **45**, 6600 (2011).
5. H. M. Braakhuis, M. Park, I. Gosens, W. H. De Jong, F. R. Cassee, *Part. Fibre Toxicol.* **11**, 18 (2014).
6. G. K. Bielmeyer-Fraser, T. A. Jarvis, H. S. Lenihan, R. J. Miller, *Environ. Sci. Technol.* **48**, 13443 (2014).
7. J. P. Stegemeyer *et al.*, *Environ. Sci. Technol.* **49**, 8451 (2015).
8. H. F. Krug, *Angew. Chem. Int. Ed.* **53**, 12304 (2014).
9. S. Buck, *Science* **348**, 1403 (2015).
10. A. E. Nel *et al.*, *ACS Nano* **9**, 5627 (2015).
11. E. J. Petersen *et al.*, *Environ. Sci. Technol.* **49**, 9532 (2015).
12. A. Ivask *et al.*, *ACS Nano* **8**, 374 (2014).
13. G. Harris *et al.*, *Nanotoxicology* **9**, 87 (2015).
14. C. D. Walkey *et al.*, *ACS Nano* **8**, 2439 (2014).
15. B. Sun *et al.*, *ACS Nano* **9**, 9357 (2015).



Dark matter in the galaxy cluster CI 0024+17 distorts the light of more distant galaxies, an optical illusion called gravitational lensing.

PHYSICS

The dark side of the universe

A provocative theory takes readers on a journey through the cosmos

By Jan Smit¹* and Renske Smit²

To put us, as book reviewers, in context, like many scientists, we study our surroundings in an effort to understand where we came from. Jan, the historical geologist, likes to begin with the birth of our solar system 4.56 billion years ago. Before that, in his mind, there was nothing. Renske, the astrophysicist, works on much larger time scales, beginning with the birth of the earliest galaxies 13.2 billion years ago. For her, our solar system is just a little speck in recent history. It is therefore rare to come across a publication that piques the interest of both of us. Such was the case with particle physicist Lisa Randall's new book, *Dark Matter and the Dinosaurs*.

The first thought that crossed both our minds when reading the title of this book was: "Oh, no, not again, another outlandish proposal for the extinction of dinosaurs..." However, we were relieved to find that, right from the start, Randall dismisses almost all connections between dark matter and the mass-extinction event that wiped out the dinosaurs. Instead, the book takes the reader on a journey through the cosmos, describing what we know about dark matter and what

more we are poised to learn as new and better equipment becomes available.

Randall starts with an outline of "The Big Questions": Why is there something rather than nothing? What happened during the Big Bang? What came before the Big Bang? She explains that there has to be dark matter because the behavior of merged galaxy clusters like the Bullet Cluster cannot be explained otherwise. She skims through the Big Bang, cosmic inflation, and how the galaxies formed when normal matter hitchhiked along with dark matter to form the seeds of the first stars. Without dark matter, we learn, our Milky Way and Earth as we know it would not exist.

Having covered the creation of stars, the book turns to our solar system. Here, Randall vividly describes the comets and asteroids that have hit or will hit Earth. She recounts how meteorites may have brought essential amino acids and perhaps some water to Earth and describes the Chicxulub asteroid/comet and its role in the mass extinction at the end of the Cretaceous. The story of the Chicxulub impact and its role in the extinction of the dinosaurs is highly entertaining and largely correct.

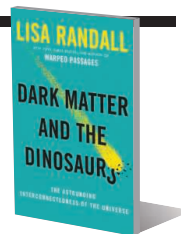
In the last chapters of the book, Randall outlines an important new way of thinking that applies to the search for viable dark matter models. The only way to find out whether something is allowed or even preferred is to evaluate the consequences

Dark Matter and the Dinosaurs

The Astounding Interconnectedness of the Universe

Lisa Randall

Ecco, 2015. 432 pp.



of new assumptions and determine their experimental implications. Although observations indicate that dark matter consists of a mostly noninteracting substance, no experiment can currently rule out that dark matter may have a weak interaction with its own particles or, alternatively, that a small fraction of particles of dark matter have a moderately large interaction with one another. If true, these new models would be an extension of current theories, some of which can be tested in new experiments over the next few years.

One model explored in this book shows how a narrow disk of dark matter in the galactic plane could potentially explain the periodicity in the crater records on Earth and could have contributed to the impact 66 million years ago that generated the mass extinction of the dinosaurs. Randall is quick to admit that the data that favor such a model are still tenuous and that the theory requires further testing. So does that mean that dark matter and dinosaurs are connected? Likely not, although there is a chance that they could be. In the end, drawing a definitive connection between the two is not really the aim of the book.

Randall has a manner of writing that is pleasant and compelling: Cliff-hangers at the end of each chapter reel you into the next. Her method of using everyday situations as metaphors for explaining complicated concepts in physics is also very effective. For example, she describes how scientists know that dark matter is present in much the same way that you may be able to infer that George Clooney is in busy downtown New York: You may not see, smell, or hear him, but you can observe that all faces on the street are directed toward him.

Despite the provocative title, the scientific reasoning set out in this book is sound and interesting. Randall succeeds in guiding the reader through the history of the cosmos and the Earth from the Big Bang to the emergence of life as we know it in a fun and captivating way. The rich metaphors and personal anecdotes peppered throughout the book make this a very enjoyable read for both lay readers and scientists of various backgrounds.

¹Faculty of Earth and Life Sciences, VU University Amsterdam, 1081 HV Amsterdam, Netherlands. ²Department of Physics, Durham University, Durham DH1 3LE, UK. *Corresponding author. E-mail: jansmit2@icloud.com

SCIENCE COMMUNICATION

The storytelling scientist

Practical tools for crafting compelling scientific narratives

By Rafael E. Luna

In Randy Olson's new book, *Houston, We Have a Narrative*, he boldly states that the single biggest problem facing science today is "narrative deficiency." "Science is a narrative process," he argues, "...therefore science needs a story." I agree that narratives have not been universally adopted in scientific communications, yet that tide appears to be turning.

Houston, We Have a Narrative fits into a growing list of publications, scientific conferences, and academic institutions encouraging scientists to integrate narrative elements into research and public communications.

A former tenured professor, Olson left academia for Hollywood in 1994. This book offers his insights gained from over 20 years of experience as a writer and director. In the book, Olson presents a series of anecdotes and useful tools that provide a strong justification for incorporating storytelling into science.

Olson begins by showing the reader how the "Introduction-Methods-Results-And-Discussion" or "IMRAD" approach for publishing research manuscripts is basically a narrative structure. "It is simple in form and essentially identical to the three-act structure that is at the heart of virtually every movie or play written today," he argues. "It is the structure of a story, which has a beginning (I), middle (M&R), and end (D)."

In an effort to preempt boisterous critics who fear that narratives will overrun and dilute scientific data, Olson spends a considerable portion of the book describing

ing why a lack of narrative in science is a problem and why better narratives could mean better scientific communication. He outlines how bad storytelling and exaggerated claims negatively affect the scientific enterprise and describes the difficulty that scientists often experience as they struggle to effectively communicate their data. He then sets the stage for Hollywood to aid scientists in the development of their narratives.



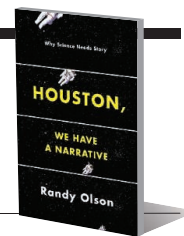
"...when crafting a scientific narrative, it is important to proceed with the same caution and precision as one would approach a scientific experiment..."

Among the communication strategies that he discusses is the "And, But, Therefore" or "ABT" method, which Olson argues is a concise and compelling way to describe one's research. "A scientist could say, for example, 'I can tell you that in my laboratory we study physiology AND biochemistry, BUT in recent years we've realized the important questions are at the molecular level, THEREFORE we are now investigating the following molecular questions...'" He contrasts the ABT method with the "And, And, And" or "AAA" structure ("People are walking AND some have dogs AND some are alone..."),

Houston, We Have a Narrative

Randy Olson

University of Chicago Press,
2015. 260 pp.



which Olson suggests is a tedious continuum of data.

Olson also describes a method for identifying the central theme of your scientific message via a technique he dubs "The Dobzhansky Template" in reference to the famous quote from the geneticist Theodosius Dobzhansky, "Nothing in biology makes sense except in the light of evolution." Olson argues that if you can effectively tell a granting agency that nothing in [insert your field here] makes sense except in light of [insert your work here], "you're probably going to get their attention." I would counter that if a scientist were to use this type of language in a grant application, he or she may be criticized for making statements that are a bit far-reaching. However, this approach would be appropriate in settings such as at a dinner party or a community outreach event.

Do scientists need to improve their scientific communication? The answer is a resounding "yes." However, when crafting a scientific narrative, it is important to proceed with the same caution and precision as one would approach a scientific experiment and to remember that a narrative is only as good as the data on which it is based.

As a minor point of clarification, the book could have done a better job of describing which tools would work best for which audiences. Nonetheless, Olson presents useful narrative techniques that scientists at various career stages could easily implement. The speed with which scientists can hope to achieve narrative proficiency using the tools in the book is one of its remarkable strengths and a testament to Olson's straightforward advice.

10.1126/science.aad2179

The reviewer is the author of *The Art of Scientific Storytelling: Transform Your Research Manuscript with a Step-By-Step Formula* (Amado International, Cambridge, 2013). E-mail: rafael_luna@hms.harvard.edu

LETTERS

Edited by Jennifer Sills

Iran's environment under siege

THE SPECIAL ISSUE on Science in Iran (4 September, Editorial by M. Farhadi, p. 1029 and News Feature by R. Stone, p. 1038) highlights the promise of a new era for my country. However, to achieve that promise, Iranians must learn how to be environmental stewards.

When I was growing up in Senejan village near Arak, 260 km south of Tehran, our community depended on qanats—ancient tunnels for transporting water from aquifers to settlements. But by the 1970s and 1980s, those qanats had been drained by Arak's rapid industrialization and heavy water consumption.

Before the 1980s, Iran had 18 dams (1). Now it has 647 dams, with 146 more under construction and 537 in planning (2). Campaigns against dam construction in Iran started in 2004, when nongovernmental organizations, activists, and scientists protested the loss of the Tange Bolaghi (3) archaeological sites submerged by Sivand Dam in Fars Province, as well as the dam's threat to Persepolis and Pasargadae, UNESCO World Heritage Sites. The dam also led to the drying up of lakes and wetlands, submergence of forests, and desertification (4). Because of desiccation of wetlands, dust storms commonly blight large swathes of Iran. On 8 February 2015, the entire city of Ahvaz, the capital of Khuzestan Province, was covered by yellow soil (5). Ahvaz now ranks first on the list of the world's most polluted cities according to the World Health Organization (6).

The outcry over dams reached a crescendo with the \$3 billion Gotvand Dam, built on a saline formation, now operating. The dam increased the salinity of the Karun River, damaging cropland in Khuzestan Province. Extensive damming combined with groundwater pumping from approximately 780,000 wells has ravaged aquifers, decreasing Iran's water table by around 20 m and accelerating subsidence (7). Water consumption stands at 85% of renewable resources.

Another practice that degrades Iran's nature is overgrazing. According to official statistics, Iran has 90 million grazing livestock—2.2 to 3.5 times the country's grazing capacity (8, 9). Many rare plants are threatened, and the denuded land is a source of dust and prone to catastrophic floods,



Seimareh Arch Dam, western Iran

including one on 19 July 2015, in which 18 people were killed (10). In Iran, soil erosion from flooding, wind, agriculture, and grazing amounts to approximately 25 tons per hectare a year, 4.3 times more than world average (11).

When sanctions are lifted, Iran must implement new strategies to reduce the pressures on its fragile environment.

Hossein Akhiani

School of Biology, University of Tehran, Tehran, Iran.
E-mail: akhiani@khayam.ut.ac.ir

REFERENCES

1. M. Najmaei, *Dam and Environment* (Bulletin No. 55, IRCOLD, 2003).
2. Iran Water Resources Management Company: Iranian dams according to geographical divisions (2015); <http://daminfo.wrm.ir/fa/dam/stats> [in Persian].
3. A. Tsuneki, in *The Neolithisation of Iran: The Formation of New Societies*, R. Matthews, H. Fazeli Nashli, Eds. (Oxbow, Oxford, 2013), pp. 84–96.
4. F. Zafarnejad, *Int. J. Environ. Stud.* **66**, 327 (2009).
5. "How Iran's Khuzestan went from wetland to wasteland," *The Guardian* (2015); <http://gu.com/p/47ap/sbl>.
6. WHO, "Public Health and Environment (PHE): Ambient air pollution, exposure to particulate matter less than 10 µm in diameter in urban areas, 2008–2013" (2014); www.who.int/phe/health_topics/outdoorair/databases/en/index.html.
7. M. Motagh et al., *Geophys. Res. Lett.* **35**, L16403 (2008).
8. S. Velayati, A. A. Kadirav, *J. Geog. Res. Dev.* **4**, 53 (2006).
9. N. Eskandari, A. Alizadeh, F. Mahdavi, *Range Management Policy in Iran* (Forests, Range, and Watershed Management Organization, Tehran, 2008).
10. "Deputy Minister: Recent floods in the country left 18 dead and three missing" (www.irna.ir/fa/News/81695388/) [in Persian].
11. A. Jalalian, *Proceedings of the 12th Iranian Soil Science Congress*, Iran, Tabriz (2011), pp. 1–7.

Iran's education and research potential

I WAS INTRIGUED by R. Stone's 4 September News Feature "Unsanctioned science" (p. 1038). Nonetheless, as an American professor born and raised in Iran, I felt that Stone

overlooked certain factors that affect Iran's higher education and scientific R&D.

First, in my opinion, despite having endured an imposed 8-year-long war, three decades of sanctions, and myriad limitations from within and without, Iran has invested heavily in the pursuit of higher education and scientific R&D as a matter of national priority and pride. This, unrivaled in the region, is evident in Iran's skyrocketing publications and citations, the proliferation of college graduates and entrepreneurs, and—unfortunately for Iran but fortuitously for the West—brain drain to renowned universities and corporations abroad.

Second, inconsistent standards among degree programs, in addition to nepotism in elite college seating and scarce job placements, have demoralized, disenfranchised, and even curtailed opportunities for independent scholars, many of whom have returned home after establishing their credentials overseas. Consequently, even though the nation's higher education student capacity has exceeded 4.5 million (1), hundreds of thousands of college seats remain vacant every year, because more than 30% of college graduates are unemployed (2).

Third, many in Iran seek a doctorate degree to achieve stature and grab power rather than to serve the nation. This is anathema to the Persian values of humility and modesty upheld not only by many contemporary Iranian scientists and scholars worldwide, but also by classical Iranian scholars such as al-Khwarizmi (Algorithm), Avicenna, Razes, Rumi, Khayyam, and al-Biruni since antiquity (3, 4).

Finally, 60% of college students—even in medicine, health care, science, and engineering—are women. Closing the still-present gap for equal opportunities in postgraduate studies and employment will ensure a robust workforce as Iran moves into the 21st century (5, 6).

With the recent "nuclear deal" (7) and the expected removal of U.N. and U.S. sanctions, I hope that Iran will once again fully (re-)gain its duly earned stature in the international community. I further trust that organizations such as the Institute for International Education, the Fulbright Board, and the Peace Corps will enhance scientific and cultural exchanges between Iran and the West. Tens of thousands of Iranian expatriate professors and scholars in the West are well prepared to play a pivotal role toward that mutual endeavor.

Davood N. Rahni

Departments of Chemistry and Environmental Law, Pace University, New York, NY 10038, USA and Department of Dermatology, New York Medical College, Valhalla, NY 10595, USA.
E-mail: drahni1956@yahoo.com

REFERENCES

1. A. Valentine, Ed., *The Business Year: Iran 2013* (2013).
2. N. Habibi, "Iran's Over-Education Crisis: Causes and Ramifications," Middle East Brief 89 (Brandeis University, Brookline, MA, 2015); www.brandeis.edu/crown/publications/meb/meb89.html.
3. L. E. Goodman, *Avicenna* (Routledge, London, 1992).
4. P. G. Kreyenbroek, in *Persian Philosophy, Companion Encyclopedia of Asian Philosophy*, B. Carr, I. Mahalingam, Eds. (Routledge, London, 2009).
5. NationMaster, "Girls to boys ratio, countries compared" (2012); www.nationmaster.com/country-info/stats/Education/Girls-to-boys-ratio/Primary-level-enrolment.
6. G. Esfandiari, "Number of Female University Students Rising Dramatically in Iran" (2003); www.payvand.com/news/03/nov/1133.html.
7. R. Stone, *Science* **348**, 164 (2015).

With moralizing gods, exclusion reigns

WE ARE PUZZLED by some aspects of "Birth of the moralizing gods" (L. Wade, News Feature, 28 August, p. 918). It is true that a moralizing religion may enhance generosity and reduce the likelihood of cheating, but most often these behaviors are expressed only among coreligionists. Meanwhile, it is exactly this kind of selectivity and bias that can inhibit cooperation when large social

scale entails ethnic and religious diversity, as it typically does today and has in the past.

Wade cites Muslim traders in Africa, studied by Jean Ensminger, as an example consistent with the "Big Gods" hypothesis that religion promotes cooperation. Yet, if we take a broader view of Muslim trader cooperation within the larger framework of complex society, we see that religion was a path to social exclusion, not cooperation (1). As Ensminger discovered, the high cost of religious conversion to Islam served to restrict access to the profits of the long-distance trade to a small number of successful and privileged merchants.

To foster cooperation at the scale of society requires social architects to devise ways to overcome social and cultural heterogeneity and the resulting potential for exclusion and bias. Clearly this is a difficult task, as we see every day in the numerous failed states ravaged by religious sectarian conflict. In the language of collective action theory, in this kind of situation, the goal of social construction is to overcome the "assurance problem," referring to how cooperation will be limited unless potential cooperators feel confident that the behavior of other group members will be consistent with collective benefit

[e.g., (2)]. In cases of religious and ethnic heterogeneity, cooperation is enhanced when persons across ethnic and religious divides are confident that their interests will be recognized and that they will be accorded voice and meaningful forms of participation in the civic life of the community.

In ancient Egypt, the state's leadership was not concerned with solving the assurance problem. They didn't have to. The pharaohs maintained overwhelming control of society's wealth and political and military apparatuses, and they were able to sustain inequality in part through religious beliefs and rituals that endowed them with near-divine status. This kind of domineering and highly centralized state-building should never be construed as an example of cooperation at the scale of society.

Richard Blanton^{1*} and Lane Fargher²

¹Department of Anthropology, Purdue University, West Lafayette, IN 47907, USA. ²Departamento de Ecología Humana, Centro de Investigación y de Estudios Avanzados del IPN-Unidad Mérida, Yucatan, México.

*Corresponding author. E-mail: blantonr@purdue.edu

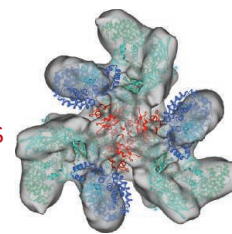
REFERENCES

1. J. Ensminger, *J. Inst. Theoret. Econ.* **153**, 4 (1997).
2. M. Levi, *Of Rule and Revenue* (Univ. of California Press, Berkeley, CA, 1988), pp. 52–55.

RESEARCH

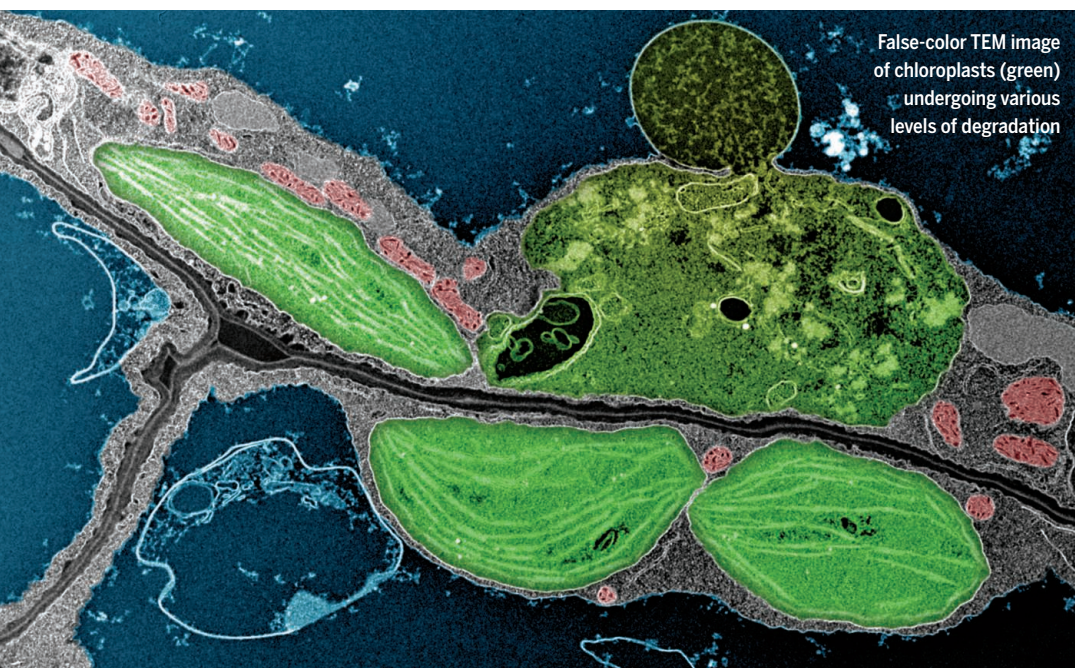
HIV proteins remodel clathrin-coated vesicles

Shen et al., p. 398



IN SCIENCE JOURNALS

Edited by Nick Wigginton



False-color TEM image of chloroplasts (green) undergoing various levels of degradation

CHLOROPLASTS

Quality control one chloroplast at a time

How do plant cells get rid of chloroplasts that are not working as they should? Woodson *et al.* describe a chloroplast quality-control pathway that allows for the selective elimination of individual chloroplasts. Damage by reactive oxygen species during photosynthesis is recognized by a ubiquitin ligase, which marks out damaged chloroplasts for degradation. The findings reveal how cells balance inherently stressful energy production with organelle turnover. — SMH

Science, this issue p. 450

INNATE IMMUNITY

Inflammasomes take the wheel

Cells require microbial ligand binding to sense pathogens (see the Perspective by Liu and Xiao). Binding to the family of NOD-like receptors triggers the assembly of large protein signaling complexes called inflammasomes, leading infected cells to die and produce inflammatory mediators. Hu *et al.* and Zhang *et al.* use cryo-electron microscopy to uncover the structural and biochemical basis of two such receptors: NAIP2, which directly binds microbial ligands, and NLRC4, a protein functioning directly downstream. A self-propagating activation mechanism of downstream inflammasome signaling starts with one molecule of NAIP4

directly binding its microbial ligand. NAIP4 then catalyzes the activation of 10 to 12 NLRC4 molecules to form a wheel-like structure. — KLM

Science, this issue p. 399, 404; see also p. 376

SUPERCONDUCTIVITY

A 3D approach to make 2D superconductors

When the thickness of a superconducting film becomes comparable to the typical size of its electron pairs, its superconductivity enters a two-dimensional (2D) regime. Thinner films usually have higher amounts of disorder, making it difficult to isolate the 2D effects. To circumvent this limitation, Saito *et al.* induced charge carriers on the surface of the 3D insulator ZrNCI. This approach

produced a clean superconducting layer thinner than the unit cell of the crystal. The superconducting state was extremely sensitive to the application of a perpendicular magnetic field, as expected for clean systems. — JS

Science, this issue p. 409

QUANTUM OPTICS

Probing the fluctuating vacuum

According to quantum mechanics, a vacuum is not empty space. A consequence of the uncertainly principle is that particles or energy can come into existence for a fleeting moment. Such vacuum or quantum fluctuations are known to exist, but evidence for them has been indirect. Riek *et al.* present an ultrafast optical based technique that probes the vacuum

fluctuation of electromagnetic radiation directly. — ISO

Science, this issue p. 420

MICROBIAL METABOLISM

Methane cycling gets more diverse

The production and consumption of methane by microorganisms play a major role in the global carbon cycle. Although these processes can occur in a range of environments, from animal guts to the deep ocean, these metabolisms are confined to the Archaea. Evans *et al.* used metagenomics to assemble two nearly complete archaeal genomes from deep groundwater methanogens (see the Perspective by Lloyd). The two reconstructed genomes are members of the recently described Bathyarchaeota

and not the phylum to which all previously known methane-metabolizing archaea belonged. — NW

Science, this issue p. 434,
see also p. 384

REPRODUCTIVE BIOLOGY

Mouse work may lead to male contraceptive

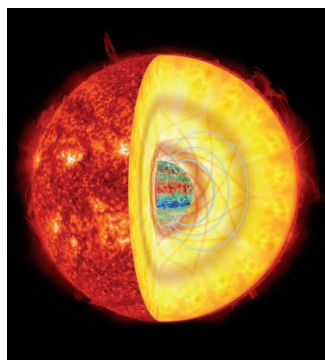
Unintended pregnancies are a major health issue worldwide. Although oral contraceptives were developed decades ago for use in women, there are no male oral contraceptives. Miyata *et al.* show that genetic deletion or drug inhibition of sperm-specific calcineurin enzymes in mice cause male sterility (see the Perspective by Castaneda and Matzuk). Although calcineurin inhibitors resulted in male infertility within 2 weeks, fertility recovered 1 week after halting drug administration. Because the sperm-specific calcineurin complex is also found in humans, its inhibition may be a strategy for developing reversible male contraceptives. — BAP

Science, this issue p. 442,
see also p. 385

ASTEROSEISMOLOGY

Stellar oscillations as magnetic probes

Unlike magnetic fields on the surfaces of stars, those within a star have so far remained difficult to observe. Fuller *et al.* have developed a method of delving into the magnetic depths by exploiting the oscillations of



Artistic representation of a magnetized red giant star

red giant stars. A high magnetic field can cause sound waves to become trapped within the central regions of the star, damping certain vibration modes. Using seismological techniques, this suppression can help infer the core magnetic field for several red giants. — KTS

Science, this issue p. 423

VASCULAR BIOLOGY

Stopping aneurysms before they start

The smooth muscle cells in aortas are connected to the extracellular matrix. Mutations in components of the extracellular matrix, such as fibulin-4, can lead to the enlargement of the aortic lumen, otherwise known as an aneurysm. Yamashiro *et al.* found that mice lacking fibulin-4 in smooth muscle cells had disrupted connections with the extracellular matrix. The mice also had abnormal increases in mechanosensitive proteins and enhanced activity of an actin cytoskeleton-remodeling enzyme called cofilin. Inhibiting the activity of cofilin or its upstream activators could therefore prevent the development of aneurysms. — WW

Sci. Signal. **8**, ra105 (2015).

BIOENGINEERING

Drugs ride waves across tissue barriers

Drugs that travel through the gastrointestinal (GI) tract meet tissue barriers that limit their uptake and dilute potency. Schoellhammer *et al.* used a common handheld ultrasonic probe to temporarily disrupt the barriers, allowing drugs to pass. The ultrasonic waves drove drugs into pig colonic tissue faster than natural absorption, without damage to the tissue. The approach also encouraged drug delivery into mouse colon tissue, leading to the healing of acute colitis. Ultrasound-mediated drug delivery may offer a versatile solution to barrier challenge in the GI tract. — MLF

Sci. Transl. Med. **7**, 310ra168 (2015).

IN OTHER JOURNALS

Edited by **Sacha Vignieri**
and **Jesse Smith**

LIGHT POLLUTION

Stay away from the light

We live in a world flooded with light 24 hours a day. Before our recent harnessing of electricity, light was a reliable indicator of seasonal variability in resources and many species evolved to take advantage of this signal. Robert *et al.* show that artificial light can alter these species physiological responses and desynchronize their seasonal reproduction. Specifically, they found that nocturnal tammar wallabies that lived near a continuously lighted military base secreted less melatonin at night and that this delayed reproduction by nearly a month, as compared to animals living without artificial light nearby. Animals living near the base attempted to avoid lighted areas, but these results suggest that light pollution may have unavoidable physiological effects. — SNV

Proc. R. Soc. London Ser. B 10.1098/rspb.2015.1745 (2015).



Exposure to continual light conditions delays reproduction in tammar wallabies

NANOMATERIALS

A tough shell for nanoparticles

Nanoparticles made from compound semiconductors such as cadmium sulfide (CdS) can exhibit useful luminescent properties but can also be

unstable with respect to ambient air and humidity, especially under conditions of strong illumination. Li *et al.* show that the passivation of metals by forming self-protecting oxides can be extended to nanoparticles. They added aluminum isopropoxide to the reaction mixture

ALSO IN SCIENCE JOURNALS

Edited by Nick Wigginton

CLATHRIN ADAPTORS

HIV proteins exploit clathrin coats

Clathrin-coated vesicles are involved in the sorting of membrane and cargo at the trans-Golgi network. Clathrin coats exploit adaptor proteins, including AP-1 and AP-2, in selecting their cargoes, assisted by the small membrane-trafficking associated GTPase Arf1. Shen *et al.* were interested in how the HIV-1 Nef protein affected this process. They leveraged a structure solved in the presence of Nef to show that the AP-1:clathrin coat is far more intricately organized than previously thought. Furthermore, Arf1 played a central structural role in these coated vesicles. It seems that HIV-1 Nef hijacks the clathrin pathway to its own ends through very sophisticated structural perturbations. — SMH

Science, this issue p. 398

MAGNETIC RESONANCE

EPR, one atom at a time

Electron paramagnetic resonance (EPR) usually detects atoms with unpaired electrons as ensemble averages. Baumann *et al.* used a spin-polarized scanning tunneling microscope tip to measure EPR spectra of single iron atoms adsorbed on a magnesium oxide surface at cryogenic temperatures. The measurement depends on the atomic orbital symmetry; no signal was observed for cobalt atoms under the same conditions — PDS

Science, this issue p. 417

ENVIRONMENT

Detectives of the nanoscale

Many consumer products contain nanometer-sized components. Are these nanomaterials harmful when they are

released into the environment? As Valsami-Jones and Lynch explain in their Perspective, answers to this question are not easy to come by. Nanoparticles undergo drastic changes that are difficult to predict and that affect their uptake by biological systems, including the human body. A lack of consensus on laboratory protocols further impedes progress. Application of state-of-the-art techniques holds promise for clearer answers to emerge on whether engineered nanomaterials are safe to use. — JFU

Science, this issue p. 388

AUTOIMMUNITY

An Aluring new autoantibody target

Autoimmunity is the immune system's ultimate act of betrayal. Cells designed to protect against invading microbes suddenly target the host instead. In the autoimmune disease systemic lupus erythematosus, antibodies target DNA and host proteins, including the RNA binding protein Ro60. Hung *et al.* discovered that Ro60 bound to endogenous Alu retroelements. They detected antibody-Ro60-Alu RNA immune complexes in the blood of individuals with lupus and an enrichment of Alu transcripts. Ro60 bound to Alu probably primes RNA-binding innate immune receptors within B cells, leading these cells to make antibodies that target Ro60-Alu RNA and drive disease-causing inflammation. — KLM

Science, this issue p. 455

TOPOLOGICAL MATTER

Breaking chiral symmetry in a solid

Dirac semimetals have graphene-like electronic structure, albeit in three rather than two dimensions. In a magnetic

field, their Dirac cones split into two halves, one supporting left-handed and the other right-handed fermions. If an electric field is applied parallel to the magnetic field, this "chiral" symmetry may break: a phenomenon called the chiral anomaly. Xiong *et al.* observed this anomaly in the Dirac semimetal Na₃Bi (see the Perspective by Burkov). Transport measurements lead to the detection of the predicted large negative magnetoresistance, which appeared only when the two fields were nearly parallel to each other. — JS

Science, this issue p. 413.
see also p. 378

PLANT SCIENCE

Metered rehydration in pollen grains

When a desiccated pollen grain lands on fertile territory, it rehydrates on the way to activating its growth and metabolic processes. Studying the small plant *Arabidopsis*, Hamilton *et al.* have identified a mechanosensory ion channel that responds to the distention of the plasma membrane as the pollen grain rehydrates. With this channel damaged or absent, the pollen grains germinated overenthusiastically but then showed a tendency to burst. — PJH

Science, this issue p. 438

ROOT DEVELOPMENT

Multifunctional root regulators

The growing plant root undergoes a variety of developmental steps that determine thickness and branching as the roots elaborate. Moreno-Risueno *et al.* identify a suite of transcription factors, some of which mobilize shifting fates during root growth. The same set of transcription

factors governs identity and proliferation of the stem cells as well as the fates of daughter cells. — PJH

Science, this issue p. 426

ALZHEIMER'S DISEASE

Early signs of dementia

There is currently no cure for Alzheimer's disease. One of the reasons could be that interventions start too late, when there is already irreversible damage to the brain. Developing a biomarker that would help to effectively start therapy at very early stages of the disease is thus of high interest. Kunz *et al.* studied neural correlates of spatial navigation in the entorhinal cortex in control study participants and individuals at risk of developing Alzheimer's. The at-risk group showed a different brain signal many decades before the onset of the disease, and they navigated differently in a virtual environment. — PRS

Science, this issue p. 430

PROTEIN DYNAMICS

Observing ultrafast myoglobin dynamics

The oxygen-storage protein myoglobin was the first to have its three-dimensional structure determined and remains a workhorse for understanding how protein structure relates to function. Barends *et al.* used x-ray free-electron lasers with femtosecond short pulses to directly observe motions that occur within half a picosecond of CO dissociation (see the Perspective by Neutze). Combining the experiments with simulations shows that ultrafast motions of the heme couple to subpicosecond protein motions, which in turn couple to large-scale motions. — VV

Science, this issue p. 445,
see also p. 381

and not the phylum to which all previously known methane-metabolizing archaea belonged. — NW

Science, this issue p. 434,
see also p. 384

REPRODUCTIVE BIOLOGY

Mouse work may lead to male contraceptive

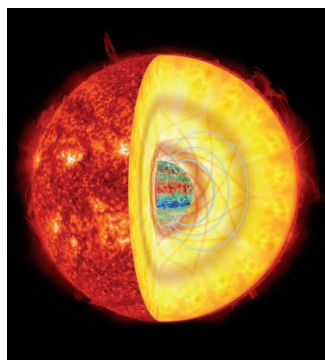
Unintended pregnancies are a major health issue worldwide. Although oral contraceptives were developed decades ago for use in women, there are no male oral contraceptives. Miyata *et al.* show that genetic deletion or drug inhibition of sperm-specific calcineurin enzymes in mice cause male sterility (see the Perspective by Castaneda and Matzuk). Although calcineurin inhibitors resulted in male infertility within 2 weeks, fertility recovered 1 week after halting drug administration. Because the sperm-specific calcineurin complex is also found in humans, its inhibition may be a strategy for developing reversible male contraceptives. — BAP

Science, this issue p. 442,
see also p. 385

ASTEROSEISMOLOGY

Stellar oscillations as magnetic probes

Unlike magnetic fields on the surfaces of stars, those within a star have so far remained difficult to observe. Fuller *et al.* have developed a method of delving into the magnetic depths by exploiting the oscillations of



Artistic representation of a magnetized red giant star

red giant stars. A high magnetic field can cause sound waves to become trapped within the central regions of the star, damping certain vibration modes. Using seismological techniques, this suppression can help infer the core magnetic field for several red giants. — KTS

Science, this issue p. 423

VASCULAR BIOLOGY

Stopping aneurysms before they start

The smooth muscle cells in aortas are connected to the extracellular matrix. Mutations in components of the extracellular matrix, such as fibulin-4, can lead to the enlargement of the aortic lumen, otherwise known as an aneurysm. Yamashiro *et al.* found that mice lacking fibulin-4 in smooth muscle cells had disrupted connections with the extracellular matrix. The mice also had abnormal increases in mechanosensitive proteins and enhanced activity of an actin cytoskeleton-remodeling enzyme called cofilin. Inhibiting the activity of cofilin or its upstream activators could therefore prevent the development of aneurysms. — WW

Sci. Signal. **8**, ra105 (2015).

BIOENGINEERING

Drugs ride waves across tissue barriers

Drugs that travel through the gastrointestinal (GI) tract meet tissue barriers that limit their uptake and dilute potency. Schoellhammer *et al.* used a common handheld ultrasonic probe to temporarily disrupt the barriers, allowing drugs to pass. The ultrasonic waves drove drugs into pig colonic tissue faster than natural absorption, without damage to the tissue. The approach also encouraged drug delivery into mouse colon tissue, leading to the healing of acute colitis. Ultrasound-mediated drug delivery may offer a versatile solution to barrier challenge in the GI tract. — MLF

Sci. Transl. Med. **7**, 310ra168 (2015).

IN OTHER JOURNALS

Edited by **Sacha Vignieri**
and **Jesse Smith**

LIGHT POLLUTION

Stay away from the light

We live in a world flooded with light 24 hours a day. Before our recent harnessing of electricity, light was a reliable indicator of seasonal variability in resources and many species evolved to take advantage of this signal. Robert *et al.* show that artificial light can alter these species physiological responses and desynchronize their seasonal reproduction. Specifically, they found that nocturnal tammar wallabies that lived near a continuously lighted military base secreted less melatonin at night and that this delayed reproduction by nearly a month, as compared to animals living without artificial light nearby. Animals living near the base attempted to avoid lighted areas, but these results suggest that light pollution may have unavoidable physiological effects. — SNV

Proc. R. Soc. London Ser. B 10.1098/rspb.2015.1745 (2015).



Exposure to continual light conditions delays reproduction in tammar wallabies

NANOMATERIALS

A tough shell for nanoparticles

Nanoparticles made from compound semiconductors such as cadmium sulfide (CdS) can exhibit useful luminescent properties but can also be

unstable with respect to ambient air and humidity, especially under conditions of strong illumination. Li *et al.* show that the passivation of metals by forming self-protecting oxides can be extended to nanoparticles. They added aluminum isopropoxide to the reaction mixture



Zebrafish show that the microbiome varies due to experience as animals age

MICROBIOME

Seeing through microbiome development

The transparent zebrafish is an ideal model for studying the codevelopment of the vertebrate gut and its microbiome. Stephens *et al.* took a pair of zebrafish and kept about 250 of their offspring in identical conditions, from hatching until they died of old age. Despite high levels of replication, variation is the order of the day. Young fish are variably colonized with environmental organisms. As the fish continue to develop, distinct bacterial communities emerge at different life stages, driven by the changing morphology of the gut and diet. Ultimately, despite the general patterns, adult gut communities are as distinct from each other as they are from their environment. — CA

ISME J. 10.1038/ismej.2015.140 (2015).

for synthesizing particles 8 nm in diameter, with a cadmium selenide core and a CdS shell. The aluminum dopant was transformed into a protective aluminum oxide coating that greatly improved photoprotection against blue light. — PDS

J. Am. Chem. Soc. 10.1021/jacs.5b05462 (2015).

CELL RENEWAL

Factor adjusts cell number in gut

Cells read their environment to trigger an appropriate response

for tissue homeostasis. Work now shows that intestinal progenitor cells use the RNA-binding protein Lin-28 to detect such a change and trigger insulin signaling as well as promote

symmetric cell division to make full use of increased nutrient availability. Progenitor cells in the embryo and adult maintain their cell number by symmetric division but also generate specific cell types through asymmetric division. Lin-28 functions in early development to ramp up cell number, but an adult role is less clear. Work by Chen *et al.* identifies Lin-28 in the fly adult intestine as a factor controlling adult stem cell division, and it does so via the insulin-like receptor InR and independently of its well-known target Let-7.

— BAP

Development 10.1242/dev.127951 (2015).

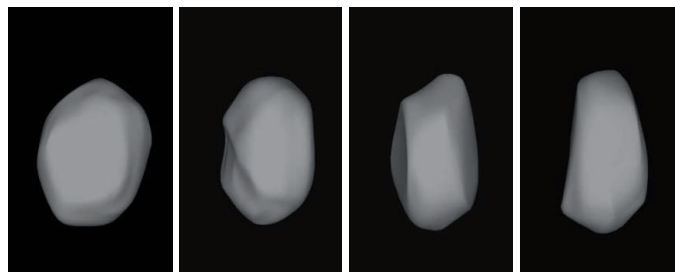
MINOR PLANETS

What shape is the asteroid Juno?

3 Juno was the third asteroid to be discovered. However, no spacecraft has ever been very close to it, so its shape and surface features have remained poorly understood. Viikinkoski *et al.* have produced a model of Juno's shape by combining constraints from a full array of available data: optical light curves, near-infrared adaptive optics images, submillimeter interferometry, and the occultations of background stars. They find that the asteroid has a distorted lozenge-like shape with evidence of concave features, suggesting impact craters. The shape appears to be intermediate between that of the lumpy irregular smaller bodies and the near-spherical larger asteroids.

— KTS

Astron. Astrophys. **581**, L3 (2015).



Plausible reconstructed shapes of the asteroid Juno

TEAM BUILDING

Lab management: Lessons over 35 years

A principal investigator is assembling her lab team. Whom should she hire? With this question in mind, Conti and Liu collected annual reports from the MIT Department of Biology that identified every principal investigator, postdoc, student, and lab technician who worked there from 1966 to 2000. They found that postdoc hiring drove a doubling in average lab size and in the number of publications per lab. The number of a lab's "breakthrough" papers in *Science*, *Nature*, or *Cell* was also influenced by postdoc numbers but was limited to those who had secured external fellowships. The numbers of graduate students and technicians, neither of which influenced overall publication rates, affected breakthrough work. Although the amount of NIH funding influenced productivity, this effect was eliminated after controlling for lab size and composition. — BW

Res. Policy **44**, 1633 (2015).

HEART DISEASE

Patching up the injured heart

During a heart attack, heart muscle is deprived of oxygen and nutrients and dies as a result. Because heart muscle cells, or cardiomyocytes, have a limited capacity to divide, this damage is often permanent. Wei *et al.* describe an intervention that may help minimize the damage. Working with mice, they applied a collagen patch containing a protein called follistatin-like 1 to the heart immediately after a heart attack. Four weeks later, they saw signs of cardiomyocyte division, new blood vessel growth, and reduced scarring, which are consistent with heart muscle regeneration. Mysteriously, follistatin-like 1 has this beneficial activity only when it is synthesized by cells in the epicardium (a membrane layer surrounding the heart); myocardial-derived follistatin-like 1 was inactive. — PAK

Nature **525**, 479 (2015).

RESEARCH ARTICLE SUMMARY

CLATHRIN ADAPTORS

HIV-1 Nef hijacks clathrin coats by stabilizing AP-1:Arf1 polygons

Qing-Tao Shen,* Xuefeng Ren,* Rui Zhang,* Il-Hyung Lee, James H. Hurley†

INTRODUCTION: Clathrin-coated vesicles mediate endocytosis and sorting from the trans-Golgi network (TGN) and endosomes to lysosomes. Adaptor protein (AP) complexes such as AP-1 connect membrane proteins to clathrin. AP-1 needs to be “unlocked” by activators in order to bind cargo and clathrin. The small guanine triphosphatase Arf1 unlocks AP-1 at the TGN by coupling AP-1:Arf1 dimerization to conformational changes. Major histocompatibility class I (MHC-I) proteins and the viral restriction factor tetherin are normally present on the cell surface. The viruses HIV-1, HIV-2, and simian immunodeficiency virus (SIV) use their Nef proteins to hijack clathrin and AP-1 and thus redirect MHC-I and tetherin to lysosomes.

RATIONALE: The down-regulatory functions of Nef are important for HIV-1 infectivity. Previous structural studies of Nef and AP complexes revealed that Nef only binds to unlocked APs. We sought to determine whether Nef could potentiate the physiological unlocking mechanisms in down-regulation of tetherin and

MHC-I. We used Förster resonance energy transfer (FRET) to determine the conformation of AP-1 complexes bound to Arf1, Nef, and cargo. To understand the mechanism by which Nef hijacks AP-1, we determined the structures of trimeric AP-1:Arf1:tetherin-Nef complexes by cryo-electron microscopy (cryo-EM) in active and inactive conformations. We predicted that the active AP-1:Arf1 trimer could form hexagonal lattices, which we visualized directly. To study the function of the hexagons, we reconstituted clathrin cage formation in vitro and showed that mutations in the lattice contacts blocked Arf1- and Nef-promoted cage formation.

RESULTS: In the presence of a tetherin-Nef fusion protein, AP-1:Arf1 complexes became trimeric. FRET analysis revealed that individual AP-1 complexes in the trimer were in the unlocked state. With the use of cryo-EM, we identified two kinds of trimers: closed and open. The closed trimer yielded a 7 Å reconstruction, which allowed docking of known atomic models of unlocked AP-1, Arf1, and Nef. The trimer is centered on a trimeric Arf1 interface. Although AP-1

was unlocked, the closed trimer hides the membrane binding sites and is thus inactive. The open trimer was more mobile, and the structure was resolved to 17 Å. The open trimer preserved the Arf1 trimeric interface while exposing mem-

ON OUR WEB SITE

Read the full article at <http://dx.doi.org/10.1126/science.aac5137>

brane binding sites. Docking the open trimer with the known AP-1:Arf1 dimer yielded a hexagonal model that matched the dimensions of clathrin. The hexagons were visualized in

AP-1:Arf1:MHC-I-Nef mixtures. Efficient clathrin cage assembly at neutral pH required Nef and intact Arf1 dimer and trimer interfaces.

CONCLUSION: Although we set out to explain how HIV-1 Nef hijacked the AP-1 complex, we also found that the inner layer of the AP-1 clathrin coat is far more intricately organized than anticipated. AP-1 and its Arf1 binding sites are conserved throughout eukaryotes; thus, the organization of the inner layer is ancient. HIV-1 has taken advantage of this complexity to subvert membrane traffic. The degree to which HIV-1 Nef can drive AP-1 hexagon formation seems to be coupled to its cargo preferences, as Nef recruits MHC-I more effectively than tetherin. Our findings elucidate the structured organization of the inner layer of clathrin coats that is conserved across eukaryotes, as well as the means by which HIV-1 uses Nef to subvert this structure. ■

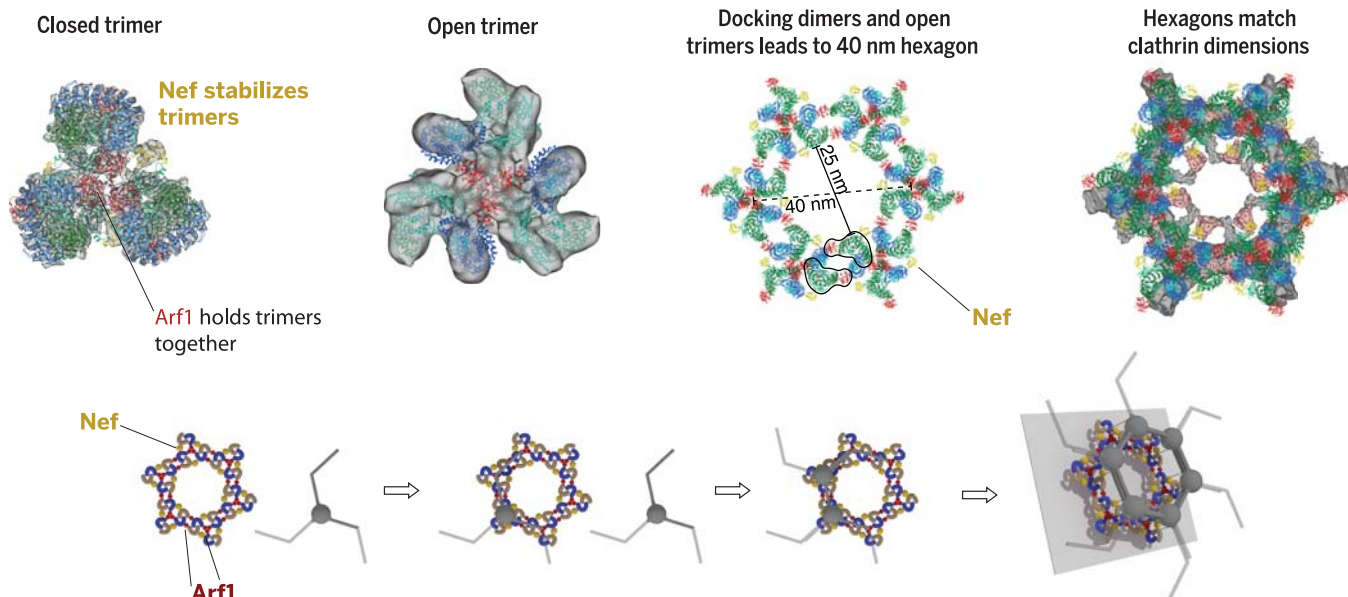
The list of author affiliations is available in the full article online.

*These authors contributed equally to this work.

†Corresponding author. E-mail: jimhurley@berkeley.edu

Cite this article as Q.-T. Shen *et al.*, *Science* 350, aac5137 (2015). DOI: 10.1126/science.aac5137

HIV-1 Nef, Arf1, and the hexagonal inner layer of an AP-1 clathrin coat. (Top) Cryo-EM reconstructions of closed (far left) and open (center left) trimers of tetherin-HIV-1 Nef fusion protein, Arf1, and the AP-1 core. Combining the open trimer and known dimer structure leads to a hexagonal model (center right) that matches the dimensions of the clathrin coat (right). (Bottom) Concept for Nef-activated assembly of the AP-1-clathrin coat.



RESEARCH ARTICLE

CLATHRIN ADAPTORS

HIV-1 Nef hijacks clathrin coats by stabilizing AP-1:Arf1 polygons

Qing-Tao Shen,^{1*} Xuefeng Ren,^{1*} Rui Zhang,^{2*} Il-Hyung Lee,¹ James H. Hurley^{1,2,†}

The lentiviruses HIV and simian immunodeficiency virus (SIV) subvert intracellular membrane traffic as part of their replication cycle. The lentiviral Nef protein helps viruses evade innate and adaptive immune defenses by hijacking the adaptor protein 1 (AP-1) and AP-2 clathrin adaptors. We found that HIV-1 Nef and the guanosine triphosphatase Arf1 induced trimerization and activation of AP-1. Here we report the cryo-electron microscopy structures of the Nef- and Arf1-bound AP-1 trimer in the active and inactive states. A central nucleus of three Arf1 molecules organizes the trimers. We combined the open trimer with a known dimer structure and thus predicted a hexagonal assembly with inner and outer faces that bind the membranes and clathrin, respectively. Hexagons were directly visualized and the model validated by reconstituting clathrin cage assembly. Arf1 and Nef thus play interconnected roles in allosteric activation, cargo recruitment, and coat assembly, revealing an unexpectedly intricate organization of the inner AP-1 layer of the clathrin coat.

Vesicular coats are involved in intracellular membrane traffic and are central to the organization of eukaryotic cells (1). Coats consist of (i) a structural scaffold and (ii) adaptor elements that link the scaffold to membrane proteins and lipids. The scaffold and adaptor may exist as separate layers, or they may be combined. Clathrin is the archetypal two-layer vesicular coat (2) and is responsible for much of the vesicular traffic originating at the plasma membrane and trans-Golgi network (TGN), as well as intraendosomal traffic. The clathrin heavy and light chains form the scaffold, and the heterotetrameric adaptor protein (AP) complexes are the most prevalent adaptor components for clathrin (3, 4). Clathrin does not bind directly to cargo or membranes; rather, the AP complexes connect cargo and membranes to clathrin. The AP-1 complex functions at the TGN, where it is recruited and activated by the small guanosine triphosphatase (GTPase) Arf1 (ADP-ribosylation factor 1) (5, 6). AP-1 consists of two large subunits (β 1 and γ), a medium subunit (μ 1), and a small subunit (σ 1) (3). The large subunits contain flexibly tethered C-terminal ear domains, and constructs lacking the linkers and ears are referred to as AP cores. AP-1 cargoes contain either tyrosine-based sorting signals, which bind to the C-terminal domain (CTD) of μ 1, or dileucine signals, which bind to a site spanning the γ and σ 1 subunits (4). The activity of AP complexes is tightly regulated, and in the absence of activation, the cargo binding sites are sequestered in a state known as the locked conformation (7, 8). AP-1 is “unlocked” by

Arf1-GTP through an allosteric mechanism coupled to the formation of a 2:2 AP-1:Arf1 dimer (9).

The lentiviruses HIV-1, HIV-2, and simian immunodeficiency virus (SIV) hijack the clathrin pathway via their accessory proteins Nef (negative factor) and Vpu (viral protein unique) (10, 11). Lentiviral hijacking facilitates viral immune evasion, assembly, and release by down-regulating cell surface receptors and restriction factors, including CD4 (cluster of differentiation 4) (12, 13), major histocompatibility complex I (MHC-I) (14), and tetherin (15). AP-1 mediates the ability of Nef and Vpu to reroute MHC-I and tetherin from the plasma membrane to lysosomes (16, 17). Nef hijacks AP-1 to down-regulate MHC-I via the tyrosine motif binding site on the CTD of μ 1 (18), whereas AP-2 is hijacked to down-regulate CD4 via the dileucine binding site on the α -2 complex (19, 20). Both Nef binding sites are occluded in the locked conformation (21, 22). Nef subversion of membrane traffic thus requires that AP complexes be unlocked. One report has suggested that Nef can drive membrane localization of AP-1 independent of Arf1 (23), whereas another found that Nef stabilizes the AP-1 coat only in the presence of Arf1 (24) and a third showed that Arf1 is required for Nef-driven down-regulation of MHC-I (25). Along with the subunits of AP-1 and MHC-I, Arf1 is one of ~50 Nef-interacting proteins detected in the human proteome (26). We set out to determine whether Nef, in combination with host cargo, could either bypass or amplify the endogenous Arf1-dependent unlocking mechanism.

HIV-1 Nef and Arf1 trimerize AP-1

We fused the cytosolic 21 amino acids of tetherin, which bind tightly to AP-1 (17), to full-length HIV-1 NL4-3 Nef. We co-incubated tetherin-Nef, the AP-1 core (henceforward referred to as AP-1), and the GTP-locked and N-terminally truncated

Arf1 mutant Gln⁷¹→Leu⁷¹ (Q71L) (27) (henceforward Arf1). These molecules formed a complex that had a molecular weight of 850 kD, as determined by multiangle light scattering (MALS) (Fig. 1, A and B). This value corresponds to three AP-1:Arf1:tetherin-Nef complexes. In contrast, the AP-1 complex alone migrated at a mass consistent with that of a single heterotetramer (Fig. 1B). AP-1:Arf1 contained two peaks, with the higher-mass peak corresponding to a species with a known dimeric crystal structure (9) (Fig. 1A). Other combinations of AP-1, Arf1, and Nef in the presence or absence of a physiological cargo peptide (TGN38) or fused to the tail of MHC-I were also tested. These complexes manifested an apparent mixture of monomer, dimer, and trimer, or in the case of MHC-I, a heterogeneous mixture of higher-order species (Fig. 1A and fig. S1).

The AP-1:Arf1:tetherin-Nef trimers appeared to be promising for structural characterization on the basis of their monodispersity. To determine whether these trimers corresponded to the unlocked conformation, we developed a Förster resonance energy transfer (FRET) reporter for AP-1 unlocking (Fig. 1, C and D). In the locked conformation (28), the separation between β 1-E471 and μ 1-K333 was 17 Å, whereas the distance increased to 58 Å in both the unlocked (9) and the even more open hyperunlocked (17) conformations (Fig. 1D). We constructed an AP-1 variant in which all 34 native Cys residues were replaced by Ala. The mutation β 1E471C μ 1K333C was generated in the Cys-free context and fluorescently labeled with Cy3 and Cy5. The labeled AP-1 formed the same 850-kD complex with tetherin-Nef and Arf1, so we compared the spectra of the labeled AP-1 alone and in complex with tetherin-Nef and Arf1 (Fig. 1C). The spectra indicated a loss of FRET in the presence of tetherin-Nef and Arf1, consistent with AP-1 unlocking.

Cryo-EM reconstruction of AP-1:Arf1:tetherin-Nef trimers

We collected negative-stain and cryo-electron microscopy (cryo-EM) images for the gel filtration peak corresponding to the 850-kD complex and carried out two-dimensional (2D) and 3D classifications (Fig. 2A and figs. S2 and S3). The complex consisted of two different types of trimers, with a small proportion of dimers (Fig. 2, A and B). Roughly 24% of the population consisted of trilobed particles, whereas ~72% corresponded to triangles. The reconstruction of the trilobed particles was improved by masking a subassembly to yield a 7 Å reconstruction (Fig. 2, C and D; figs. S4 and S5; and movie S1). The density was readily interpretable, and three crystal structures—one copy of the hyperunlocked conformation of AP-1 (17); one copy of Nef in the conformation bound to the μ 1 CTD (20); and two Arf1 molecules, as bound to β 1 (Arf1 ^{β}) (9) and to the coatamer [coat protein complex I (COPI)] counterpart of γ (Arf1 ^{γ}) (29)—easily docked into each of the three lobes (fig. S5). These molecules collectively accounted for essentially all of the density (Figs. 2D and 3A).

Arf1 ^{γ} and Arf1 ^{β} contacted AP-1 via their GTP-responsive switch I and II (SwI/II) regions,

¹Department of Molecular and Cell Biology and California Institute for Quantitative Biosciences, University of California, Berkeley, Berkeley, CA 94720, USA. ²Life Sciences Division, Lawrence Berkeley National Laboratory, Berkeley, CA 94720, USA.

*These authors contributed equally to this work. †Corresponding author. E-mail: jimhurley@berkeley.edu

consistent with the GTP-dependence of Arf1 activation of AP-1 (Fig. 3B). The region of Arf1^γ comprising residues H80, Q83, E113, D114, and E115 (outside the SwI/II regions) contacts the tip of the cargo-binding μ1 CTD (Fig. 3C). This part of the μ1 CTD moves ~27 Å from its position in the conventional unlocked structure to make these contacts. These μ1-CTD contacts with Arf1 presumably help drive the hyperunlocked conformation in the Arf1-linked trimer. The trimer is held together in part by direct contacts between three copies of Arf1^γ. The N175-R178 region and the C-terminal K181 of one Arf1 molecule contact the H146-W153 region and the Q176-N179 residues

of the next Arf1 (Fig. 3D). Arf1 is not known to trimerize in isolation, and we surmise that either (i) AP-1 promotes a distinct conformation of Arf1 that is prone to trimerization or (ii) additional contacts elsewhere in the assembly cooperate to promote the trimer. With respect to (i), at 7 Å resolution it is not possible to determine whether AP-1 induces subtle conformational changes in Arf1. With respect to (ii), a major interleaf bridge that stabilizes the trimer is formed by a contact between the N termini of Nef and β1 (Figs. 2D and 3E). This trimer structure sequesters the cargo-binding site of the three μ1 CTDs such that they face the center of the trimer; hence, mem-

brane interactions are precluded. Even though the individual AP-1 complexes are in the hyperunlocked conformation, the overall trimer is closed (Fig. 3F). Thus, we refer to this minority population of trimers as “closed” and conclude that this state would be inactive for vesicle formation.

The majority population of triangle-shaped particles yielded a 17 Å reconstruction (Fig. 4A, figs. S6 to S8, and movie S2). The resolution was limited by heterogeneity in the position of the three monomers within the triangle, which visibly contact one another only in the center. The density can be reasonably explained by docking three copies of the monomeric AP-1:Arf1^γ unit of the closed-state model described above (Fig. 4A). Each AP-1:Arf1^γ complex was docked as a rigid body while maintaining the central nucleus of three Arf1^γ molecules. Owing to the mobility of the monomers, we could not visualize clear density for Nef or Arf1^β, although Nef was stoichiometrically bound in the sample (Fig. 1A). The C termini of the β1 subunit come into close approach at the center. In this structure, the tyrosine and dileucine binding sites, the myristoylation site at the N terminus of Arf1, and the phosphatidylinositol 4-phosphate binding site of AP-1 fall into an approximate plane (Fig. 4B). Because all of the sites are accessible, we refer to this state as “open.”

AP-1:Arf1 hexagonal rings

A previous crystal structure of a 2:2 unlocked AP-1:Arf1 complex solved in the absence of Nef and cargo led to a model for Arf1 activation in the context of a dimeric assembly (9). In that structure, the SwI/II Arf1^β contact was present, and a second contact was made between W172 of the back side of Arf1^β and the α12-α16 region of the γ subunit (Fig. 4C). The mutation W172D prevents Arf1 from activating AP-1, which validated the role of the dimer contact in activation. This finding prompted us to consider the relation between the previous dimer and the current trimer structure. In the open trimer structure, the Arf1^β site and γ-α12-α16 are unobstructed and aligned in a plane parallel to the membrane. We docked the dimeric crystal structure onto these sites (Fig. 4C). Iterative docking of the dimers and trimers linked by Arf1^β bridges generated a hexagonal ring consisting of 18 AP-1 complexes and 36 Arf1 molecules (Fig. 4D). The

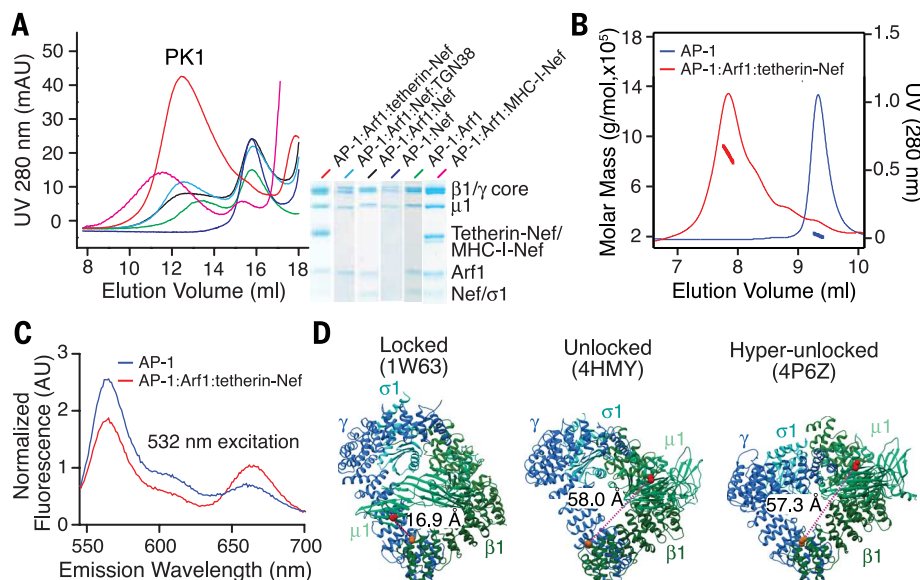


Fig. 1. Arf1, cargo, and Nef trimerize and unlock AP-1. (A) Size exclusion chromatography of AP-1 complexes. Partners are indicated with color codes at right. Peak 1 (PK1) indicates the high-molecular weight AP-1:Arf1:tetherin-Nef complex, whose central fraction was used for subsequent biophysical and cryo-EM studies. The gel shown at right was loaded with samples from PK1 for AP-1:Arf1:tetherin-Nef, and the highest-molecular weight peak eluted for each of the other samples tested. UV, ultraviolet; mAU, milliabsorbance units. (B) Multiangle light scattering (MALS) of AP-1:Arf1:tetherin-Nef (red) and free AP-1 (blue). (C) Emission spectra of free AP-1 and the AP-1:Arf1:tetherin-Nef complex, with excitation at 532 nm. The increase in Cy3 emission and the decrease in Cy5 emission illustrate the FRET efficiency decreases in the complex. The original intensity counts were normalized by the estimation of the total Cy5 amount. AU, arbitrary units. (D) Distance changes anticipated between the locked and unlocked AP-1 complexes, obtained from the indicated PDB entries. The distance increase from 17 to 58 Å corresponds to a twofold decrease in FRET efficiency difference for the Cy3-Cy5 pair ($R_0^6 = 60$ Å) and $E = R_0^6 / (R_0^6 + R^6)$ (R , distance between fluorophores; E , FRET efficiency).

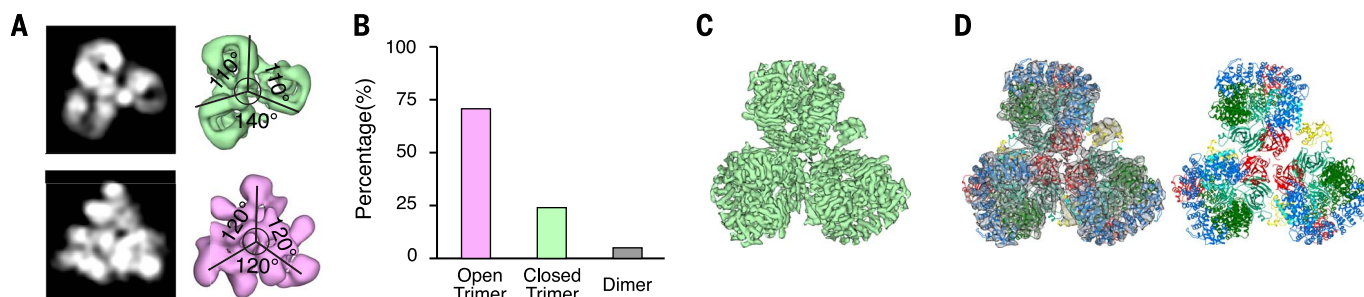


Fig. 2. Cryo-EM reconstruction of two types of AP-1:Arf1:tetherin-Nef trimers. (A) Representative 2D and 3D classes of trimers. (B) Relative populations of dimers and closed and open trimers. (C) Submasking and 7 Å reconstruction of a subassembly of the closed trimer. (D) Overall view of the docking of the hyperunlocked AP-1 structure, Arf1, and Nef into the closed trimer reconstruction.

ring is essentially identical in diameter to the hexagons seen in the cryo-EM reconstruction of the clathrin cage (30) (Fig. 4E). The clathrin binding sequence of the $\beta 1$ subunit is located directly under the projections of the clathrin density corresponding to the clathrin terminal domain (Fig. 4F). Thus, the AP-1:Arf1 hexagon is in almost perfect alignment to template the recruitment and organization of clathrin.

Spurred by this model, we revisited the high-molecular weight tail of the polydisperse AP-1:Arf1:MHC-I-Nef sample (Fig. 1A and fig. S9). We had originally considered this material too heterogeneous for EM analysis, even though MHC-I is the best known substrate for HIV-1 Nef down-regulation via AP-1. The earliest-eluting fractions of this material were subjected to negative-stain EM (Fig. 5A). We observed an abundance of polygons, including a substantial population of closed hexagons, with dimensions that were consistent with the mode of oligomerization suggested by the model. To quantitate the relative numbers of different particles, we subjected them to 2D class averaging (Fig. 5A). The particles were not perfectly identical, so the class averages lost density near the edges. Nevertheless, when atomic models were superimposed on the raw images, convincing fits were obtained (Fig. 5B).

Clathrin cage assembly promoted by AP-1 hexagons

To validate the Arf1-mediated dimer and trimer interfaces, we constructed Arf1 mutants in the

SwI region (I49D) (31), the dimer contact with the back side of Arf1^B (W172D) (9), and the two regions involved in the central trimer contacts (Fig. 5C). All of these mutants were stable and purified in isolation as monomers (fig. S10). We then tested their ability to oligomerize in the context of the AP-1:Arf1:unfused Nef complex. The wild-type (WT) complex runs as a mixture of trimer and higher-order species (Fig. 5D). No isolated dimeric species was seen in the size exclusion chromatography (SEC) of this complex, but the higher-order species were presumed to arise via a combination of dimer and trimer interactions. The dimer interface mutant W172D yields a sharper trimer peak and reduces the proportion of higher-order species (Fig. 5D). The SwI mutant I49D and the trimer-interface loop replacement Arf1 ^{Δ 148-152GS} completely eliminate the trimer and larger species. The C-terminal deletion Arf1 ^{Δ 178-181} reduces but does not eliminate the trimer. These findings are all consistent with the observed set of structural contacts.

We went on to reconstitute clathrin cages in vitro (Fig. 5E) to determine whether the formation of Nef- and Arf1-promoted polygons in turn led to clathrin assembly. WT Arf1 and Nef supported efficient cage assembly (Fig. 5F). In contrast, the SwI and dimer mutants and one of the trimer interface mutants had near-background levels of cage assembly (Fig. 5F). The second trimer interface mutant, the deletion of the C-terminal four residues, had a modest effect of marginal importance (Fig. 5F). The limited effect of this

mutant is consistent with the modest reduction in the trimer peak seen in Fig. 5D. Thus, the Arf1 bridges that hold the dimer and trimer together are essential for the promotion of clathrin cage assembly.

We mutated key residues in Nef contacts with AP-1 to probe their role in the activation of clathrin cage formation. Nef is capable of binding to the γ - $\sigma 1$ hemicomplex of AP-1 via its dileucine motif (32) (Fig. 6A). The dileucine- γ - $\sigma 1$ interaction is not essential for down-regulation of MHC-I by AP-1, and Nef is not visualized at this site in the EM density. Nevertheless, we reasoned that WT Nef can still bind to this site and could promote AP-1 unlocking. We tested the ability of Nef^{LL164-165AA} and MHC-I-Nef^{LL164-165AA} to promote AP-1 oligomerization and clathrin cage assembly. In the presence of Nef^{LL164-165AA}, AP-1 and Arf1 migrated as if Nef were absent (Fig. 6B), and clathrin cage assembly was reduced to the same background level seen without Nef (Fig. 6C). MHC-I and tetherin cooperate with Nef to bind to the $\mu 1$ CTD via an interface that does not involve the dileucine motif but does involve Asp¹²³ (21). This is the site that is well ordered in the EM density of the closed trimer in the presence of cargo. MHC-I-Nef^{LL164-165AA} still trimerizes AP-1 (Fig. 6D), although the presence of higher-order oligomers was reduced. MHC-I-Nef^{LL164-165AA} promotes clathrin cage assembly (Fig. 6E) with efficiency relatively near that of the wild type, consistent with the biological finding that MHC-I down-regulation does not require the dileucine motif (33). Conversely, MHC-I-Nef^{D123R}, which destabilizes the $\mu 1$ -CTD interface, decreased the proportion of trimeric AP-1 (Fig. 6D) and reduced clathrin cage assembly to ~30% of WT levels (Fig. 6E). In the absence of MHC-I, Nef^{D123R} displayed near-WT oligomerization (Fig. 6B) and cage assembly behavior (Fig. 6C), consistent with the dependence of the Nef- $\mu 1$ -CTD interaction on the presence of $\mu 1$ -CTD-directed cargo (21).

Conclusions

Previous models of AP-mediated clathrin recruitment have emphasized the plasma membrane adaptor AP-2, which is activated principally by phosphatidylinositol 4,5-bisphosphate, not Arf1 (34). In the reconstruction of an AP-2 clathrin coat, the AP-2 complexes were disordered and substoichiometric (30). The recruitment of clathrin to the plasma membrane appears to be coupled to recruitment of AP-2 complex pairs (35) rather than a larger scaffold. Our contrasting observations of an ordered inner layer for AP-1 point to a fundamental difference between the AP-1 and AP-2 coats. Our findings for AP-1 will likely also apply to the Arf1-activated AP-3 adaptor complex. In a very recent cryo-EM tomographic study of COPI vesicles, Dodonova *et al.* noted Arf1-mediated trimers similar to those seen here (36). In other ways, the two-layer hexagonal organization described here for AP-1 and clathrin differs from the interwoven assembly of COPI. In summary, our results show that the inner layer of the AP-1 clathrin coat, and probably other Arf1-dependent clathrin coats, has a far more

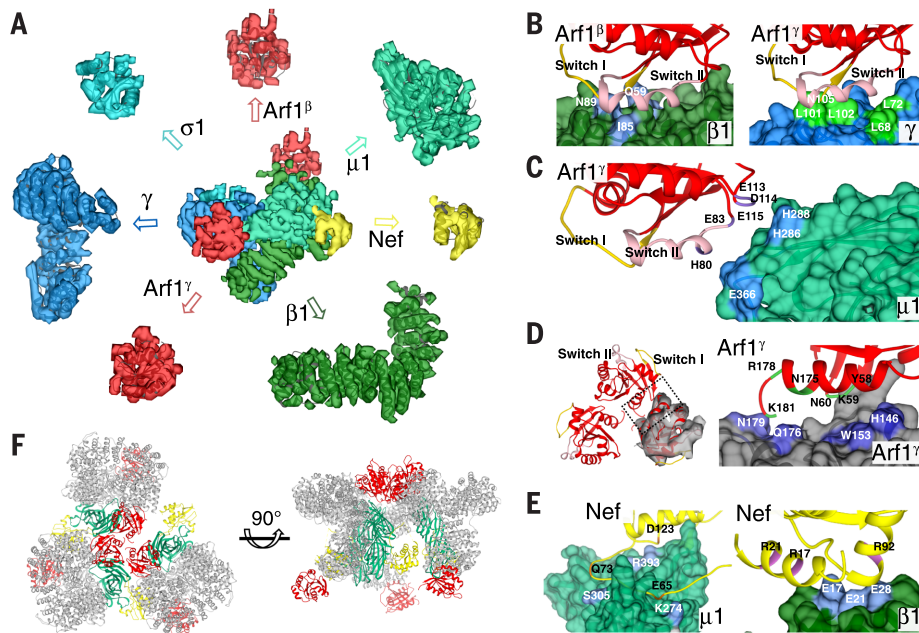


Fig. 3. Molecular interactions in the closed AP-1:Arf1:tetherin-Nef trimer. (A) Exploded view of subunit-by-subunit fits into the closed trimer reconstruction. (B) Details of interactions between Arf1 and the $\beta 1$ and γ subunits. (C) Interactions between Arf1 and the $\mu 1$ CTD drive hyperunlocking. (D) Interactions at the center of the Arf1 nucleus stabilize the trimer. (E) Interactions between Nef and the $\mu 1$ CTD (left) mirror those seen previously (21), whereas a distinct trimer-bridging interaction is observed between Nef and the N terminus of $\beta 1$ (right). (F) The closed AP-1:Arf1:tetherin-Nef trimer. The reported membrane and cargo binding subunits including Arf1, $\mu 1$, and Nef are illustrated with the same colors used previously, whereas the other parts are shown in gray.

organized structure than previously appreciated. Moreover, Arf1 plays a far more central role than previously understood. Not only does Arf1 drive recruitment and allosteric activation of AP-1, but it is also an integral component of the structure of the inner layer, bridging the individual AP-1 complexes into dimers and trimers and thence to hexagons.

The highly organized inner-layer structure introduces an additional level at which regulation can occur. HIV-1 Nef appears to take advantage of the additional complexity by promoting trimer formation, which could allow it to template clathrin cages under conditions that would otherwise fall short of full activation (Fig. 6F). Trimer promotion appears to occur by both indirect and direct mechanisms. The structural observation that Nef can bridge between different AP-1 complexes within the trimer suggests that Nef can also drive trimerization directly. The loss of function for Nef^{Δ1164-165AA} in the absence of MHC-I is consistent with an indirect mechanism, wherein Nef binds tightly to γ - σ 1 (32), driving the thermodynamic equilibrium toward the unlocked state, which in turn is capable of forming a trimer.

We currently believe that these two mechanisms can work either alone or together in different contexts.

MHC-I-Nef is much more effective than tetherin-Nef at promoting polygon formation, even though both constructs bind tightly to AP-1. HIV-1 NL4-3 (the source of Nef used in this study and a member of group M) down-regulates MHC-I via Nef and tetherin via Vpu. However, HIV group O, like SIV, uses Nef to down-regulate tetherin (37). Perhaps HIV-1 O-Nef and SIV Nef might be more effective than HIV-1 NL4-3 or other M- and N-Nefs at promoting polygon formation in the presence of tetherin. If confirmed, this would provide a molecular mechanism for virus-specific differences in the mode of tetherin down-regulation.

Our observations of the ordered inner layer of the AP-1 clathrin coat were made in the stabilizing presence of HIV-1 Nef and cargo. The conservation of the Arf1-binding sites in the evolution of AP-1 from yeast to humans leaves little doubt that the ordered inner layer is far more ancient than the appearance of the primate lentiviruses. The elaborate organization of the AP-1:Arf1 inner layer

might offer advantages to the cell in terms of clathrin assembly speed, regulatory versatility, or both. Clathrin coats can be generated on synaptic endosomes within a span of 2 s (38), a pathway that most likely involves the Arf1-activated AP-1 and/or AP-3 complexes. Cooperative assembly of a symmetry-matched hexagonal inner layer would be a clear asset in catalyzing the rapid nucleation of an endosomal clathrin coat. These benefits could have been adaptive early in the evolution of eukaryotes.

Materials and methods

Plasmid construction

The His₆- and glutathione *S*-transferase (GST)-tagged AP-1 core expression construct was described by Ren *et al.* (9). In the variant FL β :AP-1 complex used for clathrin assembly experiments, β 1 (residues 1 to 584) was replaced with full-length β 1 DNA. A tobacco etch virus (TEV) cleavage site and His₆ tag were fused to the C terminal of full-length β 1. To generate the Cys-free construct, DNAs encoding the AP-1 core subunits were codon-optimized and synthesized (Genescript, Piscataway, NJ). The Cys-free (C2A) construct was then used as a template for site-directed mutagenesis to produce the desired Cys pair construct. HIV-1 NL4-3 Nef, tetherin (1 to 21)-10 amino acid linker-Nef, and MHC-I (338 to 365)-Nef were expressed as TEV-cleavable N-terminal His₆ fusions. His₆-tagged full-length Nef was used for clathrin cage assembly. The N-terminal truncation of Nef (56 to 206) was used for SEC of AP1:Arf1: Nef trimer complexes. Human Arf1 (17 to 181) Q71L or other Arf1 mutants made in this background were expressed with a TEV-cleavable N-terminal His₆ tag.

Protein expression and purification

The AP-1 complexes were expressed in BL21 (DE3) Star (Life Technologies, Grand Island, NY) or BL21 (DE3) pLysS (Promega, Madison, WI) strains and induced with 0.3 mM isopropyl- β -D-thiogalactopyranoside (IPTG) at 20°C overnight. The cells were lysed by sonication in 50 mM Tris at pH 8.0, 300 mM NaCl, 10% glycerol, 3 mM β -mercaptoethanol (β -ME), and a protease inhibitor cocktail (Sigma-Aldrich, St. Louis, MO). The clarified lysate was first purified on a Ni-nitrilotriacetic acid (NTA) column (Qiagen, Valencia, CA). The eluate was further purified on glutathione-Sepharose 4B resin (GE Healthcare, Piscataway, NJ). After TEV cleavage at 4°C overnight, the sample was concentrated and then loaded onto a HiLoad 16/60 Superdex 200 column (GE Healthcare) in 20 mM Tris at pH 8.0, 200 mM NaCl, and 0.3 mM tris(2-carboxyethyl)phosphine (TCEP). The sample fractions were pooled together, adjusted to 30 mM imidazole, and passed through 1 ml of glutathione-Sepharose 4B and then onto a Ni-NTA column (Qiagen) to capture the residual GST- and His-tag fragments. The sample was adjusted to 20 mM Tris at pH 8.0, 200 mM NaCl, and 0.3 mM TCEP by buffer exchange in the concentrator.

His₆-tagged tetherin-Nef and other Nef constructs were expressed in BL21 (DE3) Star cells

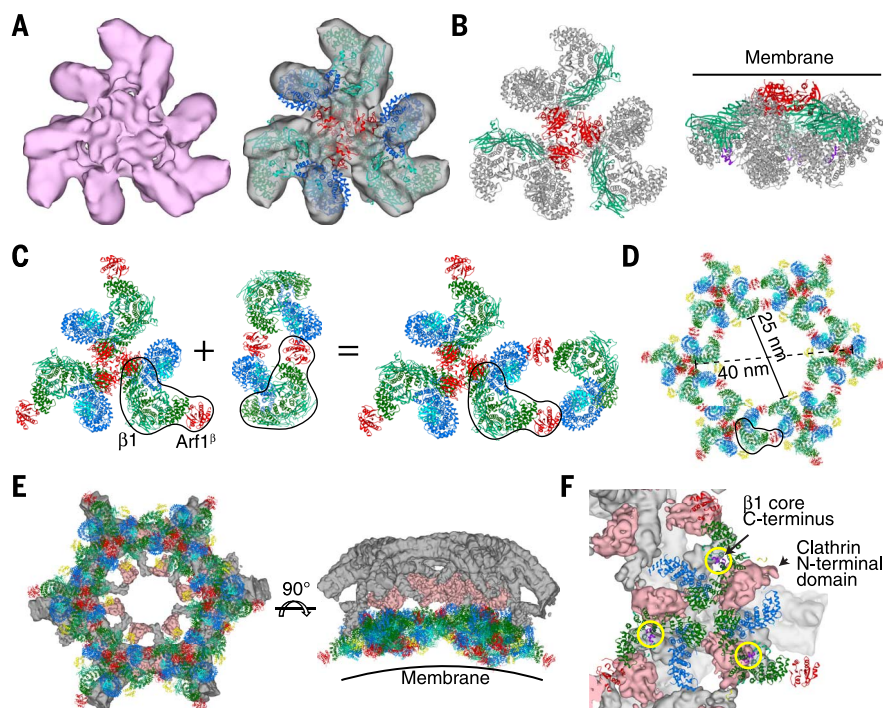


Fig. 4. The open AP-1:Arf1:tetherin-Nef trimer suggests a hexagonal assembly model. (A) Reconstruction and docking of the open AP-1:Arf1:tetherin-Nef trimer. (B) The open AP-1:Arf1:tetherin-Nef trimer. The reported membrane and cargo binding subunits including Arf1, μ 1, and Nef are colored as before, whereas the other parts are shown in gray. The membrane is represented by a horizontal line. The C terminus of the β 1 core, which is the location of the clathrin binding region, is shown in purple. (C) The open AP-1:Arf1 trimer formed in the presence of Nef (left) and the known Nef-free AP-1:Arf1 dimer (to the right of the plus sign) (9) were docked onto one another by overlaying one copy each of the β 1 subunit and Arf1 β (outlined in black) to yield the composite structure at far right. (D) Iterating the docking operation shown in (C) generates the hexagon illustrated here. Nef was docked onto all copies of AP-1 in the mode identified in the closed trimer and is shown in yellow. (E) Juxtaposition of the modeled hexagon and one hexagonal segment of the cryo-EM reconstruction of the clathrin D6-barrel (30). The membrane binding face is represented by a curved line. (F) A close-up view of the hexagon model and the clathrin D6-barrel density shows that the clathrin binding site on β 1 adjoins the AP-1 binding site on clathrin.

and induced with 0.3 mM IPTG at 20°C overnight. The purification was carried out using Ni-NTA resin, and the eluate was loaded onto a HiLoad 16/60 Superdex 200 column in the sample buffer. His₆-tagged Arf1 constructs were expressed in BL21 (DE3) Star cells by induction at 20°C overnight. The cell pellet was lysed by sonication and purified on a Ni-NTA column in 50 mM Tris at pH 8.0, 300 mM NaCl, 20 mM imidazole, 5 mM MgCl₂, 3 mM β-ME, and a protease inhibitor cocktail. The proteins were eluted with 100 mM imidazole and then loaded onto a HiLoad 16/60 Superdex 75 column (GE Healthcare) in sample buffer containing 5 mM MgCl₂. Proteins were quantified by the bicinchoninic acid assay (Pierce BCA protein assay kit) using bovine serum albumin as a standard.

For clathrin purification, a bovine brain was homogenized using a Waring blender in 500 mM Tris at pH 7.0, 2 mM EDTA, and 3 mM β-ME. The clarified lysate was precipitated at 10% saturated ammonium sulfate. The pellet was resuspended in 500 mM Tris at pH 7.0, 2 mM EDTA, and 3 mM β-ME and was purified by dialysis overnight at 4°C in a buffer containing 30 mM Tris at pH 8.5 and 2 mM EDTA. The dialyzed sample was purified through a monoQ 5/50GL

column (GE Healthcare), and the clathrin fractions were eluted in 28 to 35 mS/cm of NaCl concentration. The sample was pooled together and then loaded onto a Superose6 10/100GL column in 30 mM Tris at pH 8.0.

Size exclusion chromatography with multiangle light scattering (SEC-MALS)

The AP-1 core was incubated with Arf1 and tetherin-Nef at 4°C overnight in 20 mM Tris at pH 8.0, 200 mM NaCl, 0.3 mM TCEP, 5 mM MgCl₂, and 1 mM GTP. The molar ratio of AP-1 core:Arf1 (17 to 181) Q71L:tetherin-Nef was fixed at 1:4:6. The final concentration of the AP-1 core was 4 mg/ml (20 μM). SEC-MALS experiments were performed using an Agilent 1200 high-performance liquid chromatography system (Agilent Technologies, Santa Clara, CA) coupled to a Wyatt DAWN HELEOS-II MALS instrument and a Wyatt Optilab rEX differential refractometer (Wyatt, Santa Barbara, CA). For chromatographic separation, a WTC-050S5 size-exclusion column (Wyatt) with a 20-μl sample loop was used at a flow rate of 0.3 ml/min in phosphate-buffered saline at pH 7.4, 5 mM MgCl₂, and 0.2 mM TCEP. The outputs were analyzed by the ASTRA V software (Wyatt). MALS signals, combined with the protein concentration determined by the refrac-

tive index, were used to calculate the molecular mass of the AP-1:Arf1:tetherin-Nef complex and AP-1 alone.

AP-1:Arf1:Nef complex assembly for EM

The recombinant AP-1 core was mixed with Arf1 and Nef or tetherin-Nef proteins at a molar ratio of 1:4:6 and then incubated with 1 mM GTP at 4°C overnight. The mixture was then subjected to a Superose 6 10/100GL column in 20 mM Tris at pH 8.0, 200 mM NaCl, 5 mM MgCl₂, and 0.3 mM TCEP.

Clathrin cage assembly

The total volume of each reaction was 30 μl in HKM buffer [25 mM HEPES at pH 7.2, 125 mM potassium acetate, 2 mM MgCl₂, and 1 mM GppCp (Jena Bioscience, Jena, Germany)]. His₆-tagged Arf1 (17 to 181) Q71L proteins (final concentration: 0.4 μM) were incubated at 37°C for 15 min for GTP loading. The mixture was further supplemented with FLβ-AP-1 (final concentration: 0.1 μM) and His-Nef or His-MHC-I-Nef (final concentration: 0.4 μM) on ice for 15 min. At the last step, clathrin was added into the mixture at the final concentration of 0.3 μM on ice for 15 min and then warmed to 37°C for 15 min.

Fluorescent dye labeling

The AP-1 double cysteine mutant β1E471C μ1K333C, in which all 34 native Cys residues were replaced by Ala, was purified and labeled with Cy3 and Cy5 through the simultaneous incubation of AP-1^{34CAβ1E471C μ1K333C} (20 μM) with an 8-fold molar excess of Cy3-maleimide and a 10-fold excess of Cy5-maleimide. After overnight incubation at 4°C, unreacted materials were removed on a HiTrap desalting column (GE Healthcare, USA). The final concentration and labeling efficiency were determined by Nanodrop (Thermo Scientific) measurement and the BCA protein concentration assay (Pierce). For Arf1:tetherin-Nef complex formation, the mutant AP-1 was diluted with a 50-fold excess of WT AP-1. Incubation and purification conditions were identical to those in other experiments.

Bulk FRET assay

A Fluorolog spectrofluorometer (Horiba, Kyoto, Japan) was used for bulk FRET measurements. Micro square open-top fluorometer cells (Starna Cells, Atascadero, CA) were used to contain samples. Emission spectra of samples were obtained by scanning emission wavelengths from 600 to 900 nm with a 532-nm excitation wavelength. A 5-nm slit width was used. The same emission-wavelength scan was also performed with 640-nm excitation to estimate the total amount of Cy5. We summed emission counts from 660 to 664 nm to normalize the 532-nm excitation spectrum to facilitate comparison between spectra.

Negative-stain EM

The AP-1 core, Arf1, Nef, tetherin-Nef, MHC-I-Nef, and their derivatives at different conditions

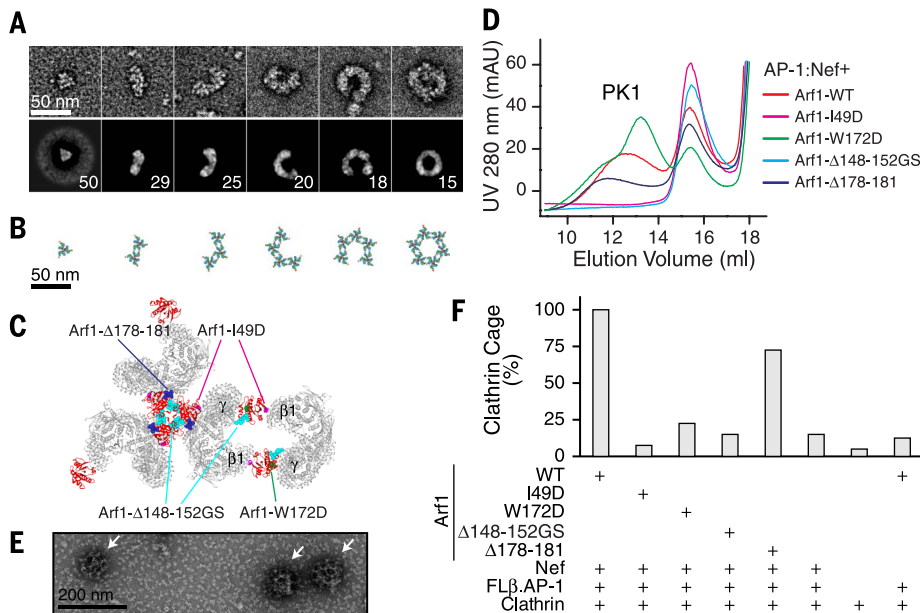


Fig. 5. Visualization and validation of AP-1 polygons. (A) Negative-stain EM of the high-molecular weight tail of the size exclusion separation of AP-1:Arf1:MHC-I-Nef. The top row shows representative particles. The bottom row shows 2D class averages, which were carried out to quantitate the relative frequency of different assemblies. The number of particles within each class is indicated. The class averages show blurring and loss of density at the edges, which suggests heterogeneity within the classes. (B) The corresponding docked model. The scale is the same as in (A), indicating good agreement with the single-particle images. (C) Location of Arf1 mutants at interfaces. Arf1 is shown in red, whereas the other parts are in gray. (D) Size exclusion chromatography of AP-1:Arf1:Nef mixtures, showing that Arf1 mutants interfere with dimerization or trimerization of AP-1. In Arf1^{Δ148-152GS}, residues L148-RHR-N152 were replaced by AGSGS. (E) Negative-stain EM of clathrin cages assembled in vitro from purified clathrin; the AP-1 core, including full-length β1 [FLβ-AP-1, following terminology used for AP-2 (39)]; WT Arf1; Nef; and the nonhydrolyzable GTP analog GppCp. Arrows indicate clathrin cages. (F) The relative percentage of clathrin cages was counted in 22 randomly chosen fields of view for the indicated mixtures of WT and/or mutant Arf1 proteins.

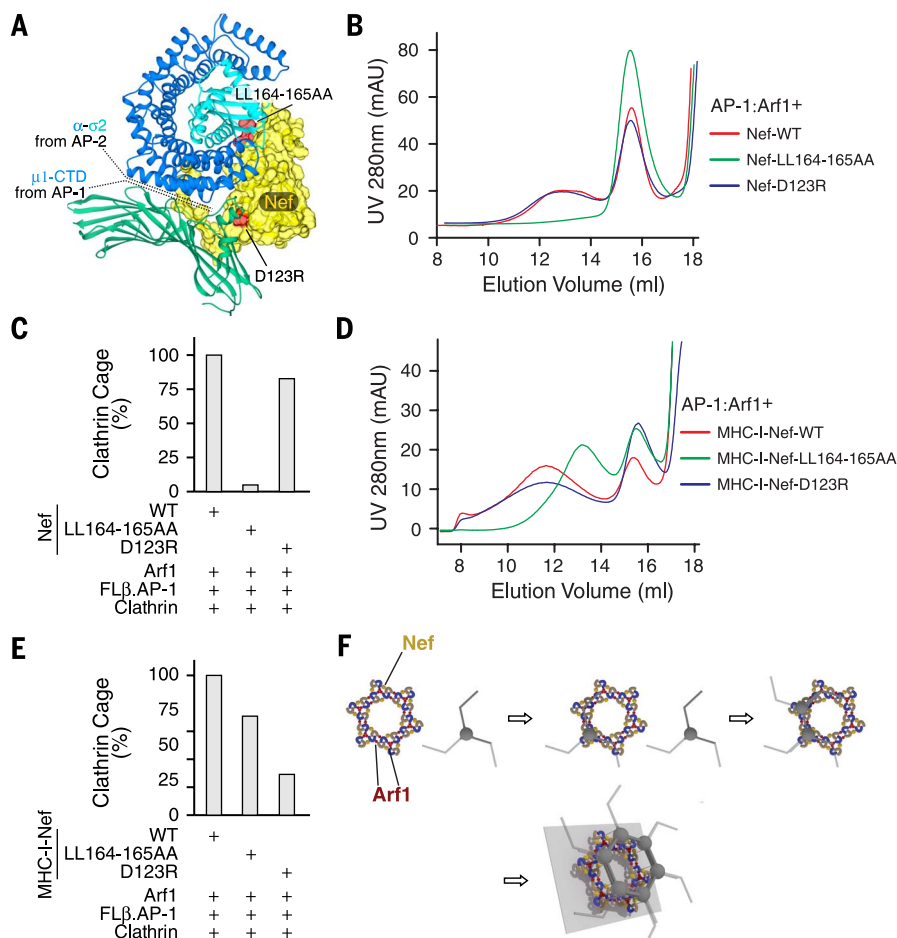


Fig. 6. The hexagonal inner coat promotes clathrin cage assembly. (A) Diagram of Nef mutants. Structures from AP-2- α -2:Nef (PDB ID 4NEE) and AP-1- μ 1:MHC-I-Nef (PDB ID 4EMZ) were combined. Homologs are colored as before. (B) Size exclusion chromatography of AP-1:Arf1:Nef mixtures, showing that Nef mutants interfere with dimerization or trimerization of AP-1. (C) The relative percentage of clathrin cages was counted in 20 randomly chosen fields of view for the indicated mixtures of WT and/or mutant Nef proteins. (D) Size exclusion chromatography of AP-1:Arf1:MHC-I-Nef mixtures, showing that MHC-I-Nef mutants interfere with dimerization or trimerization of AP-1. (E) The relative percentage of clathrin cages was counted in 20 randomly chosen fields of view for the indicated mixtures of WT and/or mutant MHC-I-Nef proteins. (F) Concept for the role of AP-1:Arf1 polygons in clathrin assembly with Nef. Nef (yellow) stabilizes the AP-1:Arf1 polygon such that closed polygons can form even without clathrin, creating a preformed template for rapid clathrin assembly.

were adjusted to total protein concentrations of 0.02 mg/ml for negative-stain EM. Four-microliter droplets of the sample were placed on glow-discharged carbon-coated copper grids and were negatively stained using 2% (w/v) uranyl acetate. For clathrin-related samples, we allowed an extra 5 min of incubation time on the grid with 3% glutaraldehyde to fix clathrin cages before the application of uranyl acetate, as described previously, with minor modifications (39). Negatively stained samples were examined under a Tecnai F20 microscope (FEI, Eindhoven, Netherlands) operated at an accelerating voltage of 120 keV with a defocus from -1.0 to -1.5 μ m at tilts of 0° or 45° . Micrographs were recorded on a charge-coupled device camera (Ultrascan 4000, 4 k \times 4 k; Gatan, Pleasanton, CA) at a nominal magnifica-

tion of 80,000 \times with a 1.37 \AA calibrated pixel size at the specimen level, using the semiautomated Leginon data collection software (40).

Cryo-EM

Droplets of 2.5- μ l AP-1, Arf1, and the tetherin-Nef complex sample at a concentration of 0.06 mg/ml were applied to Quantifoil grids with continuous carbon support and plunge frozen into liquid ethane using a Vitrobot Mark IV (FEI). The vitrified samples were examined using a Titan microscope (FEI) operated at 300 keV. The vitrified samples were imaged under parallel illumination conditions, with a beam diameter of ~ 2 mm on the specimens and a defocus range from -1.5 to -3.5 μ m. All cryo-EM images were recorded on a K2 Summit direct electron detector camera

(Gatan) at a nominal magnification of 27,500 \times , corresponding to a calibrated pixel size of 1.32 \AA . The camera was operated in counting mode, with a dose rate of about eight electrons per pixel per s on the camera. A total exposure time of 10 s, corresponding to an accumulated dose of 45.9 electrons/ \AA^2 on the specimen, was fractionated into 25 movie frames, with 0.4-s exposure time and a dose of 1.84 electron/ \AA^2 for each frame. The data were collected semiautomatically, using the Leginon data collection software (40). Drift correction for movie frames was performed using the University of California, San Francisco (UCSF) MotionCorr program (41). The parameters of the contrast transfer function (CTF) were estimated from the drift-corrected micrographs using CTFFIND4 (<http://grigoriefflab.janelia.org/ctffind4>).

Image processing

The program XMIPP/3.1 was used for 2D analysis and random conical tilt (RCT) analysis of negatively stained samples (42). A total of 11,589 untilted and tilted particle pairs was manually selected from 176 micrograph pairs. The untilted image stack was subjected to reference-free 2D classification (50 classes) (43). For 38 representative classes, the corresponding tilted particle images were used to compute 3D reconstructions via the RCT approach (44). The obtained 3D reconstructions were classified into three groups (open triangles, closed three-leaf clover, and dimer-like) by visual inspection. Both untilted and tilted particles corresponding to each trimeric shape were combined and used to generate a final structure based on projection match. The final resolutions for the open and closed trimers were determined to be 27 and 26 \AA , respectively, based on the 0.5 criterion of the Fourier shell correlation (FSC).

Further cryo-EM data analysis of images obtained from the Titan microscope was performed using the RELION/1.4-beta-1 program (45). Particles were picked from 1445 drift-corrected micrographs using the DoG Picker software (46) inside the APPION image processing suite (47), and the particle coordinates were transferred to RELION for particle extraction. A total of 144,261 individual particles were subject to reference-free 2D classification (using 100 classes) to remove poor-quality particles. The remaining data set comprising 111,183 particles was used for further analyses. With the RCT structure low-pass filtered to 60 \AA as an initial model, we performed 3D classification with 10 classes, which, after 50 iterations, revealed two major conformations: closed (one class) and open trimers (eight classes). Further 3D classification of the closed class (26,069 particles) into five subclasses revealed that the third subunit is wobbling with respect to the other two subunits (fig. S5D). The flexibility of the third subunit limited the refinement resolution of the whole trimer to 9.0 \AA . To improve the resolution of the round-edge class, we masked the third subunit during the autorefinement process and produced a reconstruction for the two rigid subunits at 8.1 \AA . A similar strategy to mask only one subunit from the trimer during autorefinement

further improved the resolution to 7.0 Å. The other eight open-state classes were reorganized into four classes, and 32,535 particles were selected for the subsequent autorefinement process. Due to the sample heterogeneity, the refinement was limited to 23.8 Å resolution. All classes superimpose reasonably well with respect to each other, revealing an apparent C3 symmetry, at least at low-to-medium resolution. Therefore, we enforced C3 symmetry during the refinement, which resulted in a final resolution of 16.7 Å. All reported resolutions for the RELION reconstruction are based on the gold standard 0.143 FSC criterion, using two independent half-maps, with correction of the effects from the soft-edged mask. The angular distribution of each structure was also calculated with the RELION package.

Docking and structural analysis

Crystal structures of the hyperunlocked AP-1 core bound to tetherin [Protein Data Bank identification code (PDB ID) 4P6Z] (17), the unlocked AP-1 core with Arf1 (PDB ID 4HMY) (9), and the closed AP-1 core (PDB ID 1W63) (28) were used as trial structures for docking. The docking was fulfilled in UCSF Chimera on the basis of a rigid-body docking strategy (48). In closed trimer, the crystal structure of hyperunlocked AP-1 fit well into the EM density map as an intact unit. Most of the α helices of the β and γ subunits in AP-1 were clearly visualized in the density, and the β sandwich of the μ 1 subunit also fit well in the density. In addition to densities occupied by AP-1 core, two of the three unassigned EM densities were identified as Arf1 (PDB ID 1O3Y) (49), based on excellent matching of α helices with the EM densities. The third unoccupied EM density lies close to the μ 1 domain and was docked well using Nef (PDB ID 4EMZ), which is further verified by the known interface between AP-1:Arf1:Nef (9) and the solved structure of the μ 1 domain, Nef, and MHC-I (21). Hyperunlocked AP-1 with Arf1^Y fit into the EM density map for the open trimer, with or without C3 symmetry, as an intact unit. Preliminary docking results were selected from 500 random placements with the best cross-correlation values and the most hits. The possible candidates were further screened on the basis of both symmetrized C3 docking and the position of Arf1^Y in the EM density.

REFERENCES AND NOTES

- R. Schekman, L. Orci, Coat proteins and vesicle budding. *Science* **271**, 1526–1533 (1996). doi: [10.1126/science.271.5255.1526](#); pmid: [8599108](#)
- T. Kirchhausen, Clathrin. *Annu. Rev. Biochem.* **69**, 699–727 (2000). doi: [10.1146/annurev.biochem.69.1.699](#); pmid: [10966473](#)
- D. J. Owen, B. M. Collins, P. R. Evans, Adaptors for clathrin coats: Structure and function. *Annu. Rev. Cell Dev. Biol.* **20**, 153–191 (2004). doi: [10.1146/annurev.cellbio.20.010403.104543](#); pmid: [15473838](#)
- L. M. Traub, J. S. Bonifacino, Cargo recognition in clathrin-mediated endocytosis. *Cold Spring Harbor. Perspect. Biol.* **5**, a016790 (2013). doi: [10.1101/cshperspect.a016790](#); pmid: [24186068](#)
- M. A. Stamnes, J. E. Rothman, The binding of AP-1 clathrin adaptor particles to Golgi membranes requires ADP-ribosylation factor, a small GTP-binding protein. *Cell* **73**, 999–1005 (1993). doi: [10.1016/0092-8674\(93\)90277-W](#); pmid: [8500185](#)
- L. M. Traub, J. A. Ostrom, S. Kornfeld, Biochemical dissection of AP-1 recruitment onto Golgi membranes. *J. Cell Biol.* **123**, 561–573 (1993). doi: [10.1083/jcb.123.3.561](#); pmid: [8227126](#)
- L. P. Jackson *et al.*, A large-scale conformational change couples membrane recruitment to cargo binding in the AP2 clathrin adaptor complex. *Cell* **141**, 1220–1229 (2010). doi: [10.1016/j.cell.2010.05.006](#); pmid: [20603002](#)
- B. J. Canagarajah, X. Ren, J. S. Bonifacino, J. H. Hurley, The clathrin adaptor complexes as a paradigm for membrane-associated allostery. *Protein Sci.* **22**, 517–529 (2013). doi: [10.1002/pro.2235](#); pmid: [23424177](#)
- X. Ren, G. G. Farias, B. J. Canagarajah, J. S. Bonifacino, J. H. Hurley, Structural basis for recruitment and activation of the AP-1 clathrin adaptor complex by Arf1. *Cell* **152**, 755–767 (2013). pmid: [23415225](#)
- M. H. Malim, M. Emerman, HIV-1 accessory proteins—Ensuring viral survival in a hostile environment. *Cell Host Microbe* **3**, 388–398 (2008). doi: [10.1016/j.chom.2008.04.008](#); pmid: [18541215](#)
- D. R. Collins, K. L. Collins, HIV-1 accessory proteins adapt cellular adaptors to facilitate immune evasion. *PLOS Pathog.* **10**, e1003851 (2014). doi: [10.1371/journal.ppat.1003851](#); pmid: [24465204](#)
- J. V. Garcia, A. D. Miller, Serine phosphorylation-independent downregulation of cell-surface CD4 by nef. *Nature* **350**, 508–511 (1991). pmid: [2014052](#)
- C. Aiken, J. Konner, N. R. Landau, M. E. Lenburg, D. Trono, Nef induces CD4 endocytosis: Requirement for a critical dileucine motif in the membrane-proximal CD4 cytoplasmic domain. *Cell* **76**, 853–864 (1994). doi: [10.1016/0092-8674\(94\)90360-3](#); pmid: [8124721](#)
- O. Schwartz, V. Maréchal, S. Le Gall, F. Lemonnier, J.-M. Heard, Endocytosis of major histocompatibility complex class I molecules is induced by the HIV-1 Nef protein. *Nat. Med.* **2**, 338–342 (1996). doi: [10.1038/nm0396-338](#); pmid: [8612235](#)
- S. J. D. Neil, T. Zang, P. D. Bieniasz, Tetherin inhibits retrovirus release and is antagonized by HIV-1 Vpu. *Nature* **451**, 425–430 (2008). doi: [10.1038/nature06553](#); pmid: [18200009](#)
- J. F. Roeth, M. Williams, M. R. Kasper, T. M. Filzen, K. L. Collins, HIV-1 Nef disrupts MHC-I trafficking by recruiting AP-1 to the MHC-I cytoplasmic tail. *J. Cell Biol.* **167**, 903–913 (2004). doi: [10.1083/jcb.200407031](#); pmid: [15569716](#)
- X. Jia *et al.*, Structural basis of HIV-1 Vpu-mediated BST2 antagonism via hijacking of the clathrin adaptor protein complex 1. *eLife* **3**, e02362 (2014). pmid: [24834023](#)
- S. Le Gall *et al.*, Nef interacts with the μ subunit of clathrin adaptor complexes and reveals a cryptic sorting signal in MHC I molecules. *Immunity* **8**, 483–495 (1998). doi: [10.1016/S1074-7613\(00\)80553-1](#); pmid: [9586638](#)
- R. Chaudhuri, O. W. Lindwasser, W. J. Smith, J. H. Hurley, J. S. Bonifacino, Downregulation of CD4 by human immunodeficiency virus type 1 Nef is dependent on clathrin and involves direct interaction of Nef with the AP2 clathrin adaptor. *J. Virol.* **81**, 3877–3890 (2007). doi: [10.1128/JVI.02725-06](#); pmid: [17267500](#)
- B. Doray, I. Lee, J. Knisely, G. Bu, S. Kornfeld, The γ/α 1 and α/α 2 hemicomplexes of clathrin adaptors AP-1 and AP-2 harbor the dileucine recognition site. *Mol. Biol. Cell* **18**, 1887–1896 (2007). doi: [10.1091/mbc.E07-01-0012](#); pmid: [17360967](#)
- X. Jia *et al.*, Structural basis of evasion of cellular adaptive immunity by HIV-1 Nef. *Nat. Struct. Mol. Biol.* **19**, 701–706 (2012). doi: [10.1038/nsmb.2328](#); pmid: [22705789](#)
- X. Ren, S. Y. Park, J. S. Bonifacino, J. H. Hurley, How HIV-1 Nef hijacks the AP-2 clathrin adaptor to downregulate CD4. *eLife* **3**, e01754 (2014). doi: [10.7554/eLife.01754](#); pmid: [24473078](#)
- K. Janvier *et al.*, HIV-1 Nef stabilizes the association of adaptor protein complexes with membranes. *J. Biol. Chem.* **278**, 8725–8732 (2003). doi: [10.1074/jbc.M210115200](#); pmid: [12486136](#)
- S. H. Coleman, D. Hitchin, C. M. Novello, J. C. Guatelli, HIV-1 Nef stabilizes AP-1 on membranes without inducing ARF1-independent de novo attachment. *Virology* **345**, 148–155 (2006). pmid: [16253302](#)
- E. R. Wonderlich *et al.*, ADP ribosylation factor 1 activity is required to recruit AP-1 to the major histocompatibility complex class I (MHC-I) cytoplasmic tail and disrupt MHC-I trafficking in HIV-1-infected primary T cells. *J. Virol.* **85**, 12216–12226 (2011). doi: [10.1128/JVI.0056-11](#); pmid: [21917951](#)
- S. Jäger *et al.*, Global landscape of HIV-human protein complexes. *Nature* **481**, 365–370 (2012). pmid: [22190034](#)
- Single-letter abbreviations for the amino acid residues are as follows: A, Ala; C, Cys; D, Asp; E, Glu; F, Phe; G, Gly; H, His; I, Ile; K, Lys; L, Leu; M, Met; N, Asn; P, Pro; Q, Gln; R, Arg; S, Ser; T, Thr; V, Val; W, Trp; and Y, Tyr.
- E. E. Heldwein *et al.*, Crystal structure of the clathrin adaptor protein 1 core. *Proc. Natl. Acad. Sci. U.S.A.* **101**, 14108–14113 (2004). doi: [10.1073/pnas.0406102101](#); pmid: [15377783](#)
- X. Yu, M. Breitman, J. Goldberg, A structure-based mechanism for Arf1-dependent recruitment of coatamer to membranes. *Cell* **148**, 530–542 (2012). doi: [10.1016/j.cell.2012.01.015](#); pmid: [22304919](#)
- A. Fotin *et al.*, Molecular model for a complete clathrin lattice from electron cryomicroscopy. *Nature* **432**, 573–579 (2004). doi: [10.1038/nature03079](#); pmid: [15502812](#)
- J. Cherfils, Arf GTPases and their effectors: Assembling multivalent membrane-binding platforms. *Curr. Opin. Struct. Biol.* **29**, 67–76 (2014). doi: [10.1016/j.sbi.2014.09.007](#); pmid: [25460270](#)
- K. Janvier *et al.*, Recognition of dileucine-based sorting signals from HIV-1 Nef and LIMP-II by the AP-1 γ/α 1 and AP-3 δ/α 3 hemicomplexes. *J. Cell Biol.* **163**, 1281–1290 (2003). doi: [10.1083/jcb.200307157](#); pmid: [14691137](#)
- N. L. Riggs, H. M. Craig, M. W. Pandori, J. C. Guatelli, The dileucine-based sorting motif in HIV-1 Nef is not required for down-regulation of class I MHC. *Virology* **258**, 203–207 (1999). doi: [10.1006/viro.1999.9736](#); pmid: [10366557](#)
- M. S. Robinson, J. S. Bonifacino, Adaptor-related proteins. *Curr. Opin. Cell Biol.* **13**, 444–453 (2001). doi: [10.1016/S0955-0674\(00\)00235-0](#); pmid: [11454451](#)
- E. Cocucci, F. Aguet, S. Boulant, T. Kirchhausen, The first five seconds in the life of a clathrin-coated pit. *Cell* **150**, 495–507 (2012). doi: [10.1016/j.cell.2012.05.047](#); pmid: [22863004](#)
- S. O. Dodonova *et al.*, A structure of the COPI coat and the role of coat proteins in membrane vesicle assembly. *Science* **349**, 195–198 (2015). doi: [10.1126/science.aab1121](#); pmid: [26160949](#)
- S. F. Kluge *et al.*, Nef proteins of epidemic HIV-1 group O strains antagonize human tetherin. *Cell Host Microbe* **16**, 639–650 (2014). doi: [10.1016/j.chom.2014.10.002](#); pmid: [25525794](#)
- S. Watanabe *et al.*, Clathrin regenerates synaptic vesicles from endosomes. *Nature* **515**, 228–233 (2014). doi: [10.1038/nature13846](#); pmid: [25296249](#)
- B. T. Kelly *et al.*, AP2 controls clathrin polymerization with a membrane-activated switch. *Science* **345**, 459–463 (2014). doi: [10.1126/science.1254836](#); pmid: [25061211](#)
- C. Suloway *et al.*, Automated molecular microscopy: The new Legion system. *J. Struct. Biol.* **151**, 41–60 (2005). doi: [10.1016/j.jsb.2005.03.010](#); pmid: [15890530](#)
- X. Li *et al.*, Electron counting and beam-induced motion correction enable near-atomic-resolution single-particle cryo-EM. *Nat. Methods* **10**, 584–590 (2013). doi: [10.1038/nmeth.2472](#); pmid: [23644547](#)
- S. H. W. Scheres, R. Núñez-Ramírez, C. O. S. Sorzano, J. M. Carazo, R. Marabini, Image processing for electron microscopy single-particle analysis using XMIPP. *Nat. Protoc.* **3**, 977–990 (2008). doi: [10.1038/nprot.2008.62](#); pmid: [18536645](#)
- S. H. W. Scheres *et al.*, Maximum-likelihood multi-reference refinement for electron microscopy images. *J. Mol. Biol.* **348**, 139–149 (2005). doi: [10.1016/j.jmb.2005.02.031](#); pmid: [15808859](#)
- M. Radermacher, T. Wagenknecht, A. Verschoor, J. Frank, Three-dimensional reconstruction from a single-exposure, random conical tilt series applied to the 50S ribosomal subunit of *Escherichia coli*. *J. Microsc.* **146**, 113–136 (1987). doi: [10.1111/j.1365-2818.1987.tb01333.x](#); pmid: [3302267](#)
- S. H. W. Scheres, RELION: Implementation of a Bayesian approach to cryo-EM structure determination. *J. Struct. Biol.* **180**, 519–530 (2012). doi: [10.1016/j.jsb.2012.09.006](#); pmid: [23000701](#)

46. N. R. Voss, C. K. Yoshioka, M. Radermacher, C. S. Potter, B. Carragher, DoG Picker and TiltPicker: Software tools to facilitate particle selection in single particle electron microscopy. *J. Struct. Biol.* **166**, 205–213 (2009). doi: [10.1016/j.jsb.2009.01.004](https://doi.org/10.1016/j.jsb.2009.01.004); pmid: [19374019](https://pubmed.ncbi.nlm.nih.gov/19374019/)
47. G. C. Lander *et al.*, Appion: An integrated, database-driven pipeline to facilitate EM image processing. *J. Struct. Biol.* **166**, 95–102 (2009). doi: [10.1016/j.jsb.2009.01.002](https://doi.org/10.1016/j.jsb.2009.01.002); pmid: [19263523](https://pubmed.ncbi.nlm.nih.gov/19263523/)
48. E. F. Pettersen *et al.*, UCSF Chimera—A visualization system for exploratory research and analysis. *J. Comput. Chem.* **25**, 1605–1612 (2004). doi: [10.1002/jcc.20084](https://doi.org/10.1002/jcc.20084); pmid: [15264254](https://pubmed.ncbi.nlm.nih.gov/15264254/)
49. T. Shiba *et al.*, Molecular mechanism of membrane recruitment of GGA by ARF in lysosomal protein transport. *Nat. Struct. Biol.* **10**, 386–393 (2003). doi: [10.1038/nsb920](https://doi.org/10.1038/nsb920); pmid: [12679809](https://pubmed.ncbi.nlm.nih.gov/12679809/)

ACKNOWLEDGMENTS

We thank E. Nogales for suggestions and advice; J. Bonifacino for discussions; P. Grob, S. Wu, Y. Cheng, and B. LaFrance for assistance at the outset of the project; and A. Johnson for assistance with figure preparation. This work was supported by the HARC Collaborative Opportunity Fund (J.H.H.; subaward of NIH grant P50GM082250 to A. Frankel) and NIH grant R01AI120691 (J.H.H.). EM facilities were supported by the Howard Hughes

Medical Institute (E. Nogales). All EM maps have been deposited in the Electron Microscopy Data Bank (accession codes: EMD-6385 for closed trimer, EMD-6388 for closed monomer, EMD-6389 for open trimer).

SUPPLEMENTARY MATERIALS

www.sciencemag.org/content/350/6259/aac5137/suppl/DC1

Figs. S1 to S10

Movies S1 and S2

5 May 2015; accepted 4 September 2015

10.1126/science.aac5137

RESEARCH ARTICLE

INNATE IMMUNITY

Structural and biochemical basis for induced self-propagation of NLRC4

Zehan Hu,^{1*} Qiang Zhou,^{2*} Chenlu Zhang,^{1*} Shilong Fan,¹ Wei Cheng,³ Yue Zhao,⁴ Feng Shao,⁴ Hong-Wei Wang,¹ Sen-Fang Sui,^{2†} Jijie Chai^{1†}

Responding to stimuli, nucleotide-binding domain and leucine-rich repeat-containing proteins (NLRs) oligomerize into multiprotein complexes, termed inflammasomes, mediating innate immunity. Recognition of bacterial pathogens by NLR apoptosis inhibitory proteins (NAIPs) induces NLR family CARD domain-containing protein 4 (NLRC4) activation and formation of NAIP-NLRC4 inflammasomes. The wheel-like structure of a PrgJ-NAIP2-NLRC4 complex determined by cryogenic electron microscopy at 6.6 angstrom reveals that NLRC4 activation involves substantial structural reorganization that creates one oligomerization surface (catalytic surface). Once activated, NLRC4 uses this surface to catalyze the activation of an inactive NLRC4, self-propagating its active conformation to form the wheel-like architecture. NAIP proteins possess a catalytic surface matching the other oligomerization surface (receptor surface) of NLRC4 but not those of their own, ensuring that one NAIP is sufficient to initiate NLRC4 oligomerization.

Nucleotide-binding domain (NBD)- and leucine-rich repeat (LRR)-containing proteins (NLRs) are critical for the cytosolic immunosurveillance system of mammals (1–4). Dysregulation of NLR function is associated with several human diseases (5–8). NLRs are pattern recognition receptors that recognize pathogen-associated molecular patterns (PAMPs) or host-derived danger components, resulting in NLR activation and oligomerization (1, 4). The oligomerized NLRs then recruit procaspase-1 (pro-Casp1) either directly or through the adaptor protein apoptosis-associated speck-like protein containing CARD (caspase activation and recruitment domain) (ASC), forming inflammasomes that catalyze Casp-1 activation (1, 9). Once activated, Casp-1 proteolytically processes pro-interleukin 1 β (pro-IL-1 β) and pro-IL-18 to initiate host innate immune responses.

NLR proteins contain a varied N-terminal domain such as CARD or pyrin domain (PYD), a central nucleotide binding and oligomerization domain (NOD), and a C-terminal LRR domain (4). The NOD module, containing an NBD and a helical domain 1 (HD1) followed by a winged-helical domain (WHD) (10), is an adenosine

diphosphate-adenosine triphosphate binding motif conserved in the apoptotic proteins Apaf-1 and CED-4 (11). NLRs are maintained in an autoinhibited state by their C-terminal LRR domains (12, 13). Recent studies support a unified model of NLR activation in which ligand-induced clustering of PYD from an NLR [or absent in melanoma 2 (AIM2)] serves to nucleate the ASC^{PYD} filament for Casp-1 polymerization and activation (14, 15).

NLRC4 inflammasomes are activated by bacterial pathogens carrying flagellin or the components of type III secretion system (T3SS) (16–23). Specificity of the NLRC4 inflammasomes for different bacterial ligands is dictated by NLR apoptosis inhibitory proteins (NAIPs) (24, 25) that contain three baculoviral inhibitor of apoptosis (IAP) repeat (BIR) domains at their N-terminal sides. In mice, direct recognition of the bacterial flagellin and the T3SS rod protein PrgJ is mediated by NAIP5/6 and NAIP2, respectively (24, 25). The structural determinants for recognition of the two bacterial PAMPs lie in the NOD module of a NAIP protein (26). Ligand binding induces NAIP interaction with NLRC4, followed by oligomerization of their complex (24, 25). Assembly of flagellin-NAIP5-NLRC4 inflammasomes was proposed to follow a sequential manner (27), but evidence for this model is lacking.

Results

The wheel-like structure of a PrgJ-NAIP2-NLRC4 complex revealed by cryo-EM

A protein complex composed of PrgJ, NAIP2, and full-length NLRC4 (NLRC4^{FL}, fig. S1A) but not a CARD-truncated NLRC4 (residues 90 to 1024, NLRC4^{ACARD}) (fig. S1B) contained double-ring structures as revealed by cryogenic electron mi-

croscopy (cryo-EM) (figs. S2A and S3A), indicating that the double-ring structures are mediated by the CARD of NLRC4. Two-dimensional (2D) class averages of the latter complex revealed particles featuring wheel-like structures containing mainly 11, some 10 (fig. S2A, bottom panel), and a small fraction of 12 protomers, and multilayer structures (fig. S2, B and C). The wheel-like architectures are further supported by comparison of the single-layer side-view averages with their mirrored images (fig. S2D).

Intriguingly, particles of the NLRC4^{FL}-containing complex mainly contained 11 and 12 protomers (fig. S3, A to F, and table S1), similar to those purified from mammalian cells (27). In the 2D class averages without imposing any symmetry, the 10, 11, or 12 protomers within one particle are highly similar (figs. S2A and S3A), suggesting that NAIP2 and NLRC4 have a conserved structure, as evidenced by sequence alignment of NLR proteins (fig. S4). Further supporting their conserved structures, the 3D reconstructions of the 11- and 10-protomer without imposing any symmetry revealed wheel-like structures with pseudosymmetry (fig. S2E). We thus performed 3D reconstruction refinement of the two types of complexes with c11 or c10 symmetry averaging. The resulting cryo-EM maps (Fig. 1A) had an overall resolution of 6.6 Å for the 11-protomer (NLRC4^{ACARD}-containing complex) and 6.7 Å for the 10-protomer complex (fig. S2, F to K, and table S1). These two types of complexes slightly differ in diameter and height (Fig. 1A). Separate rigid-body fitting of the NBD-HD1 module and its following C-terminal segment (WHD-HD2-LRR) from the inactive NLRC4 (13) into the EM volumes demonstrated a high compatibility with the 3D reconstructions (Fig. 1A). Local resolution analysis indicated that the inner part of the 11-protomer wheel-like structure was of significantly higher resolution (5.5 Å) (Fig. 1B), allowing an easy assignment of secondary structure elements of the NOD module (Fig. 1C).

Some registry errors will be present in our models, as NAIP2 was approximated to NLRC4, but the models are sufficient to characterize domain organization and interactions between secondary structural elements, the main focuses of our current study. We limit our discussions to the 11-protomer model of the PrgJ-NAIP2-NLRC4^{ACARD} complex that is nearly identical with that of the 11-protomer PrgJ-NAIP2-NLRC4^{FL} complex (fig. S3G).

A single NAIP2 initiates progressive assembly of the wheel-like structure

To determine the stoichiometry of the PrgJ-NAIP2-NLRC4^{ACARD} complex, we performed Ni-NTA-nanogold labeling EM (against the N-terminally His-tagged NAIP2) for the oligomerized complex eluted at higher molecular weights (fig. S1C, bottom panel). The results showed that each single particle of the complex was bound by one gold particle (Fig. 1D and fig. S5A), suggesting that the complex contained one NAIP2 molecule. Ni-NTA-nanogold labeling EM against the

¹Ministry of Education Key Laboratory of Protein Science, Center for Structural Biology, School of Life Sciences, Tsinghua-Peking Joint Center for Life Sciences, Tsinghua University, Beijing 100084, China. ²State Key Laboratory of Biomembrane and Membrane Biotechnology, Center for Structural Biology, School of Life Sciences, Tsinghua University, Beijing 100084, China. ³Division of Respiratory and Critical Care Medicine, State Key Laboratory of Biotherapy, West China Hospital, Sichuan University, and Collaborative Innovation Center of Biotherapy, Chengdu, China. ⁴National Institute of Biological Sciences, Beijing 102206, China.

*These authors contributed equally to this work. †Corresponding author. E-mail: chaijj@tsinghua.edu.cn (J.C.); suisf@mail.tsinghua.edu.cn (S.F.S.)

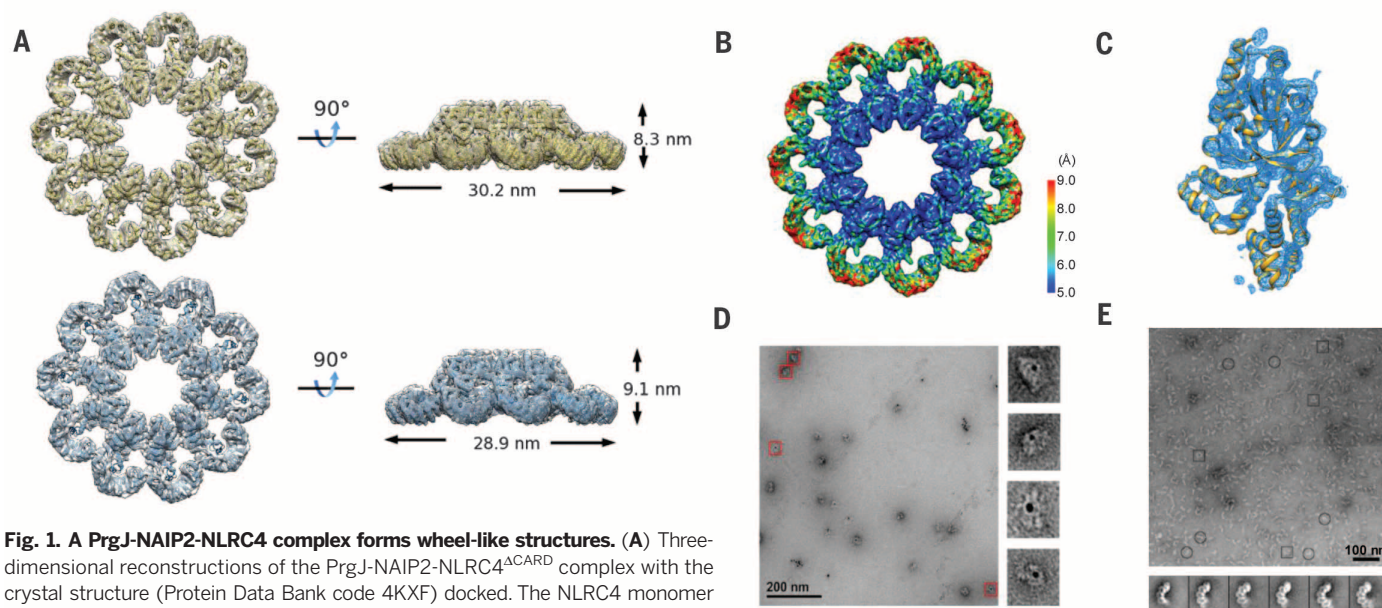


Fig. 1. A PrgJ-NAIP2-NLRC4 complex forms wheel-like structures. (A) Three-dimensional reconstructions of the PrgJ-NAIP2-NLRC4^{ACARD} complex with the crystal structure (Protein Data Bank code 4KXF) docked. The NLRC4 monomer was divided into two halves between HD1 and WHD domains. The two halves were joined together again with Modeller after rigid-body docking into the cryo-EM density map by UCSF Chimera. (Top) the 11-protomer complex; (bottom) the 10-protomer complex. (B) The local resolution of cryo-EM density map of the PrgJ-NAIP2-NLRC4^{ACARD} complex with c11 symmetry. (C) Finally refined cryo-EM density map surrounding the NOD module of NLRC4. (D) Ni-NTA-nanogold labeling (5.0 nm) of the N-terminally His-tagged NAIP2 in complex with PrgJ and NLRC4^{ACARD} eluted at positions of higher molecular weights (see fig. S1C). On the left is a representative negative-stain micrograph of the nanogold-labeled complex. Particles highlighted in red squares are shown in the insets. (E) Partially oligomerized structures of the PrgJ-NAIP2-NLRC4^{ACARD} complex eluted at lower molecular weights (see fig. S1C). (Top) A representative negative-stain micrograph of the PrgJ-NAIP2-NLRC4^{ACARD} complex. (Bottom) Representative 2D class averages of PrgJ-NAIP2-NLRC4^{ACARD} particles.

N-terminally His-tagged PrgJ for the same complex gave a similar result (fig. S5B). Consistently, gel filtration analysis showed that PrgJ-NAIP2-NLRC4^{FL} and PrgJ-NAIP2-NLRC4^{ACARD} were substoichiometric complexes (fig. S1C).

PrgJ-NAIP2-NLRC4^{ACARD} eluted at the positions of lower molecular weights (fig. S1C, bottom panel) formed unclosed and twisted structures with variable sizes (Fig. 1E). Owing to the absence of pseudo-symmetry in these complexes, the 2D classification tends to align the open ends of the particles for maximal overlap and thus likely reveals subtle structural differences between NAIP2 and NLRC4 if the single NAIP2 in one structure is not randomly positioned. Indeed, for each particle type the protomer at one end appears different from the remaining copies in the 2D class averages (Fig. 1E, bottom panel), suggesting that it corresponds to NAIP2. This agrees with the concept that assembly of the NAIP-NLRC4 inflammasomes starts with ligand-induced activation of a NAIP molecule (24, 25). Further supporting our conclusion, a nanogold-labeling EM (against NAIP2) study showed that a single nanogold particle bound to one partially oligomerized complex particle (fig. S5C). This conclusion is also in line with our observation that NAIP2 and NAIP5, although highly conserved in their sequences, failed to coexist in the same single-ring structure (fig. S6).

NOD-mediated formation of the wheel-like structure of PrgJ-NAIP2-NLRC4^{ACARD}

One side of the NOD module from each protomer packs against the opposite side of the

NOD from the adjacent protomer in an invariant fashion (Fig. 2, A and B), providing the major protomer-protomer interactions that stabilize the wheel-like structure. Two adjacent LRRs contact each other largely through complementary charged surfaces (fig. S7). The wheel-like architecture (Fig. 2A) is reminiscent of the structures of Apaf-1 (28), DARK (29, 30) and CED-4 (31) apoptosomes. However, marked differences exist between NLRC4 and Apaf-1 in oligomeric assembly (fig. S8, A and B). Apaf-1 and DARK oligomerization is predominantly mediated by the structural elements from NBD and HD1 (28, 30). By contrast, the WHD of NLRC4 is also involved in the formation of a lateral dimer besides NBD and HD1 (Fig. 2B).

Structural remodeling creates one oligomerization surface during NLRC4 activation

Structure comparison revealed that NLRC4 undergoes striking structural remodeling during activation, with WHD-HD2-LRR rotating largely as a rigid body ~90 degrees around the hinge region (residues 354 to 356) between HD1 and WHD (Fig. 2C and figs. S9 and S10). One dimeric surface, formed by structural elements from NBD and HD1, is largely exposed in the inactive NLRC4 (Fig. 2D and fig. S11, right panel). This surface (hereafter called receptor surface) is preformed, because NBD and HD1 undergo little change relative to each other during activation. Interaction of the inactive NLRC4 with an activated NLRC4 is sterically hindered by the C-terminal end of $\alpha 15$ (labeled in red) from the WHD of the inactive

NLRC4 (Fig. 2D), located immediately after the hinge region (Fig. 2C). By contrast, the LRR domain is positioned by the other oligomeric surface (hereafter called catalytic surface) in the inactive NLRC4 and completely overlaps with its neighboring NLRC4 protomer from a lateral dimer (Fig. 2E and fig. S11, left panel). In further contrast with the receptor surface, half of the catalytic surface is composed of structural elements from the WHD (Fig. 2E), indicating that this oligomerization surface is activation-created and can be fully formed only after structural reorganization of NLRC4 during activation. By comparison, both of the two oligomeric surfaces of Apaf-1 are preexistent in an inactive Apaf-1 (28, 32) (fig. S8C).

The catalytic surface initiates NLRC4 autoactivation

Formation of the unclosed structures (Fig. 1E) starting with NAIP2 indicates that their assembly is a unidirectional process. The propagation direction of these structures can be unambiguously determined by the observation that the C-terminal portion of LRR domain from each protomer is located at the same side as the catalytic surface of NLRC4 (Figs. 1E and 2B). These results strongly suggest that an activated NLRC4 uses the catalytic surface for interaction with and activation of an inactive NLRC4 (Fig. 3, A and B), leading to progressive intermolecular autoactivation of NLRC4. On the other hand, the equivalent positioning of NAIP2 to NLRC4 in the 2D class averages (Fig. 1E) suggests that the receptor surface of NLRC4 contacts NAIP2. Fully supporting

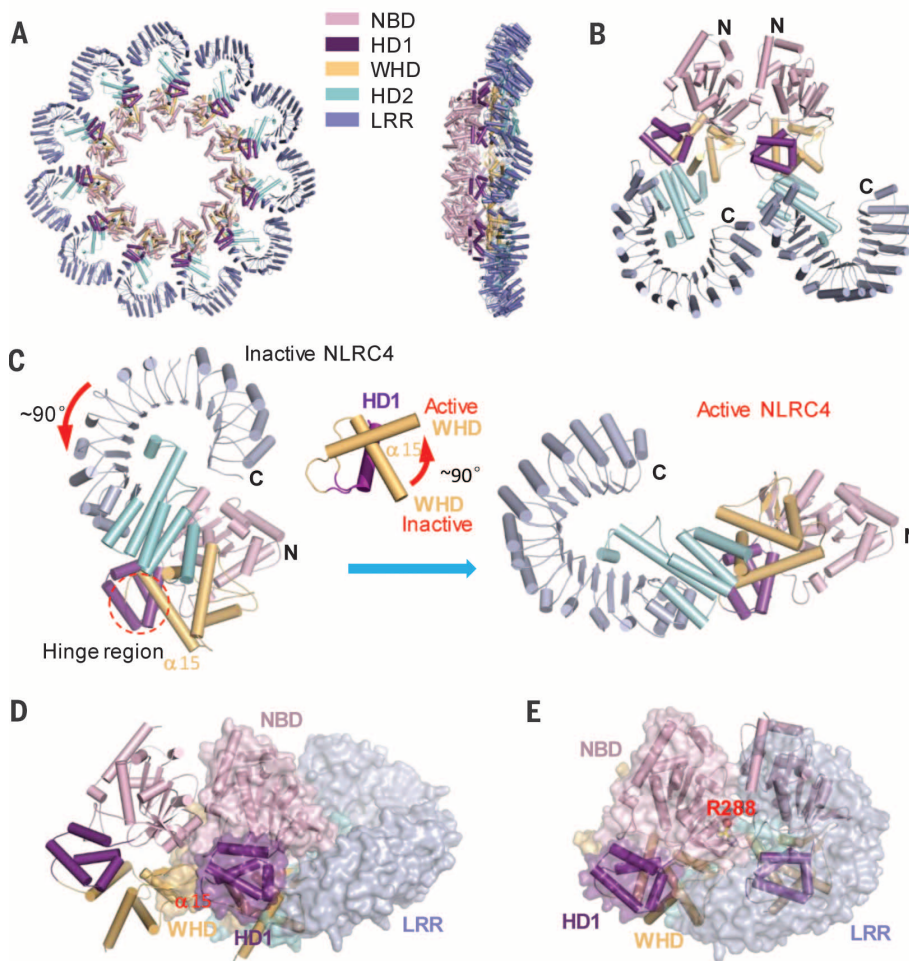


Fig. 2. NLRC4 activation creates the catalytic surface for oligomerization. (A) Cartoon representations of oligomerized NLRC4^{ACARD} in top and side views. Color codes for domains of NLRC4 are indicated. (B) A lateral dimer of NLRC4^{ACARD}. The N- and C-terminal sides of NLRC4 are labeled. (C) Striking structural reorganization occurs to NLRC4 during activation. Cartoon representations of the inactive (left) and active (right) structures of NLRC4. The two structures superimposed with the NOD module of the inactive NLRC4 as the template are shown in the same orientation. The red arrow indicates the direction of the C-terminal LRR domain movement from inactive to active state. The hinge region is highlighted in the red circle. The middle panel illustrates a structure comparison of the hinge region from the inactive and active structure. (D) The NOD module of the inactive NLRC4 (in transparent surface) was aligned with one NLRC4 monomer (right) from a lateral dimer (in cartoon). (E) The NOD module of the inactive NLRC4 (in transparent surface) was aligned with one NLRC4 monomer (left) from a lateral dimer (in cartoon).

this conclusion, NLRC4^{R288A} from the catalytic surface still displayed flagellin-induced interaction with NAIP5 but failed to form higher-order oligomeric complexes (13). Gel filtration analysis and negative staining EM 3D reconstruction showed that the flagellin-NAIP5-NLRC4^{R288AACARD} complex was dimeric in solution (Fig. 3C; fig. S12, A to E; and table S1). The 3D reconstruction (Fig. 3D) revealed a region of extra density for one of the two protomers, which is probably from NAIP5.

NLRC4^{L435DACARD} located at the same side as NLRC4^{R288AACARD} (Fig. 3B) generated similar effects on flagellin-induced NLRC4 oligomerization and interaction with NAIP5 (Fig. 3, C and E). Consistently, NLRC4^{L435D} and NLRC4^{Q433A} but not NLRC4^{R288A} and NLRC4^{R434A} abrogated flagellin-NAIP5 or PrgJ-NAIP2 mediated production of

IL-1 β , phenocopying NLRC4^{R288A} (fig. S13, A and B). Further supporting these results, NLRC4^{R285AACARD} and NLRC4^{R434AACARD} interacted with NAIP5 in a stoichiometry similar to the wild NLRC4^{ACARD} but different from NLRC4^{R288AACARD}, NLRC4^{L435DACARD}, and NLRC4^{Q433AACARD} (Fig. 3E and fig. S14).

Asp¹²⁵ from the receptor surface was modeled to form polar interactions with Arg²⁸⁸ (Fig. 3B) from the catalytic surface. Consistently, NLRC4^{D125A} abrogated flagellin-NAIP5 or PrgJ-NAIP2 mediated generation of IL-1 β (fig. S13, C and D). Similar results were obtained with the mutants NLRC4^{D123A} and NLRC4^{I124D} (Fig. 3B) located at the same oligomeric surface. However, a higher level of NLRC4^{D123A} protein was still responsive to flagellin or PrgJ (fig. S13, C and D), indicating

that this mutation only partially inhibited NLRC4 activation. NLRC4^{I124DACARD} and NLRC4^{D125AACARD} displayed no detectable interaction with NAIP5 induced by flagellin in our pull-down assay (Fig. 3E), in sharp contrast with NLRC4^{L435DACARD} and NLRC4^{R288AACARD} from the catalytic surface (Fig. 3, C and E).

Our model (Figs. 3A and 4A) predicts that an activated NAIP or NLRC4 molecule can interact with and activate the inactive mutant NLRC4^{R288A} that has an intact receptor surface. The NLRC4 mutant, however, is unable to activate a second inactive NLRC4 molecule due to its impaired catalytic surface. Thus, NLRC4^{R288A} is expected to inhibit formation of the wheel-like structure of the PrgJ-NAIP2-NLRC4^{FL} complex by terminating the propagation of NLRC4, forming partially oligomerized structures. Indeed, the complex containing the four proteins was shifted to the lower molecular weight species as compared with the PrgJ-NAIP2-NLRC4^{FL} complex (Fig. 4B). As predicted, structures similar to those of the partially oligomerized PrgJ-NAIP2-NLRC4^{ACARD} were observed in the NLRC4^{R288AACARD}-containing complex (Fig. 4C). In further support of our model (Fig. 3A and fig. S15A), the constitutively active mutant NLRC4^{H443LACARD} (13) interacted with and induced oligomerization of wild-type NLRC4^{FL} (fig. S15, B to E).

NAIPs possess catalytic surfaces matching the receptor surface of NLRC4

Our data (Figs. 1E, 3D, and 3E) support the idea that NAIP5 interacts with the receptor surface of NLRC4 (Fig. 5A). Well agreeing with this conclusion, Arg²⁸⁸ and the β -hairpin tip of WHD from the catalytic surface of NLRC4 are highly conserved in the NAIP members (Fig. 5B). In contrast, the critical amino acids from the receptor surface of NLRC4 are highly variable in all the NAIP members (Fig. 5B). Further supporting our model (Fig. 5A), mutations of Arg⁵⁹⁰ (Arg⁵⁹⁰Ala) and Leu⁷³⁷ (Leu⁷³⁷Asp) from NAIP5 or Arg⁶³⁴ (Arg⁶³⁴Ala) and Leu⁷⁸⁰ (Leu⁷⁸⁰Asp) from NAIP2 that are equivalents of Arg²⁸⁸ and Leu⁴³⁵ of NLRC4, respectively (Fig. 5B), resulted in no detectable activity of NLRC4-mediated production of IL-1 β (fig. S16, A and B). Substantial increases in protein expression, however, resulted in partial activity of the NAIP5 or NAIP2 mutants in producing IL-1 β (fig. S16, A and B). Interestingly, the two NAIP5 mutations were less effective in inhibiting flagellin-induced NAIP5-NLRC4^{ACARD} interaction (Fig. 5C, top panel) than those from the receptor surface of NLRC4 (Fig. 3E). The reason for this might be that the residual activity of these NAIP5 mutants still activated a small amount of NLRC4 that can proceed with autocatalytic activation. This differs from the mutations from the receptor surface that have an accumulating effect on inhibiting the assembly of NAIP-NLRC4 inflammasomes. Supporting these ideas, the two NAIP5 mutants exhibited nearly no detectable flagellin-induced interaction with NLRC4^{R288AACARD} (Fig. 5C, bottom panel) that has an impaired catalytic surface. By contrast, the immunoactive mutants NAIP5^{R587A} and NAIP5^{Q735A}

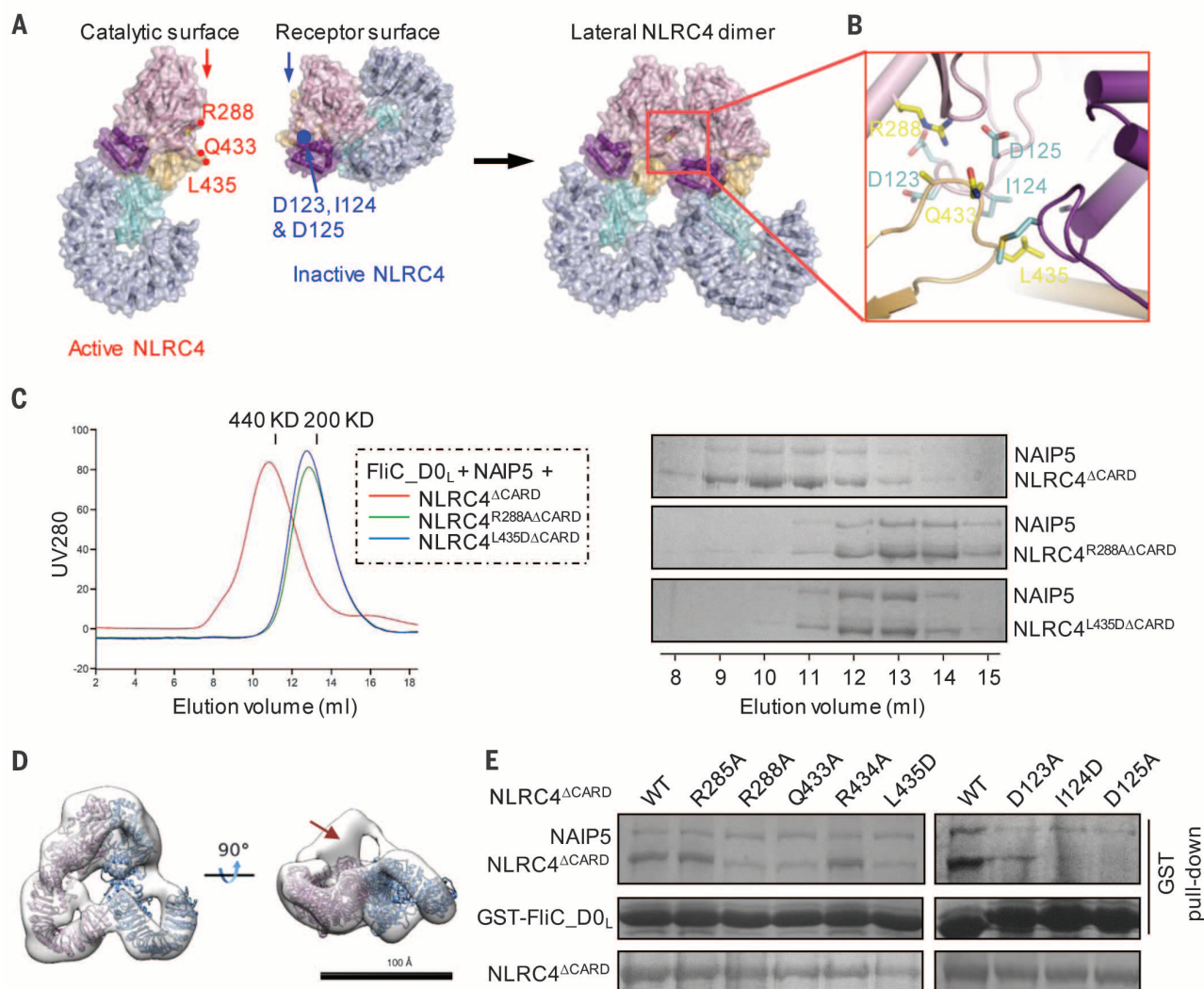


Fig. 3. The catalytic surface initiates NLRC4 self-oligomerization. (A) A model depicting formation of a lateral NLRC4 dimer through the interaction of an activated NLRC4 and with an inactive NLRC4. The red and blue arrows indicate the catalytic surface (in active NLRC4) and receptor surface, respectively. Positions of some residues from the catalytic surface and receptor surface are indicated. (B) Amino acids located at a lateral NLRC4 dimeric interface. Residues from the catalytic surface and receptor surface are colored in yellow and cyan, respectively. (C) GST-FluCD_L, NAIP5, and NLRC4^{ACARD} wild type or mutants as indicated were coexpressed in insect cells, and the purified proteins were subjected to gel filtration analysis after removal of

displayed similar interactions with either wild-type NLRC4^{ΔCARD} or NLRC4^{R288AΔCARD} as compared with the wild-type NAIP5.

Together, our data showed that NAIP members do not possess a receptor surface matching the conserved catalytic surface of their own or NLRC4's, thus precluding them from self-oligomerization and further recruitment into an existing NAIP-NLRC4-containing complex by an activated NLRC4. These ensure incorporation of a single NAIP molecule into one NAIP-NLRC4 inflammasome.

Discussion

Our present study, together with others (33, 34), supports a sequential ligand-induced assembly of

glutathione S-transferase (GST). (Left) Gel filtration profiles of protein complexes as indicated. (Right) Samples of peak fractions shown in the left panel were visualized by Coomassie staining after SDS–polyacrylamide gel electrophoresis (SDS–PAGE). **(D)** Surface representation of 3D reconstruction of the FliC_{DO_L}-NAIP5-NLRC4^{R288AΔCARD} complex shown in (C), with two NLRC4^{ΔCARD} monomers docked. The red arrow indicates the extra density map in which NLRC4^{ΔCARD} cannot be fitted. **(E)** GST-FliC_{DO_L}, NAIP5, and wild-type NLRC4^{ΔCARD} or its mutants as indicated were coexpressed in insect cells. The proteins were purified using GS4B resin. Proteins bound to the resin were detected by Coomassie blue staining after SDS–PAGE.

NAIP-NLRC4 inflammasomes (fig. S17). The partially exposed receptor surface in the inactive NLRC4 (Figs. 2D and 3A) may adopt a metastable active state that has a higher binding affinity with the catalytic surface of an activated NLRC4. This interaction might also involve an induced-fit mechanism. Regardless of conformational selection or induced fit or both pathways, to avoid the clashes between the β -hairpin tip of WHD from an activated NLRC4 and the receptor surface of an inactive NLRC4 (Fig. 2D and fig. S11), their interaction may induce a concerted reorientation of the WHD from the inactive NLRC4 (Fig. 2C and fig. S9). This results in NLRC4 activation and formation of the catalytic

surface that activates a second inactive NLRC4 molecule, thus self-propagating the active conformation of NLRC4 to assemble the wheel-like structure of inflammasomes (fig. S17). Apaf-1 likely follows a different paradigm for oligomerization. Cryo-EM studies clearly showed a 1:1 stoichiometry between Apaf-1 and cytochrome c in apoptosome (28), suggesting that each Apaf-1 molecule needs activation by cytochrome c for oligomerization. This is supported by the observation that both of the two oligomerization surfaces of inactive Apaf-1 are completely buried (fig. S8C), ruling out the possibility of self-propagation.

The properties of NLRC4 oligomerization are reminiscent of the replication mechanism of a

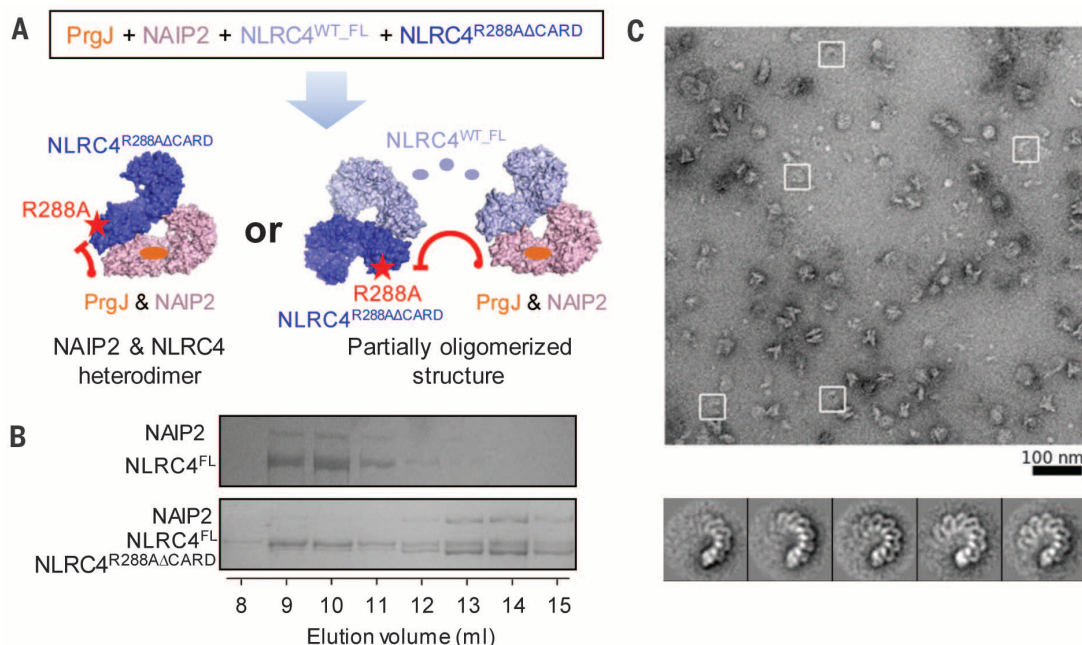


Fig. 4. NLRC4 is activated in a self-propagated manner. (A) A cartoon illustrating inhibition of the wheel-like structure of the PrgJ-NAIP2-NLRC4^{FL} complex by the mutant protein NLRC4^{R288A}CARD. The red star represents the position of Arg²⁸⁸Ala mutation from the catalytic surface. (B) Gel filtration analysis of the PrgJ-NAIP2-NLRC4^{FL} and PrgJ-NAIP2-NLRC4^{FL}-NLRC4^{R288A}CARD complexes. The peak fractions were visualized by SDS-PAGE with Coomassie blue staining. (C) Partially oligomerized structures of the PrgJ-NAIP2-NLRC4^{FL}-NLRC4^{R288A}CARD complex [sample from elution volume of 11 ml in (B)]. (Top) A representative negative-stain micrograph of the complex. (Bottom) Representative 2D class averages of the complexes.

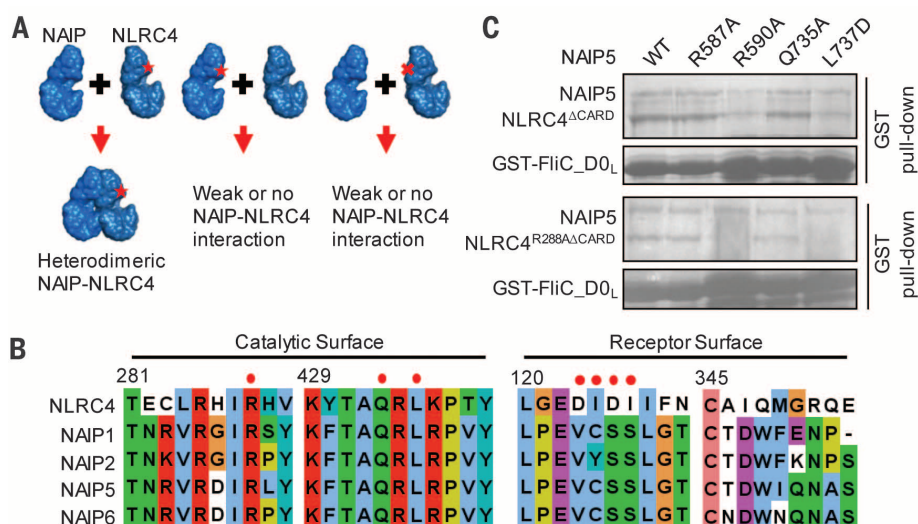


Fig. 5. NAIP members have a conserved catalytic surface with NLRC4.

(A) A cartoon showing effects of mutations from NAIP or NLRC4 on their ligand-induced interaction. The red star and the red cross indicate mutations of key amino acids in the catalytic and receptor surface, respectively. **(B)** Sequence alignment of NAIP members with NLRC4 around the catalytic and receptor surface of NLRC4. The red dots on the top indicate the amino acids whose mutations disrupt or compromise formation of the wheel-like structures of NAIP-NLRC4 complexes. Numbers indicate the

positions of NLRC4 residues. Single-letter abbreviations for the amino acid residues are as follows: A, Ala; C, Cys; D, Asp; E, Glu; F, Phe; G, Gly; H, His; I, Ile; K, Lys; L, Leu; M, Met; N, Asn; P, Pro; Q, Gln; R, Arg; S, Ser; T, Thr; V, Val; W, Trp; and Y, Tyr. **(C)** GST-FluC_D0L, wild-type NALP5 or its mutants, and wild-type NLRC4^{ΔCARD} or NLRC4^{R288AΔCARD} as indicated were coexpressed in insect cells. The proteins were purified using GS4B resin. Proteins bound to the resin were detected by Coomassie blue staining after SDS-PAGE.

prior in which conformational conversion from its properly folded isoform into the prior form (misfolded) is propagated in an autocatalytic manner (35). Such a mechanism would render the gain-of-function mutations mapped to de-

stabilize the inactive conformation of NLRC4 (36–38) more efficient to induce NLRC4 activation. However, self-propagation of NLRC4 differs from that of a canonical prion in that the former is initiated by the PAMP-activated

NAIPs rather than self-seeded. Furthermore, self-propagation of NLRC4 leads to a soluble wheel-like structure with finite copies, whereas replication of a prion is self-perpetuating and thus results in formation of insoluble aggregates. Nonetheless,

the homologies between NLRC4 oligomerization and prion replication may help to better understand their underlying mechanisms. It remains unknown whether the prion-like mechanism is conserved in other immune NLR sensors for oligomerization. However, one apparent advantage of this mechanism is that a single PAMP or a host-derived danger molecule is sufficient for inducing formation of a fiber assembly, which in principle contains endless ASC because of its self-perpetuation property (39) and thus generates an all-or-none response (40). The requirement of ligand for initiation of this activity could serve to minimize inadvertent activation of an NLR protein through intermolecular collisions.

REFERENCES AND NOTES

- K. Schroder, J. Tschopp, *Cell* **140**, 821–832 (2010).
- L. Franchi, R. Muñoz-Planillo, G. Núñez, *Nat. Immunol.* **13**, 325–332 (2012).
- V. A. Rathinam, S. K. Vanaja, K. A. Fitzgerald, *Nat. Immunol.* **13**, 333–342 (2012).
- J. von Moltke, J. S. Ayres, E. M. Kofoed, J. Chavarría-Smith, R. E. Vance, *Annu. Rev. Immunol.* **31**, 73–106 (2013).
- B. K. Davis, H. Wen, J. P. Ting, *Annu. Rev. Immunol.* **29**, 707–735 (2011).
- M. Lamkanfi, V. M. Dixit, *Annu. Rev. Cell Dev. Biol.* **28**, 137–161 (2012).
- T. Strowig, J. Henao-Mejia, E. Elinav, R. Flavell, *Nature* **481**, 278–286 (2012).
- H. Wen, J. P. Ting, L. A. O'Neill, *Nat. Immunol.* **13**, 352–357 (2012).
- F. Martinon, K. Burns, J. Tschopp, *Mol. Cell* **10**, 417–426 (2002).
- O. Danot, E. Marquet, D. Vidal-Ingligiardi, E. Richet, *Structure* **17**, 172–182 (2009).
- N. Yan, Y. Shi, *Annu. Rev. Cell Dev. Biol.* **21**, 35–56 (2005).
- W. Chuenchor, T. Jin, G. Ravilious, T. S. Xiao, *Curr. Opin. Immunol.* **26**, 14–20 (2014).
- Z. Hu et al., *Science* **341**, 172–175 (2013).
- X. Cai et al., *Cell* **156**, 1207–1222 (2014).
- A. Lu et al., *Cell* **156**, 1193–1206 (2014).
- L. Franchi et al., *Nat. Immunol.* **7**, 576–582 (2006).
- K. L. Lightfield et al., *Nat. Immunol.* **9**, 1171–1178 (2008).
- E. A. Miao et al., *Nat. Immunol.* **7**, 569–575 (2006).
- E. A. Miao et al., *Proc. Natl. Acad. Sci. U.S.A.* **107**, 3076–3080 (2010).
- A. B. Molofsky et al., *J. Exp. Med.* **203**, 1093–1104 (2006).
- T. Ren, D. S. Zamboni, C. R. Roy, W. F. Dietrich, R. E. Vance, *PLoS Pathog.* **2**, e18 (2006).
- F. S. Sutterwala et al., *J. Exp. Med.* **204**, 3235–3245 (2007).
- J. Yang, Y. Zhao, J. Shi, F. Shao, *Proc. Natl. Acad. Sci. U.S.A.* **110**, 14408–14413 (2013).
- E. M. Kofoed, R. E. Vance, *Nature* **477**, 592–595 (2011).
- Y. Zhao et al., *Nature* **477**, 596–600 (2011).
- J. L. Tenthorey, E. M. Kofoed, M. D. Daugherty, H. S. Malik, R. E. Vance, *Mol. Cell* **54**, 17–29 (2014).
- E. F. Halft et al., *J. Biol. Chem.* **287**, 38460–38472 (2012).
- S. Yuan, M. Topf, T. F. Reubold, S. Eschenburg, C. W. Akey, *Biochemistry* **52**, 2319–2327 (2013).
- S. Yuan et al., *Structure* **19**, 128–140 (2011).
- Y. Pang et al., *Genes Dev.* **29**, 277–287 (2015).
- S. Qi et al., *Cell* **141**, 446–457 (2010).
- T. F. Reubold, S. Wohlgenuth, S. Eschenburg, *Structure* **19**, 1074–1083 (2011).
- R. E. Vance, *Curr. Opin. Immunol.* **32**, 84–89 (2015).
- L. Zhang et al., *Science* **350**, 404–409 (2015).
- P. Chien, J. S. Weissman, A. H. DePace, *Annu. Rev. Biochem.* **73**, 617–656 (2004).
- S. W. Canna et al., *Nat. Genet.* **46**, 1140–1146 (2014).
- N. Romberg et al., *Nat. Genet.* **46**, 1135–1139 (2014).
- A. Kitamura, Y. Sasaki, T. Abe, H. Kano, K. Yasutomo, *J. Exp. Med.* **211**, 2385–2396 (2014).
- X. Cai, Z. J. Chen, *Trends Immunol.* **35**, 622–630 (2014).
- Q. Yin, T. M. Fu, J. Li, H. Wu, *Annu. Rev. Immunol.* **33**, 393–416 (2015).

ACKNOWLEDGMENTS

We thank Y. Xu and T. Yang at Tsinghua University Branch of China National Center for Protein Sciences Beijing for data collection and computational support, and X. Li for technical instructions of using the K2-Summit camera. We acknowledge the computational facility support on the Explorer 100 cluster system of Tsinghua National Laboratory for Information Science and Technology. The data presented in this paper are tabulated in the main paper and in the supplementary materials. The EM maps have been deposited in the Electron Microscopy Data Bank with accession codes EMD-3139/3140 for the 12- or 11-protomer PrgJ-NAIP2-NLRC4^{FL} complex, EMD-3141/3142 for the 11- or 10-protomer PrgJ-NAIP2-NLRC4^{ΔCARD} complex, and EMD-3143 for the

FliC_{DO1}-NAIP5-NLRC4^{R288AΔCARD} complex. This research was funded by the Chinese Ministry of Science and Technology (2014CB910101 to J.C., 2011CB910501 to S.-F.S., and 2012CB917303 to H.-W.W.) and the National Natural Science Foundation of China (31230016 to S.-F.S.). Z.H. was supported by a China Postdoctoral Science Foundation-funded project and the Center for Life Sciences (CLS) Postdoctoral Fellowship Foundation. Q.Z. was supported by the CLS Postdoctoral Fellowship Foundation.

SUPPLEMENTARY MATERIALS

www.sciencemag.org/content/350/6259/399/suppl/DC1
Materials and Methods
Figs. S1 to S18
Table S1
References (41–56)

11 May 2015; accepted 14 September 2015
Published online 8 October 2015
10.1126/science.aac5489

REPORTS

INNATE IMMUNITY

Cryo-EM structure of the activated NAIP2-NLRC4 inflammasome reveals nucleated polymerization

Liman Zhang,^{1,2*} Shuobing Chen,^{3,4*} Jianbin Ruan,^{1,2} Jiayi Wu,^{3,4} Alexander B. Tong,^{1,2} Qian Yin,^{1,2} Yang Li,^{1,2} Liron David,^{1,2} Alvin Lu,^{1,2} Wei Li Wang,^{4,5} Carolyn Marks,⁶ Qi Ouyang,³ Xinzheng Zhang,⁷ Youdong Mao,^{3,4,5†} Hao Wu^{1,2†}

The NLR family apoptosis inhibitory proteins (NAIPs) bind conserved bacterial ligands, such as the bacterial rod protein PrgJ, and recruit NLR family CARD-containing protein 4 (NLRC4) as the inflammasome adapter to activate innate immunity. We found that the PrgJ-NAIP2-NLRC4 inflammasome is assembled into multisubunit disk-like structures through a unidirectional adenosine triphosphatase polymerization, primed with a single PrgJ-activated NAIP2 per disk. Cryo-electron microscopy (cryo-EM) reconstruction at subnanometer resolution revealed a ~90° hinge rotation accompanying NLRC4 activation. Unlike in the related heptameric Apaf-1 apoptosome, in which each subunit needs to be conformationally activated by its ligand before assembly, a single PrgJ-activated NAIP2 initiates NLRC4 polymerization in a domino-like reaction to promote the disk assembly. These insights reveal the mechanism of signal amplification in NAIP-NLRC4 inflammasomes.

The nucleotide-binding domain (NBD) and leucine-rich repeat (LRR)-containing protein (NLR) family participates in the formation of inflammasomes that activate caspase-1 for cell death induction and cytokine maturation. NLR family apoptosis inhibitory proteins (NAIPs) are so far the only NLR family members with specifically defined ligands (1–4). NAIP2 detects the inner rod protein of the bacterial type III secretion system, including *Salmonella typhimurium* PrgJ, whereas NAIP5 and NAIP6 detect bacterial flagellin such as *Salmonella typhimurium* FliC (2, 4, 5). NLR family caspase recruitment domain (CARD)-containing protein 4 (NLRC4) was initially found to participate in caspase-1 activation and inter-

leukin (IL)-1β secretion in response to cytoplasmic flagellin (6) and was only recently shown to be the common adapter for NAIPs (2, 4). The NAIP-NLRC4 inflammasomes perform effector functions against intracellular bacteria (7, 8), play protective roles in mouse models of colitis-associated colorectal cancer (9, 10), and serve as a potential strategy in tumor immunotherapy (11). Mutations in NLRC4 also induce auto-inflammatory diseases in humans (10, 12–14).

We assembled the FliC-activated NAIP5-NLRC4 complex and the PrgJ-activated NAIP2-NLRC4 complex with the use of CARD-deleted NLRC4 (NLRC4Δ) to avoid potential CARD-mediated aggregation (Fig. 1A). Either full-length NAIP2 or N-terminal baculovirus inhibitor of apoptosis protein repeat

(BIR) domain-deleted NAIP2 (NAIP2 Δ BIR) was used. During purification, sucrose gradient fractions showed variable molar ratios between NAIP2 and NLRC4 Δ (Fig. 1B). The fraction with the highest amount of NLRC4 Δ relative to NAIP2, by

approximately one order of magnitude, contained mostly single, complete disk-like particles (Fig. 1C and fig. S1A). Similarly, overstoichiometry of NLRC4 Δ to NAIP5 was observed in the reconstituted FliC-NAIP5-NLRC4 Δ complex (Fig. 1D), also with mostly complete disks under electron microscopy (fig. S1B). In contrast, our earlier PrgJ-NAIP2-NLRC4 Δ preparations exhibited much lower NLRC4 Δ /NAIP2 molar ratios (fig. S1C), with mostly incomplete disks (fig. S1D). Labeling of NAIP2 with 5-nm Ni-NTA gold particles in the PrgJ-NAIP2 Δ BIR-His-NLRC4 Δ inflammasome revealed singularly labeled complexes (Fig. 1E). These data, together with the previous report that NAIP5 did not oligomerize in the presence of flagellin (15), demonstrated that a single NAIP exists in each complex, whether in a full disk or a partially assembled disk (Fig. 1F).

We collected cryo-electron microscopy (cryo-EM) data on the PrgJ-NAIP2-NLRC4 Δ complex (Fig. 1G and figs. S2 and S3A). Reference-free two-dimensional (2D) classification revealed mostly 11-bladed, but also 12- and 10-bladed in-

flammasome complexes (fig. S3B), implying conformational flexibility. From the top or bottom view, an inflammasome disk comprises an inner ring and an outer ring (Fig. 1H); 3D classification yielded models with apparent C_{10} , C_{11} , and C_{12} symmetries (fig. S2). The individual blades did not show observable differences to indicate the single PrgJ-NAIP2 complex in each disk, probably due to similar domain organizations of NAIP2 and NLRC4 (Fig. 1A). Upon imposing the apparent symmetry, the C_{11} , C_{12} , and C_{10} reconstructions were refined to resolutions of 4.7 Å, 7.5 Å, and 12.5 Å, respectively (Fig. 2, A to F, and fig. S3, C to G). Local resolution estimation of the C_{11} reconstruction suggests that the inner ring possesses resolutions of 4.0 to 6.0 Å (Fig. 2A and fig. S4), with secondary structural features consistent with a resolution of at least 6.0 Å (Fig. 2, A to D, and fig. S5). Using the crystal structure of NLRC4 Δ in the inactive conformation (PDB ID 4KXF) (16), we built and refined an atomic model of the active NLRC4 Δ (table S1). All structures have a domed center and a prominent

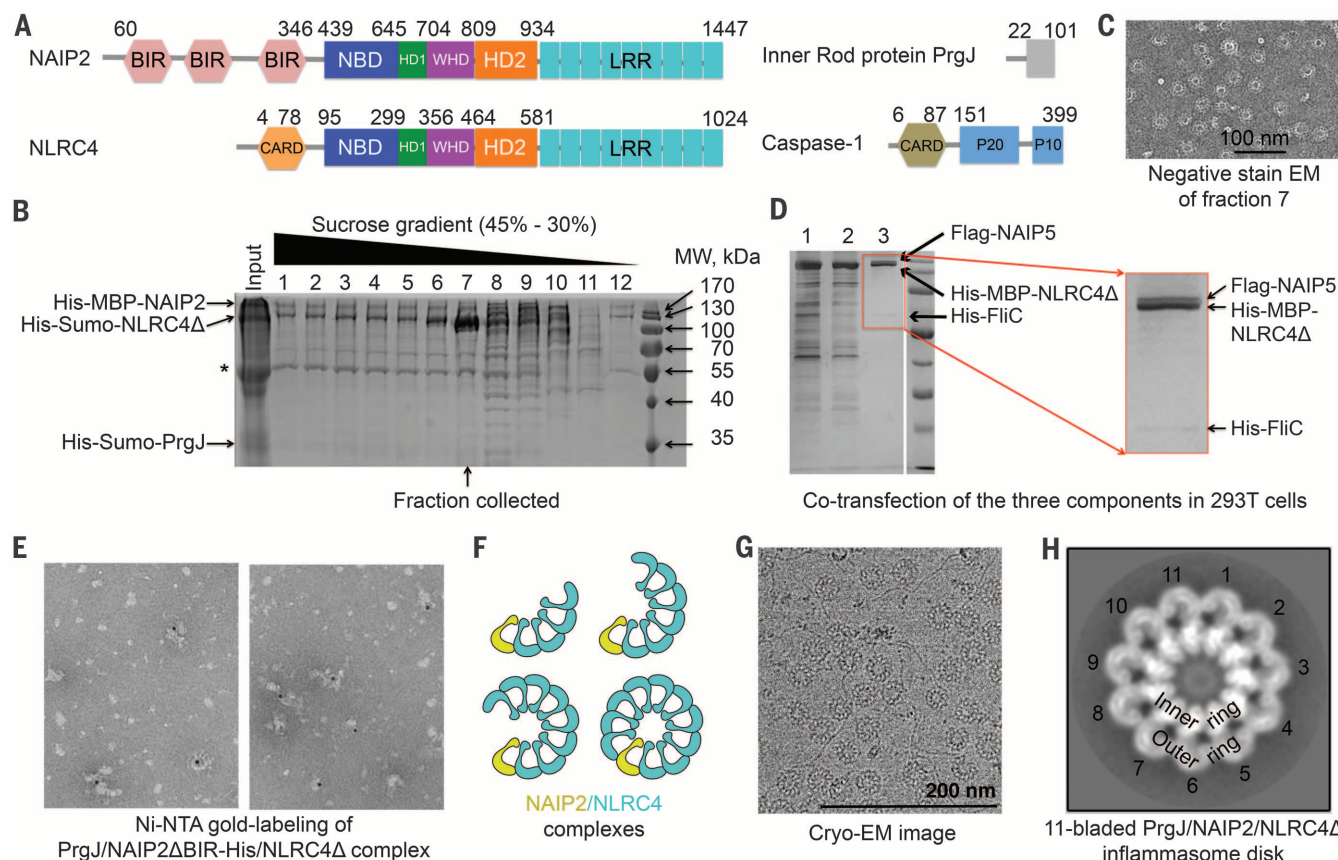


Fig. 1. Preparation and characterization of NAIP-NLRC4 Δ complexes. (A) Domain organizations of *Salmonella typhimurium* PrgJ, mouse NAIP2, mouse NLRC4, and mouse caspase-1. Domain size is drawn approximately to scale; residue numbers are labeled. (B) SDS-polyacrylamide gel electrophoresis (PAGE) of different fractions of the sucrose gradient ultracentrifugation during the purification of the PrgJ-NAIP2-NLRC4 Δ complex. Locations of the three component proteins are labeled. The asterisk indicates a contaminating band. (C) A representative negative-stain EM image from fraction 7 in (B). (D) SDS-PAGE of amylose resin elution (lane 1), anti-Flag flow-through (lane 2), and anti-Flag

elution (lane 3) fractions during the purification of the coexpressed His-FliC-Flag-NAIP5-His-MBP-NLRC4 Δ complex. An enlarged image of lane 3 is shown. (E) Ni-NTA gold labeling (5 nm) of purified His-Sumo-PrgJ-NAIP2 Δ BIR-His-Sumo-NLRC4 Δ complex upon removal of the His-Sumo tag. (F) Schematic diagram of partial and complete inflammasome particles that contain variable ratios between NAIP2 (yellow) and NLRC4 (cyan). (G) Representative cryo-EM micrograph of PrgJ-NAIP2-NLRC4 Δ particles. (H) An averaged 2D class of the 11-bladed PrgJ/NAIP2-NLRC4 Δ inflammasome complex. The dimensions of the image are 43.5 nm \times 43.5 nm.

inner hole (Fig. 2, B, E, and F). The inner ring of the disk contains the NBD, helical domain 1 (HD1), and the winged helix domain (WHD); the outer ring comprises helical domain 2 (HD2) and the LRR domain (Fig. 1A and Fig. 2B).

We focus our further discussions on the 11-bladed structure with the highest resolution. The conformation of active NLRC4 Δ in the 11-bladed inflammasome exhibits differences from that of inactive NLRC4 Δ (16). When the NBD-

HD1 regions of NLRC4 in the two states are aligned, the WHD-HD2-LRR module needs to rotate 87.5° along an axis at the junction between HD1 and WHD to turn from the inactive state to the active state (Fig. 2, G and H). The pivot point of the long-range hinge motion is where the inactive and active conformations of the α 14 helix of WHD intercept (Fig. 2H). The rotation rearranges the intramolecular interactions between WHD and the NBD-HD1 module.

Several missense mutations in human NLRC4 that are associated with auto-inflammatory conditions (12–14)—Thr³³⁷ → Ser, Val³⁴¹ → Ala, and His⁴⁴³ → Pro—localize to this highly dynamic region (fig. S6A).

We do not know whether NLRC4 conformational transition is accompanied by exchange of adenosine diphosphate (ADP) in the inactive state to adenosine triphosphate (ATP) in the active state, as observed for apoptosome assembly by

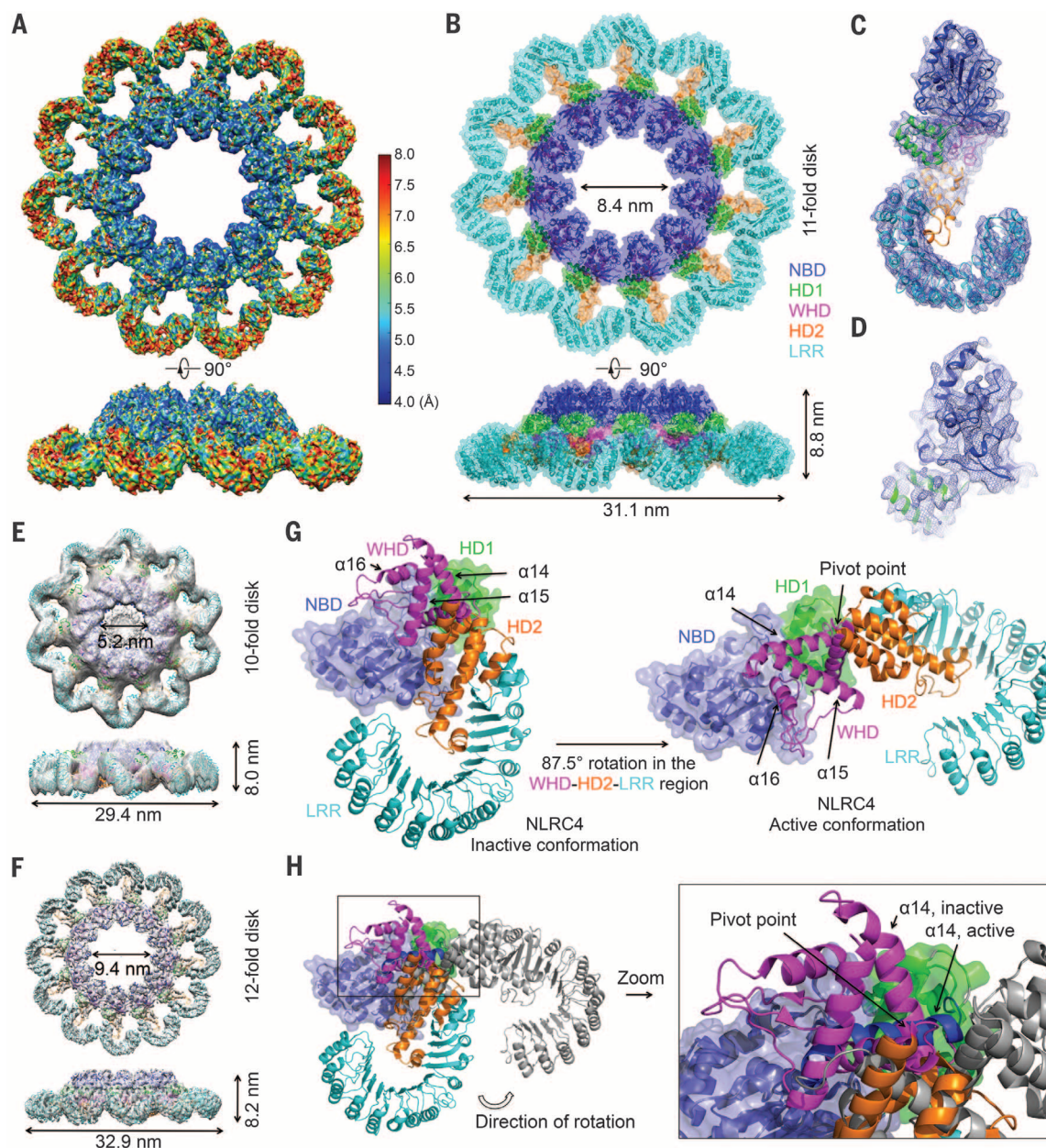


Fig. 2. Cryo-EM structure determination and conformational activation of NLRC4. (A) Cryo-EM map of the C₁₁ PrgJ-NAIP2-NLRC4 Δ complex colored with local resolution calculated by ResMap using two separately refined half maps. (B) Superimposed ribbon diagram and transparent surface of the C₁₁ NLRC4 Δ structure. (C) Cryo-EM density superimposed with one NLRC4 Δ subunit. (D) A close-up view of the structure of the NBD of NLRC4 Δ superimposed with the cryo-EM density. (E and F) Cryo-EM maps and fitted NLRC4 Δ models for the C₁₀ reconstruction at 12.5 Å resolution (E) and the C₁₂

reconstruction at 7.5 Å resolution (F). (G) The WHD-HD2-LRR domain of NLRC4 swings 87.5° to transit from the inactive conformation (left, PDB ID 4KXF) to the active conformation (right). NBD and HD1 are shown in superimposed ribbon diagram and transparent surface, and the WHD-HD2-LRR module is shown in ribbon diagram. (H) Superimposed inactive (colored) and active (gray, except for α 14 helix, which is in dark blue) conformations of NLRC4 Δ . The α 14 helices in the two conformations are labeled to show the relative rotations and the rotational pivot point.

Calculation of surface electrostatics revealed charge complementarity between the mostly basic NLRC4-A surface and the opposing, largely acidic NLRC4-B surface (Fig. 4, A and B); this finding supports unidirectional polymerization nucleated by NLRC4-A. Structural analysis identified interfacial residues including His¹⁴⁴, Arg¹⁴⁵, His²⁶⁹, Arg²⁸⁵, His²⁸⁶, Arg²⁸⁸, His²⁸⁹, Glu⁴³³, and Arg⁴³⁴ of NLRC4-A, and Asn¹¹⁶, Glu¹²², Asp¹²³, Asp¹²⁵, Ile¹²⁷, Leu²²⁰, Leu³¹³, and Asp³⁶⁸ of the

opposing NLRC4-B (Fig. 4C). We mutated NLRC4-A residues Arg²⁸⁸ and His²⁸⁹ to Asp (mutation RH2D) and Arg²⁸⁵ to Asp (mutation R285D) and tested their interactions using the same 293T cell coexpression system of His-Flc, Flag-NAIP5, and His-MBP-NLRC4Δ. Both RH2D and R285D mutations reduced the amount of NLRC4Δ in the inflammasome complex (Fig. 4D). Therefore, like a ligand-activated NAIP2, a newly activated NLRC4 triggers activation of another NLRC4 molecule by

inducing conformational changes (fig. S7F). The NBD-NBD interactions between adjacent NLRC4 subunits differ from those in the heptameric apoptosome, with distinct angular relationships that may have explained the existence of more subunits in each NLRC4 disk (21, 22) (fig. S8, A to C).

ASC, like NLRC4, is an inflammasome adapter protein. We showed previously that ASC-dependent inflammasomes activate caspase-1 by ASC^{CARD}-mediated caspase-1^{CARD} polymerization

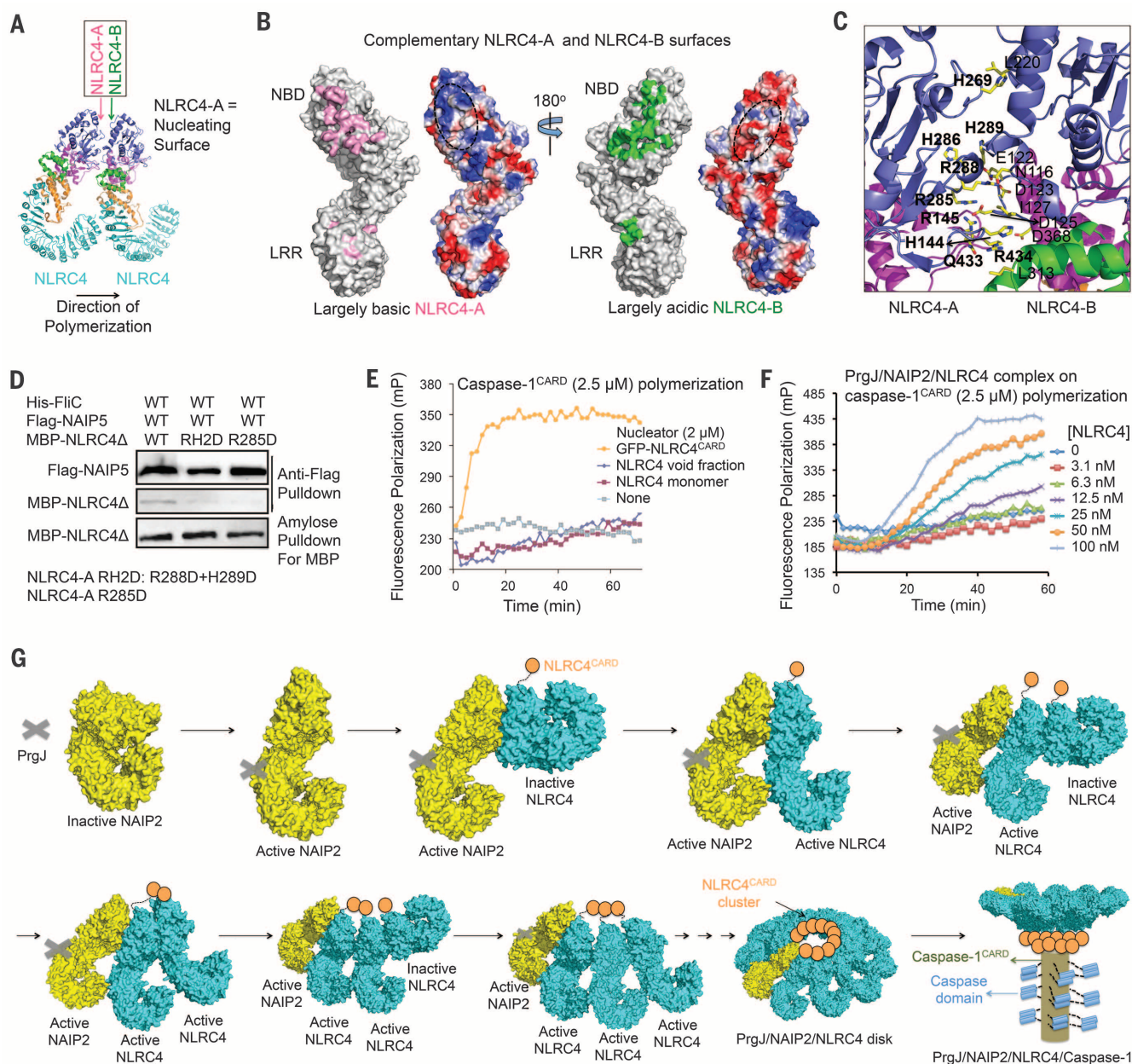


Fig. 4. NLRC4 polymerization and caspase-1 activation. (A) Locations of NLRC4-A and NLRC4-B surfaces. (B) Mapped interactions at NLRC4-A (pink) and NLRC4-B (green) surfaces and the surface electrostatic potentials. (C) Detailed interactions between two neighboring NLRC4 molecules. Those on the A surface are labeled in boldface. (D) Mutations at the NLRC4-A surface impaired NLRC4 recruitment. Three proteins were coexpressed in 293T cells. The Flag tag was used to pull down the complex; component proteins were

detected using Western blots. **(E)** NLRC4^{CARD}, instead of NLRC4^{FL}, nucleates filament formation of labeled caspase-1^{CARD}, as shown by increase in fluorescence polarization. **(F)** The PrgJ-NAIP2-NLRC4^{FL} inflammasome nucleates filament formation of labeled caspase-1^{CARD} at substoichiometric ratios, as shown by increase in fluorescence polarization. **(G)** Schematic diagram for mechanism of PrgJ-NAIP2-nucleated polymerization of NLRC4, followed by caspase-1 dimerization and activation.

(24). To examine whether the PrgJ-NAIP2-NLRC4 inflammasome may directly activate caspase-1 through the CARD in NLRC4, we adopted the same fluorescence polarization assay of caspase-1^{CARD} (24). We reconstituted the full-length PrgJ-NAIP2-NLRC4 inflammasome, which showed stacked disk-like structures similar to the previously reconstituted FliC-NAIP5-NLRC4 complex (15) (fig. S8D), and expressed NLRC4^{CARD} fused to green fluorescent protein (GFP-NLRC4^{CARD}), which was filamentous under EM (fig. S8E). GFP-NLRC4^{CARD} augmented the rate of caspase-1^{CARD} polymerization, whereas full-length NLRC4 from either the monomeric or the void fraction had little effect (Fig. 4E). The PrgJ-NAIP2-NLRC4 inflammasome robustly promoted filament formation of caspase-1^{CARD} even at a 1:100 substoichiometric ratio (Fig. 4F).

Given that NLRC4^{CARD} alone is filamentous, we expect that the ~10 molecules of NLRC4^{CARD} in each NAIP2-NLRC4 inflammasome form a short filament at the center of the disk. The observed stacking in full-length NAIP-NLRC4 inflammasomes (15) is likely due to interactions between unengaged NLRC4 CARDS. In the presence of caspase-1, the inflammasome may change into single disks, just like the transition of the *Drosophila* apoptosome from double rings to single rings in the presence of the caspase (21). Curiously, the central hole of the inflammasome has a diameter just a bit smaller than that of CARD filaments at ~9 nm, which may provide a perfectly sized “basin” to cradle the protruded CARD filament. These studies demonstrate that ASC-independent NAIP-NLRC4 inflammasomes make use of a similar mechanism for caspase-1 activation, as shown for ASC-dependent inflammasomes (24).

Our studies suggest that activation of NAIP-NLRC4 inflammasomes may proceed through the following steps (Fig. 4G), a conclusion also reached independently by the accompanying study (25): (i) Because of the domain similarity of NAIPs to NLRC4, we propose that the NAIP resting state is similar to the NLRC4 inactive conformation. After a cell is infected and bacterial products appear in the cytosol, a NAIP recognizes its specific bacterial ligand, likely through a surface on the HD1, WHD, and HD2 region (26). The specific ligand drives the NAIP into the open, activated conformation. (ii) The ligand-bound NAIP uses its nucleating surface to interact with the adapter NLRC4 that is yet to be activated. The interaction forces the WHD and its linked C-terminal region to change into the activated conformation, overcoming NLRC4 auto-inhibition. The activated NLRC4 uses its newly exposed nucleating surface to repeat recruitment and activation of additional NLRC4 molecules, until a complete disk is formed or until the NLRC4 concentration falls below the dissociation constant of the interaction. (iii) NLRC4 clustering induces oligomerization of the CARD of NLRC4, enabling the recruitment of caspase-1 through CARD-CARD interactions and triggering caspase-1 dimerization, autoproteolysis, and activation. The activation mechanism ensures signal amplification from the receptor to the adapter, and then to the effector.

As the most abundant energy source in living organisms, ATP is used widely in enzymes to mediate force generation, conformation change, oligomerization, and transport. The ATPase-mediated nucleated polymerization through a domino-like chain reaction identified here adds an important, elegant mechanism to this universal and already complex enzyme family. Nucleated polymerization in NAIP-NLRC4 inflammasomes also presents yet another mode of higher-order oligomerization, which may play a role in facilitating proximity-induced enzyme activation, threshold response, and prion-like propagation in immune signaling (27–30).

REFERENCES AND NOTES

1. J. D. Grouney, W. F. Dietrich, *Genome Res.* **10**, 1158–1171 (2000).
2. E. M. Kofoed, R. E. Vance, *Nature* **477**, 592–595 (2011).
3. E. Diez et al., *Nat. Genet.* **33**, 55–60 (2003).
4. Y. Zhao et al., *Nature* **477**, 596–600 (2011).
5. J. Yang, Y. Zhao, J. Shi, F. Shao, *Proc. Natl. Acad. Sci. U.S.A.* **110**, 14408–14413 (2013).
6. E. A. Miao et al., *Nat. Immunol.* **7**, 569–575 (2006).
7. E. A. Miao et al., *Nat. Immunol.* **11**, 1136–1142 (2010).
8. L. Franchi et al., *Nat. Immunol.* **13**, 449–456 (2012).
9. B. Hu et al., *Proc. Natl. Acad. Sci. U.S.A.* **107**, 21635–21640 (2010).
10. A. M. Janowski, R. Kolb, W. Zhang, F. S. Sutterwala, *Front. Immunol.* **4**, 370 (2013).
11. J. Garaude, A. Kent, N. van Rooijen, J. M. Blander, *Sci. Transl. Med.* **4**, 120ra16 (2012).
12. S. W. Canna et al., *Nat. Genet.* **46**, 1140–1146 (2014).
13. A. Kitamura, Y. Sasaki, T. Abe, H. Kano, K. Yasutomo, *J. Exp. Med.* **211**, 2385–2396 (2014).
14. N. Romberg et al., *Nat. Genet.* **46**, 1135–1139 (2014).
15. E. F. Halff et al., *J. Biol. Chem.* **287**, 38460–38472 (2012).
16. Z. Hu et al., *Science* **341**, 172–175 (2013).
17. T. F. Reubold, S. Wohlgemuth, S. Eschenburg, *J. Biol. Chem.* **284**, 32717–32724 (2009).
18. Q. Bao, W. Lu, J. D. Rabinowitz, Y. Shi, *Mol. Cell* **25**, 181–192 (2007).
19. M. Proell, S. J. Riedl, J. H. Fritz, A. M. Rojas, R. Schwarzenbacher, *PLOS ONE* **3**, e2119 (2008).

20. M. A. Martí-Renom et al., *Annu. Rev. Biophys. Biomol. Struct.* **29**, 291–325 (2000).
21. S. Yuan, C. W. Akey, *Structure* **21**, 501–515 (2013).
22. S. Yuan et al., *Structure* **19**, 128–140 (2011).
23. S. Qi et al., *Cell* **141**, 446–457 (2010).
24. A. Lu et al., *Cell* **156**, 1193–1206 (2014).
25. Z. Hu et al., *Science* **350**, 399–404 (2015).
26. J. L. Tenthorey, E. M. Kofoed, M. D. Daugherty, H. S. Malik, R. E. Vance, *Mol. Cell* **54**, 17–29 (2014).
27. H. Wu, *Cell* **153**, 287–292 (2013).
28. B. S. Franklin et al., *Nat. Immunol.* **15**, 727–737 (2014).
29. X. Cai et al., *Cell* **156**, 1207–1222 (2014).
30. A. Baroja-Mazo et al., *Nat. Immunol.* **15**, 738–748 (2014).

ACKNOWLEDGMENTS

We thank G. Bozkurt for technical assistance; H. Ploegh for providing engineered, Ca²⁺-independent sortase and the peptide-fluorophore conjugate Gly-Gly-Gly-TAMRA (GGG-TAMRA); and M. Ericsson for use of the Harvard Medical School EM facility. The data presented in this manuscript are tabulated in the main paper and in the supplementary materials. Cryo-EM maps and atomic coordinates have been deposited in the Electron Microscopy Data Bank (EMDB IDs EMD-6458, EMD-6459, and EMD-6460 for C₁₁, C₁₂, and C₁₀ reconstructions, respectively) and Protein Data Bank (PDB ID 3JBL for the C₁₁ reconstruction). Supported by NIH K99 grant AI08793 (Q.Y.), a Cancer Research Institute postdoctoral fellowship (L.D.), an Intel academic grant, research funds at Peking University, and NIH grant IDP1HD087988. The cryo-EM facility was funded through the NIH grant AI100645 Center for HIV/AIDS Vaccine Immunology and Immunogen Design (CHAVI-ID). The experiments were performed in part at the Center for Nanoscale Systems at Harvard University, a member of the National Nanotechnology Infrastructure Network (NNIN), which is supported by NSF award ECS-0335765.

SUPPLEMENTARY MATERIALS

www.sciencemag.org/content/350/6259/404/suppl/DC1
Materials and Methods
Figs. S1 to S8
Table S1
References (31–48)

14 May 2015; accepted 14 September 2015
Published online 8 October 2015
10.1126/science.aac5789

SUPERCONDUCTIVITY

Metallic ground state in an ion-gated two-dimensional superconductor

Yu Saito,¹ Yuichi Kasahara,^{1,2*} Jianting Ye,^{1,3,4†}
Yoshihiro Iwasa,^{1,4‡} Tsutomu Nojima^{5‡}

Recently emerging two-dimensional (2D) superconductors in atomically thin layers and at heterogeneous interfaces are attracting growing interest in condensed matter physics. Here, we report that an ion-gated zirconium nitride chloride surface, exhibiting a dome-shaped phase diagram with a maximum critical temperature of 14.8 kelvin, behaves as a superconductor persisting to the 2D limit. The superconducting thickness estimated from the upper critical fields is ≈ 1.8 nanometers, which is thinner than one unit-cell. The majority of the vortex phase diagram down to 2 kelvin is occupied by a metallic state with a finite resistance, owing to the quantum creep of vortices caused by extremely weak pinning and disorder. Our findings highlight the potential of electric-field-induced superconductivity, establishing a new platform for accessing quantum phases in clean 2D superconductors.

Recent technological advances of materials fabrication have led to discoveries of a variety of superconductors at heterogeneous interfaces and in ultrathin films; examples include superconductivity at oxide interfaces (1, 2), electric-double-layer interfaces (3), and mechan-

ically cleaved (4), molecular-beam-epitaxy-grown (5, 6), or chemical-vapor-deposited (7) atomically thin layers. These systems are providing opportunities for searching for superconductivity at higher temperatures, as well as investigating the intrinsic nature of two-dimensional (2D)

superconductors, which are distinct from bulk superconductors because of enhanced thermal and quantum fluctuations.

One of the issues to be addressed is how zero electrical resistance is achieved or destroyed. In 2D superconductors exposed to magnetic fields, vortex pinning, which is necessary to achieve zero electrical resistance under magnetic fields, may be too weak. To address this question, superconductivity in vacuum-deposited metallic thin films has been studied (8). The conventional way to approach the 2D limit is to reduce the film thickness, but this concomitantly increases disorder. In such thin films, a direct superconductor-to-insulator transition (SIT) is observed in most cases when the system is disordered (8). This SIT has been understood in the framework of the so-called “dirty boson model” (9); however, this simple picture needed to be modified because an intervening metallic phase between the superconducting (SC) and insulating phases under magnetic fields was observed in less-disordered systems (8, 10). Therefore, investigating 2D superconductivity in even cleaner systems is desirable.

In contrast to the conventional metallic films, the recently discovered 2D superconductors are highly crystalline, displaying lower normal state sheet resistance. The electric-double-layer transistor (EDLT), which is composed of the interface between crystalline solids and electrolytes, can be a good candidate to realize such a clean system, because the conduction carriers are induced electrostatically at the atomically flat surfaces without introducing extrinsic disorder. In addition, the EDLT has the greatest advantage of their applicability to a wide range of materials, as exemplified by gate-induced superconductivity in 3D SrTiO₃ (3, 11, 12), KTaO₃ (13), quasi-2D layered ZrNCl (14), transition metal dichalcogenides (15–17), and cuprates (18–22). Here, we report comprehensive transport studies on a ZrNCl-EDLT, which provide evidence of 2D superconductivity in this system based on several types of analyses. In particular, we found that the zero-resistance state is immediately destroyed by the application of finite out-of-plane magnetic fields, and, consequently, a metallic state is stabilized in a wide range of magnetic fields. This is a manifestation of the quantum tunneling of vortices due to the extremely weak pinning in the ultimate 2D system.

ZrNCl is originally an archetypal band insulator with a layered crystal structure (23, 24), in which a unit cell comprises three (ZrNCl)₂ layers (Fig. 1A). Bulk ZrNCl becomes a superconductor with a critical temperature, T_c , as high as 15.2 K by alkali-metal intercalation (25–28). Figure 1B shows the

relation between the sheet conductance, σ_{sheet} , and the gate voltage, V_G , for a ZrNCl-EDLT with a 20-nm-thick flake without any monolayer steps (29), measured at a source-drain voltage of $V_{\text{DS}} = 0.1$ V and at a temperature of $T = 220$ K. σ_{sheet} abruptly increased at $V_G > 2$ V, demonstrating a typical n -type field-effect transistor behavior. As shown in the temperature dependence of the sheet resistance, R_{sheet} , at different V_G values (Fig. 1C), the insulating phase is dramatically suppressed with increasing V_G , and finally a resistance drop due to a SC transition appears at $V_G = 4$ V. Zero resistance (below $\sim 0.05 \Omega$) was achieved at $V_G = 6$ and 6.5 V. Despite such relatively large gate voltages, any signature of electrochemical process was not observed (figs. S1 and S2) (29). The tail of the resistance drop at 6.5 V can be explained in terms of the Berezinskii-Kosterlitz-Thouless (BKT) transition (Fig. 1D), which realizes a zero-ohmic-resistance state driven by the binding of vortex-antivortex pairs. To determine the BKT transition temperature, we used the Halperin-Nelson equation (30, 31), which shows a square-root-cusp behavior that originates from the energy dissipation due to the Bardeen-Stephen vortex flow above the BKT transition temperature. On the other hand, a gradual decrease of R_{sheet} at temperatures far above T_c , leading to a broadened SC onset (Fig. 1D, inset), was observed. This feature can be well reproduced by an analysis that takes both the Aslamazov-Larkin and Maki-Thompson terms (32–34) for the 2D fluctuation conductivities into account (fig. S4) (29). These results suggest that 2D superconductivity is achieved at zero magnetic field.

Figure 2, A and B, display temperature-dependent $R_{\text{sheet}}(T)$ values at $V_G = 6.5$ V for magnetic fields applied perpendicular and parallel to the surface

of ZrNCl, respectively. For the out-of-plane magnetic fields, T_c is dramatically suppressed with a considerable broadening of the SC transition even at a small magnetic field of $\mu_0 H = 0.05$ T, which is in marked contrast to those observed in the in-plane magnetic field geometry (see also fig. S5). Such a large anisotropy suggests that the superconductivity is strongly 2D in nature and indicates a large contribution of the vortex motion in the out-of-plane magnetic field geometry. Figure 2C shows the angular dependence of the upper critical field, $\mu_0 H_{c2}(\theta)$ (θ represents the angle between the c axis of ZrNCl and applied magnetic field directions), at 13.8 K, which is just below $T_c (= 14.5$ K at zero magnetic field). $T_c(H_{c2})$ was defined as the temperature (magnetic field) where R_{sheet} becomes 50% of the normal state resistance, R_N , at 30 K (29). A cusp-like peak is clearly resolved at $\theta = 90^\circ$ (Fig. 2C, inset) and is qualitatively distinct from the 3D anisotropic mass model but is well described by the 2D Tinkham model (35). Similar observations have been reported in a SrTiO₃-EDLT (36), implying that the EDLT is a versatile tool for creating 2D superconductors. Figure 2D shows the temperature dependence of $\mu_0 H_{c2}$ at $\theta = 90^\circ$ ($\mu_0 H_{c2}^\perp$) and at $\theta = 0^\circ$ ($\mu_0 H_{c2}^\parallel$), which exhibits a good agreement with the phenomenological Ginzburg-Landau (GL) expressions for 2D SC films.

$$\mu_0 H_{c2}^\perp = \frac{\Phi_0}{2\pi\zeta_{\text{GL}}(0)} \left(1 - \frac{T}{T_c}\right) \quad (1)$$

$$\mu_0 H_{c2}^\parallel = \frac{\Phi_0\sqrt{12}}{2\pi\zeta_{\text{GL}}(0)d_{\text{SC}}} \sqrt{1 - \frac{T}{T_c}} \quad (2)$$

where Φ_0 is the flux quantum, $\zeta_{\text{GL}}(0)$ is the extrapolation of the GL coherence length,

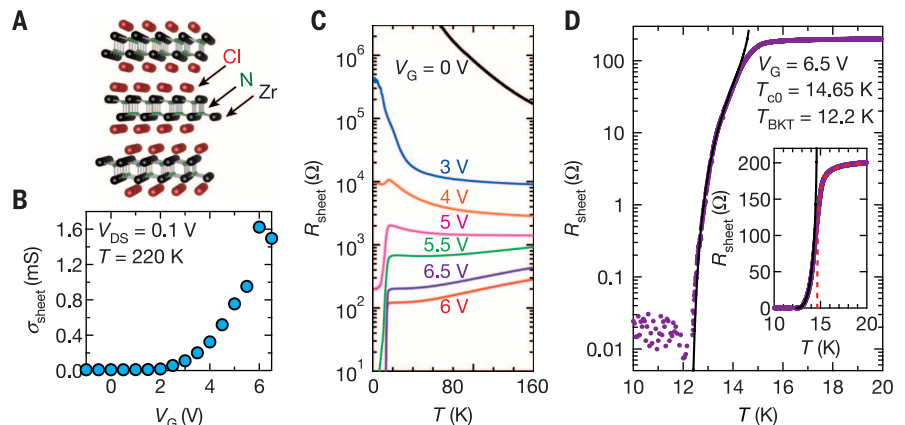


Fig. 1. Crystal structure of ZrNCl and transport properties of a ZrNCl-EDLT. (A) Ball-and-stick model of a ZrNCl single crystal. The monolayer is 0.92 nm thick. (B) Sheet conductance, σ_{sheet} , of a ZrNCl-EDLT as a function of gate voltage, V_G , at 220 K. (C) Temperature, T , dependence of the sheet resistance, R_{sheet} , at different gate voltages, V_G , from 0 to 6.5 V. The device was cooled down to low temperatures after applying V_G gate voltages at 220 K. (D) Resistive transition at zero magnetic field and $V_G = 6.5$ V, plotted on a semilog scale (linear scale in the inset). The black solid line represents the BKT transition using the Halperin-Nelson equation (30), $R = R_0 \exp\left\{-2b\left(\frac{T_0 - T}{T - T_{\text{BKT}}}\right)^{1/2}\right\}$, where R_0

and b are material parameters. This gives a BKT transition temperature of $T_{\text{BKT}} = 12.2$ K with $b = 1.9$. The red dashed line in the inset represents the superconducting amplitude fluctuation taking into account both the 2D Aslamazov-Larkin (32) and Maki-Thompson terms (33, 34), which give the temperature, T_{co} , at which the finite amplitude of the order parameter develops (fig. S4) (29).

¹Quantum-Phase Electronics Center (QPEC) and Department of Applied Physics, The University of Tokyo, Tokyo 113-8656, Japan. ²Department of Physics, Kyoto University, Kyoto 606-8502, Japan. ³Zernike Institute for Advanced Materials, University of Groningen, Nijenborgh 4, 9747 AG Groningen, The Netherlands. ⁴RIKEN Center for Emergent Matter Science (CEMS), Wako 351-0198, Japan. ⁵Institute for Materials Research, Tohoku University, Sendai 980-8577, Japan.

*Present address: Department of Physics, Kyoto University, Kyoto 606-8502, Japan. †These authors contributed equally to this work.

‡Corresponding author. E-mail: iwasa@ap.t.u-tokyo.ac.jp (Y.I.); nojima@imr.tohoku.ac.jp (T.N.)

ξ_{GL} , at $T = 0$ K, and d_{sc} is the temperature-independent SC thickness. As a result of the fit, we obtained $\xi_{\text{GL}}(0) \cong 12.8$ nm and $d_{\text{sc}} \cong 1.8$ nm. The latter parameter approximately corresponds to the bilayer thickness of the $(\text{ZrNCl})_2$ layer, which is less than one unit-cell thick. The estimated thickness is indeed in the atomic scale and demonstrates that the superconductivity persists to the extreme 2D limit. The d_{sc} for this system is much smaller than the reported value of ~ 11 nm for the interface superconductivity on SrTiO_3 (1, 36), which is presumably owing to the huge dielectric constant in the incipient ferroelectric SrTiO_3 . Recently, it was suggested based on theoretical calculations that the depth of the induced charge carriers in ion-gated superconducting ZrNCl is only one layer (37). The difference from the present observation might be ascribed to the proximity effect of the superconductivity, which is a phenomenon whereby the Cooper pairs in a SC layer (the topmost layer, in the present case) diffuse into the neighboring non-SC layers (the second layer), resulting in broadening of the effective thickness. This could occur even if there are only a small number of electrons in the second layer. Another possibility for this discrepancy might come from the

situation that the measured H_{c2} is suppressed because of the paramagnetic effect as compared with the orbital limit, leading to an estimated d_{sc} thicker than the real value.

In the present system, we found that the Pippard coherence length, ξ_{Pippard} , is equal to 43.4 nm, as calculated from $\xi_{\text{Pippard}} = \hbar v_F / \pi \Delta(0)$ by using $v_F = \hbar k_F / m^*$, $k_F = (4\pi n_{2D} / ss')^{1/2}$, and the Bardeen-Cooper-Schrieffer (BCS) energy gap of $\Delta(0) = 1.76 k_B T_c = 2.2$ meV, where v_F , k_F , m^* , \hbar , s , and s' are the Fermi velocity, the Fermi wave number, the effective mass, Planck's constant divided by 2π , the spin degree of freedom, and the valley degree of freedom, respectively, for $V_G = 6.5$ V (the sheet carrier density of $n_{2D} = 4.0 \times 10^{14} \text{ cm}^{-2}$) with $T_c = 14.5$ K and the effective mass of $m^* = 0.9 m_0$ (38). Here, s and s' are both 2. The Pippard coherence length is larger than $k_F^{-1} = 0.28$ nm and much larger than $d_{\text{sc}} \cong 1.8$ nm. We also note that the H_{c2} may exceed the Pauli limit for weak-coupling BCS superconductors, $\mu_0 H_P^{\text{BCS}} = 1.86 T_c = 27.0$ T. However, to confirm this phenomenon, it is necessary to investigate H_{c2} at lower temperatures and higher magnetic fields.

Having estimated d_{sc} , we can now compare the phase diagrams of electric-field-induced 2D

and bulk superconductors (28) (Fig. 3). A direct comparison is made by using n_{2D} estimated from Hall-effect measurements in ZrNCl -EDLTs (fig. S6) (29) and n_{2D} in the $(\text{ZrNCl})_2$ bilayer for the bulk. In contrast to the bulk, where T_c abruptly appears at $n_{2D} = 1.5 \times 10^{14} \text{ cm}^{-2}$, followed by a decrease with increasing n_{2D} , ZrNCl -EDLTs exhibit a gradual increase of T_c , forming a dome-like SC phase with a maximum T_c of 14.8 K at $n_{2D} = 5.0 \times 10^{14} \text{ cm}^{-2}$. The different phase diagrams between electric-field-induced and intercalated superconductivity in Fig. 3 suggest the importance of two dimensionality and broken inversion symmetry in the presence of an electric field, which may lead to exotic superconducting phenomena such as the spin-parity mixture state and the helical state. On the other hand, the coincidence of the critical n_{2D} in the 2D and bulk system implies that the mysterious phase diagram in the bulk Li_xZrNCl —that is, an abrupt drop of T_c near $n_{2D} \sim 1 \times 10^{14} \text{ cm}^{-2}$ —might be related to the quantum SIT phenomena realized in the 2D limit (8). Similar dome-like SC phases have already been reported in EDLTs based on the band insulators KTaO_3 (13) and MoS_2 (15), suggesting a commonality among electric-field-induced superconductors.

In an Arrhenius plot of $R_{\text{sheet}}(T)$ for out-of-plane magnetic fields at $V_G = 6.5$ V (Fig. 4A), $R_{\text{sheet}}(T)$ exhibits an activated behavior just below T_c described by $R = R' \exp(-U(H)/k_B T_c)$, where k_B is Boltzmann's constant, as shown by the dashed lines. The magnetic field dependence of the extracted activation energy $U(H)$ (Fig. 4B), and the relation between $U(H)/k_B T_c$ and $\ln R'$ (Fig. 4B, inset) are consistent with the thermally assisted collective vortex-creep model in two dimensions (39), $U(H) \propto \ln(H_0/H)$ and $\ln R' = U(H)/k_B T_c + \text{const}$. The activation energy becomes almost zero at $\mu_0 H \cong 1.3$ T, allowing the vortex

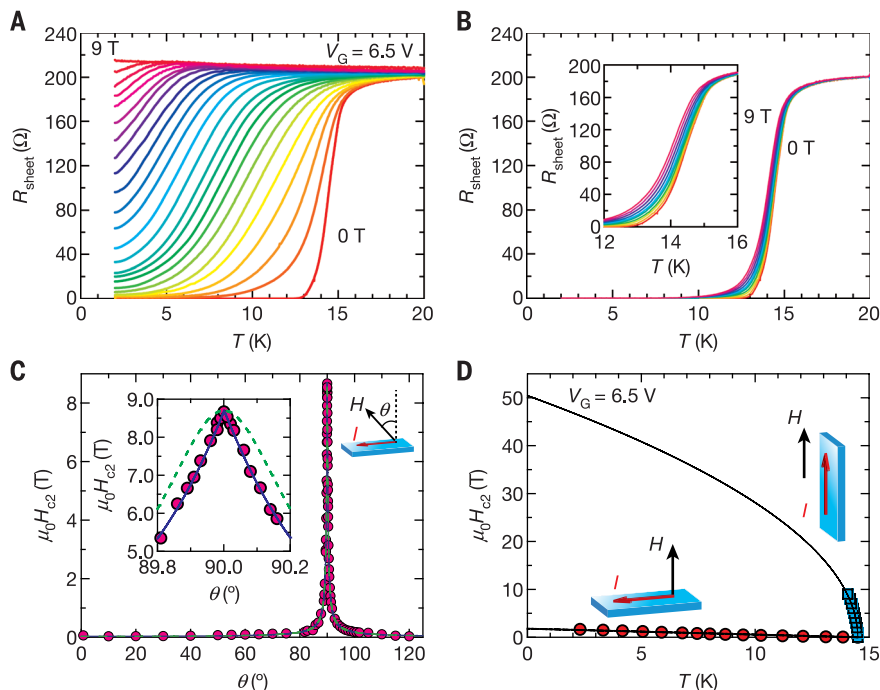


Fig. 2. Two-dimensional superconductivity in ion-gated ZrNCl . (A and B) Sheet resistance of a ZrNCl -EDLT as a function of temperature at $V_G = 6.5$ V, for (A) perpendicular magnetic fields, $\mu_0 H_{c2}^\perp$, varying in 0.05 T steps from 0 to 0.1 T, in 0.1 T steps from 0.1 to 0.9 T, and in 0.15 T steps from 0.9 to 2.7 T, and of 3 T and 9 T, and (B) parallel magnetic fields, $\mu_0 H_{c2}^\parallel$, varying in 1 T steps from 0 to 9 T, respectively. The inset of Fig. 2B is a magnified view of the region between 12 and 16 K. (C) Angular dependence of the upper critical fields $\mu_0 H_{c2}(\theta)$ (θ represents the angle between a magnetic field and the perpendicular direction to the surface of ZrNCl). The inset shows a close-up of the region around $\theta = 90^\circ$. The blue solid line and the green dashed line are the theoretical representations of $H_{c2}(\theta)$, using the 2D Tinkham formula $(H_{c2}(\theta) \sin \theta / H_{c2}^\perp)^2 + |H_{c2}(\theta) \cos \theta / H_{c2}^\parallel| = 1$ and the 3D anisotropic mass model $H_{c2}(\theta) = H_{c2}^\perp / (\sin^2 \theta + \gamma^2 \cos^2 \theta)^{1/2}$ with $\gamma = H_{c2}^\perp / H_{c2}^\parallel$, respectively. (D) Temperature dependence of $\mu_0 H_{c2}$ perpendicular and parallel to the surface, $\mu_0 H_{c2}^\perp(T)$ and $\mu_0 H_{c2}^\parallel(T)$. Solid black curves are theoretical curves obtained from the 2D Ginzburg-Landau equations.

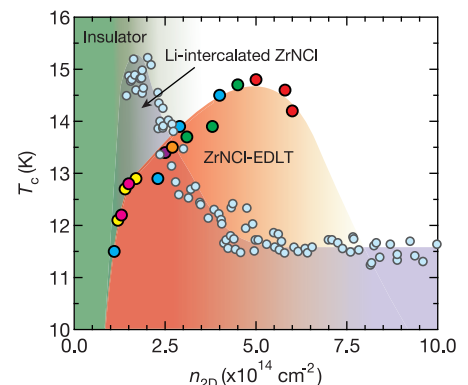


Fig. 3. Electronic phase diagram of electric-field-induced and bulk superconductivity in ZrNCl . The SC transition temperatures, T_c (defined as the temperature at which R_{sheet} reaches half the value of R_N at 30 K), for ZrNCl -EDLTs were measured in seven different devices, indicated by the colored circles. The data for Li-intercalated ZrNCl was taken from (28), and the thickness of a bilayer was used to calculate n_{2D} from the 3D carrier density. The sheet carrier density for ZrNCl -EDLTs was determined by Hall-effect measurements at 60 K (fig. S6) (29).

flow motion above this field, as explained below.

At low temperatures, on the other hand, each $R_{\text{sheet}}-T$ curve clearly deviates from the activated behavior and then is flattened at a finite value down to the lowest temperature (≈ 2 K) even at $\mu_0 H$ (≈ 0.05 T) $\sim \mu_0 H_{c2}/40$. This implies that a metallic ground state exists for at least $\mu_0 H > 0.05$ T and may be a consequence of the vortex motion driven by quantum mechanical processes. Our results are markedly distinct from conventional theories that predict a vortex-glass state and a direct SIT at $T = 0$ with R_N close to the quantum resistance $R_Q = h/4e^2 = 6.45$ k Ω , where h and e are Planck's constant and the elementary charge, respectively. The metallic ground state has been reported in MoGe (10) and Ta (40) thinfilms, where R_N values (≥ 1 k Ω)

are smaller than R_Q . In the ZrNCl-EDLT, R_N values at $V_G = 6$ and 6.5 V are ~ 120 and ~ 200 Ω , respectively, which are even lower, reaching values as small as $\sim 1/50$ of R_Q . This leads to $k_F l = \frac{1}{88} \frac{2\hbar}{e^2} \frac{1}{R_N} \sim 77 - 130$ (for $R_N \sim 120 - 200$ Ω), with the mean free path l , which is much larger than the Ioffe-Regel limit ($k_F l \sim 1$), indicating that the normal states are relatively clean. We also note that the estimated values of $l \sim 35$ nm (6 V) and 18 nm (6.5 V) result in the relation $\xi_{\text{Pippard}} \approx 1.1 - 2.4$ l , which is far from the dirty limit ($\xi_{\text{Pippard}} \gg l$). Indeed, the expression for $\xi_{\text{GL}}(0)$ in the dirty limit $0.855(\xi_{\text{Pippard}} l)^{1/2}$ is not applicable to our result. Furthermore, our $R_{\text{sheet}}-T$ data under magnetic fields do not follow the scaling relations for a magnetic-field-induced SIT, which have been

demonstrated in disordered systems (8). All of these features indicate that the ZrNCl-EDLT at $V_G = 6.5$ V is out of the disordered regime and may be entering a moderately clean regime with weak pinning.

The most plausible description of the metallic state is temperature-independent quantum tunneling of vortices (quantum creep). In this model, the resistance obeys a general form in the limit of the strong dissipation (41).

$$R_{\text{sheet}} \sim \frac{\hbar}{4e^2} \frac{\kappa}{1 - \kappa}, \quad \kappa \sim \exp \left\{ C \frac{\hbar}{e^2 R_N} \left(\frac{H - H_{c2}}{H} \right) \right\} \quad (3)$$

where C is a dimensionless constant. As seen in Fig. 4C, the $R_{\text{sheet}}-H$ relation at 2 K is well fitted by Eq. 3 up to 1.3 T, indicating that the quantum-creep model holds for a wide range. It should be noted that (i) finite-size effects (42) or (ii) the model of random Josephson junction arrays that originate from surface roughness (for example, amorphous Bi thin films) (31) or inhomogeneous carrier accumulation, both of which can cause the flattening of the resistance with a finite value, can be excluded because of the following reasons: (i) a BKT transition, and a zero resistance state (below ~ 0.05 Ω) are observed (see Fig. 1D); and (ii) the channel surface preserved atomically flat morphology with an average mean square roughness of ~ 0.068 nm, which is less than 4% of d_{sc} even after all the measurements (fig. S3) (29). Also, all the different voltage probes used to measure the longitudinal resistances and the transverse Hall resistances in four-terminal geometry (29) showed almost the same values with the differences of less than 5% at the high carrier concentrations ($V_G = 6$ and 6.5 V), which suggests that the surface carrier accumulation in the present system is homogeneous. Above 1.3 T, R_{sheet} is well described by an H -linear dependence (Fig. 4C, inset), indicating pinning-free vortex flow. The crossover from the creep to the flow motion occurs at ≈ 1.3 T, where $U(H)$ for the thermal creep approaches zero (Fig. 4B), implying that the pinning or the elastic potential effectively disappears at high magnetic fields. Based on the above observations, we obtained the field-temperature phase diagram of ion-gated ZrNCl shown in Fig. 4D. A true zero-resistance state occurs only at very small magnetic fields below 0.05 T. The key parameters here are the dimensionality and R_N of the system. The former enhances the quantum fluctuations, whereas the latter controls the coupling of vortices to a dissipative bath, which stabilizes the metallic region when R_N is low (43). Our results indicate that the EDLT provides a model platform of clean 2D superconductors with weak pinning and disorder, which may potentially lead to realizing intrinsic quantum states of matter.

REFERENCES AND NOTES

1. N. Reyren et al., *Science* **317**, 1196–1199 (2007).
2. A. Gozar et al., *Nature* **455**, 782–785 (2008).
3. K. Ueno et al., *Nat. Mater.* **7**, 855–858 (2008).

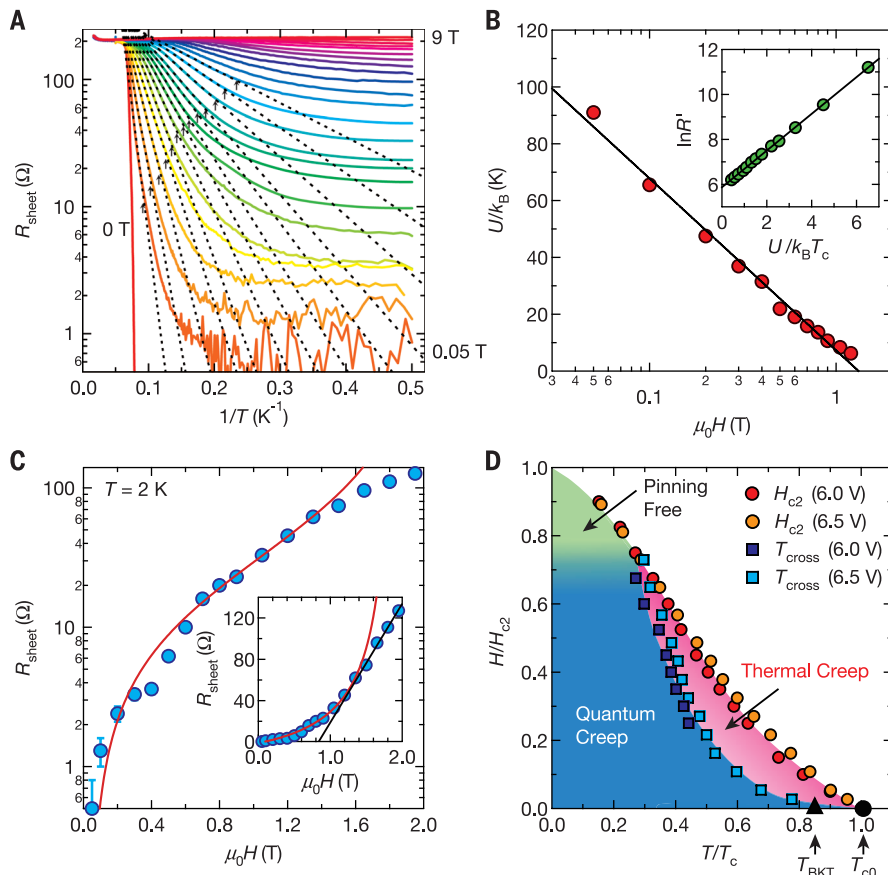


Fig. 4. Vortex dynamics in ion-gated ZrNCl. (A) Arrhenius plot of the sheet resistance of a ZrNCl-EDLT at $V_G = 6.5$ V for different magnetic fields perpendicular to the surface of ZrNCl. The black dashed lines demonstrate the activated behavior described by $R_{\text{sheet}} = R' \exp(-U(H)/k_B T)$. The arrows separate the thermally activated state in the high-temperature limit and the saturated state at lower temperatures. (B) Activation energy, $U(H)/k_B$, which is derived from the slopes of the dashed lines in Fig. 4A, is shown on a semilogarithmic plot as a function of magnetic field. The solid line is a fit by using the equation $U(H) = U_0 \ln(H_0/H)$. The inset shows the same data plotted as $\ln R'$ versus $U/k_B T_c$. These plots indicate that the resistance is governed by the thermally activated motion of dislocations of the 2D vortex lattice (2D thermal collective creep). (C) Low-temperature saturated values of the resistance as a function of magnetic field at 2 K. The red solid line is a fit using Eq. 3, which gives $C \approx 4.8 \times 10^{-3}$. The inset shows H -linear dependence of R_{sheet} above 1.3 T (black solid line). (D) Vortex phase diagram of the ZrNCl-EDLT. The boundary between the thermally assisted vortex-creep regime (thermal creep) and the quantum creep regime, T_{cross} , is determined from the Arrhenius plot as shown by the arrows in Fig. 4A. T_{BKT} and T_{c0} are the BKT transition temperature and the temperature obtained by analyses of the superconducting amplitude fluctuation, respectively (fig. S4) (29).

4. D. Jiang *et al.*, *Nat. Commun.* **5**, 5708 (2014).
5. S. Qin, J. Kim, Q. Niu, C. K. Shih, *Science* **324**, 1314–1317 (2009).
6. Q. Y. Wang *et al.*, *Chin. Phys. Lett.* **29**, 037402 (2012).
7. C. Xu *et al.*, *Nat. Mater.* **2015**, 10.1038/nmat4374 (2015).
8. A. M. Goldman, *Int. J. Mod. Phys. B* **24**, 4081–4101 (2010).
9. M. P. A. Fisher, *Phys. Rev. Lett.* **65**, 923–926 (1990).
10. D. Ephron, A. Yazdani, A. Kapitulnik, M. R. Beasley, *Phys. Rev. Lett.* **76**, 1529–1532 (1996).
11. Y. Lee *et al.*, *Phys. Rev. Lett.* **106**, 136809 (2011).
12. P. Gallagher, M. Lee, J. R. Williams, D. Goldhaber-Gordon, *Nat. Phys.* **10**, 748–752 (2014).
13. K. Ueno *et al.*, *Nat. Nanotechnol.* **6**, 408–412 (2011).
14. J. T. Ye *et al.*, *Nat. Mater.* **9**, 125–128 (2010).
15. J. T. Ye *et al.*, *Science* **338**, 1193–1196 (2012).
16. S. Jo, D. Costanzo, H. Berger, A. F. Morpurgo, *Nano Lett.* **15**, 1197–1202 (2015).
17. W. Shi *et al.*, *Sci. Rep.* **5**, 12534 (2015).
18. S. G. Haupt, D. R. Riley, J. T. McDevitt, *Adv. Mater.* **5**, 755–758 (1993).
19. S. G. Haupt *et al.*, *Proc. SPIE* **2158**, 238–249 (1994).
20. A. T. Bollinger *et al.*, *Nature* **472**, 458–460 (2011).
21. X. Leng, J. Garcia-Barriocanal, S. Bose, Y. Lee, A. M. Goldman, *Phys. Rev. Lett.* **107**, 027001 (2011).
22. S. W. Zeng *et al.*, *Phys. Rev. B* **92**, 020503 (2015).
23. S. Shamoto *et al.*, *Physica C* **306**, 7–14 (1998).
24. X. Chen, L. Zhu, S. Yamanaka, *J. Solid State Chem.* **169**, 149–154 (2002).
25. S. Yamanaka, H. Kawaji, K. Hotehama, M. Ohashi, *Adv. Mater.* **8**, 771–774 (1996).
26. T. Ito *et al.*, *Phys. Rev. B* **69**, 134522 (2004).
27. T. Takano, A. Kitora, Y. Taguchi, Y. Iwasa, *Phys. Rev. B* **77**, 104518 (2008).
28. Y. Taguchi, A. Kitora, Y. Iwasa, *Phys. Rev. Lett.* **97**, 107001 (2006).
29. See the supplementary materials on Science Online.
30. B. I. Halperin, D. R. Nelson, *J. Low Temp.* **36**, 599–616 (1979).
31. Y.-H. Lin, J. Nelson, A. M. Goldman, *Phys. Rev. Lett.* **109**, 017002 (2012).
32. L. G. Aslamazov, A. I. Larkin, *Phys. Lett.* **26A**, 238–239 (1968).
33. K. Maki, *Prog. Theor. Phys.* **39**, 897–906 (1968).
34. R. S. Thompson, *Phys. Rev. B* **1**, 327–333 (1970).
35. M. Tinkham, *Introduction to Superconductivity* (Dover, New York, ed. 2, 2004).
36. K. Ueno *et al.*, *Phys. Rev. B* **89**, 020508 (2014).
37. T. Brumme, M. Calandra, F. Mauri, *Phys. Rev. B* **89**, 245406 (2014).
38. T. Takano *et al.*, *J. Phys. Soc. Jpn.* **80**, 023702 (2011).
39. M. V. Feigel'man, V. B. Geshkenbein, A. I. Larkin, *Physica C* **167**, 177–187 (1990).
40. Y. Qin, C. L. Vicente, J. Yoon, *Phys. Rev. B* **73**, 100505 (2006).
41. E. Shimshoni, A. Auerbach, A. Kapitulnik, *Phys. Rev. Lett.* **80**, 3352–3355 (1998).
42. T. Schneider, S. Weyeneth, *Phys. Rev. B* **90**, 064501 (2014).
43. N. Mason, A. Kapitulnik, *Phys. Rev. Lett.* **82**, 5341–5344 (1999).

ACKNOWLEDGMENTS

We thank M. Nakano and Y. Nakagawa for technical support, M. Yoshida for fruitful discussions, and N. Shiba for useful comments on the manuscript. Y.S. was supported by the Japan Society for the Promotion of Science (JSPS) through a research fellowship for young scientists. J.T.Y. acknowledges the funding from the European Research Council (consolidator grant no. 648855 Ig-QPD). This work was supported by the Strategic International Collaborative Research Program (SICORP-LEMSUPER) of the Japan Science and Technology Agency, Grant-in-Aid for Specially Promoted Research (no. 25000003) from JSPS and Grant-in Aid for Scientific Research on Innovative Areas (no. 22103004) from MEXT of Japan.

SUPPLEMENTARY MATERIALS

www.sciencemag.org/content/350/6259/409/suppl/DC1
Materials and Methods
Supplementary Text
Figs. S1 to S6
References (44–49)

31 July 2014; accepted 15 September 2015
Published online 1 October 2015
10.1126/science.1259440

TOPOLOGICAL MATTER

Evidence for the chiral anomaly in the Dirac semimetal Na₃Bi

Jun Xiong,¹ Satya K. Kushwaha,² Tian Liang,¹ Jason W. Krizan,² Max Hirschberger,¹ Wudi Wang,¹ R. J. Cava,² N. P. Ong^{1*}

In a Dirac semimetal, each Dirac node is resolved into two Weyl nodes with opposite “handedness” or chirality. The two chiral populations do not mix. However, in parallel electric and magnetic fields ($\mathbf{E}||\mathbf{B}$), charge is predicted to flow between the Weyl nodes, leading to negative magnetoresistance. This “axial” current is the chiral (Adler-Bell-Jackiw) anomaly investigated in quantum field theory. We report the observation of a large, negative longitudinal magnetoresistance in the Dirac semimetal Na₃Bi. The negative magnetoresistance is acutely sensitive to deviations of the direction of \mathbf{B} from \mathbf{E} and is incompatible with conventional transport. By rotating \mathbf{E} (as well as \mathbf{B}), we show that it is consistent with the prediction of the chiral anomaly.

The notion of handedness, or chirality, is ubiquitous in the sciences. A fundamental example occurs in quantum field theory. Massless fermions segregate into left- or right-handed groups (they spin clockwise or anticlockwise, respectively, if viewed head on). Because the two groups never mix, we say that chirality is conserved. However, mixing occurs once electromagnetic fields are switched on. This induced breaking of chiral symmetry, known as the chiral anomaly (*1*), was first studied in pion physics, where it causes neutral pions to decay faster than charged pions by a factor of 3×10^8 (*1–3*). In 1983, it was proposed that the anomaly may be observed in a crystal (*4*). This goal now seems attainable (*5–11*) in the nascent field of Dirac/Weyl semimetals (*12–15*).

In Na₃Bi (*14*), strong spin-orbit coupling inverts the bands derived from the Na-3s and Bi-6p orbitals, forcing them to cross at the wave vectors $\mathbf{K}_{\pm} = (0, 0, \pm k_D)$, with $k_D \sim 0.1 \text{ \AA}^{-1}$ (*16, 17*). Because symmetry constraints forbid hybridization (*13, 15*), we have topologically protected Dirac states with energy $E(\mathbf{k}) = \hbar v|\mathbf{k}|$, where the wave vector \mathbf{k} is measured from \mathbf{K}_{\pm} and v is the Fermi velocity (Fig. 1A). Furthermore, symmetry dictates that each Dirac node resolves into two massless Weyl nodes with chiralities $\chi = \pm 1$ that preclude mixing [we calculate χ in (*18*)]. As discussed in (*4*), parallel electric and magnetic fields $\mathbf{E}||\mathbf{B}$ should cause charge pumping between the Weyl nodes, observable as a negative longitudinal magnetoresistance (LMR) (*6–11*).

Inspired by these ideas, experimental groups have recently reported negative LMR in Bi_{1-x}Sb_x (*19*), Cd₃As₂ (*20, 21*), ZrTe₅ (*22*), and TaAs (*23*). However, because negative LMR also exists in semimetals that do not have a Dirac dispersion [e.g., Cd_xHg_{1-x}Te (*24*) and PdCoO₂ (*25*)], it is desirable to go beyond this observation. Here, we

found that in Na₃Bi the enhanced current is locked to the \mathbf{B} vector and hence can be steered by rotating \mathbf{B} , even for weak fields.

Crystals of Na₃Bi grow as millimeter-sized, deep purple, hexagonal plates with the largest face parallel to the *a-b* plane (*26*). We annealed the crystals for 10 weeks before opening the growth tube. Crystals were contacted using silver epoxy in an argon glovebox to avoid oxidation, and were then immersed in paratone in a capsule before rapid cooling. Initial experiments in our lab (*27*) on samples with a large Fermi energy E_F (400 mV) showed only a positive magnetoresistance (MR) with the anomalous *B*-linear profile reported in Cd₃As₂ (*20*).

Progress in lowering E_F in Na₃Bi has resulted in samples that display a nonmetallic resistivity ρ versus T profile, a low Hall density $n_H \sim 1 \times 10^{17} \text{ cm}^{-3}$ (Fig. 1C), and a notably large, negative LMR (Fig. 1D). We explain why the negative LMR is not from localization in (*18*). We estimate the Fermi wave vector $k_F = 0.013 \text{ \AA}^{-1}$ (smaller than k_D by a factor of 8). Below ~ 10 K, the conductivity is dominated by conduction band carriers with mobility $\mu \sim 2600 \text{ cm}^2 \text{ V}^{-1} \text{ s}^{-1}$. Because the energy gap is zero, holes in the valence band are copiously excited even at low T . Above 10 K, the increased hole population leads to a steep decrease in ρ and an inversion of the sign of R_H at 62 K. From the maximum in R_H at 105 K, we estimate that $E_F \sim 3k_B T \sim 30$ mV. These numbers are confirmed by Shubnikov-de Haas (SdH) oscillations observed in the resistivity matrix element ρ_{xx} when \mathbf{B} is tilted toward \mathbf{c} (Fig. 2A). The index plot of $1/B_n$ (Fig. 2B), where B_n locates the SdH extrema, yields a Fermi surface (FS) cross section $S_F = 4.8 \pm 0.3 \text{ T}$, which gives $E_F = 29 \pm 2 \text{ mV}$, in good agreement with R_H . The density inferred from S_F ($n_c = 1.4 \times 10^{17} \text{ cm}^{-3}$) is slightly higher than n_H . The deviation from the straight line in Fig. 2B is consistent with a (spin gyromagnetic) g factor of ~ 20 , whereas $g \approx 40$ has been estimated for Cd₃As₂ (*28*). The SdH oscillations imply that E_F enters the $N = 0$ Landau level at $B = 6$ to 8 T.

¹Department of Physics, Princeton University, Princeton, NJ 08544, USA. ²Department of Chemistry, Princeton University, Princeton, NJ 08544, USA.

*Corresponding author. E-mail: npo@princeton.edu

Fig. 1. Weyl nodes and negative longitudinal magnetoresistance in Na₃Bi. (A) Sketch of a Dirac cone centered at K_+ represented as two massless Weyl nodes (slightly displaced) with distinct chiralities $\chi = -1$ (gray cone) and $+1$ (yellow). (B) An intense B field widens the node separation due to the spin Zeeman energy (separation exaggerated for clarity). The Weyl states are quantized into LLs. The $N = 0$ LL has a linear dispersion with slopes determined by χ . The yellow and green balls represent χ . An E -field $\parallel B$ generates an axial current observed as a large, negative LMR. (C) The T dependence of the resistivity ρ in $B = 0$, as inferred from $R_{14,23}$ (I applied to contacts 1 and 4, voltage measured across contacts 2 and 3) and the Hall coefficient R_H (inferred from $R_{14,35}$). Inset shows the hexagonal crystal J4 (1 mm on each side and 0.5 mm thick), contact labels, and the x and y axes. R_H is measured in $B < 2$ T applied $\parallel c$. At 3 K, R_H corresponds to a density $n = 1.04 \times 10^{17} \text{ cm}^{-3}$. The excitation of holes in the valence band leads to a sign change in R_H near 70 K and a steep decrease in ρ . (D) Longitudinal magnetoresistance $\rho_{xx}(B, T)$ at selected T from 4.5 to 300 K measured with $B \parallel \hat{x}$ and I applied to contacts 1 and 4. The steep decrease in $\rho_{xx}(B, T)$ with increasing B at 4.5 K reflects the onset of the axial current in the lowest LL. As T increases, occupation of higher LLs in conduction and valence bands overwhelms the axial current.

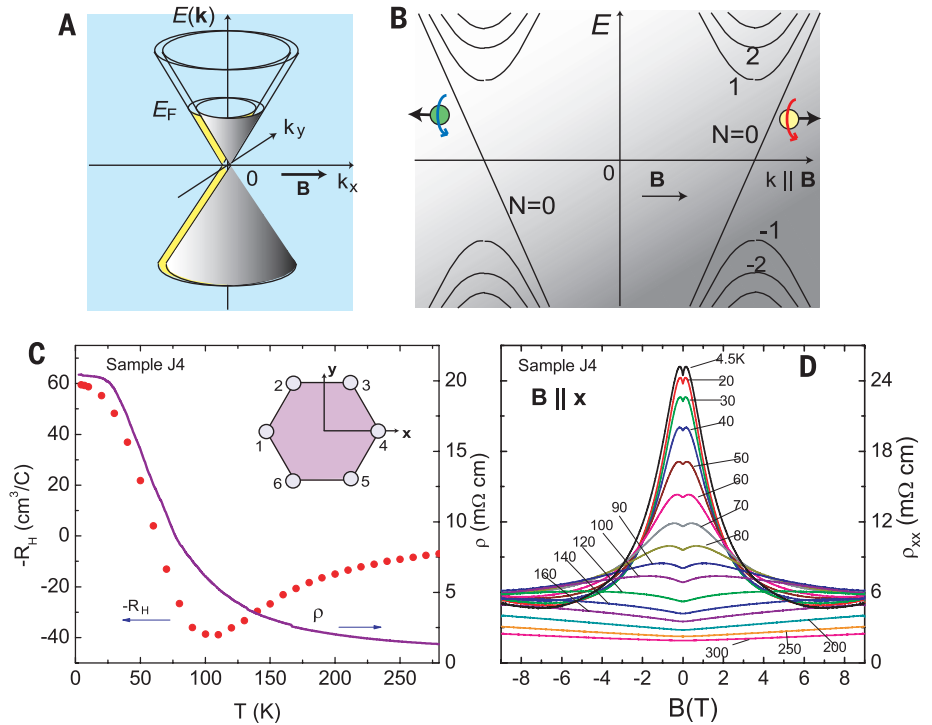
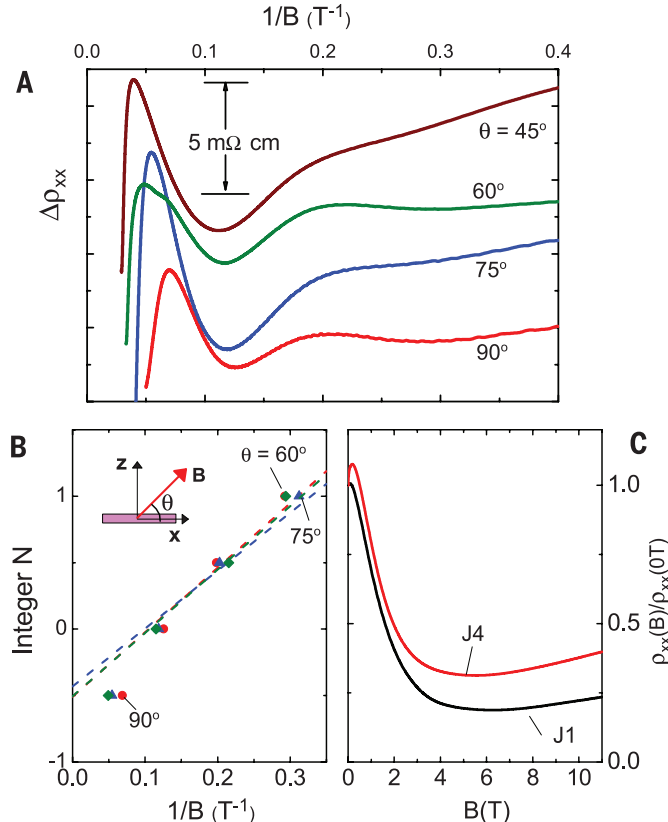


Fig. 2. Shubnikov–de Haas oscillations in Na₃Bi. (A) SdH oscillations resolved in ρ_{xx} for several tilt angles θ (relative to \hat{x}) after subtraction of the positive B -linear MR background (vertical scale as shown). The subtraction is explained in (18). (B) Landau level index N versus $1/B_n$, where B_n locates the extrema of the oscillations at selected θ (θ is defined in the inset). Uncertainties in $1/B_n$ are less than 10% (18). The slope at small B yields $S_F = 4.8 \pm 0.3$ T, $k_F = 0.013 \text{ \AA}^{-1}$, and $E_F = 29 \pm 2$ mV. The deviation at large B is consistent with a g^* value of ~ 20 (18). (C) Field profiles of ρ_{xx} (inferred from $R_{14,23}$) in samples J1 and J4, with $B \parallel \hat{z}$. The $N = 0$ LL is entered at $B = 6$ to 8 T. The slight increase for $B > 5$ T reflects the narrow width of the axial current. A slight misalignment of B (the uncertainty here is $\pm 1^\circ$) allows the B -linear positive MR component to appear as a background at large B .



The Landau levels (LLs) of the Weyl states in a strong B are sketched in Fig. 1B. In addition to the LLs, the spin Zeeman energy shifts the nodes away from K_+ by $\delta k_N = \chi g^* \mu_B B / (\hbar v)$, where \hbar is the Planck constant divided by 2π and μ_B is the Bohr magneton (14, 18). For clarity, we show the shifts exaggerated. A distinguishing feature of Weyl states is that the lowest LL ($N = 0$) disperses linearly to the right or left depending on χ . Application of $E \parallel B$ leads to a charge pumping rate between the two branches

$$W = \chi \frac{e^3}{4\pi^2 \hbar^2} \mathbf{E} \cdot \mathbf{B} \quad (1)$$

This is the chiral anomaly (4–11). The longitudinal (axial) current relaxes at a rate $1/\tau_a \sim |M|^2 eB / \hbar v$, where M is the matrix element for impurity scattering and $eB/\hbar v$ is the LL degeneracy (8). Hence, the chiral conductivity $\sigma_\chi \sim W\tau_a$ is independent of B in the quantum limit. Equation 1 and the expression for $1/\tau_a$ apply in the quantum limit at high fields (when only the lowest LL is occupied). However, we emphasize that even in weak fields when many LLs are occupied, the axial current remains observable. In the weak- B limit, Son and Spivak (9) showed that

$$\sigma_\chi = \frac{e^2}{4\pi^2 \hbar c} \frac{v}{c} \frac{(eBv)^2}{E_F^2} \tau_a \quad (2)$$

with $1/\tau_a$ now independent of B . As B increases, σ_χ grows as B^2 [see also (29)] but saturates to a B -independent value in the quantum limit.

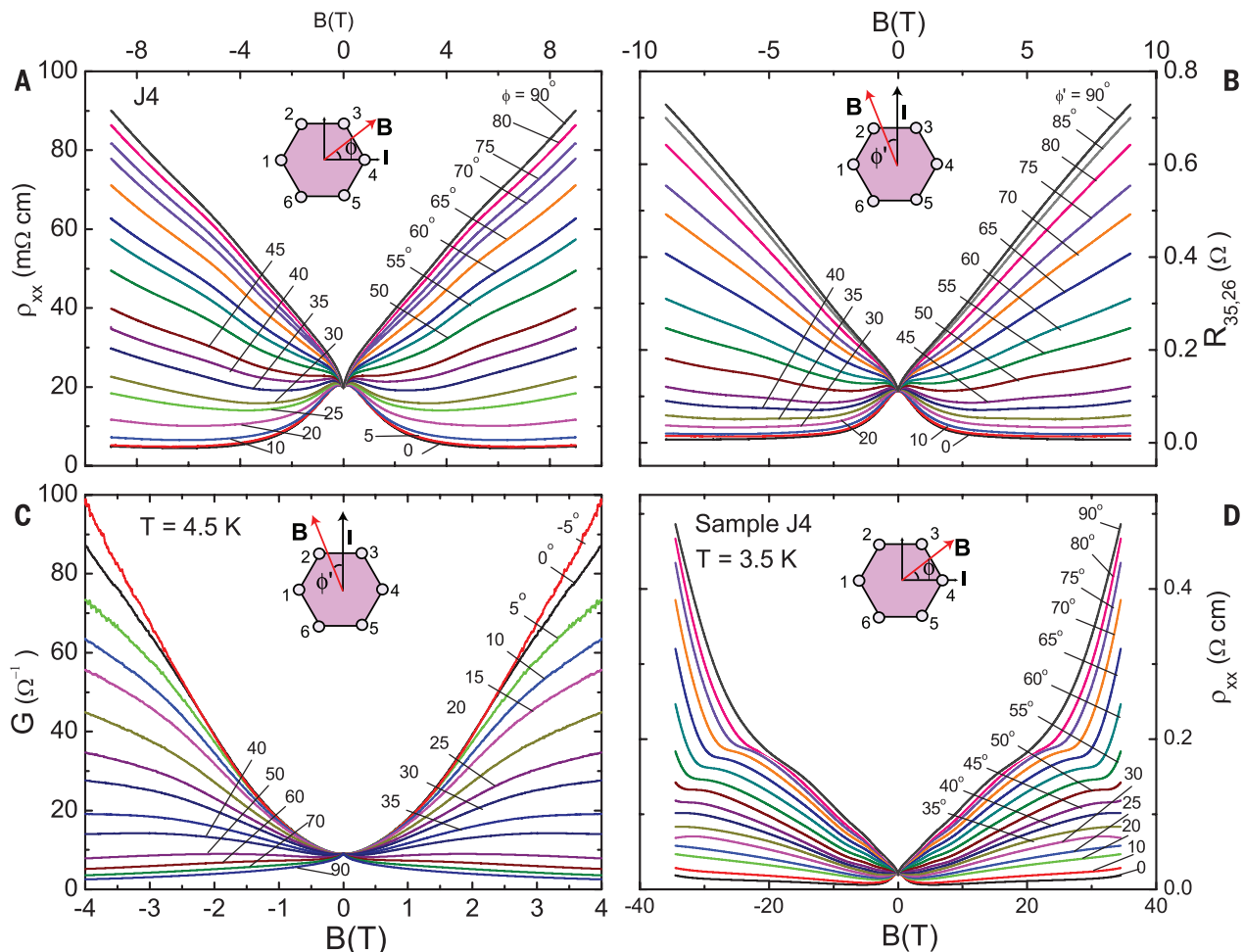


Fig. 3. Evidence for axial current in Na_3Bi . Transport measurements were taken on sample J4 in an in-plane field \mathbf{B} . **(A)** Resistivity ρ_{xx} versus B at selected field-tilt angles ϕ to the x axis (inferred from resistance $R_{14,23}$; see inset). For $\phi = 90^\circ$, ρ_{xx} displays a B -linear positive MR. However, as $\phi \rightarrow 0^\circ$ ($\mathbf{B} \parallel \hat{x}$), ρ_{xx} is strongly suppressed. **(B)** $R_{35,26}$ with \mathbf{E} rotated by 90° relative to **(A)** (\mathbf{B} makes an angle ϕ' relative to \hat{y} ; see inset). The resistance $R_{35,26}$ changes

from a positive MR to negative as $\phi' \rightarrow 0^\circ$. In both configurations, the negative MR appears only when \mathbf{B} is aligned with \mathbf{E} . **(C)** Conductance $G \equiv 1/R_{35,26}$. In weak B , it has the B^2 form predicted in Eq. 2 (9). A fit to the parabolic form gives $\tau_a/\tau_0 = 40$ to 60 . **(D)** ρ_{xx} [as in **(A)**] extended to 35 T. Above 23 T, a knee-like kink appears at H_k . Above H_k , ρ_{xx} increases very steeply (for $\phi > 35^\circ$).

As shown in Fig. 1D, the resistivity ρ_{xx} displays a large negative LMR ($\mathbf{B} \parallel \hat{x} \parallel \mathbf{I}$, the current; the notch at $B = 0$ is discussed below). The resistance measured is $R_{14,23}$ (see Fig. 1C, inset). Raising T above ~ 100 K suppresses the peak. In Fig. 2C, ρ_{xx} (in samples J1 and J4) falls rapidly to saturate to an almost B -independent value above 5 T (the slight upturn is a hint that the axial current is sensitive to misalignment of \mathbf{B} at the level $\pm 1^\circ$). A large negative LMR is anomalous in a conventional conductor, even with band anisotropy (18).

The axial current is predicted to be large when \mathbf{B} is aligned with \mathbf{E} . A crucial test then is the demonstration that, if \mathbf{E} is rotated by 90° , the negative MR pattern rotates accordingly; that is, the axial current maximum is locked to \mathbf{B} and \mathbf{E} rather than being pinned to the crystal axes, even for weak \mathbf{B} .

To carry out this test, we rotated \mathbf{B} in the x - y plane while still monitoring the resistance $R_{14,23}$. Figure 3A shows the curves of the resistivity ρ_{xx} versus B measured at 4.5 K at selected values of ϕ (the angle between \mathbf{B} and \hat{x}). The MR is positive for $\phi = 90^\circ$ ($\mathbf{B} \parallel \hat{y}$), displaying the nominal B -linear

form observed in Cd_3As_2 (20) and Na_3Bi (27) with $\mathbf{B} \parallel \mathbf{c}$. As \mathbf{B} is rotated toward \hat{x} (ϕ decreased), the MR curves are pulled toward negative values. At alignment ($\phi = 0$), the longitudinal MR is very large and fully negative [see (18) for the unsymmetrized curves and results from sample J1].

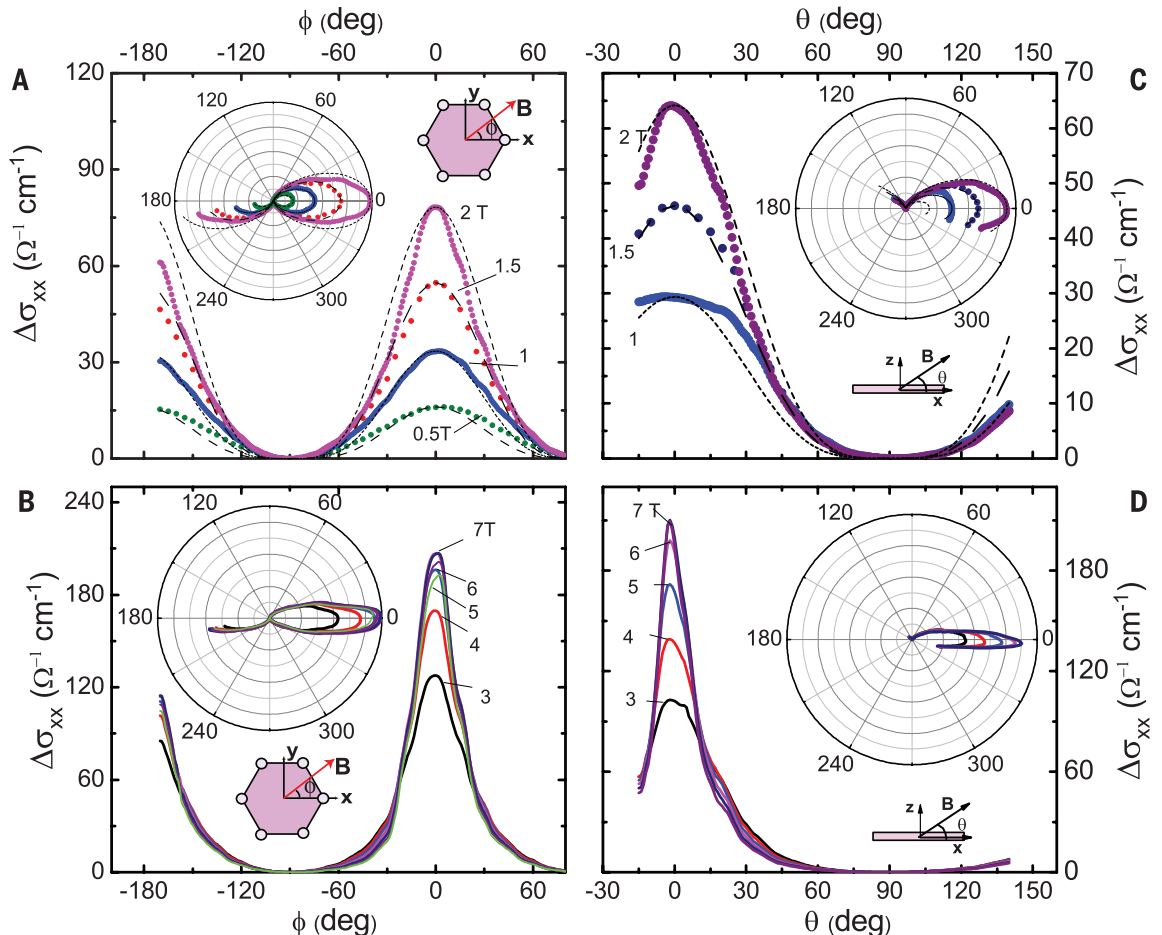
We then repeated the experiment in situ with \mathbf{I} applied to contacts 3 and 5, so that \mathbf{E} is rotated by 90° (the measured resistance is $R_{35,26}$). Remarkably, the observed MR pattern is also rotated by 90° , even when $B < 1$ T. Defining the angle of \mathbf{B} relative to \hat{y} as ϕ' , we now find that the MR is fully negative when $\phi' = 0$. The curves in Fig. 3, A and B, are nominally similar, except that $\phi = 0$ and $\phi' = 0$ refer to \hat{x} and \hat{y} , respectively. As we discuss below, we identify the locking of the negative MR direction to the common direction of $\mathbf{E} \parallel \mathbf{B}$ as a signature of the chiral anomaly.

The acute sensitivity of the axial current to misalignment at large B , as hinted in Fig. 2C, is surprising. To determine the angular variation, we performed measurements in which $R_{14,23}$ is measured continuously in fixed field versus tilt

angle (with \mathbf{B} either in the x - y or the x - z plane). Figure 4 displays the curves of $\Delta\sigma_{xx}(B, \phi) = \sigma_{xx}(B, \phi) - \sigma_{xx}(B, 90^\circ)$ versus ϕ (\mathbf{B} in the x - y plane at angle ϕ to \hat{x}), with B fixed at values $0.5 \rightarrow 2$ T (Fig. 4A) and $3 \rightarrow 7$ T (Fig. 4B). Shown in Fig. 4, C and D, are the same measurements but now with \mathbf{B} in the x - z plane at an angle θ to \hat{x} . In both cases, the low-field curves ($B \leq 2$ T) are reasonably described with $\cos^p \phi$ (or $\cos^p \theta$) with $p = 4$. However, for $B > 2$ T, the angular widths narrow considerably. Hence, at large B , the axial current is observed as a strongly collimated beam in the direction selected by \mathbf{B} and \mathbf{E} as ϕ or θ is varied. The strong collimation has not been predicted.

The large negative MR in Fig. 3 implies a long relaxation time τ_a for the axial current. By fitting Eq. 2 to the parabolic profile of $G = 1/R_{35,26}$ shown in Fig. 3C, we find that $\tau_a = 40$ to $60 \times \tau_0$, the Drude lifetime. Despite its importance, the matrix element M in $1/\tau_a$ is not well studied. There is debate on whether a large node separation $2\delta k_N$ is needed to obtain a long τ_a [using the estimate (18) of $g^* \sim 20$, we find that $\delta k_N > k_F$ when

Fig. 4. Angular dependence of the axial current. The dependence is inferred from measurements of $R_{14,23}$ in tilted $\mathbf{B}(\theta, \phi)$ in sample J4 at 4.5 K. (A and B) \mathbf{B} lies in the x - y plane at an angle ϕ to \hat{x} (sketch in insets). The conductance enhancement $\Delta\sigma_{xx}$ at fixed \mathbf{B} is plotted against ϕ for values of $B \leq 2$ T (A) and for $3 \leq B \leq 7$ T (B). Fits to $\cos^4 \phi$ (dashed curves), although reasonable below 2 T, become very poor as B exceeds 2 T. The insets show the polar representation of $\Delta\sigma_{xx}$ versus ϕ . (C and D) \mathbf{B} is tilted in the x - z plane. As sketched in the insets, θ is the angle between \mathbf{B} and \hat{x} . Curves of $\Delta\sigma_{xx}$ versus θ for $B = 1, 1.5$, and 2 T are shown in (C); shown in (D) are curves for $3 \leq B \leq 7$ T. The axial current is peaked when $\phi \rightarrow 0$ ($\theta \rightarrow 0$) with an angular width that narrows as B increases.



$B > 12$ T]. Recently, however, it was shown (29) that the ratio τ_a/τ_0 can be very large (in a superlattice model) even for negligible δk_N because Berry curvature effects hinder axial current relaxation and chiral symmetry is only weakly violated. This issue should be resolvable by LMR experiments.

A notable feature in the LMR profile (Fig. 1D) is the notch at $B = 0$, which persists to 120 K. Above 140 K, the notch expands to a V-shaped positive LMR profile. The insensitivity of this feature to the tilt angle of \mathbf{B} implies that it is associated with the Zeeman energy. A similar feature is seen in Cd_3As_2 (20).

We extended measurements of $R_{14,23}$ to $B = 35$ T. From the curves of ρ_{xx} versus B (Fig. 3D), we find a new feature at the kink field $H_k \sim 23$ T when $\mathbf{B} \parallel \hat{y}$. As \mathbf{B} is tilted away from \hat{y} ($\phi \rightarrow 55^\circ$), the feature at H_k becomes better resolved as a kink. The steep increase in ρ_{xx} above H_k suggests an electronic transition that opens a gap. However, as we decrease ϕ below 45° , $H_k(\phi)$ moves rapidly to above 35 T. The negative MR curve at $\phi = 0$ remains unaffected by the instability up to 35 T (the small rising background is from a weak B_z due to a slight misalignment).

Within standard MR theory, the feature that is most surprising is the locking of the MR pattern to the \mathbf{B} vector in Fig. 3, A and B. If one postulates that the narrow plume in Fig. 4 arises from anisotropies in the FS properties (v and τ_0

versus \mathbf{k}), the direction of maximum conductivity should be anchored to the crystal axes. We should not be able to rotate the resistivity tensor by orienting the weak E and B fields (this violates linear response). However, it agrees with the prediction of the chiral anomaly; the axial current peaks when \mathbf{E} aligns with \mathbf{B} , even for weak fields.

We believe that this locking pattern in weak B is the quintessential signature of the axial current. The experiment confirms the B^2 behavior in weak B and provides a measurement of τ_a . The narrow angular width of the axial current may provide further insight into its properties.

REFERENCES AND NOTES

- E. M. Peskin, D. V. Schroeder, *Introduction to Quantum Field Theory* (Westview, Boulder, CO, 1995), chap. 19.
- S. L. Adler, *Phys. Rev.* **177**, 2426–2438 (1969).
- J. S. Bell, R. Jackiw, *Nuovo Cim.* **60A**, 4 (1969).
- H. B. Nielsen, M. Ninomiya, *Phys. Lett. B* **130**, 389–396 (1983).
- X. G. Wan, A. M. Turner, A. Vishwanath, S. Y. Savrasov, *Phys. Rev. B* **83**, 205101 (2011).
- A. A. Burkov, M. D. Hook, L. Balents, *Phys. Rev. B* **84**, 235126 (2011).
- K.-Y. Yang, Y.-M. Lu, Y. Ran, *Phys. Rev. B* **84**, 075129 (2011).
- V. Aji, *Phys. Rev. B* **85**, 241101 (2012).
- D. T. Son, B. Z. Spivak, *Phys. Rev. B* **88**, 104412 (2013).
- S. A. Parameswaran, T. Grover, D. A. Abanin, D. A. Pesin, A. Vishwanath, *Phys. Rev. X* **4**, 031035 (2014).
- P. Hosur, X. Qi, *C. R. Phys.* **14**, 857–870 (2013).
- S. M. Young *et al.*, *Phys. Rev. Lett.* **108**, 140405 (2012).
- C. Fang, M. J. Gilbert, X. Dai, B. A. Bernevig, *Phys. Rev. Lett.* **108**, 266802 (2012).
- Z. J. Wang *et al.*, *Phys. Rev. B* **85**, 195320 (2012).
- B.-J. Yang, N. Nagaosa, *Nat. Commun.* **5**, 4898 (2014).

- Z. K. Liu *et al.*, *Science* **343**, 864–867 (2014).
- S.-Y. Xu *et al.*, *Science* **347**, 294–298 (2015).
- See supplementary materials on Science Online.
- H.-J. Kim *et al.*, *Phys. Rev. Lett.* **111**, 246603 (2013).
- T. Liang *et al.*, *Nat. Mater.* **14**, 280–284 (2015).
- C. Zhang *et al.*, <http://arxiv.org/abs/1504.07698> (2015).
- Q. Li *et al.*, <http://arxiv.org/abs/1412.6543> (2014).
- C. Zhang *et al.*, <http://arxiv.org/abs/1503.02630> (2015).
- I. M. Tsidikovskii, W. Giriat, G. I. Kharus, E. A. Neifeld, *Phys. Status Solidi B* **64**, 717–727 (1974).
- N. Kikugawa *et al.*, <http://arxiv.org/abs/1412.5168> (2014).
- S. K. Kushwaha *et al.*, *APL Materials* **3**, 041504 (2015).
- J. Xiong *et al.*, <http://arxiv.org/abs/1502.06266> (2015).
- S. Jeon *et al.*, *Nat. Mater.* **13**, 851–856 (2014).
- A. A. Burkov, *Phys. Rev. B* **91**, 245157 (2015).

ACKNOWLEDGMENTS

We thank B.A. Bernevig and Z. Wang for valuable discussions. Supported by Army Research Office grant ARO W911NF-11-1-0379, a MURI award for topological insulators (ARO W911NF-12-1-0461), and the Gordon and Betty Moore Foundation's EPIQS Initiative through grant GBMF4539 (N.P.O.). The growth and characterization of crystals were performed by S.K.K., J.W.K., and R.J.C. with support from NSF grant DMR 1420541. Some experiments were performed at the National High Magnetic Field Laboratory (NHMFL), which is supported by NSF Cooperative Agreement no. DMR-1157490, the State of Florida, and the U.S. Department of Energy; we thank E. S. Choi for assistance at NHMFL.

SUPPLEMENTARY MATERIALS

www.sciencemag.org/content/350/6259/413/suppl/DC1
Materials and Methods
Supplementary Text
Figs. S1 to S6
References (30, 31)

3 February 2015; accepted 19 August 2015
Published online 3 September 2015
10.1126/science.aac6089

MAGNETIC RESONANCE

Electron paramagnetic resonance of individual atoms on a surface

Susanne Baumann,^{1,2*} William Paul,^{1,*†} Taeyoung Choi,¹ Christopher P. Lutz,¹ Arzhang Ardavan,³ Andreas J. Heinrich¹

We combined the high-energy resolution of conventional spin resonance (here ~10 nano-electron volts) with scanning tunneling microscopy to measure electron paramagnetic resonance of individual iron (Fe) atoms placed on a magnesium oxide film. We drove the spin resonance with an oscillating electric field (20 to 30 gigahertz) between tip and sample. The readout of the Fe atom's quantum state was performed by spin-polarized detection of the atomic-scale tunneling magnetoresistance. We determine an energy relaxation time of $T_1 \approx 100$ microseconds and a phase-coherence time of $T_2 \approx 210$ nanoseconds. The spin resonance signals of different Fe atoms differ by much more than their resonance linewidth; in a traditional ensemble measurement, this difference would appear as inhomogeneous broadening.

In a spin resonance experiment, radio-frequency (RF) radiation excites transitions between low-energy electron or nuclear spin states. Electron paramagnetic resonance (EPR), also known as electron spin resonance (ESR), reveals, for example, the electronic environment of paramagnetic defects in solids (1) and distances between spin labels in biological macromolecules (2). Conventionally, magnetic resonance depends on absorption and emission of electromagnetic radiation and generally requires a large ensemble of nearly identical spins. However, in certain systems, magnetic resonance can be detected on individual spin centers, notably by optical readout (3) or by force microscopy (4). Couplings between itinerant and localized spins have been exploited to electrically detect magnetic resonance in small ensembles (5), in individual spins in quantum dots (6), in individual P atoms in Si (7, 8), and in individual magnetic molecules in an electromigration device (9).

A promising avenue to improve the spatial resolution of spin measurements is the use of scanning tunneling microscopy (STM). STM can drive inelastic excitations in spin systems (spin excitation spectroscopy), revealing the energy spacing between levels of a quantum spin (10, 11). In addition, spin-polarized STM can measure the spin orientation in magnetic nanostructures via a change in the tunnel current caused by atomic-scale tunneling magnetoresistance (12–14). Although spectroscopy in STM offers atomic-scale spatial resolution, it suffers from temperature-limited energy resolution. Previous attempts to combine ESR and STM have focused on the detection of increased noise in the tunnel current I at the spin precession frequency (15–17), and a number of theoretical mechanisms for

non-spin-polarized contrast have been proposed (18). However, the experiments operated at room temperature, and the presence of a frequency-dependent current signal has been sporadic (18). A recent STM experiment applied an RF electric field to a magnetic molecule (19) and attributed an RF-frequency-dependent dI/dV signal to spin resonance, where V is the tunneling voltage.

A schematic of our experimental setup (Fig. 1A) shows that Fe atoms are separated from the Ag substrate via a one-monolayer MgO film.

Iron atoms adsorb on the oxygen binding site of MgO and have four Mg atoms as second-nearest neighbors, in a C_{4v} symmetry (Fig. 1C). This bonding structure results in a strong easy-axis magnetic anisotropy perpendicular to the surface (z direction), i.e., along the Fe-O bond. Figure 1B and fig. S1 (20) show STM topographic images of the Fe atoms studied. The energy landscape of the lowest five states of the Fe atom (Fig. 1D) consists of low-energy states $|0\rangle$ and $|1\rangle$ that are degenerate states except for the Zeeman splitting, separated by an anisotropy barrier formed by the additional spin states.

A spin-polarized (SP) STM tip was fabricated by transferring one Fe atom from the surface to the nonmagnetic tip apex (20). The SP tip was positioned over the Fe atom under study, and a gigahertz frequency voltage V_{RF} was applied between tip and sample, in addition to the DC bias voltage V_{DC} . The RF voltage created a time-dependent electric field between tip and sample (Fig. 1A, blue). This RF electric field drove the resonant transition between states $|0\rangle$ and $|1\rangle$. During EPR measurements, we swept the RF frequency and varied the source power to compensate for the frequency-dependent transmission of the wiring, and thereby obtained a constant-amplitude V_{RF} at the tunnel junction (figs. S2 and S3). The DC voltage was used to measure the tunneling magnetoresistance of the tunnel junction with the SP tip, which resulted in a tunnel current that depended on the relative population of states $|0\rangle$ and $|1\rangle$ (14).

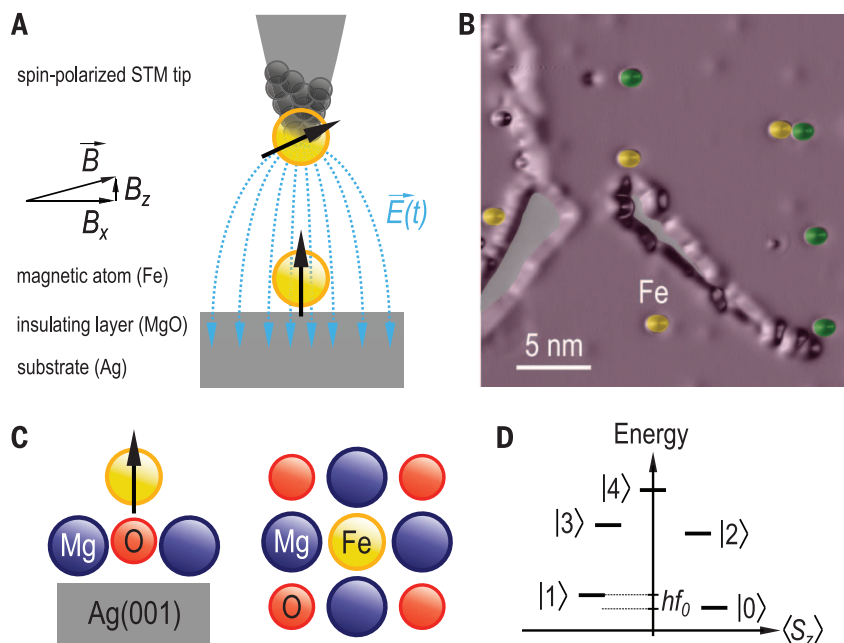


Fig. 1. Experimental setup for EPR of Fe on MgO. (A) Schematic model: a spin-polarized STM tip is brought close to an Fe atom on a thin MgO film. A magnetic field is applied to produce a large in-plane field B_x and a small proportional out-of-plane field B_z . Spin resonance of the Fe atom is driven by a gigahertz frequency electric field $\vec{E}(t)$. (B) Constant-current STM image of Fe (yellow) and Co (green) atoms on a single atomic layer of MgO. EPR curves shown in subsequent figures were measured on the indicated Fe atom. Imaging conditions: 10 pA at 0.1 V, $T = 1.2$ K, $B = 5.375$ T. (C) Geometry of Fe atom (yellow) binding on top of O (red) on an MgO layer. (D) Diagram of the five lowest energy levels of the Fe atom. The B_z field splits the lowest two energy levels, $|0\rangle$ and $|1\rangle$, by an amount $hf_0 \approx 0.1$ meV, where h is Planck's constant.

¹IBM Research Division, Almaden Research Center, 650 Harry Road, San Jose, CA 95120, USA. ²Department of Physics, University of Basel, Klingelbergstrasse 82, CH-4056 Basel, Switzerland. ³Clarendon Laboratory, Department of Physics, University of Oxford, Oxford OX1 3PU, UK.

*These authors contributed equally to this work. †Corresponding author. E-mail: wmpaul@gmail.com

We applied a large static magnetic field, $B = |\vec{B}|$, mostly in the plane of the sample but tilted out by $\sim 2^\circ$, which created a strong in-plane magnetic field, B_X , and a small out-of-plane field, B_Z . The out-of-plane B_Z established an energy splitting between states $|0\rangle$ and $|1\rangle$, and the in-plane magnetic field B_X modified the spin components of these two quantum states to strengthen the spin resonance transition between them (see below). We set B_Z so that the frequency f_0 of the RF electric field needed to excite the transition between states $|0\rangle$ and $|1\rangle$ fell at ~ 25 GHz (~ 100 μ eV). Given the known magnetic moment $5.2 \mu_B$ (Bohr magneton) of Fe on MgO (21), this energy spacing was obtained for $B_Z \approx 0.18$ T. At the STM operating temperature of 0.6 K and at low tunnel currents, the spin system was mostly ($>75\%$) in state $|0\rangle$, except when resonantly excited.

To obtain EPR spectra, we swept the frequency f of the RF electric field and monitored the time-average tunnel current. Figure 2A shows a constant tunnel-current signal over the entire frequency sweep, except for a single EPR peak. The peak position changed linearly with the magnetic field (Fig. 2D). On resonance, the tunnel current increased from the set-point current of 1.0 pA to 1.1 pA. The full-width at half-maximum (FWHM) of the resonance signal was 21 ± 2 MHz, which is limited here by the strong driving RF field and tip-sample vibrations (20). When a non-spin-polarized tip was used, the EPR signal was absent (fig. S11), so the contrast observed represented spin-polarized detection. We excited spin resonance in the Fe on the MgO surface, not on the Fe atom on the tip apex, which served only as spin-polarized detector, owing to its subpicosecond excited-state lifetimes (22).

To understand the mechanism of coherent transition, we describe the spin and orbital nature of the magnetic states $|0\rangle$ and $|1\rangle$. Fe on MgO was recently measured with spin excitation spectroscopy and x-ray absorption spectroscopy to determine its low-energy quantum states (21). When bound to MgO, the free-atom's spin and a large portion of its orbital angular momentum are preserved (21). By using the approximation that the Fe atom is in the d^6 configuration and in the lowest Hund's rule term (orbital moment $L = 2$ and spin $S = 2$), the quantum states determined previously (21) are well approximated by the ligand-field Hamiltonian

$$H_0 = D L_z^2 + F_0 (L_+^4 + L_-^4) + \lambda \vec{L} \cdot \vec{S} + \mu_B (\vec{L} + 2\vec{S}) \cdot \vec{B} \quad (1)$$

Here $D = -433$ meV gives the axial (out-of-plane) anisotropy; $F_0 = 2.19$ meV is the tetragonal (fourfold rotational) ligand field that describes the splitting between in-plane orbitals (d_{xy} and $d_{x^2-y^2}$) that results from the four nearest Mg atoms; $\lambda = -12.6$ meV gives the spin-orbit coupling; and the last term determines the Zeeman energy. Operators L_z , L_- , and L_+ refer to the orbital moment's z -axis and ladder operators. The use of this Hamiltonian, rather than an effective-spin Hamiltonian (1, 11, 14), gives richer insight into the effects of electric fields (20).

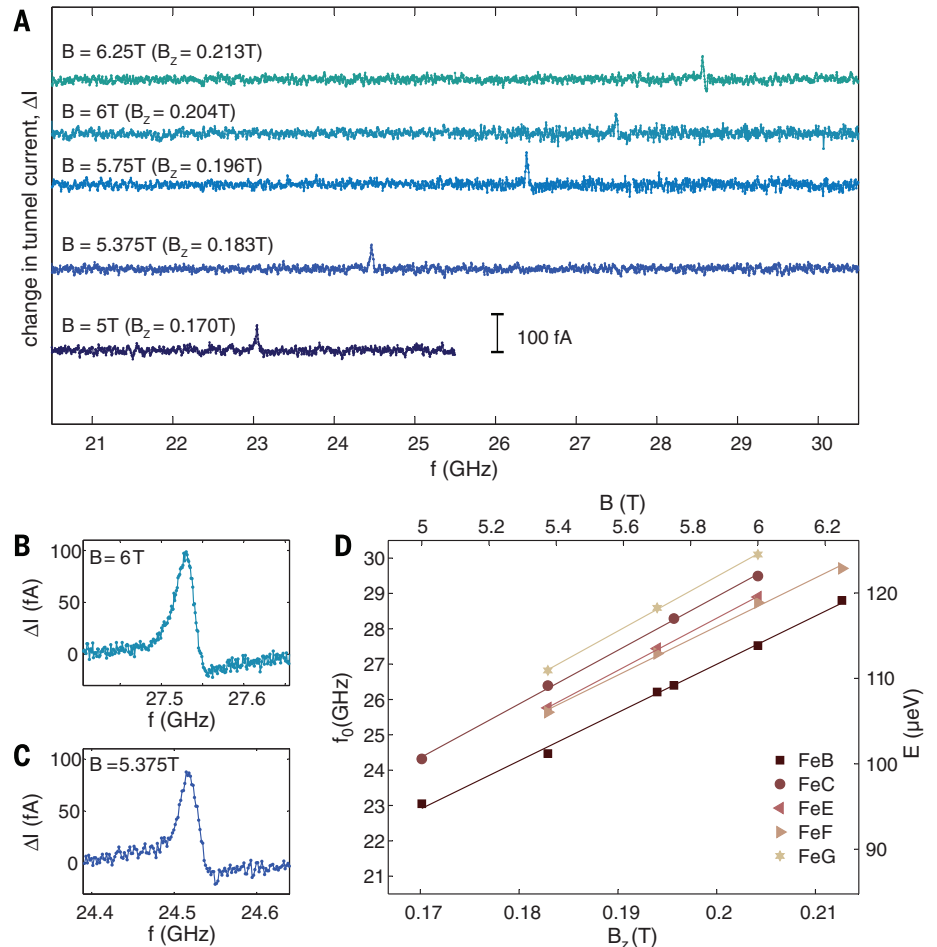


Fig. 2. EPR spectra of individual Fe atoms. (A) EPR peaks in the tunnel current as a function of frequency of RF electric field at five different values of B . Tip height setpoint 1 pA at 5 mV, $T = 0.6$ K, $V_{RF} = 5$ mV. Plots show the change in tunnel current, ΔI , between RF on and RF off, obtained by chopping V_{RF} at 95 Hz. The spin-polarized tip is positioned at the topographic peak of Fe atom indicated in Fig. 1B (and identified as “FeB” in Fig. 2D). For clarity, traces are offset vertically in proportion to the magnetic field. (B and C) Enlargement of a small frequency window at two B fields as labeled, using the same conditions as in (A). Averaging time was 50 min per data set. (D) EPR peak positions of five different Fe atoms as a function of B_z and B . The $B = 0$ intercepts of the linear fits (lines) for each atom fall at -0.8 ± 0.9 GHz. We use the mean value of the measured slopes and compare it to the known magnetic moment $5.2 \mu_B$ of Fe on MgO (21) to infer B_z relative to B (20). STM images of all five atoms are shown in fig. S1.

We propose that the large RF electric field $\vec{E}(t)$, applied mostly along z , moves the Fe atom with respect to the MgO lattice. This structural change modifies the ligand field parameters, which results in a time-dependent Hamiltonian H_1 that can drive coherent transitions between states $|0\rangle$ and $|1\rangle$

$$H_1(t) = F_1(t)(L_+^4 + L_-^4) \quad (2)$$

In the absence of an in-plane magnetic field, the largest terms of the eigenstates of H_0 , expressed in the basis of z -axis orbital and spin quantum numbers $|M_L, M_S\rangle$, are

$$|0\rangle = 0.92|+2, +2\rangle - 0.40|-2, +2\rangle + \dots \quad (3)$$

$$|1\rangle = 0.92|-2, -2\rangle - 0.40|+2, -2\rangle + \dots \quad (4)$$

These two states overlap in their orbital components under application of H_1 (both contain

$M_L = \pm 2$), but are effectively polarized in their spin component. The absence of overlap in the spin component leads to a nearly vanishing coherent transition rate $\langle 0|H_1|1\rangle$. In accordance, we did not observe any EPR signals on Fe at $B_X \approx 0$. When $B_X \gg 0$, the states $|0\rangle$ and $|1\rangle$ contain other $|M_L, M_S\rangle$ components [see (20)] making the spin component less polarized, thus increasing the coherent transition rate.

We did not observe a spin resonance signal for Co atoms on the MgO surface, even though Co's magnetic moment is similar to that of Fe (21, 23) (fig. S11). The orbital symmetry of Fe matches the fourfold symmetry of the binding site and leads to resonant transitions, whereas the same binding site symmetry does not lead to resonant transitions in Co because its lowest-energy states are dominantly composed of $M_L = \pm 3$ components. These are not mixed by the fourfold symmetric effect of $(L_+^4 + L_-^4)$, so no

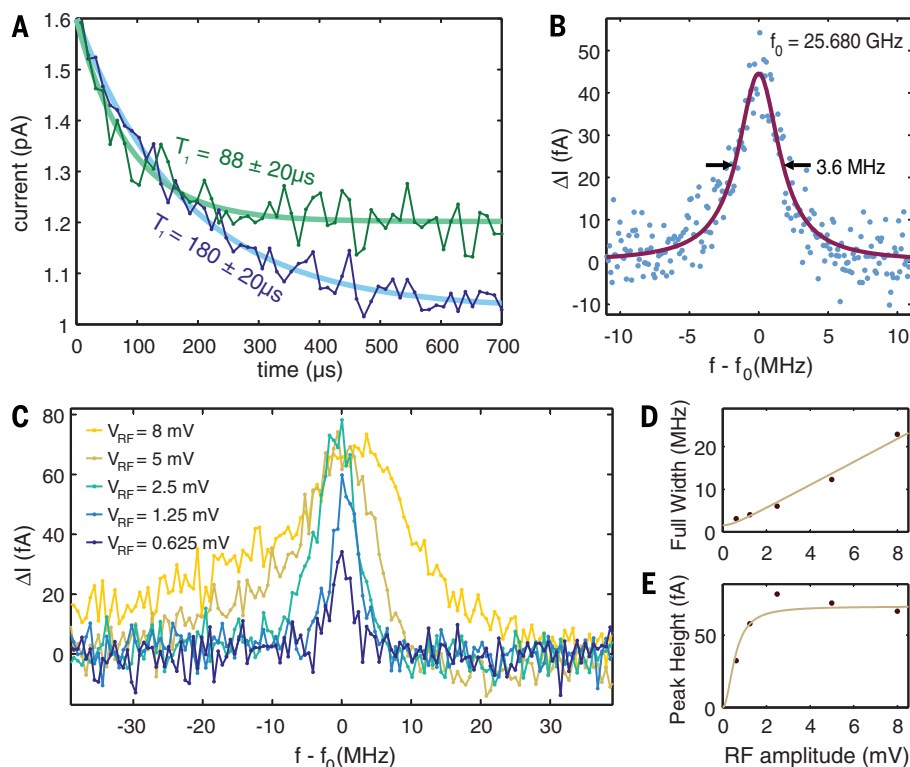


Fig. 3. Determining spin resonance parameters. (A) Electrical pump-probe measurements to determine T_1 . Tunnel current shows magnetic state of the Fe atom (indicated in Fig. 1B) as a function of delay time after exciting it with a pulse of $V_{DC} = 75$ mV lasting 16 μs. Signal decays with time constant $T_1 = 180 \mu s$ (blue curve) when $V_{DC} = 0$ during the delay time. When $V_{DC} = 5$ mV to match EPR conditions of Fig. 2, T_1 is reduced to $88 \mu s$ (green curve), and the signal amplitude is reduced, owing to direct transitions induced by the tunneling electrons. Tip apex and tip position are the same as in the spectra in Fig. 2; $T = 0.6$ K, $B = 5.7$ T. (B) EPR peak at conditions that reduce broadening: small drive amplitude $V_{RF} = 1$ mV, and tip positioned at minimum in f_0 (20), setpoint $I = 0.56$ pA, $V_{DC} = 5$ mV. Fit of Lorentzian line shape (solid line) gives width $\Delta f = 3.6$ MHz and $T_2 = 88$ ns. (C) EPR signal at five drive amplitudes V_{RF} . Same conditions as in (B). The low-amplitude spectra are symmetric. The origin of the asymmetry in the saturated spectra is not known. (D and E) Peak width (FWHM) and height for the spectra in (C). Points show width and height of a Lorentzian fit for each V_{RF} in (C). Curves show simultaneous fit to all points in (C) (20). Fit uses $T_1 = 139 \mu s$ [obtained by interpolating (A) for 0.56 pA] to yield phase coherence time $T_2 = 210 \pm 50$ ns and Rabi flop time $\pi/\Omega = 1.2 \pm 0.1 \mu s$ at $V_{RF} = 8$ mV.

resonant transitions between states $|0\rangle$ and $|1\rangle$ under application of the time-dependent H_1 are expected.

To estimate the magnitude of the driving RF electric field available in our STM geometry, we used a simple plate capacitor model. The distance from the tip to the surface of the Ag substrate is ~ 0.8 nm, and applying $V_{RF} = 5$ mV results in an electric field of $\sim 6 \times 10^6$ V/m. The effects of similar strengths of electric fields were studied in bulk EPR to modulate parameters of a spin Hamiltonian (24, 25), nitrogen vacancy centers in diamond for the purpose of electric-field sensing (26), and P in Si to electrically control quantum gates (27).

In a traditional EPR experiment, an ensemble average over a large number of spins is required to obtain sufficient signal. Variations in the local environments of individual spins in the ensemble inhomogeneously broaden the EPR peak. We compared the EPR signal of five different Fe atoms in our experiment (Fig. 2D), whose

resonance energies at a given magnetic field differ from each other by up to 3 GHz ($\sim 10 \mu eV$). However, all resonances move in proportion to the magnetic field. The subtly different local environments lead either to different magnetic moments or to variable tilting of the easy axis relative to the magnetic field. STM images of the local environment of each Fe atom (fig. S1) show no detectable imperfections within ~ 1 nm of each Fe atom. This comparison demonstrates the importance of single-atom measurement, as the linewidth in the equivalent ensemble measurement would be broadened to ~ 1 GHz.

To investigate the influence of the tip on the measured EPR spectra, we measured the same set of atoms for a different Fe-terminated tip. The EPR frequency shifted by a constant ~ 800 MHz for all (except one) atom on the surface (fig. S8). Thus, differences in resonance frequency remain independent of the tip, and energy differences can be interpreted with high accuracy even though the absolute frequencies are somewhat tip de-

pendent. A plausible origin of the observed shift is a local magnetic field created by the spin-polarized tip.

A resonantly driven magnetic moment is typically described with three parameters: (i) the energy relaxation time T_1 ; (ii) the quantum phase coherence time T_2 ; and (iii) the strength of the driving field, or equivalently, the rate at which the driving field coherently rotates the quantum system (Rabi rate Ω).

The energy relaxation time T_1 describes the time to relax from the excited state $|1\rangle$ to the ground state $|0\rangle$. More precisely, it is the time to relax to steady-state population, which typically is thermally distributed. We used an electrical pump-probe technique (28) and observed an exponentially decaying tunnel current yielding $T_1 = 88 \pm 20 \mu s$ (Fig. 3A) at the tip height and voltage used in the EPR measurements of Fig. 2. A lower bound of the coherence time T_2 (20) can be obtained from the resonance peak width of $\Delta f = 3.6 \pm 0.4$ MHz (Fig. 3B), which gives T_2 exceeding $1/\pi\Delta f \approx 100$ ns.

The Rabi rate Ω and a more accurate value of T_2 can be determined from the EPR signal as a function of RF drive amplitude (Fig. 3C). Simultaneous fits to all five spectra of Fig. 3C yielded a coherence time $T_2 = 210 \pm 50$ ns, and a driving strength of $\Omega = 2.6 \pm 0.3$ rad/μs for a driving voltage $V_{RF} = 8$ mV (20). This gives a Rabi flop time, the time needed to reverse the magnetic state coherently, of $\pi/\Omega = 1.2 \pm 0.1 \mu s$. Despite the flop time exceeding T_2 by a factor of ~ 6 , the EPR peaks reached saturation. As is known from traditional EPR, this saturation occurs because of the long T_1 time, which allows the spin to perform a random walk consisting of many successive periods of coherent evolution before T_1 elapses (1). We did not observe any Rabi oscillations in pulsed EPR experiments; instead, we observed a simple exponential change in polarization because of the small ratio of T_2 to Rabi flop time. We cannot increase V_{RF} much further to improve this ratio without exceeding the spin excitation at 14 meV. Thus, we expect that fully coherent reversal of the spin will require further increases in T_2 —for example, by increasing the MgO thickness.

REFERENCES AND NOTES

1. A. Abragam, B. Bleaney, *Electron Paramagnetic Resonance of Transition Ions* (Oxford Univ. Press, Oxford, Reprint ed., 2012).
2. G. Jeschke, Y. Polyhach, *Phys. Chem. Chem. Phys.* **9**, 1895–1910 (2007).
3. A. Gruber, Scanning confocal optical microscopy and magnetic resonance on single defect centers. *Science* **276**, 2012–2014 (1997).
4. D. Rugar, R. Budakian, H. J. Mamin, B. W. Chui, *Nature* **430**, 329–332 (2004).
5. A. R. Stegner et al., *Nat. Phys.* **2**, 835–838 (2006).
6. F. H. L. Koppens et al., *Nature* **442**, 766–771 (2006).
7. J. J. Pla et al., *Nature* **489**, 541–545 (2012).
8. J. T. Muhonen et al., *Nat. Nanotechnol.* **9**, 986–991 (2014).
9. S. Thiele et al., *Science* **344**, 1135–1138 (2014).
10. A. J. Heinrich, J. A. Gupta, C. P. Lutz, D. M. Eigler, *Science* **306**, 466–469 (2004).
11. N. Tsukahara et al., *Phys. Rev. Lett.* **102**, 167203 (2009).
12. M. Julliere, *Phys. Lett. A* **54**, 225–226 (1975).
13. R. Wiesendanger, *Rev. Mod. Phys.* **81**, 1495–1550 (2009).
14. S. Loth, C. P. Lutz, A. J. Heinrich, *New J. Phys.* **12**, 125021 (2010).

15. Y. Manassen, R. J. Hamers, J. E. Demuth, A. J. Castellano Jr., *Phys. Rev. Lett.* **62**, 2531–2534 (1989).
16. Y. Manassen, I. Mukhopadhyay, N. Rao, *Phys. Rev. B* **61**, 16223–16228 (2000).
17. C. Durkan, M. E. Welland, *Appl. Phys. Lett.* **80**, 458 (2002).
18. A. V. Balatsky, M. Nishijima, Y. Manassen, *Adv. Phys.* **61**, 117–152 (2012).
19. S. Müllegger *et al.*, *Phys. Rev. Lett.* **113**, 133001 (2014).
20. Supplementary materials are available on Science Online.
21. S. Baumann *et al.*, Interplay between orbital magnetic moment and crystal field symmetry: Fe atoms on MgO. Available at <http://arxiv.org/abs/1506.07807> (2015).
22. B. Chilian *et al.*, *Phys. Rev. B* **84**, 212401 (2011).
23. I. G. Rau *et al.*, *Science* **344**, 988–992 (2014).
24. A. Kiel, W. B. Mims, *Phys. Rev.* **153**, 378–385 (1967).
25. R. E. George, J. P. Edwards, A. Ardavan, *Phys. Rev. Lett.* **110**, 027601 (2013).
26. F. Dolde *et al.*, *Nat. Phys.* **7**, 459–463 (2011).
27. A. Laucht *et al.*, *Sci. Adv.* **1**, e1500022 (2015).
28. S. Loth, M. Etzkorn, C. P. Lutz, D. M. Eigler, A. J. Heinrich, *Science* **329**, 1628–1630 (2010).

ACKNOWLEDGMENTS

We thank B. Melior for expert technical assistance and B. A. Jones, S. Gangopadhyay, and R. M. Macfarlane for fruitful discussions. We

gratefully acknowledge financial support from the Office of Naval Research. W.P. thanks the Natural Sciences and Engineering Research Council of Canada for fellowship support.

SUPPLEMENTARY MATERIALS

www.sciencemag.org/content/350/6259/417/suppl/DC1
Supplementary Text

Figs. S1 to S13

Table S1

References (29, 30)

27 June 2015; accepted 18 September 2015

10.1126/science.aac8703

QUANTUM OPTICS

Direct sampling of electric-field vacuum fluctuations

C. Riek, D. V. Seletskiy, A. S. Moskalenko, J. F. Schmidt, P. Krauspe, S. Eckart, S. Eggert, G. Burkard, A. Leitenstorfer*

The ground state of quantum systems is characterized by zero-point motion. This motion, in the form of vacuum fluctuations, is generally considered to be an elusive phenomenon that manifests itself only indirectly. Here, we report direct detection of the vacuum fluctuations of electromagnetic radiation in free space. The ground-state electric-field variance is inversely proportional to the four-dimensional space-time volume, which we sampled electro-optically with tightly focused laser pulses lasting a few femtoseconds. Subcycle temporal readout and nonlinear coupling far from resonance provide signals from purely virtual photons without amplification. Our findings enable an extreme time-domain approach to quantum physics, with nondestructive access to the quantum state of light. Operating at multiterahertz frequencies, such techniques might also allow time-resolved studies of intrinsic fluctuations of elementary excitations in condensed matter.

Vacuum fluctuations give rise to a variety of phenomena, from spontaneous photon emission (1, 2) and the Lamb shift (3) via the Casimir force (4) to cosmological perturbations (5, 6). Representing the ground state, the quantum vacuum does not possess intensity. However, finite noise amplitudes of electric and magnetic fields should exist because of Heisenberg's uncertainty principle. These fluctuations are best explained by analogy with a harmonic oscillator of mass m , resonance angular frequency Ω , and total energy

$$H_{\text{HO}} = \frac{1}{2} \left(\frac{p^2}{m} + m\Omega^2 x^2 \right) = \frac{m}{2} (\dot{x}^2 + \Omega^2 x^2) \quad (1)$$

Quantization results in noncommuting operators for momentum p and displacement x . The Gaussian wave function of the ground state exhibits a root-mean-square (RMS) standard deviation of $\Delta x = (\hbar/2m\Omega)^{1/2}$ (7, 8), where \hbar is the reduced Planck constant. The total energy of a radiation field of wavevector \mathbf{k} in free space, with electric

and magnetic amplitudes E and B (respectively), and vector potential \mathbf{A} in the Coulomb gauge is (9)

$$H_{\text{RF}} = \frac{\epsilon_0 V}{2} (E^2 + c^2 B^2) = \frac{\epsilon_0 V}{2} (\dot{\mathbf{A}}^2 + c^2 |\mathbf{k} \times \mathbf{A}|^2) \quad (2)$$

Considering one polarization direction and the transverse character of electromagnetic waves, Eq. 1 maps onto Eq. 2 by replacing x with A (amplitude of vector potential \mathbf{A}), m with $\epsilon_0 V$ (ϵ_0 , vacuum permittivity; V , spatial volume), and Ω with $ck \equiv \Omega$ (c , speed of light; $k = |\mathbf{k}|$). Instead of x and p , an uncertainty product now links E and B or the amplitudes and phases of E , B , or A . An RMS amplitude of vacuum fluctuations $\Delta A = (\hbar/2\Omega\epsilon_0 V)^{1/2}$ results. In contrast to the mechanical case where Δx is known, understanding ΔA is less straightforward: Outside any cavities, there are no obvious boundaries that define a normalization volume V . This situation raises the question of whether direct measurement of the vacuum field amplitude in free space is physically meaningful and feasible.

The quantum properties of light (10) are typically analyzed either by photon correlation (11–14), homodyning (15–18), or hybrid measurements (19). In those approaches, information is averaged over multiple cycles, and accessing the vacuum state requires amplification. Femtosecond studies

still rely on pulse envelopes that vary slowly relative to the carrier frequency (20–23). In our work, we directly probed the vacuum noise of the electric field on a subcycle time scale using laser pulses lasting a few femtoseconds. In ultrabroadband electro-optic sampling (24–27), a horizontally polarized electric-field waveform (red in Fig. 1A) propagates through an electro-optic crystal (EOX), inducing a change Δn of the linear refractive index n_0 that is proportional to its local amplitude E_{THz} (Fig. 1A and fig. S1). The geometry is adjusted so that a new index ellipsoid emerges under 45° to the polarization of E_{THz} , with $n_{y'}$ and $n_{x'} = n_0 \pm \Delta n$. An ultrashort optical probe pulse at a much higher carrier frequency ν_p (green in Fig. 1A; intensity, I_p ; electric field, E_p) copropagates with E_{THz} at a variable delay time t_d . The envelope of I_p has to be on the order of half a cycle of light at the highest frequencies $\Omega/2\pi$ of E_{THz} that are detected. We used probe pulses as short as $t_p = 5.8$ fs, corresponding to less than 1.5 optical cycles at $\nu_p = 255$ THz (fig. S2). Upon passage through the EOX, the x' and y' components of E_p acquire a relative phase delay proportional to Δn and $E_{\text{THz}}(t_d)$. The final polarization state of the probe is analyzed with ellipsometry. The differential photocurrent $\Delta I/I$ is proportional to the electric field $E_{\text{THz}}(t_d)$. We used a radio-frequency lock-in amplifier (RFLA) for readout.

We adjusted for optimal conditions to measure the vacuum signal by studying classical multiterahertz transients, which were synchronized to the probe (8). In Fig. 1B, $\Delta I/I$ is plotted in red against delay time t_d . Figure 1C shows the amplitude spectrum (red) and phase deviations (blue) within $\pm\pi$, corroborating calculations (8) of an effective sampling bandwidth of $\Delta\nu = \Delta\Omega/2\pi = 66$ THz (figs. S3 and S4) around a center frequency of $\nu_c = \Omega_c/2\pi = 67.5$ THz (free-space wavelength $\lambda_c = 4.4$ μm). The electric-field amplitude $\bar{E}_{\text{THz}}(t_d)$ is calibrated using (28–30)

$$\frac{\Delta I}{I} = \sin \left(\frac{2\pi \nu_p r_{41} n_0^3 l |R(\Omega_c)|}{c} \bar{E}_{\text{THz}} \right) \approx \frac{2\pi \nu_p r_{41} n_0^3 l |R(\Omega_c)|}{c} \bar{E}_{\text{THz}} \quad (3)$$

r_{41} denotes the electro-optic coefficient, and l is the thickness of the EOX. The amplitude response $|R(\Omega_c)|$ includes the pulse duration of the probe and velocity matching to the multiterahertz phase (8). The classical field transient in Fig. 1B was

Department of Physics and Center for Applied Photonics, University of Konstanz, D-78457 Konstanz, Germany.

*Corresponding author. E-mail: alfred.leitenstorfer@uni-konstanz.de

sampled with a signal-to-noise ratio better than 10^3 at a RFLA detection bandwidth set to 94 Hz. From the confocal amplitude trace and cross section, we estimated a mean photon number below 900 per pulse. This result proves the capability of our approach to characterize ultrabroadband coherent wave packets containing less than 10^{-3} photons, on average, within 1 s.

But can we directly access the ground state Φ_0 of the radiation field? With the pump branch switched off, electro-optic phase shifts might still be caused by vacuum fluctuations copropagating with the probe. This effect should lead to a statistical distribution of the signal around the average of $\langle \bar{E}_{\text{vac}} \rangle = 0$. The ground-state expectation value of the squared operator for the

electric field in free space (31) yields the RMS amplitude

$$\begin{aligned} \Delta \bar{E}_{\text{vac}} &= \sqrt{\left\langle \Phi_0 \left| \sum_{\Omega=\Omega_c-\Delta\Omega/2}^{\Omega_c+\Delta\Omega/2} \frac{-\hbar\Omega}{2\epsilon_0 V} (\hat{a}_\Omega - \hat{a}_\Omega^\dagger)^2 \right| \Phi_0 \right\rangle} \\ &= \sqrt{\left\langle \Phi_0 \left| \sum_{\Omega=\Omega_c-\Delta\Omega/2}^{\Omega_c+\Delta\Omega/2} \frac{\hbar\Omega}{2\epsilon_0 V} (-\hat{a}_\Omega^2 + \hat{a}_\Omega \hat{a}_\Omega^\dagger + \hat{a}_\Omega^\dagger \hat{a}_\Omega - \hat{a}_\Omega^{\dagger 2}) \right| \Phi_0 \right\rangle} \\ &= \sqrt{\sum_{\nu=\nu_c-\Delta\nu/2}^{\nu_c+\Delta\nu/2} \frac{\hbar\nu}{2\epsilon_0 V}} \quad (4) \end{aligned}$$

\hat{a}_Ω and \hat{a}_Ω^\dagger are the operators for annihilation and creation of a photon with angular frequency Ω , respectively (ν , frequency; \hbar , Planck constant).

Because of the commutation relation $[\hat{a}_\Omega, \hat{a}_\Omega^\dagger] = 1$, only $\hat{a}_\Omega \hat{a}_\Omega^\dagger$ provides a nonvanishing contribution. Summing frequencies over our finite sensitivity interval ensures convergence of Eq. 4. The lateral extension of the volume V is now identified with the effective cross section A_{eff} , defined by the Gaussian intensity profile of the near-infrared probe beam inside the EOx. Theoretical modeling based on Laguerre-Gaussian modes (30) yields $A_{\text{eff}} = w_0^2 \pi$, where w_0 is the probe spot radius (8). Because $V = A_{\text{eff}} L$, only the length L remains to be determined. Periodic boundary conditions are applicable when the EOx is short relative to the Rayleigh range of the multiterahertz transverse mode, resulting in a density of free-space modes L/c . Summing over all longitudinal modes within a bandwidth of $\Delta\nu$ eliminates L , and we obtain

$$\Delta \bar{E}_{\text{vac}} = \sqrt{\frac{\hbar\nu_c \Delta\nu}{2\pi c n_0 \epsilon_0 w_0^2}} = 20.2 \frac{\text{V}}{\text{cm}} \quad (5)$$

A factor of $n_0^{-1/2}$ accounts for dielectric screening inside the EOx (8). Thus, the vacuum amplitude is maximized when averaging over a minimal space-time volume, determined in the transverse directions by $w_0 = 4.25 \mu\text{m}$ (fig. S5). The longitudinal cross section $c n_0 / (\nu_c \Delta\nu)$ is defined by the Fourier transform of $R(\Omega)$, containing the intensity envelope of the 5.8-fs probe pulse and phase-matching conditions within the EOx (8).

Are such fluctuations discernible on top of the shot noise due to the Poissonian photon statistics of the coherent probe? An average number of $N_p = 5 \times 10^8$ photons detected per pulse causes a relative RMS shot-noise current of $\Delta I_{\text{SN}}/I = N_p^{-1/2}$. With Eq. 3, we obtain the noise-equivalent field

$$\begin{aligned} \Delta E_{\text{SN}} &= \frac{c}{2\pi\nu_p r_{41} n_0^3 l \sqrt{N_p} |R(\Omega_c)|} \\ &= 65.0 \frac{\text{V}}{\text{cm}} \quad (6) \end{aligned}$$

Because the shot noise of the near-infrared probe, which is centered around ν_p , and the vacuum fluctuations at multiterahertz frequencies Ω are uncorrelated with each other and lack spectral overlap, the two contributions add up in quadrature. Therefore, the RMS width of the total detected noise distribution is expected to rise by a factor of

$$\frac{\Delta E_{\text{total}}}{\Delta E_{\text{SN}}} = \sqrt{\frac{\Delta E_{\text{SN}}^2 + \Delta \bar{E}_{\text{vac}}^2}{\Delta E_{\text{SN}}^2}} = 1.047 \quad (7)$$

corresponding to a 4.7% increase, due to the multiterahertz vacuum noise.

To experimentally access the statistics of the quantum vacuum, we extended the RFLA bandwidth to 1.6 MHz and sampled the probability distribution of the electric field $P(E_{\text{total}})$ every 5 μs . The contribution of the multiterahertz vacuum noise can be modified to discriminate against the shot-noise baseline by longitudinal or transverse expansion of the probed space-time volume (Eq. 5). In the first approach, we decreased ν_c and $\Delta\nu$ by chirping the probe pulse to 100 fs (fig. S3), via

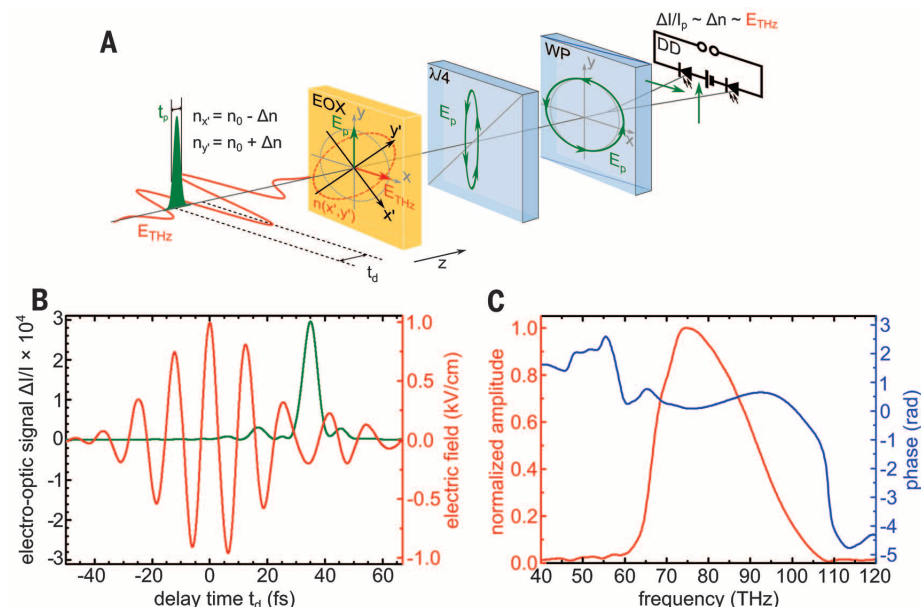


Fig. 1. Our experimental principle, with a demonstration of ultrahigh bandwidth and sensitivity. (A) Scheme of electro-optic sampling of an electric-field waveform (red) by an ultrafast probe pulse (green), consisting of an EOx, a quarter-wave plate ($\lambda/4$), a Wollaston polarizer (WP), and a differential photocurrent detector (DD). (B) Classical electro-optic signal $\Delta I/I$ and corresponding electric-field amplitude versus delay time t_d (red line). The intensity envelope of the 5.8-fs probe pulse is shown in arbitrary units for comparison (green line). (C) Spectral multiterahertz amplitude (red) and phase (blue) obtained by Fourier transform.

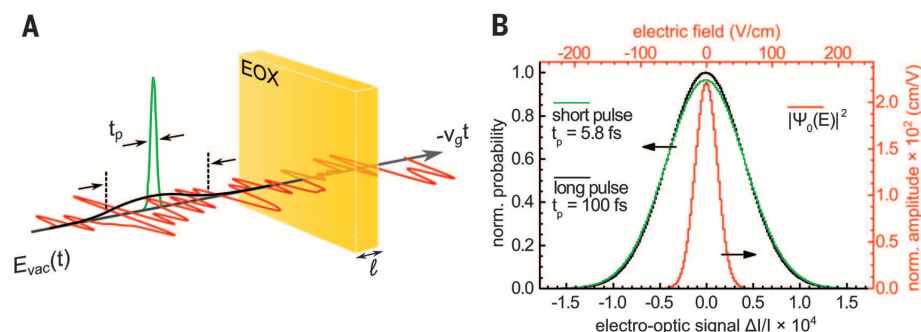


Fig. 2. Studying vacuum fluctuations via statistic readout and longitudinal modification of the probed space-time volume. (A) Diagram showing longitudinal expansion of the probe volume: Stretching the sampling pulse from 5.8 fs (green) to 100 fs (black) causes temporal averaging over the vacuum field (red), leading to a reduction of the detected noise amplitude (t_p , pulse duration; v_g , group velocity). (B) Normalized counting probability as a function of electro-optic readout by the short pulse (green) and long pulse (stretched to 100 fs; black). The deconvolved wave function $|\Psi_0|^2$ of the electric-field ground state is shown in red.

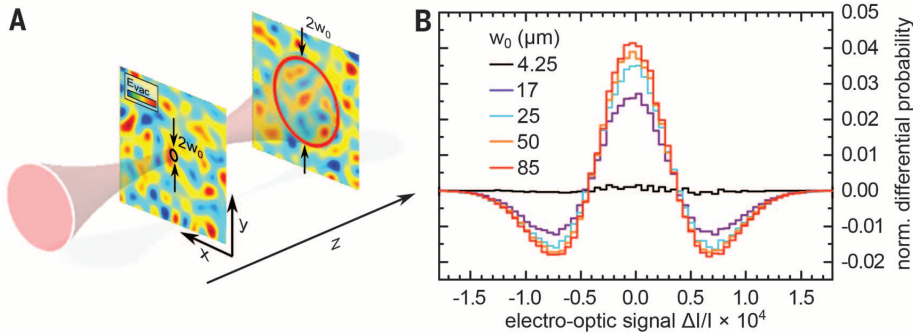


Fig. 3. Detection by transverse expansion of the space-time segment. (A) Sketch showing the lateral increase of the sampling cross section, which leads to averaging over noise patterns within the circled areas. (B) Differential histograms obtained by subtracting the result for the confocal detector position with $w_0 = 4.25 \mu\text{m}$ from the results for positions with the beam diameter at $4.25 \mu\text{m}$ (black), $17 \mu\text{m}$ (purple), $25 \mu\text{m}$ (cyan), $50 \mu\text{m}$ (orange), and $85 \mu\text{m}$ (red).

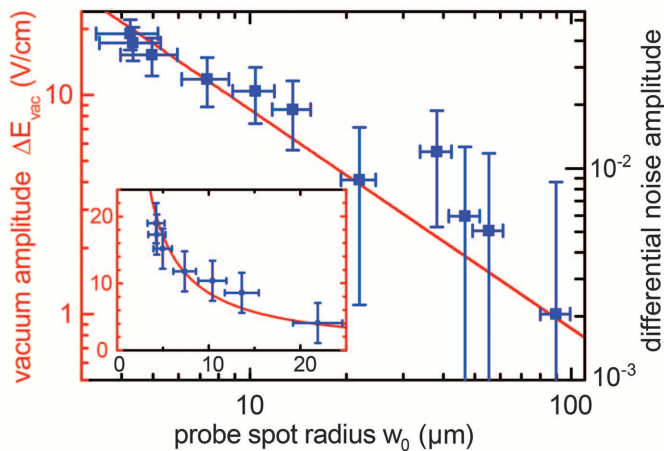


Fig. 4. Dependence of the vacuum amplitude on transverse extension of the probed space-time volume. Relative excess noise of electro-optic signal $\Delta I/I$ (right vertical axis) and RMS vacuum amplitude ΔE_{vac} (left vertical axis) versus probe radius w_0 (blue squares). Red lines represent a theoretical assessment based on Eq. 5.

translation of an SF10 prism in the compressor stage (Fig. 2A). A distinct reduction in peak counts around $P(E_{\text{total}} = 0)$ is observed when comparing the probability distribution obtained with the 5.8-fs probe (green in Fig. 2B) to the measurement with a stretched pulse (black). Also, the probabilities in the wings of the distribution including the multiterahertz vacuum (5.8-fs probe) are consistently higher than the corresponding values in the stretched-pulse distribution. The total change of the normalized noise amplitude amounts to 4%, in good agreement with the theoretical considerations underlying Eqs. 5 to 7. The red histogram in Fig. 2B emerges from a deconvolution algorithm that searches for the best link between distributions of $P(E_{\text{total}})$ obtained with and without vacuum noise. This result directly mirrors the ground-state wave function $|\Psi_0(E)|^2$ of the electromagnetic field in the polarization plane and space-time volume that we probed. From $|\Psi_0(E)|^2$, a RMS standard deviation of $\Delta \vec{E}_{\text{vac}} = 18 \text{ V/cm}$ is obtained, in good agreement with the theoretical prediction of 20.2 V/cm in Eq. 5.

In the transverse option, we kept the short pulse duration and expanded the probe radius w_0 by

translating the EOX out of the confocal plane (Fig. 3A). Averaging over a larger cross section causes a decrease in fluctuation amplitude, which is projected onto the transverse mode of the gate. The effect of progressive narrowing is emphasized with differential probabilities obtained by subtracting a distribution at $w_0 = 4.25 \mu\text{m}$ from $P(E_{\text{total}})$ sampled at increasing spot radii (Fig. 3B). When all original histograms are normalized, the maximum change in probability $\Delta P(E_{\text{total}} = 0)$ of $0.04 \equiv 4\%$ directly corresponds to the difference between the relative noise amplitudes measured with and without multiterahertz vacuum fluctuations, in quantitative agreement with Eq. 7. The dependence of the vacuum RMS amplitude on the transverse extension of the probed space-time volume is shown in Fig. 4. The normalized increase of total noise, measured with respect to bare shot noise (right vertical axis), is plotted against the probe spot radius w_0 (blue squares). Conversion to the vacuum electric amplitude ΔE_{vac} (left vertical axis) has been carried out analogously to $|\Psi_0(E)|^2$ in Fig. 2B. The functional dependence expected from Eq. 5 is shown as a red line. The inset in Fig. 4 illustrates the data recorded at low beam cross sections on a

linear scale to highlight the hyperbolic increase of vacuum fluctuations for the smaller space-time volumes that we probed.

In our study, we directly monitored vacuum fluctuations without amplifying them. The only effective part $\sum_{\Omega>0} \hat{a}_{\Omega} \hat{a}_{\Omega}^{\dagger}$ of the operator that extracts the variance of the field in Eq. 4 indicates that vacuum fluctuations correspond to photons, which spontaneously arise and vanish in the ground state Φ_0 . Time-energy uncertainty demands that virtual excitations have a limited lifetime on the order of their oscillation cycle (32). The subcycle temporal resolution provided by the ultrashort probe ensures that we can directly detect effects originating from purely virtual photons. Phase-matched copropagation of the vacuum field and probe inside the EOX maximizes those signals. But does this measurement influence the quantum vacuum at all? Based on the electro-optic change of the refractive index $\Delta n_p \sim r_{41} E_{\text{THz}}$, the local multiterahertz field imprints a phase shift onto the ultrashort probe, which we detected. Because sum- and difference-frequency mixing occur simultaneously in this process (29), it requires no net transfer of energy, momentum, or angular momentum, and it even avoids modulation of the refractive index at frequencies $\Omega/2\pi \ll \nu_p$. Our second-order nonlinear element operates far from resonance. Virtual driving of the transitions avoids problems with decoherence, distinguishing our experiment from detection approaches in quantum optics or circuit quantum electrodynamics in which resonant two-level systems are involved (33). In consequence, our approach may be used to study the multiterahertz ground state while imposing negligible influence on it. Back-action might arise only in third order: The nonlinear refractive index n_2 generates a local anomaly of phase velocity copropagating with the intensity envelope of the probe, because $\Delta n_2 \sim n_2 |E_p|^2$. When $N_p/w_0^2 t_p$ suffices to induce phase shifts of the multiterahertz field during passage through the EOX, depletion of the vacuum amplitude in the sampled space-time volume and enhanced fluctuations in an adjacent interval are expected.

REFERENCES AND NOTES

- W. Vogel, D.-G. Welsch, *Quantum Optics* (Wiley-VCH, Weinheim, Germany, ed. 3, 2006).
- D. F. Walls, G. J. Milburn, *Quantum Optics* (Springer-Verlag, Berlin, ed. 2, 2008).
- W. E. Lamb Jr., R. C. Retherford, *Phys. Rev.* **72**, 241–243 (1947).
- H. Casimir, *Proc. Kon. Ned. Akad. Wetensch.* **B 51**, 793–795 (1948).
- E. P. Tryon, *Nature* **246**, 396–397 (1973).
- V. F. Mukhanov, H. A. Feldman, R. H. Brandenberger, *Phys. Rep.* **215**, 203–333 (1992).
- F. Schwabl, *Quantum Mechanics* (Springer-Verlag, Berlin, ed. 4, 2007).
- Materials and methods are available as supplementary materials on Science Online.
- J. D. Jackson, *Classical Electrodynamics* (Wiley, New York, ed. 3, 1999).
- I. A. Walmsley, *Science* **348**, 525–530 (2015).
- R. Hanbury Brown, R. Q. Twiss, *Nature* **177**, 27–29 (1956).
- H. J. Kimble, M. Dagenais, L. Mandel, *Phys. Rev. Lett.* **39**, 691–695 (1977).
- P. Michler et al., *Nature* **406**, 968–970 (2000).
- B. Lounis, W. E. Moerner, *Nature* **407**, 491–493 (2000).

15. R. E. Slusher, L. W. Hollberg, B. Yurke, J. C. Mertz, J. F. Valley, *Phys. Rev. Lett.* **55**, 2409–2412 (1985).
16. L.-A. Wu, H. J. Kimble, J. L. Hall, H. Wu, *Phys. Rev. Lett.* **57**, 2520–2523 (1986).
17. D. T. Smithey, M. Beck, M. G. Raymer, A. Faridani, *Phys. Rev. Lett.* **70**, 1244–1247 (1993).
18. A. I. Lvovsky *et al.*, *Phys. Rev. Lett.* **87**, 050402 (2001).
19. N. B. Grosse, T. Symul, M. Stobiriska, T. C. Ralph, P. K. Lam, *Phys. Rev. Lett.* **98**, 153603 (2007).
20. A. M. Fox, J. J. Baumberg, M. Dabbicco, B. Huttner, J. F. Ryan, *Phys. Rev. Lett.* **74**, 1728–1731 (1995).
21. M. E. Anderson, M. Beck, M. G. Raymer, J. D. Bierlein, *Opt. Lett.* **20**, 620–622 (1995).
22. C. Silberhorn *et al.*, *Phys. Rev. Lett.* **86**, 4267–4270 (2001).
23. P. J. Mosley *et al.*, *Phys. Rev. Lett.* **100**, 133601 (2008).
24. Q. Wu, X.-C. Zhang, *Appl. Phys. Lett.* **71**, 1285–1286 (1997).
25. A. Leitenstorfer, S. Hunsche, J. Shah, M. C. Nuss, W. H. Knox, *Appl. Phys. Lett.* **74**, 1516–1518 (1999).
26. K. Liu, J. Z. Xu, X.-C. Zhang, *Appl. Phys. Lett.* **85**, 863–865 (2004).
27. C. Kübler, R. Huber, S. Tübel, A. Leitenstorfer, *Appl. Phys. Lett.* **85**, 3360–3362 (2004).
28. S. Namba, *J. Opt. Soc. Am.* **51**, 76–79 (1961).
29. G. Gallot, D. Grischkowsky, *J. Opt. Soc. Am. B* **16**, 1204–1212 (1999).
30. A. S. Moskalenko, C. Riek, D. V. Seletskiy, G. Burkard, A. Leitenstorfer, <http://arxiv.org/abs/1508.06953> (2015).
31. R. Loudon, P. L. Knight, *J. Mod. Opt.* **34**, 709–759 (1987).
32. C. Fürst, A. Leitenstorfer, A. Laubereau, R. Zimmermann, *Phys. Rev. Lett.* **78**, 3733–3736 (1997).
33. A. A. Clerk, M. H. Devoret, S. M. Girvin, F. Marquardt, R. J. Schoelkopf, *Rev. Mod. Phys.* **82**, 1155–1208 (2010).

ACKNOWLEDGMENTS

Support by the European Research Council (Advanced Grant 290876 “UltraPhase”), by Deutsche Forschungsgemeinschaft (SFB767), and by NSF via a postdoctoral fellowship for D.V.S. (award no. 1160764) is gratefully acknowledged.

SUPPLEMENTARY MATERIALS

www.sciencemag.org/content/350/6259/420/suppl/DC1
Materials and Methods
Figs. S1 to S5
References (34–40)

8 July 2015; accepted 16 September 2015
Published online 1 October 2015
10.1126/science.aac9788

ASTEROSEISMOLOGY

Asteroseismology can reveal strong internal magnetic fields in red giant stars

Jim Fuller,^{1,2,*†} Matteo Cantiello,^{2,*†} Dennis Stello,^{3,4} Rafael A. Garcia,⁵ Lars Bildsten^{2,6}

Internal stellar magnetic fields are inaccessible to direct observations, and little is known about their amplitude, geometry, and evolution. We demonstrate that strong magnetic fields in the cores of red giant stars can be identified with asteroseismology. The fields can manifest themselves via depressed dipole stellar oscillation modes, arising from a magnetic greenhouse effect that scatters and traps oscillation-mode energy within the core of the star. The Kepler satellite has observed a few dozen red giants with depressed dipole modes, which we interpret as stars with strongly magnetized cores. We find that field strengths larger than $\sim 10^5$ gauss may produce the observed depression, and in one case we infer a minimum core field strength of $\approx 10^7$ gauss.

Despite rapid progress in the discovery and characterization of magnetic fields at the surfaces of stars, very little is known about internal stellar magnetic fields. This has prevented the development of a coherent picture of stellar magnetism and the evolution of magnetic fields within stellar interiors.

After exhausting hydrogen in their cores, most main sequence stars evolve up the red giant branch (RGB). During this phase, the stellar structure is characterized by an expanding convective envelope and a contracting radiative core. Acoustic waves (p modes) in the envelope can

couple to gravity waves (g modes) in the core (1). Consequently, nonradial stellar oscillation modes become mixed modes that probe both the envelope (the p-mode cavity) and the core (the g-mode cavity), as illustrated in Fig. 1. Mixed modes (2) have made it possible to distinguish between hydrogen- and helium-burning red giants (3, 4) and have been used to measure the rotation rate of red giant cores (5, 6).

A group of red giants with depressed dipole modes were identified using observations from the Kepler satellite [(7), see also Fig. 2]. These stars show normal radial modes (spherical harmonic degree $\ell = 0$) but exhibit dipole ($\ell = 1$) modes whose amplitude is much lower than usual. Until now, the suppression mechanism was unknown (8). Below, we demonstrate that dipole mode suppression may result from strong magnetic fields within the cores of these red giants.

Red giant oscillation modes are standing waves that are driven by stochastic energy input from turbulent near-surface convection (9, 10). Waves excited near the stellar surface propagate downward as acoustic waves until their angular frequency ω is less than the local Lamb frequency for waves of angular degree ℓ ; i.e., until $\omega = L_\ell = \sqrt{\ell(\ell+1)}v_s/r$, where v_s is the local sound speed and r is the radial coordinate. At this bound-

dary, part of the wave flux is reflected, and part of it tunnels into the core.

The wave resumes propagating inward as a gravity wave in the radiative core where $\omega < N$, where N is the local buoyancy frequency. In normal red giants, wave energy that tunnels into the core eventually tunnels back out to produce the observed oscillation modes. We show here that suppressed modes can be explained if wave energy leaking into the core never returns back to the stellar envelope.

The degree of wave transmission between the core and envelope is determined by the tunneling integral through the intervening evanescent zone. The transmission coefficient is

$$T \sim \left(\frac{r_1}{r_2} \right)^{\sqrt{\ell(\ell+1)}} \quad (1)$$

where r_1 and r_2 are the lower and upper boundaries of the evanescent zone, respectively. The fraction of wave energy transmitted through the evanescent zone is T^2 . For waves of the same frequency, larger values of ℓ have larger values of r_2 , thus Eq. 1 demonstrates that high ℓ waves have much smaller transmission coefficients through the evanescent zone.

The visibility of stellar oscillations depends on the interplay between driving and damping of the modes (10, 11). To estimate the reduced mode visibility due to energy loss in the core, we assume that all mode energy that leaks into the g-mode cavity is completely lost. The mode then loses a fraction T^2 of its energy in a time $2t_{\text{cross}}$, where t_{cross} is the wave crossing time of the acoustic cavity. Due to the larger energy loss rate, the mode has less energy E_{ac} within the acoustic cavity and produces a smaller luminosity fluctuation V at the stellar surface, whose amplitude scales as $V^2 E_{\text{ac}}$. We show (12) that the ratio of visibility between a suppressed mode V_{sup} and its normal counterpart V_{norm} is

$$\frac{V_{\text{sup}}^2}{V_{\text{norm}}^2} = [1 + \Delta\nu \tau T^2]^{-1} \quad (2)$$

where $\Delta\nu \approx (2t_{\text{cross}})^{-1}$ (13) is the large frequency separation between acoustic overtone modes, and τ is the damping time of a radial mode with similar frequency. We evaluate T^2 from our stellar models using Eq. 6, whereas $\tau \approx 5$ to 10 days (10, 14–16) for stars ascending the RGB.

¹TAPIR, Walter Burke Institute for Theoretical Physics, Mailcode 350-17 California Institute of Technology, Pasadena, CA 91125, USA. ²Kavli Institute for Theoretical Physics, University of California, Santa Barbara, CA 93106, USA. ³Sydney Institute for Astronomy, School of Physics, University of Sydney, New South Wales 2006, Australia. ⁴Stellar Astrophysics Centre, Department of Physics and Astronomy, Aarhus University, Ny Munkegade 120, DK-8000 Aarhus C, Denmark. ⁵Laboratoire Astrophysique Interactions Multi-échelles, Commissariat à l’Énergie Atomique/Direction des Sciences de la Matière, CNRS, Université Paris Diderot, Institut de Recherches sur les lois Fondamentales de l’Univers/Service d’Astrophysique Centre de Saclay, 91191 Gif-sur-Yvette Cedex, France. ⁶Department of Physics, University of California, Santa Barbara, CA 93106, USA.

*Corresponding author. E-mail: jfuller@caltech.edu (J.F.); matteo@kitp.ucsb.edu (M.C.). †These authors contributed equally to this work.

Most observed modes are near the frequency ν_{\max} , which is determined by the evolutionary state of the star. On the RGB, more-evolved stars generally have smaller ν_{\max} . Figure 2 compares our estimate for suppressed dipole mode visibility (Eq. 2) with Kepler observations (7, 8). The objects identified by (7) as depressed dipole mode stars lie very close to our estimate. The striking agreement holds over a large baseline in ν_{\max} extending from the very early red giants KIC8561221 (8) and KIC9073950 at high ν_{\max} to near the luminosity bump at low ν_{\max} . The observations are consistent with nearly total wave energy loss in the core, because partial energy loss would create stars with less-depressed modes, which seem to be rare.

We conclude that the cores of stars with depressed dipole modes efficiently trap or disrupt waves tunneling through the evanescent region. This is further supported by their normal $\ell = 0$ mode visibility, because radial modes do not propagate within the inner core, and because much larger field strengths are required to alter acoustic waves. The absence (or perhaps smaller degree) of depression observed for $\ell = 2$ modes (7) occurs because quadrupole modes have a smaller transmission coefficient T , and less of their energy leaks into the core.

An additional consequence is that the larger effective damping rate for depressed modes will lead to larger linewidths in the oscillation power spectrum. The linewidth of a depressed dipole mode is $\tau^{-1} + \Delta\nu T_{\ell}^2$ and is generally much larger than that of a normal mode. The depressed dipole modes in KIC8561221 (8) indeed have much larger linewidths than normal dipole modes in similar stars.

Magnetic fields can provide the mechanism for trapping oscillation mode energy in the core by altering gravity wave propagation. The nearly horizontal motions and short radial wavelengths of gravity waves in RGB cores will bend radial magnetic field lines, creating strong magnetic tension forces. The acceleration required to restore a wave of angular frequency ω and horizontal displacement ξ_h is $\xi_h \omega^2$, whereas the magnetic tension acceleration due to a radial magnetic field of strength B_r is $\xi_h B_r^2 k_r^2 / (4\pi\rho)$, where k_r is the radial wavenumber and ρ is the density. Gravity waves are strongly altered by the magnetic fields when the magnetic tension force dominates, which for dipole waves occurs at a critical magnetic field strength (12)

$$B_c = \sqrt{\frac{\pi\rho}{2}} \frac{\omega^2 r}{N} \quad (3)$$

This field strength approximately corresponds to the point at which the Alfvén speed becomes larger than the radial group velocity of gravity waves.

Magneto-gravity waves cannot exist in regions with $B_r > B_c$, where magnetic tension overwhelms the buoyancy force; i.e., the stiff field lines cannot be bent by the placid gravity wave motion. Consequently, dipole magneto-gravity waves become evanescent when $\omega < \omega_{\text{MG}}$,

where the magneto-gravity frequency ω_{MG} is defined as

$$\omega_{\text{MG}} = \left[\frac{2 B_r^2 N^2}{\pi \rho r^2} \right]^{1/4} \quad (4)$$

Figure 3 shows a wave propagation diagram in which a strong internal magnetic field prevents magneto-gravity wave propagation in the core.

Fig. 1. Wave propagation in red giants with magnetized cores.

Acoustic waves excited in the envelope couple to gravity waves in the radiative core. In the presence of a magnetic field in the core, the gravity waves are scattered at regions of high field strength. Because the field cannot be spherically symmetric, the waves are scattered to high angular degree ℓ and become trapped within the core, where they eventually dissipate (dashed wave with arrow). We refer to this as the magnetic greenhouse effect.

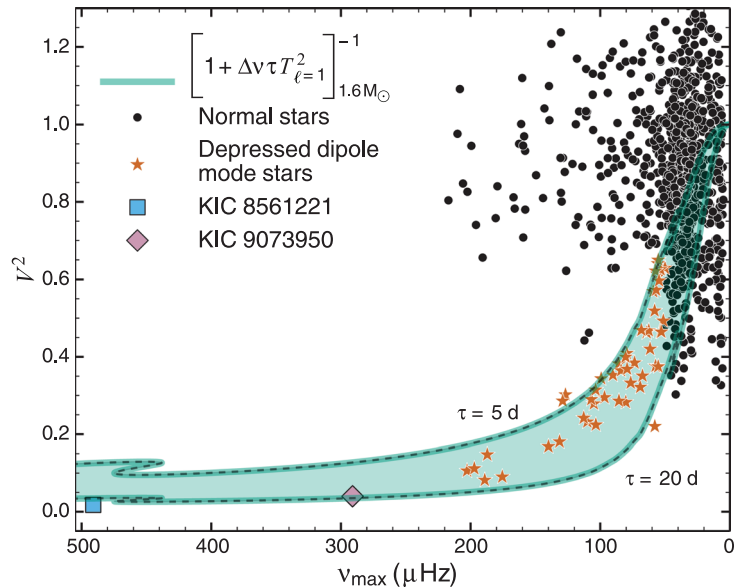
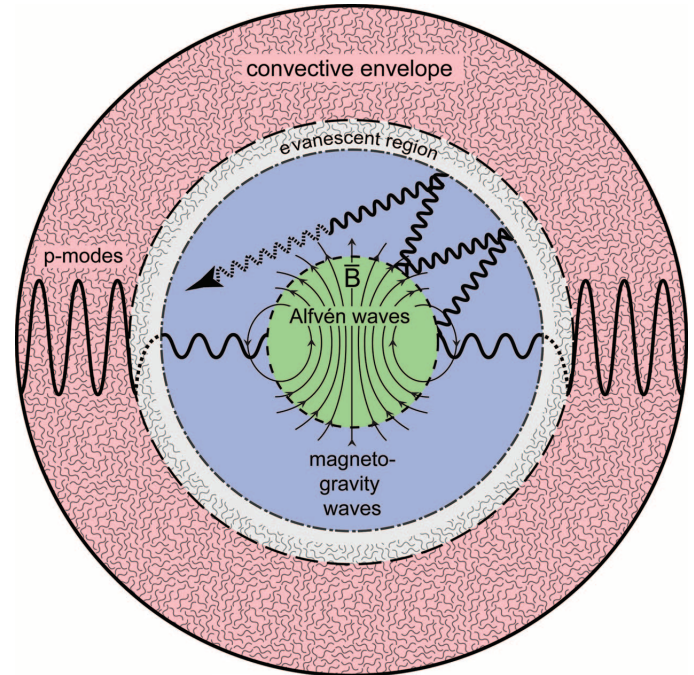


Fig. 2. Normalized visibility of dipolar modes as a function of ν_{\max} . The star and circle symbols represent the observed visibility V^2 of $\ell = 1$ modes (12). The data are taken from (7) and divided by 1.54, so that in normal oscillators, the average visibility is $V^2 = 1$ (22). Stars with depressed dipole modes (orange stars) are identified following the same criteria as in (7). The theoretical band shows the visibility of depressed dipole modes in a $1.6 M_{\odot}$, where M_{\odot} is the mass of the sun, star, as predicted by Eq. 2, and is quite insensitive to the mass of the model. The visibility of the depressed dipoles in KIC 8561221 (8) and KIC 9073950 is also shown (square and diamond symbols, respectively). We used values for τ in the range of 5 to 20 days, consistent with (10, 16).

Fig. 3. Propagation diagram for a magnetized red giant model. The model has $M = 1.6 M_{\odot}$, $R = 6.6 R_{\odot}$, $\nu_{\max} = 120 \mu\text{Hz}$, and a core magnetic field of $\approx 6 \times 10^6 \text{ G}$ (fig. S1).

(A) The red, blue, and green lines are the dipole Lamb frequency L_1 , the buoyancy frequency N , and the magneto-gravity frequency ω_{MG} (defined in Eq. 4), respectively. Regions are colored by the types of waves they support: The red region is the acoustic wave cavity, the blue region is the magneto-gravity wave cavity, and the green region hosts only Alfvén waves. The horizontal line is the frequency of maximum power, ν_{\max} , for this stellar model. Waves at this frequency behave like acoustic waves near the surface, magneto-gravity waves in the outer core, and Alfvén waves in the inner core. (B) Critical radial magnetic field strength B_c needed to suppress dipole modes. B_c (Eq. 3) is evaluated at the angular frequency $\omega = 2\pi\nu_{\max}$. B_c has a sharp minimum at the H-burning shell, which determines the minimum field strength $B_{c,\min}$ required for dipole mode suppression.

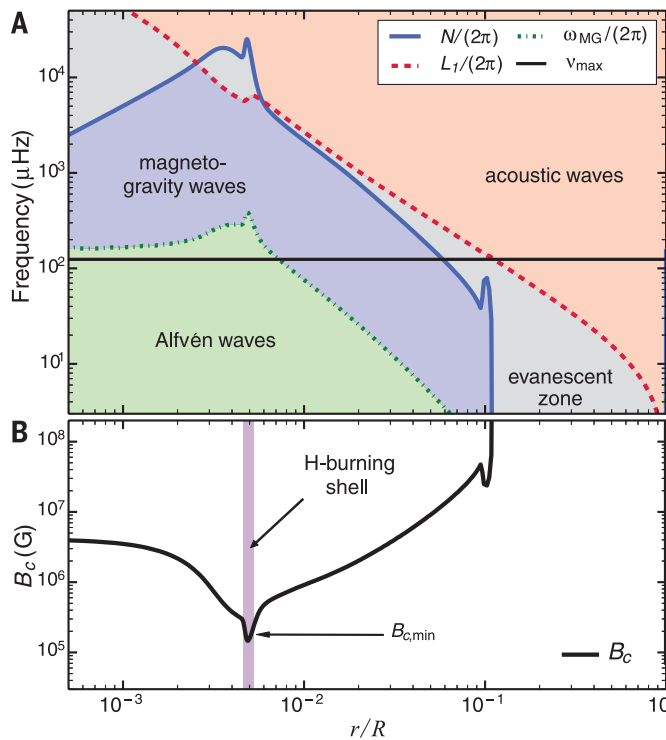
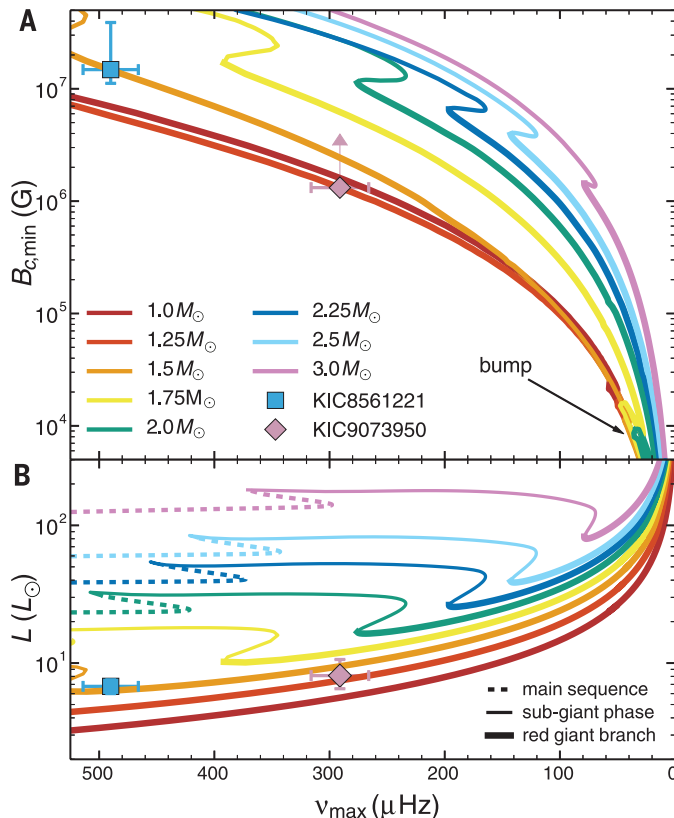


Fig. 4. Minimum field strength $B_{c,\min}$ required for magnetic suppression of dipole oscillation modes in stars evolving up the RGB. (A) $B_{c,\min}$ is shown as a function of the frequency of maximum power, ν_{\max} , for stars of different mass. L , luminosity; L_{\odot} , luminosity of the Sun. $B_{c,\min}$ has been computed for modes with angular frequency $\omega = 2\pi\nu_{\max}$. We have labeled the observed value of ν_{\max} and inferred core field strength B_r for the lower RGB star KIC8561221 (8) and a lower limit to the field strength in KIC9073950. (B) Asteroseismic HR diagram showing stellar evolution tracks over the same range in ν_{\max} . Stars evolve from left to right as they ascend the RGB. Dashed lines show the end of main sequence evolution, thin solid lines are the sub-giant phase, and thick solid lines are the RGB. We do not show any evolution beyond the RGB (i.e., no clump or asymptotic giant branch).



suppression via horizontal fields can also occur, but in general requires much larger field strengths.

In stars with field strengths exceeding B_c (Eq. 3) somewhere in their core, incoming dipole gravity waves will become evanescent where $B_r > B_c$. At this point, the waves must either reflect or be transmitted into the strongly magnetized region as Alfvén waves. In either case, the reflection/transmission process modifies the angular structure of the waves so that their energy is spread over a broad spectrum of ℓ values (12). Once a dipole wave has its energy transferred to higher values of ℓ , it will not substantially contribute to observable oscillations at the stellar surface, because higher- ℓ waves are trapped within the radiative core by a thicker evanescent region (Eq. 1 and Fig. 1) separating the core from the envelope. Even if some wave energy does eventually return to the surface to create an oscillation mode, the increased time spent in the core results in a very large mode inertia, greatly reducing the mode visibility. Additionally, high- ℓ waves will not be detected in Kepler data because of the geometric cancellation, which makes $\ell > 3$ modes nearly invisible (17).

The magnetic greenhouse effect arises not from the alteration of incoming wave frequencies but rather from modification of the wave angular structure. Such angular modification originates from the inherently nonspherical structure of even the simplest magnetic field configurations.

Dipole oscillation modes can be suppressed if the magnetic field strength exceeds B_c (Eq. 3) at some point within the core. We therefore posit that stars with depressed dipole oscillation modes have minimum core field strengths of $B_{c,\min}$. Stars with normal dipole oscillation modes cannot have radial field strengths in excess of $B_{c,\min}$ within their H-burning shells. However, they may contain larger fields away from the H-burning shell, or they may contain fields that are primarily horizontal (e.g., strong toroidal fields).

Figure 4 shows the value of $B_{c,\min}$ as stars evolve up the RGB. We have calculated $B_{c,\min}$ for angular frequencies $\omega = 2\pi\nu_{\max}$ and evaluated ν_{\max} using the scaling relation proposed by (18). On the lower RGB, where $\nu_{\max} \geq 250 \mu\text{Hz}$, field strengths on the order of $B_{c,\min} \geq 10^6 \text{ G}$ are required for magnetic suppression. As stars evolve up the RGB, the value of $B_{c,\min}$ decreases sharply, primarily because ν_{\max} decreases. By the luminosity bump (near $\nu_{\max} \sim 40 \mu\text{Hz}$), field strengths of only $B_{c,\min} \sim 10^4 \text{ G}$ are sufficient for magnetic suppression. Magnetic suppression during the sub-giant phase (higher ν_{\max}) and in higher-mass stars ($M \geq 2 M_{\odot}$) may be less common due to the larger field strengths required.

For a given field strength, there is a transition frequency ν_c below which modes will be strongly suppressed and above which modes will appear normal. Stars that show this transition are especially useful because they allow for an inference of B_r at the H-burning shell via Eq. 3, evaluated at the transition frequency $\omega = 2\pi\nu_c$. The RGB star KIC8561221 shows this transition (8). Using the observed value of $\nu_c \approx 600 \mu\text{Hz}$, we infer that the radial component of the magnetic field

within the H-burning shell is $B_r \approx 1.5 \times 10^7$ G, although we cannot rule out the presence of stronger fields away from the H-burning shell. This large field strength may indicate that KIC8561221 is the descendant of a magnetic A-type star whose internal field was much stronger than the typical surface fields of $B \sim 3$ kG of A-type stars (19).

In principle, it is possible that another symmetry-breaking mechanism within the core could suppress dipole mode amplitudes. The only other plausible candidate is rapid core rotation. In order for rotation to strongly modify the incoming waves so that they will be trapped in the core, the core must rotate at a frequency comparable to ν_{max} , roughly two orders of magnitude faster than the values commonly measured in red giant cores (2, 6, 20). The depressed dipole mode star KIC8561221 (8) does not exhibit rapid core rotation and disfavors the rotation scenario.

A magnetic field of amplitude $B > 10^4$ G (Fig. 4) could be present in the core of a red giant if it was retained from previous phases of stellar formation and evolution (12). These strong fields may reside within the inner core with little external manifestation apart from the reduced visibility of the dipole modes. However, fields of similar amplitude have been discussed in order to explain the suppression of thermohaline mixing in a small fraction of red giant stars, as inferred from the observations of their surface abundances (21). The inferred core field strength of $B_r \gtrsim 1.5 \times 10^7$ G in KIC8561221 shows that very strong magnetic fields ($B \gg 10^6$ G) can exist within the radiative cores of early RGB stars. Because these fields are probably inherited from previous stages of stellar evolution, slightly weaker ($B \gg 10^5$ G) fields could exist in the cores of exceptional very highly magnetized main sequence stars.

REFERENCES AND NOTES

1. T. R. Bedding, *Solar-like Oscillations: An Observational Perspective* (Cambridge Univ. Press, Cambridge, 2014).
2. P. G. Beck et al., *Science* **332**, 205 (2011).
3. T. R. Bedding et al., *Nature* **471**, 608–611 (2011).
4. B. Mosser et al., *Astron. Astrophys.* **572**, L5 (2014).
5. P. G. Beck et al., *Nature* **481**, 55–57 (2011).
6. B. Mosser et al., *Astron. Astrophys.* **548**, A10 (2012).
7. B. Mosser et al., *Astron. Astrophys.* **537**, A30 (2012).
8. R. A. García et al., *Astron. Astrophys.* **563**, A84 (2014).
9. P. Goldreich, D. A. Keeley, *Astrophys. J.* **212**, 243 (1977).
10. M.-A. Dupret et al., *Astron. Astrophys.* **506**, 57–67 (2009).
11. O. Benomar et al., *Astrophys. J.* **781**, L29 (2014).
12. See the supplementary materials on Science Online.
13. W. J. Chaplin, A. Miglio, *Annu. Rev. Astron. Astrophys.* **51**, 353–392 (2013).
14. E. Corsaro et al., *Astrophys. J.* **757**, 190 (2012).
15. M. Grosjean et al., *Astron. Astrophys.* **572**, A11 (2014).
16. E. Corsaro, J. De Ridder, R. A. García, *Astron. Astrophys.* **579**, A83 (2015).
17. T. R. Bedding et al., *Astrophys. J.* **713**, L176–L181 (2010).
18. T. M. Brown, R. L. Gilliland, R. W. Noyes, L. W. Ramsey, *Astrophys. J.* **368**, 599 (1991).
19. M. Aurière et al., *Astron. Astrophys.* **475**, 1053–1065 (2007).
20. S. Deheuvels et al., *Astron. Astrophys.* **564**, A27 (2014).
21. C. Charbonnel, J.-P. Zahn, *Astron. Astrophys.* **476**, L29–L32 (2007).
22. J. Ballot, C. Barban, C. V. Veer-Menneret, *Astron. Astrophys.* **531**, A124 (2011).

ACKNOWLEDGMENTS

The authors of this paper thank the Kavli Institute for Theoretical Physics and the organizers of the Galactic Archaeology and Precision Stellar Astrophysics program held from January to April 2015. J.F. acknowledges partial support from NSF under grant no. AST-1205732 and through a Lee DuBridge Fellowship at the California Institute of Technology. R.A.G. acknowledge the support of the European Community's Seventh Framework Programme (FP7/2007-2013) under grant agreement no. 312844 (SPACEINN), and from the Centre National d'Études Spatiales. D.S. acknowledges support from the Australian Research Council. This project was supported by NASA under Theory and

Computational Astrophysics Network grant no. NNX14AB53G and NSF under grants PHY 11-25915 and AST 11-09174.

SUPPLEMENTARY MATERIALS

www.sciencemag.org/content/350/6259/423/suppl/DC1
Supplementary Text
Figs. S1 to S3
Table S1
References (23–56)

29 May 2015; accepted 15 September 2015
10.1126/science.aac6933

PLANT DEVELOPMENT

Transcriptional control of tissue formation throughout root development

Miguel A. Moreno-Risueno,¹ Rosangela Sozzani,^{2*} Galip Gürkan Yardımcı,^{2†} Jalean J. Petricka,^{2‡} Teva Vernoux,³ Ikram Bililou,⁴ Jose Alonso,⁵ Cara M. Winter,² Uwe Ohler,⁶ Ben Scheres,⁴ Philip N. Benfey^{2§}

Tissue patterns are dynamically maintained. Continuous formation of plant tissues during postembryonic growth requires asymmetric divisions and the specification of cell lineages. We show that the BIRDS and SCARECROW regulate lineage identity, positional signals, patterning, and formative divisions throughout *Arabidopsis* root growth. These transcription factors are postembryonic determinants of the ground tissue stem cells and their lineage. Upon further activation by the positional signal SHORT-ROOT (a mobile transcription factor), they direct asymmetric cell divisions and patterning of cell types. The BIRDS and SCARECROW with SHORT-ROOT organize tissue patterns at all formative steps during growth, ensuring developmental plasticity.

Organs are formed, patterned, and maintained during growth. In the root of *Arabidopsis*, tissues are organized as concentric cylinders around the internal vascular tissue. Much progress has been made in identifying factors responsible for patterning some of these tissues, such as the ground tissue. The ground tissue lineage is continuously generated by the cortex endodermis initial stem cell (CEI), which divides in the transverse orientation (anticlinal division) to produce a daughter cell (CEID) and regenerate itself. The ground tissue is patterned when the CEID divides asymmetrically in the longitudinal (periclinal) orientation, gen-

erating two cell types: endodermis and cortex (1). The mobile transcription factor SHORT-ROOT (SHR) moves from the stele to the ground tissue, where SCARECROW (SCR) and the C_2H_2 transcription factor JACKDAW (JKD) sequester it in the nucleus. Nuclear SHR is required for the periclinal asymmetric divisions of the CEID that pattern the ground tissue (2, 3). These divisions are activated through a bistable switch involving SHR, SCR, and other components and correlate with the temporal activation of transcriptional programs (4, 5). Absence of SHR results in abnormal ground tissue patterning, with loss of the endodermis and a remaining single layer of ground tissue due to absence of asymmetric cell divisions (5, 6). Because the ground tissue lineage remains, this indicates that other factors participate in its specification.

Specific roles for JKD and several close relatives have been recently identified (7). JKD and BALD-IBIS regulate SHR movement by promoting its nuclear retention, and cooperatively with MAGPIE (MGP) and NUTCRACKER (NUC) are required for the formative divisions that pattern the ground tissue into cortex and endodermis. Here we show that JKD, MGP, and NUC, along with two new members of this family (collectively known as the BIRDS; table S1) named BLUEJAY (BLJ) and IMPERIAL EAGLE (IME), organize the ground tissue after embryogenesis. They function

¹Department of Biotechnology, Center for Plant Genomics and Biotechnology, Universidad Politécnica de Madrid, 28223 Pozuelo de Alarcón (Madrid), Spain. ²Department of Biology and Howard Hughes Medical Institute, Duke University, Durham, NC 27708, USA. ³Laboratoire de Reproduction et Développement des Plantes, CNRS, INRA, ENS Lyon, UCBL, Université de Lyon, 69364 Lyon, France. ⁴Department of Plant Biology, Wageningen University Research, Wageningen, Netherlands. ⁵Department of Plant and Microbial Biology, North Carolina State University, Raleigh, NC 27695, USA. ⁶Berlin Institute for Medical Systems Biology, Max Delbrück Center for Molecular Medicine, 13125 Berlin, Germany. *Present address: Department of Plant and Microbial Biology, North Carolina State University, Raleigh, NC 27695, USA. †Present address: Department of Genome Sciences, University of Washington, Seattle, WA 98195, USA. ‡Present address: Carleton College, Northfield, MN 55057, USA. §Corresponding author. E-mail: philip.benfey@duke.edu

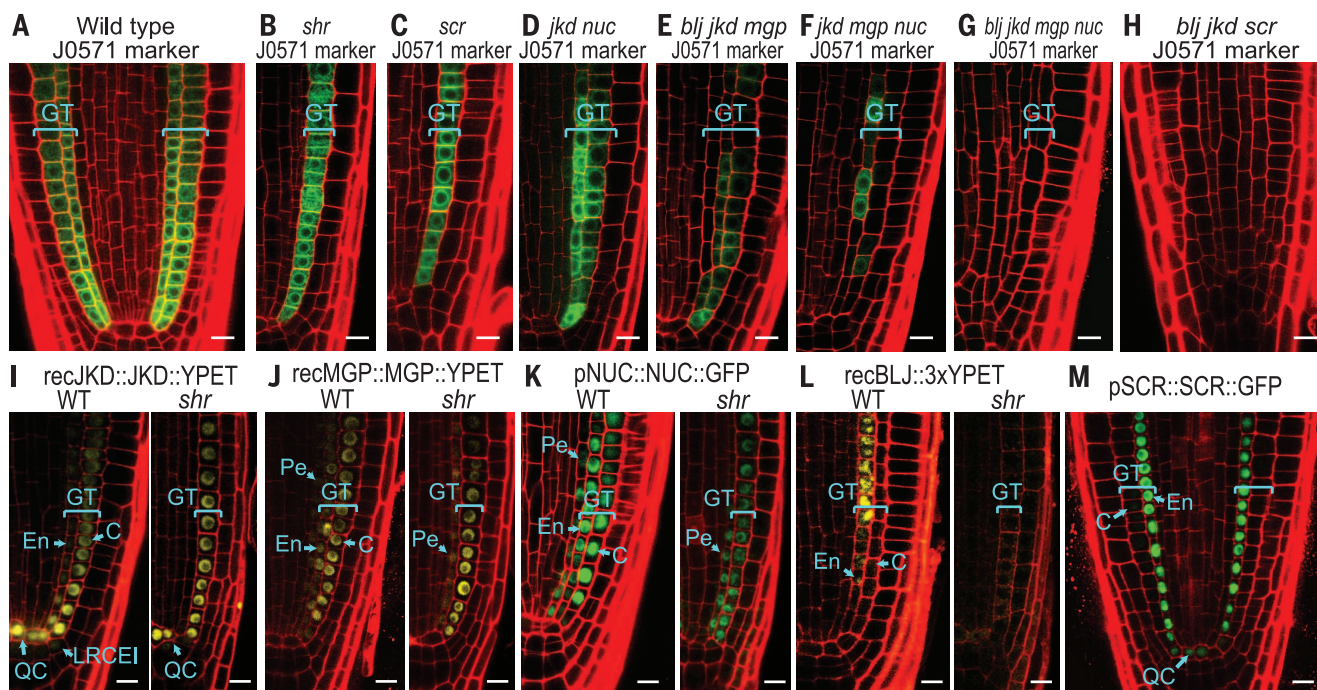


Fig. 1. BIRDs are required for ground tissue maintenance and are expressed in the ground tissue. (A to H) Confocal images of roots of wild-type (WT), *shr*, *scr*, *jkd*, *nuc*, *blj*, and *mgp*, at 6 days post-imbibition (dpi), showing the ground tissue (GT) marked by J0571. (I to L) Expression patterns of the BIRDs in WT or *shr* roots at 6 dpi; rec: regulatory regions using recombineering; p: promoter. (M) SCR expression. En, endodermis; C, cortex; QC, quiescent center; LRCEI, lateral root cap/epidermis initial; Pe, pericycle. Scale bars, 10 μ m.

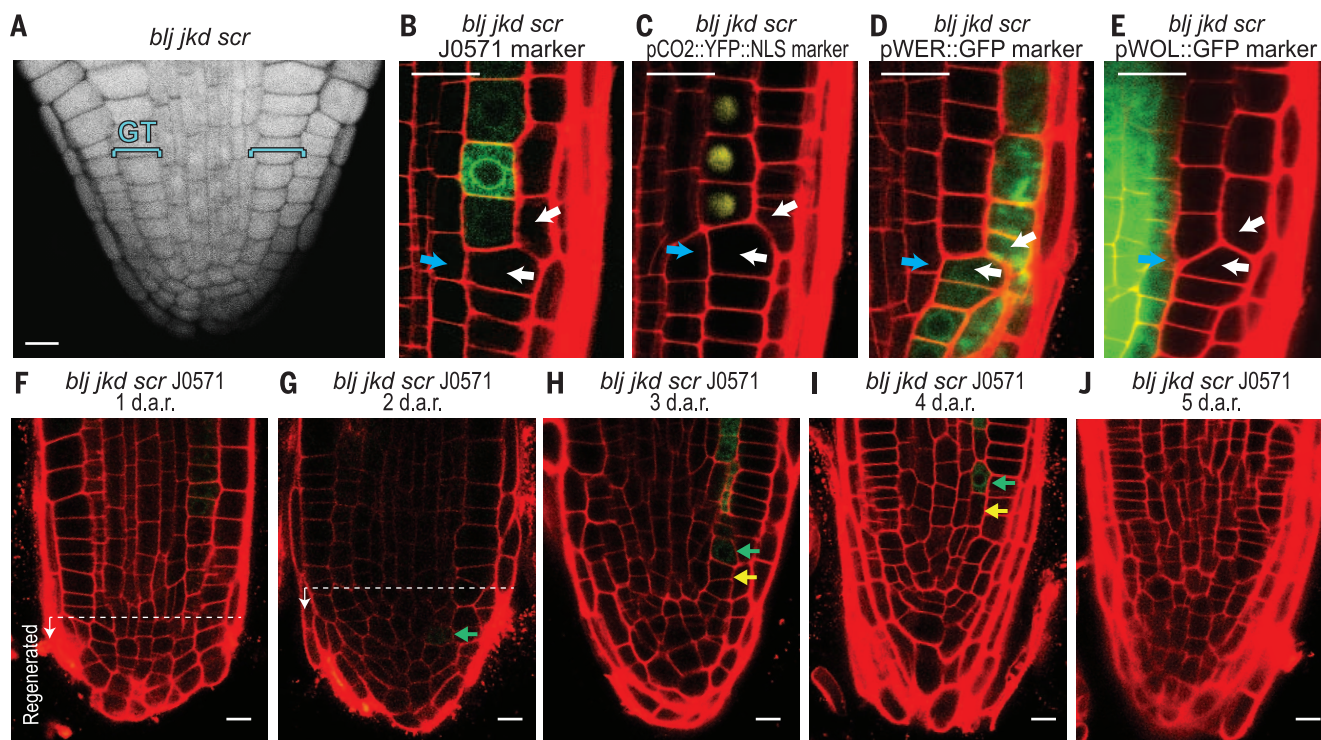


Fig. 2. BLJ, JKD, and SCR specify identity of ground tissue initial cells. (A) Mature embryos of *blj jkd scr*. (B to E) Lineage analyses in *blj jkd scr* using the J0571, cortex (CO2), epidermis (WER), and stele (WOL) markers. Blue arrows: stele; white arrows: epidermis. (F to J) *blj jkd scr* roots from 1 to 5 days after resection (d.a.r.). Regenerated ground tissue (green arrows) is visualized with J0571 marker. Yellow arrows: cells missing J0571 expression. Scale bars, 10 μ m.

as identity determinants of the CEI, which maintains and gives rise to the lineage, and act as effectors of asymmetric cell divisions of the CEID

upon SHR activation. Furthermore, the BIRDs regulate the transcriptional identity of the two ground tissue cell types and form a regulatory

network associated with lineage determination, asymmetric division, cell-type specification, and differentiation.

To explore the role of the BIRDs in ground tissue specification, we used expression from the J0571 enhancer trap line as a robust marker for ground tissue identity (Fig. 1A). This is exemplified by its expression in the mutant layer of *shr* (Fig. 1B). However, its expression was lost in some cells of double- and triple-mutant combinations of BIRDs, and was almost undetectable in the quadruple mutant, *blj jkd mgp nuc* (Fig. 1, D to G), suggesting that these transcription factors play a role in ground tissue identity. We next introgressed combinations of the BIRD mutants into *scr*. In both *jkd scr* and *blj jkd scr*, ground tissue marker expression was reduced, and a number of *blj jkd scr* roots lacked the entire ground tissue (Fig. 1H). These results indicate that the BIRDs and SCR are required for maintenance of ground tissue identity in addition to their established role in patterning divisions and endodermis specification (1, 7).

The mRNAs of *JKD*, *MGP*, and *NUC* are primarily expressed in the ground tissue (6, 7). To accurately determine where the encoded proteins and BLJ and IME accumulate, we tagged the proteins with green fluorescent protein (GFP) (8). BLJ was specifically expressed in the ground tissue, more highly in the shootward part of the meristem, although it was occasionally detected in ground tissue stem cells. Similarly, IME was also expressed more strongly in the shootward part of the meristem. By contrast, *JKD*, *MGP*, and *NUC* expression was higher toward the root tip (fig. S1). Previously, expression of the BIRDs and SCR appeared to require SHR (5, 6). How-

ever, when we introgressed the expression constructs into *shr*, we could detect all of the BIRD fusion proteins, although BLJ expression was reduced in this background (Fig. 1, I to L). SCR is also detectable in the ground tissue of *shr* (9). Taken together, our results indicate that the BIRDs and SCR can be regulated in a manner that is both dependent and independent of SHR, which is consistent with the difference in the phenotypes of *blj jkd scr* and *shr*.

The ground tissue lineage is initially specified in the embryo (10). Inspection of *blj jkd scr* embryos revealed that they developed ground tissue during embryogenesis (Fig. 2A). In seedling roots, we found that the ground tissue was present in mature zones but frequently did not continue to the meristem (fig. S2, A to L). Loss of the ground tissue was detected after germination but became more severe over time (fig. S2M). When the ground tissue disappeared, the epidermis became directly juxtaposed with the stele, as shown by tissue-specific markers (Fig. 2, B to E). These results indicate that the combined activity of the BIRDs and SCR is crucial to maintain the ground tissue lineage postembryonically.

The ground tissue marker J0571 was also lost in cells that were apparently formed by division of ground tissue cells (Fig. 1, D to G) and thus, the critical role of BLJ, JKD, and SCR in maintaining the ground tissue appears to be more than maintenance of the division potential of the CEI. Consistent with this hypothesis, other mutations affecting stem cell niche activity or the orientation plane of niche asymmetric cell divisions do

not result in loss of cell lineages (11, 12). To determine if the loss of ground tissue was due to incorrect specification of the CEI, we regenerated roots from wild-type, *scr*, and *blj jkd scr* mutants after resection of the root tip (fig. S3, A to C). In *blj jkd scr*, there was a low regeneration frequency (fig. S3D), but in those meristems that did regenerate, we found severely impaired regeneration of ground tissue with, at most, one or two cells after 2 days (Fig. 2, F and G). These cells failed to establish a new ground tissue lineage and, although a small amount of division occurred, expression of the ground tissue marker was normally lost (Fig. 2, H to J). *scr* mutants also showed impaired regeneration of the ground tissue lineage and failed to complete an entire layer (fig. S4). Our results indicate that BLJ, JKD, and SCR maintain CEI stem cells and their progeny postembryonically through specification of CEI identity.

The BIRDs and SCR are involved in regulation of transcription associated with formative divisions of the CEID and ground tissue cells (2, 6, 7). To further investigate the dual role of the BIRDs and SCR in generating and patterning the ground tissue, we reconstructed a gene regulatory network. Among the BIRDs, we focused on BLJ and JKD because they have a specific role in ground tissue establishment and identified their direct targets through chromatin immunoprecipitation (ChIP) followed by sequencing (table S2). To reconstruct the network, we used transcriptionally regulated targets that were identified by the intersection of ChIP-bound genes with previous genome-wide expression data (for SHR), as well

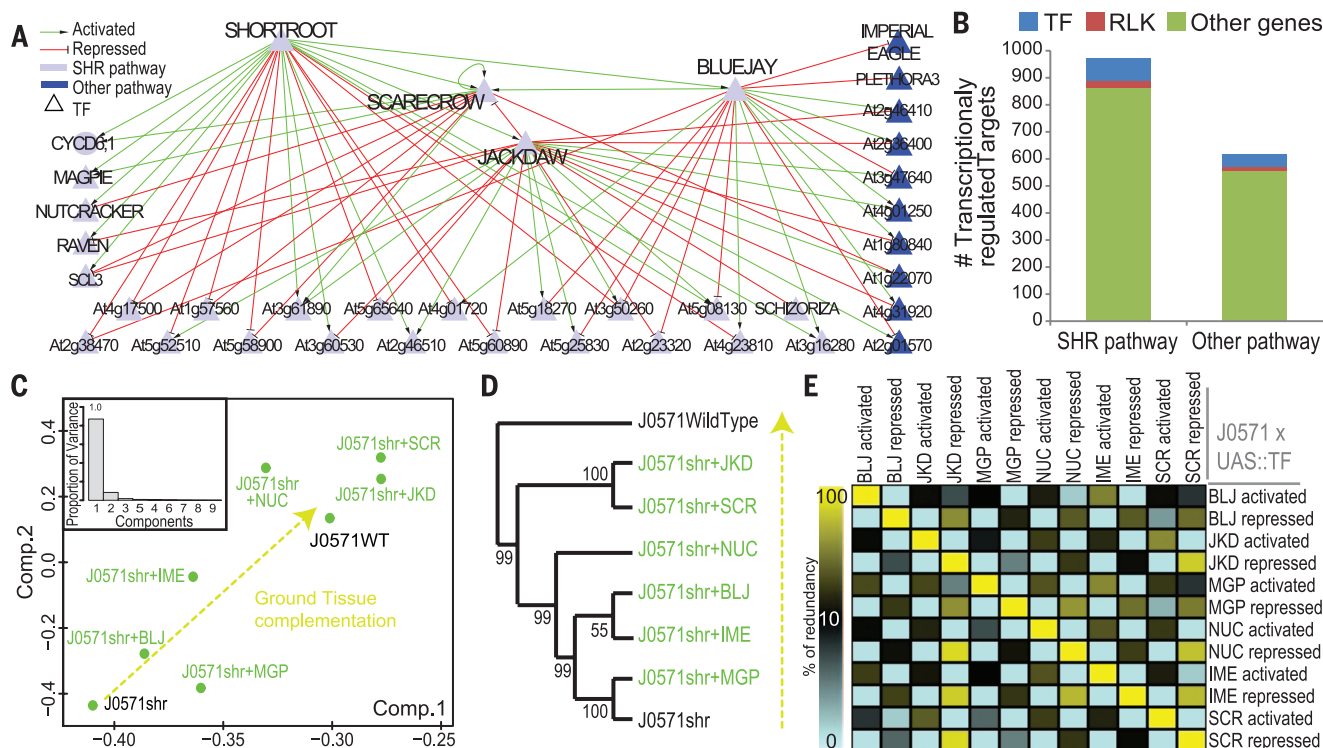


Fig. 3. BIRDs are determinants of ground tissue gene expression and form a network with SHR and SCR. (A) Network of SHR, BIRDs, SCR, and downstream transcription factor hubs. (B) Comparison of transcriptionally regulated targets. (C) Principal component analysis of the transcriptional profiles of ground tissue-expressed genes in different mutants; inset: component weights. (D) Same profiles hierarchically clustered. (E) Redundancy among regulated genes.

as with new microarray data that we generated from *blj jkd scr* root meristems and from ground tissue sorted cells of *shr* mutants in which we amplified BIRDS and SCR expression using the J0571xUAS system [tables S3 and S4; a detailed description of network reconstruction is in (13)]. The resulting network (table S5) showed pronounced overlaps between the genes regulated by more than one transcription factor (Fig. 3A and fig. S5). A more detailed analysis of the network showed that in addition to directly regulating genes (~55%) in the SHR pathway (table S6), the BIRDS and SCR also directly regulate genes in other pathways, suggesting that genes not in the SHR pathway are likely to be involved in maintaining ground tissue identity and may be activated through a transcriptional cascade (Fig. 3B).

To better understand how the BIRDS and SCR regulate ground tissue identity, we analyzed their ability to “rescue” ground tissue gene expression in the *shr* background. As these factors are down-regulated in *shr*, we amplified their expression using the J0571xUAS-driven lines in *shr* (see Methods). We then compared mRNA expression profiles of sorted ground tissue cells from these lines with the expression profile of wild-type ground tissue using principal component analysis (PCA) and hierarchical clustering. As an initial test, we asked if PCA could distinguish between the ground tissue and other root tissues as profiled in the RootMap (14) and found clear

separation (fig. S6, A and B). This provided confidence to use PCA to infer the identity of the transcriptome when each of the BIRDS was expressed in the *shr* ground tissue. Consistently, PCA localized the BIRDS’ ground tissue transcriptomes between *shr* and wild type (Fig. 3C). This was also true for SCR, indicating that a degree of rescue had occurred. In agreement with the PCA, hierarchical clustering separated the ground tissue transcriptome from other root tissues and showed different levels of rescue provided by the BIRDS and SCR (Fig. 3D and fig. S6, C and D). JKD and SCR were able to rescue the ground tissue transcriptome more effectively than did BLJ. This suggests that BLJ’s role may be to regulate a set of genes that are complementary to those regulated by JKD and SCR, leading to a combinatorial action responsible for the phenotype of *blj jkd scr*. The contrasting expression patterns of BLJ and JKD are consistent with complementary activities. In addition, there was greater overlap among genes regulated by SCR and the BIRDS that showed a higher level of rescue of the ground tissue transcriptome than with the BIRDS that showed a lower level of rescue (Fig. 3E).

Our network indicated that SCR, BLJ, JKD, MGP, and NUC are direct targets of SHR, whereas IME is regulated through an intermediate transcription factor. SCR, NUC, and MGP are activated upon SHR induction (5). To better understand the role of BLJ, JKD, and IME downstream of SHR, we

performed a real-time polymerase chain reaction analysis of gene expression after SHR induction (Fig. 4A). We found that mRNA levels of *SCR*, *BLJ*, *JKD*, *MGP*, *NUC*, and *IME* genes peaked at 6 hours, coincident with the time of onset of asymmetric divisions patterning the ground tissue. A large proportion of the genes down-regulated in *shr* are activated by the BIRDS and SCR (Fig. 4B), and some of these had been previously identified to be activated by the BIRDS and SCR (Fig. 4B, S7A). This indicates that SHR activates the BIRDS and SCR to induce gene expression associated with patterning. It is, therefore, possible that activation of downstream targets could be dependent on the level of SCR and the BIRDS, with SHR being the amplifying signal required for patterning. Inspection of the ground tissue in the J0571xUAS lines showed formative divisions (fig. S7, B to H) with high penetrance when BLJ was expressed in the *shr* background (80% of roots, $n = 20$), whereas other BIRDS and SCR could induce these divisions only with substantially lower penetrance (IME: 50%; others: 10%; $n = 20$).

As suggested by our network, we next asked if BLJ, JKD, and SCR are required for SHR function in the ground tissue. For this purpose, we fused SHR to a nuclear localization signal and expressed it directly in the ground tissue under a two-component system driven by the En7 promoter, which is specific to the endodermis and CEI (fig. S7, I to L). When expressed in a wild-type

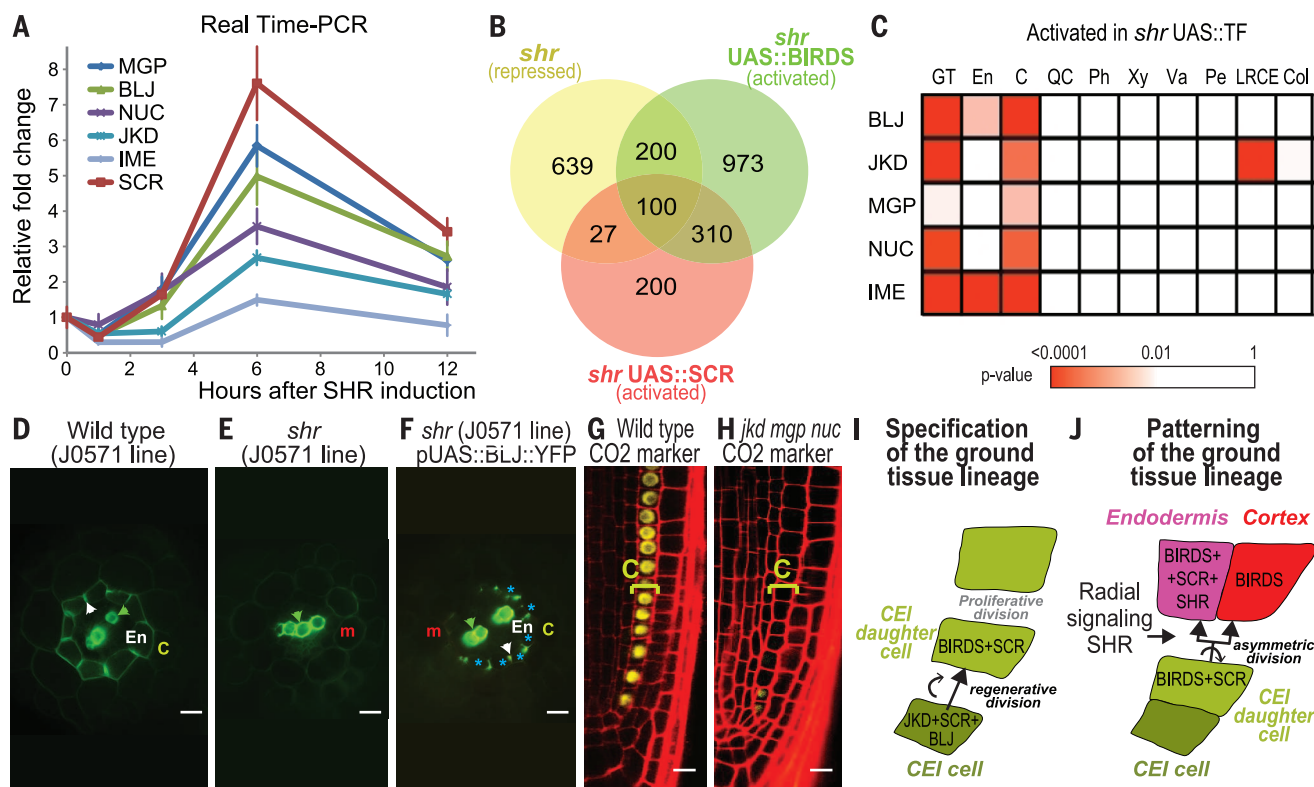


Fig. 4. BIRDS are activated by SHR and specify endodermis and cortex. (A) BIRD expression in ground tissue cells at different times after SHR induction. (B) Venn diagrams comparing genes activated by BIRDS and SHR. (C) Heatmap of BIRD contribution to tissue-enriched expression. Ph: phloem; Xy: xylem; Va: vasculature; Col: columella. (D to F) Optical root sections at 10 dpi. White arrows: Casparian strip; green arrows: lignin in xylem. (G to H) Cortex marker in 6 dpi roots. (I and J) Model of postembryonic formation and maintenance of ground tissue. Scale bars, 10 μ m.

background, SHR generated additional ground tissue layers, as previously described (7, 9). However, when expressed in combinations of mutants involving *blj jkd* and *scr*, SHR failed to rescue the formative cell divisions within the ground tissue. These results indicate that BLJ, JKD, and SCR are essential for SHR to carry out ground tissue patterning. Furthermore, analysis of the contribution of the BIRDs and SCR to generate specific gene expression patterns showed that these transcription factors were able to activate expression of endodermis and cortex genes (Fig. 4C). Staining for endodermis-specific attributes (the Casparian strip) in the *shr* J0571xUAS lines showed that BLJ (Fig. 4, D to F), along with the other BIRDs and SCR (fig. S7, M to Q), could induce Casparian strip formation subsequent to periclinal divisions of the ground tissue. Expression of cortex-specific markers required at least JKD, MGP, and NUC (Fig. 4, G and H). SCZ, which is required for expression of some cortex-specific markers (15), is also a target in the network. Our analysis suggests that cortex identity requires multiple inputs from the BIRDs. Therefore, the BIRDs and SCR, in addition to mediating SHR transcriptional competence (7), are endogenous effectors of ground tissue patterning and can provide all the necessary information for the asymmetric divisions that are activated by SHR to pattern the ground tissue.

Cell fate choices in all multicellular organisms are governed by transcription factors. Their combinatorial expression and interactions are key to tissue identity. The BIRDs and SCR play critical roles in maintaining ground tissue identity in postembryonic roots by specifying the CEI stem cells that generate the ground tissue lineage (Fig. 4I). In addition, they are effectors of asymmetric divisions that pattern the progeny of the CEIs (Fig. 4J). The continuous control of multiple steps of tissue formation by the same set of transcription factors, independently of and dependent on positional cues, is a sophisticated mechanism ensuring plasticity in the regulation of cell fate.

REFERENCES AND NOTES

1. J. J. Petricka, J. M. Van Norman, P. N. Benfey, *Cold Spring Harb. Perspect. Biol.* **1**, a000497 (2009).
2. D. Welch et al., *Genes Dev.* **21**, 2196–2204 (2007).
3. H. Cui et al., *Science* **316**, 421–425 (2007).
4. A. Cruz-Ramirez et al., *Cell* **150**, 1002–1015 (2012).
5. R. Sozzani et al., *Nature* **466**, 128–132 (2010).
6. M. P. Levesque et al., *PLoS Biol.* **4**, e143 (2006).
7. Y. Long et al., *Plant Cell* **27**, 1185–1199 (2015).
8. R. Zhou, L. M. Benavente, A. N. Stepanova, J. M. Alonso, *Plant J.* **66**, 712–723 (2011).
9. Y. Helariutta et al., *Cell* **101**, 555–567 (2000).
10. M. Pernas, E. Ryan, L. Dolan, *Curr. Biol.* **20**, 818–823 (2010).
11. M. Aida et al., *Cell* **119**, 109–120 (2004).
12. V. Willemssen et al., *Dev. Cell* **15**, 913–922 (2008).
13. Materials and methods are available as supplementary materials on Science Online.
14. S. M. Brady et al., *Science* **318**, 801–806 (2007).
15. C. A. ten Hove et al., *Curr. Biol.* **20**, 452–457 (2010).

ACKNOWLEDGMENTS

This work was supported by grants from the NIH (R01-GM043778) and the Gordon and Betty Moore Foundation (GBMF3405) to P.N.B.; from the NSF (IOS-1021619-002) to U.O. and P.N.B.; and from MINECO, FEDER/EFDR (BFU2013-41160-P), and FP7 (PCIG11-GA-2012-322082) to M.A.M.-R. M.A.M.-R. is supported by the Ramon y Cajal program (MINECO), C.M.W. by a NRSA F32 GM106690-01 fellowship, I.B. by a NWO VIDI grant, and

B.S. by an ERC Advanced Grant SysArc. J.J.P. was supported by a NIH Ruth L. Kirschstein NRSA F32 GM086976 fellowship I.B. by a NWO VIDI grant, and B.S. by an ERC Advanced Grant SysArc. We thank D. R. McClay, D. M. Pernas, and Y. Long for critical reading of the manuscript. Additional data are in the supplementary materials. The National Center for Biotechnology Information Gene Expression Omnibus accession numbers are GSE60157 (microarrays) and GSE60011 (ChIP-Seq). The authors declare that they have no competing interests.

SUPPLEMENTARY MATERIALS

www.sciencemag.org/content/350/6259/426/suppl/DC1
Materials and Methods
Figs. S1 to S7
Table S1 to S6
References (16–30)

30 July 2015; accepted 22 September 2015
10.1126/science.121171

ALZHEIMER'S DISEASE

Reduced grid-cell-like representations in adults at genetic risk for Alzheimer's disease

Lukas Kunz,^{1,2} Tobias Navarro Schröder,³ Hweeling Lee,¹ Christian Montag,⁴ Bernd Lachmann,⁴ Rayna Sariyska,⁴ Martin Reuter,^{5,6} Rüdiger Stirnberg,¹ Tony Stöcker,¹ Paul Christian Messing-Floeter,^{1,2} Juergen Fell,² Christian F. Doeller,^{3*} Nikolai Axmacher^{1,2,7,*†}

Alzheimer's disease (AD) manifests with memory loss and spatial disorientation. AD pathology starts in the entorhinal cortex, making it likely that local neural correlates of spatial navigation, particularly grid cells, are impaired. Grid-cell-like representations in humans can be measured using functional magnetic resonance imaging. We found that young adults at genetic risk for AD (*APOE-ε4* carriers) exhibit reduced grid-cell-like representations and altered navigational behavior in a virtual arena. Both changes were associated with impaired spatial memory performance. Reduced grid-cell-like representations were also related to increased hippocampal activity, potentially reflecting compensatory mechanisms that prevent overt spatial memory impairment in *APOE-ε4* carriers. Our results provide evidence of behaviorally relevant entorhinal dysfunction in humans at genetic risk for AD, decades before potential disease onset.

Late-onset AD is the most common form of dementia and one of the most challenging diseases of modern society (1). Curative therapies are still lacking, presumably because they start too late (2). Therefore, the elucidation of early pathomechanisms underlying symptoms of AD is of high interest. We aimed at identifying one of the potentially earliest neurocognitive pathomechanisms in the development of AD symptoms: We hypothesized entorhinal dysfunction in young *APOE-ε4* carriers. Our hypothesis was built on three previous findings: First, the *ε4* allele of the *APOE* gene is the strongest genetic risk factor for late-onset AD (3). Individuals carrying one *APOE-ε4* allele are at threefold increased risk of AD, and those carrying two *APOE-ε4* alleles are at more than 10-fold increased risk (4). Second, early AD histopathology appears in the entorhinal cortex (EC) (5), where tau abnormal-

ities can already be observed in adults under the age of 30 (6), especially in *APOE-ε4* carriers (7). Third, the EC contains grid cells, a cell type involved in spatial navigation. Grid cells fire whenever animals (8) or humans (9) traverse the vertices of an internally generated grid tiling the spatial environment into equilateral triangles. Their function has been linked to path integration (10, 11), error correction (12), and the maintenance of place cells (13), which exhibit only a singular firing field (14). Hence, a possible dysfunction of grid cells may provide an explanation for the symptom of spatial disorientation in patients suffering from AD. Proxies for grid cells, termed grid-cell-like representations, are detectable in humans by functional magnetic resonance imaging (fMRI). The blood oxygenation level-dependent signal of the EC depends on movement direction with sixfold rotational symmetry. More specifically, the contrast of brain activity during movements aligned versus misaligned to the main axes of a putative grid in a virtual arena leads to a macroscopically visible fMRI signal in the right EC (15).

We examined the effect of *APOE-ε4* on grid-cell-like representations by comparing two groups of healthy young adults ($n = 38$ *APOE-ε4/ε3* carriers, termed "risk participants" from now on; $n = 37$ *ε3/ε3* carriers, "control participants"; table S1). Participants completed a previously established

¹German Center for Neurodegenerative Diseases (DZNE), Bonn, Germany. ²Department of Epileptology, University of Bonn, Bonn, Germany. ³Donders Institute for Brain, Cognition and Behaviour, Radboud University, Nijmegen, Netherlands. ⁴Department of Psychology, Ulm University, Ulm, Germany. ⁵Department of Psychology, University of Bonn, Bonn, Germany. ⁶Center for Economics and Neuroscience, University of Bonn, Bonn, Germany. ⁷Department of Neuropsychology, Institute of Cognitive Neuroscience, Ruhr-University Bochum, Bochum, Germany. *These authors contributed equally to this work. †Corresponding author. E-mail: nikolai.axmacher@rub.de

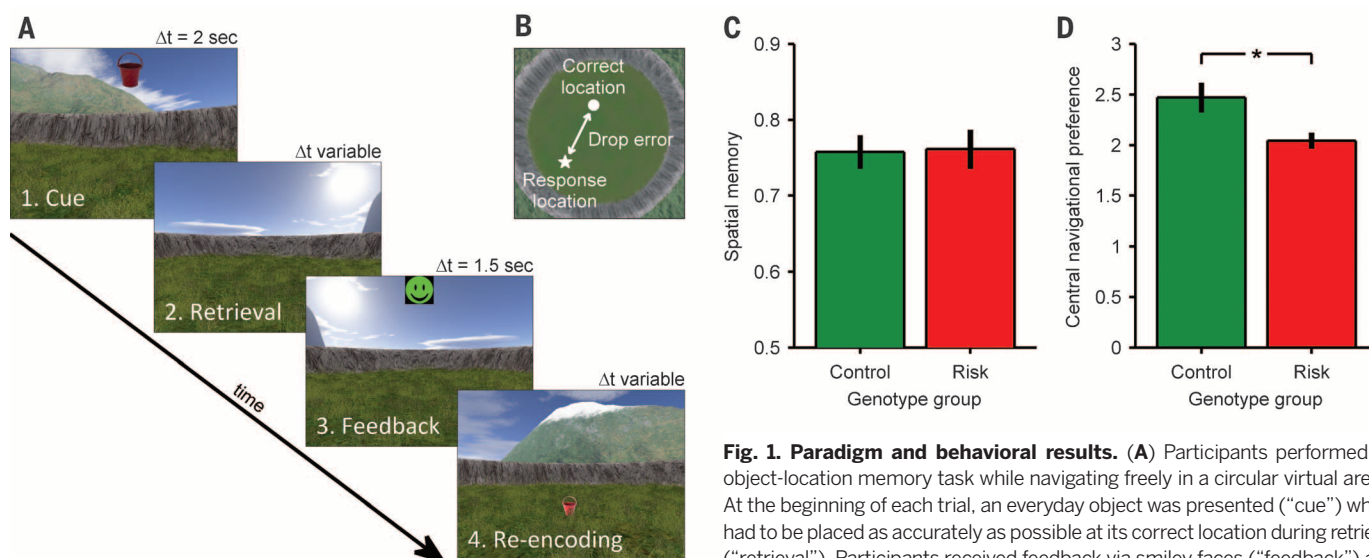


Fig. 1. Paradigm and behavioral results. (A) Participants performed an object-location memory task while navigating freely in a circular virtual arena. At the beginning of each trial, an everyday object was presented (“cue”) which had to be placed as accurately as possible at its correct location during retrieval (“retrieval”). Participants received feedback via smiley faces (“feedback”) and re-encoded the object position afterward (“re-encoding”). Δt , time for specific trial phase. (B) For each participant, the drop error was calculated as the difference between response locations and correct locations averaged across trials. To improve readability, drop error values were transformed into spatial memory performance values (methods). (C) Spatial memory performance does not differ between control ($APOE-\epsilon 3/\epsilon 3$; $n = 37$) and risk ($APOE-\epsilon 4/\epsilon 3$; $n = 38$) participants. (D) Risk participants show a reduced preference to navigate within the arena center as compared to control participants. All bars show mean and standard error of the mean (SEM) across participants. $*P < 0.05$.

paradigm for the detection of grid-cell-like representations (15), during which they performed an object-location memory task while navigating freely in a virtual environment (Fig. 1 and figs. S1 and S2). Briefly, the analysis split the fMRI data into two halves (Fig. 2 and tables S4 and S5): The first half served to identify the angular orientation of the putative grid axes (separated by angles of 60° , which is equivalent to the sixfold rotational symmetry of the grid) relative to the environment in each participant’s right EC (16). The second half of the data was then used to contrast brain activity during movements aligned with these grid axes versus brain activity during misaligned movements. The averaged contrast values of aligned versus misaligned movements across all voxels in the right EC reflect the magnitude of grid-cell-like representations [exemplary participant-specific EC region of interest (ROI); Fig. 2D]. We found significant grid-cell-like representations in control participants ($t_{36} = 2.318$, $P = 0.026$) but not in risk participants ($t_{37} = -1.730$, $P = 0.092$). In fact, the magnitude of grid-cell-like representations was strongly reduced in risk participants as compared to control participants [$t_{73} = 2.875$, $P = 0.005$; Fig. 2; two-way genotype \times sex analysis of variance (ANOVA): main effect of genotype, $F_{1,71} = 8.695$, $P = 0.004$; no main effect of sex, $F_{1,71} = 0.709$, $P = 0.403$; no interaction, $F_{1,71} = 1.838$, $P = 0.179$]. Control analyses showed that our finding in control participants was specific for sixfold rotational symmetry and specific for the right EC (fig. S3). No structural changes of the right EC, which could potentially account for the functional changes, were observed (fig. S4).

In contrast to the genotype effect on grid-cell-like representations, both genetic subgroups showed similar spatial memory performance

($t_{73} = -0.109$, $P = 0.913$; Fig. 1) as well as similar basic behavioral characteristics (table S2). We assume that the detrimental effect of $APOE-\epsilon 4$ on spatial memory becomes apparent only at older age (17), when histopathological changes due to presymptomatic AD have reached adjacent limbic regions such as the hippocampus. However, risk participants exhibited altered navigational behavior. They showed a reduced preference to navigate in the center of the arena (“central navigational preference”; methods) as compared to control participants ($t_{73} = 2.551$, $P = 0.014$; Fig. 1 and fig. S1; two-way genotype \times sex ANOVA: main effect of genotype, $F_{1,71} = 6.293$, $P = 0.014$; no main effect of sex, $F_{1,71} = 0.094$, $P = 0.761$; no interaction, $F_{1,71} = 1.978$, $P = 0.164$). This finding was also reflected in a greater mean distance of all virtual positions relative to the arena center in risk participants ($t_{73} = -3.003$, $P = 0.004$; fig. S5).

Next, we examined whether the $APOE$ -dependent changes of grid-cell-like representations and central navigational preference were related to spatial memory performance. Using linear multiple regression (Table 1), we found that greater grid-cell-like representations (in addition to higher values of central navigational preference, younger age and male sex) were positively related to spatial memory performance (supplementary text and fig. S6). This result strengthens the hypothesis that EC-specific representations of space guide behavior in humans (15, 18). Nevertheless, this result also seemed paradoxical to us: Given that $APOE-\epsilon 4$ reduces grid-cell-like representations and that reduced grid-cell-like representations are associated with impaired spatial memory performance, how can we explain similar performance between both genetic subgroups? Therefore, we hypothesized that there are compensatory mechanisms in risk participants (19).

We anticipated hippocampal task-related activity to be a compelling option for a potential compensatory mechanism because the importance of the hippocampus for spatial memory is well established (20), and hippocampal activity is altered in $APOE-\epsilon 4$ carriers (21). Hippocampal task-related activity (contrast of task versus implicit baseline; methods and table S6) was negatively correlated with grid-cell-like representations across all participants (bilateral hippocampus: Pearson’s $r = -0.317$, $P = 0.006$; Fig. 2; right hippocampus: $r = -0.292$, $P = 0.011$; left hippocampus: $r = -0.320$, $P = 0.005$). Particularly in the posterior hippocampus, which is especially relevant for spatial navigation [the bilateral posterior third; see (22)], this relationship was significantly more pronounced in risk participants than in control participants (risk participants: $r = -0.545$, $P < 0.001$; control participants: $r = -0.064$, $P = 0.707$; difference between correlation coefficients, $z = -2.27$, $P = 0.023$; fig. S7). Because reduced grid-cell-like representations were also correlated with increased task-related activity of the EC and amygdala (fig. S8), we then examined the behavioral relevance of hippocampal task-related activity. Detailed analyses revealed that increased task-related activity, particularly in the left posterior hippocampus, was associated with better spatial memory performance (supplementary text, tables S3 and S7, and fig. S9). In short, increased hippocampal activity could serve as a behaviorally relevant compensatory mechanism for reduced grid-cell-like representations. Nevertheless, increased hippocampal activity may also indicate a broader disruption of medial temporal lobe computations promoting pathological processes [(23, 24); for further discussion, see the supplementary text].

Next, we aimed at understanding the reduction of grid-cell-like representations in risk participants in greater detail. In principle, reduced grid-cell-like representations in fMRI could be due to (i) temporal instability of the putative grid axes across the entire experiment, (ii) spatial instability of the putative grid axes within each half of the experiment, or—similar temporal and spatial stability between genetic subgroups in smaller data segments provided—(iii) a relatively weaker right EC contrast of aligned versus misaligned movements. We sought to disentangle this ambiguity by first calculating one temporal stability and one spatial stability value for each participant (methods; Fig. 3). Temporal stability values differed between genetic subgroups ($t_{73} = 2.408$, $P = 0.019$), were positively correlated with grid-cell-like representations (Pearson's $r = 0.736$, $P < 0.001$; Fig. 3B), and were also negatively correlated with hippocampal task-related activity ($r = -0.311$, $P = 0.007$). Reduced temporal stability values were related to decreased functional connectivity between the right EC and hippocampus, possibly indicating a decoupling of both regions associated with entorhinal dysfunction ($r = 0.298$, $P = 0.009$; supplementary text and fig. S10). In contrast, spatial stability values did not differ between genetic subgroups and were not related to the grid-cell-like representations ($t_{73} = -0.143$, $P = 0.887$; $r = -0.079$, $P = 0.501$; Fig. 3). Finally, to disentangle reduced grid-cell-like representations from reduced temporal stability, we analyzed grid-cell-like representations on shorter data segments (methods). This analysis revealed significant grid-cell-like representations in control participants ($t_{36} = 2.708$, $P = 0.010$) but not in risk participants ($t_{37} = -0.788$, $P = 0.436$), with a significant difference between both groups ($t_{73} = 2.315$, $P = 0.023$; fig. S11), although the corresponding temporal and spatial stability values did not differ between groups (temporal stability: $t_{73} = 1.459$, $P = 0.149$; spatial stability: $t_{73} = -0.421$, $P = 0.675$). Taken together, this demonstrates that grid-cell-like representations in risk participants were less robust than in control participants (on a shorter time scale) and that the grid orientations of potential grid-cell-like representations were additionally temporally unstable in risk participants (on a longer time scale).

Our results (summarized in fig. S12) support the hypothesis that AD involves the dysfunction of entorhinal grid cells. Adults at genetic risk for AD exhibit strongly reduced fMRI representations of grid cells, and reduced grid-cell-like representations are related to impaired spatial memory performance (for a speculative interpretation of the underlying mechanistic basis, see the supplementary text). We also found a reduced preference of risk participants to navigate in the center of a virtual arena. This change in navigational strategy may be interpreted (i) as an attempt to correct errors in the grid code by encounters with environmental boundaries (25), (ii) as an uncertainty to rely on entorhinal path integration mechanisms, (iii) as a shift toward a response-based strategy relying on different mountain-wall conjunctive features, or (iv) as a

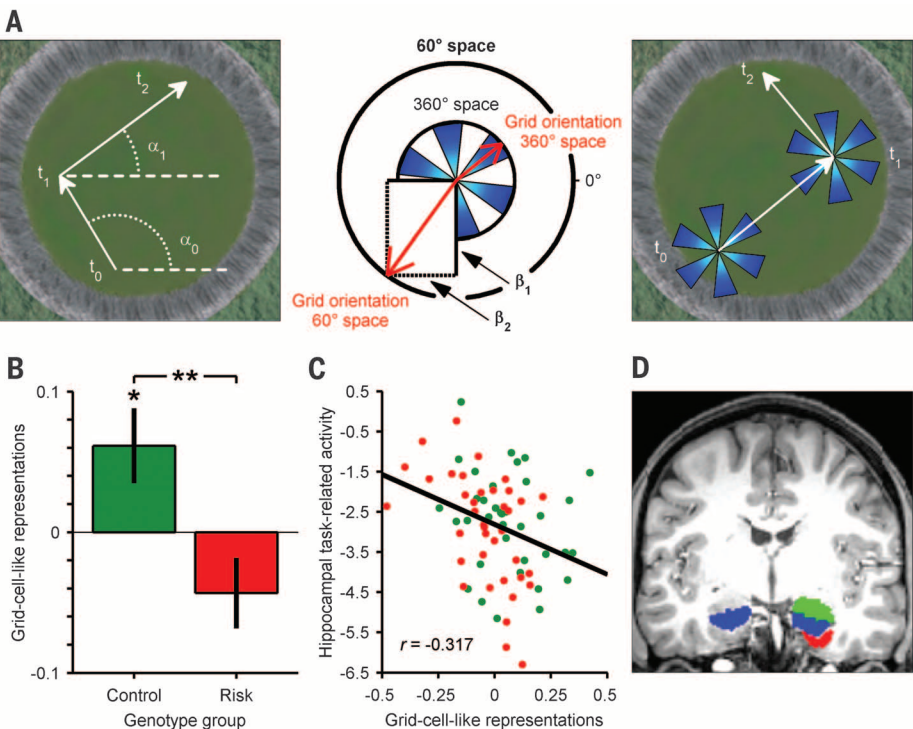


Fig. 2. Grid-cell-like representations and compensatory hippocampal activity. (A) Analysis procedure. (Left) The first half of the data was modeled with a general linear model (GLM), including one regressor for movement in the virtual arena. Two parametric modulators model movement direction in 60° space (sixfold rotational symmetry). t , time; α , running angle. (Middle) The putative grid orientation in 60° space is calculated via the β values of these parametric modulators (β_1 and β_2). Dividing by 6 yields the grid orientation in 360° space. Blue areas depict resulting aligned bins. (Right) Fitting a new GLM to the second half of the data allows the contrast of aligned versus misaligned movements to be calculated. (B) Grid-cell-like representations in the right entorhinal cortex (EC) are present for control participants but not for risk participants. In fact, grid-cell-like representations are reduced for risk participants as compared to control participants. (C) Negative correlation of task-related hippocampal activity with the magnitude of grid-cell-like representations ($P = 0.006$). (D) Exemplary ROIs of one participant, created using Freesurfer (methods). Red, right EC; blue, bilateral hippocampus; green, right amygdala. All bars show mean and SEM across participants. Green dots represent control participants; red dots represent risk participants. Units of all contrasts are parameter estimates. * $P < 0.05$. ** $P < 0.01$.

Table 1. Multiple regression to predict spatial memory performance (N = 75 participants). Adjusted coefficient of determination (R^2) = 0.170. Multicollinearity was not a concern (all variance inflation factors < 1.214).			
Predictor	β	t	P
Grid-cell-like representations	0.237	2.077	0.042
Central navigational preference	0.236	2.130	0.037
Genotype (control/ risk)	0.138	1.179	0.242
Sex (male/female)	-0.282	-2.643	0.010
Age (years)	-0.306	-2.830	0.006

result of inaccurate place fields in the arena center due to impaired grid cell input on place cells (26). Moreover, our results offer an explanation for the previously observed hyperactivity of certain brain areas in *APOE-ε4* carriers (27): They may compensate for entorhinal dysfunction. Specifically, our data would be in line with behaviorally relevant compensatory hyperactivity of the hippocampus that could indicate a stronger hippocampus-dependent boundary-based strat-

egy (28) or enhanced hippocampal path integration computations (29, 30) to counter impaired entorhinal path integration. Such neuronal hyperactivity could cause partial benefits at a young age (31) but may induce further pathological spreading afterward (24), including the degradation of place cell firing, which has already been shown in a mouse model of AD (32). Thus, the increased hippocampal activation may also reflect an adverse condition. Our results could provide a

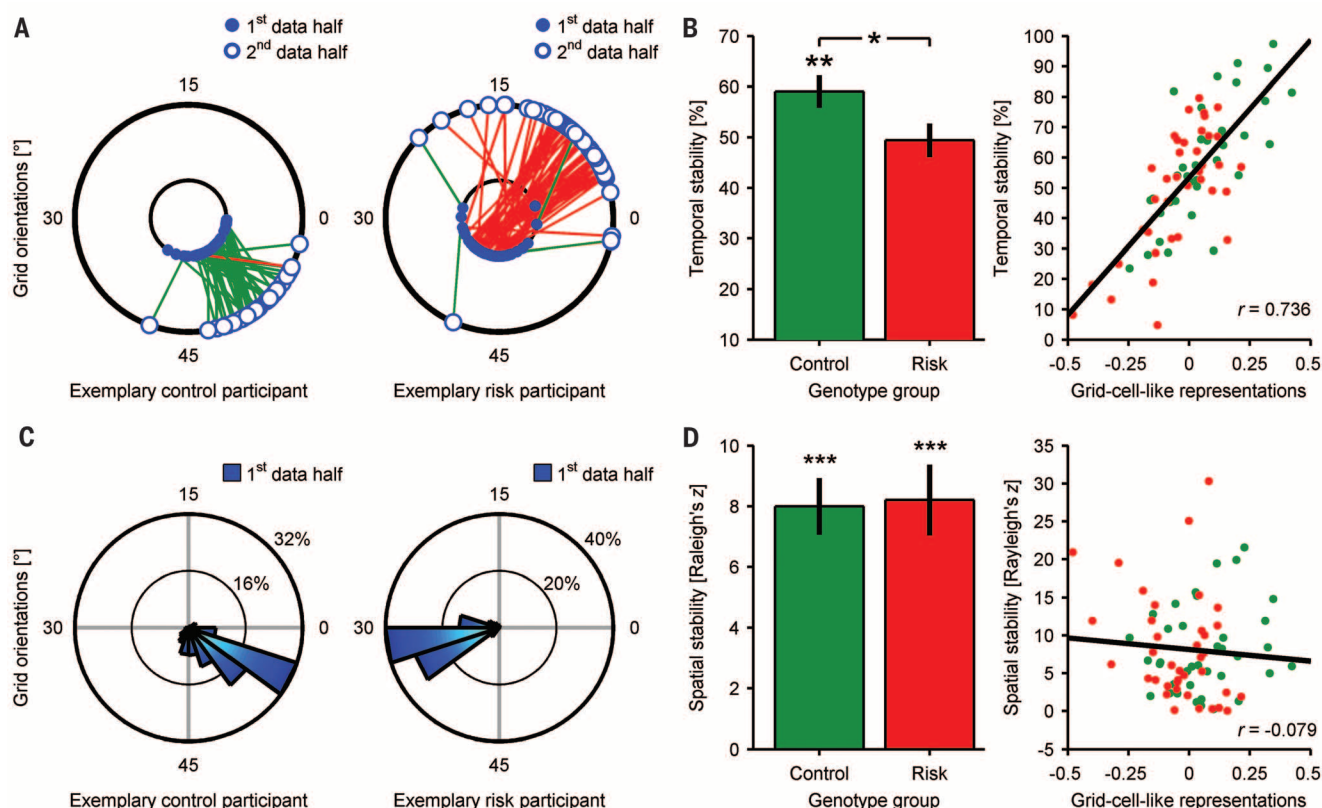


Fig. 3. Stability metrics of grid-cell-like representations. (A) Exemplary plots from one participant per group show temporally stable grid orientations (connected by green lines) and temporally instable grid orientations (red lines) of individual voxels, leading to one percentage value per participant ("temporal stability"). The exemplary plot for the risk participant indicates that the voxel-wise grid orientations change between the two halves of the data (lines between circles), but that within each half, the voxel-wise grid orientations are clustered (dots placed on the different circles, see spatial stability). (B) Temporal stability values show a reduction in risk participants and are highly

correlated with grid-cell-like representations ($P < 0.001$), suggesting temporal instability as a cause of reduced grid-cell-like representations. (C) Exemplary plots showing spatially stable grid orientations estimated from the first half of the data (Rayleigh's $z > 11$ for both). (D) Contrarily to temporal stability, spatial stability values do not differ between genetic subgroups and are not related to grid-cell-like representations. All bars show mean and SEM across participants, separately for both groups. Green dots represent control participants; red dots represent risk participants. Units of all contrasts are parameter estimates. * $P < 0.05$, ** $P < 0.01$, *** $P < 0.001$.

new basic framework for preclinical research on AD and may provide a neurocognitive explanation of spatial disorientation in AD. We emphasize their early occurrence in young adulthood, which may help to determine treatment onset and to establish entorhinal dysfunction as a prognostic marker. The amelioration of entorhinal dysfunction might be a new therapeutic target in the treatment of AD.

REFERENCES AND NOTES

- H. W. Querfurth, F. M. LaFerla, *N. Engl. J. Med.* **362**, 329–344 (2010).
- R. A. Sperling, C. R. Jack Jr., P. S. Aisen, *Sci. Transl. Med.* **3**, 111cm33 (2011).
- E. H. Corder et al., *Science* **261**, 921–923 (1993).
- C. C. Liu, T. Kanekiyo, H. Xu, G. Bu, *Nat. Rev. Neurol.* **9**, 106–118 (2013).
- H. Braak, E. Braak, *Acta Neuropathol.* **82**, 239–259 (1991).
- H. Braak, K. Del Tredici, *Acta Neuropathol.* **121**, 171–181 (2011).
- E. Ghebremedhin, C. Schultz, E. Braak, H. Braak, *Exp. Neurol.* **153**, 152–155 (1998).
- T. Hafting, M. Fyhn, S. Molden, M. B. Moser, E. I. Moser, *Nature* **436**, 801–806 (2005).
- J. Jacobs et al., *Nat. Neurosci.* **16**, 1188–1190 (2013).
- G. Buzsáki, E. I. Moser, *Nat. Neurosci.* **16**, 130–138 (2013).
- M. E. Hasselmo, M. P. Brandon, *Neural Plast.* **2008**, 658323 (2008).
- S. Sreenivasan, I. Fiete, *Nat. Neurosci.* **14**, 1330–1337 (2011).
- D. Bush, C. Barry, N. Burgess, *Trends Neurosci.* **37**, 136–145 (2014).
- A. D. Ekstrom et al., *Nature* **425**, 184–188 (2003).
- C. F. Doeller, C. Barry, N. Burgess, *Nature* **463**, 657–661 (2010).
- Materials and methods are available as supplementary materials on Science Online.
- F. Bertheau-Pavy, B. Park, J. Raber, *Neuroscience* **147**, 6–17 (2007).
- M. J. Chadwick, A. E. Jolly, D. P. Amos, D. Hassabis, H. J. Spiers, *Curr. Biol.* **25**, 87–92 (2015).
- S. Y. Bookheimer et al., *N. Engl. J. Med.* **343**, 450–456 (2000).
- B. A. Strange, M. P. Witter, E. S. Lein, E. I. Moser, *Nat. Rev. Neurosci.* **15**, 655–669 (2014).
- N. Filippini et al., *Proc. Natl. Acad. Sci. U.S.A.* **106**, 7209–7214 (2009).
- M. S. Fanselow, H. W. Dong, *Neuron* **65**, 7–19 (2010).
- A. Bakker et al., *Neuron* **74**, 467–474 (2012).
- A. W. Bero et al., *Nat. Neurosci.* **14**, 750–756 (2011).
- K. Hardcastle, S. Ganguli, L. M. Giacomini, *Neuron* **86**, 827–839 (2015).
- L. Muessig, J. Hauser, T. J. Wills, F. Cacucci, *Neuron* **86**, 1167–1173 (2015).
- A. J. Trachtenberg, N. Filippini, C. E. Mackay, *Neurobiol. Aging* **33**, 323–334 (2012).
- C. F. Doeller, J. A. King, N. Burgess, *Proc. Natl. Acad. Sci. U.S.A.* **105**, 5915–5920 (2008).
- T. Wolbers, J. M. Wiener, H. A. Mallot, C. Büchel, *J. Neurosci.* **27**, 9408–9416 (2007).
- K. R. Sherrill et al., *J. Neurosci.* **33**, 19304–19313 (2013).
- C. R. Mondadori et al., *Cereb. Cortex* **17**, 1934–1947 (2007).
- F. Cacucci, M. Yi, T. J. Wills, P. Chapman, J. O'Keefe, *Proc. Natl. Acad. Sci. U.S.A.* **105**, 7863–7868 (2008).

ACKNOWLEDGMENTS

The authors thank H. Boecker, V. Heise, W. Huijbers, T. Reber, and S. Remy for comments on the manuscript and A. Rühling and Y. Sagik for their help with fMRI scanning. We also thank all of the participants for their participation in this study. L.K. was supported by a Bonfor dissertation stipend of the Medical Faculty of the University of Bonn and a stipend of the German National Academic Foundation (Studienstiftung des deutschen Volkes). C.M. is funded by a Heisenberg grant awarded to him by the German Research Foundation (DFG, MO 2363/3-1). P.C.M.F. was supported by a stipend of the Konrad Adenauer Foundation (Konrad-Adenauer-Stiftung). C.F.D. and T.N.S. are supported by the European Research Council (grant ERC-StG 261177) and the Netherlands Organisation for Scientific Research (grant NWO-Vidi 452-12-009). N.A. received DFG funding from Emmy Noether grant AX82/2 and together with J.F. via the Sonderforschungsbereich 1089. The authors declare no conflicts of interest. All raw data are archived at the German Center for Neurodegenerative Diseases (DZNE), Bonn.

SUPPLEMENTARY MATERIALS

www.sciencemag.org/content/350/6259/430/suppl/DC1
Materials and Methods
Supplementary Text
Figs. S1 to S12
Tables S1 to S7
References (33–62)

17 June 2015; accepted 23 September 2015
10.1126/science.aac8128

MICROBIAL METABOLISM

Methane metabolism in the archaeal phylum Bathyarchaeota revealed by genome-centric metagenomics

Paul N. Evans,^{1*} Donovan H. Parks,^{1*} Grayson L. Chadwick,² Steven J. Robbins,¹ Victoria J. Orphan,² Suzanne D. Golding,³ Gene W. Tyson^{1,4,†}

Methanogenic and methanotrophic archaea play important roles in the global flux of methane. Culture-independent approaches are providing deeper insight into the diversity and evolution of methane-metabolizing microorganisms, but, until now, no compelling evidence has existed for methane metabolism in archaea outside the phylum Euryarchaeota. We performed metagenomic sequencing of a deep aquifer, recovering two near-complete genomes belonging to the archaeal phylum Bathyarchaeota (formerly known as the Miscellaneous Crenarchaeotal Group). These genomes contain divergent homologs of the genes necessary for methane metabolism, including those that encode the methyl-coenzyme M reductase (MCR) complex. Additional non-euryarchaeotal MCR-encoding genes identified in a range of environments suggest that unrecognized archaeal lineages may also contribute to global methane cycling. These findings indicate that methane metabolism arose before the last common ancestor of the Euryarchaeota and Bathyarchaeota.

Anaerobic archaea are major contributors to global methane cycling. Methanogenic archaea are estimated to produce one billion tons of methane per year, with an equal amount estimated to be oxidized by archaeal methanotrophs (1). All previously described archaeal methane-metabolizing microorganisms belong to the phylum Euryarchaeota (2) and share a core set of bidirectional enzymes responsible for their respective metabolisms (3). This restricted phylogenetic distribution has led to the hypothesis that archaeal methane metabolism originated within the Euryarchaeota (4), although an origin outside this phylum has also been proposed (5). Recent advances in metagenomic techniques are allowing population genomes to be recovered en masse across many previously uncultivated archaeal lineages and from increasingly complex environments (6, 7). This has greatly expanded our understanding of the metabolic capabilities of these lineages; however, no methanogenic or methanotrophic archaea have been discovered thus far outside of the Euryarchaeota phylum.

The recently proposed Bathyarchaeota phylum (formerly the Miscellaneous Crenarchaeotal Group, MCG) represents an evolutionarily diverse group of microorganisms (8–11) found in a wide range of environments, including deep-

ocean and freshwater sediments (9, 12, 13). The high abundance of bathyarchaeotal 16S ribosomal RNA (rRNA) genes and lipid biomarkers within sulfate-methane transition zones has led to speculation that members of this lineage may be involved in dissimilatory anaerobic oxidation of methane, coupled to organic carbon assimilation (14). However, no Bathyarchaeota have been successfully cultured, and the only genomic representative is a ~21% complete single-cell genome, AB-536-E09 (E09), which was obtained from marine sediments (13). Although the E09 genome appears to belong to a peptide fermenter, its full metabolic potential is not understood because of its genome being incomplete. Given the wide environmental and phylogenetic diversity of Bathyarchaeota, additional genomes are required

to understand the metabolic capabilities of this understudied phylum.

In this study, we collected microbial biomass from filtered formation waters in 11 coal-bed methane wells within the Surat Basin (Queensland, Australia; fig. S1). Recovered DNA was sequenced, assembled, and binned into population genomes (supplementary materials). From the CX-10 sample, 19 population genomes were recovered (table S1), including two Bathyarchaeota genomes estimated to be ~92% (BA1) and ~94% (BA2) complete, as determined by the presence of single-copy marker genes (Table 1). A genome tree, inferred from 144 phylogenetically informative genes, places the BA1 and BA2 genomes and the E09 single-cell genome in a well-supported phylum that is sister to the Thaumarchaeota and Aigarchaeota phyla (Fig. 1A). The 16S rRNA gene tree is congruent with the genome tree and places these genomes with environmental clones belonging to Bathyarchaeota (Fig. 1B). The BA1 and BA2 genomes only share 656 genes (31.5%), with an average amino acid identity of 67.0%, and they have a 16S rRNA sequence identity of 90.5% (table S2), indicating that they represent separate genera or families (15, 16). E09 represents a distinct bathyarchaeotal family from BA1 and BA2, based on 16S rRNA sequence identity (81.5% to BA1, 83.5% to BA2), and shares 56 of its 603 genes (9.3%) with these genomes (fig. S2 and table S3).

Metabolic reconstruction of the BA1 genome revealed the presence of many genes in the Wood-Ljungdahl pathway and key genes associated with archaeal methane metabolism (Fig. 2 and table S4)—most importantly, those that encode the methyl-coenzyme M reductase complex (MCR) (*mcrABG* and putatively *mcrCD*; supplementary text). The BA1 genome contains genes for methanogenesis from methyl sulfides (*mtsA*), methanol (*mtbA*), and methylated amines (*mtaA*, *mttBC*, *mtbBC*), as well as three *mtrH* subunits, each collocated with a corrinoid protein (Fig. 2). The presence of these genes suggests the potential for diverse methyl compound utilization,

Table 1. Summary statistics of Bathyarchaeota genomes.

	BA1 (this study)	BA2 (this study)	E09 [from (13)]
Completeness*	91.6%	93.8%	21.5%
Contamination*	2.8%	3.7%	0.0%
Total length (base pairs)	1,931,714	1,455,689	529,171
GC content	47.1%	44.2%	43.3%
Number of scaffolds	89	57	87
Number of contigs	96	58	87
N50 of contigs	32,677	43,519	13,721
Number of coding sequences†	2403	1761	603
Coding density	80.8%	83.6%	81.7%
Average coverage	35.8	49.8	no data
Relative abundance‡	0.92%	1.03%	no data

*Based on lineage-specific marker sets determined with CheckM (28). †Inferred with Prodigal (29). ‡Estimated from the proportion of reads mapped to the genome.

¹Australian Centre for Ecogenomics, School of Chemistry and Molecular Biosciences, University of Queensland, St Lucia 4072, Queensland, Australia. ²Division of Geological and Planetary Sciences, California Institute of Technology, Pasadena, CA 91125, USA. ³School of Earth Sciences, University of Queensland, St Lucia 4072, Queensland, Australia. ⁴Advanced Water Management Centre, University of Queensland, St Lucia 4072, Queensland, Australia. *These authors contributed equally to this work. †Corresponding author. E-mail: g.tyson@uq.edu.au

similar to that found in obligate H_2 -utilizing methylotrophic methanogens belonging to the order Methanomassiliicoccales (17). Additionally, these genes may be sufficient for methyl group transfer directly to tetrahydromethanopterin (H_4 MPT) for carbon assimilation (18). Further, 12 novel methyltransferases with high similarity to each other, but divergent from known methyltransferases, were also identified in the genome, suggesting that this microorganism may use additional methylated compounds. However, the absence of most subunits of the Na^+ -translocating methyl- H_4 MPT:coenzyme M methyltransferase (MTR; encoded by *mtrABCDEFG*) suggests that BA1 is unable to perform hydrogenotrophic methanogenesis.

BA1 also contains genes (*hdrABC* and *mvhADG*) that encode a conventional heterodisulfide reductase- F_{420} nonreducing hydrogenase electron-bifurcating complex, which is needed for the cycling of coenzyme M (CoM) and coenzyme B (CoB). In addition, three copies of the gene for heterodisulfide reductase subunit D (*hdrD*) were found collocated with the gene for cytoplasmic flavin adenine dinucleotide-containing dehydrogenases (*gldD*), a gene arrangement also found in the lactate utilization operon of *Archaeoglobus fulgidis* (19). This indicates that lactate may also

serve as an electron donor for the reduction of the heterodisulfide in methanogenesis, functionally replacing methanophenazine and HdrE as the source of electrons for HdrD. The absence of HdrE is also seen in some methylotrophic methanogens belonging to the recently described order Methanomassiliicoccales, which also lack the genes for the MTR complex (17). In addition to the missing MTR subunits, the BA1 genome also lacks most other energy-conserving complexes, including the $F_{420}H_2$ dehydrogenase (encoded by *fpo*), energy-converting hydrogenases A and B (*eha* and *ehb*), Rhodobacter Nitrogen Fixation complex, and V/A-type adenosine triphosphate (ATP) synthase. The only complex capable of conserving energy via ion pumping is an energy-converting hydrogenase (encoded by *ech*), which may be sufficient for energizing the membrane for solute transport in the absence of energy-generating mechanisms. To ensure that our results did not reflect contamination within the BA1 population genome, we examined contigs encoding genes associated with methane metabolism to ensure that they agreed with the average guanine-cytosine (GC) content, coverage, and tetranucleotide frequencies of the genome (fig. S3).

Similar to BA1, the BA2 genome contains genes that encode the MCR complex (*mcrABGCD*) and

a number of additional genes typical of methane metabolism (*hdrABC*, *hdrD*, and *mvhADG*) (Fig. 2 and fig. S4). These include homologs to the genes for the novel methyltransferases found in BA1, suggesting that BA2 may also be capable of methylotrophic methanogenesis. However, in contrast to BA1, the majority of genes involved in the methyl branch of the Wood-Ljungdahl pathway either were not identified or appeared to be repurposed. For example, the gene for formylmethanofuran- H_4 MPT formyltransferase (*ftr*) was present in the BA2 genome, but it was found in an operon for purine biosynthesis and may have been co-opted into the formyl transferase reactions in this pathway. Additionally, the H_4 MPT biosynthesis genes (*mptBN*) have greater sequence similarity to bacterial homologs than to euryarchaeotal or BA1 homologs. Chemiosmotic energy-conserving complexes were also absent in the BA2 genome, including the energy-conserving hydrogenase complex (*ech*) found in BA1.

In addition to the differences between their methane-metabolism pathways, comparative genomic analysis identified other metabolic differences between the BA1 and BA2 genomes. Similar to the peptide-fermenting lifestyle inferred from the E09 single-cell genome (13), BA1 can generate acetyl-coenzyme A (CoA) from oxidative

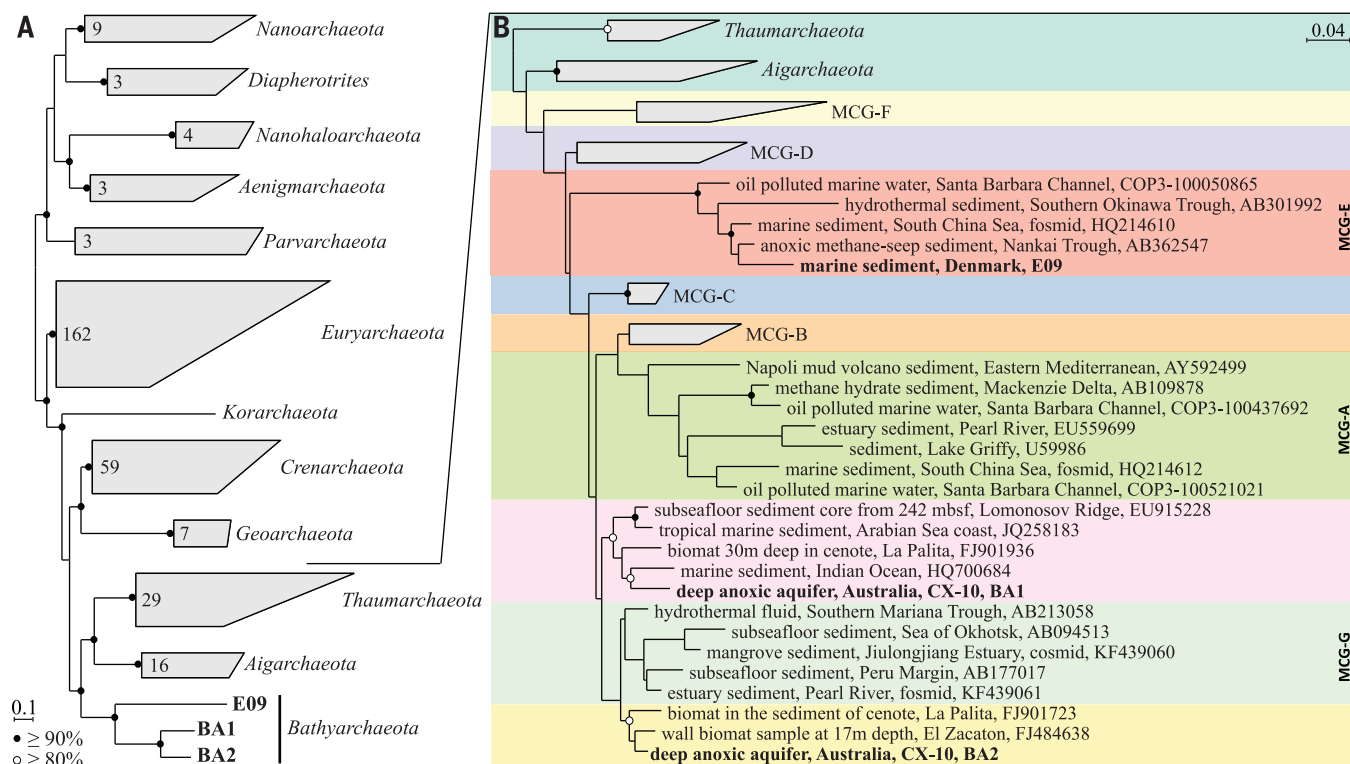


Fig. 1. Phylogenetic trees showing the placement of the BA1, BA2, and E09 genomes in the archaeal phylum Bathyarchaeota. (A) Maximum-likelihood tree of 295 archaea, inferred from a concatenated alignment of 144 proteins and rooted with the DPANN (Diapherotrites Parvarchaeota Aenigmarchaeota Nanoarchaeota Nanohaloarchaeota) superphyla (27). Support values are shown with white ($\geq 80\%$) and black ($\geq 90\%$) circles and indicate the minimum support under nonparametric bootstrapping, gene jackknifing, and taxon jackknifing (supplementary materials). (B) Maximum-likelihood 16S rRNA gene tree

showing the placement of bathyarchaeotal representatives relative to environmental sequences, including genes recovered from Coal Oil Point. Thaumarchaeota and Aigarchaeota 16S rRNA sequences from reference genomes were used as an outgroup. Bathyarchaeota (formerly MCG) groups are based on the classification in (9). Nonparametric support values are shown with white ($\geq 80\%$) and black ($\geq 90\%$) circles. Environmental context and genomes or National Center for Biotechnology Information accession numbers are given. Scale bars indicate expected number of substitutions per site.

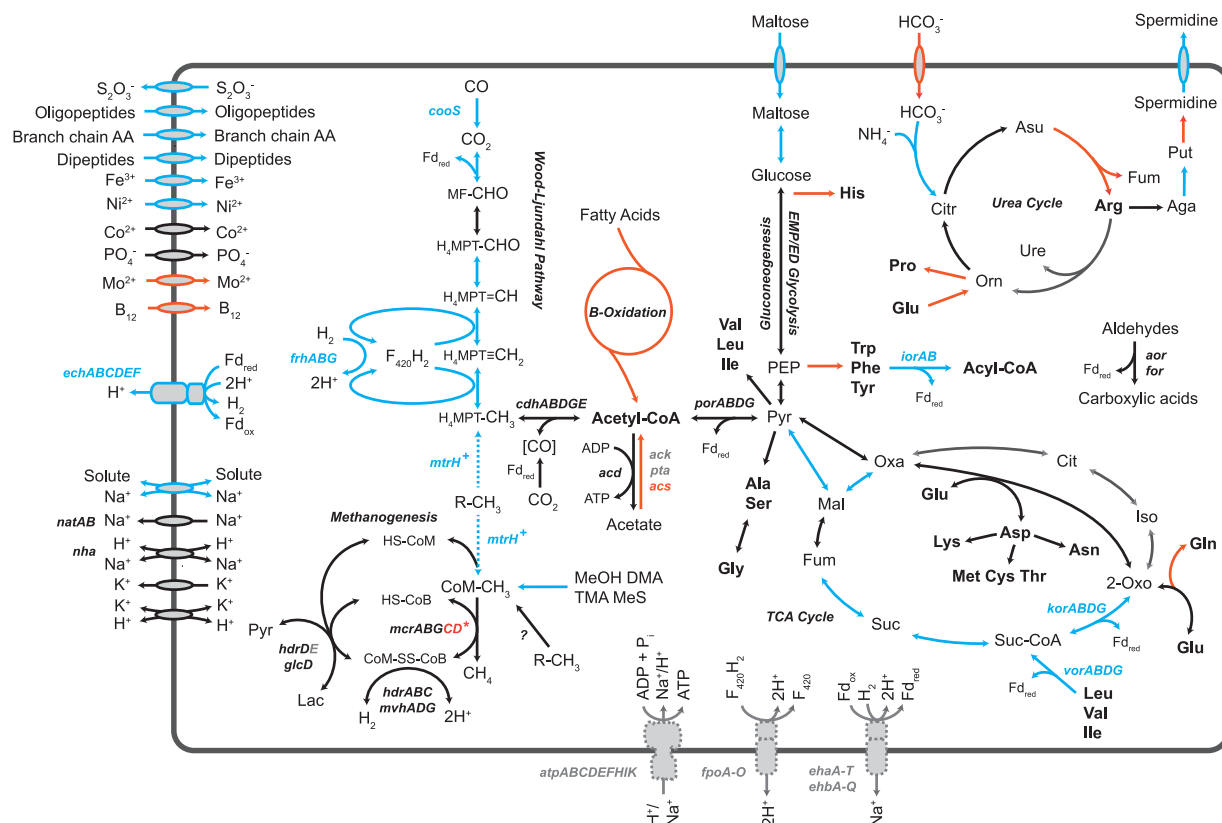


Fig. 2. Key metabolic pathways in the BA1 and BA2 genomes. Genes and pathways found in both BA1 and BA2 (black), only found in BA1 (blue), only found in BA2 (orange), or missing from both genomes (gray) are indicated. Genes associated with the pathways highlighted in this figure are presented in tables S9 (BA1) and S10 (BA2). In the BA1 genome, **mtrH* genes are adjacent to corrinoid proteins. A bathyarchaeotal contig containing *mcrCD* genes was identified in the metagenome, which probably belongs to the BA1 genome (supplementary text). EMP/ED, Embden-Meyerhof-Parnas/Entner-Doudoroff pathway; TCA, tricarboxylic acid.

deamination of amino acids by glutamate dehydrogenase (encoded by *gdh*), aspartate aminotransferases (*aspC*), and 2-oxoacid:ferredoxin oxidoreductases (*kor*, *ior*, *por*, and *vor*). Aldehydes generated by these oxidoreductases can also be used to generate reduced ferredoxin and oxoacids via multiple aldehyde:ferredoxin oxidoreductases (*aor* or *for*) (20). Consistent with peptide fermentation, the BA1 genome contains multiple peptidases and amino acid and oligopeptide transporters (Fig. 2). Acetyl-CoA generated in the above reactions, or through the reductive acetyl-CoA pathway, can be used for ATP formation through the adenosine diphosphate (ADP)-forming acetyl-CoA synthase (encoded by *acd*). The BA1 genome also contains a putative maltose transporter and an α -1-4 glycosyl hydrolase (GH family 38), indicating that glucose may be used as a carbon or energy source. Similar characteristics of peptide fermentation and maltose utilization are seen in *Pyrococcus* and other nonmethanogenic archaea (20). In contrast, BA2 appears to be a fatty-acid oxidizer, generating ATP from acetyl-CoA formed through β -oxidation and oxidation of pyruvate via the pyruvate:ferredoxin oxidoreductase (encoded by *por*). Genes for acetate assimilation via phosphotransacetylase (*pta*) or acetate kinase (*ack*) were not identified in either

genome. BA2 is predicted to be able to synthesize all 20 standard amino acids, whereas BA1 appears to be auxotrophic for histidine, proline, tryptophan, tyrosine, and phenylalanine, consistent with its ability to take up amino acids from the environment (Fig. 2).

MCR is the only catabolic enzyme shared by all methane-metabolizing organisms and has not previously been identified in microorganisms outside Euryarchaeota. To further explore the distribution and diversity of this complex, *mcrA* gene sequences from BA1 and BA2 were used to identify homologs across the Surat Basin and 2705 publicly available metagenomes. Non-euryarchaeotal *mcrA* genes were recovered from 8 of the 11 Surat Basin samples, and these genes cluster with those from BA1 and BA2 (Fig. 3 and table S5). An additional five nearly full-length *mcrA* genes were recovered from hydrocarbon-seep samples from Coal Oil Point (Santa Barbara, California), and these sequences constitute sister lineages to the Surat Basin *mcrA* sequences (Fig. 3 and table S5). Non-euryarchaeotal *mcrA* gene fragments (50 to 98% amino acid similarity) were also identified in other high-methane flux environments, including tar sand tailing ponds (Alberta, Canada), petroleum reservoir sediments (North Sea, UK), and several aquatic environments (table S6).

These results show that there is substantial *mcrA* diversity outside of the Euryarchaeota phylum, which may even extend beyond the Bathyarchaeota phylum. This diversity has previously gone unrecognized, because commonly used polymerase chain reaction primers for *mcrA* fail to amplify these divergent genes (fig. S5). Our results also indicate that not all Bathyarchaeota encode *mcrA*. Bathyarchaeotal *mcrA* genes were not identified in many metagenomes, where a substantial proportion of the community were inferred to belong to this phylum (table S7), which explains conflicting observations about Bathyarchaeota and their role in methane metabolism (11, 21). Consistent with the MCR subunit A (McrA) tree (Fig. 3), trees for McrB and McrG show substantial divergence between euryarchaeotal sequences and homologs from the Surat Basin and Coal Oil Point, including the gene sequences identified within the BA1 and BA2 genomes (figs. S6 to S8). The congruent topologies of these gene trees support the hypothesis that the MCR complex has coevolved as a functional unit and that methane metabolism was present in the last common ancestor of Euryarchaeota and Bathyarchaeota.

Despite the divergence of these novel *McrA* genes from their euryarchaeotal homologs (Fig. 3), they appear to be functionally conserved. The

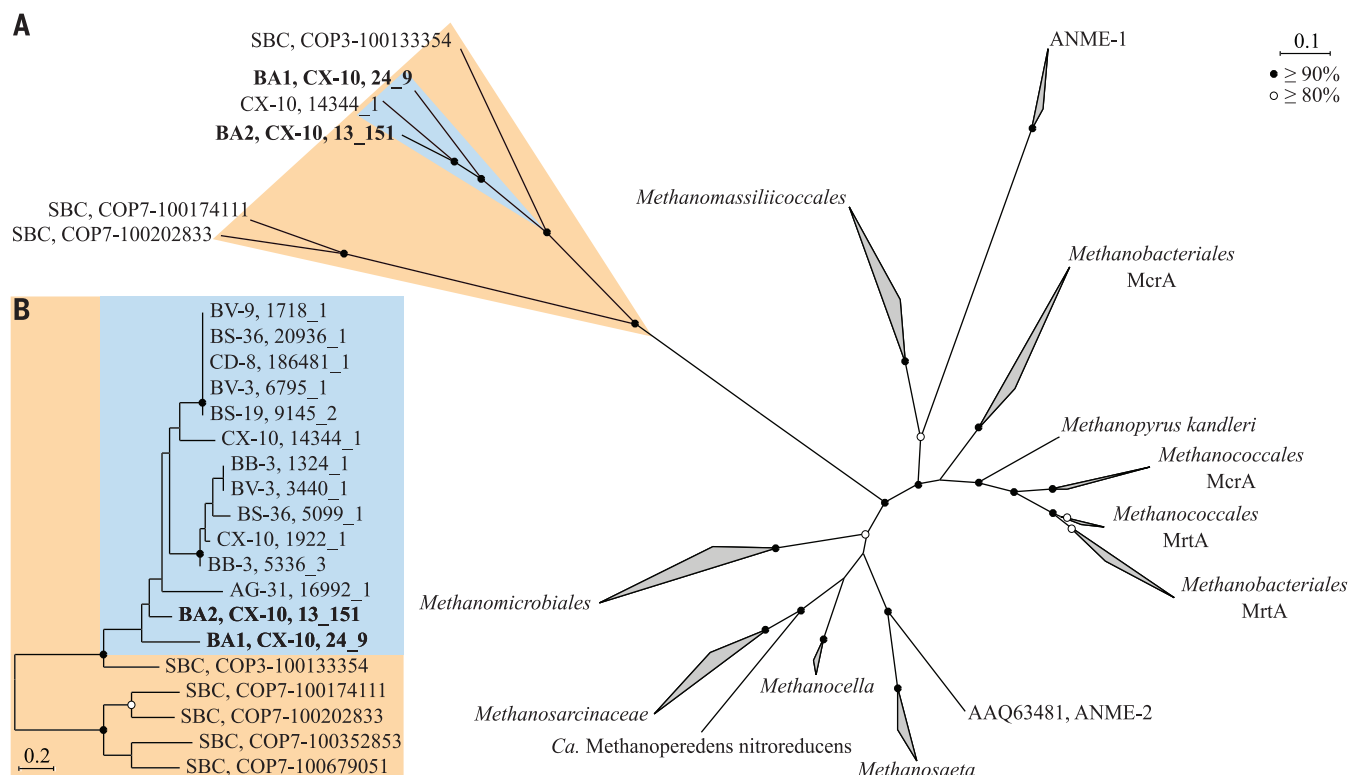


Fig. 3. Maximum-likelihood trees of McrA. (A) Placement of nearly full-length McrA protein sequences (≥400 amino acids) identified within the Surat Basin and Coal Oil Point metagenomes, in relation to 153 proteins obtained from GenBank. Lineages were collapsed (depicted as wedges) and labeled according to the lowest common ancestor of all taxa in the lineage. (B) Maximum-likelihood tree of nearly full-length and partial McrA sequences identified within the Surat Basin and Coal Oil Point metagenomes. Nonparametric support values are shown with white (≥80%) and black (≥90%) circles. Information about the Surat Basin wells is given in fig. S1. SBC, Santa Barbara Channel.

ligand-binding sites for CoB, CoM, and cofactor F_{430} (22) are largely conserved or have complementary amino acid substitutions to extant proteins (fig. S9 and table S8). Additionally, all functionally important residues in McrB and McrG proteins are conserved across the BA1 and BA2 proteins and their euryarchaeotal homologs (table S8). This strongly suggests that the MCR complex in these genomes can perform the same chemistry as its euryarchaeotal counterparts. Structure prediction of the McrA, McrB, and McrG proteins within the BA1 genome revealed high conservation with the crystal structures from *Methanopyrus kandleri* (fig. S10), indicating the potential for protein-ligand binding of CoB, CoM, and F_{430} (fig. S11). Despite the absence of almost all genes required for the synthesis of CoM and CoB in BA1 and BA2 (tables S9 and S10), these compounds remain the most likely substrates, based on the conserved nature of the MCR active sites. An N-terminal extension and a 19-amino acid insertion specific to the non-euryarchaeotal McrA protein sequences reside close to each other in the tertiary structure, despite being separated by ~300 amino acids in the primary sequence, suggesting that these may be involved in novel interactions with other protein complexes (fig. S10). Additionally, BA2 contains a homolog of the ATP-binding protein AtwA (component A2) that was recently shown to be necessary for MCR

activation in vitro (23), providing further evidence that a functional MCR complex is present in Bathyarchaeota (table S10).

The ability of BA1 and BA2 to carry out complex fermentation and β -oxidation, respectively, is unique among archaeal methanogens and methanotrophs (2). The presence of methane-metabolizing genes in a genome capable of complex fermentation leads us to hypothesize that BA1 is a methylotrophic methanogen that uses reduced ferredoxin, generated during fermentation of amino acids and maltose, to reduce methyl groups from diverse organic sources to methane (Fig. 2 and supplementary text). In contrast, we predict that BA2 derives its energy from fatty acid metabolism, and the presence of a gene for acetyl-CoA synthase (*acs*) suggests that carbon can be incorporated into biomass from acetate. However, like BA1, BA2 also appears to have the potential for methylotrophic methanogenesis using a wide range of methylated compounds (Fig. 2). Both BA1 and BA2 appear to lack ATP synthase genes, suggesting that they are restricted to substrate-level phosphorylation to gain energy. Although bacterial and archaeal genomes lacking ATP synthase genes have been recovered from a contaminated aquifer (7, 24), the absence of these genes in microorganisms with a methanogenic lifestyle is unexpected. These genes may be contained in the missing fraction

(<10%) of the BA1 or BA2 genome, although this is unlikely, because they are absent in both genomes and could not be identified in the metagenomic data. Given the outstanding questions about these bathyarchaeotal genomes and the bidirectionality of the enzymes involved in archaeal methane metabolism, it remains possible that these organisms could gain energy from the oxidation of methane (14). Although no genes were identified for coupling methane oxidation to known electron acceptors (25, 26), it is possible that CO_2 could act as an electron acceptor in the reversal of acetoclastic methanogenesis, producing acetate for a syntrophic association (supplementary text). The discovery of bathyarchaeotal and non-euryarchaeotal methane-metabolizing lineages has potentially important consequences for our understanding of the carbon cycle and directly affects our interpretation of the origin and evolutionary history of the MCR complex.

REFERENCES AND NOTES

1. W. Reeburgh, *Chem. Rev.* **107**, 486–513 (2007).
2. R. K. Thauer, A. K. Kaster, H. Seedorf, W. Buckel, R. Hedderich, *Nat. Rev. Microbiol.* **6**, 579–591 (2008).
3. R. K. Thauer, *Curr. Opin. Microbiol.* **14**, 292–299 (2011).
4. S. Gribaldo, C. Brochier-Armanet, *Philos. Trans. R. Soc. London B Biol. Sci.* **361**, 1007–1022 (2006).
5. S. Kelly, B. Wickstead, K. Gull, *Proc. Biol. Sci.* **278**, 1009–1018 (2011).
6. V. Iverson et al., *Science* **335**, 587–590 (2012).
7. C. J. Castelle et al., *Curr. Biol.* **25**, 690–701 (2015).

8. E. J. Gagen, H. Huber, T. Meador, K. U. Hinrichs, M. Thomm, *Appl. Environ. Microbiol.* **79**, 6400–6406 (2013).
9. J. Meng *et al.*, *ISME J.* **8**, 650–659 (2014).
10. C. S. Lazar *et al.*, *Environ. Microbiol.* **17**, 2228–2238 (2015).
11. K. Kubo *et al.*, *ISME J.* **6**, 1949–1965 (2012).
12. C. Vetriani, H. W. Jannasch, B. J. MacGregor, D. A. Stahl, A. L. Reysenbach, *Appl. Environ. Microbiol.* **65**, 4375–4384 (1999).
13. K. G. Lloyd *et al.*, *Nature* **496**, 215–218 (2013).
14. J. F. Biddle *et al.*, *Proc. Natl. Acad. Sci. U.S.A.* **103**, 3846–3851 (2006).
15. K. T. Konstantinidis, J. M. Tiedje, *Proc. Natl. Acad. Sci. U.S.A.* **102**, 2567–2572 (2005).
16. P. Yarza *et al.*, *Nat. Rev. Microbiol.* **12**, 635–645 (2014).
17. K. Lang *et al.*, *Appl. Environ. Microbiol.* **81**, 1338–1352 (2015).
18. U. Harms, R. K. Thauer, *Eur. J. Biochem.* **250**, 783–788 (1997).
19. W. P. Hocking, R. Stokke, I. Roalkvam, I. H. Steen, *Front. Microbiol.* **5**, 95 (2014).
20. K. Ma, A. Hutchins, S. J. Sung, M. W. Adams, *Proc. Natl. Acad. Sci. U.S.A.* **94**, 9608–9613 (1997).

21. J. F. Biddle, S. Fitz-Gibbon, S. C. Schuster, J. E. Brenchley, C. H. House, *Proc. Natl. Acad. Sci. U.S.A.* **105**, 10583–10588 (2008).
22. U. Ermler, W. Grabarse, S. Shima, M. Goubeaud, R. K. Thauer, *Science* **278**, 1457–1462 (1997).
23. D. Prakash, Y. Wu, S. J. Suh, E. C. Duin, *J. Bacteriol.* **196**, 2491–2498 (2014).
24. C. T. Brown *et al.*, *Nature* **523**, 208–211 (2015).
25. M. F. Haroon *et al.*, *Nature* **500**, 567–570 (2013).
26. E. J. Beal, C. H. House, V. J. Orphan, *Science* **325**, 184–187 (2009).
27. C. Rinke *et al.*, *Nature* **499**, 431–437 (2013).
28. D. H. Parks, M. Imelfort, C. T. Skennerton, P. Hugenholtz, G. W. Tyson, *Genome Res.* **25**, 1043–1055 (2015).
29. D. Hyatt *et al.*, *BMC Bioinformatics* **11**, 119 (2010).

ACKNOWLEDGMENTS

We thank E. Gagen and P. Hugenholtz for valuable comments and suggestions; K. Baublys, SGS-Leeder, and Australian Laboratory Services staff for sample collection; and M. Butler and S. Low for library preparation and sequencing. This study was supported by the Australian Research Council (ARC) Linkage Project (grant LP100200730) and the U.S. Department of Energy's Office of Biological Environmental Research (award no. DE-SC0010574). D.H.P. is supported by the Natural Sciences and Engineering

Research Council of Canada. S.J.R. is supported by an Australian Postgraduate Award Industry scholarship. G.W.T. is supported by an ARC Queen Elizabeth II Fellowship (grant DP1093175). The authors declare no conflicts of interest. Our Whole Genome Shotgun projects have been deposited in the DNA DataBank of Japan, the European Molecular Biology Laboratory repository, and NIH's GenBank under the accession numbers LIHJ000000000 (BA1) and LIHK000000000 (BA2). The versions described in this paper are LIHJ010000000 (BA1) and LIHK010000000 (BA2). Non-euryarchaeotal Surat Basin *mcrA* sequences have been deposited under the accession numbers KT387805 to KT387832, and unprocessed reads have been deposited under the accession number SRX1122679.

SUPPLEMENTARY MATERIALS

www.sciencemag.org/content/350/6259/434/suppl/DC1
Materials and Methods
Supplementary Text
Figs. S1 to S14
Tables S1 to S13
References (30–87)

11 June 2015; accepted 14 September 2015
10.1126/science.aac7745

PLANT SCIENCE

Mechanosensitive channel MSL8 regulates osmotic forces during pollen hydration and germination

Eric S. Hamilton, Gregory S. Jensen, Grigory Maksaev, Andrew Katims,*
Ashley M. Sherp, Elizabeth S. Haswell†

Pollen grains undergo dramatic changes in cellular water potential as they deliver the male germ line to female gametes, and it has been proposed that mechanosensitive ion channels may sense the resulting mechanical stress. Here, we identify and characterize MscS-like 8 (MSL8), a pollen-specific, membrane tension-gated ion channel required for pollen to survive the hypoosmotic shock of rehydration and for full male fertility. MSL8 negatively regulates pollen germination but is required for cellular integrity during germination and tube growth. MSL8 thus senses and responds to changes in membrane tension associated with pollen hydration and germination. These data further suggest that homologs of bacterial MscS have been repurposed in eukaryotes to function as mechanosensors in multiple developmental and environmental contexts.

Mechanosensitive (stretch-activated) ion channels provide an evolutionarily conserved mechanism for the perception of mechanical force at the membrane (1). The mechanosensitive channel of small conductance (MscS) from *Escherichia coli* belongs to a large and structurally diverse family of proteins encoded in bacterial, archaeal, plant, and fungal genomes (2, 3). Bacterial MscS homologs prevent cellular lysis upon hypoosmotic shock by releasing osmolytes from the cell in direct response to increased lateral membrane tension (4). MscS-like (MSL) proteins in plants exhibit homology to the pore-lining domain of *E. coli* MscS;

outside of this region, they show diverse domains and topologies (3) (fig. S1, A and B). *Arabidopsis thaliana* mutants lacking functional MSL genes respond normally to externally applied osmotic or mechanical stresses (5).

We therefore hypothesized that MscS homologs in plants may sense and respond to rapid changes in water status (and therefore membrane tension) that are intrinsic to the plant life cycle rather than environmentally imposed. Several such events occur during the development of pollen, the multicellular haploid life stage of plants that harbors the male gametes (6). In most angiosperms, including *A. thaliana*, the last stage of pollen maturation is partial dehydration (<30% water content) (7). Once the desiccated pollen grain contacts the stigma cells of a compatible female flower, stigma exudate enters the grain and reactivates its metabolism (8). The pollen tube

germinates, breaking through the grain cell wall and proceeding via polarized tip growth toward female gametes inside the ovaries (9). The mechanical stress exerted on pollen membranes and cell walls (10, 11) and the spatially and temporally dynamic ion fluxes known to be essential for pollen grain germination and tube growth (12) suggest a role for stretch-activated ion channels (13). Mechanosensitive cation channel activities have been detected in pollen grain and tube membranes (14), but their molecular identity and physiological functions remain unknown.

A. thaliana MSL8 (At2g17010) transcripts were detected in mRNA isolated from floral but not leaf or root tissue (fig. S1C). In transgenic plants expressing genomic MSL8 fused to green fluorescent protein (*gMSL8-GFP*) under the control of native sequences, fluorescence was observed inside half of the pollen grains within the anthers of the hemizygous first transformed T1 generation (Fig. 1A). *gMSL8-GFP* signal was observed in tricellular and mature pollen (Fig. 1, B to F) (6) but not in any other tissue. MSL8 transcripts were identified in an RNA-sequencing data set from mature, dry pollen (15) (fig. S1D). Phylogenetic analysis suggests that male-specific expression of MSL genes evolved in both monocot and dicot lineages (fig. S2).

MSL8-GFP expressed from endogenous sequences localized both to the plasma membrane and to endomembrane compartments in pollen grains, and upon germination was mobilized to the tube periphery (Fig. 1, G and H), as did MSL8-YFP (yellow fluorescent protein) expressed from the strong pollen-specific promoter *LAT52* (Fig. 1I) (16). MSL8-YFP colocalized with the pollen plasma membrane protein CPK34 (17) but not with an endoplasmic reticulum marker (maximum Pearson's correlation coefficients of 0.66 and 0.09, respectively) (Fig. 1, J to L, and fig. S3), and there was no substantial overlap with Golgi or vacuole markers (fig. S4). A similar internal localization pattern has been observed with other pollen plasma membrane proteins (18, 19).

Department of Biology, Washington University in Saint Louis, Saint Louis, MO 63130, USA.

*Present address: University of Miami, Miller School of Medicine, 1600 NW 10th Avenue, Miami, FL, USA. †Corresponding author. E-mail: ehaswell@wustl.edu

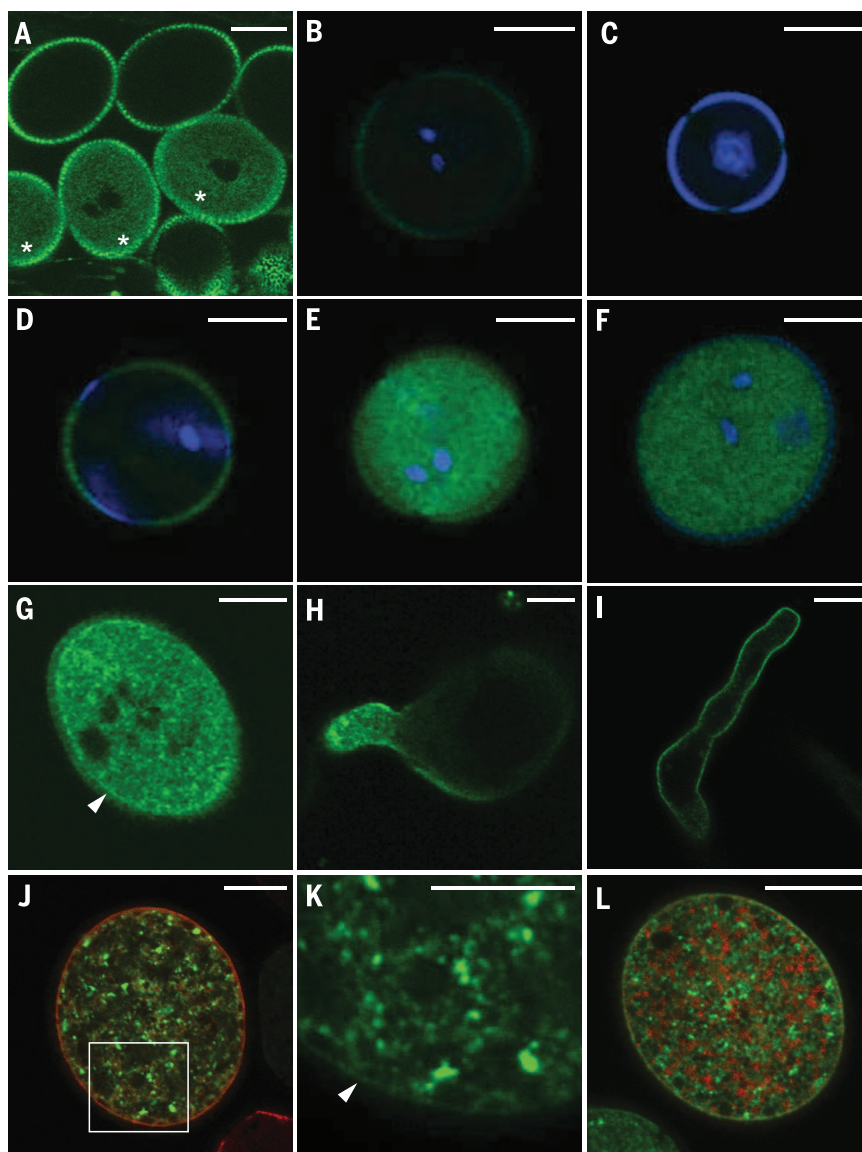


Fig. 1. MSL8 is expressed in mature pollen grains and localizes to the plasma membrane and endomembranes of pollen grains and germinating tubes. (A) Confocal image of GFP signal in a dissected anther from stage 12 flowers of a *gMSL8-GFP* T1 plant. Asterisks mark transgenic pollen. The pollen cell wall is autofluorescent, but internal fluorescence is ascribed to MSL8-GFP. (B to F) Confocal images of GFP (green) and 4',6-diamidino-2-phenylindole (DAPI) signal (blue) during pollen development. (B) Tricellular pollen from a nontransformed line. Pollen was isolated from a *gMSL8-GFP*-expressing line at the (C) microspore, (D) bicellular, (E) tricellular, and (F) mature stages of development. (G and H) Confocal images of ungerminated (G) and in vivo germinated (H) pollen grains in a *gMSL8-GFP*-expressing line. (I) A germinated pollen tube from a line expressing *LAT52pMSL8-YFP*. (J) MSL8-YFP (green) overlaid with CPK34-mCherry (red). (K) Magnification of box indicated in (J), green channel only. (L) MSL8-YFP overlaid with endoplasmic reticulum-mCherry (red). Arrow indicates plasma membrane. Scale bars, 10 μ m [(B) to (J) and (L)] or 5 μ m (K).

MSL8 produced mechanosensitive ion channel activity when expressed in *Xenopus laevis* oocytes (Fig. 2A and fig. S5, A and B). In this system, MSL8 (or MSL8-YFP, which was indistinguishable) (fig. S5C) had a unitary conductance of 57 pS under negative membrane potentials and 39 pS under positive membrane potentials (Fig. 2B); the conductance of MscS is ~300 pS under similar conditions (20). MSL8 exhibited a 6.3-fold pref-

erence for chloride over sodium (Fig. 2C) and is therefore more anion-selective than MscS, which has a permeability ratio ($P_{Cl}:P_K$) of 1.2 to 3.0 (21). Finally, the gating threshold pressure for MSL8 was higher than that of MscS (-48.2 ± 14.8 mm Hg and -19.1 ± 5.1 mm Hg, respectively; $n = 9$ patches) (fig. S5, D and E). MSL8 activity was unaffected by treatment with $MgCl_2$, ruthenium red, or tetramethylammonium-Cl (figs. S5C and S6, A to C). A

mechanosensitive channel activity with conductance similar to MSL8 under the same conditions was occasionally detected in wild-type Col-0 pollen protoplasts (5 of 58 patches) and may correspond to the endogenous MSL8 channel (Fig. 2D and fig. S6, D to F). Final confirmation will require demonstrating the loss of channel activity in *msl8* mutant pollen grains.

Two transfer DNA (T-DNA) insertion alleles were identified that resulted in the reduction and loss of detectable *MSL8* transcripts in the flower, *msl8-1* and *msl8-4*, respectively (fig. S7, A and B). The null *msl8-4* allele was transmitted through the male germ line with reduced efficiency, while it was transmitted normally through the female germ line (Fig. 3A). Even modest transmission defects will result in rapid purification from a natural population, as pollen-specific genes are subject to strong selection against deleterious mutations (22). We detected no obvious morphological defects in the coat or cell wall of desiccated *msl8-4* pollen grains (Fig. 3B).

To test the hypothesis that *MSL8* is required for pollen to survive the osmotic downshift experienced during rehydration, we quantified the viability of mature pollen after rehydration in distilled water. Whereas wild-type pollen exhibited 83 to 95% viability over the 2-hour time course, *msl8-4* pollen viability dropped from 38% to 21%, and *msl8-1* pollen viability dropped from wild-type levels to 46% (Fig. 3C-D). This phenotype was rescued by the *gMSL8-GFP* transgene in both mutant backgrounds (fig. S7, C and D).

While the osmotic shock of in vitro hydration in distilled water is more extreme than pollen grains are likely to experience in vivo, *msl8-4* pollen also shows a defect in viability when hydrated in low concentrations of polyethylene glycol (PEG) 3350 (Fig. 3E). These results are consistent with previous work showing that even slow rates of osmotic downshock are lethal to an *E. coli* strain lacking mechanosensitive ion channels (23). Increasing the osmolarity of the hydration medium led to corresponding increases in pollen viability. The in vivo hydration rate of *msl8-4* pollen did not differ from the wild type (fig. S7E). Finally, *msl8-4* pollen grains dissected from anthers before desiccation showed wild-type viability upon hydration (Fig. 3F). Thus, *msl8* pollen developed normally and was fully viable before dehydration, and its loss of viability when hydrated can be attributed to the hypoosmotic challenge of water entering the desiccated grain.

MSL8 also plays a role in pollen germination. During in vitro germination assays, *msl8-4* pollen grains and germinated tubes burst 26% of the time, whereas only 3% of the wild type burst (Fig. 4, A to C). Pollen bursting is associated with cell-wall defects and lesions in ion channel genes and is thus thought to result from a failure to balance osmotic pressure with the strength of the cell wall (19). *msl8-4* and *msl8-1* pollen germinated at a higher rate than the corresponding wild type (both burst and intact tubes: 43% in *msl8-4* and 57% in *msl8-1*; compare to 20% and 23% in Ler and Col-0, respectively) (Fig. 4, A to C). Conversely, overexpression of *LAT52pMSL8-YFP*

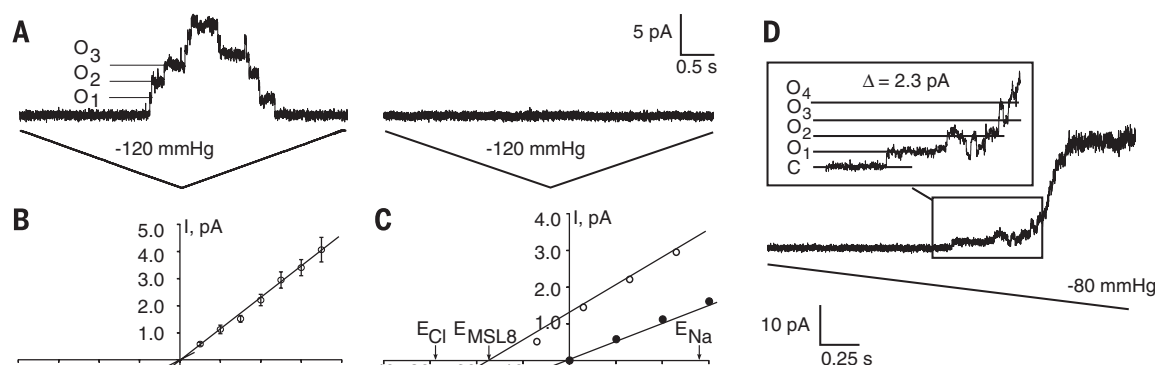


Fig. 2. MSL8 forms a small-conductance mechanosensitive ion channel with a preference for anions that is similar to a channel present in pollen membranes. (A) Represent-

ative trace from an excised inside-out patch of plasma membrane from a *Xenopus laevis* oocyte expressing MSL8-YFP capped RNA (cRNA) (left) or water-injected (right) at -60 mV membrane potential. Channels were gated by negative tension (suction) applied to the patch pipette. The first three channel openings are labeled O_1 to O_3 . (B) The current-voltage relationship of untagged tension-gated MSL8 in symmetric ND96 buffer. $N = 8$ oocytes. (C) The current-voltage relationship of tension-gated MSL8 under symmetric (filled circles, 100 mM NaCl) and asymmetric (open circles, 100 mM NaCl pipette/300 mM NaCl bath) conditions. $N = 3$ oocytes. (D) Representative trace from an excised inside-out patch of membrane from a Col-0 pollen protoplast at a transmembrane potential of -60 mV. Inset, four channel openings with characteristics similar to MSL8 are labeled O_1 to O_4 .

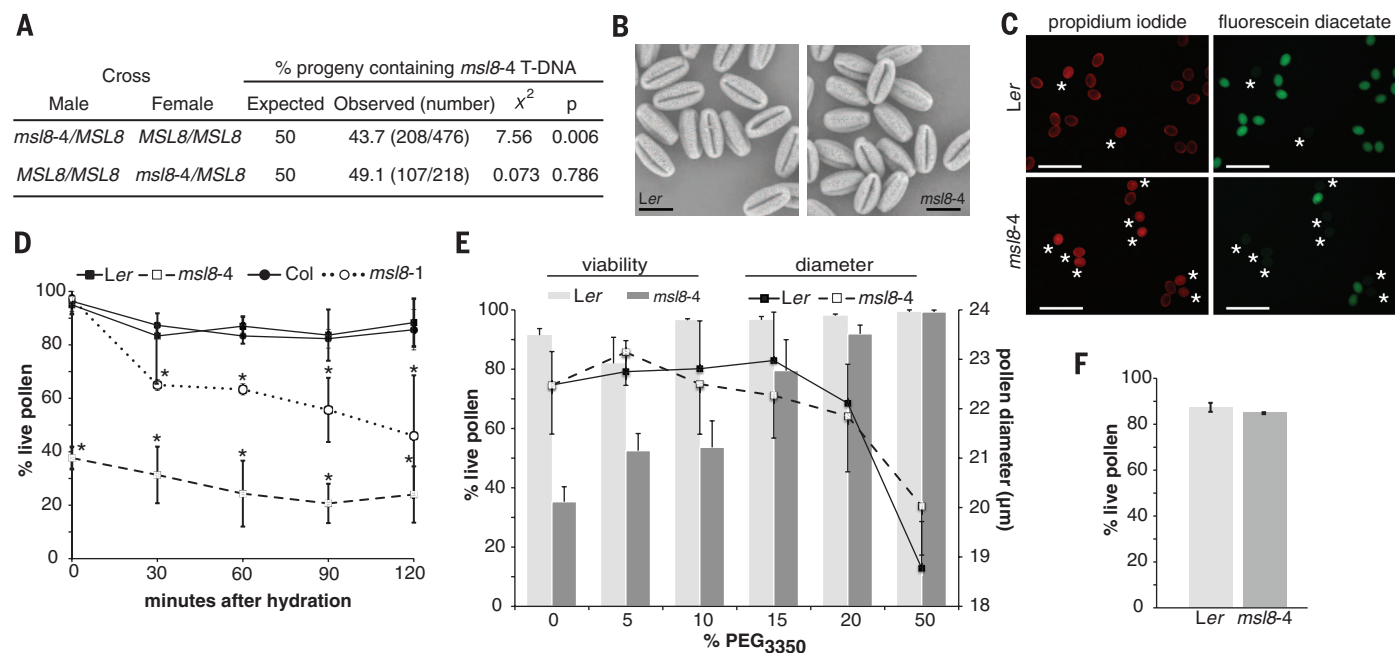


Fig. 3. MSL8 is required for mature pollen grains to survive hypoosmotic shock during rehydration. (A) Transmission ratio analysis of the *msl8-4* allele. The progeny of reciprocal crosses between *msl8-4* heterozygotes and wild-type plants were genotyped. P values were determined by a chi-square test against the expected ratio of 50:50. (B) Scanning electron micrograph of desiccated pollen from the indicated genotypes. Scale bar is $20\ \mu\text{m}$. (C) Viability of wild-type and mutant pollen after hydration. Pollen was incubated for 30 min in distilled water containing fluorescein diacetate and propidium iodide, dyes that stain viable and unviable pollen, respectively. Asterisks

mark compromised pollen. Scale bar, $100\ \mu\text{m}$. (D) Hydration viability time course. The average of three experiments with $N = 55\ 170$ pollen grains is shown. Error bars, mean \pm SD. Asterisks indicate significant ($P < 0.05$) differences from the wild type by Student's t test. (E) Effect of a PEG series on viability (bars, 3 to 5 trials per genotype; $N = 48$ to 440 pollen grains per trial; error bars, mean \pm SE) and pollen diameter (lines, $N = 15$ pollen grains per genotype; error bars, mean \pm SD) after hydration. (F) Viability after hydration of nondehiscent tricellular pollen grains dissected from the anther of the indicated genotypes. $N > 50$ pollen grains per genotype. Error bars, mean \pm SD.

inhibited germination, and three independent homozygous lines exhibited only 4 to 39% of wild-type germination rates (Fig. 4D). The germination rate was inversely correlated with the level of MSL8-YFP transcript in these lines (Fig. 4E),

confirming that MSL8 negatively regulates in vitro germination. MSL8-YFP overexpression lines were impaired in transmission of the transgene to the next generation (Fig. 4F and fig. S8A), but only through the male parent (Fig. S8B-C). Because

these lines exhibited wild-type hydration survival (fig. S8D), this defect can be attributed to reduced rates of pollen germination.

Changes in osmotic potential are part of normal pollen function, in addition to being environmental

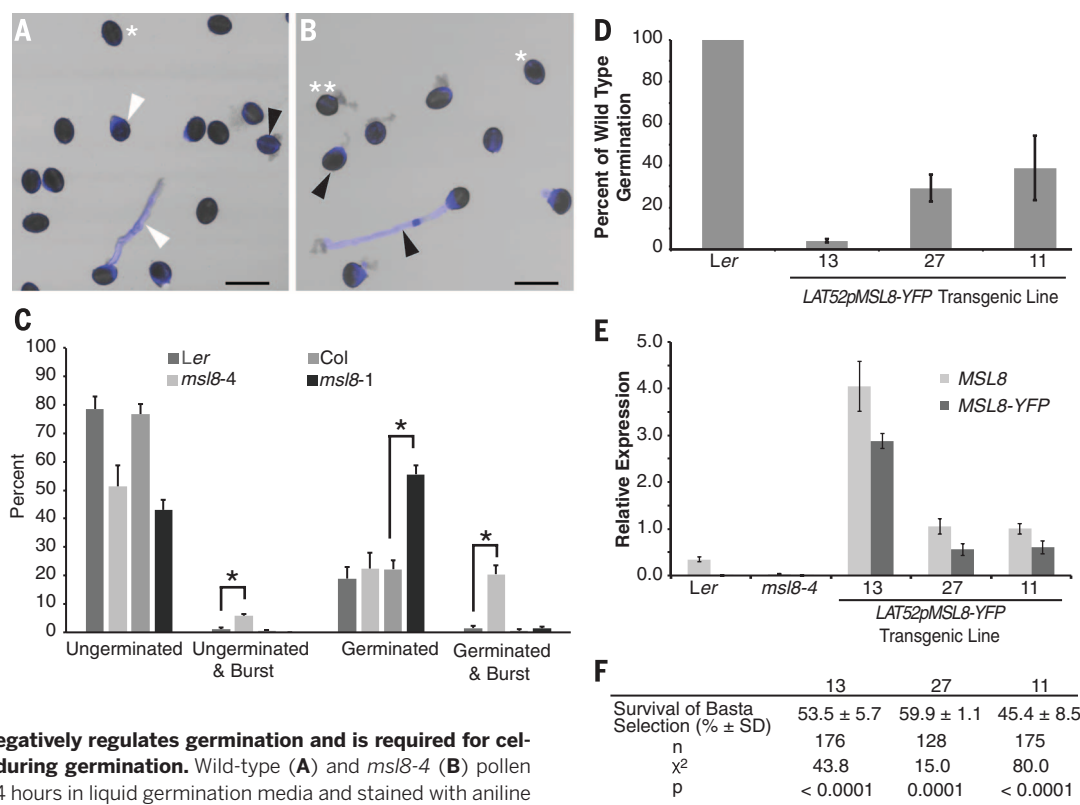


Fig. 4. MSL8 negatively regulates germination and is required for cellular integrity during germination. Wild-type (A) and *msl8-4* (B) pollen grains germinated for 4 hours in liquid germination media and stained with aniline blue for callose, a marker of germination. Examples of ungerminated (single asterisk), ungerminated and burst (double asterisk), germinated (white arrow), or germinated and burst (black arrow) pollen are indicated. Scale bar, 50 μ m. (C) Germination rate and bursting frequency in the indicated genotypes. $N \geq 396$ pollen grains per genotype. Asterisks indicate significant ($P < 0.05$) differences by Student's *t* test. (D) Percentage germination overnight on solid media of pollen from wild-type and three independent homozygous *LAT52pMSL8-YFP* transgenic lines. Error bars, mean \pm SE. (E) Quantitative reverse-transcription polymerase chain reaction of *MSL8-YFP* and *MSL8* transcripts relative to *ACTIN* in flowers from Ler, *msl8-4*, and the *LAT52pMSL8-YFP* lines in (D). Two technical replicates of three biological replicates are presented. Error bars, mean \pm SE. (F) Survival of selection for the Bialaphos resistance gene in offspring of the *LAT52pMSL8-YFP* lines in (D). *P* values were determined by a chi-square test against 75% expected survival.

stresses that must be tolerated. Here, we show that MSL8 is required for a tuned response to developmentally normal osmotic challenges. During pollen rehydration, MSL8 maintains cellular integrity upon osmotic downshift, playing a role analogous to that of *E. coli* MscS. During pollen germination, however, MSL8 maintains the optimal osmotic potential required to drive germination yet prevent lysis of the nascent pollen tube. MSL8 may accomplish these functions by releasing osmolytes directly in response to membrane tension and/or function indirectly in pathways that regulate pollen desiccation, membrane trafficking, or cell-wall dynamics. This study illustrates how MSL8, a eukaryotic homolog of the bacterial osmotic safety valve MscS, has been repurposed to help pollen cope with predictable osmotic changes that are characteristic of pollen development. It also contributes to a growing body of evidence that mechanical signaling plays a critical role in plant and animal development (24, 25).

stresses that must be tolerated. Here, we show that MSL8 is required for a tuned response to developmentally normal osmotic challenges. During pollen rehydration, MSL8 maintains cellular integrity upon osmotic downshift, playing a role analogous to that of *E. coli* MscS. During pollen germination, however, MSL8 maintains the optimal osmotic potential required to drive germination yet prevent lysis of the nascent pollen tube. MSL8 may accomplish these functions by releasing osmolytes directly in response to membrane tension and/or function indirectly in pathways that regulate pollen desiccation, membrane trafficking, or cell-wall dynamics. This study illustrates how MSL8, a eukaryotic homolog of the bacterial osmotic safety valve MscS, has been repurposed to help pollen cope with predictable osmotic changes that are characteristic of pollen development. It also contributes to a growing body of evidence that mechanical signaling plays a critical role in plant and animal development (24, 25).

REFERENCES AND NOTES

1. A. Anishkin, S. H. Loukin, J. Teng, C. Kung, *Proc. Natl. Acad. Sci. U.S.A.* **111**, 7898–7905 (2014).
2. C. D. Pivetti et al., *Microbiol. Mol. Biol. Rev.* **67**, 66–85 (2003).
3. E. S. Hamilton, A. M. Schlegel, E. S. Haswell, *Annu. Rev. Plant Biol.* **66**, 113–137 (2015).
4. I. R. Booth, P. Blount, *J. Bacteriol.* **194**, 4802–4809 (2012).
5. E. S. Haswell, R. Peyronnet, H. Barbier-Brygoo, E. M. Meyerowitz, J. M. Frachisse, *Curr. Biol.* **18**, 730–734 (2008).
6. N. Firon, M. Nepi, E. Pacini, *Ann. Bot.* **109**, 1201–1214 (2012).
7. G. G. Franchi et al., *J. Exp. Bot.* **62**, 5267–5281 (2011).
8. A. F. Edlund, R. Swanson, D. Preuss, *Plant Cell* **16** (suppl. 1), S84–S97 (2004).
9. H. J. Wang, J. C. Huang, G. Y. Jauh, *Adv. Bot. Res.* **54**, 1–52 (2010).
10. L. Beauzamy, N. Nakayama, A. Boudaoud, *Ann. Bot.* **114**, 1517–1533 (2014).
11. J. Kroeger, A. Geitmann, *Curr. Opin. Plant Biol.* **15**, 618–624 (2012).
12. E. Michard, F. Alves, J. A. Feijó, *Int. J. Dev. Biol.* **53**, 1609–1622 (2009).
13. J. A. Feijó, R. Mahlo, G. Obermeyer, *Protoplasma* **187**, 155–167 (1995).
14. R. Dutta, K. R. Robinson, *Plant Physiol.* **135**, 1398–1406 (2004).
15. A. E. Lorraine, S. McCormick, A. Estrada, K. Patel, P. Qin, *Plant Physiol.* **162**, 1092–1109 (2013).
16. D. Twell, T. M. Klein, M. E. Fromm, S. McCormick, *Plant Physiol.* **91**, 1270–1274 (1989).
17. C. Myers et al., *Plant J.* **59**, 528–539 (2009).
18. S. Frietsch et al., *Proc. Natl. Acad. Sci. U.S.A.* **104**, 14531–14536 (2007).
19. M. Tunc-Ozdemir et al., *PLOS ONE* **8**, e55277 (2013).
20. G. Maksaev, E. S. Haswell, *J. Gen. Physiol.* **138**, 641–649 (2011).
21. G. Maksaev, E. S. Haswell, *Channels* **7**, 215–220 (2013).
22. R. Arunkumar, E. B. Josephs, R. J. Williamson, S. I. Wright, *Mol. Biol. Evol.* **30**, 2475–2486 (2013).
23. M. Bialecka-Fornal, H. J. Lee, R. Phillips, *J. Bacteriol.* **197**, 231–237 (2015).
24. O. Hamant, *Curr. Opin. Plant Biol.* **16**, 654–660 (2013).
25. C. J. Miller, L. A. Davidson, *Nat. Rev. Genet.* **14**, 733–744 (2013).

ACKNOWLEDGMENTS

This work was funded by NSF MCB1253103 and NIH 2R01GM084211 to E. S. Haswell and by the Monsanto Excellence Fund Fellowship to E. S. Hamilton. We acknowledge M. Wilson and the Donald Danforth Plant Science Center imaging facility for technical assistance, J. Harper for plasmid ps819, M. Johnson for line *msl-1*, and the Arabidopsis Biological Resource Center for T-DNA insertion lines and ER-rk (CD3-959) and G-rk (CD3-967) membrane markers. The authors do not have any conflicts of interest. The supplementary materials contain additional data.

SUPPLEMENTARY MATERIALS

www.sciencemag.org/content/350/6259/438/suppl/DC1
Materials and Methods
Figs. S1 to S8
Table S1
References (26–32)

22 May 2015; accepted 10 September 2015
10.1126/science.aac6014

REPRODUCTIVE BIOLOGY

Sperm calcineurin inhibition prevents mouse fertility with implications for male contraceptive

Haruhiko Miyata,¹ Yuhkoh Satouh,¹ Daisuke Mashiko,^{1,2} Masanaga Muto,^{1,3} Kaori Nozawa,^{1,2} Kogiku Shiba,⁴ Yoshitaka Fujihara,¹ Ayako Isotani,⁵ Kazuo Inaba,⁴ Masahito Ikawa^{1,2,3,5*}

Calcineurin inhibitors, such as cyclosporine A and FK506, are used as immunosuppressant drugs, but their adverse effects on male reproductive function remain unclear. The testis expresses somatic calcineurin and a sperm-specific isoform that contains a catalytic subunit (PPP3CC) and a regulatory subunit (PPP3R2). We demonstrate herein that male mice lacking *Ppp3cc* or *Ppp3r2* genes (knockout mice) are infertile, with reduced sperm motility owing to an inflexible midpiece. Treatment of mice with cyclosporine A or FK506 creates phenocopies of the sperm motility and morphological defects. These defects appear within 4 to 5 days of treatment, which indicates that sperm-specific calcineurin confers midpiece flexibility during epididymal transit. Male mouse fertility recovered a week after we discontinued treatment. Because human spermatozoa contain PPP3CC and PPP3R2 as a form of calcineurin, inhibition of this sperm-specific calcineurin may lead to the development of a reversible male contraceptive that would target spermatozoa in the epididymis.

Calcineurin is a Ca^{2+} - and calmodulin-dependent serine-threonine phosphatase that plays a major role in calcium signaling (1, 2). In the immune system, calcineurin activates T cells by dephosphorylating the transcription factor NFAT (nuclear factor of activated T cells), and the dephosphorylated NFAT up-regulates the expression of interleukin-2 (1, 2). This process is suppressed by calcineurin inhibitors, such as cyclosporine A (CsA) and FK506, that are mainstays of immunosuppressive therapy after organ transplantation (1, 2). In the male re-

productive system, animal experiments have revealed that CsA and FK506 have deleterious effects on spermatogenesis and epididymal sperm maturation (3, 4). Further, in vitro treatment of spermatozoa with these drugs impairs sperm motility and the acrosome reaction (5, 6). These data suggest important roles of calcineurin in male fertility; however, the existence of several isoforms expressed in the testis hampered the clarification of their functions and pharmacological processes.

Calcineurin exists as a heterodimer composed of a catalytic and a regulatory subunit. In mammals, three isoforms of the catalytic subunit (PPP3CA, PPP3CB, and PPP3CC) and two isoforms of the regulatory subunit (PPP3R1 and PPP3R2) have been identified. *Ppp3ca*, *Ppp3cb*, and *Ppp3r1* are expressed ubiquitously, whereas *Ppp3cc* and *Ppp3r2* are expressed strongly in the mouse testis (fig. S1A) (7). PPP3CC and PPP3R2 were not detected in the testis and epididymis of *c-Kit^{wt/wv}*

mice, which lack differentiating germ cells (Fig. 1A). This indicates that *Ppp3cc* and *Ppp3r2* are the only subunits expressed in spermatogenic cells. In mature spermatozoa, both PPP3CC and PPP3R2 are localized in the tail (Fig. 1B). Consistent with the existence of the calcineurin isoforms, Ca^{2+} -dependent phosphatase activity is inhibited by CsA in mouse spermatozoa (fig. S1B). When mouse *Ppp3cc* and *Ppp3r2* were expressed in human embryonic kidney 293T (HEK293T) cells, heterodimerization of PPP3CC and PPP3R2 stabilized the calcineurin complex (Fig. 1C). This is consistent with genetic deletion of *Ppp3r1*, which leads to loss of PPP3CA and/or PPP3CB (8). Protein extracts from transfected cells contain Ca^{2+} -dependent phosphatase activity that was blocked by CsA (Fig. 1D). Thus, we conclude that the PPP3CC-PPP3R2 complex is the sperm-specific calcineurin (sperm calcineurin).

To elucidate the physiological functions of sperm calcineurin, we deleted (i.e., knocked out) the *Ppp3cc* gene in mice (fig. S2, A and B). We confirmed that PPP3CC was depleted in both testis and spermatozoa in *Ppp3cc*^{-/-} males (fig. S2C). The PPP3R2 signal was less in *Ppp3cc*-null testis and spermatozoa, which further indicated that PPP3CC stabilizes PPP3R2 (fig. S2D). As expected, Ca^{2+} -dependent phosphatase activity was reduced in *Ppp3cc*-null spermatozoa (fig. S2E). In *Ppp3cc*^{-/-} mice, there were no overt abnormalities in spermatogenesis, epididymal sperm morphology, or sperm counts (fig. S3, A to F).

Although *Ppp3cc*^{-/-} males copulated, they were infertile (Fig. 2A). When we investigated sperm migration in the female reproductive tract using transgenic spermatozoa that have DsRed2 in the mitochondria (9), fewer spermatozoa reached the ampulla compared with those of controls (fig. S4A). Although this could explain, in part, the male infertility, the presence of spermatozoa in the ampulla suggests that there are other factors that render the *Ppp3cc*^{-/-} males infertile. To examine other possible factors, we performed in vitro fertilization (IVF) and found that *Ppp3cc*-null spermatozoa cannot fertilize cumulus-intact oocytes (Fig. 2B). Further analysis revealed that *Ppp3cc*-null spermatozoa could pass through the cumulus cell layers (fig. S4B) and could bind to the zona pellucida (ZP) (Fig. 2C) but failed to fertilize cumulus-free ZP intact oocytes (fig. S4C);

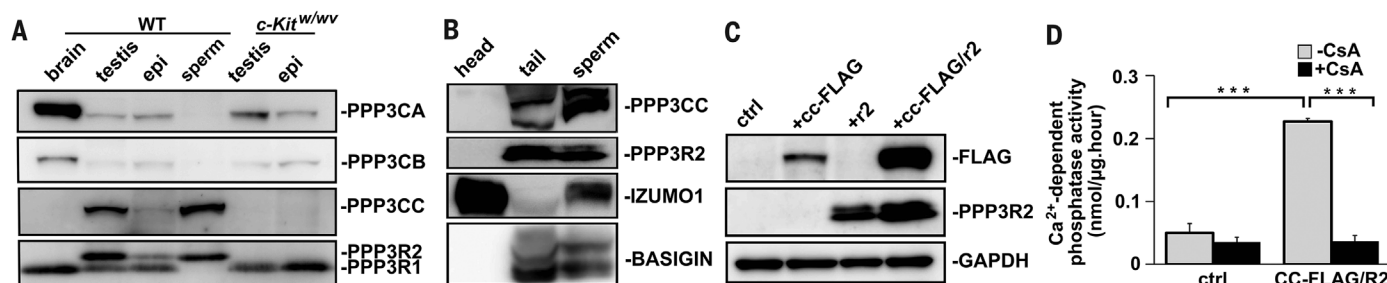


Fig. 1. Sperm calcineurin is a complex of PPP3CC and PPP3R2. (A) Both PPP3CC and PPP3R2 were detected in differentiating germ cells. (B) Both PPP3CC and PPP3R2 are localized in the sperm tail. IZUMO1 localized in the head and BASIGIN localized in the tail were used as controls. (C) Mouse PPP3CC-FLAG (cc-FLAG) and/or mouse PPP3R2 (r2) were overexpressed in HEK293T cells. (D) HEK293T cells that overexpressed both PPP3CC-FLAG and PPP3R2 have Ca^{2+} -dependent phosphatase activity that is blocked by 100 nM CsA. $n = 3$.

therefore, the ZP was the site of the problem. Once the ZP was removed, *Ppp3cc*-null spermatozoa could fuse with oocytes (fig. S4D), which confirmed that *Ppp3cc*-null spermatozoa are defective in zona penetration. When IVF was performed in a medium containing glutathione as a reducing agent to destabilize the ZP (fig. S5A) (10, 11), oocytes were fertilized by *Ppp3cc*-null spermatozoa (Fig. 2D and fig. S5A). These fertilized eggs developed to term (Fig. 2E and fig. S5B), which indicates that sperm calcineurin is not required for sperm genomic integrity. Fertility of *Ppp3cc*^{-/-} males was also rescued by expressing mCherry-tagged *Ppp3cc* transgene under a testis-specific *Ctgn* promoter (fig. S6, A to C) (12).

To understand why null spermatozoa could not penetrate the ZP, we investigated the acrosome reaction, as this is a prerequisite for spermatozoa to penetrate through the ZP (13). However, the acrosome reaction occurred normally in *Ppp3cc*-null spermatozoa (fig. S7, A and B). Next, we investigated sperm motility using computer-assisted sperm analysis. Although there were no differences in the percentage of motile spermatozoa (fig. S7C), velocity parameters of *Ppp3cc*-null spermatozoa (C57BL6/DBA2 background) were lower than those of control C57BL6/DBA2 spermatozoa (Fig. 3A). However, knockout (KO) sperm motility was still comparable to that of C57BL6 wild-type (WT) mice (table S1). Therefore, differences in velocities alone cannot explain the penetration defect.

We then investigated the percentage of hyperactivated spermatozoa and discovered that it was significantly lower in *Ppp3cc*^{-/-} mice than in control spermatozoa (Fig. 3B and fig. S7D), which suggests that *Ppp3cc*-null spermatozoa are defective in ZP penetration due to impaired hyperactivation. To elucidate why *Ppp3cc*-null

spermatozoa fail to exhibit hyperactivation, we further analyzed sperm motility. Although beat frequencies of *Ppp3cc*-null spermatozoa were normal (fig. S7E), the midpiece of null spermatozoa bent slightly in a direction opposite from the hook of the acrosome (anti-hook) (99%, 110 out of 111 spermatozoa) (14) and was inflexible (Fig. 3, C and D, and movies S1 to S4). In contrast, defects were not observed in the principal piece of null spermatozoa (Fig. 3C). When WT spermatozoa are hyperactivated, the curvature of the midpiece bend increases (14); however, *Ppp3cc*-null spermatozoa do not exhibit this increase. Thus, PPP3CC is required to develop the flexible midpiece for hyperactivation and to penetrate the ZP. Identical phenotypes were observed in *Ppp3r2* KO mice (fig. S8, A to F), which reconfirmed the importance of sperm calcineurin in midpiece flexibility and male fertility.

PPP3CC is localized close to CATSPER1, a Ca²⁺ channel required for hyperactivation (15, 16). To investigate whether PPP3CC is downstream of CATSPER1, we analyzed sperm motility of *Catsper1*^{-/-} mice. However, the midpiece of *Catsper1*-null spermatozoa was not rigid (fig. S8G), which indicates that sperm calcineurin is activated by calcium influx from different calcium channels and/or internal calcium stores.

To understand why the *Ppp3cc*-null midpiece remains rigid, we investigated microtubule (MT) sliding using spermatozoa from which membranes had been removed. MTs extend from the neck region in both control and null spermatozoa with comparable frequencies, which suggests that axonemal dyneins can slide the MTs even in the KO midpiece (fig. S9, A to C, and movie S5). The midpiece that was bent in the direction of the hook of the acrosome (pro-hook) appeared in null spermatozoa (fig. S9A) (32% ± 8.0, no. of

males = 3, no. of spermatozoa = 55). Because the mitochondrial sheath was removed in this assay (17), the mitochondrial sheath may contribute to the rigid midpiece bending in an anti-hook direction. Interaction between the mitochondrial sheath and the outer dense fibers may keep the midpiece rigid (18).

To further analyze the function of sperm calcineurin, we treated WT spermatozoa in vitro with CsA or FK506. Sperm motility and midpiece flexibility of these mature spermatozoa were not affected by calcineurin inhibitors (fig. S10, A and B). Furthermore, WT spermatozoa were able to fertilize normally in vitro, even in the presence of CsA or FK506 in the media (fig. S10C). Thus, sperm calcineurin activity is no longer necessary to confer midpiece flexibility in mature spermatozoa collected from the cauda epididymis.

To determine the effects of immunosuppressant drugs on immature spermatozoa, WT male mice were treated with CsA or FK506 for 2 weeks; these males became infertile (Fig. 4A), and spermatozoa from treated mice did not fertilize in vitro (Fig. 4B). When sperm motility was investigated, their midpiece was as inflexible as *Ppp3cc*- or *Ppp3r2*-null spermatozoa (Fig. 4C, movie S6 to S9). These results indicate that sperm calcineurin activity is important during the later stages of spermatogenesis or during sperm maturation in the epididymis. To elucidate where sperm calcineurin works, we administered CsA or FK506 for short periods. Spermatozoa with rigid midpieces appeared as early as 5 days after CsA administration and 4 days after FK506 administration (Fig. 4D). Because it takes ~10 days for spermatozoa to transit the epididymis (19), these results indicate that sperm calcineurin is essential to confer midpiece flexibility during epididymal transit. This is consistent with the fact that the sperm midpiece becomes flexible during epididymal transit (fig. S11A) (20). Fast transit of spermatozoa through the epididymis suggests that male fertility may recover quickly after stopping drug administration. As expected, fertility of male mice treated with CsA or FK506 recovered 1 week after halting drug administration (Fig. 4E). Sperm motility and midpiece flexibility also recovered after treatment (fig. S11, B to D). Considering these results in mice, we suggest that sperm calcineurin may be a target for reversible and rapidly acting human male contraceptives.

In human spermatozoa, the catalytic subunit of calcineurin was detected using a pan-calcineurin antibody (21). With specific antibodies, we confirmed the existence of PPP3CC and PPP3R2 but not PPP3CA and PPP3CB in human spermatozoa (fig. S12A). The recombinant human PPP3CC-PPP3R2 exhibited Ca²⁺-dependent phosphatase activity that was blocked by CsA (fig. S12, B and C). Thus, human spermatozoa contain PPP3CC-PPP3R2 as a functional calcineurin. In support of this idea, it has been reported that human spermatozoa exhibit Ca²⁺-dependent phosphatase activity (22). In humans, sperm motility develops during epididymal transit (22). Although male patients treated with a therapeutic dosage of CsA did not show signs of infertility (23), there are

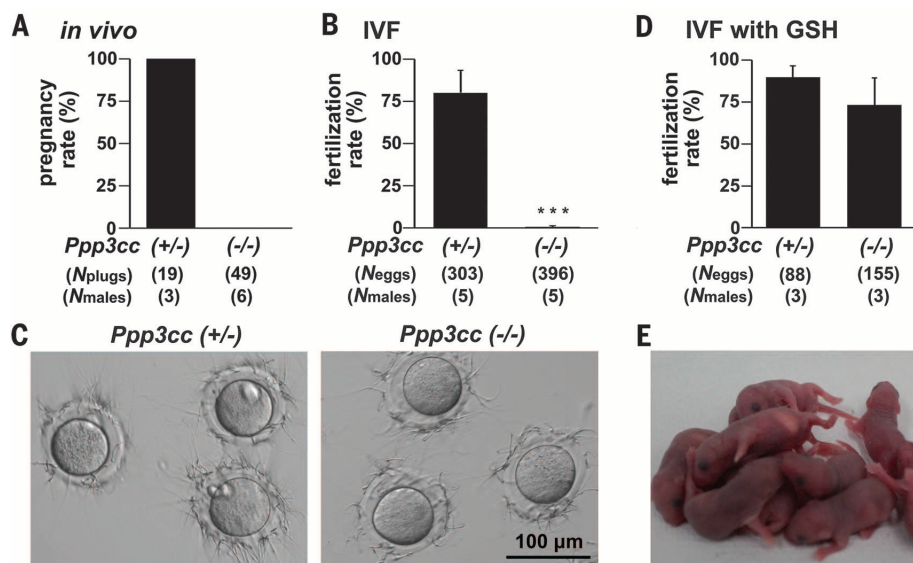


Fig. 2. *Ppp3cc*^{-/-} male is infertile because of impaired ZP penetration. (A) Pregnancy rate (pregnancy over vaginal plug) is presented as a percentage. (B) IVF with cumulus-intact oocytes. (C) Sperm-ZP binding assay in vitro. (D) IVF with cumulus-intact oocytes in medium containing glutathione (GSH). (E) Pups were obtained from eggs fertilized with *Ppp3cc*-null spermatozoa in (D).

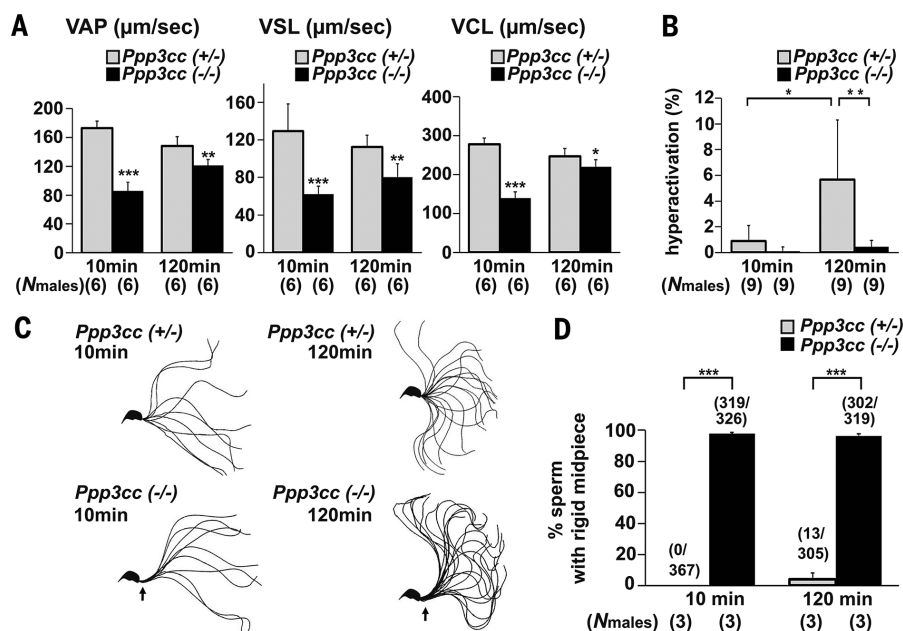


Fig. 3. Sperm calcineurin is necessary for a flexible midpiece. (A) Sperm motility at 10 min and 120 min after sperm suspension. VAP, average path velocity; VSL, straight-line velocity; and VCL, curvilinear velocity. (B) The percentage of hyperactivated spermatozoa. (C) Flagellar bending patterns. Single frames throughout one beating cycle are superimposed. The midpiece (black arrow) was inflexible in the *Ppp3cc*-null spermatozoa. (D) The percentage of the spermatozoa with a rigid midpiece. The number of spermatozoa with a rigid midpiece over the number of spermatozoa examined is presented in the parentheses above the column.

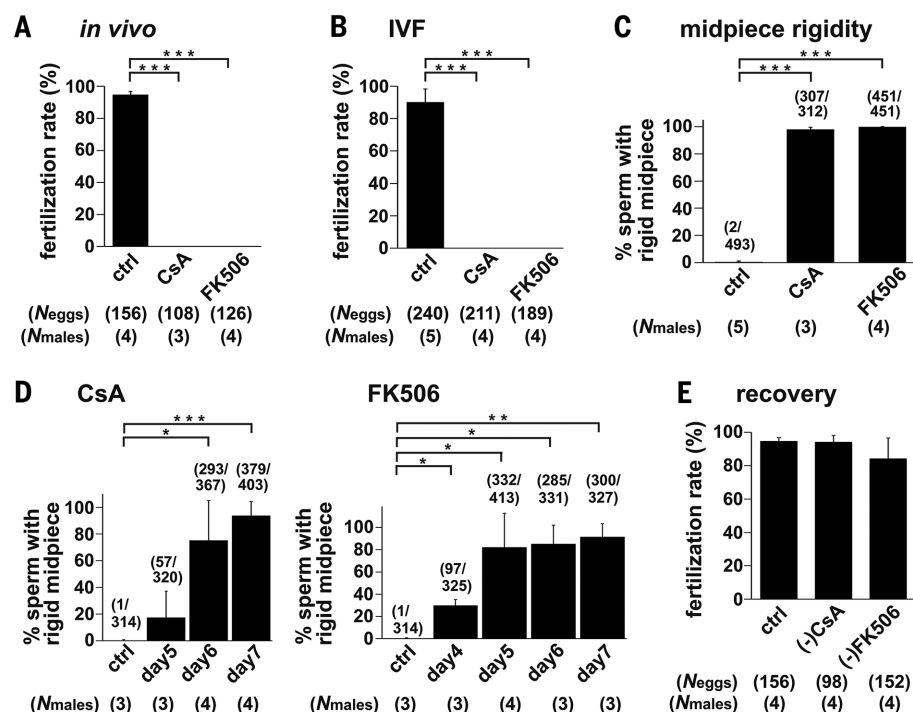


Fig. 4. Sperm calcineurin confers midpiece flexibility during epididymal transit. (A and B) Male mice were treated with CsA or FK506 for 2 weeks, and we analyzed their *in vivo* fertility using superovulated females (A), and fertilization rate *in vitro* (with cumulus cells) (B). (C) The percentage of spermatozoa with a rigid midpiece. The number of spermatozoa with a rigid midpiece over the number of spermatozoa examined was presented in the parentheses above the column. (D) Male mice were treated with CsA or FK506 for a short period, and their midpiece was analyzed. (E) Male mice were treated with CsA or FK506 for 2 weeks, and their *in vivo* fertility was analyzed 1 week after stopping drug administration. Drug concentration for CsA, 80 mg/kg per day, and for FK506, 8 mg/kg per day.

studies showing that CsA treatment impairs the motility of spermatozoa (24). Further, the concentration of CsA in the blood correlates inversely with sperm motility (25), which suggests that the PPP3CC-PPP3R2 complex is also involved in sperm motility development in humans.

In the present study, we demonstrated that PPP3CC associates with PPP3R2 to form sperm calcineurin during spermatogenesis. Our KO mice reveal that sperm calcineurin is not essential for spermatogenesis. The impaired spermatogenesis reported with CsA and FK506 treatment could be attributed to the inhibition of somatic calcineurin and/or nonspecific inhibition of other molecules. We conclude that sperm calcineurin confers midpiece flexibility during epididymal transit, and this process is required to generate fertilization-competent spermatozoa. In the immune system, calcineurin dephosphorylates the transcription factor NFAT (1, 2); however, in spermatozoa, calcineurin plays roles in the epididymis after transcription has ceased. Therefore, sperm calcineurin does not confer midpiece flexibility by dephosphorylating transcription factors such as NFAT. Specific inhibition of sperm calcineurin or its interaction with substrates may lead to the development of reversible and rapidly acting male contraceptives that target spermatozoa in the epididymis but leave testicular function intact.

REFERENCES AND NOTES

- C. B. Klee, H. Ren, X. Wang, *J. Biol. Chem.* **273**, 13367–13370 (1998).
- F. Rusnak, P. Mertz, *Physiol. Rev.* **80**, 1483–1521 (2000).
- L. Seethalakshmi, M. Menon, R. K. Malhotra, D. A. Diamond, *J. Urol.* **138**, 991–995 (1987).
- A. Hisatomi et al., *Toxicology* **109**, 75–83 (1996).
- M. M. Misro, S. P. Chaki, M. Srinivas, S. K. Chaudh, *Arch. Androl.* **43**, 215–220 (1999).
- J. Castillo Bennett, C. M. Roggero, F. E. Mancifesta, L. S. Mayorga, *J. Biol. Chem.* **285**, 26269–26278 (2010).
- T. Muramatsu, P. R. Giri, S. Higuchi, R. L. Kincaid, *Proc. Natl. Acad. Sci. U.S.A.* **89**, 529–533 (1992).
- H. Zeng et al., *Cell* **107**, 617–629 (2001).
- H. Hasuwa et al., *Exp. Anim.* **59**, 105–107 (2010).
- M. L. Bath, *PLOS ONE* **5**, e9387 (2010).
- T. Takeo, N. Nakagata, *Biol. Reprod.* **85**, 1066–1072 (2011).
- M. Ikawa et al., *Dev. Biol.* **240**, 254–261 (2001).
- R. Yanagimachi, in *The Physiology of Reproduction*, E. Knobil, J. D. Neil, Eds. (Raven Press, New York, 1988), vol. 1, chap. 5.
- S. Ishijima, S. A. Baba, H. Mohri, S. S. Suarez, *Mol. Reprod. Dev.* **61**, 376–384 (2002).
- J. J. Chung et al., *Cell* **157**, 808–822 (2014).
- D. Ren et al., *Nature* **413**, 603–609 (2001).
- M. Kinukawa, M. Nagata, F. Aoki, *Reproduction* **128**, 813–818 (2004).
- D. M. Woolley, J. Neesen, G. G. Vernon, *Cell Motil. Cytoskeleton* **61**, 74–82 (2005).
- M. L. Meistrich, T. H. Hughes, W. R. Bruce, *Nature* **258**, 145–147 (1975).
- C. Jeulin, L. M. Lewin, C. Chevrier, D. Schoevaert-Brossault, *Cell Motil. Cytoskeleton* **35**, 147–161 (1996).
- K. Ahmad, G. E. Bracho, D. P. Wolf, J. S. Tash, *Arch. Androl.* **35**, 187–208 (1995).
- C. H. Yeung, T. G. Cooper, F. Oberpenning, H. Schulze, E. Nieschlag, *Biol. Reprod.* **49**, 274–280 (1993).
- J. Haberman et al., *J. Urol.* **145**, 294–296 (1991).
- Z. G. Cao et al., *Zhonghua Nan Ke Xue* **12**, 405–407 (2006).
- M. M. Eid, I. A. Abdel-Hamid, M. A. Sobh, M. A. el-Said, *Int. J. Androl.* **19**, 338–344 (1996).

ACKNOWLEDGMENTS

We thank Biotechnology Research and Development (Osaka, Japan) for generating mutant mice, D. E. Clapham (Howard Hughes

Medical Institute, Boston, MA) for providing *Catsper1* KO mice, and S. A. M. Young and F. Abbasi for review of the manuscript. We also thank M. Okabe for continuous encouragement. This work was partly supported by the Ministry of Education, Culture, Sports, Science and Technology and the Japan Society for the Promotion of Science (26830056 to H.M.; 15H05573 to Y.F.; 20670006, 25112007, and 25250014 to M.I.), JAMBIO, and Takeda Science Foundation. All of the gene-manipulated mouse lines were deposited into the Riken BioResource Center (with stock numbers as

follows: *Ppp3cc* KO, RBRC05878; *Ppp3r2* KO, RBRC09504; *Ppp3cc*-FLAG TG#1, RBRC09502; *Ppp3cc*-FLAG TG#2, RBRC09503; and *Ppp3cc-mCherry* TG, RBRC09501) and are available from M.I. under a material transfer agreement with Osaka University. The authors declare no conflict of interest.

SUPPLEMENTARY MATERIALS

www.sciencemag.org/content/350/6259/442/suppl/DC1
Materials and Methods

Figs. S1 to S12
Table S1
References (26–40)
Movies S1 to S9

23 July 2015; accepted 3 September 2015
Published online 1 October 2015
10.1126/science.1258336

PROTEIN DYNAMICS

Direct observation of ultrafast collective motions in CO myoglobin upon ligand dissociation

Thomas R. M. Barends,^{1*} Lutz Foucar,¹ Albert Ardevol,² Karol Nass,¹ Andrew Aquila,³ Sabine Botha,¹ R. Bruce Doak,¹ Konstantin Falahati,⁴ Elisabeth Hartmann,¹ Mario Hilpert,¹ Marcel Heinz,^{2,4} Matthias C. Hoffmann,⁵ Jürgen Köfinger,² Jason E. Koglin,⁵ Gabriela Kovacsova,¹ Mengning Liang,⁵ Despina Milathianaki,⁵ Henrik T. Lemke,⁵ Jochen Reinstein,¹ Christopher M. Roome,¹ Robert L. Shoeman,¹ Garth J. Williams,⁵ Irene Burghardt,⁴ Gerhard Hummer,² Sébastien Boutet,⁵ Ilme Schlichting^{1,5}

The hemoprotein myoglobin is a model system for the study of protein dynamics. We used time-resolved serial femtosecond crystallography at an x-ray free-electron laser to resolve the ultrafast structural changes in the carbonmonoxy myoglobin complex upon photolysis of the Fe-CO bond. Structural changes appear throughout the protein within 500 femtoseconds, with the C, F, and H helices moving away from the heme cofactor and the E and A helices moving toward it. These collective movements are predicted by hybrid quantum mechanics/molecular mechanics simulations. Together with the observed oscillations of residues contacting the heme, our calculations support the prediction that an immediate collective response of the protein occurs upon ligand dissociation, as a result of heme vibrational modes coupling to global modes of the protein.

Dynamics is an essential aspect of protein structure and function. This concept has been recognized ever since the first protein crystal structure—of the oxygen-storage protein myoglobin (Mb)—was solved. The Mb active site was found to be shielded from solvent, and no path for a ligand to enter or leave the binding site at the heme iron was apparent. Thus, in addition to regulating heme chemistry, structural dynamics of the protein matrix must control access to the active site. Ligand binding to and dissociation from Mb have been studied in great detail using numerous approaches, exploiting the fact that the Fe-CO bond is sensi-

tive to light and can be cleaved with a very high quantum yield (1–7). However, in synchrotron-based time-resolved x-ray crystallography, the time resolution was limited by the 100-ps duration of the x-ray pulse (8), and the structural changes emanating from the breaking ligand bond had already spread throughout the protein by the time the data could be collected.

The advent of x-ray free-electron lasers (FELs), with their high peak brilliance and femtosecond short pulses, extends the 100-ps time resolution of synchrotron-based Laue crystallography to the chemical reaction time scale of femtoseconds. The feasibility of high-resolution time-resolved serial femtosecond crystallography (SFX) measurements at FELs was established recently by Tenboer *et al.*, using pump-probe experiments on photoactive yellow proteins on the nanosecond time scale (9). Ultrafast time-resolved solution small-angle x-ray scattering (SAXS) measurements on a multiphoton-excited photosynthetic reaction center (10)—and, recently, on photodissociated carbonmonoxy Mb (7)—showed conformational changes within picoseconds, providing direct structural evidence for a protein quake (11). We analyzed the ultrafast light-induced structural

changes in the myoglobin-carbon monoxide complex (MbCO) at high spatial and temporal resolution by time-resolved SFX at the Linac Coherent Light Source (LCLS). The high peak brilliance of the x-ray laser allows analysis of micrometer-sized crystals (12), which can be fully photolyzed due to their relatively low absorption (9). In contrast, the synchrotron-based Laue measurements required the use of macroscopic crystals, resulting in partial photolysis [23% (8)] and the need for difference refinement (13).

Horse heart (hh) MbCO microcrystals were injected in random orientations in a thin liquid microjet into the FEL beam (fig. S1). We used a pump-probe scheme for data collection (14), with time delays of (nominally) 0.5, 1.0, 3, 10, 50, and 150 ps between the photolyzing optical laser flash [532 nm, 150 fs, 5 μ J, 380 GW/cm²; see (15) for multiphoton absorption and ionization effects] and the probing x-ray FEL pulse (6.7 to 6.9 keV, 80 fs). For comparison, we also collected “dark” exposures, which were interleaved nonuniformly with the “light” exposures. Data from the nominally 0.5-ps delay were sorted [using the FEL data analysis software suite CASS (16)] according to the information from a timing tool (17) and binned into groups (with approximate time delays of –0.1, 0, 0.1, 0.2, 0.3, 0.4, 0.5, and 0.6 ps) containing 20,000 indexed diffraction patterns each, with an overlap of 5000 patterns with the adjacent groups on either side of the window (see fig. S2 for details). The timing-tool correction resulted in a ~50-fs effective time jitter (timing error) between optical and x-ray pulses, which is substantially smaller than the intrinsic uncorrected shot-to-shot time jitter (~300 fs). The main contributions to the overall time resolution of our experiment, which we estimate to be ~250 fs, are the duration of the optical pump pulse and the manner in which we binned the diffraction data. The diffraction data at each time delay were indexed and integrated using the SFX data processing software suite CrystFEL (18). The hhMbCO structure [Protein Data Bank (PDB) ID 1DWR] (19) was used as a starting model for refinement, with CO and water molecules omitted. The resolution was 1.8 Å, owing to a temporarily reduced performance of the FEL, which limited the photon energy to 6.9 keV (λ = 1.8 Å). The data and refinement statistics are shown in table S1. The 1DWR (19) structure was also the starting point for quantum mechanics/molecular mechanics simulations (QM/MM) simulations. The heme cofactor, CO, His⁶⁴, and His⁹³ were treated quantum mechanically in these calculations of solvated MbCO, and photodissociation was induced by transition from the singlet to the quintet state.

¹Max-Planck-Institut für Medizinische Forschung, Jahnstraße 29, 69120 Heidelberg, Germany. ²Max-Planck-Institut für Biophysik, Max-von-Laue-Straße 3, 60438 Frankfurt am Main, Germany. ³European XFEL GmbH, Albert-Einstein-Ring 19, 22761 Hamburg, Germany. ⁴Institut für Physikalische und Theoretische Chemie, Goethe-Universität, Max-von-Laue-Straße 7, 60438 Frankfurt am Main, Germany. ⁵Linac Coherent Light Source (LCLS), SLAC National Accelerator Laboratory, 2575 Sand Hill Road, Menlo Park, CA 94025, USA.

*Corresponding author. E-mail: thomas.barends@mpimf-heidelberg.mpg.de (T.R.M.B.); ilme.schlichting@mpimf-heidelberg.mpg.de (I.S.)

Myoglobin is an α -helical hemoprotein. The CO-binding heme cofactor is coordinated by the proximal histidine residue (His⁹³), located in the F helix. In the distal pocket, the bound CO is in close contact with the residues Leu²⁹ and Phe⁴³, with His⁶⁴ and Val⁶⁸ located in the E helix, with the CD loop, and with the B helix (Fig. 1A). Consistent with the 150-fs pump-pulse duration, the -0.1-, 0-, and 0.1-ps data show a mixture of bound and photodissociated CO (fig. S3), whereas the 0.2-ps data show a mostly dissociated CO. For all later time points, the photoexcited state is fully occupied. The unbound CO is located in the primary docking site (Fig. 1, A to D) atop the pyrrole C ring, contacting Val⁶⁸, Leu²⁹, Phe⁴³, Ile¹⁰⁷, His⁶⁴, and Leu³², which is the same position as was observed in the structure of photolyzed hhMbCO determined at cryogenic temperature (19). Within the time resolution of our experiment, the heme has adopted the “domed” configuration

and the iron has moved 0.2 Å out of the heme plane, reaching its final out-of-plane position of 0.3 Å between 0.6 and 3 ps (Fig. 1E). These observations agree with the biexponential iron motion in our QM/MM simulations (Fig. 1E), which shows a 90-fs fast phase of 60% relative amplitude and a 1.3-ps slow phase. This is in line with previous classical molecular dynamics (MD) calculations (20–22) and with recent ultrafast x-ray absorption spectroscopy (23), which showed a fast initial Fe displacement occurring within 50 to 70 fs, followed by a 0.4-ps phase. Time-resolved resonance Raman studies indicate that the iron-histidine out-of-plane mode ($\nu_{\text{Fe-His}}$)—which corresponds to heme doming and, thus, iron movement—has reached 90% ($\pm 10\%$) within 700 fs (1, 2), consistent with the observation of a deoxy-like species with a time constant of 250 to 300 fs (24, 25).

The structural differences between the 5-coordinated deoxy Mb conformation and the

6-coordinated MbCO are relatively small, with a root mean square displacement of 0.11 Å for 152 C α atoms. Accordingly, the structural changes occurring during the transition are even smaller (see supplementary materials for accuracy of our structures). Nevertheless, after refinement of the structures, we observe clear differences for our time-resolved structures in comparison with the dark-state structure in the region stretching from the F helix to the beginning of the G helix, the A helix, the region spanning the C helix to the CD corner, the E helix, and the C-terminal side of the H helix. Importantly, these regions are linked directly or indirectly to the heme group (26). Sequence displacement graphs (27)—which illustrate the change in distance of the protein main-chain atoms to the center of the four porphyrin N atoms as a function of the time delay between the pump and probe pulses—show substantial main-chain changes within 1 ps throughout the whole protein (Fig. 2A), in line with the global

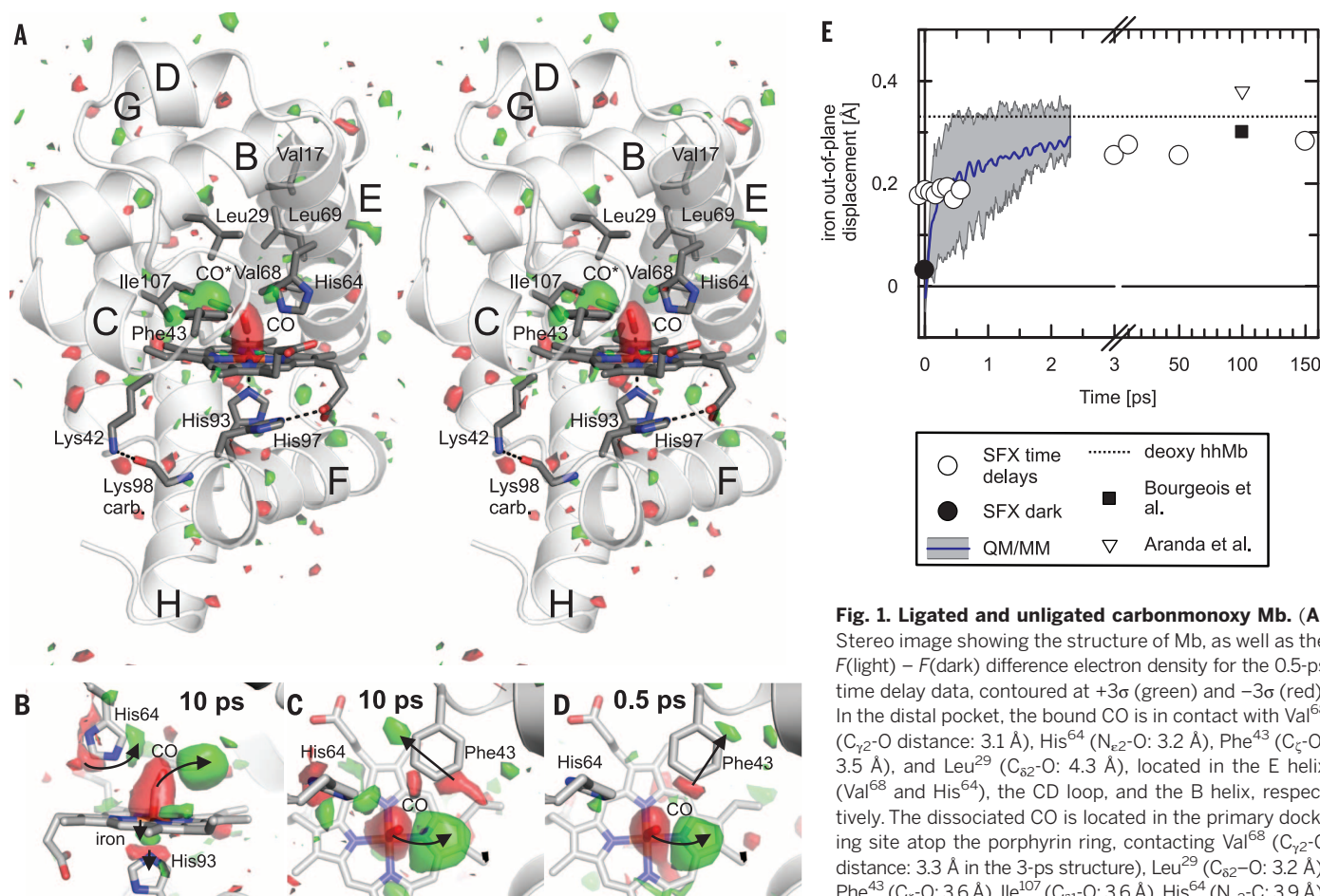


Fig. 1. Ligated and unligated carbonmonoxy Mb. (A) Stereo image showing the structure of Mb, as well as the $F(\text{light}) - F(\text{dark})$ difference electron density for the 0.5-ps time delay data, contoured at $+3\sigma$ (green) and -3σ (red). In the distal pocket, the bound CO is in contact with Val⁶⁸ ($C_{72}-O$ distance: 3.1 Å), His⁶⁴ ($N_{e2}-O$: 3.2 Å), Phe⁴³ ($C_{\gamma}-O$: 3.5 Å), and Leu²⁹ ($C_{\delta 2}-O$: 4.3 Å), located in the E helix (Val⁶⁸ and His⁶⁴), the CD loop, and the B helix, respectively. The dissociated CO is located in the primary docking site atop the porphyrin ring, contacting Val⁶⁸ ($C_{72}-C$ distance: 3.3 Å in the 3-ps structure), Leu²⁹ ($C_{\delta 2}-O$: 3.2 Å), Phe⁴³ ($C_{\gamma}-O$: 3.6 Å), Ile¹⁰⁷ ($C_{\delta 1}-O$: 3.6 Å), His⁶⁴ ($N_{e2}-C$: 3.9 Å), and Leu³² ($C_{\delta 2}-O$: 4.2 Å). The proximal histidine (His⁹³) coordinates the heme iron. Leu⁶⁹ interacts with Val¹⁷, providing a steric link between the E and A helices. (B to D) Difference electron density maps [$F(\text{light}) - F(\text{dark})$] showing bound (-3σ contour level, red) and photodissociated ($+3\sigma$, contour level green) CO, doming of the heme, out-of-plane movement of the iron, and concomitant movement of His⁹³ away from the heme, as well as rotation of His⁶⁴ and movement of Phe⁴³, which is displaced in different directions at the two time delays shown (0.5 and 10 ps). The orientation in (B) is rotated by 90° with respect to the orientation in (C) and (D). (E) Iron out-of-plane displacement, as observed in the time-resolved SFX experiments (white circles), deoxy hhMb (dashed horizontal line), Laue experiments [black square (42) and white triangle (13)], and the dark-state SFX structure (black circle). The average displacement over 146 QM/MM trajectories as a function of time is also indicated (blue line). The shaded area shows the interquartile range of displacements in individual QM/MM trajectories.

changes observed in ultrafast SAXS measurements on photolyzed MbCO (7). These motions are reproduced well by the QM/MM simulations (fig. S4). In contrast to the other structural ele-

ments, the displacement of the E helix keeps increasing until the 150-ps time point, as does that of the C-terminal end of the F helix, reaching values similar to those observed previously

with Laue crystallography after a time delay of 100 ps (8, 13) (fig. S5A). Comparison of these displacements to those observed for a room temperature synchrotron structure of deoxymyoglobin (fig. S5B) suggests that most of the motions are essentially complete after 150 ps, even though some residual displacements occur in the E and F helices. When these changes in relative position are plotted onto the protein structure (Fig. 2, B and C, and figs. S6 and S7), color-coding to illustrate whether a residue moves toward the heme center (blue) or away from it (red), “hotspots” of motion appear at subpicosecond time delays around the proximal and distal histidines, moving away from and toward the center, respectively. These displacements seem to spread out at later time points over the E helix and the regions adjacent to the C helix. This is not caused by choosing the heme as the point of reference, as it is also observed when calculating the displacements with respect to the center of mass of the protein or the dark-state atomic positions (figs. S8 and S9). In this case, it becomes even more obvious that the F-helix motion occurs before the E-helix motion, with the F helix starting to move almost instantaneously, and the E helix following later.

Plots depicting the changes in pairwise distances between all C_α atoms as a function of pump-probe delay time show that the F helix moves away from several other elements (B, C, D, E, and G helices) at subpicosecond time delays. After 3 ps, the E helix moves toward several elements, such as the FG corner and the H helix (Fig. 3 and fig. S10). As can be seen in the color-coded structures (Fig. 2C and fig. S6), the E and A helices move together, probably due to their direct steric coupling between Val¹⁷ and Val⁶⁸ through the side chain of Leu⁶⁹, as well as through the heme cofactor, Leu⁷², and Trp¹⁴ (26, 28). The rapid displacement of the A and E helices is in line with ultraviolet time-resolved resonance Raman spectroscopic experiments (6) that suggested a fast displacement of the E helix toward the heme within the instrument response time (3.3 ps) and a slower movement of the FG corner with a time constant of 2 ps. Indeed, as can be seen in fig. S10, substantial changes in relative position of the FG corner do not occur until ~3 ps. The observation of subpicosecond global structural changes is consistent with results from recent ultrafast solution scattering experiments (7) that additionally showed a 3.6-ps damped oscillation of the radius of gyration.

At several time points, residues at either side of loops between helices show marked changes in relative position, suggesting that these loops function as hinges between the various structural elements (26). For instance, at all time delays, there is a clear change in relative position with respect to the dark state of residues 43 to 45 at the N terminus of the CD loop. This includes Phe⁴³, which is mechanically coupled to the heme (26) and in contact with the CO molecule. At 150 ps, there are also marked changes in the positions of residues at the C terminus of

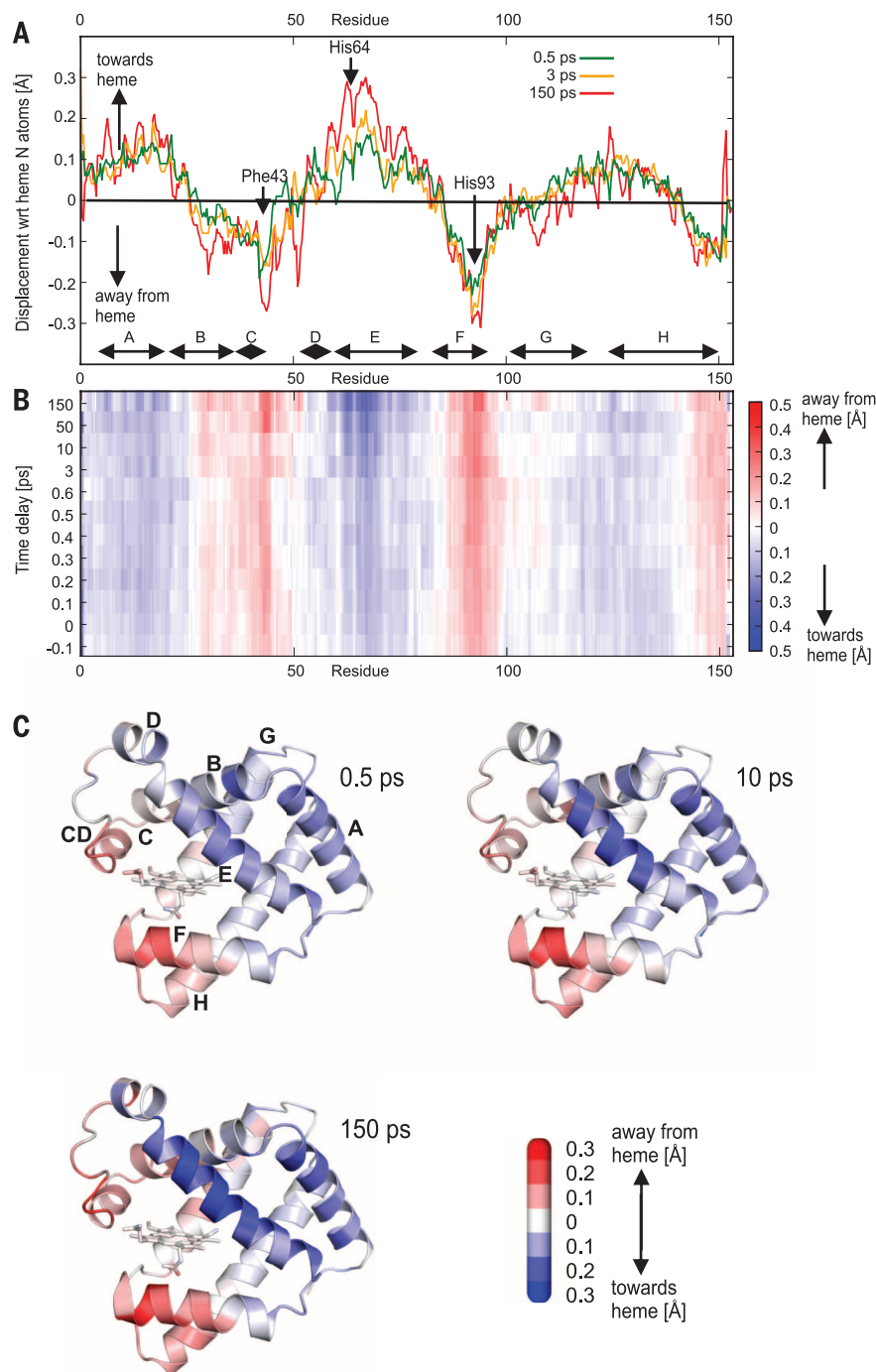


Fig. 2. Structural changes in the protein main chain. (A) Sequence displacements (27) showing the distance of the protein main-chain atoms (C, N, and C_α) to the center of the four porphyrin N atoms for time delays between the pump and probe pulses of 0.5, 3, and 150 ps. Letters at the bottom of the plot represent helices. (B) Matrix representation of the displacement shown in (A) for all time delays collected. The magnitude and direction of the displacement is color-coded, with a movement toward the heme shown in blue and movement away in red. (C) Displacement of the main-chain atoms toward or away from the center of the four porphyrin N atoms, as a function of the time delay between the pump and probe pulse, mapped onto the structure. The dark state was used as the reference.

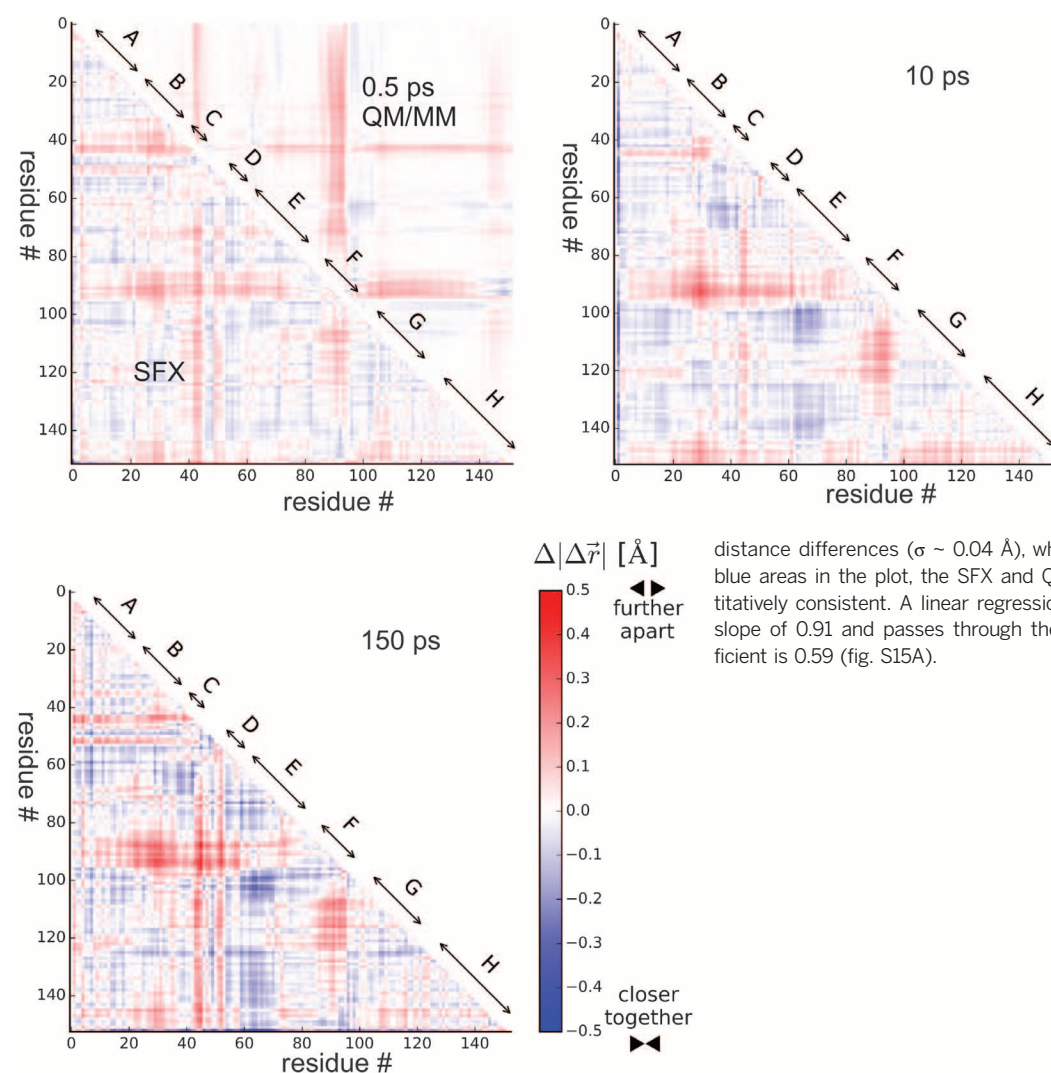


Fig. 3. Difference distance matrix plots. Matrices depicting the observed changes in pairwise distances between all C_{α} atoms (26), with respect to the dark-state structure as a function of the pump-probe delay time. Very early on, the F helix moves away from several other elements (B, C, D, E, and G helices). At longer time delays, the E helix moves toward the FG corner and the H helix. For the 0.5-ps time delay, the SFX results (top left plot, lower left corner) are compared with the QM/MM calculations (top left plot, upper right corner). Accounting for scatter in the SFX-derived

distance differences ($\sigma \sim 0.04$ Å), which also explains the somewhat larger blue areas in the plot, the SFX and QM/MM distance differences are quantitatively consistent. A linear regression of SFX against QM/MM data has a slope of 0.91 and passes through the origin. The Pearson correlation coefficient is 0.59 (fig. S15A).

the CD loop, possibly due to the much larger changes in the E helix position. The changes at the C terminus of the GH loop at 150 ps (Fig. 3) probably result from coupling to the E helix of an adjacent molecule via a crystal contact.

The data also allowed us to study the temporal evolution of the conformation of some heme-coupled residues (26). At subpicosecond time delays, the χ_1 torsion angles of Phe⁴³, Val⁶⁸, and Ile¹⁰⁷ show an exponential change with time (Fig. 4A). Their side chains have a high probability of being hit by the dissociating CO (29), which would result in a large momentum transfer, causing a movement of the side chain followed by an exponential relaxation. Interestingly, the χ_1 torsion angles of His⁹³, as well as the H-bond distance between the propionate side chain and His⁹⁷ ($O_{1A}-N_{E2}$) and between the carbonyl oxygen of Lys⁹⁸ and the amino group of Lys⁴², seem to oscillate with time at subpicosecond time delays (Fig. 4B), as do, e.g., the side-chain torsion angles of Phe⁴³ (χ_2), Leu²⁹ (χ_1, χ_2), Ile¹⁰⁷ (χ_2), and His⁹³ (χ_1, χ_2) (Fig. 4B and fig. S11). The oscillation period (500 ± 150 fs) is remi-

niscient of the 417- to 430-fs period of the heme doming motion of the photoproduct [80 cm^{-1} (30, 31) to 75 cm^{-1} (4)]. This observation is in line with a coupling of the heme doming mode to collective modes of the protein, as suggested earlier (31–33).

We can directly monitor the dynamics of the heme normal modes by QM/MM calculations. As shown in fig. S12, the amplitude of the ν_7 in-plane breathing mode of the porphyrin ring, which is excited by CO photodissociation, decays exponentially with a time constant of ~ 1.3 ps, consistent with the measured decay time of 1.9 ± 0.6 ps (34). The ν_7 mode exhibits a distinct amplitude modulation with a period of ~ 0.35 ps. The observed oscillatory dynamics in the heme environment thus appears to reflect coherent motions excited by photodissociation in the heme (35, 36).

Our high-resolution observations of ultrafast, global, and asymmetric structural changes are in line with observations from SAXS experiments (7) and femtosecond optically heterodyne-detected transient grating spectroscopy studies showing

that Mb changes shape within 500 fs upon CO dissociation (5). The dynamics of the anisotropic mass displacement and, thus, of protein strain were interpreted as evidence for the activation of low-frequency collective modes of the protein by the photodissociation of the Fe-CO bond to drive the system from its ligated to the unligated conformation (5, 32, 37). Based on femtosecond coherence spectroscopy, it has been suggested that electronic rearrangements in the heme iron upon ligand photodissociation can simultaneously excite associated low-frequency vibrational modes (38).

The experimental and computational results reported here are consistent with this conceptual view of Mb dynamics, in which ultrafast modes of the heme couple with lower-frequency protein modes and, ultimately, with large-scale motions such as the displacements of the E and F helices (Fig. 4C). This notion that functional protein dynamics are governed by a network of coupled modes spanning a broad range of frequencies and length scales is emerging as a general model for the explanation of protein function (39–41).

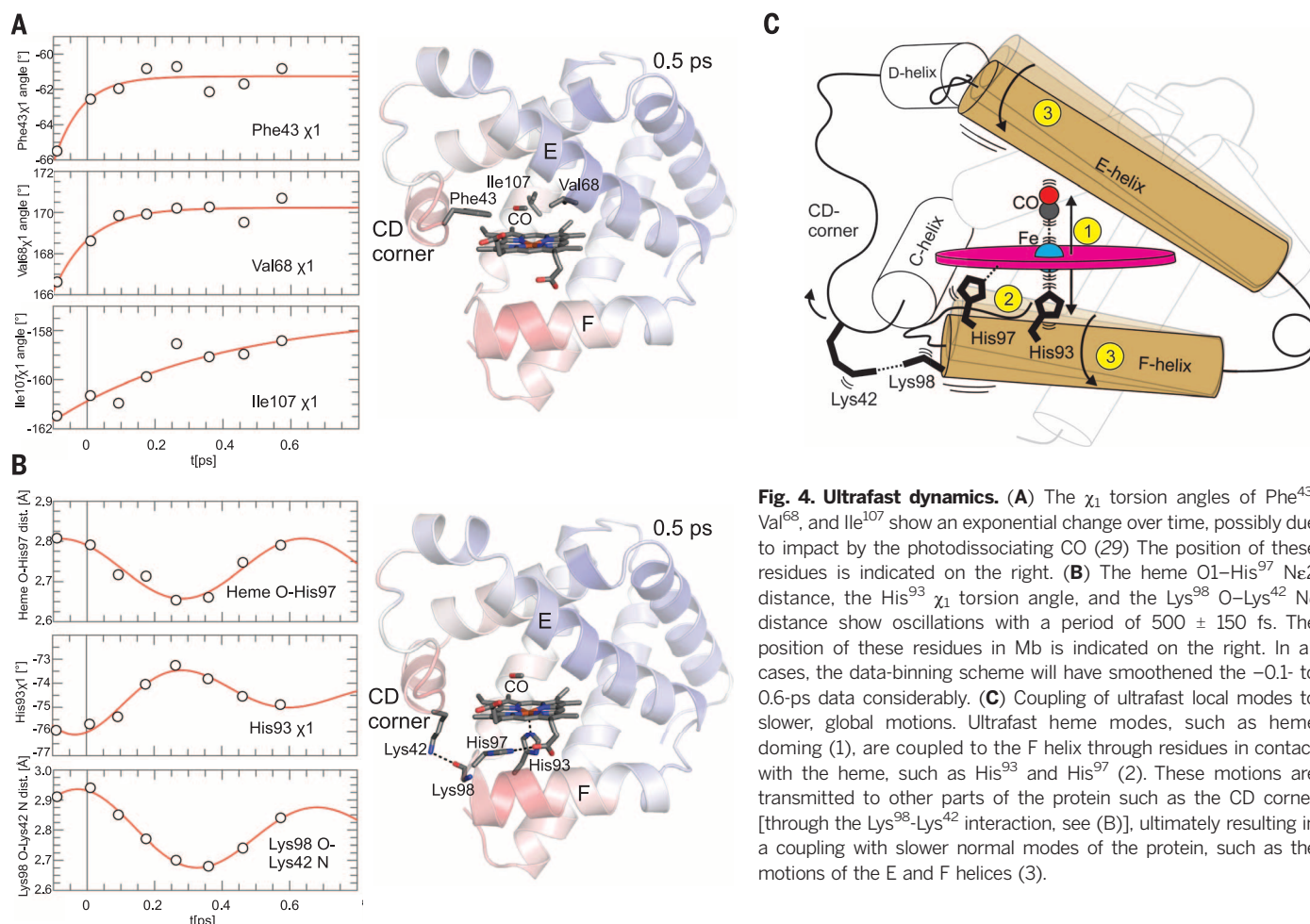


Fig. 4. Ultrafast dynamics. (A) The χ_1 torsion angles of Phe⁴³, Val⁶⁸, and Ile¹⁰⁷ show an exponential change over time, possibly due to impact by the photodissociating CO (29). The position of these residues is indicated on the right. (B) The heme O1–His⁹⁷ N π 2 distance, the His⁹³ χ_1 torsion angle, and the Lys⁹⁸ O–Lys⁴² N π 2 distance show oscillations with a period of 500 ± 150 fs. The position of these residues in Mb is indicated on the right. In all cases, the data-binning scheme will have smoothed the ~ 0.1 - to 0.6 -ps data considerably. (C) Coupling of ultrafast local modes to slower, global motions. Ultrafast heme modes, such as heme doming (1), are coupled to the F helix through residues in contact with the heme, such as His⁹³ and His⁹⁷ (2). These motions are transmitted to other parts of the protein such as the CD corner [through the Lys⁹⁸–Lys⁴² interaction, see (B)], ultimately resulting in a coupling with slower normal modes of the protein, such as the motions of the E and F helices (3).

REFERENCES AND NOTES

- S. Franzen, B. Bohn, C. Poyart, J. L. Martin, *Biochemistry* **34**, 1224–1237 (1995).
- S. Franzen et al., *J. Biol. Chem.* **270**, 1718–1720 (1995).
- J. W. Petrich, J. L. Martin, D. Houde, C. Poyart, A. Orszag, *Biochemistry* **26**, 7914–7923 (1987).
- L. Zhu, J. T. Sage, P. M. Champion, *Science* **266**, 629–632 (1994).
- G. D. Goodno, V. Astinov, R. J. D. Miller, *J. Phys. Chem. A* **103**, 10630–10643 (1999).
- A. Sato, Y. Gao, T. Kitagawa, Y. Mizutani, *Proc. Natl. Acad. Sci. U.S.A.* **104**, 9627–9632 (2007).
- M. Levantino et al., *Nat. Commun.* **6**, 6772 (2015).
- F. Schotte et al., *Science* **300**, 1944–1947 (2003).
- J. Tenboer et al., *Science* **346**, 1242–1246 (2014).
- D. Arnlund et al., *Nat. Methods* **11**, 923–926 (2014).
- A. Ansari et al., *Proc. Natl. Acad. Sci. U.S.A.* **82**, 5000–5004 (1985).
- S. Boutet et al., *Science* **337**, 362–364 (2012).
- R. Aranda IV, E. J. Levin, F. Schotte, P. A. Anfinsen, G. N. Phillips Jr., *Acta Crystallogr. D* **62**, 776–783 (2006).
- Materials and methods are available as supplementary materials on Science Online.
- Previous studies have shown that, in the high-intensity excitation regime, the directed functional protein motions become dominated by either thermal or ionization contributions rather than those of ligand dissociation (5). However, our observed structural changes are highly consistent with those expected for ligand dissociation and changes in potential energy surface at the heme. Given our structural results for the $20 \mu\text{J}$ ($1 \text{ TW}/\text{cm}^2$) excitation data (fig. S13), it seems that ionization of the heme still appears like a centralized force that displaces the heme and protein in a very similar fashion to ligand dissociation. The process seems to be occurring within a linear response, in which case the observed dynamics still captures the protein response function. We cannot exclude the possibility that the oscillations of spatial positions of residues coupled to the heme are caused or increased by heating due to high excitation conditions. However, the excellent agreement of our structural observations and their temporal dependence with previous spectroscopic data argues against photolysis artifacts. In addition, our QM/MM simulations starting from cold heme (0 K) agree with those of the normal system, as well as the experimental data (fig. S14). Moreover, our simulations are in line with the collective modes model (32) and other mode-mode coupling mechanisms (4, 38).
- F. Foucar et al., *Comput. Phys. Commun.* **183**, 2207–2213 (2012).
- M. R. Bionta et al., *Opt. Express* **19**, 21855–21865 (2011).
- T. A. White et al., *Acta Crystallogr. D* **69**, 1231–1240 (2013).
- K. Chu et al., *Nature* **403**, 921–923 (2000).
- E. R. Henry, M. Levitt, W. A. Eaton, *Proc. Natl. Acad. Sci. U.S.A.* **82**, 2034–2038 (1985).
- K. Kuczcera, J. C. Lambry, J. L. Martin, M. Karplus, *Proc. Natl. Acad. Sci. U.S.A.* **90**, 5805–5807 (1993).
- O. Schaad, H. X. Zhou, A. Szabo, W. A. Eaton, E. R. Henry, *Proc. Natl. Acad. Sci. U.S.A.* **90**, 9547–9551 (1993).
- M. Levantino et al., *J. Struct. Dyn.* **2**, 041713 (2015).
- J. L. Martin et al., *EMBO J.* **2**, 1815–1819 (1983).
- J. W. Petrich, C. Poyart, J. L. Martin, *Biochemistry* **27**, 4049–4060 (1988).
- Y. Seno, N. Go, *J. Mol. Biol.* **216**, 95–109 (1990).
- V. Guallar, A. A. Jarzecki, R. A. Friesner, T. G. Spiro, *J. Am. Chem. Soc.* **128**, 5427–5435 (2006).
- Y. Seno, N. Go, *J. Mol. Biol.* **216**, 111–126 (1990).
- R. Elber, M. Karplus, *J. Am. Chem. Soc.* **112**, 9161–9175 (1990).
- F. Rosca et al., *J. Phys. Chem. A* **104**, 4280–4290 (2000).
- F. Rosca et al., *J. Phys. Chem. A* **106**, 3540–3552 (2002).
- R. J. D. Miller, *Acc. Chem. Res.* **27**, 145–150 (1994).
- J. T. Sage et al., *Phys. Rev. Lett.* **86**, 4966–4969 (2001).
- T. Kitagawa, N. Haruta, Y. Mizutani, *Biopolymers* **67**, 207–213 (2002).
- A. M. Nagy, V. Raicu, R. J. D. Miller, *Biochim. Biophys. Acta* **1749**, 148–172 (2005).
- M. R. Armstrong, J. P. Ogilvie, M. L. Cowan, A. M. Nagy, R. J. Miller, *Proc. Natl. Acad. Sci. U.S.A.* **100**, 4990–4994 (2003).
- J. Deak, H.-L. Chiu, C. M. Lewis, R. J. D. Miller, *J. Phys. Chem. B* **102**, 6621–6634 (1998).
- P. M. Champion, F. Rosca, D. Ionescu, W. Cao, X. Ye, *Faraday Discuss.* **127**, 123–135 (2004).
- V. L. Schramm, *Acc. Chem. Res.* **48**, 1032–1039 (2015).
- H. Fujisaki, J. E. Straub, *Proc. Natl. Acad. Sci. U.S.A.* **102**, 6726–6731 (2005).
- G. Li, D. Magana, R. B. Dyer, *Nat. Commun.* **5**, 3100 (2014).
- D. Bourgeois et al., *Proc. Natl. Acad. Sci. U.S.A.* **103**, 4924–4929 (2006).

ACKNOWLEDGMENTS

Use of the LCLS, SLAC National Accelerator Laboratory, is supported by the U.S. Department of Energy, Office of Science, Office of Basic Energy Sciences under contract number DE-AC02-76SF00515. We acknowledge support from the Max Planck Society. G.K. was supported by the European Union under the program FP7-PEOPLE-2011-ITN NanoMem (project number 317079). We thank R. J. D. Miller for discussions and for pointing out the complications in the high-excitation regime, as discussed in (15); P. M. Champion and M. Huix-Rotlant for valuable discussions; C. Zeymer for assistance with the samples; G. M. Stewart, T. Anderson, and SLAC Informedia for preparing fig. S1; and T. Mueller for help in preparing Fig. 4C. T.R.M.B., L.F., K.N., A.Aq.,

S.Bot., R.B.D., M.C.H., E.H., M.Hi., J.E.K., G.K., M.L., D.M., H.L., C.M.R., R.L.S., G.J.W., S.Bou., and I.S. performed the experiment; T.R.M.B., L.F., K.N., J.R., and I.S. analyzed the data; A.Ar., K.F., M.He., J.K., I.B., and G.H. performed simulations; and T.R.M.B. and I.S. wrote the manuscript, with contributions from all authors. Structures and diffraction data have been deposited in the PDB under accession numbers 5CMV, 5CN4, 5CN5, 5CN6, 5CN7, 5CN8, 5CN9, 5CNB,

5CNC, 5CND, 5CNE, 5CNF, 5CNG, and 5D5R. Raw diffraction data will be made available at csiddb.org.

SUPPLEMENTARY MATERIALS

www.sciencemag.org/content/350/6259/445/suppl/DC1
Materials and Methods

Figs. S1 to S17
Tables S1 and S2
References (43–104)

12 May 2015; accepted 26 August 2015
Published online 10 September 2015
10.1126/science.aac5492

CHLOROPLASTS

Ubiquitin facilitates a quality-control pathway that removes damaged chloroplasts

Jesse D. Woodson,¹ Matthew S. Joens,^{2*} Andrew B. Sinson,^{1,3} Jonathan Gilkerson,^{1,4†} Patrice A. Salomé,^{5‡} Detlef Weigel,⁵ James A. Fitzpatrick,^{2*} Joanne Chory^{1,4§}

Energy production by chloroplasts and mitochondria causes constant oxidative damage. A functioning photosynthetic cell requires quality-control mechanisms to turn over and degrade chloroplasts damaged by reactive oxygen species (ROS). Here, we generated a conditionally lethal *Arabidopsis* mutant that accumulated excess protoporphyrin IX in the chloroplast and produced singlet oxygen. Damaged chloroplasts were subsequently ubiquitinated and selectively degraded. A genetic screen identified the plant U-box 4 (PUB4) E3 ubiquitin ligase as being necessary for this process. *pub4-6* mutants had defects in stress adaptation and longevity. Thus, we have identified a signal that leads to the targeted removal of ROS-overproducing chloroplasts.

In chloroplasts, an electron transport chain allows energy from sunlight to be used. When the chloroplast's capacity to transfer electrons is exceeded (owing to high irradiance, drought, or extreme temperatures) reactive oxygen species (ROS) (e.g., singlet oxygen (¹O₂) or peroxides) are generated (1). ROS can then damage DNA, proteins, lipids, and other cellular components. Thus, safeguards have evolved that allow for rapid cellular responses to these injuries.

Information about ROS damage is relayed by chloroplast-to-nucleus (retrograde) signals that broadly regulate nuclear genes involved in chloroplast function and stress adaptation (2, 3). Retrograde signals involve chloroplast-localized tetrapyrroles (hemes and chlorophylls) (4), chloroplast gene expression (5), chloroplast-produced ROS (6, 7), and metabolites (8–10). These signals are assumed to affect the function of all 50 to 100 chloroplasts in a cell. Here, we looked for other quality-control mechanisms that could work at the level of the individual chloroplast.

Plastid ferrochelatases 1 and 2 (FC1 and FC2) are conserved enzymes at the heme-chlorophyll branch point of the chloroplast-localized tetrapyrrole biosynthetic pathway (fig. S1). They convert protoporphyrin IX (Proto) to heme and may play a role in the quality control of individual chloroplasts (11–13). To test this hypothesis, we monitored *Arabidopsis thaliana* *fc1* and *fc2* mutants (fig. S2, A to C) during de-etiolation. De-etiolation involves development of nongreen plastids into mature chloroplasts and requires chloroplast signaling. When this process is disrupted, photoautotrophic growth can be inhibited (14). Seedlings were grown in the dark for 4 days and then moved to light. After 1 day of light, wild-type (wt) and *fc1-1* plants became green, whereas *fc2-1* and *fc2-2* mutants failed to do so (Fig. 1, A and B), and photosynthetic cells in cotyledons died (Fig. 1C).

To determine the cause of this phenotype, we profiled the transcriptomes of wt and *fc2-1* seedlings at the start of de-etiolation. RNA profiles were similar between these genotypes before the dark-to-light shift (Fig. 1D, table S1), but diverged after 2 hours of light. Genes enriched for plastid function (group 3) were repressed, whereas genes enriched for heat stress (group 1) and chitin response (group 2) (table S2) were more highly expressed in *fc2-1* than in wt. Thus, the dark-to-light transition appeared to cause photooxidative stress in the *fc2-1* mutant, possibly within chloroplasts.

To test this, we grew seedlings in 24-hour light/dark cycling periods (Fig. 1E and fig. S3, A and B).

Wt and *fc2* seedlings turned green when grown in constant light (24 hours) or 16 hours of light (8 hours of dark)/day. In shorter light periods [8 hours of light (16 hours of dark)/day or 4 hours of light (20 hours of dark)/day], *fc2* seedlings, unlike wt, did not become green; transgenic complementation confirmed this was an *fc2* mutant defect. For plants provided with 8 hours of light/day, the third dawn blocked their ability to turn green, and stress marker genes were induced (fig. S3, C and D, and table S3). This condition was used for most of the subsequent seedling experiments. These phenotypes were not dependent on EXE1, which mediates chloroplast-induced cell death (7) (fig. S4, A to I, and supplementary text).

We used transmission electron microscopy (TEM) to monitor the development of *fc2* chloroplasts. In constant light conditions, the ultrastructure of *fc2-1* chloroplasts was similar to that of wt (Fig. 1F). In 8 hours of light/day, *fc2-1* chloroplasts were severely damaged, with swollen thylakoid membranes, large plastoglobule structures, and disrupted outer envelope membranes. This loss of chloroplast integrity was confirmed using *fc2-1* seedlings expressing chloroplast-localized yellow fluorescent protein (YFP) (Fig. 1G and fig. S3H). When these lines were grown in 8 hours of light/day, YFP leaked into the cytoplasm after 1 hour. After 8 hours, YFP and chlorophyll fluorescence were barely detectable. Thus a chloroplast stress signal induced fast chloroplast degradation.

Because tetrapyrroles can cause photooxidative damage (15), we monitored the levels of five chlorophyll intermediates. In 8 hours of light/day growth conditions, Proto was the only one that accumulated in *fc2* mutants (Fig. 2A and fig. S5A). Genetic complementation experiments of *fc2* mutants showed that expression of *FC1* could not prevent this accumulation (Fig. 2A), but did restore wt levels of heme (Fig. 2B) and chlorophyll (Fig. 2C and fig. S5B) in constant light and protochlorophyllide (fig. S5C) in the dark. In 8 hours of light/day growth conditions, *FC1* expression did not restore the ability to turn green (Fig. 2C and fig. S5B), block chloroplast degradation (fig. S4I), or block stress marker gene induction (fig. S4H) in *fc2-1* plants. Expressing maize *FC1* or a catalytically dead variant of *FC2* (H295A) (12) also did not restore an ability to turn green to *fc2-1* plants (figs. S6 and S7, A and B). Finally, reducing excess tetrapyrrole accumulation in *fc2-1* by introducing *hema1* and *hema2* mutations that reduce the first step of tetrapyrrole synthesis (fig. S1) allowed seedlings to avoid chloroplast degradation when provided with 8 hours of light/day (Fig. 2C and fig. S4I).

¹Plant Biology Laboratory, The Salk Institute, La Jolla, CA. ²Waitt Advanced Biophotonics Center, The Salk Institute, La Jolla, CA. ³Division of Biological Sciences, University of California-San Diego, La Jolla, CA. ⁴Howard Hughes Medical Institute, The Salk Institute, La Jolla, CA. ⁵Department of Molecular Biology, Max Planck Institute for Developmental Biology, Tübingen, Germany. *Present address: Washington University Center for Cellular Imaging, Washington University School of Medicine, St. Louis, MO. †Present address: Department of Biology, Shepherd University, Shepherdstown, WV. ‡Present address: Department of Chemistry and Biochemistry, University of California-Los Angeles, Los Angeles, CA. §Corresponding author. E-mail: chory@salk.edu

Together these findings suggested that Proto accumulation correlated with chloroplast degradation and confirmed that FC2 has a specialized function in plastids (11, 12, 16).

Proto is a photosensitizing molecule that generates $^1\text{O}_2$ in cells (17). As expected, *fc2-1* mutants provided with 8 hours of light/day accumulated $^1\text{O}_2$ (Fig. 2D) and induced $^1\text{O}_2$ and oxidative stress-responsive genes within 2 hours (fig. S8A). Feeding the $^1\text{O}_2$ scavenger vitamin B6 (18) blocked

chloroplast degradation in *fc2-1* seedlings and restored their ability to become green (Fig. 2E and fig. S8B). Thus, a burst of $^1\text{O}_2$, owing to Proto accumulation in *fc2* mutants, was likely to be responsible for chloroplast degradation and an inability to turn green.

To identify genes required for $^1\text{O}_2$ -induced chloroplast degradation, we screened for second site mutations in *fc2-1* mutants that restored a wt ability to green when provided with 4 hours of light/

day. By one-step mapping and whole-genome sequencing, we identified 24 *ferrochelatase-two-suppressor* (*fts*) mutants affecting 17 independent loci (Fig. 3A). Four of these loci were characterized; three were genes that affect tetrapyrrole and $^1\text{O}_2$ accumulation (fig. S9A; fig. S10, A to E; and table S4) (19).

The fourth loci, *fts29* (called *pub4-6* hereafter), had a missense mutation in *Plant U-Box 4* (*PUB4*) *E3 ubiquitin ligase*, a broadly expressed gene

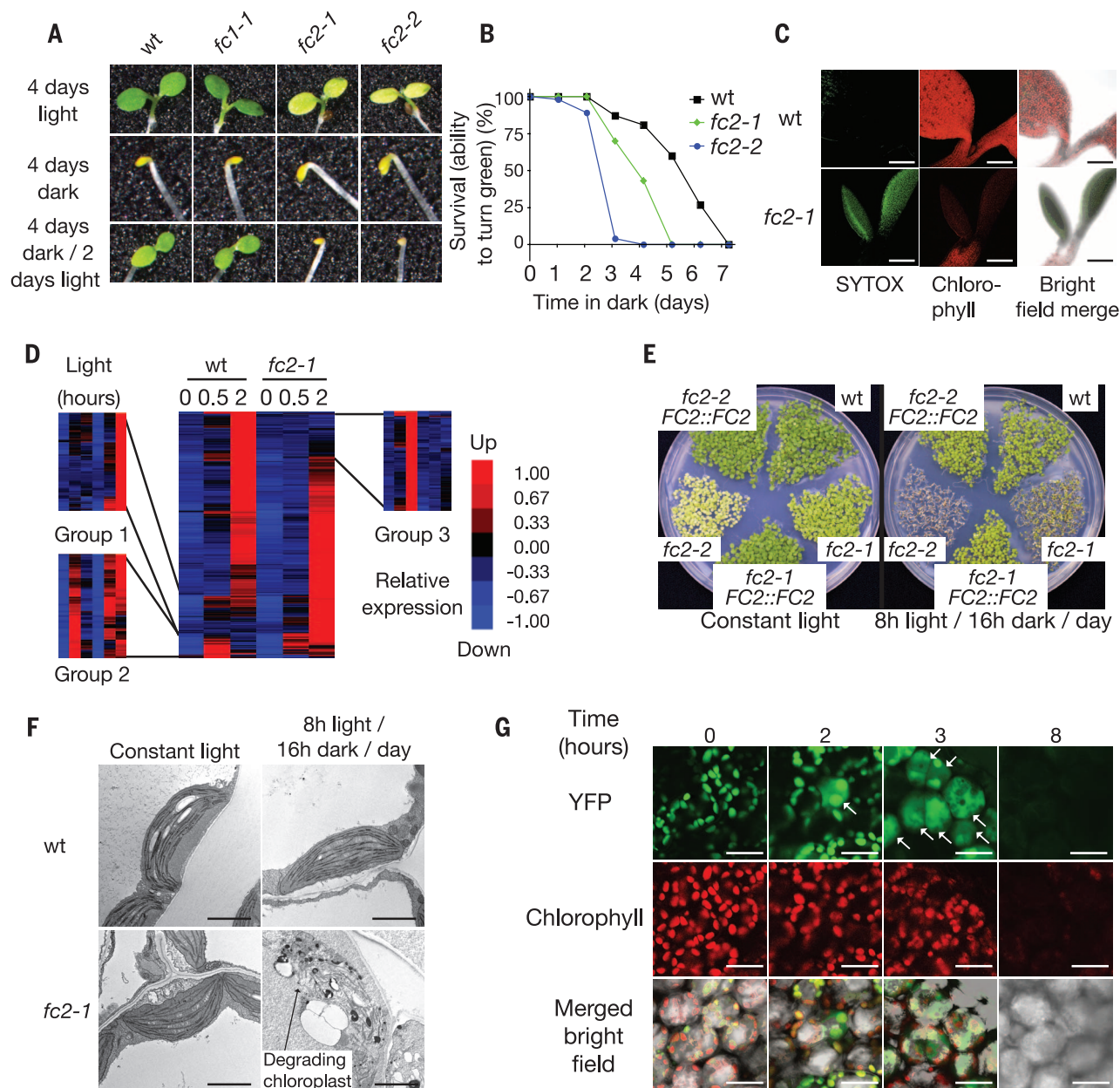


Fig. 1. *fc2* mutants suffer from chloroplast degradation and photooxidative stress during dark-to-light transitions. (A) *fc2* mutant seedlings are unable to turn green after 4 days of growth in the dark. (B) The survival rate (the ability to turn green in 48 hours of light) of 100 seedlings first grown for the indicated number of days in the dark. (C) *fc2-1* cotyledons undergo cell death, as shown by SYTOX green staining of dead nuclei. Scale bars, 200 μm . (D) A microarray analysis of transcripts induced (at least twofold, $P \leq 0.05$) in

4-day-old dark grown seedlings during the first 2 hours of de-etiolation. (E) Five-day-old seedling phenotypes under different day lengths. (F) Representative TEM micrographs of chloroplasts in 3-day-old cotyledon mesophyll cells 2 hours after dawn. Scale bars, 2 μm . (G) Confocal images of 3-day-old *fc2-1* seedling cotyledons grown in 8 hours of light/day expressing plastid-targeted YFP (RBCS-YFP) before (time 0) or after light exposure. White arrows indicate cells with cytoplasmic YFP. Scale bars, 20 μm .

encoding an active cytoplasmic-localized (Fig. 3B and fig. S11) E3 ubiquitin ligase involved in cell death and development (20, 21). E3 ubiquitin ligases catalyze the transfer of ubiquitin from an E2 ubiquitin-conjugating enzyme to a protein substrate. A wt copy of *PUB4* complemented the *pub4-6* phenotype (Fig. 3C and fig. S12, A and B) and *pub4-6* was allelic with *pub4* T-DNA lines (fig. S12, C to D). *fc2-1/pub4-6* had no reduction in tetrapyrrole synthesis [protochlorophyllide, chlorophyll, and ALA levels remained elevated (fig. S10, A to C)]. When provided with 8 hours of light/day, Proto and $^1\text{O}_2$ (Fig. 3, D and E) accumulated in *fc2-1/pub4-6*, but chloroplasts were not degraded. Instead, chloroplasts appeared stressed with irregular shapes and angular membranes (Fig. 3F). *fc2-1/pub4-6* mutants still induced many nuclear stress-associated genes (fig. S13), which suggested that chloroplast degradation

was not because of $^1\text{O}_2$ damage per se but was because of a $^1\text{O}_2$ -generated signal involving *PUB4*.

Because E3 ligases ubiquitinate protein substrates, we tested whether the ubiquitination of chloroplast proteins was linked to chloroplast degradation. Chloroplast fractions of *fc2-1* plants provided with 16 hours of light/day exhibited a *PUB4*-dependent increase in polyubiquitinated protein(s) compared with wt (Fig. 3G and fig. S14, A and B). Immuno-electron microscopy also showed a *PUB4*-dependent increase of ubiquitin on the chloroplast envelopes in *fc2-1* mutants (Fig. 3H and fig. S14C) (19), which suggested that ubiquitination was responsible for the chloroplast degradation in *fc2-1* plants.

Next, we tested if chloroplast degradation happened under permissive conditions without cell death. In constant light conditions, chloroplast degradation occurred in wt, but *fc2* mutants had

more chloroplasts being degraded (Fig. 4, A to E) (19). These aberrant chloroplasts often had starch granules (indicating that they had been photosynthetic) (Fig. 4D), large plastoglobules, and compressed grana/thylakoid membranes (Fig. 4E and fig. S15, A and B). Sometimes these chloroplasts were observed to be interacting with a globular vacuole (Fig. 4, B and C, and fig. S15, C and D). Nearby organelles appeared normal, which suggested that specific chloroplasts had been selected for degradation. Degradation depended on *PUB4*; *pub4-6* and *fc2-1/pub4-6* plants had less chloroplast degradation than their parent lines wt and *fc2-1*, respectively (Fig. 4A). *pub4-6* plants also accumulated more chloroplasts/cell area and chlorophyll (Fig. 4, F and G, and fig. S16, A to C). Thus, *PUB4* may control chloroplast degradation in healthy cells.

To test if chloroplast degradation is important for long-term maintenance of photosynthetic

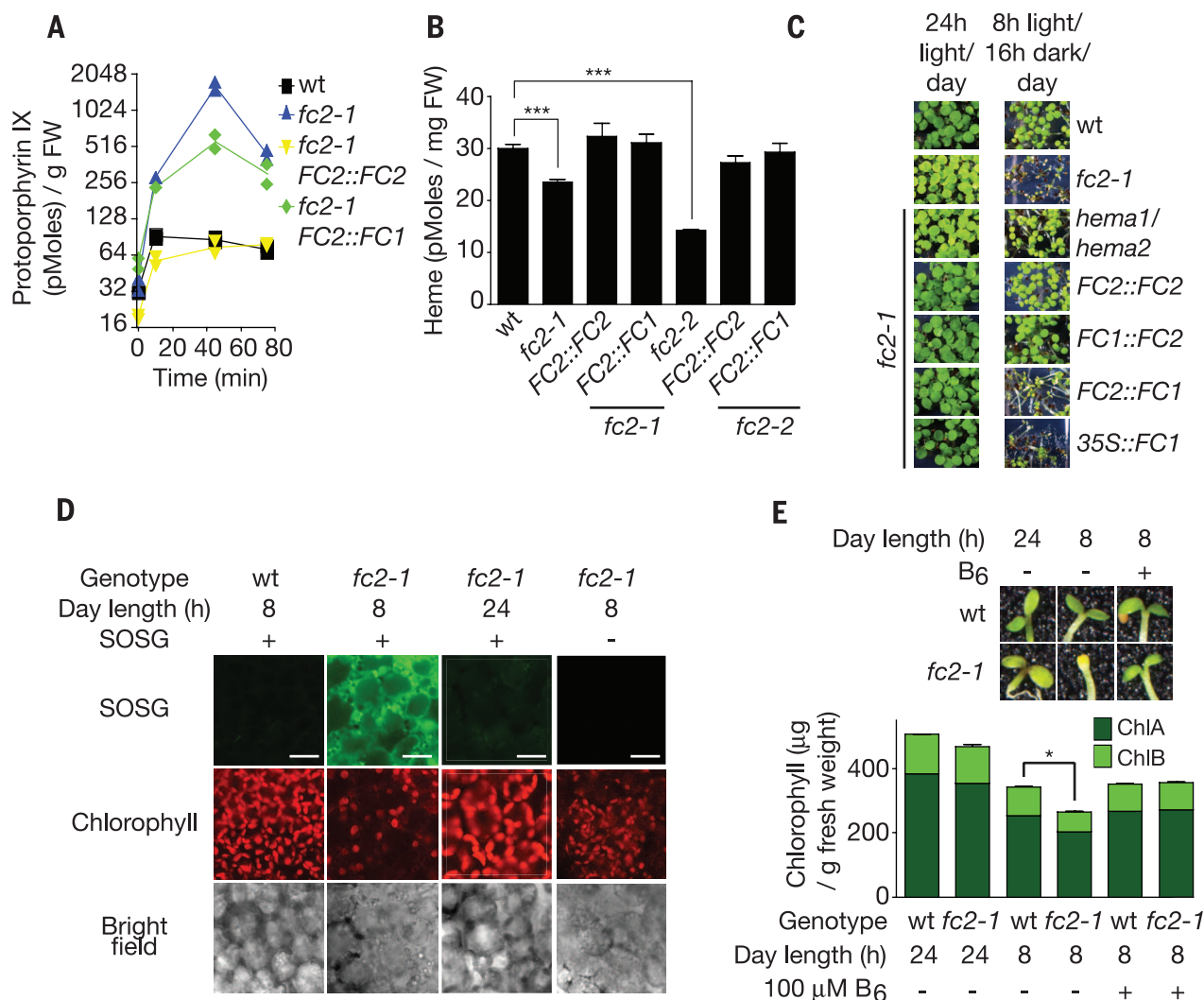


Fig. 2. *fc2* mutants accumulate Proto and $^1\text{O}_2$. (A) Time course (starting at dawn) of Proto levels in 3-day-old seedlings provided with 8 hours of light/day ($n \geq 2$ replicates). (B) Free heme levels of seedlings ($n = 3$ replicates). (C) Phenotypes of transgenic seedlings grown for 5 days in the indicated conditions. (D) Representative confocal images of singlet oxygen (as shown by singlet oxygen sensor green) accumulation in cotyledon mesophyll cells (2 hours after dawn) of 3-day-old seedlings provided with 8 hours of light/day. Scale bars, 20 μm . (E) Effect of feeding vitamin B₆ on chlorophyll levels ($n = 3$ replicates) and survival. All values are means \pm SEM. * $P \leq 0.05$, *** $P \leq 0.001$, two-tailed Student's *t* test.

cells during stress (22, 23), we characterized the phenotypes of *pub4-6* single mutants. *pub4-6* mutants senesced early (Fig. 4H and fig. S16, D and E) and were stunted in excess light that

causes long-term chloroplast oxidative damage (Fig. 4I). Thus, a ubiquitination-dependent chloroplast degradation pathway and/or PUB4 may be important for stress adaptation and longevity.

Indiscriminate chloroplast degradation can occur during osmotic stress (24) or used to recycle nutrients during starvation or senescence (25, 26). Here, we found that plant cells also use a selective

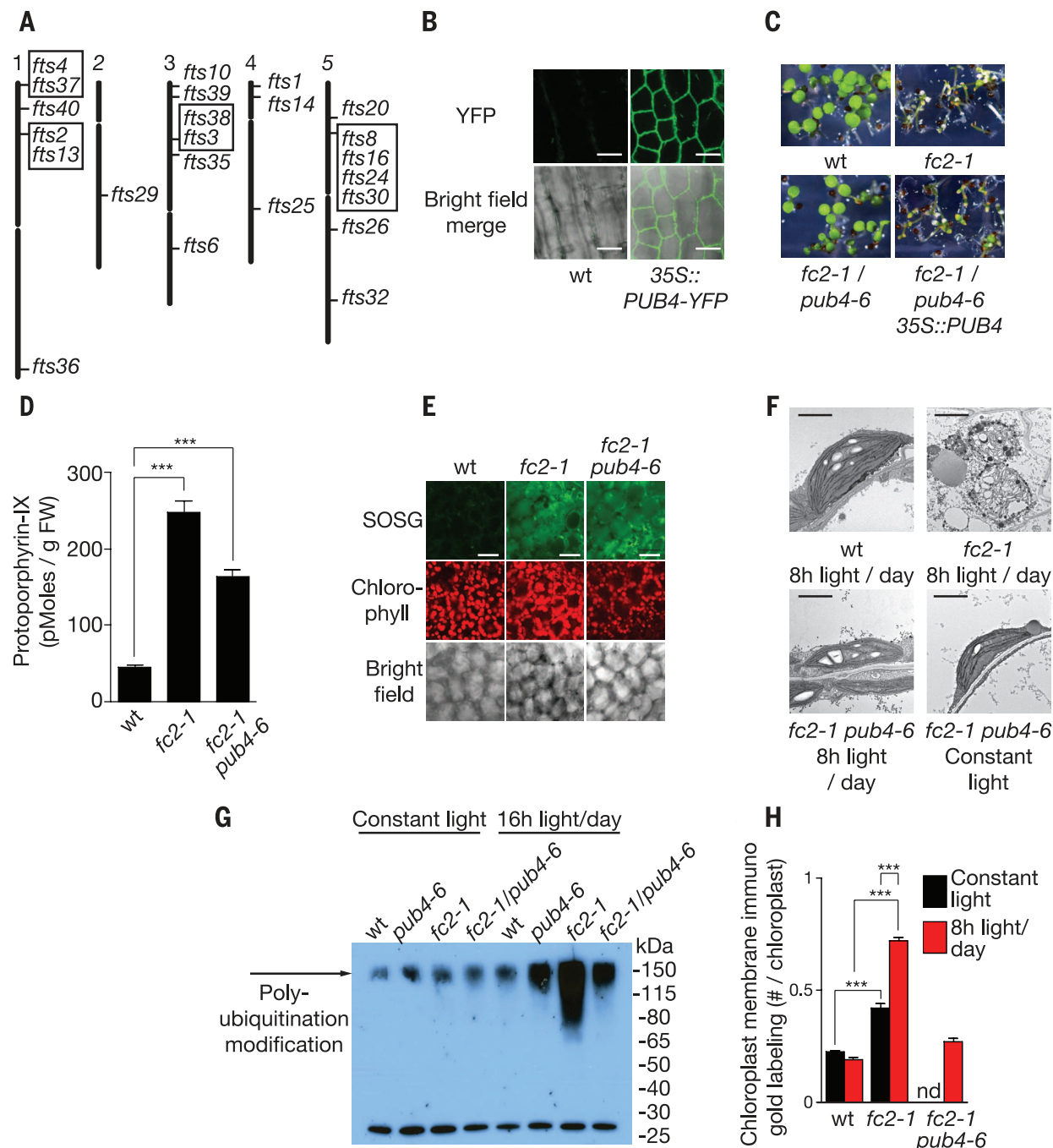


Fig. 3. A mutant screen to identify genes involved in chloroplast stress and degradation. (A) Locations of 24 independent *fts* (*ferrochelatase two suppressors*) mutations representing 17 loci. Boxed mutants are allelic. (B) Subcellular localization of stably expressed PUB4-YFP in hypocotyl cells. (C) Complementation of the *fts29* (*pub4-6*) phenotype with a wt copy of *PUB4* grown for 5 days in 8 hours of light/day. (D) Proto levels in 3-day-old seedlings provided 8 hours of light/day 10 min after dawn ($n = 3$ replicates). (E) Representative confocal images of $^{18}\text{O}_2$ accumulation in cotyledon mesophyll cells (2 hours after dawn) of 3-day-old seedlings provided with

8 hours of light/day. Scale bars, 20 μm . (F) Representative TEM micrographs of chloroplasts in 3-day-old cotyledon mesophyll cells 6 hours after dawn. Scale bars, 2 μm . (G) Antiubiquitin immunoblot of whole chloroplast fractions isolated from leaves 3 hours after dawn. Plants were grown for 2 weeks in constant light and then transferred to 16 hours of light/day or kept in constant light for 2 days. (H) Quantification of chloroplast envelope-associated ubiquitin by immunoelectron microscopy (gold labeling) (19) in 3-day-old seedlings ($n = 3$ seedlings, 10 cells each) 1 hour after dawn. All values are means \pm SEM. *** $P \leq 0.001$, two-tailed Student's *t* test.

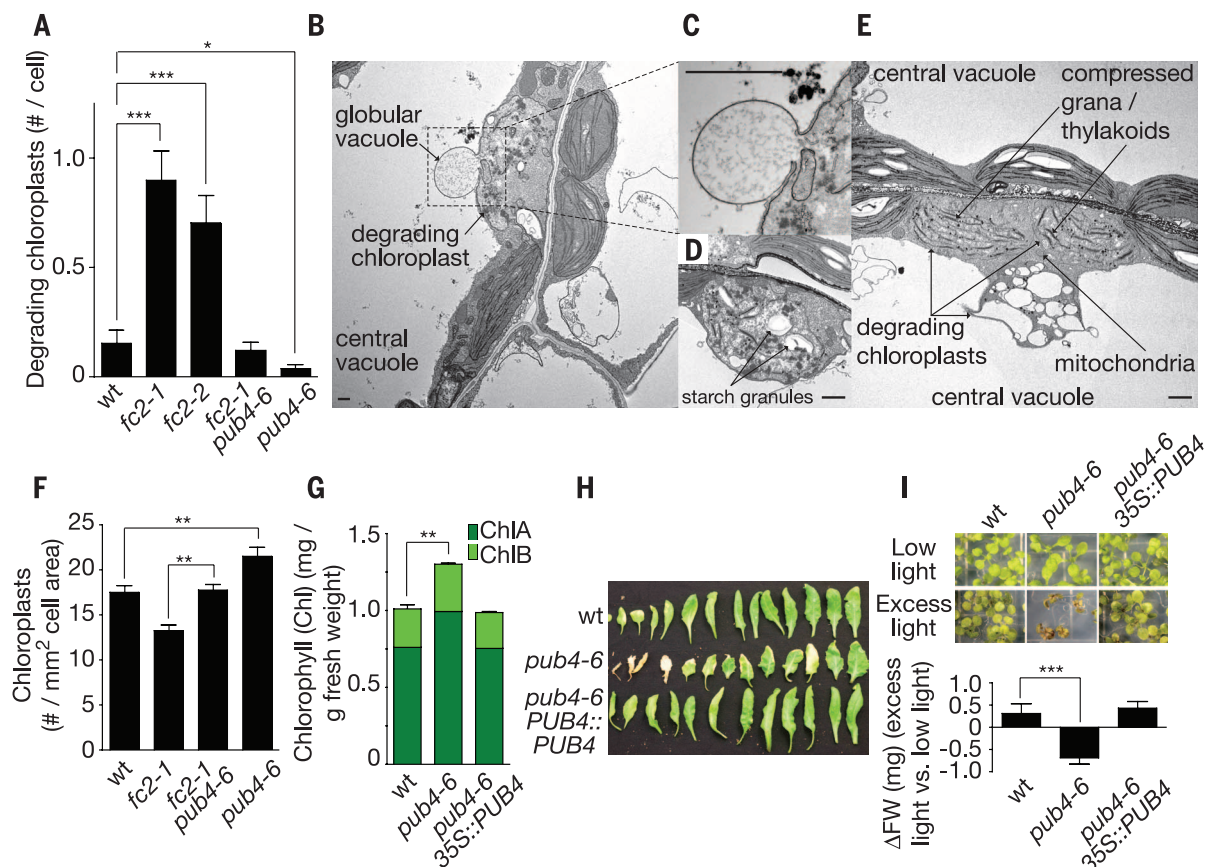


Fig. 4. PUB4 is part of a chloroplast quality-control pathway. (A) Quantification of degrading chloroplasts using scanning electron microscopy micrographs (19) of cotyledon mesophyll cells of 5-day-old seedlings grown in constant light ($n \geq 54$ cells). (B to E) TEM images of chloroplasts undergoing various levels of degradation in *fc2-1* seedlings. Scale bars, 1 μm . (F) Quantification of chloroplasts in cotyledon palisade mesophyll cells ($n \geq 6$ seedlings)

and (G) chlorophyll levels ($n = 3$ replicates) of 6-day-old seedlings grown in constant light. (H) Senescing rosette leaves of 5-week-old plants grown in constant light. (I) Phenotypes and fresh weight (FW) of seedlings ($n = 7$ groups of 10) grown for 1 week in low light ($30 \mu\text{mol} \cdot \text{m}^{-2} \cdot \text{s}^{-1}$ at 22°C) and then transferred to excess light ($275 \mu\text{mol} \cdot \text{m}^{-2} \cdot \text{s}^{-1}$ at 15°C) for 1 week. All values are means \pm SEM. * $P \leq 0.05$, ** $P \leq 0.01$, *** $P \leq 0.001$, two-tailed Student's t test.

chloroplast degradation system to remove ROS-damaged chloroplasts. When chloroplasts accumulated $^1\text{O}_2$, proteins in their envelope membranes became ubiquitinated by the direct or indirect action of PUB4, and were degraded (fig. S17). $^1\text{O}_2$ is the major ROS species generated during photosynthesis (27), but its short half-life ($\sim 4 \mu\text{s}$) ensures that it is confined only to chloroplasts in which it was generated (28) so that healthy chloroplasts are not accidentally degraded.

REFERENCES AND NOTES

1. K. Asada, *Plant Physiol.* **141**, 391–396 (2006).
2. W. Chi, X. Sun, L. Zhang, *Annu. Rev. Plant Biol.* **64**, 559–582 (2013).
3. D. Leister, *Front. Plant Sci.* **3**, 135 (2012).
4. N. Mochizuki, J. A. Brusslan, R. Larkin, A. Nagatani, J. Chory, *Proc. Natl. Acad. Sci. U.S.A.* **98**, 2053–2058 (2001).
5. J. C. Gray, J. A. Sullivan, J. H. Wang, C. A. Jerome, D. MacLean, *Philos. Trans. R. Soc. Lond. B Biol. Sci.* **358**, 135–144 (2003).
6. F. Ramel et al., *Plant Cell* **25**, 1445–1462 (2013).
7. D. Wagner et al., *Science* **306**, 1183–1185 (2004).
8. G. M. Estavillo et al., *Plant Cell* **23**, 3992–4012 (2011).
9. F. Ramel et al., *Proc. Natl. Acad. Sci. U.S.A.* **109**, 5535–5540 (2012).
10. Y. Xiao et al., *Cell* **149**, 1525–1535 (2012).
11. M. Scharfenberg et al., *Plant Cell Environ.* **38**, 280–298 (2015).
12. J. D. Woodson, J. M. Perez-Ruiz, J. Chory, *Curr. Biol.* **21**, 897–903 (2011).
13. J. D. Woodson, J. M. Perez-Ruiz, R. J. Schmitz, J. R. Ecker, J. Chory, *Plant J.* **73**, 1–13 (2013).
14. M. E. Ruckle, S. M. DeMarco, R. M. Larkin, *Plant Cell* **19**, 3944–3960 (2007).
15. R. Tanaka, A. Tanaka, *Annu. Rev. Plant Biol.* **58**, 321–346 (2007).
16. J. Papenbrock et al., *Plant J.* **28**, 41–50 (2001).
17. J. C. Kennedy, R. H. Pottier, *J. Photochem. Photobiol. B* **14**, 275–292 (1992).
18. P. Bilski, M. Y. Li, M. Ehrenshaft, M. E. Daub, C. F. Chignell, *Photochem. Photobiol.* **71**, 129–134 (2000).
19. Materials and Methods are available as supplementary materials on Science online.
20. A. Kinoshita et al., *Development* **142**, 444–453 (2015).
21. H. Wang et al., *Plant J.* **74**, 511–523 (2013).
22. M. Kusaba, A. Tanaka, R. Tanaka, *Photosynth. Res.* **117**, 221–234 (2013).
23. Z. Li, S. Wakao, B. B. Fischer, K. K. Niyogi, *Annu. Rev. Plant Biol.* **60**, 239–260 (2009).
24. S. Wang, E. Blumwald, *Plant Cell* **26**, 4875–4888 (2014).
25. S. Michaeli, A. Honig, H. Levanyon, H. Peled-Zehavi, G. Galili, *Plant Cell* **26**, 4084–4101 (2014).
26. A. Chiba, H. Ishida, N. K. Nishizawa, A. Makino, T. Mae, *Plant Cell Physiol.* **44**, 914–921 (2003).
27. C. Triantaphylides et al., *Plant Physiol.* **148**, 960–968 (2008).
28. P. R. Ogilby, *Chem. Soc. Rev.* **39**, 3181–3209 (2010).

ACKNOWLEDGMENTS

We thank S. Orchard for photographs of plants, C. Lanz for assistance with sequencing, X. Wang for help with SHORE analysis, C. Procko, E. Lee, and A. Tsang for technical assistance, and D. O'Keefe for useful discussions about the manuscript. J.D.W., A.S., J.G. and J.C. acknowledge long-term support from the Division of Chemical Sciences, Geosciences, and Biosciences, Office of Basic Energy Sciences of the U.S. Department of Energy through grant DE-FG02-04ER15540 and from the Howard Hughes Medical Institute. J.G. was supported by an NIH Kirschstein fellowship (1F32GM096610). M.S.J. and J.A.J.F. received funding from the Waitt Advanced Biophotonics Center, NCI P30 Cancer Center Support Grant CA014195 (JAJF), NINDS P30 Neuroscience Center Core Grant NS072031 and the W.M. Keck Foundation. P.S. and D.W. were supported by a Gottfried Wilhelm Leibniz Award to the Deutsche Forschungsgemeinschaft (D.F.G.), and by the Max Planck Society. We thank J. Callis for sharing the anti-ubiquitin antibody and R. Tsien and L. Gross for use of their HPLC. Microarray data are deposited at Gene Expression Omnibus (GSE71764). All biological materials in this study are available from J.C. under a materials transfer agreement with the Salk Institute for Biological Studies/HHMI.

SUPPLEMENTARY MATERIALS

www.sciencemag.org/content/350/6259/450/suppl/DC1
Materials and Methods
Supplementary Text
Figs. S1 to S17
Tables S1 to S9
References (29–63)

5 June 2015; accepted 18 September 2015
10.1126/science.aac7444

AUTOIMMUNITY

The Ro60 autoantigen binds endogenous retroelements and regulates inflammatory gene expression

T. Hung,^{1*} G. A. Pratt,² B. Sundararaman,² M. J. Townsend,¹ C. Chaivorapol,¹T. Bhargale,¹ R. R. Graham,¹ W. Ortmann,¹ L. A. Criswell,³G. W. Yeo,^{2,4,5*} T. W. Behrens^{1*}

Autoantibodies target the RNA binding protein Ro60 in systemic lupus erythematosus (SLE) and Sjögren's syndrome. However, it is unclear whether Ro60 and its associated RNAs contribute to disease pathogenesis. We catalogued the Ro60-associated RNAs in human cell lines and found that among other RNAs, Ro60 bound an RNA motif derived from endogenous Alu retroelements. Alu transcripts were induced by type I interferon and stimulated proinflammatory cytokine secretion by human peripheral blood cells. Ro60 deletion resulted in enhanced expression of Alu RNAs and interferon-regulated genes. Anti-Ro60-positive SLE immune complexes contained Alu RNAs, and Alu transcripts were up-regulated in SLE whole blood samples relative to controls. These findings establish a link among the lupus autoantigen Ro60, Alu retroelements, and type I interferon.

Autoantibodies to the RNA binding protein Ro60 (also called SSA) are present in individuals with systemic lupus erythematosus (SLE) (1), Sjögren's syndrome (2), neonatal lupus with heart block (3–5), and other autoimmune disorders (6). SLE subjects with anti-Ro60 antibodies have an increased prevalence of skin disease, photosensitivity, and nephritis, along with elevated expression of interferon (IFN)-inducible genes in immune cells and tissues (7, 8). Ro60, encoded by *TROVE2*, is a component of a ribonucleoprotein complex comprising the E3 ubiquitin ligase Ro52 (9), the

polymerase III (Pol III) transcriptional terminator La/SSB, and short noncoding Y RNAs (*HYI-4*) (10). Ro60 has a specific RNA recognition domain for Y RNAs but binds additional, possibly misfolded, RNAs through a separate cavity (11). The identity of these other RNA species and their relevance to autoimmune disease is unclear.

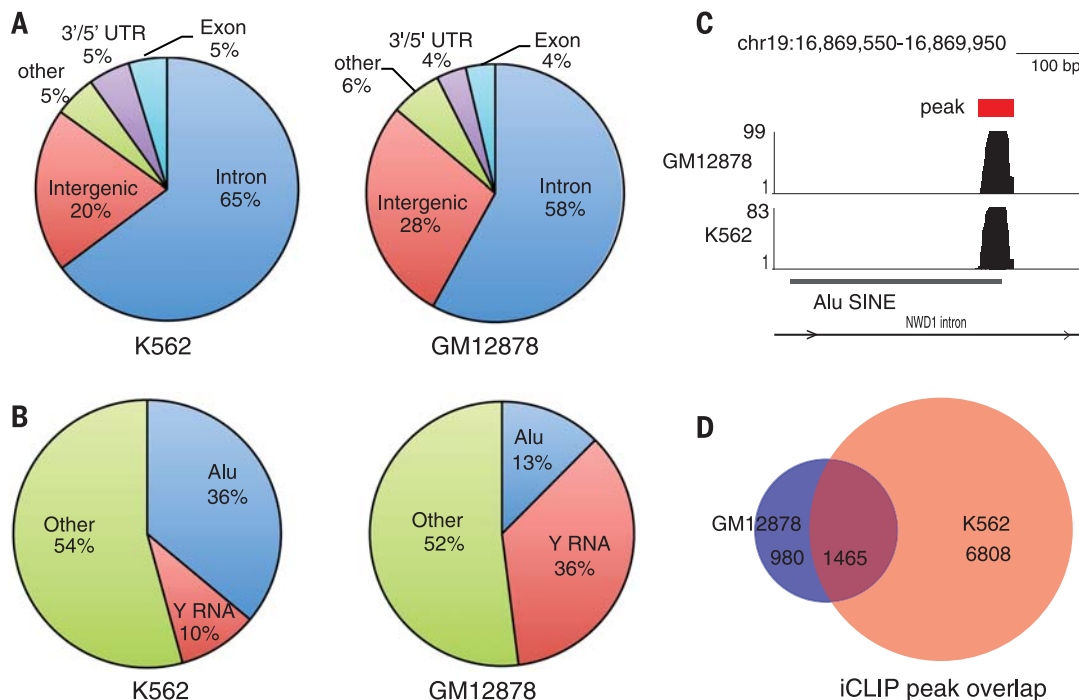
To identify RNAs bound to Ro60, we performed iCLIP (individual nucleotide cross-linking and immunoprecipitation) (12–14) followed by high-throughput sequencing in two type I interferon-stimulated ENCODE cell lines: GM12878, an Epstein-Barr virus-transformed B lymphocyte

cell line, and K562, an erythromyeloblastoid leukemia cell line (www.genome.gov/encode/) (fig. S1). Sequencing reads were aligned to the human reference genome (hg19), generating 970,667 and 1,090,671 alignments for GM12878 and K562, respectively. This analysis identified 2445 Ro60-bound sites in GM12878 and 8273 sites in K562.

Annotation of all peaks to known genomic features revealed that approximately two-thirds of the iCLIP tags localized to introns in both cell lines (Fig. 1A). As expected, Y RNAs constituted a substantial fraction of iCLIP tags in both lines (Fig. 1B). Surprisingly, iCLIP tags within Alu SINEs (short interspersed elements), a common repetitive transposable element (~1.1 M) in the human genome (15), were also represented (Fig. 1, B and C). Additional lower-frequency tags included 5' and 3' untranslated regions, LINEs (long interspersed elements), tRNAs, rRNAs, and simple repeats (fig. S1). Most of the Ro60 iCLIP peaks identified in GM12878 (1465/2445, 60%) were also found in K562 (Fig. 1D and table S1), indicating concordance of iCLIP results between the two cell lines.

Motifs enriched within shared iCLIP peaks included Y RNA consensus sequences, as well as a U-rich motif that corresponds to the 3' antisense

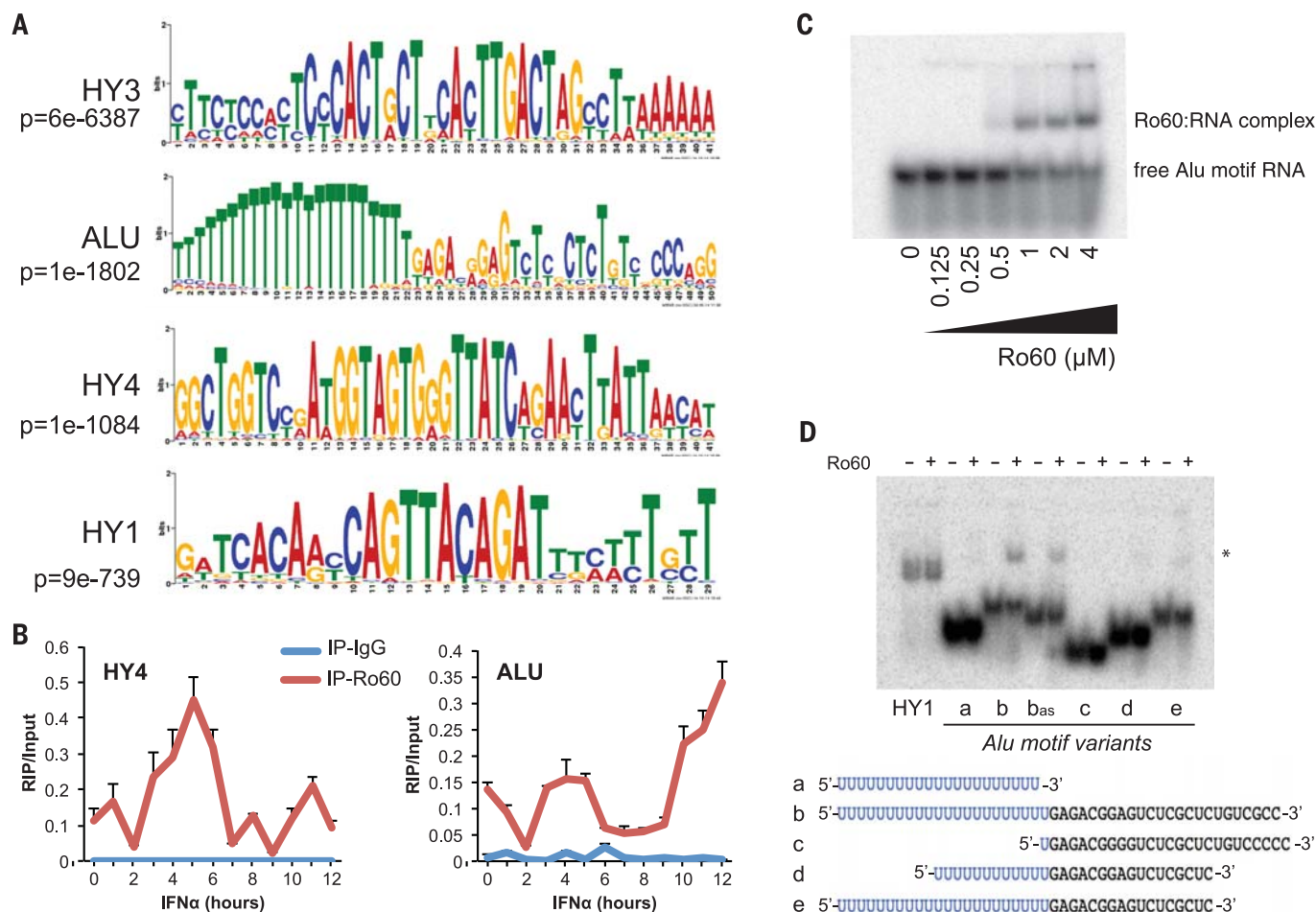
Fig. 1. iCLIP identifies RNAs bound by Ro60. (A) Pie graph showing annotation of Ro60 iCLIP peaks to gene structures in IFN- α -treated (6 hours) K562 and GM12878 cell lines. (B) Pie graph showing annotation of iCLIP peaks to Repeatmasker elements. (C) Genome browser snapshot of a representative Alu iCLIP peak; y axis indicates read counts. (D) Venn diagram representation of overlap in Ro60 iCLIP peaks between K562 and GM12878. $P < 0.001$, hypergeometric test.



We next used an electromobility shift assay (EMSA) to test the binding of radiolabeled Alu motif RNA oligonucleotides to purified recombinant Ro60 protein. Ro60 binding was observed with the full-length Alu motif (Fig. 2, C and D, oligo b), and an antisense version of the full-length motif (Fig. 2D, oligo b_{AS}). Reduced binding to Ro60 (oligos d and e), or no appreciable binding (oligos a and c), was observed for various truncated Alu motifs (Fig. 2D). Several sequence

To further explore the functional role of Ro60, we used zinc finger nuclease technology to generate three GM12878 Ro60 knockout (KO) cell lines, each containing unique biallelic frame-shift mutations within exon 2 of Ro60/*TROVE2* (fig. S5). The KO lines contained undetectable levels of Ro60 protein (Fig. 3A) and showed markedly reduced retrieval of Alu and Y RNA by Ro60 RIP-PCR (fig. S6). Surprisingly, RNA-seq at baseline and 6 hours after treatment with IFN- α demonstrated that many of the genes altered by IFN- α treatment in the parental cells (lanes 9 and 10) were dysregulated in the Ro60 KOs in the absence of treatment (Fig. 3B, lanes 3 to 5). Gene expression correlated significantly between the unstimulated Ro60 KO lines and the IFN- α -treated parental cell line (Fig. 3C) ($R = 0.64$, $n = 4520$, $P < 0.0001$). Genes dif-

We next performed a time course of IFN- α treatment to determine whether the widespread changes in gene expression included alterations in Ro60-bound RNAs. In the parental cell line, there were minimal changes in the protein levels of Ro60 during the 12-hour experiment (Fig. 3D). At all time points, Y RNAs were expressed at reduced levels in the Ro60 null cells relative to parental cells (Fig. 3E and fig. S7), whereas total Alu RNAs were found at significantly higher levels in the null cells (Fig. 3F). We confirmed these differences by quantitation of Alu reads from the RNA-seq data (Fig. 3G). Together, these findings demonstrate elevation of Alu expression and activation of IFN-induced genes in the absence of Ro60. A possible interpretation of these



[oligo b from (D)] with indicated concentrations of recombinant Ro60 protein. **(D)** EMSA of Alu motif variants with recombinant Ro60. a, PolyU sequence alone; b, representative Alu motif; b_{AS}, antisense of b; c, deleted polyU; d, partial 5' and 3' truncations; e, partial 3' truncation. Asterisk indicates RNA/Ro60 complex. RNA sequences depicted in bottom panel. See also fig. S4.

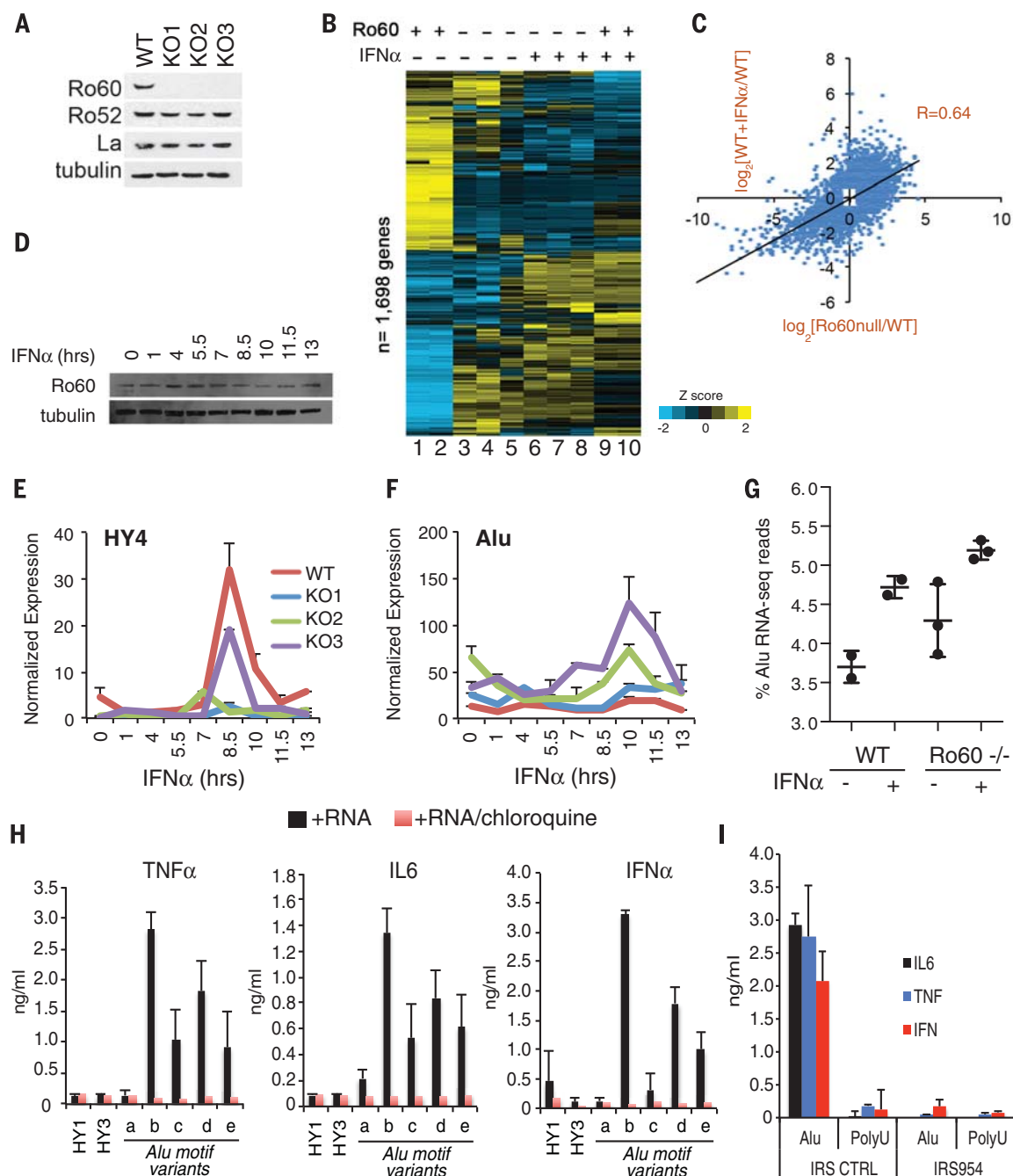


Fig. 3. Loss of Ro60 in GM12878 cells activates inflammatory gene expression and Alu RNA expression. (A) Western analysis of Ro60, Ro52, La, and tubulin in three independent GM12878 Ro60 KO clones. (B) RNA-seq heat map of 1698 genes induced or repressed by a factor of >2 upon 6 hours of IFN- α in parental GM12878 cells. Unsupervised clustering of both genes and conditions. Lanes 1 and 2: Parental cells at baseline, biologic replicates. Lane 3: KO1 at baseline. Lane 4: KO2 at baseline. Lane 5: KO3 at baseline. Lane 6: KO1 + IFN- α . Lane 7: KO2 + IFN- α . Lane 8: KO3 + IFN- α . Lanes 9 and 10: Parental cell line + IFN- α , biologic replicates. See Fig. S7 for global correlation of gene expression between clones. (C) Scatterplot of gene expression changes [\log_2 (relative change)] in Ro60 null clones (x axis) or wild-type parental cells treated with IFN- α (y axis) compared to baseline wild-type cells. Data represent all genes with induction or repression by a factor of ≥ 1.5 ; $n = 4520$, $P = 2.2 \times 10^{-16}$. $R =$ Pearson product-moment correlation. (D) Western blot of whole-cell lysates at indicated time points after IFN- α treatment of the

parental cell line. (E and F) RT-PCR of HY4 RNA (E) or Alu RNA (F) at indicated time points after IFN- α treatment of the parental cell line. Expression values normalized to GAPDH. P values of (E): KO1 versus WT ($P = 0.015$), KO2 versus WT ($P = 0.001$), KO3 versus WT ($P = 0.001$); Student's t test. (G) Quantitation of Alu reads as a percent of all RNA-seq reads from IFN- α -treated (6 hours) wild-type (biologic replicates, $n = 2$) or Ro60 null clone ($n = 3$) libraries. Error bars represent SD. (H) Enzyme-linked immunosorbent assay (ELISA) of culture supernatants of human PBMCs 15 hours after N -[1-(2,3-dioleoyloxy)propyl]- N,N,N -trimethylammonium methyl sulfate (DOTAP) transfection of the indicated RNAs (see Fig. 2D for RNA sequences). Error bars represent SD of three technical replicates from a representative experiment (1 of 3). (I) ELISA of culture supernatants of human PBMCs 15 hours after DOTAP cotransfection of the indicated RNAs with TLR7/9 inhibitory oligo IRS954 or a control oligo. Error bars represent technical replicates from a representative experiment (1 of 4).

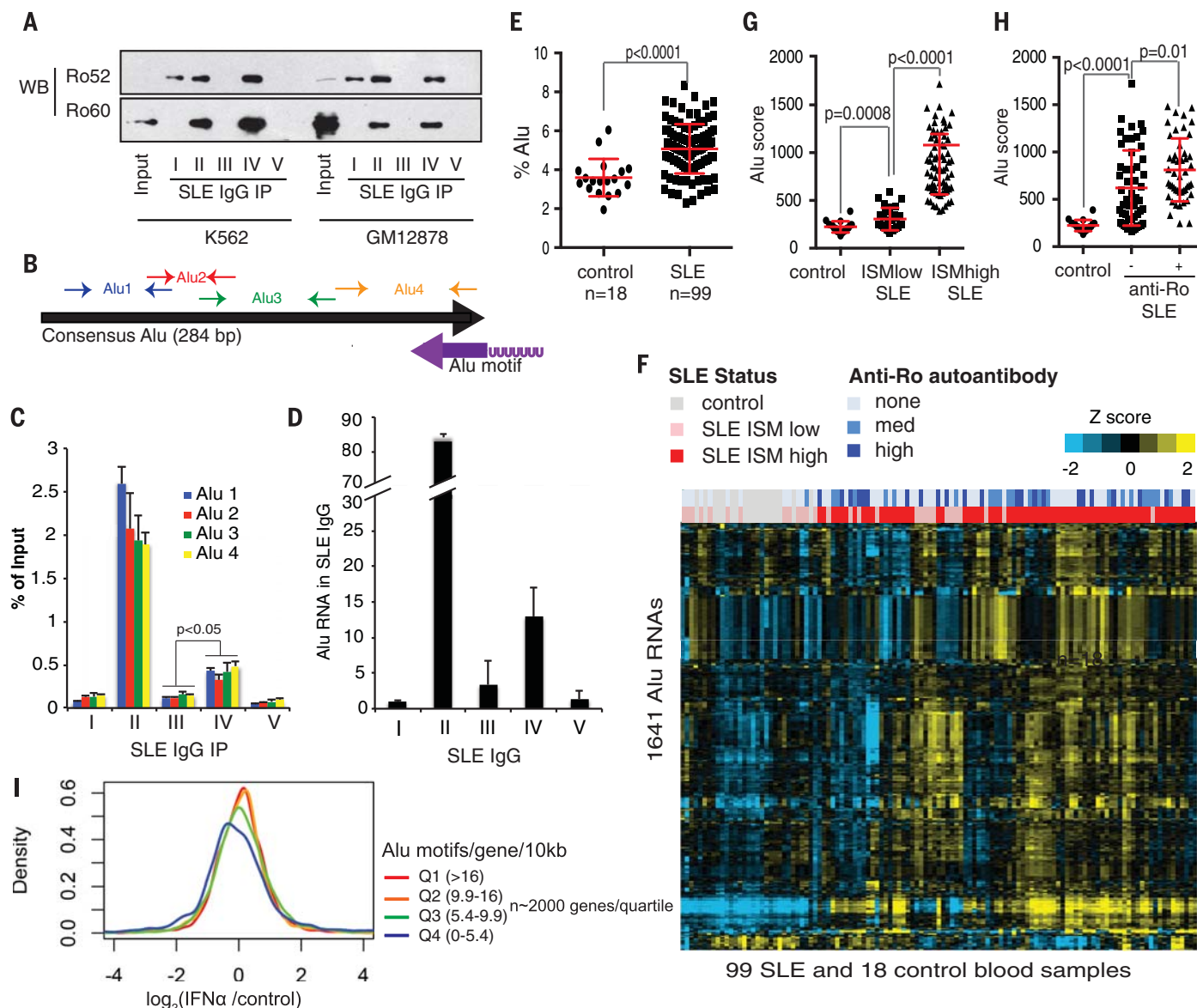


Fig. 4. Alu RNAs in Ro60-positive SLE immune complexes and SLE whole blood. (A) Immunoprecipitation from IFN- α -treated (6 hours) K562 or GM12878 cell lysates using SLE patient IgGs followed by Western blot of Ro52 or Ro60. Input lane represents 10% total lysate. (B) PCR primer map of Alu elements with respect to the consensus Alu sequence and the identified Ro60 Alu motif from Fig. 2A (purple arrow represents orientation of the motif). (C) SLE IgG immunoprecipitates from IFN- α -treated K562 lysates in (A) were subjected to RT-PCR of Alu RNA using the primers in (B). Error bars represent SD of representative experiment (of 3). (D) RT-PCR of cell-free serum IgGs purified using Protein G beads from 50 μ l of SLE sera (I–V). Values represent relative change with respect to patient I IgG. Preexisting Alu RNAs contributed

negligibly to the total Alu RNAs retrieved from cell lysates in part (C) (fig. S11C). (E) Percent of whole blood RNA-seq Alu reads in control or SLE subjects. P value calculated using Student's t test. Error bars represent SD. (F) Heat map of the top 1641 Alu elements expressed in SLE or control subject blood. Unsupervised hierarchical clustering of Alus and subjects. Bars at the top represent anti-Ro titers (blue) or Interferon Signature Metric (ISM) scores (red = ISM high, pink = ISM low). (G and H) Alu score = mean expression of top SLE Alu RNAs (14). (G) Alu scores binned by ISM status; (H) Alu scores binned by anti-Ro status. (I) Distribution of gene expression changes in IFN- α -treated (6 hours) PBMCs relative to controls; expression is the average of three donors. For Alu density calculations, see (14). $P < 0.001$ (Q4 versus Q3).

data is that aberrant expression of endogenous Alu RNAs stimulates intracellular RNA sensors to induce inflammatory responses.

To test this idea, we transfected synthesized RNAs into peripheral blood mononuclear cells (PBMCs) isolated from healthy human donors. The Alu motif RNAs potently stimulated secretion of cytokines, including IFN- α , interleukin (IL)-6, and tumor necrosis factor (TNF)- α (Fig. 3H),

consistent with a previous report (16). Cytokine induction by the Alu RNAs was blocked by co-incubation of the transfected cells with chloroquine, a molecular agent that disrupts signaling of endosome-localized Toll-like receptors (TLRs) 3, 7, and 8, all of which recognize RNA (17, 18), or by cotransfection of a TLR7/9 antagonist, phosphorothioated oligo IRS954 (19, 20) (Fig. 3I). Co-incubation of the transfected PBMCs with BX795,

an inhibitor of TBK/IKK ϵ (21) that mediates signaling downstream of cytosolic RNA receptors RIG-I, MDA-5, and TLR3, had no effect on Alu-mediated cytokine production (fig. S8).

Truncated Alu motifs (see Fig. 2D) elicited submaximal cytokine responses. Y RNAs showed no ability to elicit cytokine production in this system. Alu motif sequence variants that retained Ro60 binding in vitro (fig. S4) also elicited cytokine

responses comparable to the wild type (fig. S9). We conclude that cytokine secretion in Alu motif-transfected human PBMCs is TLR7-dependent.

Next, we purified SLE serum immunoglobulin G (IgG) using Protein G beads from subjects representing a spectrum of anti-Ro autoantibodies (fig. S10) and performed immunoprecipitations from GM12878 and K562 cell lysates. By Western blot, only sera II and IV immunoprecipitated Ro60 (Fig. 4A). Sera II and IV also precipitated Y RNA and POLG RNA (fig. S10), two of the prominent peaks identified in the Ro60 iCLIP experiments. Using primers spanning the 284-base pair consensus Alu sequence (Fig. 4B), RT-PCR showed that endogenous SLE IgGs also immunoprecipitated Alu transcripts (Fig. 4C). Parallel experiments in the Ro60 null cell lines showed reduced immunoprecipitation of Alu and Y RNAs (fig. S11). We found that Alu RNAs were enriched in primary serum IgG immune complexes from anti-Ro60-positive SLE patients (Fig. 4D), which suggests that circulating anti-Ro60 autoantibodies in SLE subjects are preloaded with Alu transcripts.

Finally, we tested the levels of Alu transcripts in blood cells of SLE patients and controls (22) using RNA-seq. (99 active SLE, 18 healthy controls; fig. S12). RNA-seq reads mapping to Alu elements were found at significantly higher levels in SLE subjects than in controls ($P = 6.5 \times 10^{-6}$) (Fig. 4E). Hierarchical clustering of the most highly expressed Alu RNAs (fig. S13) segregated Interferon Signature Metric (ISM)-high SLE subjects from control and ISM-low patients (Fig. 4F). Alu scores (14) were higher in ISM-low SLE subjects than in controls and were highest in ISM-high SLE subjects (Fig. 4G). Alu scores were also significantly elevated in anti-Ro autoantibody-positive SLE subjects relative to SLE subjects lacking anti-Ro ($P = 0.01$) (Fig. 4H). A subset of ISM-high/Alu score-high SLE subjects lacked anti-Ro antibodies, indicating that there are other mechanisms for induction of IFN and Alu RNA in SLE subjects, likely including autoantibodies to other RNA binding proteins (23).

Endogenous retroelements were recently shown to activate humoral immune responses in mice (24), and aberrant accumulation of retroelements contributes to two human genetic diseases with features of SLE: Aicardi-Goutieres syndrome

and familial chilblain lupus (25). Our investigation of the Alu RNAs bound to Ro60 supports the hypothesis that retroelements contribute to human autoimmunity. Our findings suggest a model that links Ro60 autoantibody responses and Alu retroelement stimulation of intracellular RNA sensors, including TLR7, with development of SLE, Sjögren's syndrome, and congenital heart disease in the offspring of anti-Ro60 mothers (4) (see fig. S14). We speculate that IFN-stimulated modifications to Alu RNA, such as N6-methyladenosine (m6A), may mediate this interaction (fig. S14B). These findings also provide new insights into the lupus-like disorder described in Ro60 knockout mice (26), suggesting that autoimmunity in this model may be mediated by dysregulation of murine retroelements.

Finally, this work may help to explain the maintenance of Alu sequences in the genome over the course of primate evolution. There are more than 1 million copies of the Alu retroelement in the human genome, and it has been postulated that the retention of Alu sequences in gene-rich regions and their transcription in response to stress might provide an evolutionary advantage (27). When we binned all coding genes in quartiles from high to low density of the Alu motif and plotted gene expression changes upon IFN- α treatment, we observed that genes with higher densities of the Alu motif showed increased IFN-inducible gene expression ($P < 0.001$; Fig. 4I and fig. S14A). These data support a model where the transcription of Alu-containing genes upon pathogen infection up-regulates endogenous Alu RNA "adjuvants," which serve to amplify immune responses via stimulation of intracellular RNA sensors, possibly by temporarily overwhelming the ability of endogenous Ro60 to target these RNAs for destruction. Thus, Alu sequences may have persisted in the genome by virtue of their beneficial effects for defense against infectious agents, while at the same time predisposing to anti-Ro60 autoantibody production in the setting of systemic autoimmunity.

REFERENCES AND NOTES

- G. Clark, M. Reichlin, T. B. Tomasi Jr., *J. Immunol.* **102**, 117–122 (1969).
- M. Alspaugh, P. Maddison, *Arthritis Rheum.* **22**, 796–798 (1979).

- L. A. Lee, *Autoimmun. Rev.* **4**, 207–213 (2005).
- R. M. Clancy et al., *J. Immunol.* **184**, 2148–2155 (2010).
- R. M. Clancy et al., *J. Clin. Invest.* **116**, 2413–2422 (2006).
- J. Schulte-Pelkum, M. Fritzler, M. Mahler, *Autoimmun. Rev.* **8**, 632–637 (2009).
- E. C. Baechler et al., *Proc. Natl. Acad. Sci. U.S.A.* **100**, 2610 (2003).
- K. A. Kirou et al., *Arthritis Rheum.* **52**, 1491 (2005).
- E. Ben-Chetrit, E. K. Chan, K. F. Sullivan, E. M. Tan, *J. Exp. Med.* **167**, 1560–1571 (1988).
- R. J. Maraia, N. Sasaki-Tozawa, C. T. Driscoll, E. D. Green, G. J. Darlington, *Nucleic Acids Res.* **22**, 3045–3052 (1994).
- A. J. Stein, G. Fuchs, C. Fu, S. L. Wolin, K. M. Reinisch, *Cell* **121**, 529–539 (2005).
- J. König et al., *Nat. Struct. Mol. Biol.* **17**, 909–915 (2010).
- I. Huppertz et al., *Methods* **65**, 274–287 (2014).
- See supplementary materials on Science Online.
- P. Deininger, *Genome Biol.* **12**, 236 (2011).
- N. M. Green, K. S. Moody, M. Debatis, A. Marshak-Rothstein, *J. Biol. Chem.* **287**, 39789–39799 (2012).
- M. Rutz et al., *Eur. J. Immunol.* **34**, 2541–2550 (2004).
- O. M. Hart, V. Athie-Morales, G. M. O'Connor, C. M. Gardiner, *J. Immunol.* **175**, 1636–1642 (2005).
- F. J. Barrat, T. Meeker, J. H. Chan, C. Guiducci, R. L. Coffman, *Eur. J. Immunol.* **37**, 3582–3586 (2007).
- C. Guiducci et al., *Nature* **465**, 937–941 (2010).
- K. Clark, L. Plater, M. Peggie, P. Cohen, *J. Biol. Chem.* **284**, 14136–14146 (2009).
- K. C. Kalunian et al., *Ann. Rheum. Dis.* 10.1136/annrheumdis-2014-206090 (2015).
- P. Migliorini, C. Baldini, V. Rocchi, S. Bombardieri, *Autoimmunity* **38**, 47–54 (2005).
- M. Zeng et al., *Science* **346**, 1486–1492 (2014).
- H. E. Volkman, D. B. Stetson, *Nat. Immunol.* **15**, 415–422 (2014).
- D. Xue et al., *Proc. Natl. Acad. Sci. U.S.A.* **100**, 7503–7508 (2003).
- E. S. Lander et al., *Nature* **409**, 860–921 (2001).

ACKNOWLEDGMENTS

We thank J. Lowe, E. Brown and V. Dixit for their critical review of the manuscript. The data presented in this manuscript are tabulated in the main paper and in the supplementary materials. A material transfer agreement is required for access to the GM12878 Ro60 KO cell lines. Sequencing data are available at NCBI GEO, accession number GSE72420. Supported by an Alfred P. Sloan research fellowship and NIH grants HG004659, NS075449, and HG007005 (G.W.Y.) and by NSF graduate research fellowship grant DGE-1144086 (G.A.P.).

SUPPLEMENTARY MATERIALS

www.sciencemag.org/content/350/6259/455/suppl/DC1
Materials and Methods
Figs. S1 to S14
Data Tables S1 and S2

16 June 2015; accepted 3 September 2015
Published online 17 September 2015
10.1126/science.aac7442

Cell Biology Feature

Issue date: December 4, 2015

Reserve ads by November 17

Ads accepted until November 30 on
a first-come, first-served basis



For recruitment in science, there's only one

Science

Looking to hire cell biologists? This feature covers the growing trends in cell biology and the skills scientists need for a career in this field, such as biophysics, imaging techniques, and translational research. Advice from government, university, and company representatives for building a career in these expanding areas will draw scientists to your ad.

What makes *Science* the best choice for recruiting?

- Read and respected by 570,400 readers around the globe
- 67% of our weekly readers are Ph.D.s
- Your ad dollars support AAAS and its programs, which strengthens the global scientific community.

Why choose this cell biology feature for your advertisement?

- Relevant ads lead off the career section with special cell biology banner
- Bonus distribution to the American Society for Cell Biology meeting, December 12–16 in San Diego, CA.

Expand your exposure. Post your print ad online to benefit from:

- Link on the job board homepage directly to cell biology jobs
- Dedicated landing page for cell biology positions
- Additional marketing driving relevant job seekers to the job board.

SCIENCECAREERS.ORG

ScienceCareers

FROM THE JOURNAL SCIENCE  AAAS

To book your ad: advertise@sciencecareers.org

The Americas
202-326-6577

Europe/RoW
+44 (0) 1223-326500

Japan
+81-3-3219-5777

China/Korea/Singapore/Taiwan
+86-186-0082-9345

1ST YEAR IN
PHOENIX



2016 **MRS**® SPRING MEETING & EXHIBIT
March 28–April 1, 2016 | **Phoenix, Arizona**

CALL FOR PAPERS

Abstract Submission Opens
September 15, 2015

Abstract Submission Deadline
October 15, 2015

CHARACTERIZATION AND MODELING OF MATERIALS

- CM1 New Frontiers in Aberration Corrected Transmission Electron Microscopy
- CM2 Quantitative Tomography for Materials Research
- CM3 Mechanics and Tribology at the Nanoscale—*In Situ* and *In Silico* Investigations
- CM4 Verification, Validation and Uncertainty Quantification in Multiscale Materials Simulation

ENERGY AND ENVIRONMENT

- EE1 Emerging Materials and Phenomena for Solar Energy Conversion
- EE2 Advancements in Solar Fuels Generation—Materials, Devices and Systems
- EE3 Materials and Devices for Full Spectrum Solar Energy Harvesting
- EE4 Electrode Materials and Electrolytes for Lithium and Sodium Ion Batteries
- EE5 Next-Generation Electrical Energy Storage Chemistries
- EE6 Research Frontiers on Liquid-Solid Interfaces in Electrochemical Energy Storage and Conversion Systems
- EE7 Mechanics of Energy Storage and Conversion—Batteries, Thermoelectrics and Fuel Cells
- EE8 Grid-Scale Energy Storage
- EE9 Hydrogen and Fuel Cell Technologies for Transportation—Materials, Systems and Infrastructure
- EE10 Recent Advances in Materials for Carbon Capture
- EE11 Caloric Materials for Renewable Energy Applications
- EE12 Radiation Damage in Materials—A Grand Multiscale Challenge
- EE13 Actinides—Fundamental Science, Applications and Technology
- EE14 Titanium Oxides—From Fundamental Understanding to Applications
- EE15 Materials for Sustainable Development—Integrated Approaches

ELECTRONICS AND PHOTONICS

- EP1 Organic Excitonic Systems and Devices
- EP2 Silicon Carbide—Substrates, Epitaxy, Devices, Circuits and Graphene
- EP3 Perovskite-Based Photovoltaics and Optoelectronic Devices
- EP4 Emerging Silicon Science and Technology
- EP5 Metal Oxide Hetero-Interfaces in Hybrid Electronic Platforms
- EP6 Integration of Heterovalent Semiconductors and Devices
- EP7 Material and Device Frontiers for Integrated Photonics
- EP8 Resonant Optics—Fundamentals and Applications
- EP9 Materials and Processes for Nonlinear Optics
- EP10 Optoelectronic Devices of Two-Dimensional (2D) Materials
- EP11 Novel Materials for End-of-Roadmap Devices in Logic, Power and Memory
- EP12 Materials Frontiers in Semiconductor Advanced Packaging
- EP13 Tailoring Superconductors—Materials and Devices from Basic Science to Applications
- EP14 Materials for Next-Generation Displays
- EP15 Diamond Power Electronic Devices

MATERIALS DESIGN

- MD1 Materials, Interfaces and Devices by Design
- MD2 Tuning Properties by Elastic Strain Engineering—from Modeling to Making and Measuring
- MD3 Functional Oxide Heterostructures by Design
- MD4 Phase-Change Materials and Applications
- MD5 Fundamentals of Organic Semiconductors—Synthesis, Morphology, Devices and Theory
- MD6 Electronic Textiles
- MD7 Advances in Lanthanide Materials for Imaging, Sensing, Optoelectronics and Recovery/Recycling
- MD8 Multiscale Behavior of Materials in Extreme Environments
- MD9 Magnetic Materials—From Fundamentals to Applications
- MD10 Micro-Assembly Technologies

NANOTECHNOLOGY

- NT1 Functional Nanostructures and Metamaterials for Solar Energy and Novel Optical Phenomena
- NT2 Oxide and Chalcogenide-Based Thin Films and Nanostructures for Electronics and Energy Applications
- NT3 Carbon Nanofluidics
- NT4 Emerging Non-Graphene 2D Materials
- NT5 Nanodiamonds—Fundamentals and Applications
- NT6 Colloidal Nanoparticles—From Synthesis to Applications
- NT7 Nanoparticle Characterization and Removal
- NT8 Silicon Nanostructures—Doping, Interface Effects and Sensing

SOFT MATERIALS AND BIOMATERIALS

- SM1 Liquid Crystalline Materials—Displays and Beyond
- SM2 Bioinspired Dynamic Materials—Synthesis, Engineering and Applications
- SM3 Soft Materials for Compliant and Bioinspired Electronics
- SM4 Engineering Biointerfaces with Nanomaterials
- SM5 Surfaces and Interfaces for Biomaterials
- SM6 Transient and Biologically-Inspired Electronics
- SM7 Future Healthcare Needs through Biomaterials, Bioengineering and the Cellular Building Block
- SM8 Bioinspired Metal Nanoparticles—Synthesis, Properties and Application
- SM9 Structure and Properties of Biological Materials and Bioinspired Designs
- SM10 Biofabrication-Based Biomaterials and Tissues

www.mrs.org/spring2016

Meeting Chairs

Christopher A. Bower X-Celeprint Ltd.
Andrew M. Minor University of California, Berkeley
Lawrence Berkeley National Laboratory
Roger Narayan UNC/NCSU Joint Department
of Biomedical Engineering
Izabela Szlufarska University of Wisconsin-Madison
Osamu Ueda Kanazawa Institute of Technology

Don't Miss These Future MRS Meetings!

2016 MRS Fall Meeting & Exhibit
November 27 – December 2, 2016
Boston, Massachusetts

2017 MRS Spring Meeting & Exhibit
April 17 – 21, 2017
Phoenix, Arizona

MRS MATERIALS RESEARCH SOCIETY®
Advancing materials. Improving the quality of life.

506 Keystone Drive • Warrendale, PA 15086-7573
Tel 724.779.3003 • Fax 724.779.8313
info@mrs.org • www.mrs.org



Eni Award 2015

Ideas for a brighter future

Eni has always promoted and encouraged avant-garde scientific research by awarding the most innovative projects and discoveries in the field of energy. The prestigious, internationally recognised Eni Award is assigned to researchers who have distinguished themselves in the field of renewable energy, environmental protection and the new frontiers of hydrocarbons. By valorising the best ideas of today we can ensure a brighter future.



AAAS Travels

TANZANIA
Wildlife & Eclipse Safari
August 23-September 3, 2016



FOR THE WHOLE FAMILY!
See the Annular Solar Eclipse, September 1, 2016!

Join us on a Wildlife & Eclipse Safari in Tanzania to see the Annular Solar Eclipse. Enjoy splendid days looking for lions, leopards, elephants, rare rhinos, hippos, spectacular birds, and other wildlife in the finest wildlife parks in East Africa! \$5,295 pp + air.

For a detailed brochure, call (800) 252-4910
All prices are per person twin share + air



BETCHART EXPEDITIONS Inc.
17050 Montebello Rd, Cupertino, CA 95014
Email: AAASInfo@betchartexpeditions.com
www.betchartexpeditions.com

QUAD Four-Axis Micromanipulator System

QUAD, the newest Sutter Instrument motorized manipulator is easy to use and has four independent axes. The X, Y, Z axes provide 25mm range of motion and Diagonal offers 30mm. The ROE controller has a digital display is compact, intuitive, fan-free, easy to use, and takes up minimal bench space.

FEATURES

- Four independent axes – 30mm travel in diagonal for coaxial pipette movement, 25mm travel in X, Y and Z
- Sub-micron resolution
- True diagonal assures coaxial movement
- Suited for *in vivo* electrophysiological recording
- Quiet mode eliminates electrical noise
- Push button control for multiple functions – Work, Home, Quiet, Pulse and Relative



SUTTER INSTRUMENT

PHONE: 415.883.0128 | FAX: 415.883.0572
EMAIL: INFO@SUTTER.COM | WWW.SUTTER.COM

Solid Phase Extraction

The Oasis PRiME HLB is a first-of-its-kind, next-generation solid phase extraction (SPE) product that provides cleaner samples in less time and with less effort for liquid chromatography (LC) and liquid chromatography-mass spectrometry (LC-MS) analyses. Oasis PRiME hydrophilic-lipophilic balance (HLB) cartridges and multiwell plates simplify and speed up extraction protocols to ensure consistent, reproducible LC and LC-MS results. Laboratories can now process samples up to 40% faster and deliver samples that are up to 70% cleaner with fewer LC-MS matrix effects than samples prepared using other extraction techniques. Oasis PRiME HLB Sorbent is available immediately worldwide. Whether doing bioanalysis, food analysis, or forensic toxicological screening by LC and LC-MS, few things are more important to getting quality analytical results than a clean sample. That's why today's scientists need three things from a sample preparation protocol: simplicity, speed, and cleaner eluates. For scientists working with samples containing proteins, fats, or lipids, Oasis PRiME HLB fulfills all three requirements and is now the gold standard for SPE.

Waters

For info: 800-252-4752
www.waters.com

FISH Probes

Cytocell Pathology FISH probes now include eight new probes. The new additions to the Cytocell range include high-quality pathology fluorescence in situ hybridization (FISH) probes for 1q25, 1p36, 19p13, 19q13, ROS1-GOPC, and RET. In addition to pathology probes, a large number of other probes are available, including hematology and hematopathology probes, as well as whole-chromosome and murine-chromosome painting probes. Importantly, Cytocell FISH probes provide bright signals for easy, accurate scoring, leading to consistent results. Not only does Cytocell offer an extensive range of high-quality FISH probes, the customer support is excellent and provides fast access to the probes.

Oxford Gene Technology

For info: +44-(0)-1865-856826
www.ogt.com



Biospecimen Handling/Transport System

The CryoPod Carrier is a liquid nitrogen (LN₂)-based system for the safe, reliable, and protected handling and transport of cryogenic biospecimens. The carrier is a breakthrough technology that enables more than 4 hours of < -150°C temperature stability for cryogenically frozen biospecimens and therapeutics, keeping them well below glass transition (T_g) temperature where biological activity may cease. The CryoPod Carrier provides a safe, portable, and trackable solution for hand-carrying temperature-sensitive, cryogenically frozen biological materials through the use of a special material that holds and minimizes LN₂ movement and prevents LN₂ from coming in contact with the samples. The instrument displays temperature, date, and time, and features audible and visual alarms as well as logging capabilities. The carrier can integrate with an automated filling station, ensuring hands-free, safer handling, and replenishing the LN₂ charge in less than 15 minutes. At 20 pounds, it is lightweight and compact.

BioCision

For info: 888-478-2221
www.biocision.com

Western Blotting System

Based on proprietary sequential lateral flow (SLF), the latest iBind Flex Western System is designed to enable a more versatile walk-away solution for the immunodetection step in a Western blotting workflow. Researchers now have the ability to adapt the iBind Flex Western Device to a variety of blot formats and sample throughput. Compatible with downstream chemiluminescent, colorimetric, or fluorescent detection protocols and optimized for higher sensitivity and reproducibility, the iBind Flex offers the potential for a significant reduction in primary antibody required when compared to manual blot processing. Experimental results can be achieved without the need for power, pumps, or vacuums through the use of SLF technology, which is designed to automate the blocking, primary, and secondary antibody binding and washing steps for immunodetection of proteins transferred to a nitrocellulose or polyvinylidene difluoride (PVDF) membrane. The sequential and uniform flow of solutions across a glass fiber matrix ensures a consistent antigen-antibody interaction to deliver robust protein detection.

Thermo Fisher Scientific

For info: 800-955-6288
www.thermofisher.com

Color Camera

The Leica DMC4500 Allrounder camera is an ideal tool for advanced analysis and documentation. The camera is fast, with a 5-megapixel coupled-charge device (CCD) sensor, providing a live image speed of up to 18 frames per second. Its USB 3.0 interface provides fast interaction between the camera and computer, making it compatible with desktop computers and laptops alike. The DMC4500 is an ideal choice for most analysis and documentation tasks, due

to its exceptional picture quality and ease of use. Although some cameras are dedicated to specific tasks, this versatile camera can handle many applications in industry as well as in life sciences, with the exception of fluorescence-only applications. The DMC4500's USB 3.0 interface is an upgrade from the formerly common firewire interface, and the CCD sensor provides true-color rendering in the high-resolution images it produces.

Leica Microsystems

For info: 800-248-0123
www.leica-microsystems.com

Electronically submit your new product description or product literature information! Go to www.sciencemag.org/products/newproducts.dtl for more information.

Newly offered instrumentation, apparatus, and laboratory materials of interest to researchers in all disciplines in academic, industrial, and governmental organizations are featured in this space. Emphasis is given to purpose, chief characteristics, and availability of products and materials. Endorsement by *Science* or AAAS of any products or materials mentioned is not implied. Additional information may be obtained from the manufacturer or supplier.

JOIN AAAS

Get instant access to *Science*. Support all of the sciences.



The American Association for the Advancement of Science (AAAS) is a non-profit community that is open to everyone, from Nobel laureates to high school students. Ours is a global membership of over 120,000 people who believe in the power of science to make the world a better place.

From the moment you join, you get immediate access to everything that AAAS's award-winning journal *Science* has to offer, including:

- 51 weeks of home delivery of *Science*;
- Instant online retrieval of every *Science* article ever published, from today, dating back to 1880;
- Anytime, anywhere access via the *Science* mobile site and apps for Android, iPad, and iPhone devices;
- Members-only newsletters; and more.

As a member, you are also making a critical contribution to AAAS's efforts to provide a public voice for all of science. With public skepticism about science increasing, and public funding for research more uncertain than ever, this work has never been more important.

AAAS is hard at work promoting science in government offices, in schools, and in the public commons all around the world—with programs like AAAS Senior Scientists and Engineers, which brings volunteer scientists into public school classrooms, or our sweeping petition drives calling for the preservation of federal R&D funding.

Visit promo.aaas.org/joinaaas and join today. Together we can make a difference.

Science
AAAS

A man in a black tuxedo with a red bow tie is conducting with a white baton. His eyes are closed, and he has a serene expression. Surrounding him are various 3D molecular models: purple and blue structures on the left, red and orange structures on the right, and several colorful (green, blue, pink, orange) ribbon diagrams of protein structures floating around his chest and arms. The background is dark with some glowing blue light effects.

invitrogen

One conductor, a symphony of enzymes

Finally, a complete, one-buffer system—for beautifully simple cloning

Introducing the Invitrogen™ Anza™ Restriction Enzyme Cloning System:

- One buffer for all restriction enzymes
- One digestion protocol for all DNA types
- Complete digestion in 15 minutes
- Overnight digestion without star activity

Choose simplicity at thermofisher.com/Anza

ThermoFisher
SCIENTIFIC

AAAS 2016
ANNUAL MEETING

WASHINGTON, DC
FEBRUARY 11–15

Global Science Engagement

The 2016 meeting focuses on how the scientific enterprise can meet global challenges in need of innovation and international collaboration.

aaas.org/meetings



See Inside for Details:

President's Address / Registration Rates

Plenary Lectures / Topical Lectures

Seminars / Symposia Tracks

AAAS 2016 ANNUAL MEETING

Join Us in Washington, DC

Learn about science and technology addressing current and future global challenges.

- Seminars on food security; personalized medicine; preserving artifacts; and communicating science
- 130+ symposia in 14 disciplinary tracks covering the latest research advances
- Network with colleagues and attend career development workshops

Connect with us



@AAASmeetings #AAASmtg



facebook.com/AAAS.Science

www.aaas.org/meetings

Reporters: The EurekAlert! website hosts the AAAS Annual Meeting Newsroom. For details please visit eurekalert.org/aaasnewsroom

Dear Colleagues:

On behalf of the AAAS Board of Directors, it is my honor to invite you to join us in Washington, DC for the 2016 AAAS Annual Meeting, February 11–15. The AAAS Annual Meeting is the most widely recognized global science gathering with cutting-edge scientific sessions, valuable networking opportunities, and broad international media coverage.

The 2016 meeting theme—*Global Science Engagement*—focuses on how the scientific enterprise can meet global challenges in need of innovation and international collaboration.

We hope you will join us in Washington, DC.

Geraldine Richmond, Ph.D.
AAAS President and Program Chair
Presidential Chair and Professor of Chemistry
University of Oregon

PRESIDENT'S ADDRESS



Geraldine Richmond

AAAS President and Program Chair
Presidential Chair in Science and Professor
of Chemistry
University of Oregon

Thursday, February 11
6:00 p.m. – 7:00 p.m.

Dr. Geri Richmond's research using laser spectroscopy and computational methods focuses on understanding the chemistry and physics that occur at complex interfaces, with relevance to important problems in energy production, environmental remediation, and atmospheric chemistry. She is a member of the National Academy of Sciences and American Academy of Arts and Sciences and is a fellow of the American Chemical Society (ACS), American Physical Society (APS), American Association for the Advancement of Science (AAAS), and the Association for Women in Science. Richmond

has served in leadership roles on many international, national, and state governing and advisory boards. She is a member of the National Science Board and is the U.S. Science Envoy to the Lower Mekong River Countries of Vietnam, Laos, Cambodia, Burma, and Thailand. She is founding and current director of COACH, an organization that has helped career advancement for thousands of scientists and engineers in the U.S., Asia, Africa, and Latin America. Awards for her scientific accomplishments include the ACS Olin-Garvan Medal, the Spiers Medal of the Royal Society of Chemistry, the ACS Joel H. Hildebrand Award in Theoretical and Experimental Studies of Liquids, and the APS Davisson-Germer Prize. Awards for outreach and science capacity-building efforts include the Presidential Award for Excellence in Science and Engineering Mentoring, the ACS Award for Encouraging Women in the Chemical Sciences, the Council on Chemical Research Diversity Award, and the ACS Charles L. Parsons Award.

www.aaas.org/meetings

GLOBAL SCIENCE ENGAGEMENT

PLENARY LECTURES

All plenary lectures will be held in the Washington Marriott Wardman Park.



Christopher Dye
Director of Strategy,
Office of the
Director General,
World Health
Organization

***A Problem Shared:
Teaming Up to Fight
Epidemic Diseases***

Friday, February 12
5:00 p.m. – 6:00 p.m.



Jennifer Doudna
Professor of Chemistry
and Molecular and Cell
Biology,
University of California,
Berkeley

***The CRISPR-Cas9 Genome
Editing Revolution***

Saturday, February 13
5:00 p.m. – 6:00 p.m.



Jad Abumrad
Host and Producer,
Radiolab

***Lecture title to be
announced***

Sunday, February 14
5:00 p.m. – 6:00 p.m.

TOPICAL LECTURES

Friday, February 12

Thaís Storch Bergmann

Professor of Physics and Astronomy, Federal University of
Rio Grande do Sul, Brazil
Supermassive Black Holes and the Evolution of the Universe

May-Britt Moser

Professor of Neuroscience, Norwegian University of Science
and Technology
Brain, Space, and Memory

Gary Machlis

Science Advisor to the Director, U.S. National Park Service
The Near-Horizon Future of Science in National Parks

Saturday, February 13

Robin Murphy

Professor of Computer Science and Engineering,
Texas A&M University
Disaster Management: Robots, Informatics, and People

Jennifer Richeson

John D. and Catherine T. MacArthur Professor of Psychology,
Northwestern University
*Coalition or Darogation? Psychological Perspectives on
Race Relations in the 21st Century*

David Spiegelhalter

Professor for the Public Understanding of Risk,
Cambridge University
Metaphors for Communicating Chronic Risks

Sunday, February 14

GEORGE SARTON MEMORIAL LECTURE IN THE HISTORY AND
PHILOSOPHY OF SCIENCE

David Kaiser

Germeshausen Professor of the History of Science,
Massachusetts Institute of Technology
Einstein's Legacy: Studying Gravity in War and Peace

JOHN P. MCGOVERN LECTURE IN THE BEHAVIORAL SCIENCES

Elizabeth Spelke

Professor of Psychology, Harvard University
Lecture title to be announced

Samuel Wasser

Endowed Chair and Director, Center for Conservation
Biology, University of Washington
Lecture title to be announced

SEMINARS

Thursday, February 11

Communicating Science

Scientific and technological issues may trigger societal conflict when they intersect with personal or political views. Today's scientists and engineers are increasingly obligated to engage with public audiences about emerging issues in science and technology. This seminar builds connections between scientists, science communication and public engagement professionals who can support their efforts, and social scientists whose research can inform best practices. Participants will gain actionable knowledge and join a growing community focused on public engagement with science. The panels focus on policy engagement, communicating emerging science-society topics such as synthetic biology, and using visuals for science communication.

Organized by: AAAS Center for Public Engagement with Science and Technology

Scientists Engaging in Policy

MODERATOR: Erin Heath, AAAS Office of Government Relations, Washington, DC

SPEAKERS: Carrie Wolinetz, National Institutes of Health, Bethesda, MD

Arthur Lupia, University of Michigan, Ann Arbor
Jim Gates, University of Maryland, College Park

Communicating Synthetic Biology

MODERATOR: Andrew Maynard, Arizona State University, Tempe

SPEAKERS: Gretchen Gano, University of California, Berkeley
Kristala Prather, Massachusetts Institute of Technology, Cambridge

Natalie Kuldell, BioBuilder Educational Foundation, Cambridge, MA

Dietram Scheufele, University of Wisconsin, Madison

Using Visuals for Science Communication

MODERATOR: Lena Groeger, ProPublica, New York City

SPEAKERS: Matt Hansen, University of Maryland, College Park

Alberto Cuadra, AAAS/Science, Washington, DC

Paul Martin Lester, California State University, Fullerton

Friday, February 12

Food Security

This seminar will explore food security in light of climate change and other disruptive events, changes in food production systems, and advances in technology and data-sharing. The first session focuses on managing the impacts of food shocks, coincidental extreme events that affect the stability of food production or markets, and climate projections for how weather hazards may contribute to food shocks. The next session examines approaches to sustainable intensification of agriculture, including agricultural censuses, farming practices, and the role of small farms. The final session addresses sustainable intensification specifically through use of open datasets and geospatial data to improve farming productivity and reduce environmental impacts and poverty.

Food Shocks: The Impact of Simultaneous Extreme Events on Global Food Systems

Organized by: Matt Goode and Riaz Bhunnoo, U.K. Biotechnology and Biological Sciences Research Council, Swindon

SPEAKERS: Kirsty Lewis, Met Office Hadley Center for Climate Science and Services, Exeter, United Kingdom

Joshua W. Elliott, University of Chicago Computation Institute, IL

Tim Benton, Global Food Security Program, Swindon, United Kingdom

Multiple Paths to Ensuring Global Food Security

Organized by: Linda Young, U.S. Department of Agriculture (USDA), Washington, DC

SPEAKERS: Pietro Gennari, Food and Agriculture Organization of the United Nations, Rome, Italy

Catherine Woteki, USDA, Washington, DC

Seth Cook, International Institute for Environment and Development, London, United Kingdom

DISCUSSANT: Kenneth G. Cassman, University of Nebraska, Lincoln

Using Data to Enhance Food Productivity in Subsistence Farming

Organized by: Cindy Cox and Jawoo Koo, International Food Policy Research Institute (IFPRI), Washington, DC

SPEAKERS: Stanley Wood, Bill and Melinda Gates Foundation, Seattle, WA

Paul West, University of Minnesota, St. Paul

Ousmane Badiane, IFPRI, Washington, DC

Saturday, February 13

Precision and Personalized Medicine

Precision medicine and personalized medicine offer an opportunity to transform health care by customizing treatment to an individual's genetics. The United States and United Kingdom have recently made investments into initiatives that seek to accelerate progress in this research. This seminar discusses these efforts, and others that use large datasets from insurance companies to understand response patterns, engage patient organizations in research, and use genomic medicine for patients with rare inherited diseases, cancer, or infection. The seminar also addresses emerging questions about privacy and the public good, including computational methods and algorithms for analyzing big data.

Precision Medicine's Global Reach: Solutions from the Big Data Revolution

Organized by: Kristen T. Honey, AAAS Science and Technology Policy Fellow, U.S. Department of Energy, Washington, DC

SPEAKERS: Dhanurjay "DJ" Patil, White House Office of Science and Technology Policy, Washington, DC
John N. Aucott, Johns Hopkins University School of Medicine, Baltimore, MD
Lorraine Johnson, LymeDisease.org, Los Angeles, CA

Precision Medicine and Bioethics

Organized by: Lindsay R. Chura, British Embassy, Washington, DC

SPEAKERS: Hugh Whittall, Nutfield Council on Bioethics, London, United Kingdom
Richard Barker, Innovate UK, Swindon
Willem Ouwehand, University of Cambridge, United Kingdom
DISCUSSANT: Kathy Hudson, National Institutes of Health, Bethesda, MD

Personalized Medicine: Big Data and Machine Learning

Organized by: Gabriela Chira, European Commission

SPEAKERS: Karsten Borgwardt, ETH Zurich, Switzerland
Gunnar Rätsch, Memorial Sloan-Kettering Cancer Center, New York City
Florence Demenais, French Institute of Health and Medical Research (INSERM), Paris

Sunday, February 14

Protecting Cultural Heritage Sites and Artifacts

From the destruction of ancient sites in areas of conflict to discrediting fake artifacts, this seminar covers a range of preservation needs, techniques, and practices. The seminar highlights recent work in Syria, Mali, and Iraq using satellite images. The second session demonstrates how forensic science and the humanities can work together to reveal the true history of objects. The third session discusses the application of technologies – such as 3-D printing, digital scanning, and a novel sensing system that captures spatial data – for preserving archaeological information, or for creating new products. Projects in Cambodia, Guatemala, Mexico, Europe, and the U.S. are presented.

Cultural Heritage Destruction: Evidence and Emergency Responses

Organized by: Susan Wolfenbarger, AAAS Scientific Responsibility, Human Rights, and Law Program, Washington, DC; Katharyn Hanson, University of Pennsylvania Museum's Cultural Heritage Center, Philadelphia

SPEAKERS: Susan Wolfenbarger, AAAS, Washington, DC
Corine Wegener, Smithsonian Institution, Washington, DC
Morag Kersel, Depaul University, Chicago, IL

Faked or Changed? Using Science To Reconstruct Object Biography

Organized by: Marc Walton and Katherine Faber, Northwestern University, Evanston, IL

SPEAKERS: Luigi Modini, U.S. Federal Bureau of Investigation, Chicago, IL
Marc Walton, Northwestern University, Evanston, IL
Joel Baden, Yale University, New Haven, CT; Candida Moss, University of Notre Dame, IN
DISCUSSANT: Francesca Casadio, Art Institute of Chicago, IL

Preserving World Heritage and Transforming Global Manufacturing with 3-D Scanning

Organized by: Björn Johansson, Chalmers University of Technology, Gothenburg, Sweden; Ram D. Sriram, National Institute of Standards and Technology, Gaithersburg, MD; Ramesh Jain, University of California, Irvine

SPEAKERS: Jan-Eric Sundgren, Volvo Group, Gothenburg, Sweden
Katsushi Ikeuchi, University of Tokyo, Japan
Lori Collins, University of South Florida, Tampa
DISCUSSANT: ADAM METALLO, SMITHSONIAN INSTITUTION, LANDOVER, MD

SYMPOSIA TRACKS

Organizers are listed under symposia titles.

ANTHROPOLOGY, CULTURE, AND LANGUAGE

Global Variation in Health and Aging: Cultural Contexts and Quality of Life

Lynnette Leidy Sievert, University of Massachusetts, Amherst

I Can't Hear Myself Think! Noise and the Developing Brain from Infancy to Adulthood

Nan Bernstein Ratner, University of Maryland, College Park

Bilingualism Matters

Karen Emmorey, San Diego State University, CA

Evolutionary Biology Impacts on Medicine and Public Health

Cynthia Beall, Case Western Reserve University, Cleveland, OH; Randolph Nesse, Arizona State University, Tempe

Rethinking Child Language Disorders: Insights from Sign Language Research

Richard P. Meier, University of Texas, Austin

The Science of Human Evolution in Africa

Leslea Hlusko, University of California, Berkeley

Understanding Speakers of 7,000 Languages

Robert Munro, Idibon, San Francisco, CA

BEHAVIORAL AND SOCIAL SCIENCES

Aligning Publishing Incentives with Research Transparency and Integrity

Bobbie Spellman, University of Virginia, Charlottesville; Arthur Lupia, University of Michigan, Ann Arbor

Going Public: How Science Communicators Can Break Through the Noise

Arthur Lupia, University of Michigan, Ann Arbor; Kathleen Hall Jamieson, University of Pennsylvania, Philadelphia

How the Body Shapes the Mind

Susan Goldin-Meadow and Daniel Casasanto, University of Chicago, IL

Interpersonal Violence and Conflict Escalation: Situational Dynamics

William Alex Pridemore, State University of New York, Albany

Is the Risk of Alzheimer's and Dementia Declining? Evidence From Around the World

Kenneth Langa, University of Michigan, Ann Arbor

Trying on Identities: Science Engagement of Adolescents

Julia McQuillan, University of Nebraska, Lincoln

U.S. and Global Public Opinion on Science and Technology Issues

John C. Besley, Michigan State University, East Lansing

Virtues of U.S. Scientists Guiding Scientific Practice

Robert T. Pennock, Michigan State University, East Lansing; Jon D. Miller, University of Michigan, Ann Arbor

BIOLOGY AND NEUROSCIENCE

At a Loss for Words, or Losing Your Mind? New Views on Language Problems in Aging

Margaret Rogers, American Speech-Language-Hearing Association, Rockville, MD; Nan Bernstein Ratner, University of Maryland, College Park

Artificial Intelligence: Imagining the Future

Maria Spiropulu, California Institute of Technology, Pasadena

Discovery and Development of the CRISPR-Cas Genome Editing Technology

Hong Li, Florida State University, Tallahassee

Human Gene Editing: Ethical, Legal, and Policy Implications

Anne-Marie Mazza and Kevin Finneran, National Academies of Sciences, Engineering, and Medicine, Washington, DC

From Toxins to Culture: How Environment Shapes the Infant Brain

Marie-Francoise Chesselet, University of California, Los Angeles

Neuroplasticity: Insights in Neuronal Connectivity Illuminate Brain Function

Thomas Franke, New York University, New York City; Eric Nestler, Mount Sinai School of Medicine, New York City

Neuroscience Clues to the Chemistry of Addictions and Mood Disorders

Mary Baker, European Brain Council, Brussels, Belgium; Aidan Gilligan, SciCom—Making Sense of Science, Brussels, Belgium

Oral Cancer: Epidemiology, Mechanisms, and Early Detection

Mina Mina, University of Connecticut Health Center, Farmington

COMMUNICATION AND PUBLIC PROGRAMS

Opinion Writing: Strategies for Persuasive Public Communication

Laura Helmuth, Slate magazine, Washington, DC; Bethany Brookshire, Science News, Washington, DC

A Global Village of Public Engagement in Science

Satoru Ohtake, Japan Science and Technology Agency, Tokyo; Seunghwan Kim, Korea Foundation for the Advancement of Science and Creativity, Seoul, South Korea; Tateo Arimoto, National Graduate School for Policy Studies, Tokyo, Japan

Bridging the Science-Society Gap in Africa

Thandi Mgwebi, National Research Foundation, Pretoria, South Africa

GeoJournalism: Telling the Story of Science with Data, Maps, and Sensors

James Fahn, Internews' Earth Journalism Network, Albany, CA

Maker Culture and Creativity: The Global Maker Movement

Seunghwan Kim, Korea Foundation for the Advancement of Science and Creativity, Seoul, South Korea

Science in Unexpected Places: Innovative Ways to Engage the Public

Jennifer Cutraro, WGBH Educational Foundation, Boston, MA

Using Humor to Address Serious Topics

Kasha Patel, NASA Goddard Space Flight Center, Washington, DC

What Scientists Think About Public Engagement: New Data, Insights, and Directions

Anthony Dudo, University of Texas, Austin

EDUCATION

Meeting Global Climate Goals with Energy Education

Matthew Garcia, AAAS Science and Technology Policy Fellow, U.S. Department of Energy, Washington, DC; David Blockstein, Council of Energy Research and Education Leaders, Washington, DC

Advancing Science Through Afterschool STEM: Making the Case with Evidence

Anita Krishnamurthi, Afterschool Alliance, Washington, DC

After the Dover Intelligent Design Trial: Law, Politics, and Education

Ida Chow, Society for Developmental Biology, Bethesda, MD; Jay B. Labov, National Academy of Sciences, Washington, DC; Eugenie C. Scott, National Center for Science Education, Berkeley, CA

Building a Transdisciplinary Science Workforce to Meet Contemporary Health Challenges

Sybil Pettit, Health and Environmental Sciences Initiative, Washington, DC

Enabling Effective Climate Literacy with Collective Impact

Tamara Shapiro Ledley, TERC, Cambridge, MA; Frank Niepold, National Oceanic and Atmospheric Administration, Silver Spring, MD; Lin Chambers, National Aeronautics and Space Administration (NASA), Hampton, VA

Incorporating Responsible Science into Academic Curricula

Lida Anestidou, National Academies of Sciences, Engineering, and Medicine, Washington, DC

Mathematics and Music

David Wright, Washington University, St. Louis, MO

Team Science and Convergence: Implications for Education

Katherine Bowman, Margaret Hilton, and Elizabeth O'Hare, National Research Council, Washington, DC

ENGINEERING, INDUSTRY, AND TECHNOLOGY

X-ray Imaging Innovations for Biomedicine

Ge Wang, Rensselaer Polytechnic Institute, Troy, NY; Mannudeep Kalra, Massachusetts General Hospital, Boston

Accelerating Energy-Climate Innovation

Daniel Sarewitz, Arizona State University, Tempe; John Alic, Consultant, Avon, NC

Cleaner Energy Solutions: What Can 21st Century Large-Scale Physics Deliver?

Silvana C. Westbury and Isabelle Boscaro-Clarke, Diamond Light Source, Didcot, United Kingdom

Does Hydraulic Fracturing Allow Gas to Reach Drinking Water?

David Marker, WESTAT, Rockville, MD

Global Science-Driven Entrepreneurship: Determined Pursuit of Innovative Success

Anice Anderson, Private Engineering Consulting, Carmel, IN; Katharine Blodgett Gebbie, National Institute of Standards and Technology, Gaithersburg, MD; Charles W. Clark, Joint Quantum Institute, Gaithersburg, MD

AAAS 2016 ANNUAL MEETING GLOBAL SCIENCE ENGAGEMENT

Advance Registration Rates until January 19

	AAAS Member Rates for members in good standing	New Member Reduced rates if you join AAAS today	Non-Member Rates for all other attendees
Professional	\$295	\$380	\$399
Postdoc	\$235	\$320	\$335
K-12 Teacher	\$235	\$320	\$335
Emeritus	\$235	\$320	\$335
Student	\$60	\$70	\$90

One-day rates are also available: www.aaas.org/AM16reg

Promoting Global Science, Technology, and Innovation Entrepreneurship: Best Practices

Sarah Staton and Sara Klucking, U.S. Department of State, Washington, DC

Rethinking Sustainable Housing in Sub-Saharan Africa

Esther Obonyo and Abraham Goldman, University of Florida, Gainesville

Smart Materials for Sustainable Infrastructure: Self-Healing Concrete and Asphalt

Stefanie Reiffert and Patrick Regan, Technical University of Munich, Germany

The Global Energy Landscape: 2050 and Beyond

Subhashree Mishra, David Rench McCauley, and Abigail Watrous, U.S. Department of Energy, Washington, DC

ENVIRONMENT, ECOLOGY, AND CLIMATE CHANGE

Sea Level Rise: Human and Scientific Challenges

Benjamin Hamlington, Old Dominion University, Norfolk, VA; Eric Lindstrom, NASA Earth Sciences Division, Washington DC; Michelle Covi, Mitigation and Adaptation Research Institute and Virginia Sea Grant, Norfolk, VA

The National Park System: A National Scientific Asset

Gary Machlis, U.S. Department of the Interior, National Park Service, Washington, DC; Megan F. McKenna, National Park Service, Fort Collins, CO

Advancing Knowledge of Global Amphibian Decline with International Collaboration

Karen Lips, University of Maryland, College Park; Patricia Burrowes, University of Puerto Rico, San Juan; Kelly Zamudio, Cornell University, Ithaca, NY

Air Pollution, Climate Change, and Policy in Asia

Zhanqing Li and Maureen Cribb, University of Maryland, College Park

Biodiversity, Scientists, and Religious Communities: Conservation Through Collaboration

Se Y. Kim and Jennifer Wiseman, AAAS Dialogue on Science, Ethics, and Religion, Washington, DC

Creating Resilient Cities in the Face of Global Sea Level Rise

Rita Teutonico and Tiffany Troxler, Florida International University, Miami

Dynamic Relationship Between Mountain Glaciers and Climate Change

Jeffrey Kargel, University of Arizona, Tucson

Empowering Environmental Research, Education, and Outreach in Congo Basin Forests

Mary Katherine Gonder, Drexel University, Philadelphia, PA; Thomas Smith, University of California, Los Angeles

Finding the Balance: Collaboration on Social-Ecological Tipping Points

Carrie Kappel, University of California, Santa Barbara

Global Soil Biodiversity: A Common Ground for Sustainability

Tandra Fraser, Colorado State University, Fort Collins

Global Urban Ecology Research: Addressing Novelty, Equity, and Uncertainty

Jessica Graybill, Colgate University, Hamilton, NY; Vivek Shandas, Portland State University, OR

Living with Earthquakes: Causes, Early Warning, and Damage Mitigation

David Kornhauser, Kyoto University, Japan

Sea Level Rise in a Warming World: Past is Prologue

Maureen Raymo, Columbia University Lamont-Doherty Earth Observatory, Palisades, NY

Tsunamis: An International Hazard

Costas Synolakis, University of Southern California, Los Angeles; Harry Yeh, Oregon State University, Corvallis; Philip Liu, Cornell University, Ithaca, NY

Unmanned Autonomous Systems for Climate and Environmental Research

Sally McFarlane, U.S. Department of Energy, Washington, DC

FOOD AND WATER RESOURCES

Climate Change and Agriculture: Revisiting the Evidence and Potential Solutions

Caron Gala, Council on Food, Agricultural, and Resource Economics, Washington, DC

Food Systems: Building Resilience and Partnering across Sectors

Rahel Byland, ETH Zurich, Switzerland; Ursula Oesterle, Mixing Bowl, Palo Alto, CA

Food, Water, Energy, and the American Indian Farmer

Maureen McCarthy, University of Nevada, Reno

Global Science to Protect Our Global Farm

Matt Goode, U.K. Biotechnology and Biological Sciences Research Council, Swindon; Jennifer Martin, National Institute of Food and Agriculture, Washington, DC

Pathogens Without Borders

John Bakum, Cornell University, Ithaca, NY

Unlocking Plant Genetic Diversity for Food and Nutritional Security

Patrick Byrne, Colorado State University, Fort Collins; Ann Marie Thro, National Institute of Food and Agriculture, Washington, DC; Wayne Smith, Texas A&M University, College Station

GLOBAL PERSPECTIVES AND ISSUES

Arctic Research as a Model for Responsible International Collaboration

David Moorman, Canada Foundation for Innovation, Ottawa

Engaging LGBT Scientists in the U.S. and Abroad

Arthur G. Fitzmaurice and Gregory Mack, National Science Foundation, Arlington, VA

Library of Alexandria and Global Research Engagement

Ronald LaPorte, University of Pittsburgh, PA; Faina Linkov, Magee Womens Research Institute, Pittsburgh, PA

Limiting our Planet's Nitrogen Footprint

James Galloway, University of Virginia, Charlottesville

Open Science: Global Perspectives and Prospects

Rene von Schomberg, European Commission, Brussels, Belgium

SESAME: A Scientific Source of Light in the Middle East

James Gillies, European Organization for Nuclear Research (CERN), Geneva, Switzerland; Antonella Varaschin, Infinera Corporation, Rome, Italy

Smart Cities: Utopia for Data Collection?

Eswaran Subrahmanian, Carnegie Mellon University, Pittsburgh, PA; Maryann Feldman, National Science Foundation, Arlington, VA; Ram D. Sriram, National Institute of Standards and Technology, Gaithersburg, MD

Statecraft and Scalpel: Regional and Global Health Diplomacy

Daan Du Toit, South Africa Department of Science and Technology, Pretoria; Satoru Ohtake, Japan Science and Technology Agency, Tokyo

Statisticians Building Global Science Capacity and Infrastructure

Rochelle Tractenberg, Georgetown University, Washington, DC; Eric Vance, Virginia Polytechnic Institute and State University, Blacksburg

Toward a Sustainable Future in the Middle East: Building Scientific Collaborations

Elizabeth Ann Nalley, Cameron University, Lawton, OK; Zafra Margolin Lerman, Malta Conferences Foundation, Evanston, IL

INFORMATION TECHNOLOGY AND COMPUTING

New Science Roadmaps for Global Research

Ben Shneiderman, University of Maryland, College Park

Citizen Science and Information Technology: Engaging People for a Better Planet

Daniel Rubenstein, Princeton University, NJ; Carla P. Gomes, Cornell University, Ithaca, NY; Barbara Illman, U.S. Forest Service, Madison, WI

Emergence of Intelligent Machines: Challenges and Opportunities

Bart Selman, Cornell University, Ithaca, NY; Francesca Rossi, University of Padova, Italy

Massively-Collaborative Global Research in Mathematics and Science

Edward Aboufadel, Grand Valley State University, Allendale, MI

Public-Private Partnerships to Accelerate Innovation in Intelligence Analysis

Alyson Wilson, North Carolina State University, Raleigh

The Confluence of Computing and Society: Emerging Themes in Socio-Technical Systems

Gregory D. Hager, Johns Hopkins University, Baltimore, MD; Ann Drobni, Computing Community Consortium, Washington, DC

INTERNATIONAL AND SUSTAINABLE DEVELOPMENT

Accelerating Africa's Scientific Transformation

Michela Greco, CRDF Global, Arlington, VA

Enhancing African STEM Research and Capacity with International Collaboration

Molly Haragan and Emilio Bunge, Development Finance International Inc., Bethesda, MD

Mathematics Making a Difference in Africa

Evans Harrell, Georgia Institute of Technology, Atlanta

Sustainable Development Goals: Paths Forward

Margaret Collins, International Institute for Applied Systems Analysis, Laxenburg, Austria

Using Biodiversity Science for Conservation and Development

Molly Fannon and John Kress, Smithsonian Institution, Washington, DC

Win-Win or Lose-Lose: Poverty, Human Health, and Environmental Quality

Christopher B. Barrett, Cornell University, Ithaca, NY

MEDICAL SCIENCES AND PUBLIC HEALTH

Advancing Assistive Devices Through Global Olympic-Style Competition

Rahel Byland, ETH Zurich, Switzerland

Fighting Cancer and Chronic Infections with T Cell Therapy: Promise and Progress

Patrick Regan and Ulrich Marsch, Technical University of Munich, Germany

Improving Cancer Patient Care: Trade-offs between Efficacy and Toxicity

Gabriela Chira, European Commission, Brussels, Belgium

Lessons from the Ebola Outbreak: Designing Vaccine Trials for Emerging Diseases

M. Elizabeth Halloran, University of Washington, Seattle

Measles Vaccination: Global Challenges

M. Elizabeth Halloran, University of Washington, Seattle

New and Emerging Tobacco Products: Biomarkers of Exposure and Injury

Daniel Conklin, University of Louisville, KY; Judith Zelikoff, New York University, Tuxedo

Public Health Epigenomics: Integrating Environment and Human Health

Shaun McCullough, U.S. Environmental Protection Agency, Research Triangle Park, NC; Dana Dolinoy, University of Michigan, Ann Arbor

The Burden of Disease From Air Pollution

Aaron Cohen, Health Effects Institute, Boston, MA; Michael Brauer, University of British Columbia, Vancouver, Canada

The Impact of Convergence on Innovation Across Sectoral and Global Boundaries

Katherine Bowman, National Research Council, Washington, DC; Amanda Arnold, Square Set Strategies LLC, Washington, DC; Anice Anderson, Private Engineering Consulting, Carmel, IN

PHYSICS AND ASTRONOMY

Astroparticle Physics: Unraveling Mysteries of the Universe

Tajinder Panesar, Institute of Physics, London, United Kingdom

Ghost Hunters: The Search for New Types of Neutrinos

Katie Yurkewicz, Fermi National Accelerator Laboratory, Batavia, IL; Vincenzo Napolano, National Institute for Nuclear Physics, Rome, Italy

James Webb Space Telescope: Building a Global Observatory

Jason Kalirai, Margaret Meixner, and Joel Green, Space Telescope Science Institute, Baltimore, MD

Mapping the Northern and Southern Skies: Diversity and Research Capacity for Global Astronomy

Keivan Stassun, Vanderbilt University, Nashville, TN

Megascience Global Projects Seeded in Europe, Asia, and the U.S.

Maria Spiropulu, California Institute of Technology, Pasadena; David Gross, University of California, Santa Barbara

Planet Formation Seen With Radio Eyes

Mark T. Adams, National Radio Astronomy Observatory, Charlottesville, VA

Radio Astronomy on Three Continents: First Stars and the Epoch of Reionization

Bruce G. Elmegreen, IBM T.J. Watson Research Center, Yorktown Heights, NY

**Space Weather: A Low Frequency,
High Impact Space Age Hazard**

*Michael Wiltberger, National Center for
Atmospheric Research, Boulder, CO*

**Where Did Most of the Universe Go?
Searching for Dark Matter**

*Terry O'Connor, U.K. Science and Technology
Facilities Council, Swindon; Manuel Gnida,
SLAC National Accelerator Laboratory,
Menlo Park, CA*

PUBLIC POLICY

**A War on Science? Vaccines, Climate
Change, GMOs, and the Role of Science**

*Mark A. Largent, Michigan State University,
East Lansing; Christian Young, Alverno
College, Milwaukee, WI*

**Childhood Stunting: Policy Solutions To
Address a Global Burden with Long-Term
Impacts**

*Sharon Bergquist, Bill and Melinda Gates
Foundation, Seattle, WA*

**Federal Science and the Public Good:
U.S. Agency Science-Based Decision-
Making**

*Francesca T. Grifo, U.S. Environmental
Protection Agency, Washington, DC*

**Forensic Sciences: Toward a Stronger
Scientific Framework**

Alicia Carriquiry, Iowa State University, Ames

**Fostering Integrity in Science: An Action
Agenda**

*Thomas Arrison, National Academies of
Sciences, Engineering, and Medicine,
Washington, DC*

**Future Directions for International Science
Advice**

*Peter Gluckman, New Zealand Ministry of
Foreign Affairs and Trade, Wellington*

**Grand Visions for the Future of U.S.
Science in a New Global Era**

*Pushpalatha Bhat, Fermi National Accelerator
Laboratory, Batavia, IL*

**Integrating Science into Policymaking:
What Works and Why**

*Stephen Davies and Geraldine Barry, European
Commission Joint Research Center, Brussels,
Belgium*

**Overcoming Barriers to Technology
Innovation in Established Economic
Sectors**

*Charles Weiss, Georgetown University,
Bethesda, MD; William B. Bonvillian,
Massachusetts Institute of Technology,
Washington, DC*

Peer Review for Public Trust

*Brad Wible and Marcia McNutt, AAAS/Science,
Washington, DC*

**Science Policy in the 2016 U.S.
Presidential Election: Candidates' Visions
for Science**

*Joanne P. Carney, AAAS Office of Government
Relations, Washington, DC; Tobin Smith,
American Association of Universities,
Washington, DC; Jennifer Poulakidas,
Association of Public and Land-grant
Universities, Washington, DC*

**The Global Impact of Violence Against
Children: Economic, Health, and Policy
Perspectives**

*Susan Horton, University of Waterloo, Canada;
Susan Bissell, United Nations Children's Fund
(UNICEF), New York City*

AAAS 2016 ANNUAL MEETING

GLOBAL SCIENCE ENGAGEMENT

AAAS, publisher of *Science*, thanks the sponsors and
supporters of the 2016 Annual Meeting



for its generous support of
the Science Journalism Awards

As of October 15, 2015



There's only one **Science**

Science Careers Advertising

For full advertising details, go to ScienceCareers.org and click For Employers, or call one of our representatives.

Tracy Holmes

Worldwide Associate Director
Science Careers
Phone: +44 (0) 1223 326525

THE AMERICAS

E-mail: advertise@sciencecareers.org

Fax: +1 (202) 289 6742

Tina Burks

Phone: +1 (202) 326 6577

Nancy Toema

Phone: +1 (202) 326 6578

Online Job Posting Questions

Phone: +1 (202) 312 6375

EUROPE / INDIA / AUSTRALIA / NEW ZEALAND / REST OF WORLD

E-mail: ads@science-int.co.uk

Fax: +44 (0) 1223 326532

Sarah Lelarge

Phone: +44 (0) 1223 326527

Kelly Grace

Phone: +44 (0) 1223 326528

Online Job Posting Questions

Phone: +44 (0) 1223 326528

JAPAN

Katsuyoshi Fukamizu (Tokyo)

E-mail: kfukamizu@aaas.org

Phone: +81 3 3219 5777

Hiroyuki Mashiki (Kyoto)

E-mail: hmashiki@aaas.org

Phone: +81 75 823 1109

CHINA / KOREA / SINGAPORE / TAIWAN / THAILAND

Ruolei Wu

Phone: +86 186 0082 9345

E-mail: rwu@aaas.org

All ads submitted for publication must comply with applicable U.S. and non-U.S. laws. Science reserves the right to refuse any advertisement at its sole discretion for any reason, including without limitation for offensive language or inappropriate content, and all advertising is subject to publisher approval. Science encourages our readers to alert us to any ads that they feel may be discriminatory or offensive.

ScienceCareers

FROM THE JOURNAL SCIENCE **AAAS**

ScienceCareers.org

POSITIONS OPEN

UC San Diego

Bioengineering
JACOBS SCHOOL OF ENGINEERING

FACULTY POSITIONS

University of California San Diego DEPARTMENT OF BIOENGINEERING

The Department of Bioengineering in the Jacobs School of Engineering at the University of California, San Diego is inviting applications for a **TENURE-TRACK POSITION** at the Assistant Professor.

A PhD or advancement to candidacy in bioengineering or related engineering disciplines is required for this position. Successful applicants will be expected to teach undergraduate courses in University of California San Diego's Bioengineering, Biotech and/or BioSystems Engineering Major tracks and graduate courses in Bioengineering and establish a vigorous program of high-quality federally funded bioengineering research.

To obtain more information or submit your application materials, go to website: <https://apol-recruit.ucsd.edu/apply/JPF00928>.

University of California San Diego is an Affirmative Action/Equal Opportunity Employer.

Anatomy and Cell Biology East Carolina University Tenure Track position at the Assistant or Associate Professor level is available, based on qualifications, in the Department of Anatomy and Cell Biology, Brody School of Medicine at East Carolina University (ECU) in Greenville, NC. The new faculty is expected to develop a rigorous, extramurally funded research program that will contribute to the departmental research missions in cell biology (<http://www.ecu.edu/anatomy>). Research programs must complement the strengths of ongoing research in the department or within the school of medicine. Applicants should have strong interest in graduate student education; experience in medical education in the anatomical sciences is preferred. A fixed term appointment is an option but not preferred. For more information about the position, please access the HR website and apply using the on-line application process to position #957507 https://ecu.peopleadmin.com/applicants/jsp/shared/position/JobDetails_css.jsp?postingId=346235. Applicants should submit a complete application including a cover letter, statement of interest, curriculum vitae, statement of teaching philosophy, and statement of research plans including specific aims for a potential proposal. East Carolina University is a constituent institution of the University of North Carolina and an Equal Opportunity/Affirmative Action University that accommodates the needs of individuals with disabilities.

ASSISTANT/ ASSOCIATE PROFESSOR FORENSIC BIOLOGY

The Forensic Science Program and the Department of Biology at Middle Tennessee State University invite qualified applicants for a tenure-track assistant professor position in Forensic Biology. Candidates must apply online at website: <http://www.mtsu.edu/jobs.php>, position no. 103020. Middle Tennessee State University is an Equal Opportunity/Affirmative Action Employer. Women, minorities, and persons with disabilities are encouraged to apply. Review of applications begins November 30, 2015.

Download the ScienceCareers Job App

SEARCH JOBS
ON THE GO!

apps.sciencemag.org



POSITIONS OPEN

Vice Chair for Research Pennsylvania State University

An opportunity exists for a Vice Chair for Research and Director of the Division of Musculoskeletal Sciences within the Department of Orthopaedics and Rehabilitation at The Pennsylvania State University College of Medicine. This is a tenure or tenure track faculty position at the rank of Associate or Full Professor. This position will provide administrative oversight of the Department's research programs and includes a highly competitive salary and start-up funds. This is a unique opportunity to join and direct a well-established, highly interactive research group consisting of engineers, material, clinical and basic scientists focusing on musculoskeletal research. A joint academic appointment will include a primary appointment in the College of Medicine at the Hershey, PA campus and a secondary appointment in an appropriate department at Penn State University main campus at State College, PA.

The professional qualifications for this position include: The ideal candidate will have an advanced degree of Ph.D., M.D., or M.D./Ph.D. Will have established an independent and extramurally funded research program in the area of musculoskeletal sciences or engineering. Demonstrated strong leadership skills; have experience in teaching and mentoring junior investigators, post-doctoral fellows, graduate and medical students; and have a record of strong publications in peer-reviewed journals. Will be an individual who can apply modern biomedical science and engineering concepts to the study of musculoskeletal tissues and lead others in developing their own research programs.

As part of one of the country's pre-eminent universities, our 551-bed tertiary medical center is the central Pennsylvania's region's only level I adult and pediatric trauma center and academic medical center. Also home to Penn State Children's Hospital, we are considered a resource for the most complex adult and pediatric cases. Hershey, PA, and the surrounding area offer a pleasant alternative to the pressures of urban living with a mix of well-maintained communities with quiet tree-lined streets, safe shopping districts, beautiful farmland, and state parks and game lands. It's the best of both worlds, with cultural events and nightlife both within Hershey and driving distance to Harrisburg; Philadelphia; the Pocono Mountains; Baltimore; Washington, D.C.; and New York City. The area is home to two professional sports teams, an amusement park, golf courses, professional and amateur theater, symphonies, and opportunities for hunting, fishing, and mountain biking.

Apply to job 58934 at website: <http://apptkr.com/690801>

CAMPUS SECURITY CRIME STATISTICS: For more about safety at Penn State, and to review the Annual Security Report which contains information about crime statistics and other safety and security matters, please go to website: <http://www.police.psu.edu/dery/>, which will also provide you with detail on how to request a hard copy of the Annual Security Report.

Penn State is an Equal Opportunity, Affirmative Action Employer, and is committed to providing employment opportunities to all qualified applicants without regard to race, color, religion, age, sex, sexual orientation, gender identity, national origin, disability or protected veteran status.

Post Your Jobs

1 million candidates*
151,000 job applications*



Reach Scientists.
Fill Positions.

*Jan-Dec 2014

ScienceCareers
employers.sciencecareers.org



Specialty Care Division of AstraZeneca

7389 - Director, Oncology Cambridge

MedImmune seeks an exceptionally strong individual to join their Oncology Research team in Cambridge, UK. This is a strategic position with responsibilities that are of major significance to the success of the Oncology portfolio. MedImmune's oncology research team consists of approximately 85 people roughly divided equally between Cambridge, UK and Gaithersburg, MD, USA. The Oncology Research Group in Cambridge consists of 2 teams each led by a Director. A vacancy has arisen to replace one of those Directors.

Reporting to the VP Oncology Research who is based in the US, the incumbent will lead a team of approximately 20 people consisting of scientists, technicians and post-docs. Importantly the successful candidate will bring substantial research experience in tumour-immunology and be a well-respected and recognised scientist in academia and/or bio-pharmaceutical industry. The primary responsibility of the Oncology Research Group is to bring new and innovative science that can lead to the development of new immune-therapies. The group addresses basic science including investigating new mechanisms/pathways, validation of targets and further in-vivo and in-vitro validation of models and determining mode of action.

Major Duties and Responsibilities:

- Providing scientific, operational and strategic leadership for Oncology Research activities at MedImmune, Cambridge.
- Bringing cell and molecular immunology expertise to the development of novel cancer therapeutics as well as providing scientific and managerial leadership for cross-functional teams. Direct responsibility for managing and mentoring scientists and teams, ensuring appropriate resourcing for work plans and projects.
- Using scientific knowledge and expertise to review and support key investment decisions and provide guidance to the Oncology governance committees for project progression.
- Implementation of strategies to ensure a sustainable Oncology Research pipeline.
- Establishing and maintaining innovation and capability in complex models of disease, with a particular focus on tumour immunology.
- Promoting awareness of the competitive environment and helping to build MedImmune's external presence in key areas of research.
- Providing clear communication of results with conclusions and recommendations to key stakeholders and preparing documents and reports for internal governance committees and regulatory agencies, including INDs.
- Establishing and managing external collaborations; and contributing to assessment of external business alliance and in-licensing opportunities.

This senior and highly visible position within the MedImmune organisation requires an experienced oncology research professional whose qualities and experience include the following parameters.

Education:

Your career will be built on a strong academic background. With a PhD or MD/PhD qualification and with excellent interpersonal and communication skills the incumbent will have a proven track record in tumour-immunology, preferably in aspects of innate immunology and/or immune suppressive components in the tumour microenvironment.

Experience & Skillset

A thought leader in Immuno-Oncology;

- Strong understanding of developing drugs within the field of Immuno-Oncology is a plus.
- Strong understanding of the cellular processes underlying cancer.
- Strong background in understanding, elucidating and manipulating the immune system in various solid and hematologic oncology settings.
- Experience and familiarity of cell-based assays and models with industry-standard techniques.
- Target Identification and Target Validation experience would be advantageous.
- Experience of developing data packages suitable for supporting IND filings would be beneficial.
- Able to demonstrate strong mentoring skills to scientists as well as postdocs.
- Proven ability to lead innovative research and the validation of novel targets.
- A strong background of in vitro and in vivo experimentation and functional assay development is essential.
- Experience of championing and guiding projects from inception to candidate drug.
- Ability to prioritise and clearly define those priorities to others and monitor progress.
- Motivated to work in a fast paced and highly collaborative environment.
- Leadership and Line management expertise are essential to the post with evidence of developing a strong team ethic.

Visit the MedImmune career portal (<https://www.medimmune.com/careers>) using reference 7389

Competitive remuneration and company benefits apply.

Closing date for submissions – 30th Nov 2015



Massachusetts
Institute of
Technology

Come work with us!

Tenure Track Faculty

The Department of Brain & Cognitive Sciences (BCS)

(<http://bcs.mit.edu>) at MIT is looking to hire up to five (5) tenure-track faculty at the assistant professor level. Affiliations with the Picower Institute for Learning & Memory and the McGovern Institute for Brain Research are possible. We are most excited about candidates who work in one or more of the following four (4) areas:

i. Computational and theoretical approaches to neuroscience and cognition. Possible areas of focus include but are not limited to: statistics and data science, neural circuits, neural population representations and transformations, and cognitive processes. Candidates with the ability to build bridges across empirical domains are especially attractive. An affiliation with Electrical Engineering and Computer Science (EECS), the Computer Science and Artificial Intelligence Laboratory (CSAIL), Institute for Data, Systems, and Society (IDSS), or other allied departments is possible.

ii. Systems neuroscience in non-human animals. The ideal candidate would be driven by computational questions and ideas from human cognition, with the goal of reverse engineering the underlying neural representations and processes using tools that allow access to multiple brain regions.

iii. Cognitive neuroscience in humans, especially if the candidate's work bridges levels of analysis using a variety of methods including MRI, MEG, fMRI, theoretical modeling, genetics and reverse engineering approaches.

iv. Human cognition using behavioral methods, especially in the areas of language and/or cognitive development.

Successful applicants are expected to develop and lead independent, internationally competitive research programs and to share in our commitment to excellence in undergraduate and graduate education by teaching courses and mentoring graduate and undergraduate students. PhD must be completed by start day of employment and some postdoctoral training is preferred.

Please submit application materials – cover letter, CV, statement of research and teaching interests and representative reprints – online at <https://academicjobsonline.org/ajo/jobs/5972>. Please state research area in cover letter. To help direct the application, applicants should indicate which of the four areas listed above is their main research area by answering the mandatory questions included in the application. In addition, please arrange to have three letters of recommendation submitted online. Review of applications will begin on October 31, 2015.

MIT is an affirmative action employer, and we encourage applications from women and underrepresented minorities.

<http://web.mit.edu>

CAREER OPPORTUNITY AT QBRI - PRINCIPAL INVESTIGATORS IN DIABETES, CANCER, NEUROLOGICAL DISORDERS, AND GENOMICS

Qatar Biomedical Research Institute (QBRI), an institution of Hamad bin Khalifa University which is a member of Qatar Foundation, is a national center of excellence in biomedical research that aims to transform healthcare through harnessing and converting the latest advances in science, medicine and technology into novel discoveries that will lead to more effective treatments and preventive strategies for human diseases such as diabetes, cancer, and neurological disorders. QBRI's approach is holistic and multidisciplinary, focusing on prevention, diagnosis, treatment and personalized healthcare. QBRI has plans to hire more than 50 staff members over the next two years and is slated to occupy state-of-the-art life sciences laboratories in a newly established research campus that is due to open in 2016.

Building on existing strengths, QBRI is committed to developing scientific excellence in breast cancer, type 2 diabetes, and neurogenetic/neurodevelopmental disorders.

FULL-TIME INVESTIGATOR POSITIONS

To fulfill its mission, QBRI is recruiting independent, full-time investigators at the equivalent of Assistant, Associate and Full Professor, to lead and support basic, clinical and translational research in their area of expertise in cancer, diabetes, neurological disorders, and genomics. Individuals with expertise in functional genomics, computational and systems biology, developmental and cellular biology, and animal models of human disease are encouraged to apply.

These positions offer outstanding scientific resources and generous funding opportunities amidst existing expertise, and access to state-of-the-art core laboratories and to a homogeneous and genetically unique population. In addition, there will be the opportunity to take a joint academic appointment at the College of Engineering and Science, Hamad bin Khalifa University. The positions offer ample opportunities for interaction and collaboration with national, regional and international universities, research institutes, clinical entities and organizations.

KEY RESPONSIBILITIES:

- Set research program agenda
- Build and manage research group
- Recruit research team of Associates and Scientists
- Tangible output of high impact publications, conference presentations, scientific interactions and collaborations, and patents

REQUIREMENTS:

The ideal candidate must hold a doctoral degree and demonstrate considerable research experience and thorough knowledge of the field. The candidate must demonstrate a solid record of productive scholarship; mentoring students, post-doctoral fellows and junior researchers. As such, candidates should exhibit excellent and effective communication and organizational skills as well as demonstrated ability to work in a team/matrix environment.

Applicants should provide a cover letter, a *curriculum vitae*, a research statement, publication list and reprints of the 5 most relevant publications. Please include the names and contact information of at least three referees as well. Completed applications will be reviewed and interviews will be arranged on a rolling basis until the positions are filled. Only shortlisted applicants will be contacted.

CONTACT INFORMATION

If you are interested and fulfil the criteria mentioned above, kindly send your application to qfjobs@qf.org.qa, copying qbri-info@qf.org.qa; Website: www.qbri.org.qa Virtual Tour: www.qbri.org.qa/facilities/vtour

LUNDBECK FOUNDATION FELLOWSHIPS

The Lundbeck Foundation hereby invites applications for fellowships within biomedicine, including science projects with a clear biomedical angle and research plans, which will be granted to especially promising young researchers and their research groups.

The fellowships are awarded for five years and each fellowship amounts to DKK 10 million (approx. Euro 1,3 million).

The subject area should be frontline basic- or applied research within the scope of the Foundation's grant strategy, which can be seen at www.lundbeckfonden.com

The call invites Danish or foreign researchers from abroad, who wish to move to Denmark and continue their research here. The call is also open for applicants from Danish universities and university hospitals.

The fellowships are intended for researchers who are qualified to establish or develop their own research groups within biomedicine and who have received their PhD degree within the last 5-7 years.

The application should include an account of the research plan, collaborators, budget and how the research group is envisioned to be placed within a Danish research institution. In addition, it should include a letter of intent from a resident researcher at the host institution, who makes him- or herself available as a mentor to facilitate the applicant's establishment of the research group as an integral part of the host institution. Further guidance is provided in the application form.

The application, written in English, should be sent via the Foundation's Electronic Application System for fellowships at www.lundbeckfonden.com no later than December 14, 2015. Interviews will take place during the weeks of April 18-21 or 25-29, 2016 at the Lundbeck Foundation.

For further information please contact Ulla Jakobsen, Science Manager, phone: 39 12 80 11 or email: application@lundbeckfonden.com



Lundbeck Foundation is an active industrial foundation with controlling shareholdings in H. Lundbeck, ALK and Falck. In addition, the Foundation manages financial investments of approximately € 1.3 billion. The Foundation supports biomedical research of the highest international quality. In 2014, the Foundation had a profit after tax of approx. € 217 million and made research grants of approx. € 64 million.

Lundbeckfonden
Scherfigsvej 7, DK-2100 Copenhagen Ø
Tel. +45 39 12 80 00
www.lundbeckfonden.com

LUNDBECK FOUNDATION

Be the force behind the cures.



DEVELOPMENTAL NEUROBIOLOGY FACULTY RECRUITMENT

The Department of Developmental Neurobiology at St. Jude Children's Research Hospital (St. Jude) seeks an exceptional and creative scientist for a FACULTY position in cellular or systems neuroscience. We are seeking an investigator to lead a multidisciplinary research program that addresses the basic function of neurons or neuronal circuits. Areas of interest include neural circuits and behavior, synaptic neurobiology, cell biology of neurogenesis, including stem cell biology, and neural epigenetics. Early career investigators interested in contributing to a culture of excellence at St. Jude are particularly encouraged to apply. This search is also open for mid-career investigators with a strong record of independent research.

The research environment at St. Jude is highly interactive with collaborative opportunities across all basic research and clinical departments, as well as access to state-of-the-art institutional shared resources managed by Ph.D. level scientists. Developmental Neurobiology investigators have access to specialized departmental shared resources that include animal behavior, human stem cells, live cell imaging, cell sorting and advanced image processing and analysis.

We offer very competitive packages, including generous startup funds, equipment, laboratory space, personnel support and potential institutional support beyond the start-up phase. A faculty position at the Assistant and Associate Member level may be considered. Successful applicants may hold a Ph.D. and/or M.D. degree, have at least three years of relevant postgraduate experience, and a demonstrated track record of productivity.

Interested applicants should send via email a curriculum vitae, a 2-3 page summary of research interests, and the names of three references to:

**David Solecki, Ph.D and
Stanislav S. Zakharenko, M.D./Ph.D.**
Department of Developmental Neurobiology
St. Jude Children's Research Hospital
262 Danny Thomas Place, Memphis, TN 38105
Email: DNBFaculty@stjude.org

www.stjude.org/developmental-neurobiology

EOE/M/F/Vet/Disability/Sexual Orientation/Gender Identity



**St. Jude Children's
Research Hospital**
ALSAC • Danny Thomas, Founder



MEDICINE
TEXAS A&M HEALTH SCIENCE CENTER

Tenure-Track Faculty Position Neuroscience and Experimental Therapeutics College of Medicine Texas A&M Health Science Center

The Department of Neuroscience and Experimental Therapeutics invites applications for a tenure-track faculty position at the level of ASSISTANT PROFESSOR. We are interested in outstanding scientists in the neurosciences, neuropharmacological or translational sciences with a strong record of research productivity and a commitment to graduate and medical education. The ideal candidate's research program should complement existing research strengths in the department which include molecular, cellular and behavioral approaches to study brain development, aging, neurodegeneration and addiction. (For more details see <http://medicine.tamhsc.edu/next/faculty/index.html>)

This position offers an outstanding research environment, collaborative faculty, a newly built research facility with a modern vivarium and a highly competitive start-up package, compensation and benefits. Successful candidates are expected to develop independent, extramurally-funded research programs, and to participate in teaching and service within the department. The neuroscience community at Texas A&M consists of 70+ faculty located in the departments across the University. Additional interdisciplinary collaborations are possible with the College of Engineering and the College of Pharmacy.

Applications must be submitted online through the departmental web site located at <http://medicine.tamhsc.edu/next/index.html>. Applications must include a full CV, research statement, three most relevant publications and list of three references. Applications must be received by **December 31, 2015**. Review of applications will begin as soon as they are received, and applications received after the deadline will not be guaranteed consideration.

Contact information: **Chair of Research Faculty Search Committee, Department of Neuroscience and Experimental Therapeutics, Texas A&M Health Science Center, College of Medicine, Medical Research and Education Building, 8447 State Highway 47, Bryan, TX 77807. COM-NEXTResearchFaculty@medicine.tamhsc.edu.**

The TAMHSC is an Affirmative Action/ Equal Opportunity Employer.

UAB SCHOOL OF MEDICINE

Knowledge that will change your world

The University of Alabama at Birmingham

MOLECULAR NEUROBIOLOGY ASSISTANT OR ASSOCIATE PROFESSOR

The Department of Neurobiology and the Civitan International Research Center at UAB invite applications for a tenure-track or tenured position in Molecular Neurobiology at the rank of Assistant or Associate Professor. The Department seeks to recruit an outstanding scientist who applies studies of molecular mechanisms to questions related to Intellectual Disability and autism research. At this level, a prior track record of NIH support will be an important criterion for the successful applicant. Research programs complementary to existing strengths in epigenetics and genomics/bioinformatics will also be a consideration.

The Department of Neurobiology and Civitan International Research Center offers a collegial and creative environment and UAB is one of the leading academic medical centers in the country. The Department of Neurobiology is currently ranked among the top 20 in NIH funding among all US Neuroscience Departments. More information can be found at <https://www.uab.edu/medicine/neurobiology/>. The deadline for applications will be December 1, 2015. Applicants should provide a CV, brief description of research interests and names of 3-5 references to:

Drs. Farah Lubin and David Sweatt
c/o Lissa LaRue
University of Alabama at Birmingham
Department of Neurobiology
1825 University Blvd. SHEL 903
Birmingham, AL 35294-2182
E-mail: llarue@uab.edu

UAB is an Equal Opportunity/Affirmative Action Employer committed to fostering a diverse, equitable and family-friendly environment in which all faculty and staff can excel and achieve work/life balance irrespective of race, national origin, age, genetic or family medical history, gender, faith, gender identity and expression as well as sexual orientation. UAB also encourages applications from individuals with disabilities and veterans.



UNIVERSITY of
DENVER

NATURAL SCIENCES & MATHEMATICS

**Department of Biological Sciences
Associate Professor in Biological Sciences,
Plant Ecology - Kurtz Endowed Chair in Biological Sciences**

The Division of Natural Sciences and Mathematics and the Department of Biological Sciences at the University of Denver invites applications for a Plant Ecologist in a tenure-track position at the Associate Professor level to begin September 1, 2016. Applicants at the level of Full Professor will also be considered. We are interested in candidates studying plant ecology at any scale from population to community to landscape ecology, and those interested in plant ecological interactions with other organisms, including in an evolutionary context. Candidates will have a Ph.D. in an appropriate field and demonstrated success in extramural funding with an established research program that complements the research interests of faculty. The successful candidate will be the Kurtz Endowed Chair in Biological Sciences, supervise undergraduate research projects and M.S. and Ph.D. students, teach undergraduate and graduate courses in biology and specific areas of specialty, and will serve as the Director of the Chester Alter Arboretum at the University of Denver by consulting and working with campus facilities. Information on Departmental programs can be found at <http://www.du.edu/nsm/departments/biologicalsciences/>

All candidates must submit their application through <https://dujobs.silkroad.com>. The online application should include: a cover letter, a curriculum vitae, and separate statements of research interests and teaching philosophy and two recent publications. In addition, at least three recommenders should email letters of reference to: Plant Ecology Faculty Search Committee, University of Denver, Department of Biological Sciences at biology.rec@du.edu. The review of applications will begin **November 15, 2015** and continue until the position is filled. Contact Dr. Anna Sher at Anna.Sher@du.edu if you have questions regarding the search.

The University of Denver is committed to enhancing the diversity of its faculty and staff and encourages applications from women, minorities, members of the LGBT community, people with disabilities and veterans. The University is an Equal Opportunity/Affirmative Action Employer.



**Harvard University Faculty Positions in
Paleobiology, Geobiology, and Earth History**

The Departments of Organismic & Evolutionary Biology (OEB) and Earth & Planetary Sciences (EPS)—in partnership with the Museum of Comparative Zoology (MCZ)—invite applications for two tenure-track faculty positions spanning the broadly defined fields of paleobiology, geobiology, and Earth history. We seek to attract two outstanding individuals to establish innovative research programs and teach both undergraduate and graduate students. We are especially interested in individuals whose work spans the intellectual interests of the OEB and EPS departments, possibly including—although not limited to—paleontology and/or the interactions between life, evolution, (bio)geochemistry, and the environment over geologic time, either on land or in the ocean. The positions may be associated with curatorial appointments in the MCZ with oversight responsibilities of the museum's invertebrate paleontology collections.

Basic Qualifications: Doctorate or terminal degree in geobiology, paleontology, or related disciplines required by the time the appointment begins.

Additional Qualifications: Demonstrated excellence in teaching is desired.

Please submit applications online at: <http://academicpositions.harvard.edu/postings/6418>

Required materials include a cover letter, curriculum vitae; a statement of research and teaching interests; four representative publications; and the names, institutional affiliations, and email addresses of three references. Review of applications will begin **November 9, 2015**, and conclude when the positions are filled.

Further information about EPS and OEB are available at <http://www.eps.harvard.edu/> and <http://www.oeb.harvard.edu/>. Address questions about the position to **Professor Ann Pearson** (pearson@eps.harvard.edu) or **Professor James Hanken** (hanken@oeb.harvard.edu) and about the application process to **Chenoweth Moffatt** (moffatt@eps.harvard.edu).

Harvard is an Equal Opportunity Employer and all qualified applicants will receive consideration for employment without regard to race, color, religion, sex, sexual orientation, gender identity, national origin, disability status, protected veteran status, or any other characteristic protected by law.



UNIVERSITY OF CALIFORNIA
UC RIVERSIDE

**NOW HIRING
300
LADDER FACULTY**

**Join us in defining the
new American research
university**

clusterhiring.ucr.edu



Temple University School of Pharmacy

Tenure-Track Faculty Positions in the Department of Pharmaceutical Sciences

The Department of Pharmaceutical Sciences invites applications for two tenure-track positions at the rank of Associate or Full Professor in the following areas: **Structural Biology** Applicants should possess a PhD degree in biophysics, biochemistry, bioinformatics, chemistry or computational biology with at least 5 years of experience. Expertise in applying various techniques to probe molecular structures such as X-ray crystallography or protein NMR, would be advantageous. The optimal candidate should also possess expertise in supporting technologies such as macromolecule expression/purification and computational chemistry, as well as interest and expertise in structure-based drug design. **Oxidative Stress** Applicants should hold a PhD or MD degree and although the specific research area is open, we seek a candidate with a strong record of recent accomplishments in the area of mitochondrial dysfunction and oxidative stress in areas such as; diabetes, cancer, neuroscience/aging, cardiovascular. Expertise in system biology strategies for pharmaceutical research is highly desired. In addition to the specific requirements for each of the positions, the successful candidate will show evidence of continual ability to secure extramural funding, produce high quality peer reviewed publications, develop a strong independent research program, collaborate with others, teach professional Pharmacy students (PharmD) and mentor graduate students and post-doctoral investigators. All candidates must demonstrate a strong commitment to both research and teaching.

The Department of Pharmaceutical Sciences houses the Moulder Center for Drug Discovery Research, the cGMP Facility, and the Jayne Haines Center for Pharmacogenomics and Drug Safety. The successful candidate will also be a member of the Moulder Center for Drug Discovery which will provide opportunities for their participation in multidisciplinary research initiatives based at the center and with internal and external collaborators. Applicants must provide a cover letter, curriculum vitae, statement of research plans and teaching philosophy along with contact information for three references to:

Professor Magid Abou-Gharbia, Ph.D.
Chair of Pharmaceutical Sciences Search Committee

Temple University School of Pharmacy
c/o Sophon Din
3307 N. Broad Street
Philadelphia, PA 19140

Electronic submissions supplied as a single pdf file will be accepted at Sophon.din@temple.edu.

Temple University is an Equal Opportunity Employer and complies with applicable EEO and Affirmative Action regulations.



**Stanford
MEDICINE**

Department of Radiology Faculty Positions in the Molecular Imaging Program at Stanford

We are pleased to announce that the Molecular Imaging Program at Stanford (MIPS) is recruiting up to three new faculty members at the Assistant, Associate, or Full Professor level. The MIPS is committed to advancing the fundamental basic science of molecular imaging and to translating these discoveries for improving human health care. Stanford University and the Department of Radiology have made substantial commitments towards the expansion of the MIPS including new space at the Technology & Innovation Park.

We seek applicants committed to developing a research program focused in any specific area of the field of molecular imaging of living subjects. This includes but is not limited to novel imaging instrumentation, novel chemistry/materials science for molecular imaging agent development, novel assay development, mathematical modeling, and translation of molecular imaging strategies for clinical application. We are interested in applicants who have multidisciplinary experience that can be applied to the development of disease detection and management approaches. The qualified candidate should have a Ph.D. and/or M.D. degree(s) with experience in a relevant field.

Candidates must have interest in leading an independent research program and participating in our center-wide efforts to translate novel technologies or methodologies into clinical practice and have the desire to collaborate with investigators in Stanford's multi-disciplinary molecular imaging research effort, which includes faculty in the Schools of Medicine, Engineering, and Humanities & Sciences, and external investigators. The ideal candidate will have demonstrated breadth of preparation, as exemplified by significant clinical and/or research experience resulting in high impact publications in biomedical research. Success in obtaining grant funding (e.g., NIH award(s)), and expertise in multi-disciplinary research are highly desired. We are looking for motivated individuals who are committed to excellence in research, teaching, and mentoring of students in multi-disciplinary biomedical research.

Appointments will be in the University Tenure Line. The predominant criterion for appointment in the University Tenure Line is a major commitment to research and teaching. Faculty rank will be determined by the qualifications and experience of the successful candidate.

Stanford University is an Equal Opportunity Employer and is committed to increasing the diversity of its faculty. It welcomes nominations of and applications from women and members of minority groups, protected veterans and individuals with disabilities, as well as from others who would bring additional dimensions to the university's research, teaching and clinical missions.

Applicants must submit a curriculum vitae summarizing their educational and professional background, along with a current list of published work, clinical trials they have led or contributed to if applicable, and a brief statement (4-5 pages) describing the candidate's research and teaching activities and interests and how they relate to the position described above with specific emphasis on the molecular imaging of living subjects. Interested candidates can submit their applications at <http://radiology.stanford.edu>.



Postdoctoral Fellowships Available

The Lombardi Comprehensive Cancer Center (LCCC) at Georgetown University, a multidisciplinary NCI-designated cancer research center, is currently recruiting postdoctoral fellows into positions funded by an NCI training grant. The goal is to develop strong basic and translational scientists with an interest in cancer research. Successful applicants will choose a mentor from an interdisciplinary group of investigators who are committed to cancer research. Research programs include:

- The role of growth factor signal pathways
- The development of hormone and drug resistance
- The genetic and molecular mechanisms of malignant progression
- Invasion metastasis angiogenesis
- Stem cells in cancer
- Role of metabolism in cancer
- Development of novel immunological and anticancer therapies
- The etiology of cancer, biomarkers, and molecular epidemiology
- Bioinformatics and cancer

Visit <http://tumorbiology.georgetown.edu/postdoc> for further information.

Salary is competitive and commensurate with qualifications and experience. Please send curriculum vitae, a short statement of research interests and career goals, and the names and addresses of 3 references to **Karen Shepherd** (bivinsk@georgetown.edu).

Minorities and women are strongly encouraged to apply. US citizenship or permanent residency required.

Advance
your career
with expert
advice from
Science
Careers.



**Download Free Career
Advice Booklets!**

ScienceCareers.org/booklets



Science Careers

FROM THE JOURNAL SCIENCE AAAS



東北林業大學

2015~2017 High-level Talent Introduction Announcement of Northeast Forestry University

Established in 1952 and located in Harbin – beautiful “Ice City”, Northeast Forestry University is in national “211 Project” directly under the Ministry of Education of the People’s Republic of China and key construction projects of “Advantage Discipline Innovation Platform”. It is a multidisciplinary university integrating agriculture, science, industry, economics, management, culture, law, medicine and art with forestry science as advantage and forestry engineering as specialty. To further improve the overall level of teaching staff and achieve a research university with international view, we are hereby looking for talents sincerely and mainly introducing excellent domestic and foreign talents with important complementary and supporting functions for the construction of subjects and talent team.

I. Subject Areas for Recruitment:

Agriculture, General Computing, Computer Science, Information Science and Technology, Architecture, Planning, Cell & Molecular Biology, Bioinformatics, Ecology, Genetics, Microbiology & Virology, Plant Science, Zoology & Animal Science, Civil Engineering & Construction, Electrical & Electronics Engineering, Materials Science, Mechanical Engineering, Polymer Science & Technology, Veterinary Medicine, Business, Economics, Finance, and Accounting, Analytical Chemistry, Chemical Engineering, Inorganic Chemistry, Organic Chemistry, Physical Chemistry, Botany.

II. Recruitment Plan

1. Leading Talents or Teams: to introduce leading talents or teams with international advanced level and competitive capacity in distinctive preponderant disciplines of the university and national key disciplines.
2. Distinguished Young Scholars: distinguished domestic and foreign young scholars have published high cited academic paper in the top-level publication of related field, with the potential to be selected into talent projects such as Thousands of People Plan, National Science Fund for Distinguished Young Scholars, Thousand Youth Talents Plan and Tens of Thousands of People Plan, or personnel with academic title of associate professor in overseas famous colleges and universities and above or personnel equivalent to the level of researchers in overseas famous research institutes; age under 40, and 45 for the excellences.
3. Excellent Young Scholars: excellent domestic and foreign young scholars have published high cited academic paper in the top-level publication of related secondary discipline, with the potential to be selected into talent projects such as Provincial Science Fund for Distinguished Young Scholars, Longjiang Scholars and Provincial Excellent Young and Middle-aged Experts; age under 35, and 40 for the excellences.
4. Young Backbone: domestic and foreign young backbone have published high cited academic paper in the top-level publication of related secondary discipline, with the ability of winning National Science Foundation of China and Philosophy and Social

Science Foundation of China and great development potential in academy and scientific research; age: under 35.

5. Excellent Young Teachers: doctors with strong ability of teaching and scientific research; age: under 35.

III. Treatment

1. Leading Talents: appointed to the post of professor;
 2. Distinguished Young Scholars: appointed to the post of professor;
 3. Excellent Young Scholars: appointed to the post of professor or associate professor;
 4. Young Backbone: appointed to the post of associate professor or lecturer;
- The university will provide salary standard, scientific research start-up fund and house purchase subsidies according to the level of talent introduction.

IV. Further Details and Contact Information

Please check the following links for more details about the recruitment plan:

<http://gkzp.nefu.edu.cn>

For official website, please check:

<http://www.nefu.edu.cn>

Contact Person:

Mr. Zhang Chunlei (Tel: +86-451-82190165)

Ms. Guan Bingbing or Mr. Ni Songyuan (+86-451-82192070, 82191327)

Email: nefugec@nefu.edu.cn



High-level Talents Online Job Fair 2015



**The Second action of 2015
will be held on oct 18th ,from 7AM to 24AM
in Shanghai**

Recruitment requirements:

Scholars and doctors with working position and graduating doctors domestic and overseas

Please send your curriculum vitae to:

acabridge@gmail.com

chisa.add@gmail.com

chisa_yang@163.com

For more information, please check the following web sites:

<http://www.eol.cn/cv>

http://www.chisa.edu.cn/zt/yczt/network_video/index.html



LABORATORY FOR LASER PLASMAS
SHANGHAI JIAO TONG UNIVERSITY

Multiple Faculty Positions and Postdoc Positions in Lasers, Plasma Physics, and Ultrafast Science

The Laboratory for Laser Plasmas at Shanghai Jiao Tong University, founded jointly by the University and the Ministry of Education of China in 2010, is a unique multidisciplinary research center. It brings together the best scientists, engineers, and educators from the fields of laser, plasma, accelerator physics and technologies, and ultrafast science to solve some key challenges of our modern society related to energy, environment, and health issues. The Laboratory has equipped with a series of state-of-the-art facilities including a multi-100 terawatt high power laser system, kHz terawatt laser systems, a high power mid-infrared laser system, a multi-MeV RF electron accelerator, advanced laser-target interaction chambers and diagnostics.

To further intensify our innovation capabilities, we are now seeking outstanding scholars to join us. The ideal candidates are supposed to have a PhD and a strong research record related to one of the following areas: high power laser technology, laser plasma theory and simulation, laser-plasma experiment, advanced particle accelerators and applications, high energy density physics, or ultrafast science. The following positions are available according to the candidates' experience:

- (a) Distinguished professors selected by “National 1000 Talent Plan”, “Changjiang Scholars Program”, or “National Science Fund for Distinguished Young Scholars”.
- (b) Distinguished researchers selected by “National 1000 Young Talent Plan”, “National Science Fund for Excellent Young Scholars”.
- (c) Postdoctors with a strong record of academic accomplishments (normally appointed for two years for this position).

For positions (a) and (b), the following qualifications are required at least: Working experience as a professor, associate professor or equivalent at top overseas universities or research institutes; Competence of leading a research team to carry out world-class scientific researches; Competence of cultivating young researchers and promoting international academic collaboration. For successful candidates, the University will provide attractive annual salary, start-up fund, housing allowance together with other benefits from the Laboratory. For positions (c), there is a good opportunity to be promoted to research staff provided excellent performance is achieved during the postdoc period.

All applicants should send a cover letter, a curriculum vitae with a publication list, a research proposal (3-4 pages), and a statement of teaching interest in a single pdf file by February 28, 2016 to Ms. Dan Zhang through e-mail: laser_plasma@sjtu.edu.cn. Please also arrange three reference letters directly to the above e-mail address. Applications after the deadline could be reviewed until the positions are filled.

By Carol Lynn Curchoe

The power of mentoring

I was born a scientist, but becoming one professionally required a little help. Stellar teachers nurtured my love for science and engineering in middle school. Later, after some missteps and struggles in high school, professors at Manchester Community College conspired to change my life course from high school dropout to Ph.D. holder. One of them was my first algebra teacher. On the first day of class, she wrote on the board, “You CAN do math.” “You may not believe that now,” she told us, “but you will by the end of this semester with me.”

She taught me that I could learn things even if they were hard, and that I didn’t need to know them instinctively. When I transferred to the University of Connecticut for my bachelor’s degree in molecular and cellular biology, this principle served me well in the 200-person introductory “weed-out” courses.

I thought that I would be a technician at a pharmaceutical company after graduation, so I worked in various labs on campus to gain the critical hands-on experience I would need. But my career trajectory took a turn during the last semester of my undergraduate education, when my lab adviser encouraged me to consider going to graduate school for a Ph.D.

I hardly even knew what grad school was, but once she opened my eyes to the possibilities, and we came up with a funding strategy, I was hooked on the idea.

Getting my Ph.D. was the first step on my circuitous route toward a professional life that I could never have imagined. I did a postdoc and worked on technology transfer and in university administration before starting my own business and management consulting firm, 32ATPs. I entered the political arena with a 1-year appointment as Utah’s state science adviser. In this role, I shepherded a precious allotment from the state legislature of 10 million hard-won dollars for science, technology, engineering, and mathematics (STEM) education. I then started the R&D arm of 32ATPs and recently co-founded my second startup, EduPaper Products, where I pursue my passion of making STEM education accessible to everyone.

None of this would have been possible without the encouragement I received throughout my schooling and in my professional career. Study after study shows that, beginning in early childhood and continuing throughout college,



“None of this would have been possible without the encouragement I received.”

girls are typically discouraged from entering STEM fields, and I was lucky to be an exception.

I have worked to pay it forward by acting as a mentor for girls and women in STEM, passing on the advice that has worked for me:

- Be brave enough to take the next step, whatever it is.
- Identify what you want, and don’t be afraid to ask for it.
- Don’t be afraid of rejection. It is going to happen; put yourself out there anyway.
- Build your professional network, and ask for help from those connections when you need it.
- Have your own brand: something that makes you unique and that people will remember you by.
- Get a full night’s sleep and don’t skip meals. You make mistakes when you’re tired or hungry!
- Every time you do something new, creative, innovative, or different, write up how you did it. Catalog it so you can easily advise others who may need your help in the future.

I still need advice, too. I stay in touch with many of my mentors, and I find new mentors through state- and federal-level professional services. These days, I worry just as much about giving back to my mentors as I do about learning from them, and I am honored when my grad school mentors ask me for help. Mentorship, I like to say, works up, down, and sideways. ■

Carol Lynn Curchoe is the founder of 32ATPs, a clean energy and consulting firm in San Diego, California, and co-founder of EduPaper Products. She was named among Utah Business magazine’s top 40 professionals under 40 in 2014. For more on life and careers, visit ScienceCareers.org. Got an interesting career story? Send it to SciCareerEditor@aaas.org.

ILLUSTRATION: ROBERT NEUBECKER